frontiers | Research Topics

Establishment of marker models for molecular typing of renal cell carcinoma

Edited by
Linhui Wang, Łukasz Zapała and Le Qu

Published in
Frontiers in Oncology

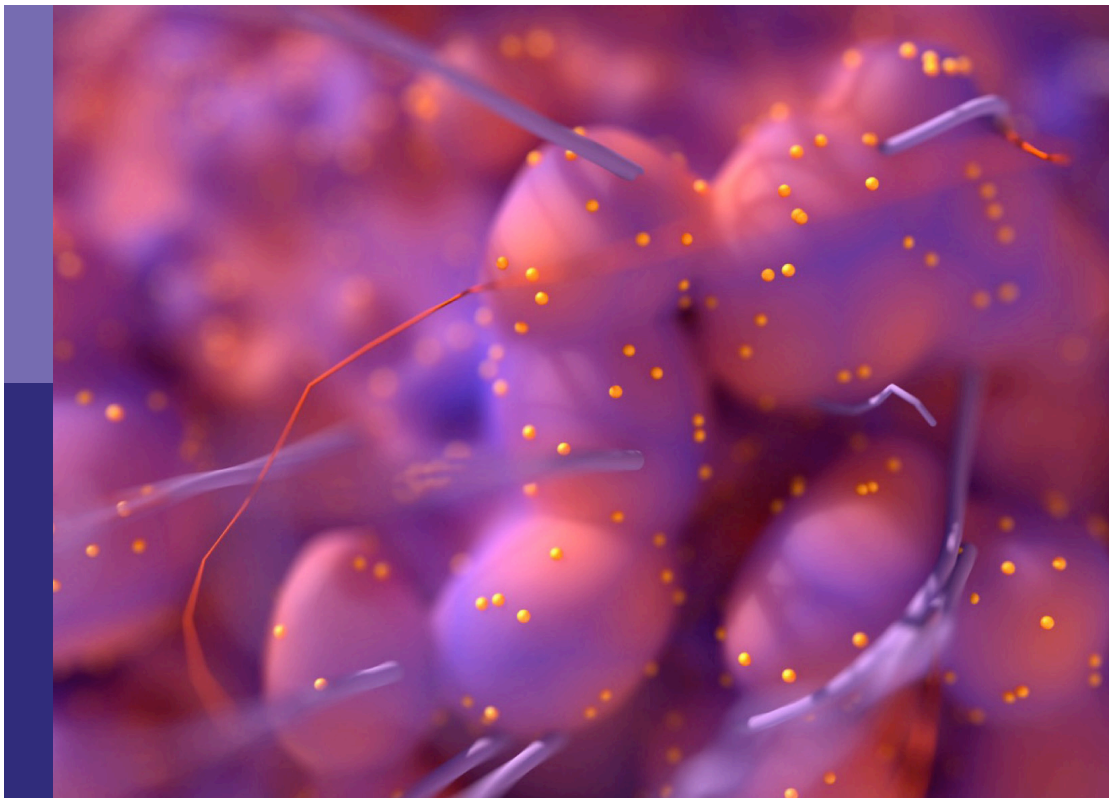

ISSN 1664-8714
ISBN 978-2-8325-3070-2
DOI 10.3389/978-2-8325-3070-2

About Frontiers

Frontiers is more than just an open access publisher of scholarly articles: it is a pioneering approach to the world of academia, radically improving the way scholarly research is managed. The grand vision of Frontiers is a world where all people have an equal opportunity to seek, share and generate knowledge. Frontiers provides immediate and permanent online open access to all its publications, but this alone is not enough to realize our grand goals.

Frontiers journal series

The Frontiers journal series is a multi-tier and interdisciplinary set of open-access, online journals, promising a paradigm shift from the current review, selection and dissemination processes in academic publishing. All Frontiers journals are driven by researchers for researchers; therefore, they constitute a service to the scholarly community. At the same time, the *Frontiers journal series* operates on a revolutionary invention, the tiered publishing system, initially addressing specific communities of scholars, and gradually climbing up to broader public understanding, thus serving the interests of the lay society, too.

Dedication to quality

Each Frontiers article is a landmark of the highest quality, thanks to genuinely collaborative interactions between authors and review editors, who include some of the world's best academicians. Research must be certified by peers before entering a stream of knowledge that may eventually reach the public - and shape society; therefore, Frontiers only applies the most rigorous and unbiased reviews. Frontiers revolutionizes research publishing by freely delivering the most outstanding research, evaluated with no bias from both the academic and social point of view. By applying the most advanced information technologies, Frontiers is catapulting scholarly publishing into a new generation.

What are Frontiers Research Topics?

Frontiers Research Topics are very popular trademarks of the *Frontiers journals series*: they are collections of at least ten articles, all centered on a particular subject. With their unique mix of varied contributions from Original Research to Review Articles, Frontiers Research Topics unify the most influential researchers, the latest key findings and historical advances in a hot research area.

Find out more on how to host your own Frontiers Research Topic or contribute to one as an author by contacting the Frontiers editorial office: frontiersin.org/about/contact

Establishment of marker models for molecular typing of renal cell carcinoma

Topic editors

Linhui Wang — Second Military Medical University, China
Łukasz Zapała — Medical University of Warsaw, Poland
Le Qu — Nanjing University, China

Citation

Wang, L., Zapała, Ł., Qu, L., eds. (2023). *Establishment of marker models for molecular typing of renal cell carcinoma*. Lausanne: Frontiers Media SA.
doi: 10.3389/978-2-8325-3070-2

Table of contents

frontiers | Frontiers in Oncology

TYPE Editorial
PUBLISHED 10 July 2023
DOI 10.3389/fonc.2023.1236980

OPEN ACCESS

EDITED BY
Ronald M Bukowski,
Cleveland Clinic, United States

REVIEWED BY
P.K. Vinod,
International Institute of Information Technology, Hyderabad, India

*CORRESPONDENCE
Linhui Wang
wanglinhui@smmu.edu.cn

RECEIVED 08 June 2023
ACCEPTED 27 June 2023
PUBLISHED 10 July 2023

CITATION
Jiang A, Zapała Ł, Qu L and Wang L (2023) Editorial: Establishment of marker models for molecular typing of renal cell carcinoma.
Front. Oncol. 13:1236980.
doi: 10.3389/fonc.2023.1236980

Editorial: Establishment of marker models for molecular typing of renal cell carcinoma

Aimin Jiang[1], Łukasz Zapała[2], Le Qu[3] and Linhui Wang[1]*

[1]Department of Urology, Changhai Hospital, Naval Medical University, Shanghai, China, [2]Clinic of General, Oncological and Functional Urology, Medical University of Warsaw, Warsaw, Poland, [3]Department of Urology, Jinling Hospital, Affiliated Hospital of Medical School, Nanjing University, Nanjing, Jiangsu, China

KEYWORDS

renal cancer (RC), tumor biomarkers, tumor prognosis, molecular subtype, multi-omics

Editorial on the Research Topic
Establishment of marker models for molecular typing of renal cell carcinoma

According to the latest cancer statistics report, renal cell carcinoma (RCC) accounts for more than 400,000 new cancer cases and causes approximately 179,000 deaths worldwide (1, 2). Clear cell renal cell carcinoma (ccRCC) comprises approximately 75-80% of all cases of RCC, with the remaining percentage being represented by several subtypes of nonclear cell carcinoma (3). While curative treatment may be possible for patients with localized disease, others may present with metastatic or locally advanced disease. In some cases, patients with aggressive tumor biology may experience recurrence despite surgical resection. Given the variability in patient outcomes, accurate risk stratification is essential to identify patients who might benefit from more intensive initial treatment, closer monitoring, or adjuvant therapies. The advent of sophisticated multiomics techniques such as whole genome sequencing, combined with innovative bioinformatic tools, has enabled researchers to delve deep into tumor etiology and stratify patients based on characteristics associated with clinical outcomes. Based on the above concerns, there is an urgent need to identify novel biomarkers and risk models.

In this Research Topic, an overview of novel biomarkers and molecular subtyping of RCC is performed through 1 review and 15 original research papers by 119 authors, and these works facilitate our better understanding of cancer progression and heterogeneity to therapy response among RCC patients (Wang et al., Zheng et al., Pan et al. Lin et al., Zhang et al. Lin et al., Tao et al., Yu et al., Chen et al., Xia et al. Zhang et al., Chang et al., Teng et al., Zeng et al., Ding et al.).

Risk models based on transcriptome signatures could be better applied in clinical practice because of interpretability and accessibility. Wang et al. performed a comprehensive in silico combined with in-house validation analysis and divided ccRCC patients into CIN25-C1 and C2 subtypes based on 25 genes related to chromosomal instability. Patients with CIN25-C2 had a poor prognosis and increased proliferation, EMT, stemness and telomerase activity but were sensitive to sunitinib. There is great promise for the routine clinical application of CIN25-based ccRCC classification, as polymerase chain reaction (PCR) quantification appears to be sufficient. Lin et al. developed a reliable risk

system based on ferroptosis and oxidative stress-associated genes and compared the differences at various levels, including clinical parameters, the immune microenvironment, and therapy resistance. They found that ccRCC patients with high risk scores had higher TMB levels and $CD8^+$ T-cell infiltration degrees and preferable responsiveness to ICI therapy. Notably, a study from Pan et al. utilized the interferon regulatory family to construct a novel risk classifier for ccRCC with the application of a nonnegative matrix factorization algorithm, and they also applied the least absolute shrinkage and selection operator to develop a risk system to guide better risk stratification, which reached a superior performance than classical clinical parameters and the ClearCode34 model.

Accumulating evidence suggests that metabolic reprogramming, especially in fatty acid metabolism, is significantly correlated with tumorigenesis and progression in RCC. Ding et al. constructed an optimal nomogram consisting of the risk score of fatty acid metabolism-related genes and verified ten signatures involved in overall survival by immunohistochemical analyses, which also participated in uncontrolled pain in advanced RCC patients. Neutrophils are a type of abundant inflammatory cell present in the tumor microenvironment and could activate cancer cells and releasing modified DNA structures coated with cytoplasmic and granular proteins. A study from Teng et al. utilized neutrophil extracellular trap-related signatures to carry out a remodelling analysis and divided ccRCC patients into three distinctive subtypes with various activated states of metabolism and immune infiltration degrees, and four promising diagnostic genes, including *SLC27A2*, *SLC16A12*, *MAP7* and *SLC3A1*, were verified through RT–PCR.

Mitogen-activated protein kinase (*MAPK*) signaling is one of the most extensively studied pathways in tumor research. Zhang et al. constructed a risk score consisting of 14 *MAPK*-related genes using Lasso regression analysis and further proved that *MAPK* activation is correlated with various malignant behaviors of tumor cells, including but not limited to invasion, migration, apoptosis, and extracellular matrix degradation. Recent studies have found that the basement membrane, comprising fundamental components, displays crucial biological functions in the body by providing resistance against mechanical stress and determining tissue morphology and cancer progression. Tao et al. established a risk scoring system involving 16 basement membrane genes, which were related to metabolic and tumor-related signaling cascades. Studies have suggested the involvement of iron channels, especially potassium channels, in the proliferation and migration of various tumors by regulating T-cell function. Notably, Zeng et al. constructed a promising prognostic signature involving hypoxia and angiogenesis signatures based on potassium ion channel-related genes for ccRCC and finally validated the differential expression of four biomarkers related to potassium transport, including *ATP1A3*, *GNB3*, *GNB4* and *NSF*. The homeobox (*HOX*) family, encoding a conserved family of transcription factors in mammals, plays an indispensable role in organogenesis and development. A study from Zheng et al. reported an eight *HOX* gene-based risk model, and patients were divided into a lower risk group with a fragile type II IFN response and para-inflammation scores. Noninvasive surveillance approaches, especially liquid biopsy, are suitable for functioning as a repeatable and personalized snapshot among patients with high clinical stage scores. Zhang et al. carried out an integrative analysis consisting of transcriptomic and proteomic profiles and finally developed a risk score (containing *VSIG4*, *TFGBI* and *P4HB*) to predict the long-term prognosis of ccRCC patients with venous tumor thrombus.

Consistently, some promising diagnostic- and therapeutic-related targets specific for ccRCC were also investigated. Aided by systematic bioinformatic analysis and *in vitro* experiments, Xia et al. proved that T-cell immunoglobulin and the *ITIM* domain, or *TIGIT*, were highly expressed in tumor tissues and identified as crucial prognostic determinants. TIGIT might promote Treg cell infiltration, and patients with high expression of this signature might benefit from sunitinib treatment. In addition, two potential drugs (PD0325901 and selumetinib) targeting *TIGIT* were identified and verified by molecular docking. Chang et al. proved that the dysregulated expression level of one amino acid metabolism regulator, L-dopa decarboxylase (*DDC*), could trigger higher intratumoral heterogeneity and an immunosuppressive state in ccRCC *via* PI3k/Akt signaling after analysing multiomics profiles across four ccRCC datasets.

For advanced ccRCC patients, a second-line therapeutic strategy of axitinib is suitable to prolong progression-free survival after first-line therapies fail, while intra- and intertumoral heterogeneity could vary the therapy response rate. Lin et al. enrolled 44 advanced ccRCC patients and applied a combination of Cox and Lasso algorithms to construct a predictive model to predict the axitinib benefit rate. This model reached satisfactory performance, since the area under the curve values of 3-, 6-, and 12-month progression-free survival were 0.975, 0.909, and 0.911, respectively.

Genetic alterations, such as mutations and chromosomal copy number variations (CNVs), have emerged as an initial step towards genomic stratification in RCC. Tai et al. collected 55 patients with RCC across different regions in China with whole genome sequences and summarized the results as follows: In patients with ccRCC, the occurrence of mutations in *VHL, PBRM1, BAP1*, and *SERD2* reached 74%, 50%, 24%, and 18%, respectively. In contrast, among patients with nonclear ccRCC, the most frequently observed mutations were those in *FH* (29%), *MLH3* (24%), *ARID1A* (18%), *KMT2D* (18%), and *CREBBP* (18%). Previous genomic analysis of clinical samples of ccRCC unveiled a high incidence of *SETD2* mutations, which could expedite cancer progression through epigenetic regulation. Yu et al. provided a comprehensive summary of *SETD2* in ccRCC occurrence and progression, which suggested that hypermutated *SETD2* could be treated as a novel therapeutic target.

Although there are numerous prognostic biomarkers found in RCC that provide novel insights into diagnosis and therapy, their accuracy and utility remain to be further investigated and verified. The clinical utility and widespread application of specific risk models or biomarkers is hindered by numerous challenges, including resource limitations, complexity, the need for repeated outhouse validation, and ideally, evaluation across different

prospective clinical trials. Nonetheless, our understanding of the biological mechanisms governing RCC initiation and progression continues to progress alongside the advances of new platforms for clinical application. In the future, it is possible that genomic or other profiling of each patient's tumor might facilitate personalized medicine, enabling the administration of appropriate treatments to the right patients at the optimal time.

Author contributions

LW and ŁZ supervised and conceived the topic. AJ and LW reviewed all articles on this Research Topic and wrote the original manuscript. LQ reviewed the manuscript. All authors approved the final version of this paper.

Conflict of interest

The authors declare that the research was conducted in the absence of any commercial or financial relationships that could be construed as a potential conflict of interest.

Publisher's note

References

1. Xia C, Dong X, Li H, Cao M, Sun D, He S, et al. Cancer statistics in China and united states, 2022: profiles, trends, and determinants. *Chin Med J* (2022) 135(5):584–90. doi: 10.1097/CM9.0000000000002108

2. Siegel RL, Miller KD, Fuchs HE, Jemal A. Cancer statistics, 2022. *CA: Cancer J Clin* (2022) 72(1):7–33. doi: 10.3322/caac.21708

3. Moch H, Cubilla AL, Humphrey PA, Reuter VE, Ulbright TM. The 2016 WHO classification of tumours of the urinary system and Male genital organs-part a: renal, penile, and testicular tumours. *Eur Urology* (2016) 70(1):93–105. doi: 10.1016/j.eururo.2016.02.029

frontiers | Frontiers in Oncology

TYPE Original Research
PUBLISHED 28 September 2022
DOI 10.3389/fonc.2022.1013324

OPEN ACCESS

EDITED BY
Łukasz Zapała,
Medical University of Warsaw, Poland

REVIEWED BY
Yibing Guan,
The Second Affiliated Hospital of Xi'an Jiaotong University, China,
Paweł Rajwa,
Medical University of Silesia, Poland
Aleksander Ślusarczyk,
Medical University of Warsaw, Poland

*CORRESPONDENCE
Jing-hui Guo
guojh@jnu.edu.cn
Jun Huang
tzhuoyumin@163.com

†These authors have contributed equally to this work and share first authorship

SPECIALTY SECTION
This article was submitted to Genitourinary Oncology, a section of the journal Frontiers in Oncology

RECEIVED 06 August 2022
ACCEPTED 12 September 2022
PUBLISHED 28 September 2022

CITATION
Zeng R, Li Y, He D-m, Sun M-z, Huang W-q, Wang Y-h, Zhuo Y-m, Chen J-j, Chen T-h, Guo J-h and Huang J (2022) Potassium channel-related genes are a novel prognostic signature for the tumor microenvironment of renal clear cell carcinoma.
Front. Oncol. 12:1013324.
doi: 10.3389/fonc.2022.1013324

Potassium channel-related genes are a novel prognostic signature for the tumor microenvironment of renal clear cell carcinoma

Rui Zeng[1†], Yi Li[2†], Dong-ming He[1], Meng-zhu Sun[3], Wen-qing Huang[3], Yu-hang Wang[2], Yu-min Zhuo[2], Jun-jiang Chen[1], Tai-heng Chen[1], Jing-hui Guo[1*] and Jun Huang[2*]

[1]Department of Physiology, School of Medicine, Jinan University, Guangzhou, China, [2]Department of Urology, The First Affiliated Hospital of Jinan University, Guangzhou, China, [3]Department of Transfusion Medicine, Shenzhen Hospital, Southern Medical University, Shenzhen, China

Clear cell renal cell carcinoma (ccRCC) accounts for 80% of renal cell carcinomas (RCCs), and its morbidity and prognosis are unfavorable. Surgical resection is the first-line treatment for ccRCC, but the oncogenesis of ccRCC is very complex. With the development of high-throughput sequencing technology, it is necessary to analyze the transcriptome to determine more effective treatment methods. The tumor microenvironment (TME) is composed of tumor cells, various immune-infiltrating cells, fibroblasts, many cytokines, and catalysts. It is a complex system with a dynamic balance that plays an essential role in tumor growth, invasion, and metastasis. Previous studies have confirmed that potassium channels can affect the immune system, especially T lymphocytes that require potassium channel activation. However, the effect of potassium channels on the TME of ccRCC remains to be studied. Therefore, this study aims to construct a prognostic signature for ccRCC patients based on potassium ion channel-related genes (PCRGs), assess patient risk scores, and divide patients into high- and low-risk groups based on the cutoff value. In addition, we investigated whether there were differences in immune cell infiltration, immune activator expression, somatic mutations, and chemotherapeutic responses between the high- and low-risk groups. Our results demonstrate that the PCRG signature can accurately assess patient prognosis and the tumor microenvironment and predict chemotherapeutic responses. In summary, the PCRG signature could serve as an auxiliary tool for the precision treatment of ccRCC.

KEYWORDS

clear cell renal cell carcinoma (ccRCC), prognostic signature, potassium channel, tumor microenvironment, immunotherapy

Introduction

Renal cell carcinoma (RCC) is the most common malignant tumor in the urinary system, and 80% of RCCs are the clear cell renal cell carcinoma (ccRCC) pathological type. This percentage is far more than the that for the mixed cell type, granulosa cell type, and undifferentiated cell type (1). According to the World Health Organization and the International Society of Urological Pathology (WHO/ISUP) classification system (2), ccRCC can be divided into four grades (grades I-IV). Even the first-line treatment of ccRCC is surgery (3), however, nearly one-third of patients with ccRCC already have metastasis at the first diagnosis, and the clinical curative effect is limited in patients with metastasis, even when combined with chemotherapy and immunotherapy. The first line of treatment for metastatic RCC patients is immune checkpoint inhibitors (ICIs) in combination with tyrosine kinase inhibitors (TKIs) (4); however, patients with locally advanced or metastatic RCC have a poor prognosis. Before metastasis, the overall survival rate for RCC is 74%, and for patients with metastasis, the 5-year survival rate decreases to 8% (5). Thus, it is important to identify new biomarkers or targets to increase the early diagnosis rate of ccRCC and enhance the effect of early intervention treatment.

Recently, the tumor microenvironment (TME), which includes tumor-infiltrating immune cells (TICs), has been shown to play a decisive role at all stages of tumor progression (6–8). ccRCC is a highly immune-infiltrated tumor, and the high immune infiltration of ccRCC has been proven in multiple studies (9). Immune cells play a key role in anticancer immunity. By immunomonitoring, TICs could predict the prognosis of ccRCC patients and enhance the effects of targeted therapy treatments (10). Most of the immune checkpoint genes are upregulated in ccRCC, and thus, they indicate a tumor in an immune-hot (high immune infiltration inside the tumor) condition. Compared with immune-cold (lack of immune infiltrates) tumors, the higher levels of infiltrating lymphocytes in the nidus could help eliminate tumor cells, resulting in a better prognosis (11). By affecting the TME and proliferation of immune cells, potassium channels are involved in the tumorigenesis, proliferation, and migration of tumors (12). As reported by Masi A (13), hERG1 voltage-dependent potassium channels promote the secretion of vascular endothelial growth factor from tumor cells, especially in high-grade gliomas. This stimulates neoangiogenesis and enhances the progression of malignancy. Moreover, high expression of TREK-1, a two-pore domain potassium channel, in prostate cancer increases the proliferation of tumors, and the overexpression of Kv1.1 potassium channels promotes the proliferation of breast cancer (14, 15).

Previous studies (16, 17) have proven that potassium channels can affect the immune system. In particular, T lymphocytes need potassium channels to activate to enhance the tumor. This leads to the avoidance of immune destruction or the promotion of inflammation, which is associated with cancer progression and prognosis. However, the effect of potassium channels on the intratumoral immune microenvironment of ccRCC remains to be investigated. Thus, this study was designed to evaluate the correlation between potassium channels and the TME of ccRCC.

Materials and methods

Public data acquisition and processing

In this study, transcriptome RNA sequencing (RNA-seq) data of human ccRCC samples were downloaded *via* The Cancer Genome Atlas (TCGA) (https://portal.gdc.cancer.gov/). All the RNA-seq data selected in our study were normalized by fragments per kilobase million (FPKM). After removing duplications and samples that were missing data, the KIRC data set consisted of 29 normal samples and 394 cancer samples and matched the clinical information of the selected data. The RNA-seq data were combined into an expression profile matrix by Perl (http://www.perl.org/). The "org.hs.eg.db" package was used to convert the Ensembl ID into a gene symbol. Our study used GeneCards (https://www.genecards.org/) to obtain PCRGs.

Human renal clinical tissues and RNA extraction

ccRCC tumor tissues and adjacent normal tissues were collected from 12 patients who underwent radical nephrectomy at The First Affiliated Hospital of Jinan University, and RNA was extracted from those tissues. These patients had WHO/ISUP grades I to IV. This study was approved by the Ethics Committee of the First Affiliated Hospital of Jinan University. Both patients and the control individuals provided written informed consent.

The total RNA of tumor tissues and adjacent normal tissues from all patients was extracted using the EZ-Press RNA Purification Kit (EZbioscience, USA). cDNA was obtained by reverse transcription using the PrimeScript RT Kit (TaKaRa, Japan).

Identification of prognostic differentially expressed PCRGs

The "limma" package was used to identify the differentially expressed genes (DEGs) between ccRCC tumor and adjacent normal tissues. Genes with an adjusted $P< 0.05$ and |log2 fold

change (FC)|>0 were defined as DEGs. Additionally, the "survival" package was used to perform univariate Cox regression, and the screening condition was P< 0.05 to identify prognostic genes. Based on the above results, the PCRGs obtained from GeneCards (https://www.genecards.org/) were used to screen differentially expressed PCRGs and prognostic PCRGs. The intersection of the two was used to identify prognostic differentially expressed PCRGs. To explore the correlations and interactions among these genes, the "igraph" package was used to draw a correlation graph of the prognostic differentially expressed PCRGs. The protein–protein interaction (PPI) network of these genes was constructed and clustered through STRING (https://string-db.org/).

Construction and evaluation of the PCRG signature

The TCGA-KIRC cohort was divided into a training cohort (n=275) and a validation cohort (n=117). Due to the large number of PCRGs, our study used least absolute shrinkage and selection operator (LASSO) regression to identify PCRGs that significantly impacted survival in the training set and calculated their regression coefficients. The PCRG signature was used to calculate the risk score of each patient, and the PCRG expression value of each patient was multiplied by the corresponding coefficient of the gene for weighting. Then, the weighted expression values of the 10 PCRGs were added to finally obtain the risk score of the patient, which was calculated as follows:

Risk score=

$$\sum_{i=1}^{n} Exp_i * Coef_i$$

where n is the number of genes in the PCRG signature, i.e., n=10, Exp_i the expression value of the ith gene of the patient, and $Coef_i$ is the coefficient of the gene in the PCRG signature.

The patients were classified into high-risk and low-risk groups according to the median risk score, and then time-dependent receiver operating characteristic (ROC) analysis was used to verify the prediction accuracy of the signature. Multivariate Cox regression was used to verify whether the risk score obtained by the signature was an independent prognostic factor, and Kaplan–Meier survival analysis was performed to detect whether there was a significant difference in survival between the high- and low-risk groups. A heatmap was used to show the expression of the 10 PCRGs that constituted this signature in ccRCC. Principal component analysis (PCA) was used for dimension reduction, and the expression pattern of PCRGs in high- and low-risk patients was studied. Furthermore, one-way ANOVA was used to analyze whether the risk scores of grade, stage, T stage, and M stage at different levels were different.

Construction and evaluation of the nomogram

A nomogram was constructed based on sex, age, stage, T stage, M stage, and the risk score to predict ccRCC patient overall survival (OS) at 1, 3, and 5 years. The concordance index (C-index), calibration curve and decision curve analysis (DCA) were used to evaluate the predictive accuracy of the nomogram.

Functional enrichment analysis and gene set enrichment analysis

After classifying the samples of the TCGA-KIRC cohort into high-risk and low-risk groups according to the median risk score, the "limma" package was used to search for DEGs. The screening conditions were P< 0.05 and |log2FC|>0. These DEGs were used for Gene Ontology (GO) and Kyoto Encyclopedia of Genes and Genomes (KEGG) functional enrichment analyses. In addition, gene set enrichment analysis (GSEA) was used to uncover which biological functions the DEGs showed statistically significant and consistent differences in.

Estimation of the TME

The "Cibersort" package was used to analyze the abundance ratios of 22 types of immune cells in the TCGA ccRCC cohort and determine whether the PCRG signature could distinguish different immune cell infiltrations. The "survival" and "survminer" packages were used to analyze the relationships between immune activators and the PCRG signature and the effect of the expression of immune activators on the survival of patients in the high- and low-risk groups.

Gene mutation analysis

The "maftools" package was used to analyze the tumor mutation burden (TMB) based on somatic mutation data from TCGA. We calculated the TMB for each patient and compared the TMB between the high-risk and low-risk groups.

Prediction of sensitivity to chemotherapy

Based on the Genomics of Drug Sensitivity in Cancer (GDSC) database, we used the "pRRophetic" package to calculate the half-maximal inhibitory concentration (IC50) for different chemotherapy drugs between the high-risk and low-risk groups.

Real–time quantitative PCR

Based on the SYBR Green (ChamQ Universal SYBR qPCR Master Mix, Vazyme Biotech, China)method, the CFX96 real-time PCR system (Bio-Rad, USA) was used for RT–qPCR detection. After the expression level of GAPDH was used for normalization, the relative expression level of mRNA was determined. The mRNA-specific primer sequences are shown in Table 1.

Statistical analysis

Statistical analyses were conducted using R 4.1.1 and GraphPad Prism 8 (GraphPad Software, Inc.). All data are expressed as the mean ± SD. A paired difference test between ccRCC samples and adjacent normal samples in the two groups by the "limma" package was used to determine the DEGs. Analysis with one-way ANOVA followed by the Student–Newman–Keuls multiple comparison test was used for the comparison of three or more experimental groups. For qPCR data, Student's t test was used for analysis.

Results

Identification of differentially expressed prognostic PCRGs in the TCGA ccRCC cohort

Among 118 PCRGs, 73 were differentially expressed. Of these, 44 were upregulated, and 29 were downregulated in tumor tissues (Figure 1A). Seventy-three prognosis-related PCRGs were obtained by univariate Cox regression, and the screening threshold was $p< 0.05$ (Figure 1B). The intersection of differentially expressed PCRGs and prognosis-related PCRGs was used to obtain 25 differentially expressed PCRGs (Figure 1C). The heatmap illustrates the different expression patterns of these PCRGs in ccRCC and normal tissues (Figure 1D). We examined the correlation between 25 differentially expressed PCRGs in the TCGA-KIRC cohort. Red dots represent a positive correlation, and blue dots represent a negative correlation (Figure 1E). Our study mapped the correlations among the 25 PCRGs and constructed the PPI network of these genes through the STRING database. The results showed that the 25 PCRGs could form 3 clusters (Figure 1F).

TABLE 1 mRNA-specific primer sequences.

Gene	Primer sequence	Tm
ATP1A3	F: GCAGTGTTTCAGGCTAACCAGG	58.9
	R: CTCCTTCACGGAACCACAGCA	60.2
GNB3	F: CGTTTGGCCCTGTGACTAT	55.0
	R: TACCAGGGTGCTACACTTTA	52.3
GNB4	F: TCCTATCCAAAGGCATCCACA	54.0
	R: TGTTCAGTTGACCACGAGTGT	56.0
NSF	F: GTGTCACATTGCCCCTCTG	56.6
	R: TCTGGTCTATTGGTCATTCCTG	53.7
GAPDH	F: ACAGTTGCCATGTAGACC	54
	R: TTTTTGGTTGAGCACAGG	52

Construction and validation of the PCRG signature

Compared with λ_{1SE}, λ_{min} has higher accuracy. Hence, λ_{min} was selected to build the model for accuracy in our study. The LASSO algorithm was used to determine $Log(\lambda_{min}) = -3.8$ (Figure 2A), and the PCRG prognostic signature consisting of 10 genes (Figure 2B) was established. The specific gene composition and coefficient of each gene are shown in Table 2. The PCRG prognostic signature was used to calculate the patients' risk scores and divide them into high-risk and low-risk groups (Figure 2C). The risk score calculated by the signature can separate surviving patients from nonsurviving patients (Figure 2D). In addition, the heatmap shows the expression patterns of the 10 genes that make up the PCRG prognostic signature between the high-risk and low-risk groups (Figure 2E).

The signature was significantly correlated with survival in the training cohort (Figure 3A) and validation cohort (Figure 3B). Nine of the 10 genes that constituted the prognostic signature were significantly associated with the Kaplan–Meier survival curve (Figures 3C–L). PCA showed that the risk score could categorize patients with different risk scores into two groups (Figure 4A). ROC curve analysis was used to illustrate the accuracy of this signature. The 1-year, 3-year, and 5-year area under the curve (AUC) values of the risk score were 0.628, 0.702, and 0.768, respectively. Interestingly, the 1-year, 3-year, and 5-year AUC values increased gradually, suggesting that the PCRG signature has an excellent ability to predict long-term prognosis (Figure 4B). The forest map shows that the hazard ratio (HR) of the risk score and 95% confidence interval (CI) were 3.333 (2.391 −4.647), $p<0.001$, in univariate Cox regression (Figure 4C) and 2.680 (1.830–3.925), $p<0.001$, in multivariate Cox regression (Figure 4D). Moreover, with the increase in T stage (Figure 4E), M stage (Figure 4F), and stage (Figure 4G), the risk score also increased. These findings suggest that the higher the malignancy degree of ccRCC was, the higher the risk score.

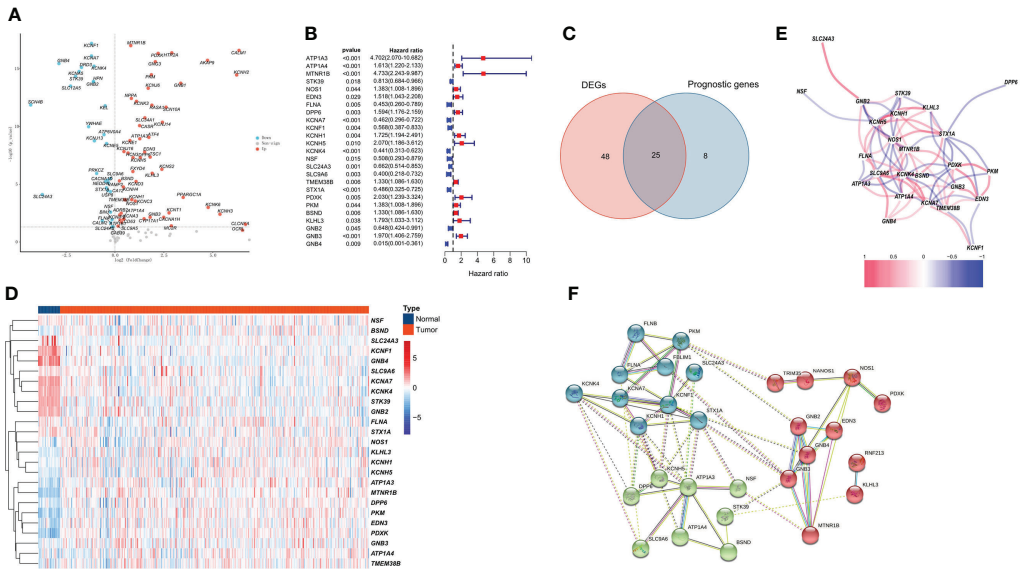

FIGURE 1
Identification of 25 prognosis-associated differentially expressed PCRGs. **(A)** Volcano plot of DEGs between ccRCC and normal tissues. **(B)** Univariate Cox analysis of 25 differentially expressed PCRGs in ccRCC. **(C)** Venn diagram showing the intersection of the DEGs and prognostic genes. **(D)** Heatmap illustrating the differential expression of 25 prognosis-associated PCRGs between ccRCC tissues and normal tissues. **(E)** Correlation between 25 differentially expressed PCRGs in the TCGA-KIRC cohort. Red represents a positive correlation, and blue represents a negative correlation. **(F)** PPI network of 25 PCRGs.

Construction and evaluation of the nomogram

To further evaluate the predictive ability of the PCRG signature, we constructed a prognostic nomogram for ccRCC based on the different weights of the risk score, stage, T stage, M stage, sex, and age (Figure 5A). Our study evaluated the consistency between nomogram-predicted survival and actual survival using the C-index, and the C-index of the nomogram was 0.76. The calibration curves (Figures 5B–D) of the nomogram showed that the OS predicted by the nomogram was in good agreement with the actual OS. The DCA curves indicated that the nomogram provided a better net benefit (Figure 5E).

Functional annotation analysis of the PCRG signature

To further explore the underlying biological mechanisms involved in the association between the PCRG signature and ccRCC, GO and KEGG were used to annotate the 84 DEGs between the high-risk and low-risk groups. According to GO enrichment analysis (Figures 6A, B), the DEGs are mainly involved in the "positive regulation of T-helper 1 type immune response", "positive regulation of T–helper cell differentiation", "positive regulation of neutrophil migration", "positive regulation of CD4 -, Alpha-beta T-cell differentiation", "T-cell activation involved in the immune response" and other immune-related pathways. The KEGG pathways (Figures 6C, D) were mainly related to metabolism, gap junctions, tumor-related signaling pathways, and other biological processes closely related to tumorigenesis and development. In addition, GSEA of the high-risk and low-risk groups showed that the high-risk group was positively correlated with hypoxia (NES=1.67, FDR=0.04), angiogenesis (NES=1.65, FDR=0.04), and vasculogenesis (NES=1.93, FDR=0). In contrast, the low-risk group was positively correlated with NK-cell activation (NES=-1.84, FDR=0.03) and germinal center formation (NES=1.72, FDR=0.04) (Figures 6E–I).

Association between immune cell infiltration and TMB and the risk score in ccRCC

To further verify the results of functional enrichment analysis and GSEA, the present study compared the infiltration of immune cells in the high- and low-risk groups (Figure 7A). Most of the immune cells were more

10.3389/fonc.2022.1013324

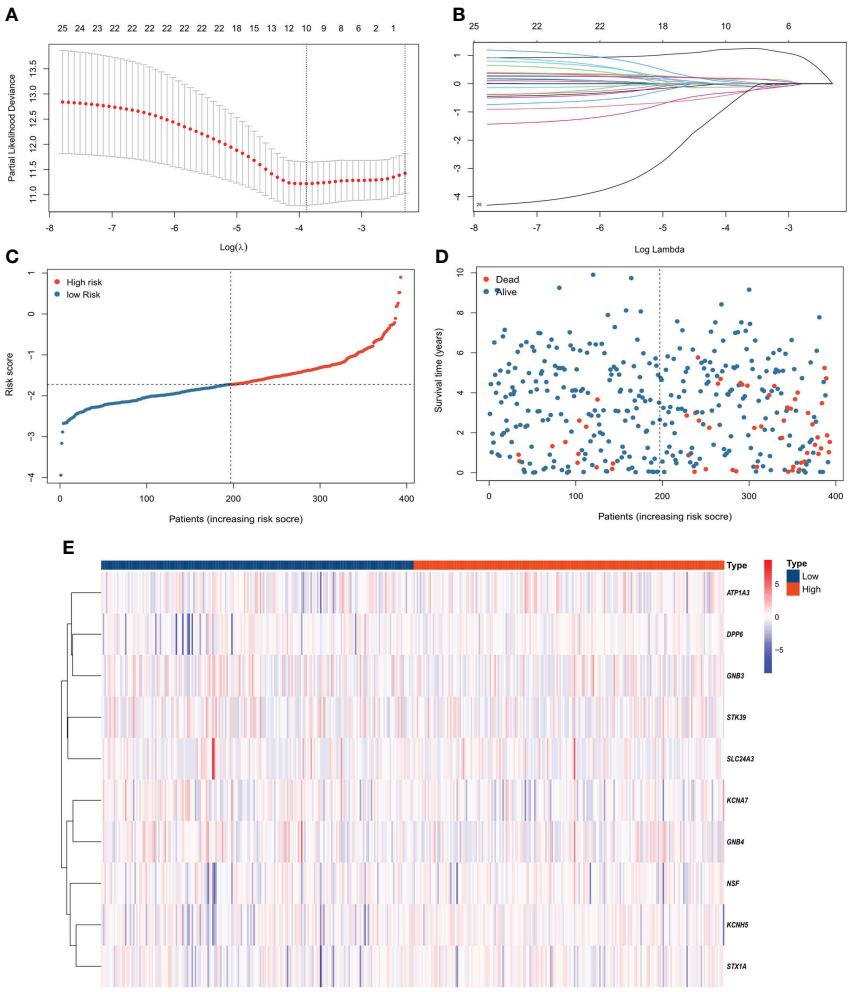

FIGURE 2
Construction of the PCRG prognostic signature. **(A)** Selection of the optimal parameter (λ) of LASSO regression through cross-validation. **(B)** LASSO coefficient profiles of the 10 genes that comprise the prognostic signature selected by λ. **(C)** The TCGA-KIRC cohort was divided into high-risk and low-risk groups according to the median risk score value. **(D)** Higher mortality was observed in the high-risk group than in the low-risk group. **(E)** Heatmap of the expression levels of 10 PCRGs in the high-risk and low-risk groups.

TABLE 2 Genes and their coefficients that constitute the PCRG signature.

Gene	Coefficient
ATP1A3	1.20856795
GNB3	0.192896088
SLC24A3	0.165657175
DPP6	0.141493127
STK39	0.087752983
STX1A	-0.0357362
KCNA7	-0.126888902
KCNH5	-0.33762536
NSF	-0.437328756
GNB4	-0.977379864

Genes in bold font we performed qPCR validation, and the remaining genes were not.

infiltrated in the low-risk group than in the high-risk group, especially memory B cells, NK cells and T helper cells, as mentioned in the above results (Figure 7B). These findings suggest that the risk score may be related to the formation of tertiary lymphatic structures (TLSs) in ccRCC. In addition, our study explored the relationship between the risk score and the immune activators TNFAIP1, MHC II and KIR2DS4. The results showed that the lower the risk score was, the higher the expression of these immune activators (Figures 7C–E). After combining these results with the PCRG signature, the prognosis of the high-risk + low immune activator group was significantly worse than that of the low-risk + high immune activator group (Figures 7F–H).

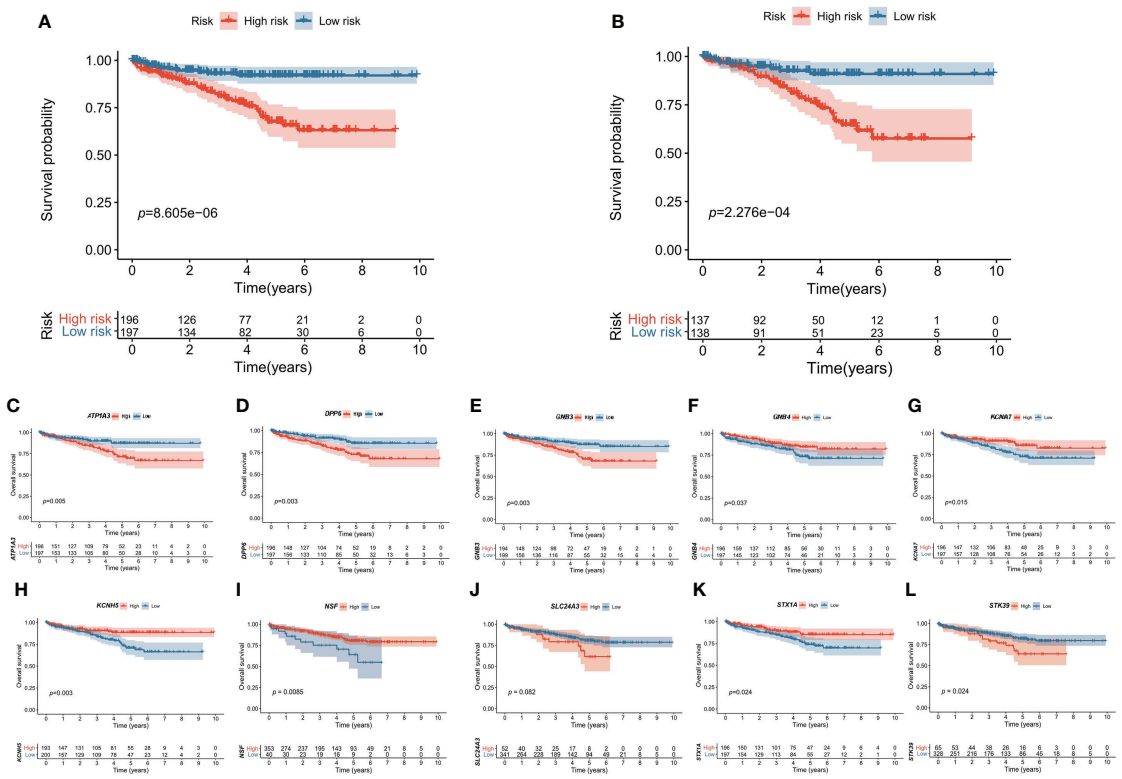

FIGURE 3
Kaplan–Meier survival curves of the high-risk and low-risk groups. The overall survival of the high-risk group was significantly lower than that of the low-risk group in the **(A)** training cohort and **(B)** validation cohort. The effect of each gene **(C–L)** expression value on OS in the prognostic signature.

Association between TMB and the risk score in ccRCC

We further analyzed the relationship between TMB and the risk score in ccRCC. The somatic mutation results showed that most genomic variants were missense mutations. The rest were frameshift deletion mutations, nonsense mutations, and frameshift insertion mutations, and C>T was the most common SNV type in both the high- and low-risk groups (Figure 8A). From an overall perspective, the samples in the low-risk group had a significantly larger number of variants than those in the high-risk groups (Figure 8B). The top 10 most frequently mutated genes in the corresponding groups are illustrated in Figure 8C. *VHL*, *PBRM1*, and *TTN* occupied the top three positions in both groups.

Prediction of chemotherapeutic drug responses

We used the "pRRophetic" package to predict the chemotherapeutic response to commonly used chemotherapy agents in the high- and low-risk groups based on drug sensitivity data from GDSC. The results showed that there was no difference in response between the two groups for sorafenib. The low-risk group demonstrated a higher response to sunitinib ($p<0.001$), gefitinib ($p<0.001$), and temsirolimus ($p=0.0097$) than the high-risk group. The response to axitinib ($p=0.045$) and pazopanib ($p=0.044$) was higher in the high-risk group than in the low-risk group (Figures 9A–F).

The expression of key genes in the PCRG signature in ccRCC

To verify the authenticity of the PCRG signature, we collected tumor and normal tissues from 12 ccRCC patients in this study. RNA was extracted for RT–qPCR to verify the PCRG signature. The gene with the most significant coefficient made the most decisive contribution to the risk score. *ATP1A3* and *GNB3* had the largest positive coefficients in the signature, and *GNB4* and *NSF* had the largest negative coefficients. Therefore, *ATP1A3*, *GNB3*, *GNB4*, and *NSF* were identified as key genes in the signature and further analyzed. The expression of *ATP1A3*

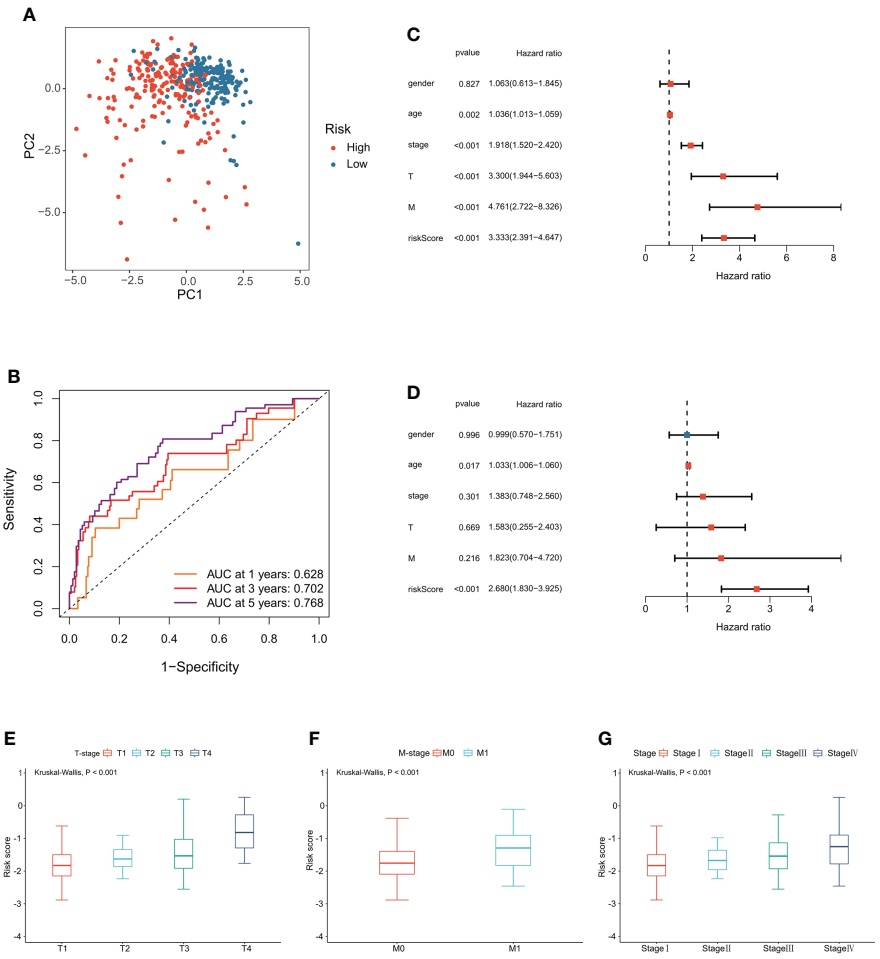

FIGURE 4
Evaluation of the PCRG prognostic signature. **(A)** The low-risk and high-risk groups can be separated into two parts using PCA. **(B)** Time-dependent ROC curves for the risk score for predicting 1-, 3-, and 5-year survival in the TCGA-KIRC cohort. **(C)** Univariate Cox and **(D)** multivariate Cox regression analyses of age, sex, grade, stage, T stage, M stage, and risk score. Relationship between the risk score and **(E)** T stage, **(F)** M stage, and **(G)** stage.

(Figure 10A) and *GNB3* (Figure 10B) in tumor tissues was significantly higher than that in normal tissues.

In comparison, the expression of *GNB4* (Figure 10C) and *NSF* (Figure 10D) in tumor tissues was significantly lower than that in normal tissues, suggesting that these key genes play an essential role in the occurrence and development of ccRCC. The results of RT–qPCR confirmed the database analysis conclusion. In addition, we used the Human Protein Atlas (HPA) online database (https://www.proteinatlas.org/) to detect the protein expression of key genes. The immunohistochemical results of *ATP1A3*, *GNB4*, and *NSF* were consistent with the RT–qPCR results (Figures 10E–L).

Conclusions

With the rapid development of high-throughput sequencing technologies, we can better understand the cancer biology of ccRCC. In this study, we constructed a novel prognostic signature composed of PCRGs. The PCRG signature could accurately classify patients in the training and validation cohorts into high- and low-risk groups. Our results demonstrate that the PCRG signature has high specificity and sensitivity and can supplement clinicopathological parameters for prognosis evaluation and treatment guidance for patients. We analyzed the TME landscapes of the high- and low-risk groups. The results showed that the low-risk group had higher proportions of immune cell infiltration and somatic mutations and a better response to chemotherapy. These findings suggest that patients in the low-risk group were more likely to benefit from immunotherapy and chemotherapy, indicating that the PCRG signature has better performance than other prognostic signatures. In addition, by combining the PCRG signature with clinical parameters such as age, T stage, and M stage, we

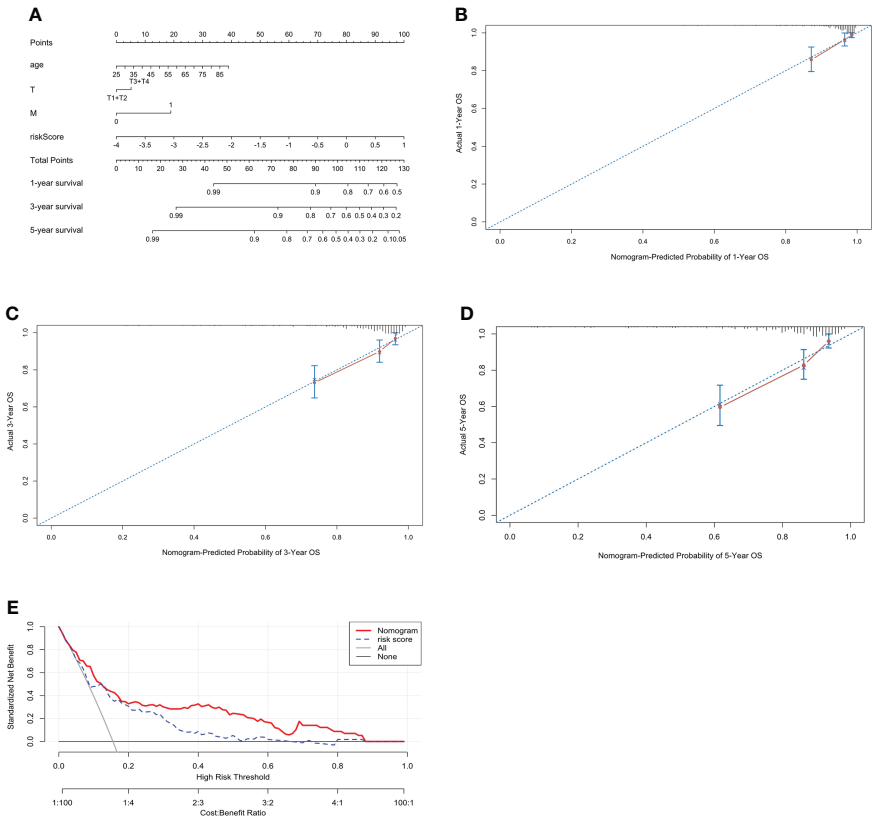

FIGURE 5
Construction of a prognostic nomogram including the risk score for ccRCC. **(A)** A nomogram for predicting the 1-, 3- and 5-year overall survival of individual ccRCC patients. The calibration curve for predicting the 1-year **(B)**, 3-year **(C)**, and 5-year **(D)** overall survival of ccRCC patients. The better the red line and the 45° dashed line fit, the better uniformity between the nomogram-predicted and actual probabilities. **(E)** DCA curves of the nomogram and risk score.

constructed a nomogram to provide clinicians with a robust and straightforward method for the personalized evaluation of ccRCC patients. Finally, we found that the mRNA expression of the four key genes in the PCRG signature in clinical samples was consistent with their coefficients.

Discussion

In this study, we established a prognostic signature consisting of potassium channel-related genes (PCRGs) to predict the prognosis of patients with clear cell renal cell carcinoma (ccRCC) by bioinformatics methods. The risk score calculated by the PCRG signature was strongly associated with the prognosis of patients with ccRCC, especially for long-term prediction. In short, the PCRG signature we propose here may be a complementary method for assessing the prognosis of patients with ccRCC.

As a fatal malignant tumor, ccRCC is a common pathological type of renal cell carcinoma (RCC) that accounts for approximately 80% of all RCCs. Due to its high degree of drug resistance and 20-40% recurrence rate after surgical resection, the prognosis of these patients is poor, and the quality of human life is seriously affected (18–20). Therefore, it is of great significance to find new biomarkers or targets for the early diagnosis and intervention of ccRCC. It has been reported that potassium channels are involved in the proliferation and migration of ccRCC. For example, overexpression of the potassium inward rectifier channel *KCNJ1* can inhibit the proliferation and migration of ccRCC and lead to apoptosis. Its low expression is related to the poor prognosis of ccRCC (21). Another study reported that the Ca^{2+}-activated potassium channel KCa3.1 is highly expressed in ccRCC and promotes ccRCC metastasis, which is associated with worse survival (22). Previous studies have shown that potassium channels, such as voltage-gated Kv1.3 and the $Ca2^{+}$-activated potassium channel *IKCa1*, are crucial for the activation and proliferation of T

10.3389/fonc.2022.1013324

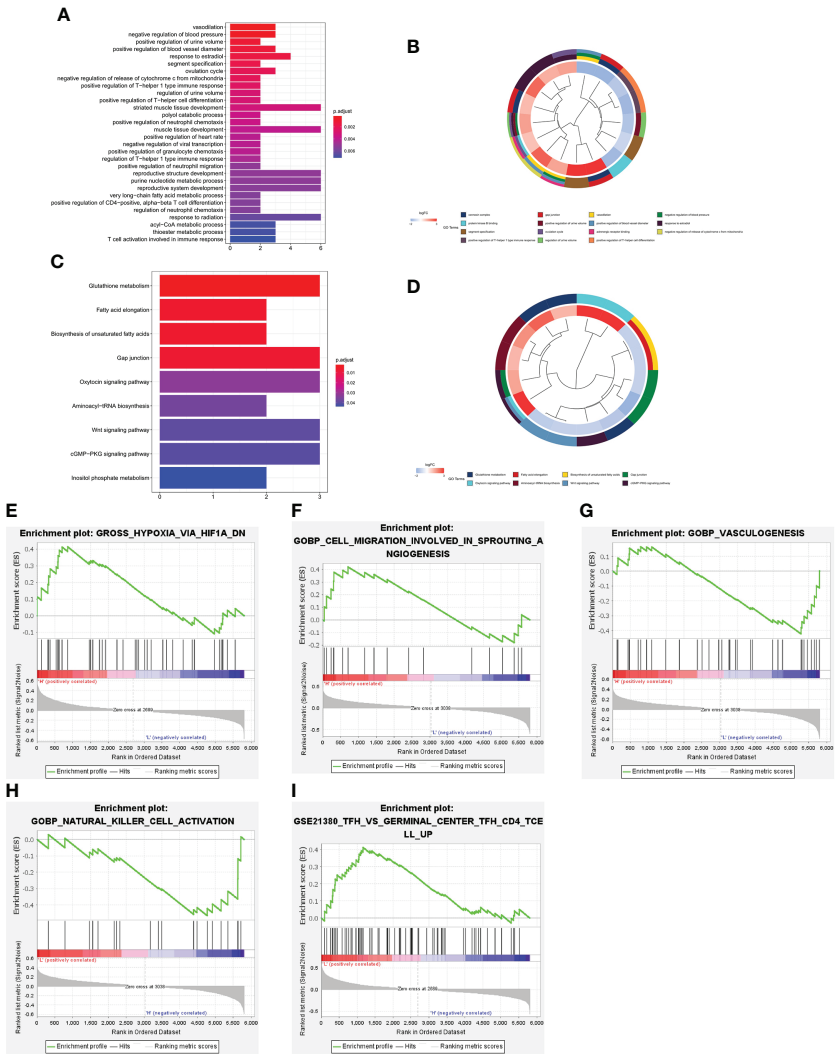

FIGURE 6
Functional enrichment analysis of the DEGs between the high-risk and low-risk groups. Bar plot **(A)** and circle plot **(B)** of the top 30 GO pathway analysis enrichment results. Bar plot **(C)** and circle plot **(D)** of KEGG pathway analysis enrichment results. **(E–I)** GSEA between the high-risk and low-risk groups.

lymphocytes (23, 24) and can be used as drug targets to regulate the function of the immune system (25). According to this research, Kv1.3 is highly expressed in the perivenular and parenchymal inflammatory infiltrates of multiple sclerosis (MS) brain tissue on T cells from the cerebrospinal fluid (26). Moreover, the use of Kv1.3 inhibitors can specifically and permanently block the proliferation and function of CD4+ T cells (27, 28). Furthermore, the activation of Kv1.3 on T lymphocytes can enhance the NLRP3 inflammasome and increase the secretion of IL-1β, which strengthens the T-cell-mediated inflammatory response (29).

Recently, the tumor microenvironment (TME), which includes tumor-infiltrating immune cells (TICs), was shown to play a decisive role at all stages of tumor progression. The high level of immune infiltration of ccRCC has been proven in many types of studies. Therefore, potassium channels are likely to affect the tumor and immune system, which could affect the modeling the TME. Ultimately, this could lead to the occurrence and development of ccRCC. How potassium channels directly lead to cancer remains unclear, and only a few studies have been carried out on the correlation between PCRGs and the development of ccRCC (21, 22).

Our study first proposed a prognostic signature consisting of 10 PCRGs that could predict the prognosis of patients with ccRCC, especially for long-term prediction. The low-risk group calculated by the PCRG signature had a better prognosis and overall survival (OS) than the high-risk group. We analyzed the differentially expressed genes (DEGs) between the high-risk

10.3389/fonc.2022.1013324

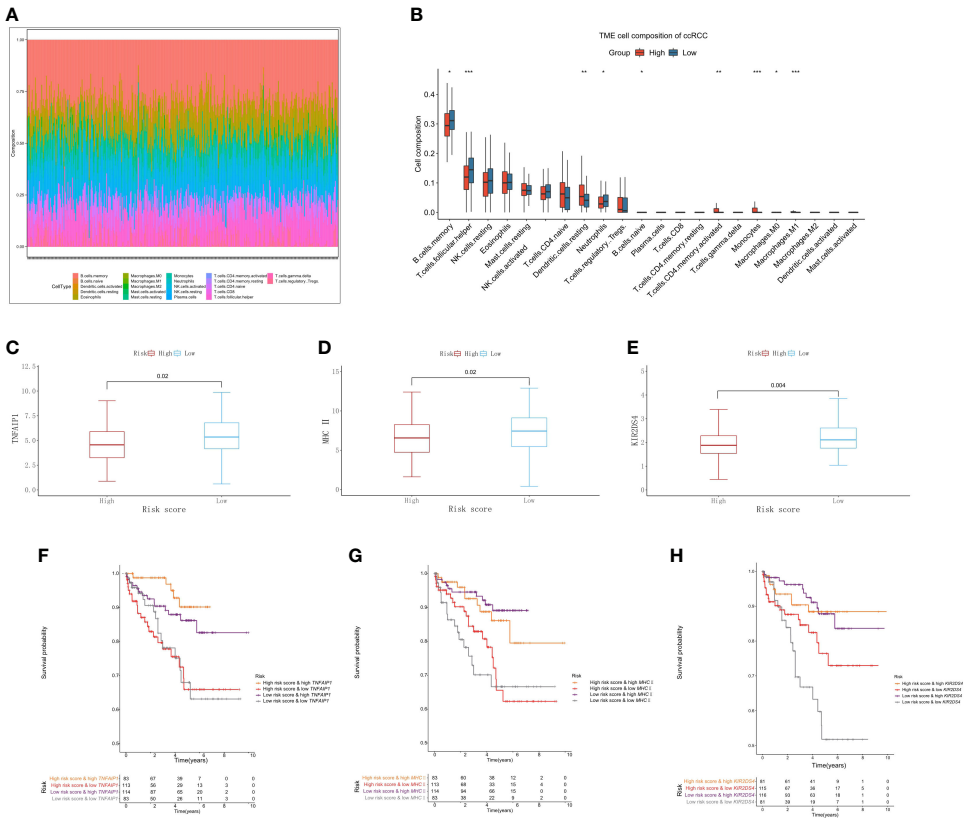

FIGURE 7
Immune cell infiltration associated with the risk score in ccRCC. **(A)** The abundance ratios of 22 immune cells in the TCGA-KIRC cohort. **(B)** Differences in immune cell abundance between the high-risk and low-risk groups. Relationship between the risk score and the immune activators TNFAIP1 **(C)**, MHC II **(D)**, and KIR2DS4 **(E)**. Relationship between the risk score and the expression of the immune activators TNFAIP1 **(F)**, MHC II **(G)**, and KIR2DS4 **(H)** with OS.

and low-risk groups predicted by the PCRG signature through GO enrichment analysis. The results showed that those genes were mainly concentrated in T lymphocyte activation and regulation, which is consistent with the previously reported literature that suggest that potassium channels could regulate T lymphocytes. Additionally, KEGG pathway analysis showed that the DEGs were mainly related to tumor-related signaling pathways and tumorigenesis. This result also supports the participation of potassium channels in the development of ccRCC. GSEA showed that the low-risk group was positively correlated with follicular helper CD4 T cells (TFHs) and germinal centers (GCs).

In contrast, the high-risk group was positively related to hypoxia, angiogenesis, vasculogenesis, and glycolysis. In addition, we compared the infiltration of immune cells in ccRCC tumor tissues and normal tissues. We found more infiltration of immune cells, especially memory B cells, NK cells, and T helper cells, in normal tissues than in ccRCC tissues. These results suggest that tertiary lymphoid structure (TLS) formation may be underway.

TLS is a lymphocyte aggregate located in nonlymphoid tissue (30). TLSs do not exist under physiological conditions but occur as the result of infection, autoimmunity, chronic inflammation, and even numerous cancers (30). They exhibit all the characteristics of structures in the lymph nodes associated with the generation of an adaptive immune response, including a T-cell zone with mature dendritic cells (DC), a germinal center with follicular DCs, proliferating B cells, and high endothelial venules (HEV) (31). Previous studies have identified TLSs as a tumor prognostic biomarker and therapeutic target that is associated with improved survival (30, 32, 33). Our results show that the numbers of TFH, GC, CD4+ T cells, and memory B cells predicted by the PCRG signature were higher in the low-risk group than in the high-risk group. These findings indicate a better prognosis and higher OS in the low-risk group. This indicates that PCRGs may affect TLS formation, including GC, by regulating T lymphocytes, such as TFH, and ultimately affect the occurrence and development of ccRCC.

Mutations in the genome of tumor cells may produce new antigens with immunogenicity that can be recognized by T

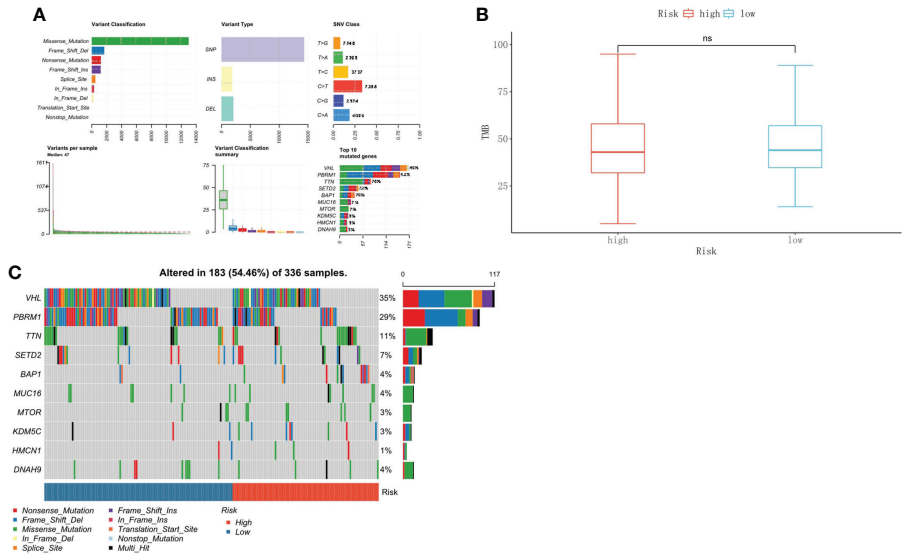

FIGURE 8
Tumor mutational burden associated with the risk score in ccRCC. **(A)** The overall landscape of somatic mutations. **(B)** TMB comparison between the high-risk and low-risk groups. **(C)** Waterfall maps of the somatic mutations in the high-risk and low-risk groups.

lymphocytes (34). Tumor mutation burden (TMB) can reflect the tumor gene mutation status. In short, the higher the TMB is, the more tumor gene mutations are present. Thus, the possibility of forming an immunogenic new antigen is greater, and the possibility of patients benefiting from tumor immunotherapy is greater (35). Therefore, we conducted a TMB prediction analysis on the high- and low-risk groups. The mean TMB scores of the low-risk group were higher than those of the high-risk group. These findings suggest that the low-risk group may be more likely to benefit from tumor immunotherapy and to have a better response to targeted drugs and chemotherapeutic drugs. This was proven by our prediction of chemotherapeutic drug

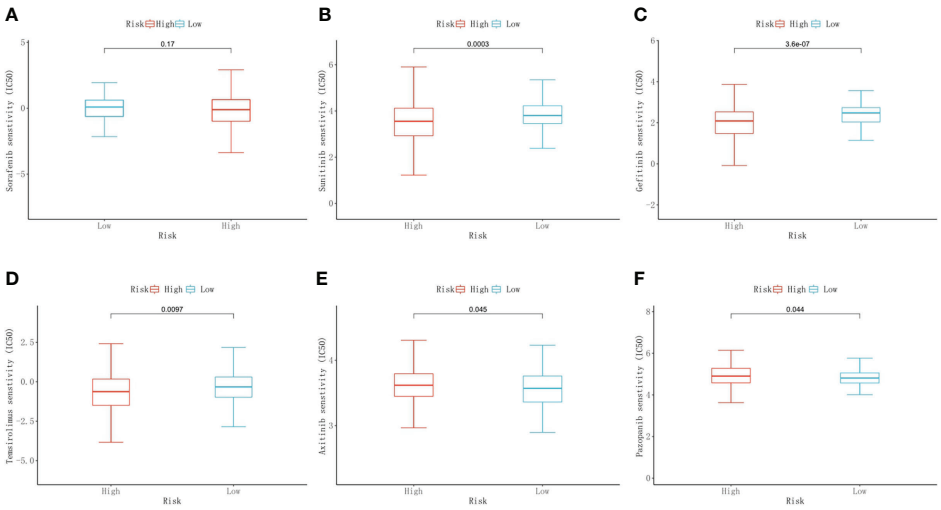

FIGURE 9
Predictive results of chemotherapeutic responses. The differences in the chemotherapeutic response to common chemotherapeutic drugs between the high- and low-risk groups **(A–F)**.

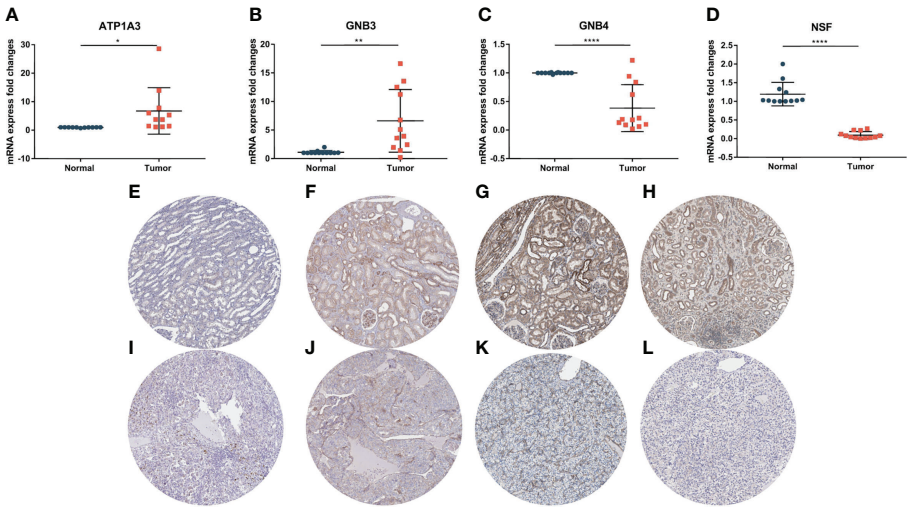

FIGURE 10
Expression of key genes in the PCRG prognostic signature in ccRCC and normal kidney tissues. The mRNA expression levels of ATP1A3 **(A)**, GNB3 **(B)**, GNB4 **(C)**, and NSF **(D)** in clinical samples were detected by qPCR. Immunohistochemistry of ATP1A3, GNB3, GNB4, and NSF in normal tissues **(E–H)** and ccRCC tissues **(I–L)** from the Human Protein Atlas (HPA) database.

response to ccRCC between the high- and low-risk groups by using the PCRG signature.

Related studies have reported that PCRGs play an important role in the development of multiple diseases. For example, the G protein beta3 subunit (*GNB3*) could be a candidate gene in disorders associated with poor immune response. It has been reported that the counts of CD4+ T cells with the *GNB3* homozygous 825T allele (TT) genotype were significantly enhanced compared to those with the C825 allele (CC) genotype (36). Na^+/K^+-ATPase is widespread in eukaryotic cell membranes, and its different α/β isoforms (*ATP1A1-1A4*, *ATP1B1-1B3*) were identified in humans in their early years (37). Moreover, the high expression of sodium pumps was shown to be closely related to the occurrence, development, and malignancy of cancer (37). Recently, *ATP1A3* has been reported to exert significant effects in various cancers, including glioblastomas (38), hepatomas (39), and medulloblastomas (40). It has been reported that bufalin inhibits the growth of hepatocellular carcinoma (HCC) cells, which is correlated with the expression level of *ATP1A3* in HCC cells (39). Another study reported that activation of *ATP1A3* could sensitize glioblastoma cells to temozolomide (41). However, the role of PCRGs in the development of ccRCC has not been reported, and further research is needed. In this study, through a series of rigorous analyses, we established a prognostic signature consisting of PCRGs that could predict the prognosis of patients with ccRCC. Our results suggest that these key genes may play a significant role in the occurrence and development of ccRCC. The PCRG signature may improve our understanding of the role of potassium channels in the occurrence and development of ccRCC and provide a reference for discovering new prognostic biomarkers and immunotherapy methods for ccRCC.

There were some limitations to our study. First, the robustness of the prognostic signature needs to be verified by external data sets. However, there is no suitable ccRCC gene expression data set, so we have to split the TCGA-KIRC cohort into training and validation cohorts to partially compensate for the study's limitations. Second, our results require further basic experiments and clinical studies to validate and further explore the potential underlying mechanisms and clinical applications of PCRGs in ccRCC. Finally, many factors, such as comorbidities, influence overall survival, but we did not study them in depth. Therefore, further studies concentrating on RFS/CSS are required.

Data availability statement

The original contributions presented in the study are included in the article/supplementary material. Further inquiries can be directed to the corresponding authors.

Ethics statement

This study was approved by the Ethics Committee of the First Affiliated Hospital of Jinan University. Both patients and controls provided written informed consent.

Author contributions

Conception and design of the research: All authors. Acquisition of data: RZ and YL. Analysis and interpretation of

data: RZ, YL, and MS. Statistical analysis: RZ and YL. Drafting manuscript: RZ, YL, DH, MS, YW, and TC. Obtaining funding: JH, JG, WH, JC, and YZ. All authors contributed to the article and approved the submitted version.

Acknowledgments

Financial support from the Science and Technology Program of Guangzhou, China (805147677069) is gratefully acknowledged. The experimental instrument support from the Medical Experimental Center, School of Medicine, Jinan University is gratefully acknowledged.

Conflict of interest

The authors declare that the research was conducted in the absence of any commercial or financial relationships that could be construed as a potential conflict of interest.

Publisher's note

References

1. Siegel RL, Miller KD, Jemal A. Cancer statistics, 2019. *CA Cancer J Clin* (2019) 69(1):7–34. doi: 10.3322/caac.21551

2. Moch H, Cubilla AL, Humphrey PA, Reuter VE, Ulbright TM. The 2016 who classification of tumours of the urinary system and Male genital organs-part a: Renal, penile, and testicular tumours. *Eur Urol* (2016) 70(1):93–105. doi: 10.1016/j.eururo.2016.02.029

3. Fisher R, Gore M, Larkin J. Current and future systemic treatments for renal cell carcinoma. *Semin Cancer Biol* (2013) 23(1):38–45. doi: 10.1016/j.semcancer.2012.06.004

4. Khan Y, Slattery TD, Pickering LM. Individualizing systemic therapies in first line treatment and beyond for advanced renal cell carcinoma. *Cancers (Basel)* (2020) 12(12). doi: 10.3390/cancers12123750

5. Choueiri TK, Motzer RJ. Systemic therapy for metastatic renal-cell carcinoma. *N Engl J Med* (2017) 376(4):354–66. doi: 10.1056/NEJMra1601333

6. Zitvogel L, Tesniere A, Kroemer G. Cancer despite immunosurveillance: Immunoselection and immunosubversion. *Nat Rev Immunol* (2006) 6(10):715–27. doi: 10.1038/nri1936

7. Grivennikov SI, Greten FR, Karin M. Immunity, inflammation, and cancer. *Cell* (2010) 140(6):883–99. doi: 10.1016/j.cell.2010.01.025

8. Zhang Y, Zhang Z. The history and advances in cancer immunotherapy: Understanding the characteristics of tumor-infiltrating immune cells and their therapeutic implications. *Cell Mol Immunol* (2020) 17(8):807–21. doi: 10.1038/s41423-020-0488-6

9. Şenbabaoğlu Y, Gejman RS, Winer AG, Liu M, Van Allen EM, de Velasco G, et al. Tumor immune microenvironment characterization in clear cell renal cell carcinoma identifies prognostic and immunotherapeutically relevant messenger rna signatures. *Genome Biol* (2016) 17(1):231. doi: 10.1186/s13059-016-1092-z

10. Lai Y, Tang F, Huang Y, He C, Chen C, Zhao J, et al. The tumour microenvironment and metabolism in renal cell carcinoma targeted or immune therapy. *J Cell Physiol* (2021) 236(3):1616–27. doi: 10.1002/jcp.29969

11. Hu FF, Liu CJ, Liu LL, Zhang Q, Guo AY. Expression profile of immune checkpoint genes and their roles in predicting immunotherapy response. *Brief Bioinform* (2021) 22(3). doi: 10.1093/bib/bbaa176

12. D'Amico M, Gasparoli L, Arcangeli A. Potassium channels: Novel emerging biomarkers and targets for therapy in cancer. *Recent Pat Anticancer Drug Discovery* (2013) 8(1):53–65. doi: 10.2174/15748928130106

13. Masi A, Becchetti A, Restano-Cassulini R, Polvani S, Hofmann G, Buccoliero AM, et al. Herg1 channels are overexpressed in glioblastoma multiforme and modulate vegf secretion in glioblastoma cell lines. *Br J Cancer* (2005) 93(7):781–92. doi: 10.1038/sj.bjc.6602775

14. Voloshyna I, Besana A, Castillo M, Matos T, Weinstein IB, Mansukhani M, et al. Trek-1 is a novel molecular target in prostate cancer. *Cancer Res* (2008) 68(4):1197–203. doi: 10.1158/0008-5472.Can-07-5163

15. Ouadid-Ahidouch H, Chaussade F, Roudbaraki M, Slomianny C, Dewailly E, Delcourt P, et al. Kv1.1 k(+) channels identification in human breast carcinoma cells: Involvement in cell proliferation. *Biochem Biophys Res Commun* (2000) 278(2):272–7. doi: 10.1006/bbrc.2000.3790

16. Hanahan D, Weinberg RA. Hallmarks of cancer: The next generation. *Cell* (2011) 144(5):646–74. doi: 10.1016/j.cell.2011.02.013

17. Becchetti A, Pillozzi S, Morini R, Nesti E, Arcangeli A. New insights into the regulation of ion channels by integrins. *Int Rev Cell Mol Biol* (2010) 279:135–90. doi: 10.1016/s1937-6448(10)79005-5

18. Williamson TJ, Pearson JR, Ischia J, Bolton DM, Lawrentschuk N. Guideline of guidelines: Follow-up after nephrectomy for renal cell carcinoma. *BJU Int* (2016) 117(4):555–62. doi: 10.1111/bju.13384

19. Penticuff JC, Kyprianou N. Therapeutic challenges in renal cell carcinoma. *Am J Clin Exp Urol* (2015) 3(2):77–90.

20. Ljungberg B, Campbell SC, Choi HY, Jacqmin D, Lee JE, Weikert S, et al. The epidemiology of renal cell carcinoma. *Eur Urol* (2011) 60(4):615–21. doi: 10.1016/j.eururo.2011.06.049

21. Guo Z, Liu J, Zhang L, Su B, Xing Y, He Q, et al. Kcnj1 inhibits tumor proliferation and metastasis and is a prognostic factor in clear cell renal cell carcinoma. *Tumour Biol* (2015) 36(2):1251–9. doi: 10.1007/s13277-014-2746-7

22. Rabjerg M, Oliván-Viguera A, Hansen LK, Jensen L, Sevelsted-Møller L, Walter S, et al. High expression of Kca3.1 in patients with clear cell renal carcinoma predicts high metastatic risk and poor survival. *PLoS One* (2015) 10(4):e0122992. doi: 10.1371/journal.pone.0122992

23. Wulff H, Beeton C, Chandy KG. Potassium channels as therapeutic targets for autoimmune disorders. *Curr Opin Drug Discovery Devel* (2003) 6(5):640–7.

24. Cahalan MD, Wulff H, Chandy KG. Molecular properties and physiological roles of ion channels in the immune system. *J Clin Immunol* (2001) 21(4):235–52. doi: 10.1023/a:1010958907271

25. Cahalan MD, Chandy KG. Ion channels in the immune system as targets for immunosuppression. *Curr Opin Biotechnol* (1997) 8(6):749–56. doi: 10.1016/s0958-1669(97)80130-9

26. Rus H, Pardo CA, Hu L, Darrah E, Cudrici C, Niculescu T, et al. The voltage-gated potassium channel Kv1.3 is highly expressed on inflammatory infiltrates in multiple sclerosis brain. *Proc Natl Acad Sci USA* (2005) 102(31):11094–9. doi: 10.1073/pnas.0501770102

27. Panyi G, Possani LD, Rodríguez de la Vega RC, Gáspár R, Varga Z. K+ channel blockers: Novel tools to inhibit T cell activation leading to specific immunosuppression. *Curr Pharm Des* (2006) 12(18):2199–220. doi: 10.2174/138161206777585120

28. Hu L, Pennington M, Jiang Q, Whartenby KA, Calabresi PA. Characterization of the functional properties of the voltage-gated potassium channel Kv1.3 in human Cd4+ T lymphocytes. *J Immunol* (2007) 179(7):4563–70. doi: 10.4049/jimmunol.179.7.4563

29. Zhu J, Yang Y, Hu SG, Zhang QB, Yu J, Zhang YM. T-Lymphocyte K(V)1.3 channel activation triggers the Nlrp3 inflammasome signaling pathway in hypertensive patients. *Exp Ther Med* (2017) 14(1):147–54. doi: 10.3892/etm.2017.4490

30. Sautès-Fridman C, Lawand M, Giraldo NA, Kaplon H, Germain C, Fridman WH, et al. Tertiary lymphoid structures in cancers: Prognostic value, regulation, and manipulation for therapeutic intervention. *Front Immunol* (2016) 7:407. doi: 10.3389/fimmu.2016.00407

31. Dieu-Nosjean MC, Goc J, Giraldo NA, Sautès-Fridman C, Fridman WH. Tertiary lymphoid structures in cancer and beyond. *Trends Immunol* (2014) 35 (11):571–80. doi: 10.1016/j.it.2014.09.006

32. Hiraoka N, Ino Y, Yamazaki-Itoh R, Kanai Y, Kosuge T, Shimada K. Intratumoral tertiary lymphoid organ is a favourable prognosticator in patients with pancreatic cancer. *Br J Cancer* (2015) 112(11):1782–90. doi: 10.1038/bjc.2015.145

33. Germain C, Gnjatic S, Tamzalit F, Knockaert S, Remark R, Goc J, et al. Presence of b cells in tertiary lymphoid structures is associated with a protective immunity in patients with lung cancer. *Am J Respir Crit Care Med* (2014) 189 (7):832–44. doi: 10.1164/rccm.201309-1611OC

34. Matsushita H, Vesely MD, Koboldt DC, Rickert CG, Uppaluri R, Magrini VJ, et al. Cancer exome analysis reveals a T-Cell-Dependent mechanism of cancer immunoediting. *Nature* (2012) 482(7385):400–4. doi: 10.1038/nature10755

35. Chan TA, Yarchoan M, Jaffee E, Swanton C, Quezada SA, Stenzinger A, et al. Development of tumor mutation burden as an immunotherapy biomarker: Utility for the oncology clinic. *Ann Oncol* (2019) 30(1):44–56. doi: 10.1093/annonc/mdy495

36. Lindemann M, Virchow S, Ramann F, Barsegian V, Kreuzfelder E, Siffert W, et al. The G protein Beta3 subunit 825t allele is a genetic marker for enhanced T cell response. *FEBS Lett* (2001) 495(1-2):82–6. doi: 10.1016/s0014-5793(01)02339-0

37. Mijatovic T, Van Quaquebeke E, Delest B, Debeir O, Darro F, Kiss R. Cardiotonic steroids on the road to anti-cancer therapy. *Biochim Biophys Acta* (2007) 1776(1):32–57. doi: 10.1016/j.bbcan.2007.06.002

38. Com E, Clavreul A, Lagarrigue M, Michalak S, Menei P, Pineau C. Quantitative proteomic isotope-coded protein label (Icpl) analysis reveals alteration of several functional processes in the glioblastoma. *J Proteomics* (2012) 75(13):3898–913. doi: 10.1016/j.jprot.2012.04.034

39. Li H, Wang P, Gao Y, Zhu X, Liu L, Cohen L, et al. Na+/K+-atpase A3 mediates sensitivity of hepatocellular carcinoma cells to bufalin. *Oncol Rep* (2011) 25(3):825–30. doi: 10.3892/or.2010.1120

40. Suñol M, Cusi V, Cruz O, Kiss R, Lefranc F. Immunohistochemical analyses of Alpha1 and Alpha3 Na+/K+-atpase subunit expression in medulloblastomas. *Anticancer Res* (2011) 31(3):953–8.

41. Lan YL, Chen C, Wang X, Lou JC, Xing JS, Zou S, et al. Gamabufotalin induces a negative feedback loop connecting Atp1a3 expression and the Aqp4 pathway to promote temozolomide sensitivity in glioblastoma cells by targeting the amino acid Thr794. *Cell Prolif* (2020) 53(1):e12732. doi: 10.1111/cpr.12732

frontiers | Frontiers in Oncology

TYPE Original Research
PUBLISHED 24 October 2022
DOI 10.3389/fonc.2022.1026331

OPEN ACCESS

EDITED BY
Linhui Wang,
Second Military Medical University, China

REVIEWED BY
Demitrios Vynios,
University of Patras, Greece
Asif Loya,
Shaukat Khanum Memorial Cancer Hospital and Research Center, Pakistan

*CORRESPONDENCE
Yi Liu
liuyi_ay@163.com
Jun Zhou
zhoujun@ahmu.edu.cn

†These authors share first authorship

SPECIALTY SECTION
This article was submitted to Genitourinary Oncology, a section of the journal Frontiers in Oncology

RECEIVED 23 August 2022
ACCEPTED 06 October 2022
PUBLISHED 24 October 2022

CITATION
Tao J, Li X, Liang C, Liu Y and Zhou J (2022) Expression of basement membrane genes and their prognostic significance in clear cell renal cell carcinoma patients.
Front. Oncol. 12:1026331.
doi: 10.3389/fonc.2022.1026331

Expression of basement membrane genes and their prognostic significance in clear cell renal cell carcinoma patients

Junyue Tao[1,2,3†], Xiao Li[1,2,3†], Chaozhao Liang[1,2,3], Yi Liu[1,2,3*] and Jun Zhou[1,2,3*]

[1]Department of Urology, The First Affiliated Hospital of Anhui Medical University, Anhui Medical University, Hefei, China, [2]Institute of Urology, Anhui Medical University, Hefei, China, [3]Anhui Province Key Laboratory of Genitourinary Diseases, Anhui Medical University, Hefei, China

Background: Clear cell renal cell carcinoma (ccRCC) is a malignant tumor with limited treatment options. A recent study confirmed the involvement of basement membrane (BM) genes in the progression of many cancers. Therefore, we studied the role and prognostic significance of BM genes in ccRCC.

Methods: Co-expression analysis of ccRCC-related information deposited in The Cancer Genome Atlas database and a BM geneset from a recent study was conducted. The differentially expressed BM genes were validated using quantitative reverse-transcription polymerase chain reaction (qRT-PCR). Least absolute shrinkage and selection operator regression and univariate Cox regression analyses were performed to identify a BM gene signature with prognostic significance for ccRCC. Multivariate Cox regression, time-dependent receiver operating characteristic, Kaplan–Meier, and nomogram analyses were implemented to appraise the prognostic ability of the signature and the findings were further verified using a Gene Expression Omnibus dataset. Additionally, immune cell infiltration and and pathway enrichment analyses were performed using ImmuCellAI and Gene Set Enrichment Analysis (GSEA), respectively. Finally, the DSIGDB dataset was used to screen small-molecule therapeutic drugs that may be useful in treating ccRCC patients.

Results: We identified 108 BM genes exhibiting different expression levels compared to that in normal kidney tissues, among which 32 genes had prognostic values. The qRT-PCR analyses confirmed that the expression patterns of four of the ten selected genes were the same as the predicted ones. Additionally, we successfully established and validated a ccRCC patient prediction model based on 16 BM genes and observed that the model function is an independent predictor. GSEA revealed that differentially expressed BM genes mainly displayed significant enrichment of tumor and metabolic signaling cascades. The BM gene signature was also associated with immune cell infiltration and checkpoints. Eight small-molecule drugs may have therapeutic effects on ccRCC patients.

Conclusion: This study explored the function of BM genes in ccRCC for the first time. Reliable prognostic biomarkers that affect the survival of ccRCC patients were determined, and a BM gene-based prognostic model was established.

KEYWORDS

clear cell renal cell carcinoma, basement membrane (BM), gene expression profile, prognostic biomarkers, gene expression analysis

Introduction

There are over 300,000 new cases of clear cell renal cell carcinoma (ccRCC), acounting for the most prevalent subtype of renal malignancy, reported worldwide in 2020 (1). In recent years, several alternative treatments, such as surgery, immunotherapy, and other targeted therapy, have been applied for ccRCC patients (2). For patients with ccRCC at early localized stage, surgery remains the first-line therapy; yet 30% of them meet post-surgery recurrence (3). Despite encouraging achievements in immunotherapy and targeted therapy, the five-year survival probability for metastatic ccRCC has only improved by 11.7% (4–6). Therefore, exploring the mechanism and mining potential biomarkers of ccRCC have become the focus of kidney cancer research.

The basement membrane (BM) is the oldest extracellular matrix (ECM) in animals, bordering all cells, including the epithelium and endothelium (7). The BM core structural components belong to the laminin family, collagen IV, heparan sulfate proteoglycans, nidogens, and perlecan (8). Utilizing these basic components, the basement membrane plays a vital biological role in the body, resisting mechanical stress, determining tissue morphology, establishing a diffusion barrier, and providing an environment for guiding cell polarity, differentiation, migration, and survival (9–12). Over 20 BM gene mutations form the basis of human diseases, highlighting their diverse and vital functions (13). As targets of autoantibody attack in immune diseases, deficiencies in the expression and turnover of BM proteins are crucial causative factors in cancer, fibrosis, and diabetes (14–16). Collagen type IV, alpha-6 (*COL4A6*) is a BM gene encoding the a6 chain of collagen IV. *COL4A6* is highly downregulated in prostate cancer, and its deletion can promote prostate cancer progression and metastasis by activating the p-focal adhesion kinase (FAK)/matrix metallopeptidase 9 (MMP-9) signaling pathway (17). Nephronectin (NPNT) has also been shown to be a key regulator of tumor metastasis (18). Huang et al. reported that in metastatic hepatocellular carcinoma, overexpressed NPNT could promote malignant progression through transcriptional regulation of the FAK/phosphatidylinositol 3–kinase (PI3K)/protein kinase B (AKT) signaling cascade (19). Peroxidasin (PXDN) is a BM-associated protein with peroxidase activity that promotes the proliferation, invasion, and migration of ovarian cancer cells, and PXDN overexpression has been correlated with an unfavorable prognosis (20). A disintegrin and metalloproteinase with thrombospondin motifs (ADAMTS) protein is a zinc metalloendopeptidase whose substrates are mostly ECM components associated with multiple malignant phenotypes, including cancer progression and metastasis (21–23).

However, we currently lack systematic studies on the relationship between BM genes and ccRCC. Herein, we used bioinformatics analyses to determine the prognostic significance of the BM gene family in ccRCC and the related mechanisms affecting prognosis to provide a reference for treating ccRCC.

Materials and methods

Acquisition of data and identification of differential expression BM genes

The gene expression and related clinical characteristics of 539 ccRCC and 72 noncancerous renal tissue specimens were acquired from The Cancer Genome Atlas (TCGA) (https://portal.gdc.cancer.gov). In a recent study of BM genes, we downloaded a set of 224 BM genes (24). We also downloaded GSE46699, GSE22541, and GSE29609 datasets of GEO (https://www.ncbi.nlm.nih.gov/geo/), totaling 128 ccRCC organization information. The downloaded data were normalized with the corresponding R package, and the R package "limma" (25) was utilized for identification of the differentially expressed BM genes (DEGs). DEGs having a |log2 fold change (FC)| > 1 and an adjusted P <0.05 were considered for subsequent analysis.

Verification of the expression levels of DEGs

Quantitative reverse transcription-polymerase chain reaction (qRT-PCR) was performed to test the transcript abundances of the DEGs. TRIzol (Invitrogen, Shanghai, China) reagent was employed for isolation of total RNA from the HEK-293 and 786-O cells. The primers used to test the

expression of selected DEGs are listed in Supplementary Table 1. The PCR program was 94°C 3 min, 22 rounds of 94°C 30 s, 55°C 30 s, and 72°C 30 s, and 72°C 5 min. All the reactions were conducted in triplicate.

Construction and validation of the BM gene signature

Genes associated with the prognosis of ccRCC were identified by univariate Cox regression from the DEGs with the R package "glmnet" (26). We also carried out a least absolute shrinkage and selection operator (LASSO)-penalized Cox regression analysis for construction of a prognostic risk model. Each screened BM gene's risk score was determined as follows:

$$\text{Risk score} = (\text{Coef 1ñmRNA1 expression}) + (\text{Coef 2ñmRNA2 expression}) + (\text{Coef nñmRNAn expression})$$ (27)

Coef represents the coefficient of the LASSO-Cox analysis for a specific mRNA. The median risk score was calculated, based on which patients with ccRCC were classified to a high- or low-risk group. For evaluation of the model's prediction ability, we conducted a time-based receiver operating characteristic (ROC) analysis of the model with the survival ROC package (28). Three downloaded GEO datasets were used as verification sets.

Identification of independent prognostic indices and establishment of the predictive nomogram

Correlations between BM gene expression features and clinical variables were also determined. Univariate and multivariate Cox regression analyses combined with other clinical variables were conducted to test the performance of the our prognostic BM gene signature. The nomogram was established through clinical variables and the BM gene-based model risk score to evaluate the 1-year, 3-year and 5-year OS in ccRCC patients. The prediction effect of the nomogram was assessed by measuring the concordance index and plotting a calibration curve.

Functional annotation and gene set enrichment analysis

Kyoto Encyclopedia of Genes and Genomes (KEGG) pathway enrichment analysis and Gene Ontology (GO) annotation were carried out for high- and low-risk populations by utilizing the R package "ClusterProfiler" (29). $P < 0.05$ was deemed to signify statistical significance.

Through GSEA, we explored the potential mechanisms underlying low-risk and high-risk populations from a molecular biology perspective. $P < 0.05$ and FDR < 25% were considered significantly enriched.

Analysis of the infiltration levels of immune cells

Based on the features of B cell-specific long non-coding RNAs, we used the MCP-counter, CIBERSORT-ABS, EPIC, XCELL, TIMER, and QUANTISEQ algorithms to evaluate the differences in immune cell infiltration levels between low-risk and high-risk populations. The expression of some immune checkpoints in the two groups was examined to explore possible immune checkpoint blocking therapies, such as *LAG3*, *ICOS*, *TIGIT*, *CTLA4*, *PDCD1*, and *BTLA*. Additionally, the association between 16 BM genes and immune cells was determined using the TIMER database (http://cistrome.shinyapps.io/timer/), which deepened our knowledge of the effects of BM genes on ccRCC.

Identification of potential small molecule drugs

Molecular identification of drugs is a crucial link in drug detection. The Drug Signatures Database (DSigDB) was searched for candidate drugs implicated with the differential expression of the BM genes. The Enrichr platform (https://amp.pharm.mssm.edu/Enrichr/) served as the access path for the DSigDB database.

Statistics analysis

R software (version 4.0.5) was utilized for analysis of statistical data. Wilcoxon test was utilized to examine differences between groups, and P <0.05 was deemed to indicate statistical significance.

Results

Establishment and validation of the BM gene-based model

From the TCGA-KIRC dataset, 108 BM genes were identified to be differentially expressed compared to that in normal kidney tissues. These DEGs included 39 downregulated and 69 upregulated BM genes (Figure 1). Subsequently, we implemented univariate Cox regression analysis for identification of the differentially expressed genes with prognostic significance. The

results revealed that 32 genes had prognostic values (Figure 2), and the qRT-PCR analyses demonstrated that four of the ten genes tested were expressed as predicted (Figure 3).

Subsequently, the top 20 genes were selected according to their significance, and a LASSO-Cox regression analysis was carried out. A risk model involving 16 genes (*COL9A2*, *COL4A6*, *NPNT*, *COL4A4*, *ITGAX*, *SEMA3B*, *HMCN1*, *ADAMTS2*, *MMP7*, *FN1*, *VCAN*, *FREM1*, *PXDN*, *VWA1*, *GPC2*, and *ADAMTS4*) was successfully constructed. The risk score was measured with coefficients for the 16 BM genes as follows (Table 1): Risk score = (0.0788 × *COL9A2* mRNA level) + (0.1435 × *COL4A6* mRNA level) + (−0.0198 × *NPNT* mRNA level) + (−0.0378 × *COL4A4* mRNA level) + (0.0082 × *ITGAX* mRNA level) + (0.0027 × *SEMA3B* mRNA level) + (−0.1336 × *HMCN1* mRNA level) + (0.0221 × *ADAMTS2* mRNA level) + (0.0003 × *MMP7* mRNA level) + (0.0001 × *FN1* mRNA level) + (0.0020 × *AN* mRNA level) + (−0.0392 × *FREM1* mRNA level) + (0.0103 × *PXDN* mRNA level) + (-0.0075 × *VWA1* mRNA level) + (0.2294 × *GPC2* mRNA level) + (0.0090 × *ADAMTS4* mRNA level).

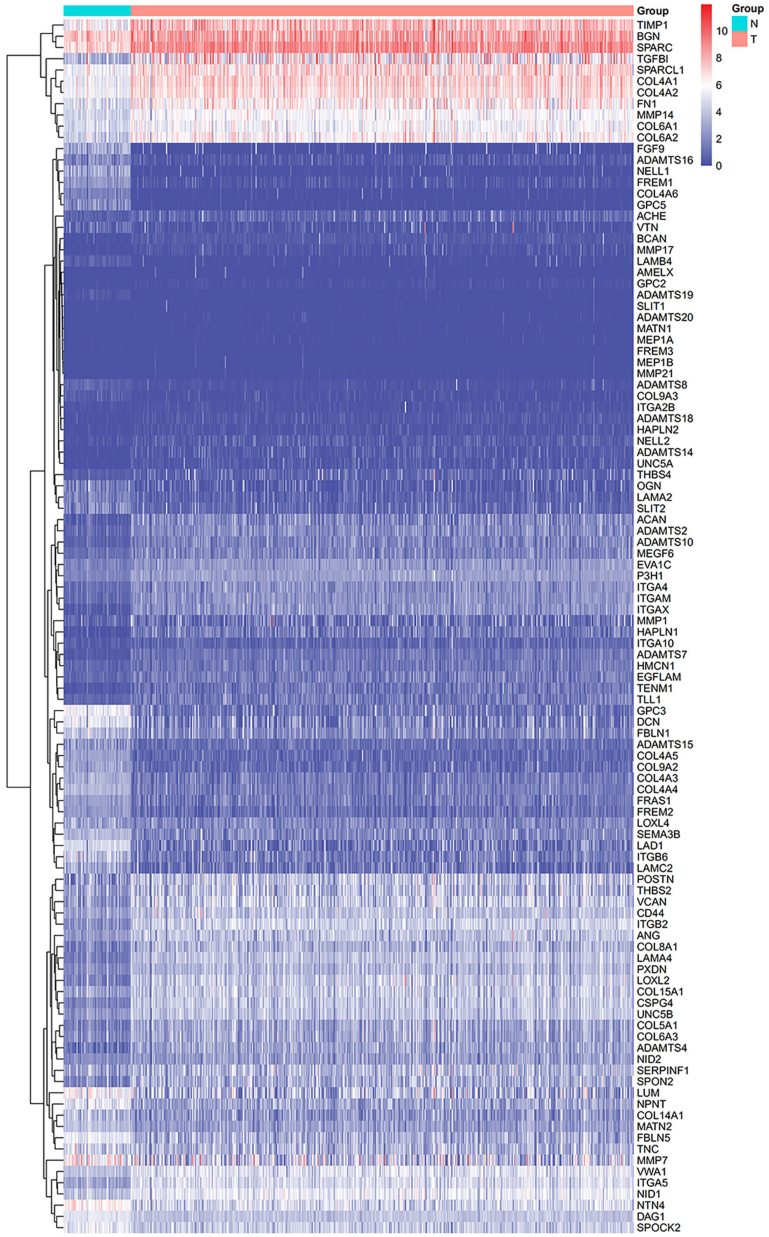

FIGURE 1
The heatmap displaying the DEGs.

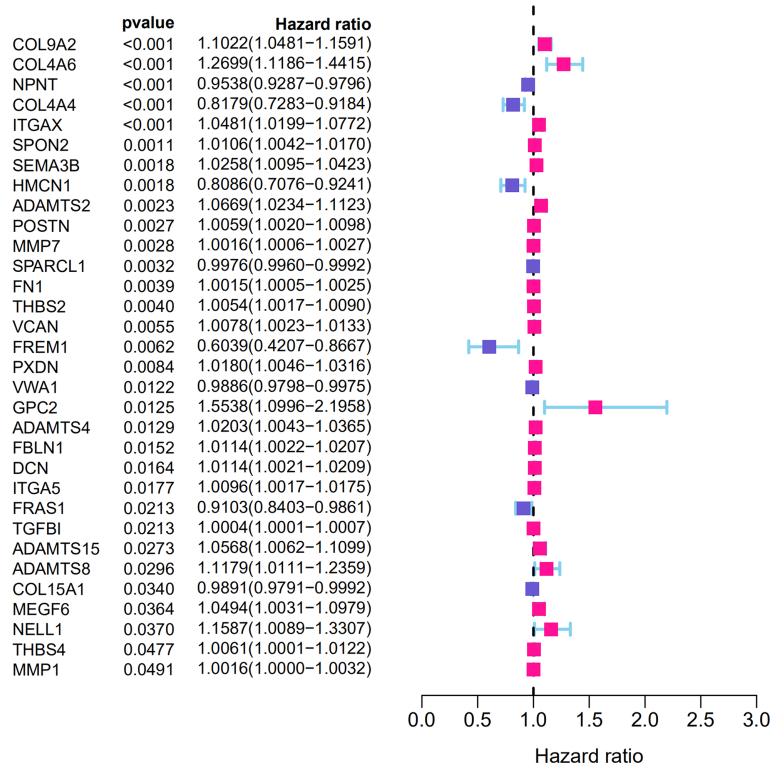

FIGURE 2
The BM genes with prognostic significance in ccRCC.

Patients were then assigned to high-risk and low-risk groups based on the median risk score. As revealed by the Kaplan–Meier analysis, high-risk patients exhibited a significantly lower survival rate compared with the low-risk ones ($P < 0.001$), suggesting a relationship between high risk score and dismal survival (Figures 4A, C). Additionally, the area under the ROC curve (AUC) values of the signature were 0.747, 0.719, and 0.715 at 1, 3, and 5 years, respectively, indicating that our model was stability for predicting the prognosis (Figures 4B, D). We used data from the GEO database for external validation (Figures 5) and observed that the risk score was inversely correlated with survival. The AUCs of time-dependent ROC were 0.867, 0.848, and 0.749 at 1, 3, and 5 years, respectively.

BM gene-based signature could predict ccRCC prognosis independently

The independent prognostic significance of the BM gene-based model was assessed in ccRCC patients using univariable and multivariable Cox analyses. As displayed in Figure 6A, univariate analysis revealed a significant correlation between age, tumor grade, pathological stage, risk score, and ccRCC patients' survival ($P < 0.001$). Notably, the multivariate analysis also showed this correlation ($P < 0.05$) (Figure 6B). Therefore, based on these findings, we confirmed that our BM gene-based signature represents an independent indicator for assessing ccRCC patient prognosis.

Relationship between clinical features and the signature

The association of our signature with the progression of ccRCC was investigated using the Chi-square test. As revealed by the test, there were significant differences in the pathological stage, T stage, and tumor grade between the two groups of ccRCC patients ($P < 0.001$) (Figures 7A,B). Further hierarchical analysis showed the outstanding role of the model in predicting prognosis in both male and female patients ($P = 0.0014$ and $P < 0.001$, respectively), patients aged both more than, less than or equal to 65 years ($P = 0.002$ and 0.001, respectively), as well as in patients with all stages ($P = 0.019$ and 0.012 for Stages I-II and III-IV, respectively), all grades (P=0.009 and $P < 0.001$ for high and lo grades, respectively), all T stages ($P = 0.007$ and 0.011 for T1–T2 and T3–T4 stages, respectively), N0 stage ($P < 0.001$),

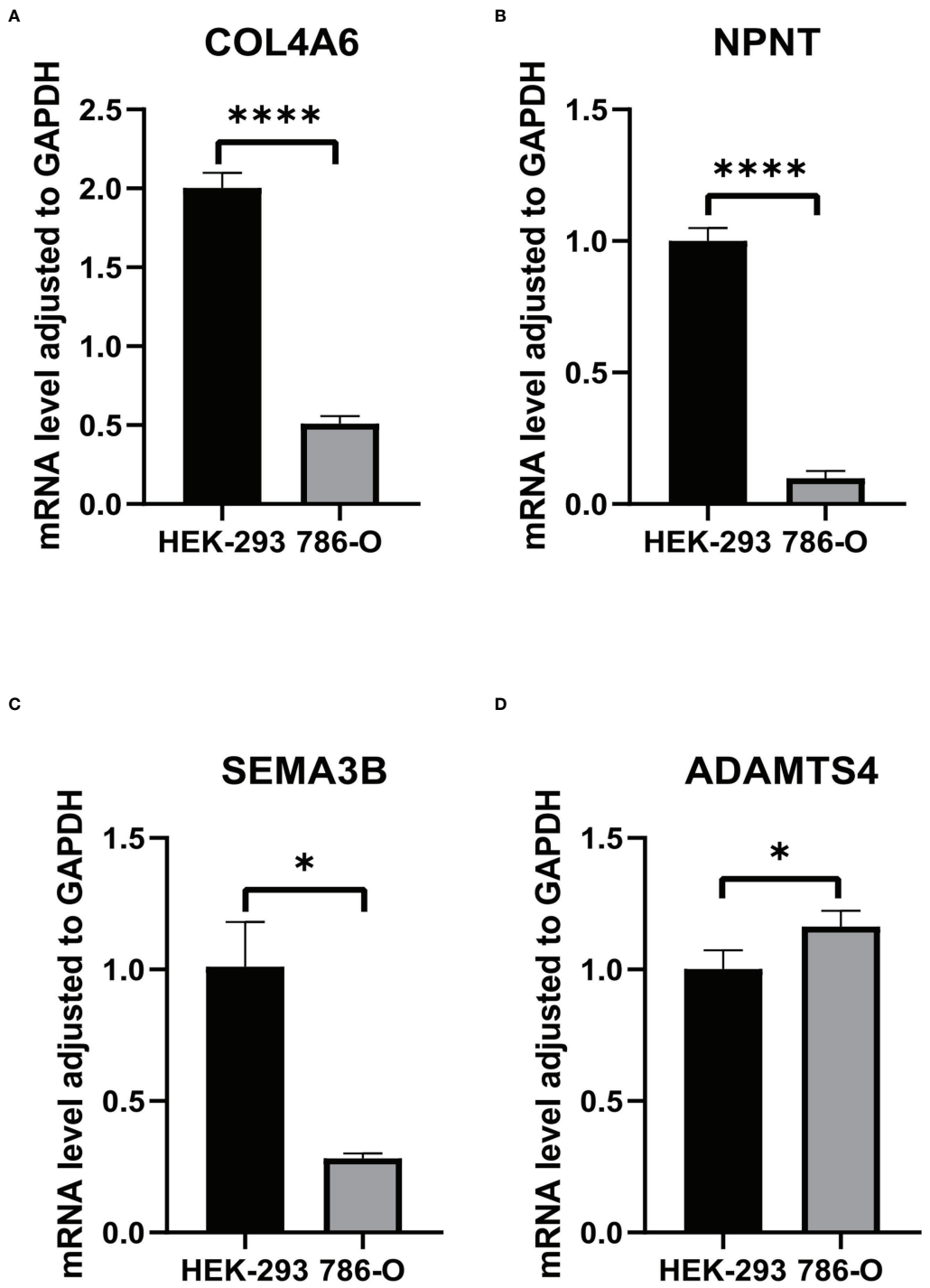

FIGURE 3
The RNA levels of **(A)** COL4A6, **(B)** NPNT, **(C)** SEMA3B, **(D)** ADAMTS4 in HEK-293 and 786-O cells. "*" represents P < 0.05, "****" represents P < 0.0001.

and all M stages ($P < 0.001$ and $P = 0.036$ for M0 and M1 stages, respectively). However, the model performed poorly in predicting the prognosis for the N1 stage ($P > 0.05$). In the TCGA-KIRC cohort, only 15 samples were recorded with N1 stage, which might be not large enough to generate statistical significance, but the overall trend is clear that the prognostic signature deeply participated in the development and progression of ccRCC (Figure 8).

TABLE 1 The list of signature genes and their coefficients.

Gene symbol	Coefficient
COL9A2	0.0788
COL4A6	0.1435
NPNT	-0.0198
COL4A4	-0.0378
ITGAX	0.0082
SEMA3B	0.0027
HMCN1	-0.1336
ADAMTS2	0.0221
MMP7	0.0003
FN1	0.0001
VCAN	0.0020
FREM1	-0.0392
PXDN	0.0103
VWA1	-0.0075
GPC2	0.2294
ADAMTS4	0.0090

Nomogram construction

We constructed a nomogram with covariates of patients' sex, age, tumor grade, pathological stage, and risk score to predict patients' survival rates at 1, 3, and 5 years. As shown in Figure 9A, each parameter has a score, and the total score was computed for survival rate prediction at the specific time point. The nomogram's performance in survival prediction was appraised by ROC analysis. We found that the AUCs of the TCGA cohort were 0.954 for 1-year survival, 0.873 for 3-year survival, and 0.781 for 5-year survival. The calibration curve revealed the consistency of the actual survival rate of the patient with the predicted value (Figure 9B).

Functional enrichment and GSEA

GO annotation and KEGG analysis were performed to explore the potential functions of the 108 DEGs. As indicated by biological process analyses, 108 BM genes were significantly associated with the GO terms of cell–substrate adhesion, extracellular structure organization, and extracellular matrix organization. Cellular component analysis suggested that the GO terms of endoplasmic reticulum lumen, basement membrane, and collagen-containing extracellular matrix were mainly enriched. Molecular function analysis revealed that glycosaminoglycan binding, extracellular matrix structural constituent, and metalloendopeptidase activity were mainly

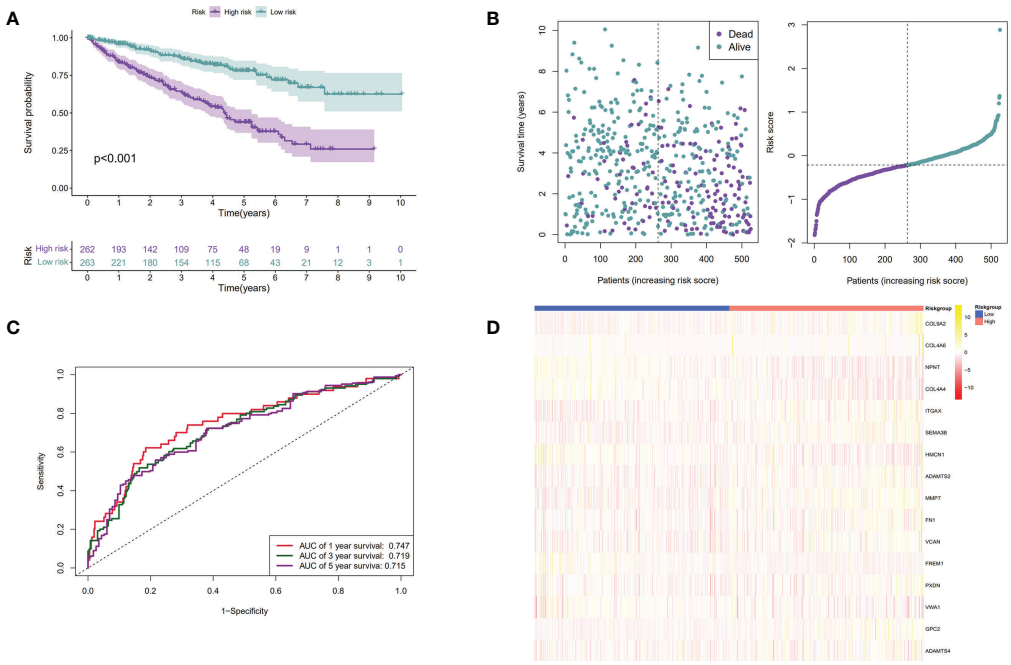

FIGURE 4
Establishment of the BM genes-based prognostic signature based on the TCGA dataset. **(A).** The Kaplan-Meier (K-M) curves of low-risk and high-risk ccRCC patients in the TCGA dataset; **(B).** The time-dependent ROC curves displaying the 1-year, 3-year, and 5-year OS of ccRCC patients in the TCGA dataset; **(C).** Survival distributions of the TCGA dataset determined according to the median risk score; **(D).** Heatmap displaying the divergences between low- and high-risk patients of 16 signature genes in the prognostic model for the TCGA dataset.

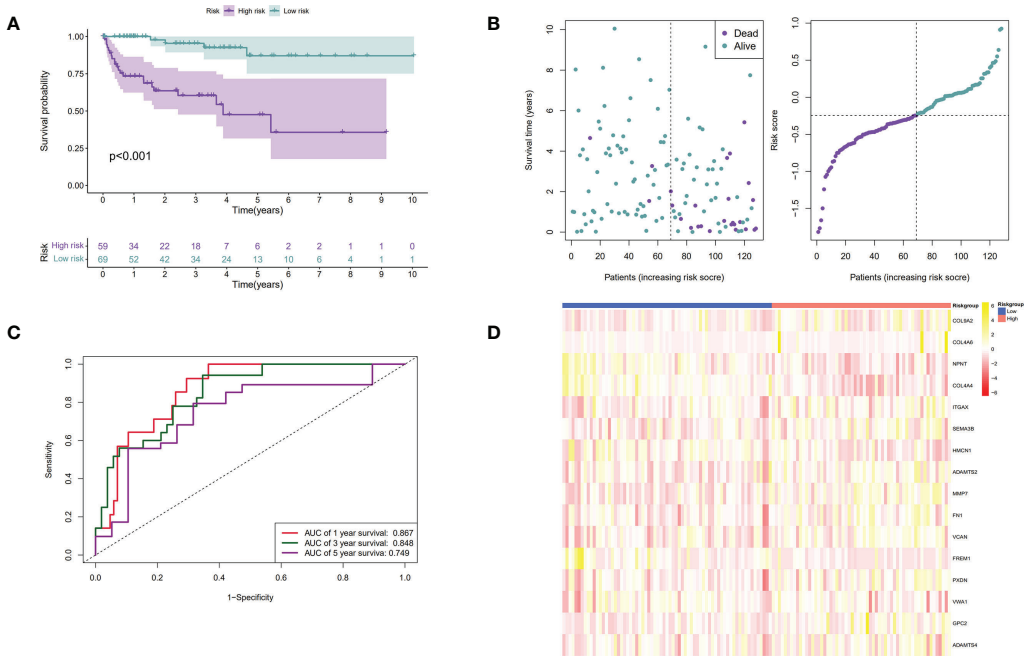

FIGURE 5
Verification of the prognostic signature by utilizing the GEO dataset. **(A).** The Kaplan-Meier curves of low-risk and high-risk ccRCC patients in the GEO dataset; **(B).** The time-dependent ROC curves displaying the 1-year, 3-year, and 5-year OS of ccRCC patients in the GEO dataset; **(C).** Survival distributions of the GEO dataset determined according to the median risk score; **(D).** Heatmap displaying the divergences between low and high-risk patients of 16 signature genes in the prognostic model for the GEO dataset.

involved in 108 DEGs (Figure 10A). In KEGG pathway analysis, the DEGs were primarily involved in pathways of protein digestion and absorption, PI3K/Akt signaling, focal adhesion, ECM–receptor interaction, and human papillomavirus infection (Figure 10B).

GSEA was carried out to investigate the specific molecular functions of the BM gene-based model. The PI3K/Akt signaling pathway, hepatitis C pathway, and estrogen signaling pathway exhibited significant enrichment for the high-risk group; whereas for the low-risk group, the adherens junction pathway, pentose and glucuronate interconversion pathway, glycine, serine, and threonine metabolism pathways, and ascorbate and aldarate metabolism pathways were enriched (Figure 11).

Analysis of the infiltration levels of immune cells based on the BM gene-based model

CIBERSORT, CIBERSORT-ABS, EPIC, MCPCOUNTER, QUANTISEQ, TIMER, and XCELL analyses were performed to explore the relationship between BM gene-based signatures and immune infiltration levels (Figure 12). Given the significance of immune checkpoints in immunotherapy, the mRNA levels of several immune checkpoint genes were compared between the two groups to explore possible immune checkpoint blocking therapies. The results showed that *LAG3*, *PDCD1*, *ICOS*, *TIGIT*, *CTLA4*, and *BTLA* mRNA levels were increased in high-risk patients, implying the existence of immunosuppressive phenotypes in these patients (Figure 13).

TIMER analysis

We explored the association of six immune cells with the 16 BM genes by employing the TIMER database and observed that *NPNT*, *COL4A6*, *ITGAX*, *HMCN1*, *ADAMTS2*, *FN1*, *VCAN*, and *PXDN* were positively associated with the levels of different immune cell infiltrations, such as those of CD4+ T cells, CD8+ T cells, B cells, dendritic cells, neutrophils, and macrophages. *COL9A2* and *ADAMTS4* were positively related to CD8+ T cells, CD4+ T cells, dendritic cells, neutrophils, and macrophages. *COL4A6* and *GPC2* exhibited positive correlations with CD4+ T cells, macrophages, neutrophils, and dendritic cells. In conclusion, these immune cells may be involved in the process of BM genes mediating ccRCC prognosis (Supplementary Figure 1; Figure 2).

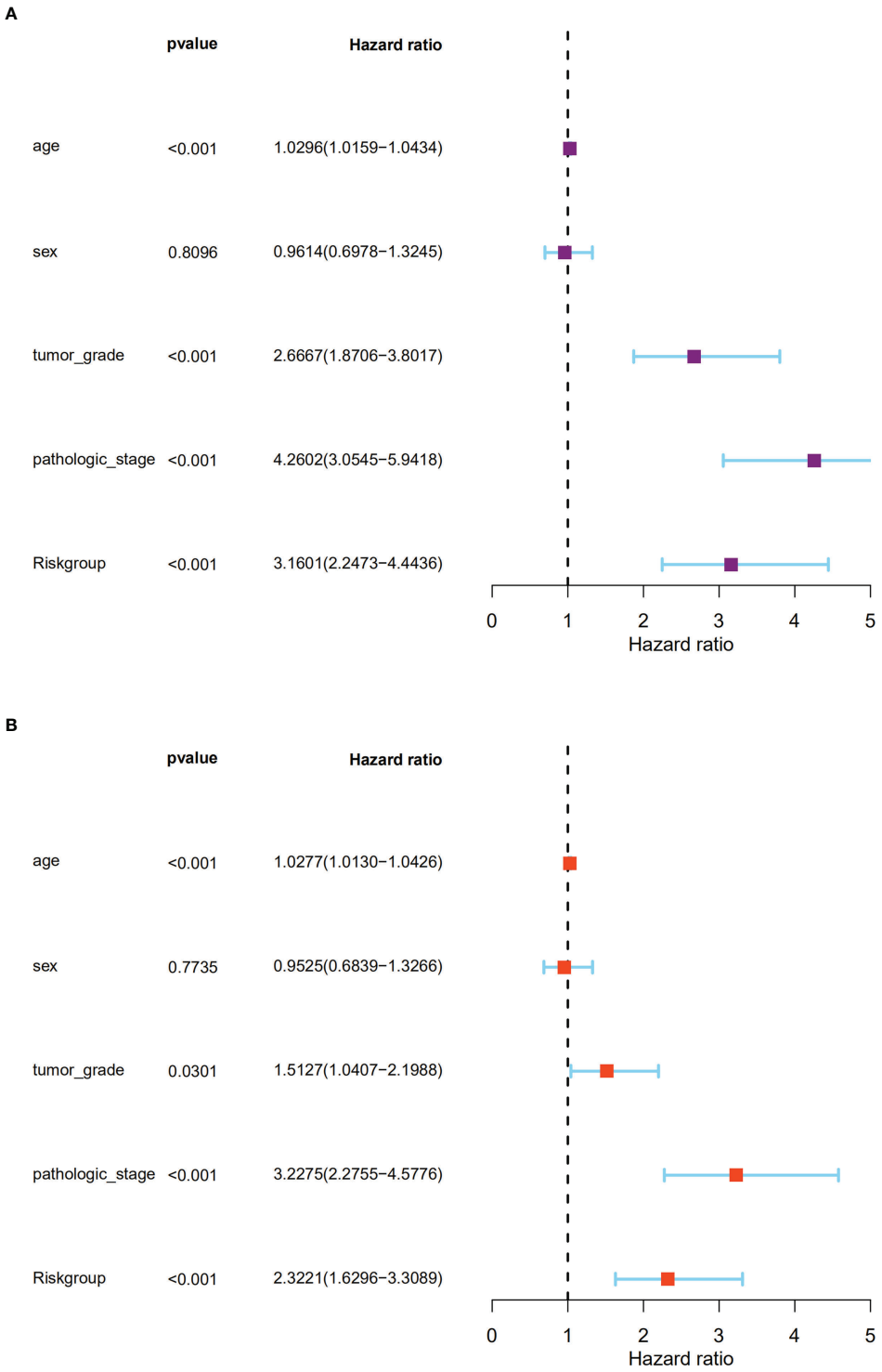

FIGURE 6
The signature could predict the prognosis of ccRCC patients in the TCGA dataset independently. **(A).** The univariate Cox regression analysis; **(B).** The multivariate Cox regression analyses showed the associations of the risk score predicting overall survival with clinicopathological indices.

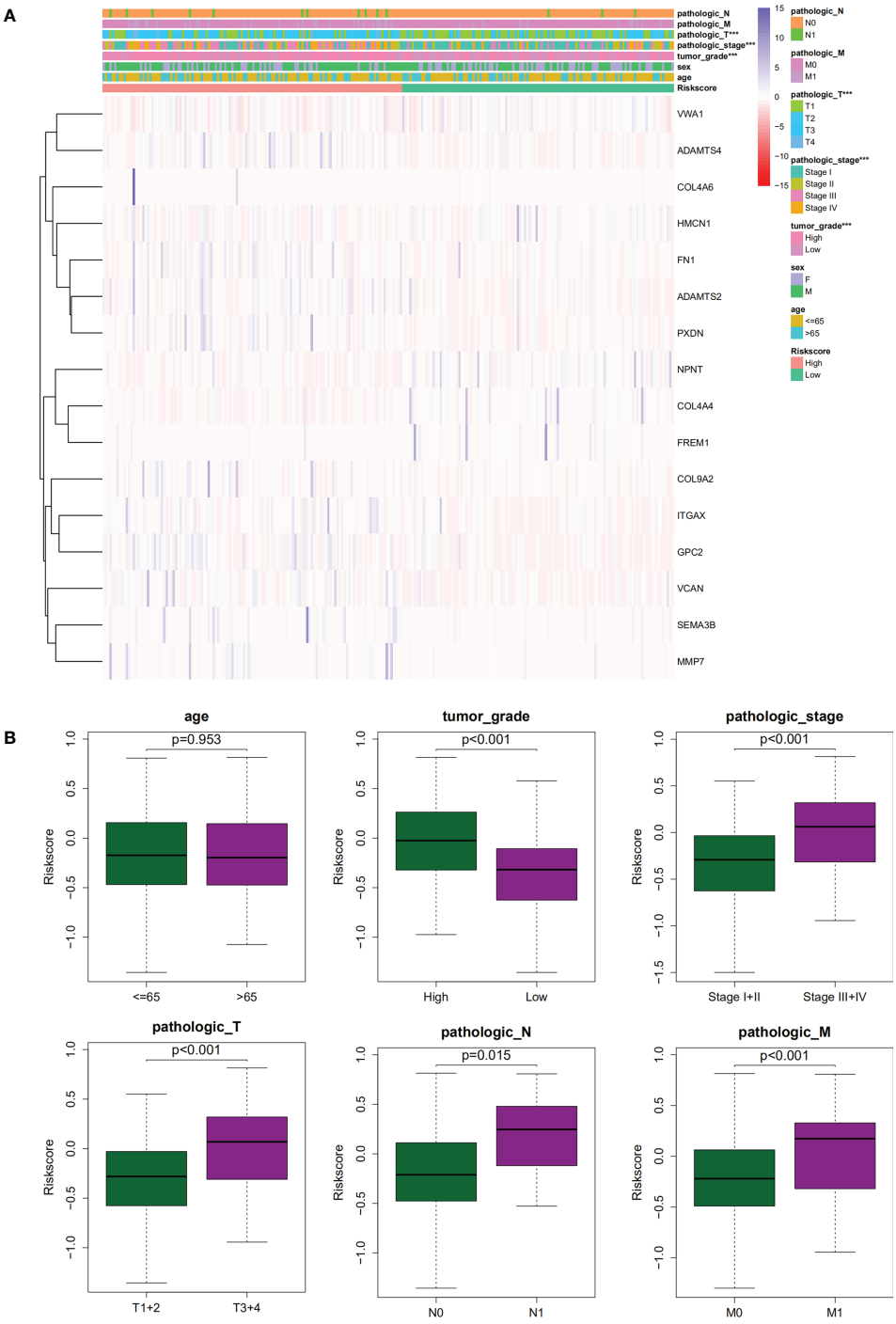

FIGURE 7
(A, B). The correlations between clinicopathological features and the gene signature.

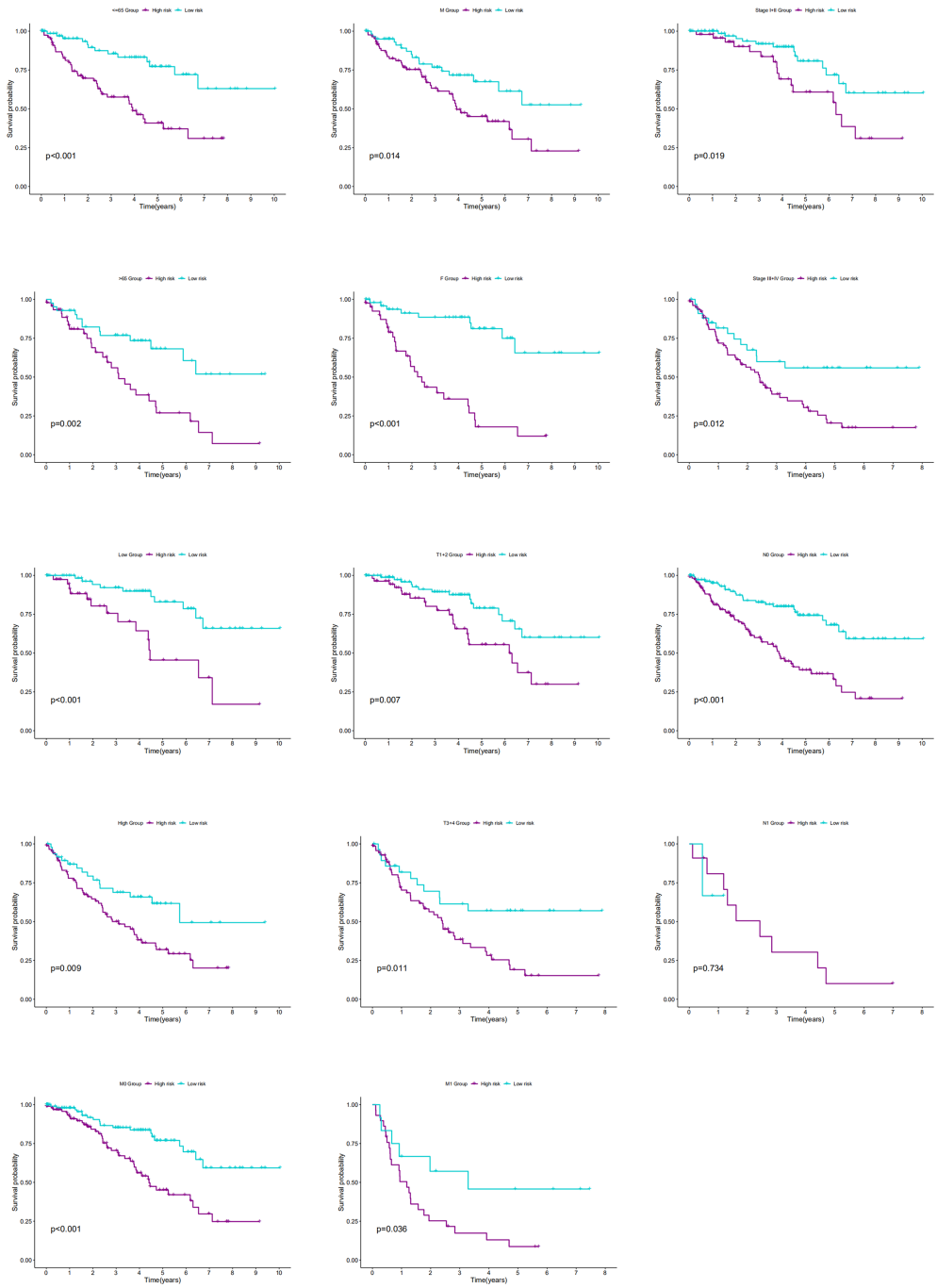

FIGURE 8
The K-M curves showed the differences of OS between low- and high-risk patients with different ages, genders, stages, T stages, N stages, M stages or grades.

Prediction of candidate drugs implicated with the differential expression of the signature genes

We identified candidate drugs related to the differential expression of BM genes using the DSigDB to further improve the therapeutic effect in patients with renal cell carcinoma. These drugs included Healon BOSS, CGS-27023A TTD 00002801, VANADIUM CTD 00006979, LAMININ BOSS, O-Phospho-L-tyrosine BOSS, Tetradioxin CTD 00006848, endosulfan CTD 00005896, and orphenadrine hydrochloride BOSS (Table 2). These small-molecule drugs exhibited a higher negative correlation and potential to treat ccRCC.

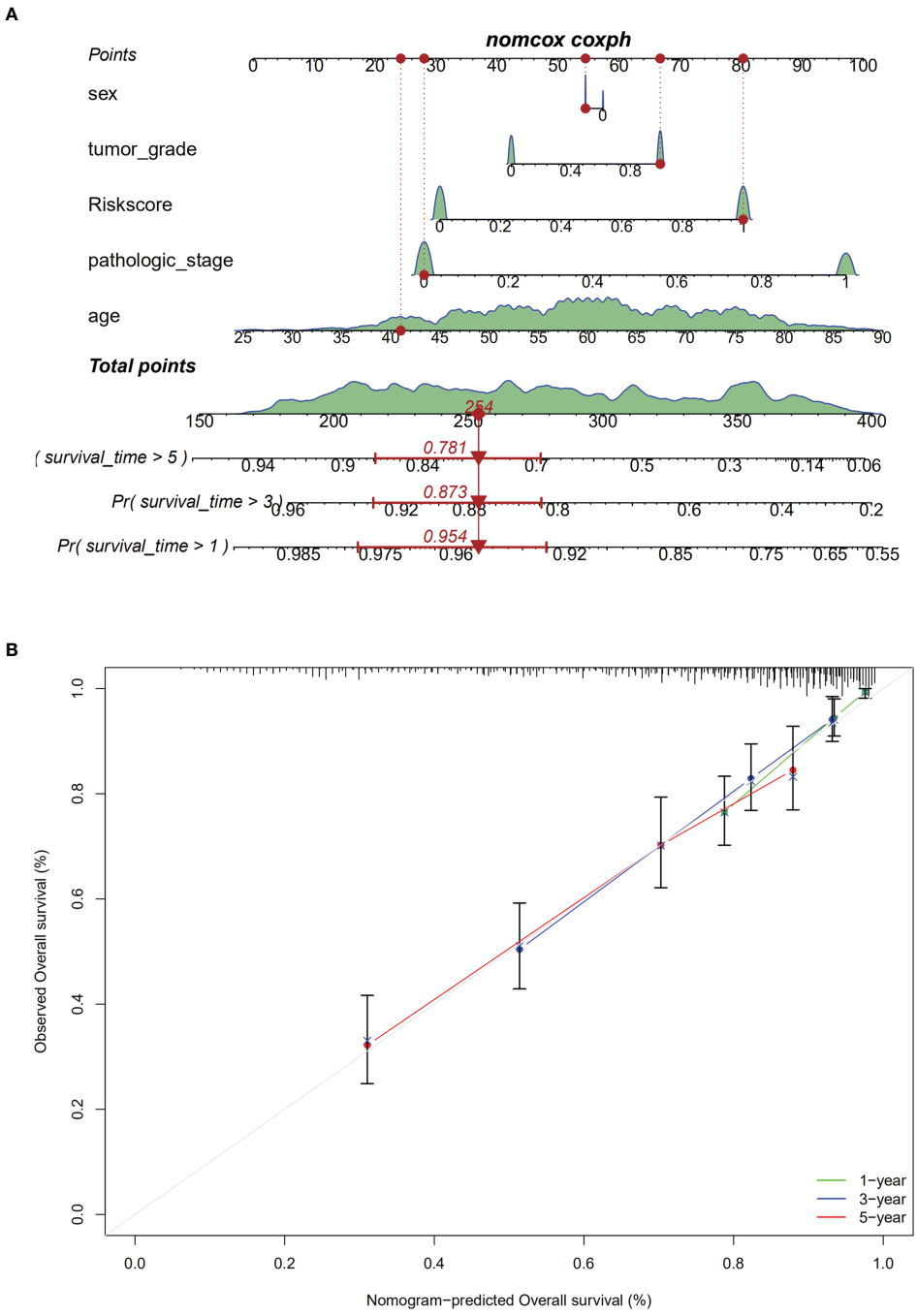

FIGURE 9
Establishment of the nomogram. **(A)**. The nomogram; **(B)**. calibration analysis for predicting1-, 3- or 5-year OS.

Discussion

Treating advanced RCC with drugs has always been a clinical challenge based on its resistance to traditional radiotherapy and chemotherapy (30). Despite the initial positive effects of emerging targeted therapies and immunotherapy in ccRCC patients, in most cases, patients develop drug resistance and disease progression within two years owing to the highly dynamic, adaptive, and heterogeneous tumor microenvironment of ccRCC (31). Therefore, research on tumor resistance and distant metastasis caused by changes in the tumor microenvironment environment may provide new strategies for ccRCC treatment. Previous

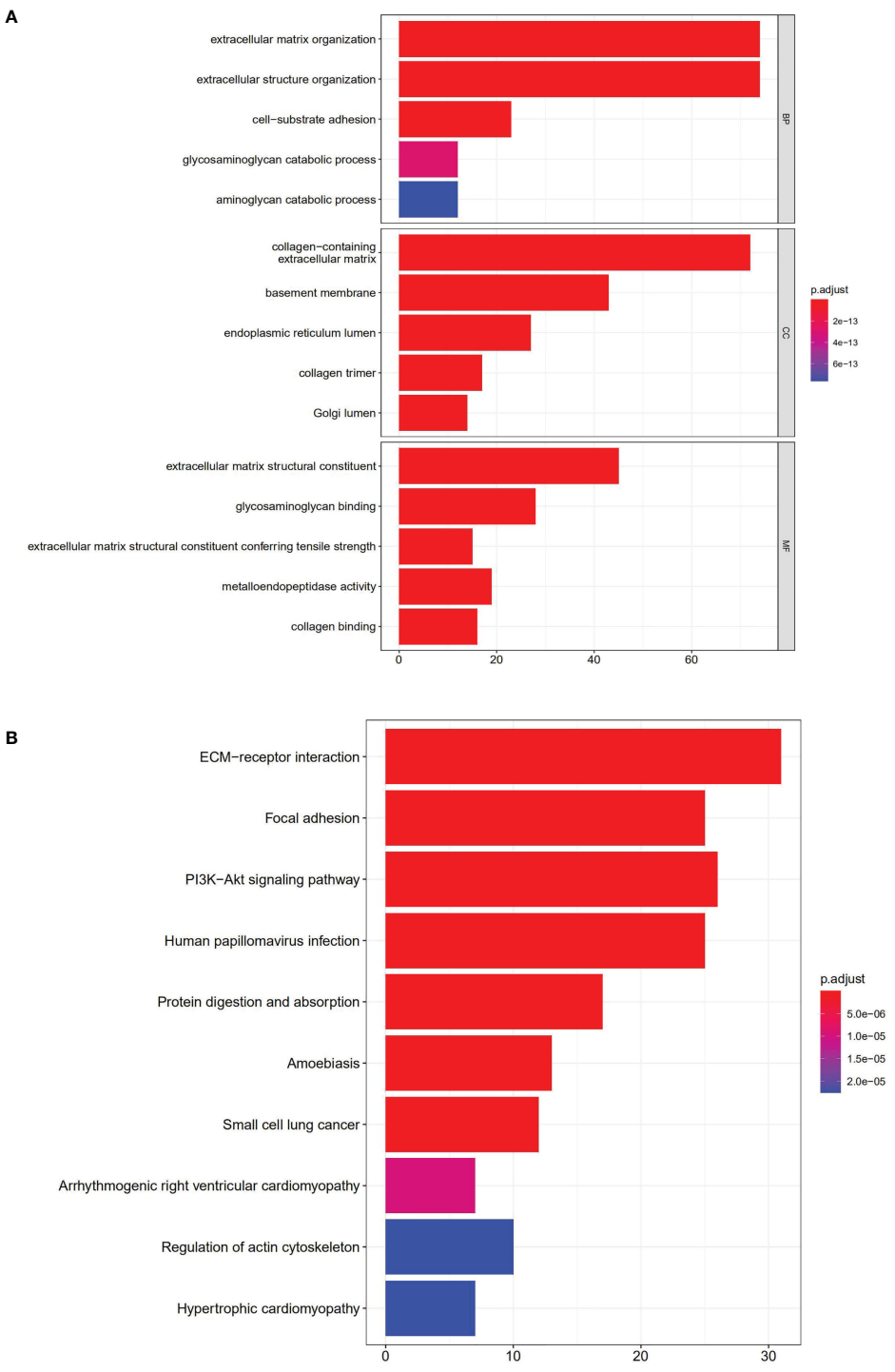

FIGURE 10
Enrichment analyses of DEGs. **(A).** GO enrichment analysis; **(B).** KEGG enrichment analysis.

research acknowledges BM remodeling as a critical step in the formation of the tumor microenvironment (32), which often results in complex disarray of pro- and anti-tumor signals from degradation products (33). Additionally, studies have demonstrated that most BM-related collagens are upregulated at the mRNA and protein levels, are associated with the formation of aggressive phenotypes of malignant cells and are involved in the regulation of key tumorigenesis steps, including proliferation,

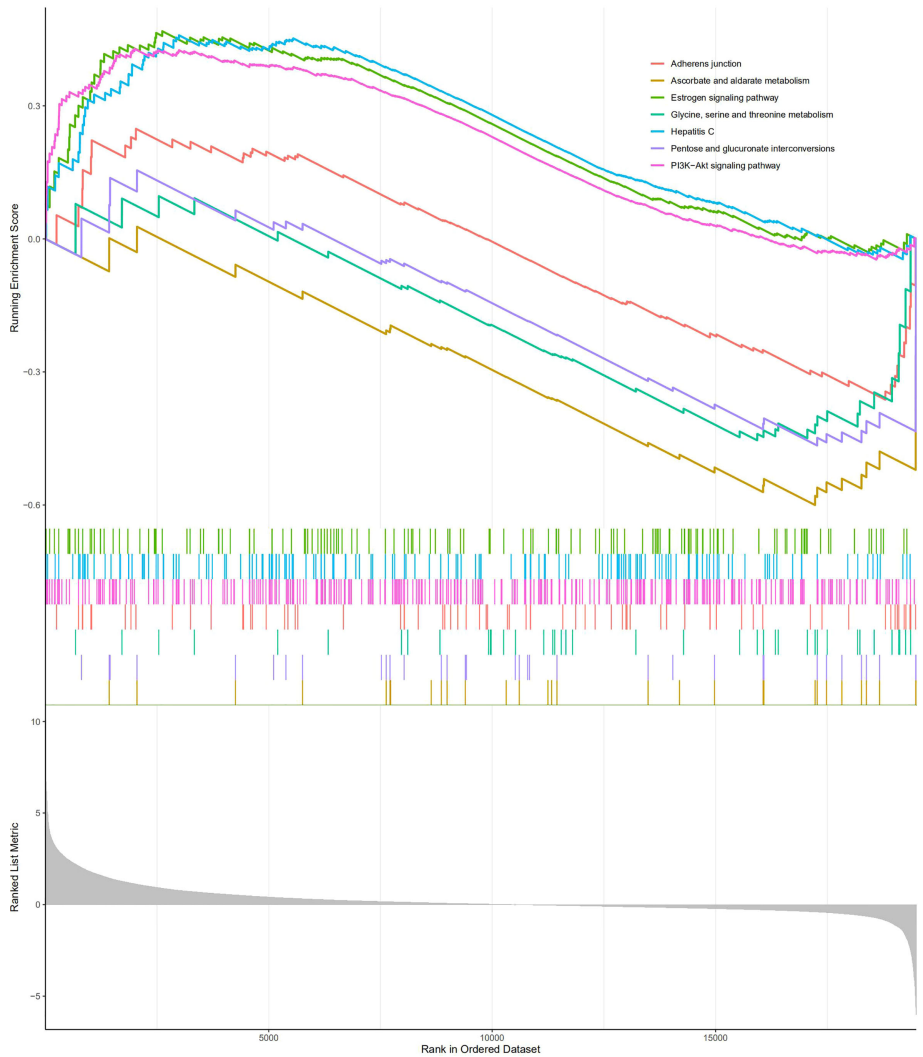

FIGURE 11
Gene Set Enrichment Analysis analysis.

invasion, metastasis, apoptosis, and angiogenesis (34–36). Therefore, BM may genes exert crucial effects on the formation of a highly heterogeneous tumor microenvironment in ccRCC and can serve as disease markers for prognosis and treatment effect prediction in patients with renal cancer.

A prognostic model was constructed that contains 16 BM genes, and its prognostic value for ccRCC was evaluated *via* ROC anlysis. Some of these genes are potentially related to ccRCC. For instance, MMP7 has been widely reported to promote tumor angiogenesis by transforming the extracellular matrix, thereby participating in the invasion and metastasis of ccRCC (37–39). A previous study identified SEMA3B as a renal tumor suppressor gene, whose downregulation was positively associated with tumor progression, stage, and grade of ccRCC (40). As a vital member of the BM gene family, *ITGAX* is responsible for encoding integrin alpha X, a critical component of leukocyte-specific complement receptor 4. Its expression in ccRCC has been reported to increase significantly, and ITGAX overexpression has association with dismal survival outcomes of ccRCC patients (41). Gong et al. recently reported that the *HMCN1* mutations are frequently detected in patients with ccRCC and are correlated with a higher tumor mutation burden and dismal clinical consequences, and may correlate with anti-tumor immunity and cell metabolism (42). In addition, *COL4A4* has been identified as an unfavorable prognostic factor for ccRCC (43). The functions of other genes in ccRCC currently remain unknown and require further exploration. Data from the TGGA and GSEA databases indicated that the BM gene signatures were positively correlated with a higher risk of adverse

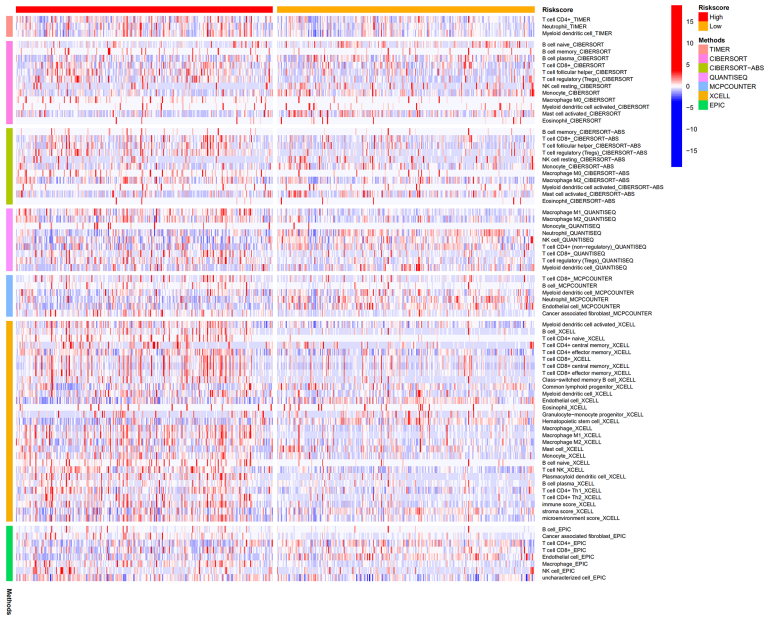

FIGURE 12
Differences in infiltration levels of immune cells between low- and high-risk patients.

TABLE 2 The eight candidate small molecule drugs predicted based on DSigDB.

Index	Name	p-value	Adjusted p-value	Odds Ratio	Combined Score
1	Healon BOSS	0.00000179	0.0007	59.68	789.76
2	CGS-27023A TTD 00002801	0.0000466	0.0095	259.39	2587.35
3	VANADIUM CTD 00006979	0.000211	0.0282	31.36	265.34
4	LAMININ BOSS	0.00048	0.0328	23.54	179.91
5	O-Phospho-L-tyrosine BOSS	0.000807	0.0438	55.83	397.64
6	Tetradioxin CTD 00006848	0.000936	0.0438	5.550	38.70
7	endosulfan CTD 00005896	0.001033676	0.0438	49.07	337.40
8	Orphenadrine hydrochloride BOSS	0.001175147	0.0438	45.90	309.68

OS. Meanwhile, the AUCs were all above 0.7 at 1, 3, and 5 years. These results indicated the admirable performance of our model for prognosis prediction.

According to KEGG pathway enrichment analysis, focal adhesions and ECM-receptor interactions were identified as the major pathways for 108 DEGs. These pathways further enriched the molecular mechanisms of ccRCC initiation and progression. GSEA revealed the involvement of BM gene-based models in tumor and metabolic pathways. These include the PI3K/Akt signaling, estrogen signaling, adherens junction, pentose and glucuronate interconversions, threonine, glycine and serine metabolism, and ascorbate and aldarate metabolism pathways. Therefore, the BM gene-based model may be crucial for cancer cell metabolism and tumor microenvironment formation.

Furthermore, the model had close association with immune cell infiltration, immune cells may be essential in BM genes mediating the prognosis of ccRCC. We also found higher expression levels of immune checkpoints in high-risk ccRCC patients, implying that the dismal prognosis of these patients is possibly due to the immunosuppressive microenvironment and may respond to treatment regimens involving checkpoint inhibitors. Finally, given that the signature BM genes we identified may be relevant therapeutic targets for patients with ccRCC, we sucessfully dentified eight potential small-molecule

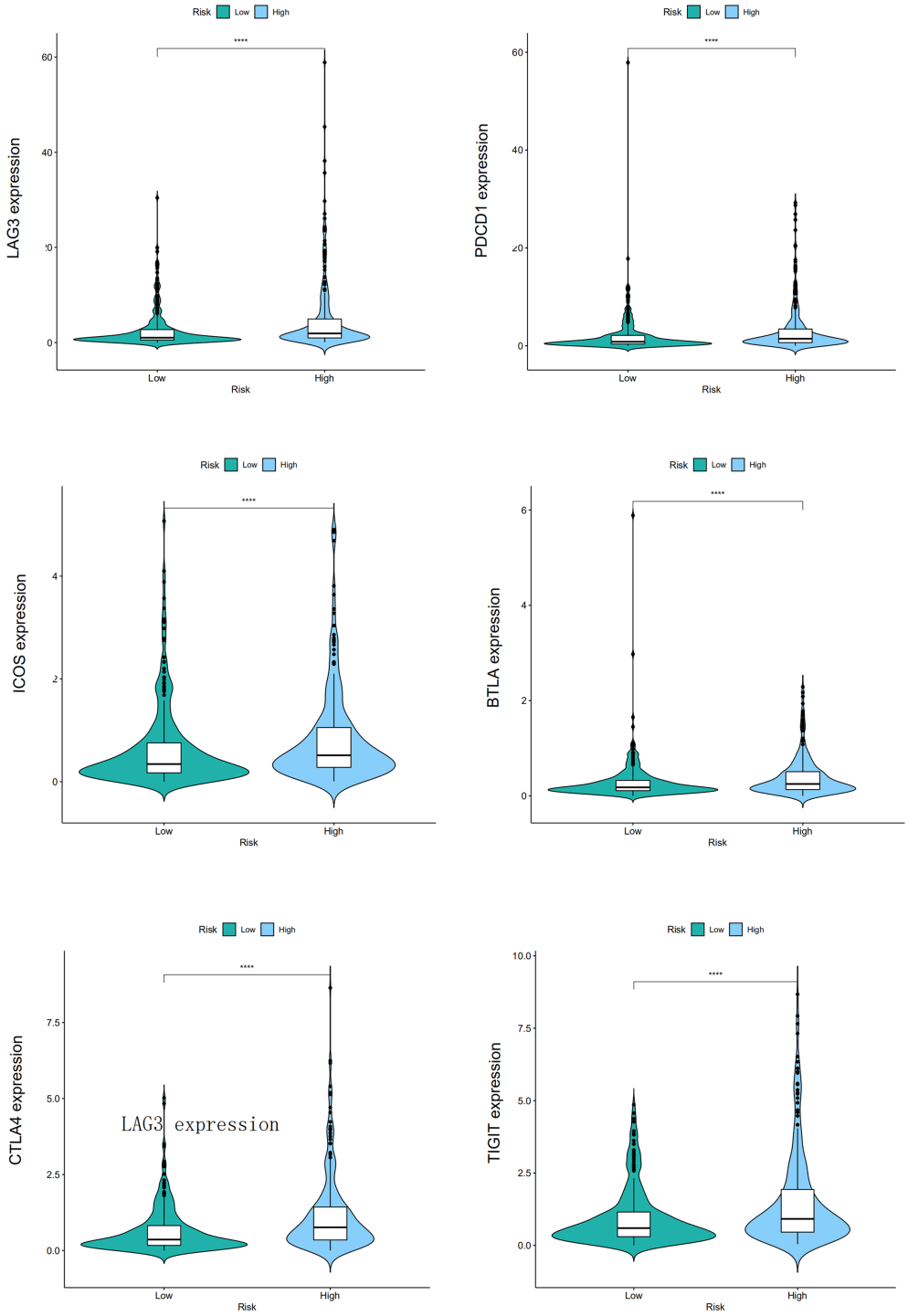

FIGURE 13
The different mRNA levels of immune checkpoint genes between low- and high-risk patients, and the "****" represents P < 0.0001.

drugs to further improve the therapeutic effect in patients with ccRCC.

Our work has certain limitations, such as predicting the prognostic value of BM genes using only data from public databases and the relatively small sample size. We could only determine how BM genes affect ccRCC based on limited clinical data, which ignored environmental and genetic factors. Finally, the underlying mechanism between the identified

signature genes and ccRCC remains unclear, and we plan to investigate this further.

In summary, this study comprehensively characterized the involvement of the BM gene family in ccRCC and its prognosis. We proposed trustworthy prognostic biomarkers for ccRCC patients and constructed a BM gene-based prognostic model. We believe this investigation could support further research on the role of BM genes in ccRCC.

Data availability statement

The original contributions presented in the study are included in the article/Supplementary Material. Further inquiries can be directed to the corresponding authors.

Ethics statement

The studies involving human participants were reviewed and approved by The Ethics Review Board of the First Affiliated Hospital of Anhui Medical University. Written informed consent for participation was not required for this study in accordance with the national legislation and the institutional requirements.

Author contributions

JT and XL conceived the experiments and performed the experiments and drafted the manuscript, CL provided supportive advice for the experiment, YL and JZ confirmed the authenticity of all the raw data and funded the research. All authors contributed to the article and approved the submitted version.

Funding

This work was supported by Natural Science Foundation of Anhui Province in China (No. 2108085MH295).

Conflict of interest

The authors declare that the research was conducted in the absence of any commercial or financial relationships that could be construed as a potential conflict of interest.

Publisher's note

Supplementary material

The Supplementary Material for this article can be found online at: https://www.frontiersin.org/articles/10.3389/fonc.2022.1026331/full#supplementary-material

References

1. Sung H, Ferlay J, Siegel RL, Laversanne M, Soerjomataram I, Jemal A, et al. Global cancer statistics 2020: GLOBOCAN estimates of incidence and mortality worldwide for 36 cancers in 185 countries. *CA Cancer J Clin* (2021) 71(3):209–49. doi: 10.3322/caac.21660

2. Escudier B, Porta C, Schmidinger M, Rioux-Leclercq N, Bex A, Khoo V, et al. Renal cell carcinoma: ESMO clinical practice guidelines for diagnosis, treatment and follow-updagger. *Ann Oncol* (2019) 30(5):706–20. doi: 10.1093/annonc/mdz056

3. Klatte T, Rossi SH, Stewart GD. Prognostic factors and prognostic models for renal cell carcinoma: a literature review. *World J Urol* (2018) 36(12):1943–52. doi: 10.1007/s00345-018-2309-4

4. Barata PC, Rini BI. Treatment of renal cell carcinoma: Current status and future directions. *CA Cancer J Clin* (2017) 67(6):507–24. doi: 10.3322/caac.21411

5. Atkins MB, Tannir NM. Current and emerging therapies for first-line treatment of metastatic clear cell renal cell carcinoma. *Cancer Treat Rev* (2018) 70:127–37. doi: 10.1016/j.ctrv.2018.07.009

6. Wiechno P, Kucharz J, Sadowska M, Michalski W, Sikora-Kupis B, Jonska-Gmyrek J, et al. Contemporary treatment of metastatic renal cell carcinoma. *Med Oncol* (2018) 35(12):156. doi: 10.1007/s12032-018-1217-1

7. Jayadev R, Sherwood DR. Basement membranes. *Curr Biol* (2017) 27(6): R207–11. doi: 10.1016/j.cub.2017.02.006

8. Pozzi A, Yurchenco PD, Iozzo RV. The nature and biology of basement membranes. *Matrix Biol* (2017) 57–58:1–11. doi: 10.1016/j.matbio.2016.12.009

9. Yurchenco PD. Basement membranes: cell scaffoldings and signaling platforms. *Cold Spring Harb Perspect Biol* (2011) 3(2):a004911. doi: 10.1101/cshperspect.a004911

10. Jayadev R, Chi Q, Keeley DP, Hastie EL, Kelley LC, Sherwood DR. Alpha-integrins dictate distinct modes of type IV collagen recruitment to basement membranes. *J Cell Biol* (2019) 218(9):3098–116. doi: 10.1083/jcb.201903124

11. Li S, Qi Y, McKee K, Liu J, Hsu J, Yurchenco PD. Integrin and dystroglycan compensate each other to mediate laminin-dependent basement membrane assembly and epiblast polarization. *Matrix Biol* (2017), 57–58:272–84. doi: 10.1016/j.matbio.2016.07.005

12. Sherwood DR. Basement membrane remodeling guides cell migration and cell morphogenesis during development. *Curr Opin Cell Biol* (2021) 72:19–27. doi: 10.1016/j.ceb.2021.04.003

13. Nystrom A, Bornert O, Kuhl T. Cell therapy for basement membrane-linked diseases. *Matrix Biol* (2017) 57–58:124–39. doi: 10.1016/j.matbio.2016.07.012

14. Naba A, Clauser KR, Whittaker CA, Carr SA, Tanabe KK, Hynes RO. Extracellular matrix signatures of human primary metastatic colon cancers and their metastases to liver. *BMC Cancer* (2014) 14:518. doi: 10.1186/1471-2407-14-518

15. Randles M, Lausecker F, Kong Q, Suleiman H, Reid G, Kolatsi-Joannou M, et al. Identification of an altered matrix signature in kidney aging and disease. *J Am Soc Nephrol* (2021) 32(7):1713–32. doi: 10.1681/ASN.2020101442

16. To M, Goz A, Camenzind L, Oertle P, Candiello J, Sullivan M, et al. Diabetes-induced morphological, biomechanical, and compositional changes in ocular basement membranes. *Exp Eye Res* (2013) 116:298–307. doi: 10.1016/j.exer.2013.09.011

17. Ma JB, Bai JY, Zhang HB, Gu L, He D, Guo P. Downregulation of collagen COL4A6 is associated with prostate cancer progression and metastasis. *Genet Test Mol Biomarkers* (2020) 24(7):399–408. doi: 10.1089/gtmb.2020.0009

18. Magnussen SN, Toraskar J, Wilhelm I, Hasko J, Figenschau SL, Molnar J, et al. Nephronectin promotes breast cancer brain metastatic colonization *via* its integrin-binding domains. *Sci Rep* (2020) 10(1):12237. doi: 10.1038/s41598-020-69242-1

19. Huang L, Guan S, Feng L, Wei J, Wu L. Integrated analysis identified NPNT as a potential key regulator in tumor metastasis of hepatocellular carcinoma. *Gene* (2022) 825:146436. doi: 10.1016/j.gene.2022.146436

20. Zheng YZ, Liang L. High expression of PXDN is associated with poor prognosis and promotes proliferation, invasion as well as migration in ovarian cancer. *Ann Diagn Pathol* (2018) 34:161–5. doi: 10.1016/j.anndiagpath.2018.03.002

21. Binder MJ, McCoombe S, Williams ED, McCulloch DR, Ward AC. ADAMTS-15 has a tumor suppressor role in prostate cancer. *Biomolecules* (2020) 10(5):682. doi: 10.3390/biom10050682

22. de Assis Lima M, da Silva SV, Serrano-Garrido O, Hulsemann M, Santos-Neres L, Rodriguez-Manzaneque JC, et al. Metalloprotease ADAMTS-1 decreases cell migration and invasion modulating the spatiotemporal dynamics of Cdc42 activity. *Cell Signal* (2021) 77:109827. doi: 10.1016/j.cellsig.2020.109827

23. Wang B, Chen S, Zhao JQ, Xiang BL, Gu X, Zou F, et al. ADAMTS-1 inhibits angiogenesis *via* the PI3K/Akt-eNOS-VEGF pathway in lung cancer cells. *Transl Cancer Res* (2019) 8(8):2725–35. doi: 10.21037/tcr.2019.10.34

24. Jayadev R, Morais M, Ellingford JM, Srinivasan S, Naylor RW, Lawless C, et al. A basement membrane discovery pipeline uncovers network complexity, regulators, and human disease associations. *Sci Adv* (2022) 8(20):eabn2265. doi: 10.1126/sciadv.abn2265

25. Phipson B, Lee S, Majewski IJ, Alexander WS, Smyth GK. Robust hyperparameter estimation protects against hypervariable genes and improves power to detect differential expression. *Ann Appl Stat* (2016) 10(2):946–63. doi: 10.1214/16-AOAS920

26. Engebretsen S, Bohlin J. Statistical predictions with glmnet. *Clin Epigenetics* (2019) 11(1):123. doi: 10.1186/s13148-019-0730-1

27. Huang R, Liao X, Li Q. Identification and validation of potential prognostic gene biomarkers for predicting survival in patients with acute myeloid leukemia. *Onco Targets Ther* (2017) 10:5243–54. doi: 10.2147/OTT.S147717

28. Heagerty PJ, Zheng Y. Survival model predictive accuracy and ROC curves. *Biometrics* (2005) 61(1):92–105. doi: 10.1111/j.0006-341X.2005.030814.x

29. Yu G, Wang LG, Han Y, He QY. clusterProfiler: an r package for comparing biological themes among gene clusters. *OMICS* (2012) 16(5):284–7. doi: 10.1089/omi.2011.0118

30. Meng J, Gao L, Zhang M, Gao S, Fan S, Liang C. Systematic investigation of the prognostic value of cell division cycle-associated proteins for clear cell renal cell carcinoma patients. *biomark Med* (2020) 14(3):223–38. doi: 10.2217/bmm-2019-0498

31. Lai Y, Tang F, Huang Y, He C, Chen C, Zhao J, et al. The tumour microenvironment and metabolism in renal cell carcinoma targeted or immune therapy. *J Cell Physiol* (2021) 236(3):1616–27. doi: 10.1002/jcp.29969

32. Pramanik D, Jolly MK, Bhat R. Matrix adhesion and remodeling diversifies modes of cancer invasion across spatial scales. *J Theor Biol* (2021) 524:110733. doi: 10.1016/j.jtbi.2021.110733

33. Nissen NI, Karsdal M, Willumsen N. Collagens and cancer associated fibroblasts in the reactive stroma and its relation to cancer biology. *J Exp Clin Cancer Res* (2019) 38(1):115. doi: 10.1186/s13046-019-1110-6

34. Bager CL, Willumsen N, Leeming DJ, Smith V, Karsdal MA, Dornan D, et al. Collagen degradation products measured in serum can separate ovarian and breast cancer patients from healthy controls: A preliminary study. *Cancer biomark* (2015) 15(6):783–8. doi: 10.3233/CBM-150520

35. Kehlet SN, Sanz-Pamplona R, Brix S, Leeming DJ, Karsdal MA, Moreno V. Excessive collagen turnover products are released during colorectal cancer progression and elevated in serum from metastatic colorectal cancer patients. *Sci Rep* (2016) 6:30599. doi: 10.1038/srep30599

36. Leeming DJ, Koizumi M, Qvist P, Barkholt V, Zhang C, Henriksen K, et al. Serum n-terminal propeptide of collagen type I is associated with the number of bone metastases in breast and prostate cancer and correlates to other bone related markers. *biomark Cancer* (2011) 3:15–23. doi: 10.4137/BIC.S6484

37. Li L, Wang LX, Xu GL, Yang F, Gao QL, Niu H, et al. Bio-informatics analysis of renal carcinoma gene matrix metalloproteinase-7. *Indian J Cancer* (2016) 53(1):13–8. doi: 10.4103/0019-509X.180835

38. Lu H, Yang Z, Zhang H, Gan M, Zhou T, Wang S. The expression and clinical significance of matrix metalloproteinase 7 and tissue inhibitor of matrix metalloproteinases 2 in clear cell renal cell carcinoma. *Exp Ther Med* (2013) 5 (3):890–6. doi: 10.3892/etm.2012.859

39. Sarkissian G, Fergelot P, Lamy PJ, Patard JJ, Culine S, Jouin P, et al. Identification of pro-MMP-7 as a serum marker for renal cell carcinoma by use of proteomic analysis. *Clin Chem* (2008) 54(3):574–81. doi: 10.1373/clinchem.2007.090837

40. Loginov VI, Dmitriev AA, Senchenko VN, Pronina IV, Khodyrev DS, Kudryavtseva AV, et al. Tumor suppressor function of the SEMA3B gene in human lung and renal cancers. *PloS One* (2015) 10(5):e0123369. doi: 10.1371/journal.pone.0123369

41. Sui Y, Lu K, Fu L. Prediction and analysis of novel key genes ITGAX, LAPTM5, SERPINE1 in clear cell renal cell carcinoma through bioinformatics analysis. *PeerJ* (2021) 9:e11272. doi: 10.7717/peerj.11272

42. Gong Z, Wu X, Guo Q, Du H, Zhang F, Kong Y. Comprehensive analysis of HMCN1 somatic mutation in clear cell renal cell carcinoma. *Genes (Basel)* (2022) 13(7):1282. doi: 10.3390/genes13071282

43. Tu B, Zhang Y, Jia Y, Wei L, Gao F, Sha Q, et al. Prognostic values of COL4As transcriptional expressions in clear cell renal cell carcinoma patients. *Comb Chem High Throughput Screen* (2022) 25. doi: 10.2174/1386207325666220707113100

frontiers | Frontiers in Oncology

TYPE Original Research
PUBLISHED 31 October 2022
DOI 10.3389/fonc.2022.1008714

OPEN ACCESS

EDITED BY
Linhui Wang,
Second Military Medical University, China

REVIEWED BY
Raj Sewduth,
VIB KU Leuven Center for Cancer Biology, Belgium
Lisha Mou,
Shenzhen Second People's Hospital, China

*CORRESPONDENCE
Fan Cheng
urology1969@aliyun.com
Yuan Ruan
10733638@qq.com

†These authors have contributed equally to this work and share first authorship

SPECIALTY SECTION
This article was submitted to Genitourinary Oncology, a section of the journal Frontiers in Oncology

RECEIVED 01 August 2022
ACCEPTED 04 October 2022
PUBLISHED 31 October 2022

CITATION
Zheng D, Ning J, Xia Y, Ruan Y and Cheng F (2022) Comprehensive analysis of a homeobox family gene signature in clear cell renal cell carcinoma with regard to prognosis and immune significance. *Front. Oncol.* 12:1008714. doi: 10.3389/fonc.2022.1008714

Comprehensive analysis of a homeobox family gene signature in clear cell renal cell carcinoma with regard to prognosis and immune significance

Di Zheng†, Jinzhuo Ning†, Yuqi Xia, Yuan Ruan* and Fan Cheng*

Department of Urology, Renmin Hospital of Wuhan University, Wuhan, China

The homeobox (HOX) family genes have been linked to multiple types of tumors, while their effect on malignant behaviors of clear cell renal cell carcinoma (ccRCC) and clinical significance remains largely unknown. Here, we comprehensively analyzed the expression profiles and prognostic value of HOX genes in ccRCC using datasets from The Cancer Genome Atlas (TCGA) and International Cancer Genome Consortium (ICGC) databases. We developed a prognostic signature comprising eight HOX genes (*HOXB1*, *HOXA7*, *HOXB5*, *HOXD8*, *HOXD9*, *HOXB9*, *HOXA9*, and *HOXA11*) for overall survival prediction in ccRCC and it allowed patients to be subdivided into high- and low-risk groups. Kaplan-Meier survival analysis in all the internal and external cohorts revealed significant difference in clinical outcome of patients in different risk groups, indicating the satisfactory predictive power of the signature. Additionally, we constructed a prognostic nomogram by integrating signature-derived risk score and clinical factors such as gender, age, T and M status, which might be helpful for clinical decision-making and designing tailored management schedules. Immunological analysis revealed that the regulatory T cells (Tregs) infiltrated differently between the two subgroups in both TCGA and ICGC cohorts. ssGSEA method showed that the enrichment scores for mast cells were significantly lower in high-risk group compared with the low-risk group, which was consistent in both TCGA and ICGC cohorts. As for the related immune function, the enrichment scores of APC co-inhibition, para-inflammation, and type II IFN response were consistently lower in high-risk group in both cohorts. Of the eight HOX genes, the mRNA and protein levels of HOXD8 were downregulated in ccRCC than that in normal tissues, and decreased expression of HOXD8 was associated with increased tumor grade and stage, and lymph node metastasis. Survival analysis revealed that lower expression of *HOXD8* predicted worse overall survival in ccRCC. In conclusion, our HOX gene-based signature was a favorable indicator to predict the prognosis of ccRCC cases and associated

10.3389/fonc.2022.1008714

with immune cell infiltration. *HOXD8* might be a tumor suppressor gene in ccRCC and a potential predictor of tumor progression.

KEYWORDS

homeobox family gene, signature, prognosis, immune microenvironment, ccRCC

Introduction

Renal cell carcinoma (RCC) is a common malignancy affecting urinary system, with a worldwide incidence rate growing 2% annual (1, 2). Clear cell renal cell carcinoma (ccRCC), characterized by robust lipid and glycogen accumulation, is the most frequent histological subtype of RCC, accounting for eighty to ninety percentage of all RCC cases. As one of the most lethal malignancies of the urological system, ccRCC is known for its high mortality rate and it causes around 175000 deaths per year worldwide (3). Early diagnosis and surgical resection could effectively improve clinical outcome for localized ccRCC, while approximately 30% of patients have developed metastasis when they are first diagnosed (4, 5). Besides, about 30%-35% ccRCC patients showed local recurrence or distant metastasis after nephrectomy (6). For relapsed or advanced RCC, patients typically undergo surgery and/or receive systemic therapy. Cytoreductive nephrectomy before systemic therapy is recommended in select patients with a potentially surgically resectable primary tumor mass (7). Patients with metastatic RCC who present with hematuria or other symptoms related to the primary tumor should be offered palliative nephrectomy if they are surgical candidates (7). Targeted therapy including tyrosine kinase inhibitors (TKIs; e.g., axitinib, cabozantinib, lenvatinib), and/or anti-VEGF antibodies are wildly used in first- and second-line treatments. The immune checkpoint inhibitors (ICIs; e.g., pembrolizumab, nivolumab) therapy, a method that can improve body's anticancer immune response by regulating the activity of immune cells, provided a revolution in treatment options and have also been increasingly recommended and investigated (8). According to the NCCN guidelines for kidney cancer, combination of TKI with ICI, including axitinib with pembrolizumab, cabozantinib with nivolumab, and lenvatinib with pembrolizumab, were regarded as first-line preferred regimens for relapsed or advanced ccRCC (7). Nevertheless, due to the extensive heterogeneity in genomic level and the existence of a highly heterogeneous tumor microenvironment, prediction patients' respond to these therapies remains a fundamental problem and patients' prognosis varies even they share similar clinicopathological features and are under standard management. Exploring novel and reliable indicators to predict prognosis and response to therapies are of great importance for developing tailored management schedules and clinical decision-making, which may assist improving the prognosis of ccRCC patients.

The homeobox (HOX) genes encode a highly conserved family of transcription factors in mammal that are essential for organogenesis and development (9). Up to now, a total of thirty-nine HOX genes have been identified in human genome. On the basis of sequence similarity and chromosomal location, HOX genes are split into four clusters, namely HOXA, HOXB, HOXC, and HOXD, which are located on chromosomes 7, 17, 12, and 2, respectively (10). Over the past decades, we have come to discovered that many genes controlling embryogenesis such as HOX genes participate in carcinogenesis likewise (11). Apart from their role as master regulators of embryonic development in physiological status, HOX genes have been linked to multiple types of tumors (12–14). Altered expression of HOX genes were oncogenes or tumor suppressor genes by acting as transcription activator or transcriptional repressor, depending on context. In tumors, the deregulation of HOX genes may affect cell proliferation, invasion, differentiation, angiogenesis, and intracellular signal transduction (15–17). For example, higher HOXB9 expression was associated with poorer prognosis in adrenocortical carcinoma and simultaneous overexpression of HOXB9 and Ctnnb1 in adrenal cortex of transgenic mice led to larger adrenal tumors (18). In gastric cancer, the upregulated HOXA10 promoted the transcription of TGFB2, which triggered the activation of TGFβ/SMAD signaling and led to accelerated lung metastasis (19). In ccRCC, little is known about the role of HOX genes on malignant behaviors and its clinical significance.

The rapid development of high-throughput sequencing technology and bioinformatic methods has permitted their widespread application in cancer research, resulting in a comprehensive understanding of genetic or epigenetic abnormalities during carcinogenesis and progression (20, 21). Many of these abnormalities were confirmed to be potential therapeutic targets and prognosis indicators in multiple types of cancers in the later research. Recently, re-analyzing publicly available statistics such as RNA-Seq data from public databases has opened the door to the discovery of novel biomarker molecules, particularly certain gene families, for overall survival prediction in cancers (22, 23). In this study, using the transcriptome data of ccRCC sample and corresponding clinical

information from public databases, we systematically analyzed the expression profiles and prognostic value of HOX genes in ccRCC. We developed an eight HOX gene-based signature for overall survival prediction and validated its accuracy in both internal and external cohorts. Additionally, we constructed a prognostic nomogram by integrating the signature-derived risk score and clinical parameters such as gender, age, T and M status for clinical decision-making. Moreover, we analyzed the association of the signature with immune microenvironment and distinct immune cell infiltration in ccRCC. Finally, we compared the expression of the eight HOX gene in tumor and adjacent normal tissues, and performed Kaplan-Meier survival analysis in ccRCC cohorts.

Materials and methods

Data sources

We downloaded transcriptome profiles (HTSeq-FPKM) of 539 ccRCC tumor tissues and 72 non-tumor tissues, and corresponding clinical information of ccRCC patients from the TCGA database (https://portal.gdc.cancer.gov/) and named as TCGA cohort. The ICGC cohort containing gene expression matrix files and clinical data was obtained from the ICGC database (https://dcc.icgc.org/projects) and was utilized for external validation. Patients without overall survival time or survival status were excluded in the subsequent analysis. Finally, a total of 621 ccRCC including 530 cases from TCGA cohort and 91 cases from ICGC cohort was collected in our study.

Construction and validation of the HOX family gene-based signature

First, we randomly split the TCGA cohort (entire cohort) into a training cohort and a testing cohort at a ratio of roughly 1:1. To reduce overfitting, in the training cohort, differentially expressed HOX family genes were submitted to LASSO (least absolute shrinkage and selection operator) Cox regression analysis with the *glmnet* package in R. Following that, a multivariate Cox regression analysis was carried out, which resulted in the development of a HOX family gene-based signature in ccRCC. The risk score derived from the signature was calculated by a liner combination of gene expression level (Expi) and associated coefficients (Coefi), with the formula:riskscore = $\sum_{i=1}^{n}(Coefi*Expi)$. We computed the risk score of all the cases in training, testing, entire, and ICGC cohorts, and it allowed patients to be classified as high- or low-risk based on the median risk score value in training cohort. Finally, Kaplan-Meier survival analysis and time-dependent receiver operating characteristic (ROC) curves analysis were used to determine the signature' predictive power in training, testing, entire, and ICGC cohorts.

Construction of a prognostic nomogram

Integrating the signature-derived risk score and clinical factors such as gender, age, T and M status, a prognostic nomogram was built by using *rms* package in R. Calibration curves were plotted in TCGA and ICGC cohorts to evaluate whether the nomogram's predicted overall survival of ccRCC patients was close to the actual clinical outcome.

Functional annotation and gene set enrichment analysis

Using the *edgeR* package in R software, we first identified genes that were differently expressed across high- and low-risk groups, with the criterion of FDR<0.05 and |log2FC| >0.5. Subsequently, these differentially expressed genes (DEGs) were subjected to Gene ontology (GO) and Kyoto Encyclopedia of Genes and Genomes (KEGG) enrichment analyses using DAVID online tool (https://david.ncifcrf.gov/), and a *P*. value less than 0.05 was considered as significantly enriched. Gene set enrichment analysis was conducted using the GSEA software (version 4.0.2) to unearth the underlying signaling pathways associated with the signature based on the KEGG terms. *P*. value<0.05 and |NES| >1 was set as the screening criterion of the enrichment results, and the results were visualized using *ggplot2* package in R.

Evaluation of immune cell infiltration and immune function

The CIBERSORT algorithm was used to calculate the proportion of infiltrated immune cells in ccRCC samples based on gene expression matrixes (24, 25), and the abundance of 22 infiltrated immune cell types were then compared between high- and low-risk groups. Using the *GSVA* package in R, single-sample gene set enrichment analysis (ssGSEA) was applied to determine the enrichment scores of immune cells and associated immunological activities, which were then compared across high- and low-risk groups.

Tissue collection

A total of 20 frozen tissue samples including 10 ccRCC tissues and 10 adjacent normal tissues were collected in Renmin hospital of Wuhan university between August 2020 and June 2022. All the samples were harvest after resection and stored at -80°C. The experiment with patient tissue specimens was authorized by the Ethics Committee of Renmin Hospital of Wuhan University.

RNA isolation and qRT-PCR

RNA isolation and quantitative real-time PCR (qRT-PCR) were performed as previously described (26). The primer sequences were list as follow: *GAPDH*, forward, 5'-CCATCTTCCAGGAGCGAGAT-3' and reverse, 5'-TGAGTCCTTCCACGATACCA-3'; *HOXD8*, 5'-CACAAGCTCCTGGTAGACGA-3' and reverse, 5'-GCTCTGTCTTCCTCCAGCTC-3'.

Statistical analysis

R software (version 4.1.0) was employed to conduct all the statistical analyses and was utilized for visualization of the results. Kaplan-Meier method and the log-rank test was used to compare the difference in overall survival between risk groups. Differences of multiple variables between risk groups were assessed using Student's *t*-test or Wilcoxon test. If not otherwise stated, *P*. value less than was deemed statistically significant.

Results

Characterization of homeobox family genes

A total of thirty-nine homeobox family genes were enrolled in our study. The transcriptional expressions of these HOX genes in ccRCC tumor tissues and adjacent normal tissues were shown in Figure 1A. Of the 39 HOX family genes, thirty-two were differentially expressed between tumor and adjacent normal tissues (with the criteria of *P*-value less than 0.05) (Figure 1B). Moreover, fourteen HOX genes were significantly associated with the prognosis of ccRCC patients based on univariate Cox regression analysis and Kaplan-Meier survival analysis, and these genes were regarded as robust prognosis-related HOX genes (Figures 1B, C). Among the fourteen HOX genes, nine genes (*HOXA2*, *HOXA13*, *HOXA3*, *HOXB13*, *HOXA1*, *HOXA11*, *HOXC4*, *HOXC11*, and *HOXD10*) were risk factors (Hazard Ratio >1) and the other six genes (*HOXD1*, *HOXD3*, *HOXD8*, *HOXC10*, and *HOXA7*) were protective factors (Hazard Ratio<1) in ccRCC (Figure 1C). Figure 1D exhibits the correlation of these prognosis-related HOX genes. We then constructed a protein-protein interaction (PPI) network using the prognosis-related HOX genes (Figure 1E), and hub gene analysis suggested that *HOXA11* and *HOXC4* were the top two ranked genes in this PPI network (Figure 1F).

Construction of a homeobox family gene-based signature in ccRCC

To construct a prognostic signature based on homeobox family genes, the TCGA ccRCC cohort was randomly classified into a training (n=266) and a testing cohort (n=264). In training cohort, the HOX family genes were subjected to LASSO regression analysis followed by multivariate Cox analysis (Figures 2A–B), and eight HOX genes (*HOXB1*, *HOXA7*, *HOXB5*, *HOXD8*, *HOXD9*, *HOXB9*, *HOXA9*, and *HOXA11*) were finally retained to construct a prognosis signature in ccRCC. The detailed information and coefficient of the eight HOX genes was shown in Figure 2C and Table 1. The risk score based on the prognosis signature was obtained by a linear combination of the expression levels of selected genes and corresponding coefficients. The formula was as follow: risk score = *HOXA11* × 0.401 + *HOXA7* × (-0.837) + *HOXA9* × 0.238 + *HOXB1* × (-4.284) + *HOXB5* × (-0.276) + *HOXB* × 0.163 + *HOXB9* × 0.163 + *HOXD8* × (-0.085) + *HOXD9* × 0.066. Then, the risk score of each patient in training cohort was computed and it allowed patients to be stratified into high- and low-risk groups according to the median value of risk score. Figure 2D shows the risk score distribution of patients in training cohort. The living status and survival time of patients in training cohort was exhibited in Figure 2E, and it suggested that the mortality rate of patients in high-risk group was higher than that in low-risk group. Figure 2F shows the transcription levels of the three HOX genes in high- and low-risk groups. Kaplan-Meier survival analysis demonstrated significant difference in the overall survival between high- and low-risk groups (Figure 2G). The area under the curve (AUC) values of the time-dependent receiver operating characteristic (ROC) curves were 0.750, 0.750, and 0.776 for 1-, 2- and 3-year overall survival, respectively (Figure 2H).

10.3389/fonc.2022.1008714

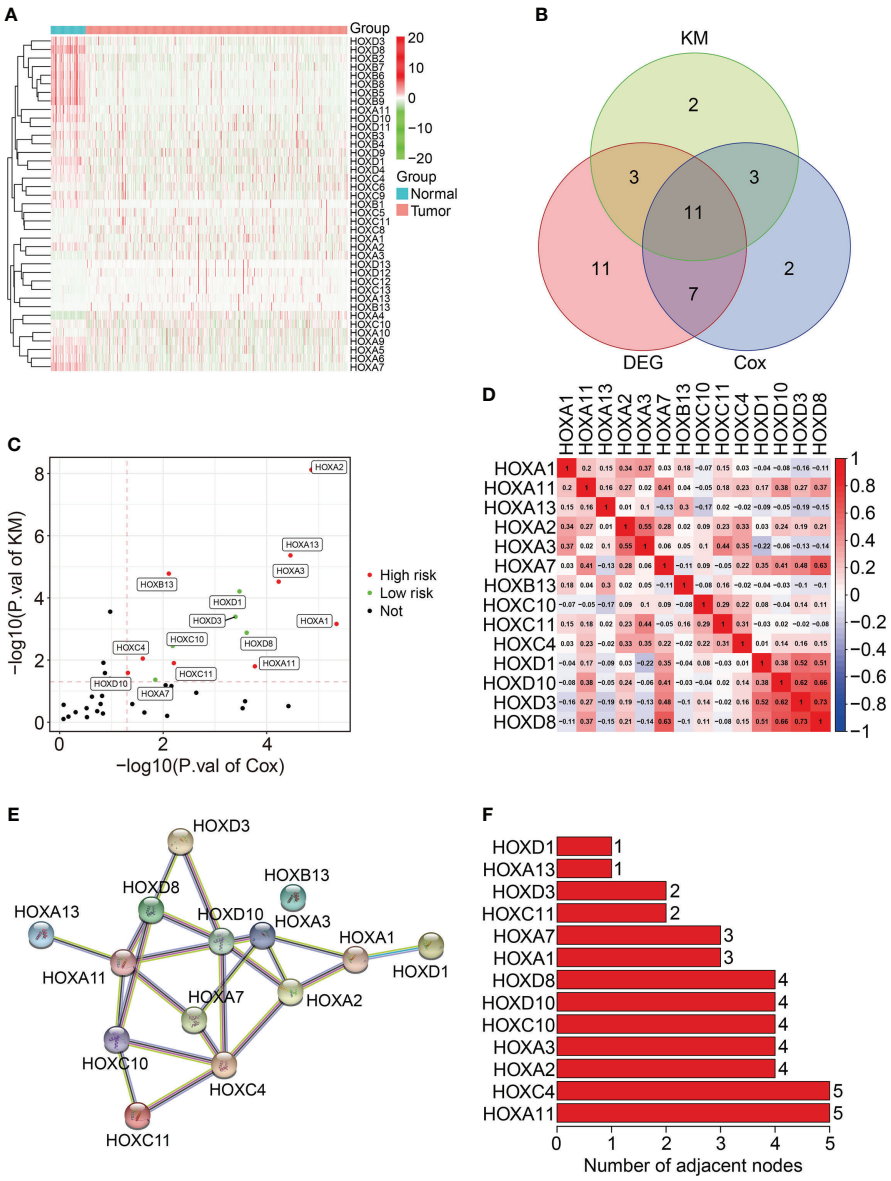

FIGURE 1
Characterization of homeobox family genes in ccRCC based on TCGA database. **(A)** Heatmap showing the expression patterns of HOX family genes in tumor tissues and adjacent normal tissues. **(B)** Venn plot showing the number of differentially expressed HOX genes and prognosis-related HOXs. **(C)** Volcano plot showing the prognosis-related HOXs based on univariate Cox regression analysis and Kaplan-Meier survival analysis. **(D)** Correlation heatmap of the 14 prognosis-related HOXs. **(E)** Protein-protein interaction network of the 14 prognosis-related HOXs. **(F)** Hub genes in the PPI network.

Validation of the homeobox family gene-based signature in internal cohorts

First, we assessed the prognostic value of the HOX gene-based signature in internal cohorts including testing cohort and entire cohort. The risk score of each case in testing cohort and entire cohort was calculated using the formula mentioned above. Then, we divided patients of the internal cohorts into high- and low-risk groups using the median risk score value in training cohort as the cutoff. Figures 3A, B show the profile of risk score in testing cohort and entire cohort. The distributions of survival time and living status were shown in Figures 3C, D. The expression patterns of the three HOX genes were exhibited in Figures 3E, F. Kaplan-Meier survival analysis determined that patient in high-risk group had

10.3389/fonc.2022.1008714

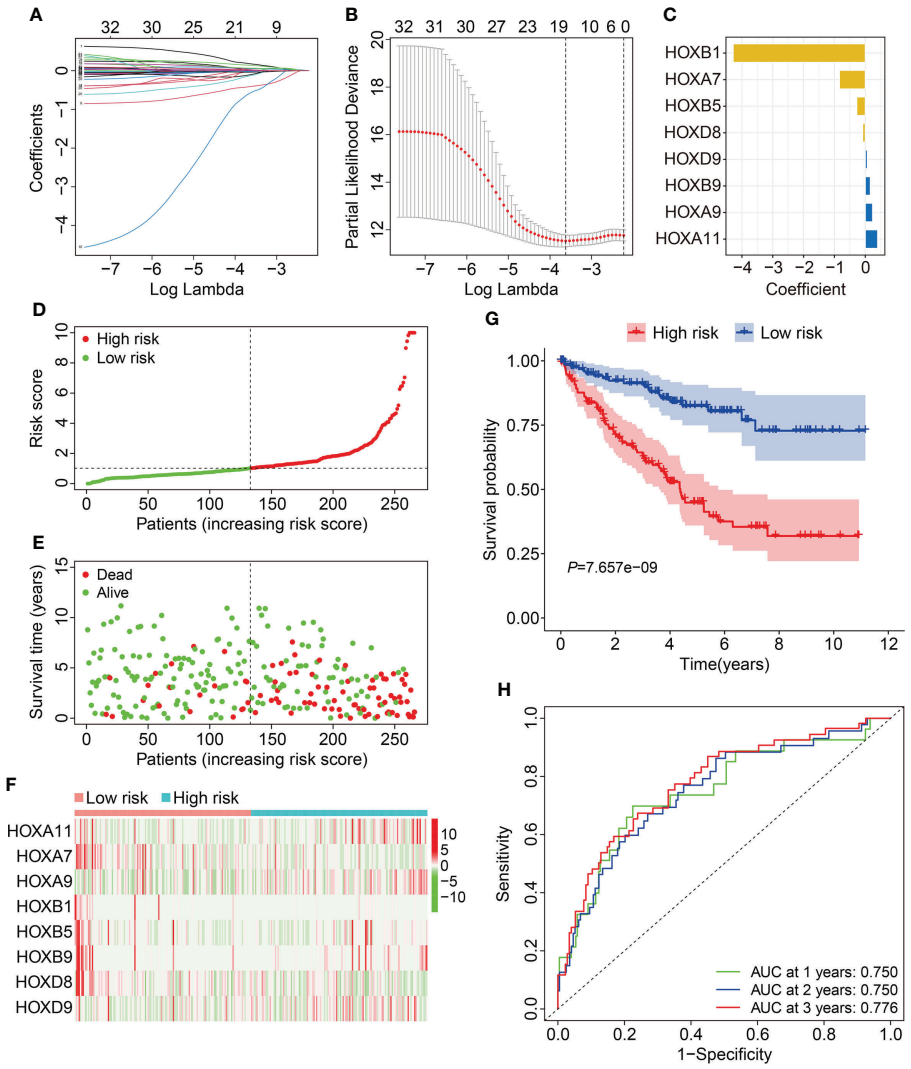

FIGURE 2
Construction of HOX family gene-based signature in ccRCC. **(A, B)** LASSO regression analysis and multivariate Cox analysis. **(C)** The distribution of the coefficient of the eight HOX family genes. **(D, E)** The distribution of risk score and survival status in high- and low-risk groups. **(F)** The transcription levels of the eight HOX family genes in high- and low-risk groups. **(G)** Kaplan-Meier survival curve for overall survival of patients in high- and low-risk groups. **(H)** Time-dependent ROC curve analysis in training cohort.

TABLE 1 Overall information of nine-HOXs constructing the prognostic model.

Gene Name	Coefficient	HR	HR.95L	HR.95H	P.value
HOXA11	0.4010	1.4933	1.1911	1.8721	0.0005
HOXA7	-0.8368	0.4331	0.2889	0.6493	0.0001
HOXA9	0.2382	1.2690	1.1587	1.3899	0.0000
HOXB1	-4.2839	0.0138	0.0000	4.4573	0.1462
HOXB5	-0.2765	0.7584	0.6211	0.9262	0.0067
HOXB9	0.1629	1.1769	1.0815	1.2807	0.0002
HOXD8	-0.0855	0.9181	0.8585	0.9818	0.0126
HOXD9	0.0662	1.0685	1.0336	1.1045	0.0001

10.3389/fonc.2022.1008714

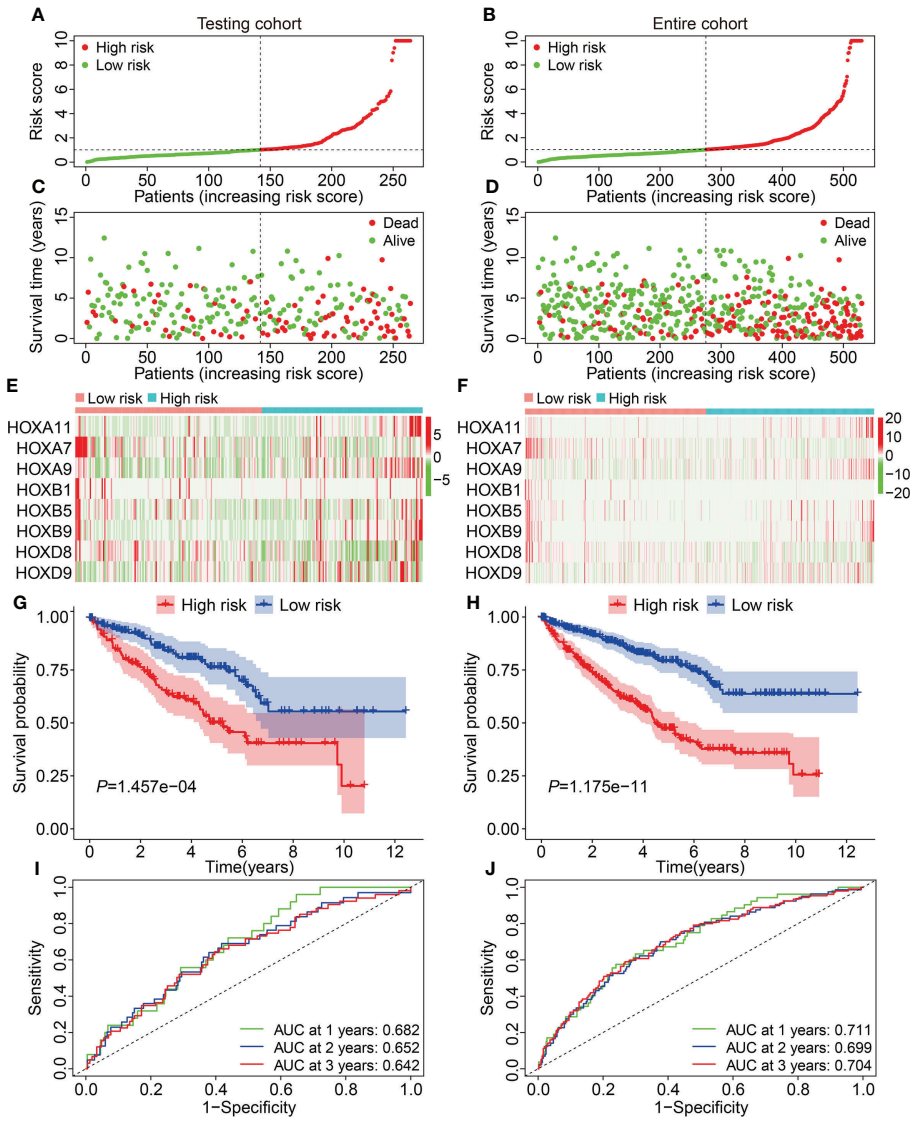

FIGURE 3
Validation of the HOX gene-based signature in internal cohorts. **(A, B)** The profile of risk score in testing cohort and entire cohort. **(C, D)** The distribution of survival time and status in testing cohort and entire cohort. **(E, F)** The expression patterns of the eight HOX genes in testing cohort and entire cohort. **(G, H)** Kaplan-Meier survival curve for overall survival of patients testing cohort and entire cohort. **(I, J)** Time-dependent ROC curve analysis in testing cohort and entire cohort.

worse overall survival than that in low-risk group, which was consistent in both testing cohort and entire cohort (Figures 3G, H). Time-dependent ROC analyses suggested that the AUC values for 1-, 2-, and 3-year overall survival were 0.682, 0.652, and 0.642 in testing cohort (Figure 3I), and 0.711, 0.699, and 0.704 in entire cohort (Figure 3J), respectively. Moreover, we classified patients of the entire cohort into multiple subgroups according to the clinical parameters including gender (female *vs* male), age (≤60 *vs* >60), grade (Grade: T1/2 *vs* Grade: T3/4), stage (stage I/II *vs* stage III/IV), T (T 1/2 *vs* T3/4), and M stage (M0 *vs* M1). Survival analyses revealed that in different strata of clinicopathological features, patients of high-risk group harbored worse overall survival (Figures 4A–F), suggesting that our HOX family gene-based signature was quite useful and perform well in prognosis prediction.

Validation of the homeobox family gene-based signature in external ICGC cohort

Subsequent, the external ICGC cohort was utilized to estimate the stability and generalizability of the prognostic signature. Using the same formula as in training cohort, the

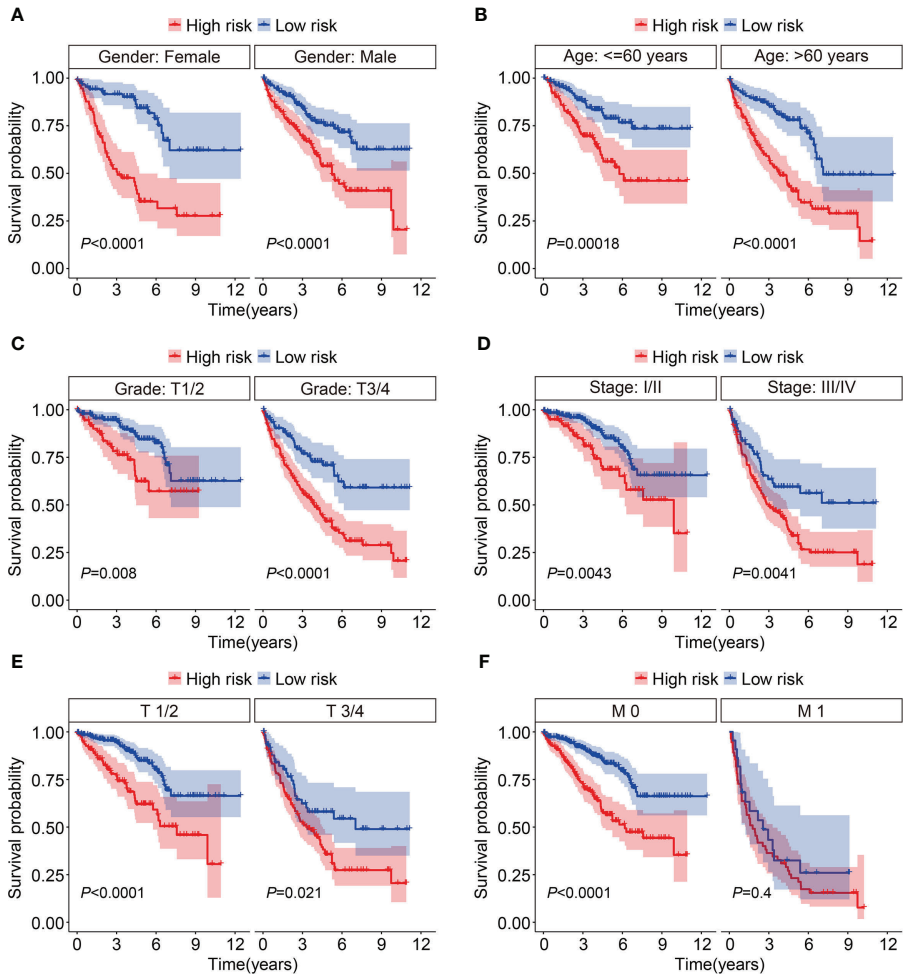

FIGURE 4
Kaplan-Meier survival curves to compare overall survival of high- and low-risk groups in subgroups stratified by gender **(A)**, age **(B)**, grade **(C)**, stage **(D)**, T and M status **(E, F)**.

risk score of patients in ICGC cohort was computed and it allowed patients to be assigned into high- and low-risk groups based on the median value of risk score in training cohort. The risk score distribution of patients in high- and low-risk groups was shown in Figure 5A. The distribution of survival time and living status of patients in ICGC cohort was exhibited in Figure 5B, and it suggested that patients of high-risk group tended to have better survival status and longer survival time. Figure 5C shows the expression profile of the eight HOX genes in ICGC cohort. Survival analysis revealed that the overall survival of patients who belonged to the high-risk group was poorer than that of the low-risk group (Figure 5D). Time-dependent ROC analysis suggested that the AUC values were 0.630, 0.659, and 0.727 for 1-, 2-, and 3-year overall survival (Figure 5E). Taken together, these analyses indicated the satisfactory predictive power of the signature in forecasting the clinical outcomes of ccRCC patients.

Estimation of the independent prognostic value of the signature and construction of a nomogram

To investigate the independence of the signature and other clinicopathological parameters (age, gender, grade, stage, T and M status), both univariate and multivariate Cox regression analyses were performed. The results indicated that age, grade, stage, M status, and the signature-derived risk score showed significance in both analyses, and they thus could be regarded as independent prognostic indicators in patients with ccRCC

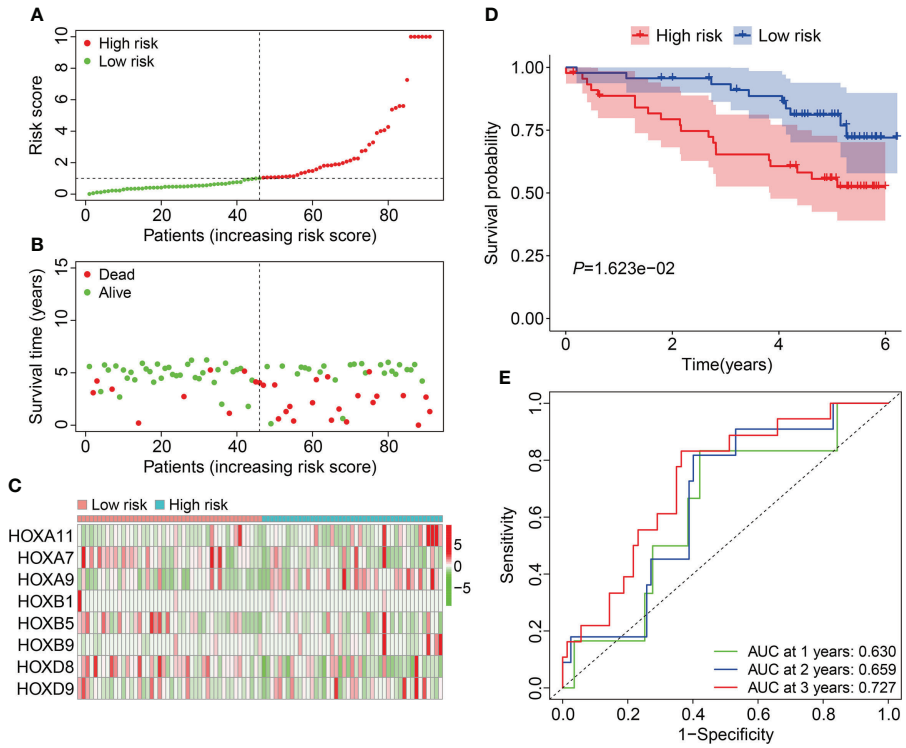

FIGURE 5
Validation of the HOX family gene-based signature in external ICGC cohort. **(A)** The profile of risk score in ICGC cohort. **(B)** The distribution of survival time and living status in ICGC cohort. **(C)** The expression patterns of the three HOX family genes in ICGC cohort. **(D)** Kaplan-Meier survival curve for overall survival of patients in ICGC cohort. **(E)** Time-dependent ROC curve analysis in ICGC cohort.

(Table 2). Furthermore, a nomogram was created by combining risk score and other four clinicopathological characteristics including gender, age, T, and M status that were shared in TCGA and ICGC cohorts (Figure 6A). As shown in Figures 6B, C, calibration curves indicated satisfactory agreement between the nomogram prediction and actual observations, showing the remarkable dependability of the nomogram in predicting the overall survival of ccRCC patients.

Functional annotation of the HOX family gene-based signature

To reveal the underlying biological mechanism of the HOX family gene-based signature, we screened differentially expressed genes (DEGs) between high- and low-risk groups using *edgeR* filtration. A total of 328 shared DEGs between different risk groups in both TCGA and ICGC cohorts were identified the

TABLE 2 Univariable and multivariable analysis of the HOX family gene-based signature and clinical factors in the TCGA cohort.

Variables	Univariable analysis				Multivariable analysis			
	HR	95% CI of HR		*P*	HR	95% CI of HR		*P*
		Lower	Upper			Lower	Upper	
Age (≤60 vs >60)	1.788	1.309	2.441	0.000	1.694	1.233	2.329	0.001
Gender (Female vs Male)	0.930	0.679	1.274	0.651	0.932	0.673	1.290	0.671
Grade (I/II vs III/IV)	2.593	1.837	3.659	0.000	1.617	1.118	2.338	0.011
Stage (I/II vs III/IV)	3.610	2.618	4.978	0.000	2.158	1.039	4.481	0.039
T (T 1/2 vs T 3/4)	3.003	2.205	4.088	0.000	0.937	0.500	1.757	0.840
M (M0 vs M1)	4.205	3.070	5.759	0.000	2.447	1.655	3.616	0.000
Risk (High vs Low)	1.005	1.001	1.008	0.000	1.006	1.002	1.009	0.002

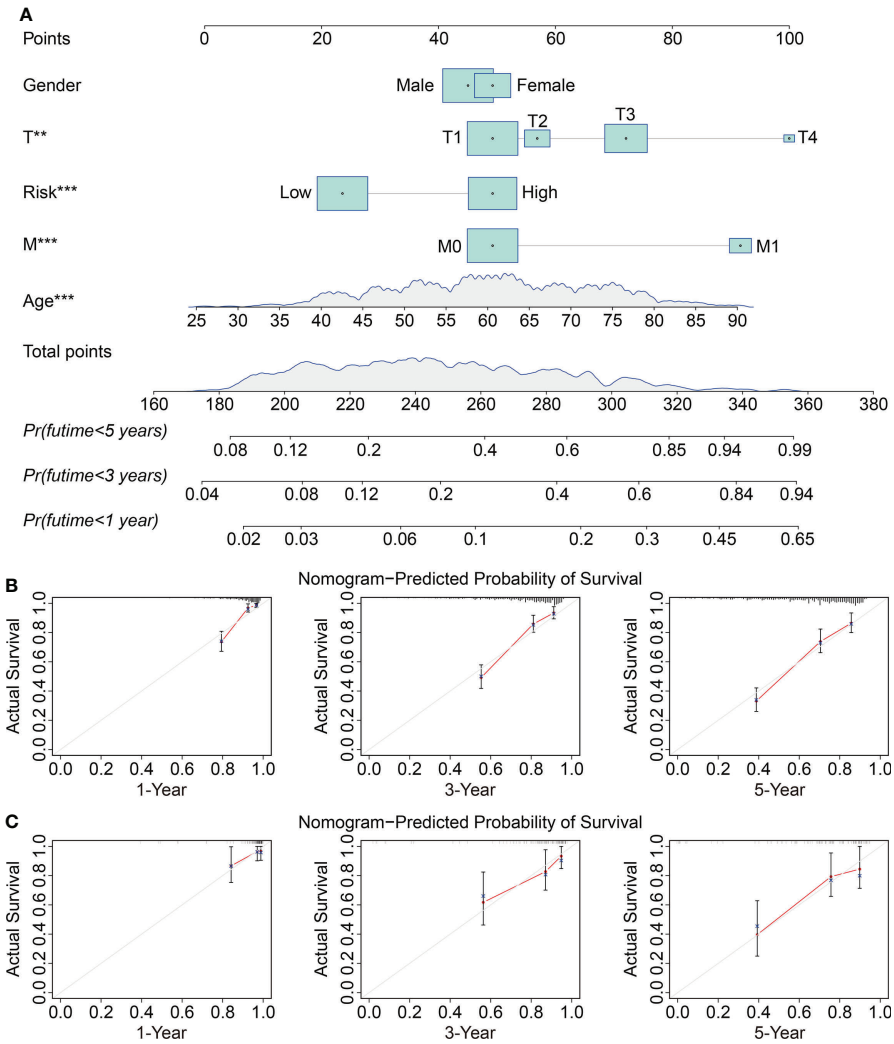

FIGURE 6
Construction and validation of a prognostic nomogram in ccRCC. **(A)** The nomogram combining risk score with clinical factors such as gender, age, T and M status for forecasting 1-, 3-, and 5-year overall survival. **(B, C)** The calibration plots of predicted and actual probabilities for the nomogram in TCGA and ICGC cohorts $^{**}P < 0.01$; $^{***}P < 0.001$.

criterion of FDR<0.05 and |log2FC| >0.5 (Figure 7A). The expression patterns of these shared DEGs in TCGA and ICGC cohorts were exhibited in Figures 7B, C. Then, we annotated the function of these shared DEGs using DAVID database. GO enrichment analysis suggested that biological processes including regulation of response to stimulus, immune system process, response to external stimulus, defense response, and regulation of immune system process, were significantly enriched. As for the cellular component, extracellular region, extracellular region part, and vesicle were the three most enriched terms. In the molecular function category, DEGs were mainly enriched in receptor binding, protein complex binding, and antigen binding (Figure 7D). KEGG enrichment analysis suggested that multiple signaling pathways including PI3K-Akt, MAPK, Ras, Rap1, and HIF-1 were significantly enriched (Figure 7E). GSEA method revealed that allograft rejection, base excision repair, complement and coagulation cascades, lysosome, primary immunodeficiency, proteasome, and pyrimidine metabolism were markedly enriched in ccRCC samples with higher risk scores in TCGA cohort. Meanwhile, hallmarks including adherens junction, fatty acid metabolism, propanoate metabolism, TGF-β signaling pathway, tight junction, valine leucine and isoleucine degradation, and WNT signaling pathway were significantly enriched in ccRCC samples of low-risk group in TCGA cohort (Figure 7F). In ICGC cohort, oxidative phosphorylation and ribosome were significantly enriched in ccRCC samples of high-risk group, while hallmarks such as apoptosis, basal transcription factors, JAK/

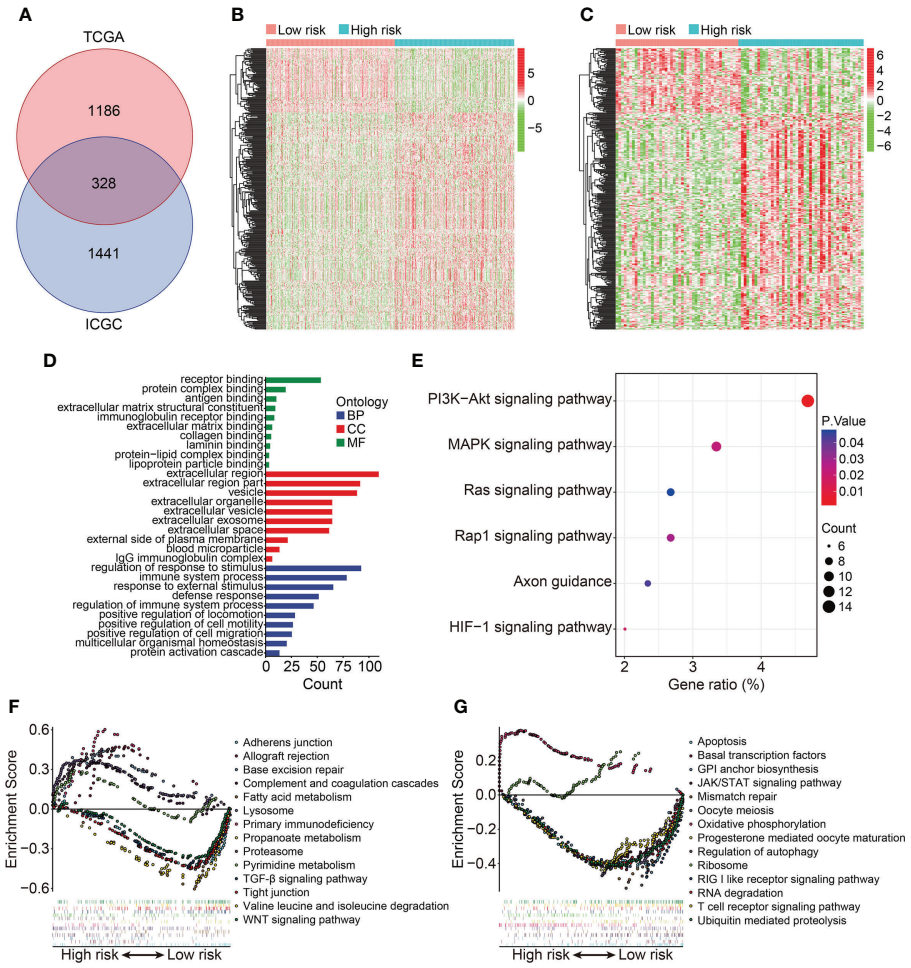

FIGURE 7
Identification of risk-related differentially expressed genes and functional enrichment analysis. **(A)** Venn plot exhibiting shared DEGs between different risk groups in TCGA and ICGC cohorts. **(B, C)** Heatmap showing the expression profiles of the DEGs in TCGA and ICGC cohorts. **(D, E)** GO and KEGG enrichment analyses. **(F, G)** Gene set enrichment analysis in TCGA and ICGC cohorts.

STAT signaling pathway, RIG I like receptor signaling pathway, and T cell receptor signaling pathway were markedly enriched in ccRCC samples of low-risk group (Figure 7G).

Association between the HOX family gene-based signature with immune cell infiltration

To explore the relationship between HOX family gene-based signature with the immune landscape of ccRCC, we estimated the proportions of immune cell infiltrated in each ccRCC sample by analyzing RNA sequencing data, and compared them between high- and low-risk groups. Figure 8A and Supplementary Figure 1A show the proportion of 22 infiltrated immune cell types in ccRCC samples of TCGA and ICGC cohorts, and it suggested that M2 macrophages, CD8 T cells, and resting memory CD4 T cells were the three most abundant immune cells in tumor microenvironment. The correlations of these infiltrated immune cells in ccRCC samples of TCGA and ICGC cohorts were shown in Figure 8B and Supplementary Figure 1B. In TCGA cohort, the regulatory T cells (Tregs) infiltrated differently between the two subgroups (Figures 10C, D). In ICGC cohort, a higher level of immune infiltration by regulatory T cells (Tregs), and a lower level of M1 macrophages and resting dendritic cell were associated with higher risk score (Supplementary Figure 1C, D). Additionally, we employed ssGSEA method to compare the enrichment scores of immune cell and related immune functions in high- and low-risk groups. As shown in Figures 9A, B, the scores for mast cells were significantly lower in high-risk group compared with the low-risk group, which was consistent in both TCGA and ICGC cohort. As for the related immune function, the enrichment scores of APC

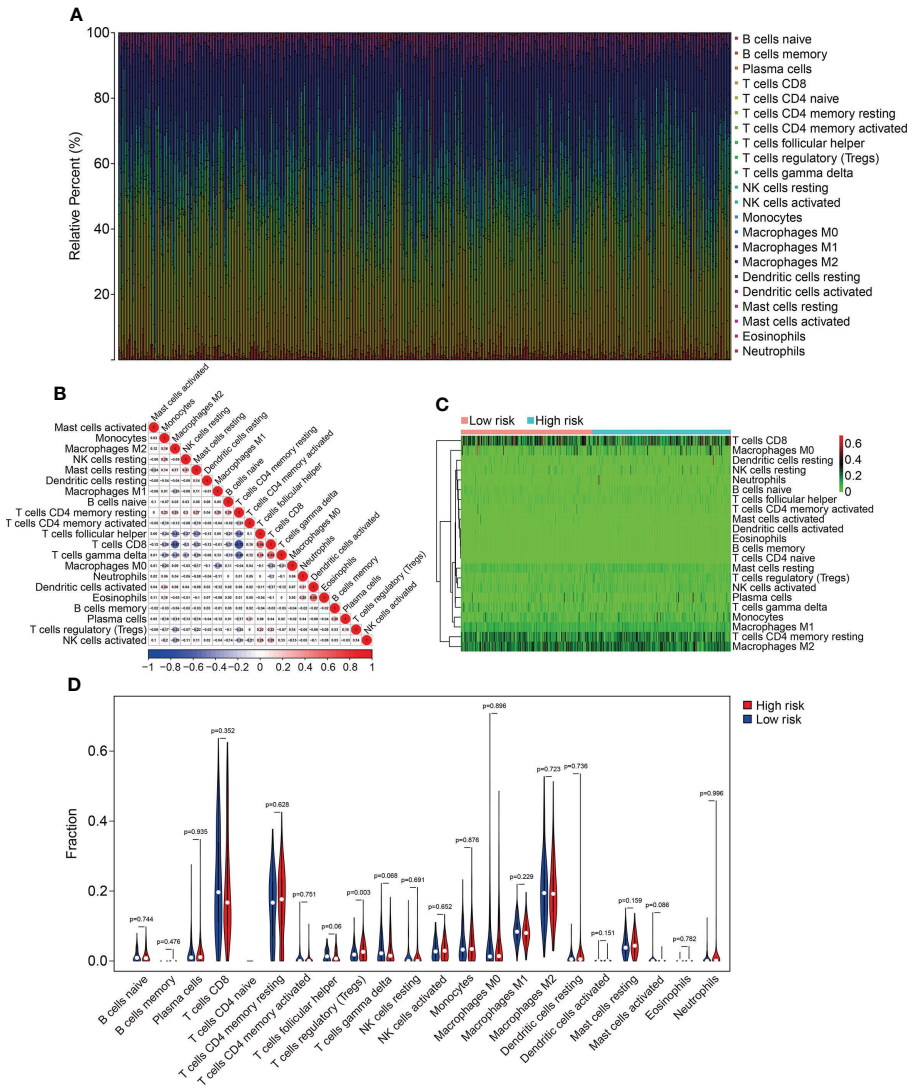

FIGURE 8
Comparison of immune cell infiltration in high- and low-risk groups in TCGA cohort. **(A)** Relative abundance of immunocyte infiltration in KIRC samples of the TCGA cohort. **(B)** The heatmap showing the correlation of infiltrating immune cells in the TCGA cohort. **(C, D)** The fraction of 22 immune cell types in high- and low- risk groups of the TCGA cohort.

co-inhibition, para-inflammation, and type II IFN response were consistently lower in high-risk group in both cohorts (Figures 9C, D).

Expression and Kaplan-Meier survival analysis of the eight HOX family genes

We then analyzed the expression levels of the eight HOX family genes in ccRCC tissues and adjacent normal tissues, and performed Kaplan-Meier survival analysis in TCGA and ICGC cohorts. As shown in Figures 10A-G, the transcript levels of *HOXB1*, *HOXA7*, *HOXB5*, *HOXD8*, *HOXB9*, *HOXA9*, and *HOXA11* were significantly lower in ccRCC tumor tissues compared to adjacent normal tissues, which was consistent in both TCGA and ICGC cohorts. Compared to normal tissues, the expression of *HOXD9* was lower in ccRCC tumor tissues of TCGA cohort, while it was higher in ccRCC tumor tissues of ICGC cohort (Figure 10H). Meanwhile, Kaplan-Meier survival analysis in TCGA cohorts revealed that lower expression of *HOXA7* and *HOXD8*, and higher expression of *HOXA9*, *HOXA11*, and *HOXB9* were associated with worse overall survival in ccRCC patients (Figures 11A–H). In ICGC cohort, survival analysis indicated that higher expression of *HOXA9* predicted poorer prognosis in ccRCC (Supplementary Figure 2A–H).

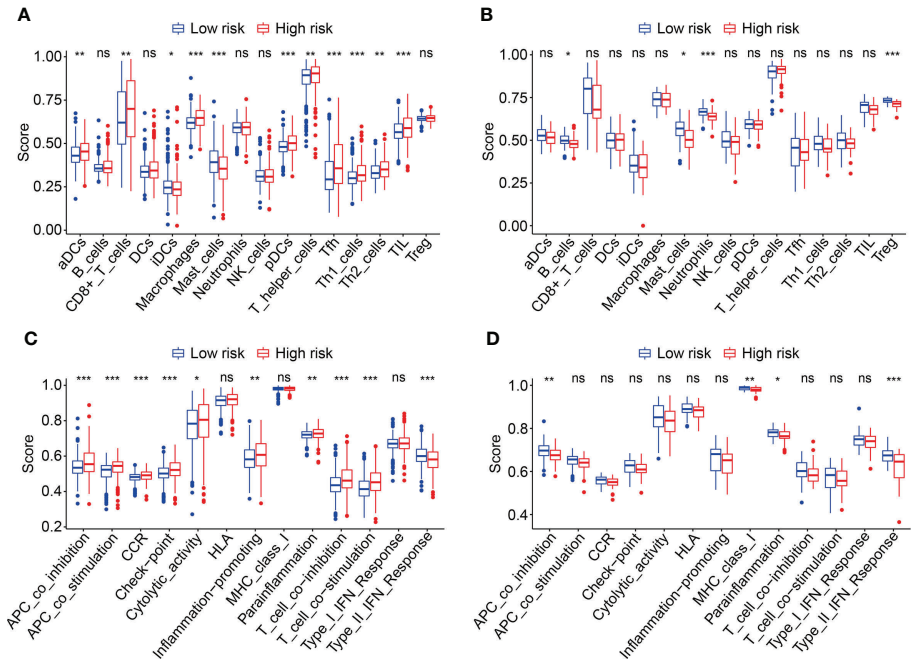

FIGURE 9
Comparison of immune cell infiltration and immune function based on ssGSEA. **(A, B)** Box plots exhibiting enrichment scores of immunocytes between the two subgroups in TCGA and ICGC cohorts. **(C, D)** Box plots exhibiting enrichment scores of the related-immune function between the two subgroups in TCGA and ICGC cohorts *$P < 0.05$; **$P < 0.01$; ***$P < 0.001$. not significant.

HOXD8 was downregulated in ccRCC and correlated with tumor progression

Finally, we comprehensively analyzed HOXD8 in ccRCC based on public resources. Figure 12A shows the expression profiles of *HOXD8* in various tumor types and it suggested that compared to adjacent normal tissues, *HOXD8* was downregulated in tumor tissues including BRCA, COAD, KIRC, KIRP, KICH, PRAD, READ, and UCEC, while it was upregulated in tumor tissues such CHOL, ESCA, HNSC, LIHC, and LUSC. Moreover, *HOXD8* expression were markedly downregulated in ccRCC tissues than that in match non-tumor tissues (Figure 12B). Besides, *HOXD8* expression was significantly decreased with the increase of tumor grade and stage, and lymph node metastasis (Figures 12C–E). Additionally, the protein level of HOXD8 was also lower in ccRCC tissues than that in normal tissues (Figure 12F), and HOXD8 protein level decreased with the increase of tumor grade (Figure 12G). Finally, we analyzed the expression of HOXD8 in three independent datasets (GSE40435, GSE46699, and GSE53757) from GEO database and performed qRT-PCR to detect *HOXD8* expression in clinical samples. Our results indicated that *HOXD8* expression were dramatically downregulated in ccRCC tissues compared to adjacent non-tumor tissues (Figures 12H–K).

Discussion

Members of HOX family genes had been found to be aberrantly expressed in multiple types of tumors. In ccRCC, although some studies have indicated that dysregulation of HOX genes such as *HOXD1*, *HOXA13*, and *HOXC11* were associated with cell proliferation, metastasis, and apoptosis (27–29), while the detailed roles of HOX family genes on malignant behaviors of ccRCC and its prognostic values remained largely to be characterized. Here, we comprehensively analyzed the expression profiles and clinical significance of HOX genes in ccRCC using transcriptome profiles of tumor samples and corresponding clinical information from the TCGA database. We are suppressed to find that over eighty percent (32/39) of HOX genes were differentially expressed between ccRCC samples and adjacent normal tissues, and about thirty-five percent (14/39) of HOX genes were robustly associated with patients' prognosis. These analyses indicated that HOX genes might exert vital role in the development and progression of ccRCC. Subsequently, we built a prognostic signature based on eight HOX genes including *HOXB1*, *HOXA7*, *HOXB5*, *HOXD8*, *HOXD9*, *HOXB9*, *HOXA9*, and *HOXA11* in ccRCC for risk stratification, which allowed patients with higher or lower risk score to be divided into different risk groups. Comparing the overall survival in subgroups of all the internal cohorts (training

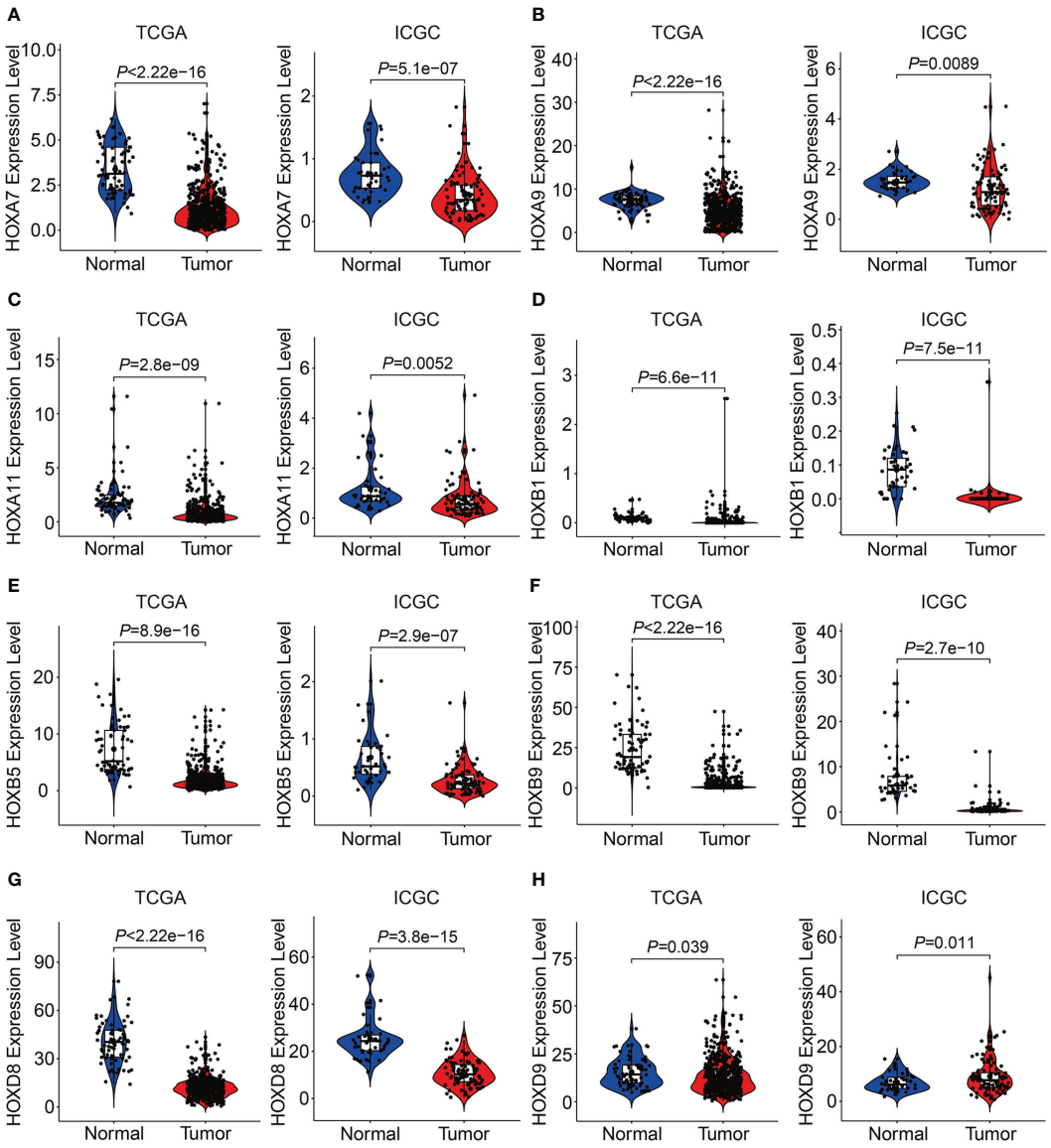

FIGURE 10
Comprising the expression of *HOXA7* **(A)**, *HOXA9* **(B)**, *HOXA11* **(C)**, *HOXB1* **(D)**, *HOXB5* **(E)**, *HOXB9* **(F)**, *HOXD8* **(G)**, and *HOXD9* **(H)** between tumor tissues and adjacent normal tissues in TCGA and ICGC cohorts.

cohort, testing cohort, entire cohort) and external cohort (ICGC cohort) by Kaplan-Meier survival method indicated that the overall survival of patients who belonged to the high-risk group was poorer than that of the low-risk group. Moreover, time-dependent ROC curve analyses suggested the favorable forecasting performance of the signature. Besides, the specificity and accuracy of our eight-gene based signature was superior to some previously reported prognostic signatures in ccRCC (30, 31), in terms of AUC values of the ROC curves (Supplementary Table 1). Taken together, our HOX gene-based signature harbored satisfactory accuracy and generalizability in prognosis prediction. Additionally, univariate and multivariate Cox regression analyses revealed that the signature-derived risk score was an independent prognostic indicator in patients with ccRCC. Furthermore, we successfully developed a nomogram by combining signature-derived risk score, gender, age, T and M status to expand the predictive ability of the signature, which exhibited good clinical application value and might be helpful in facilitating individualized treatment and clinical decision-making.

In order to reveal the underlying biological mechanism of the HOX family gene-based signature, a total of 328 shared DEGs between the two risk groups were identified and were then functionally annotated. In KEGG enrichment analysis, we found

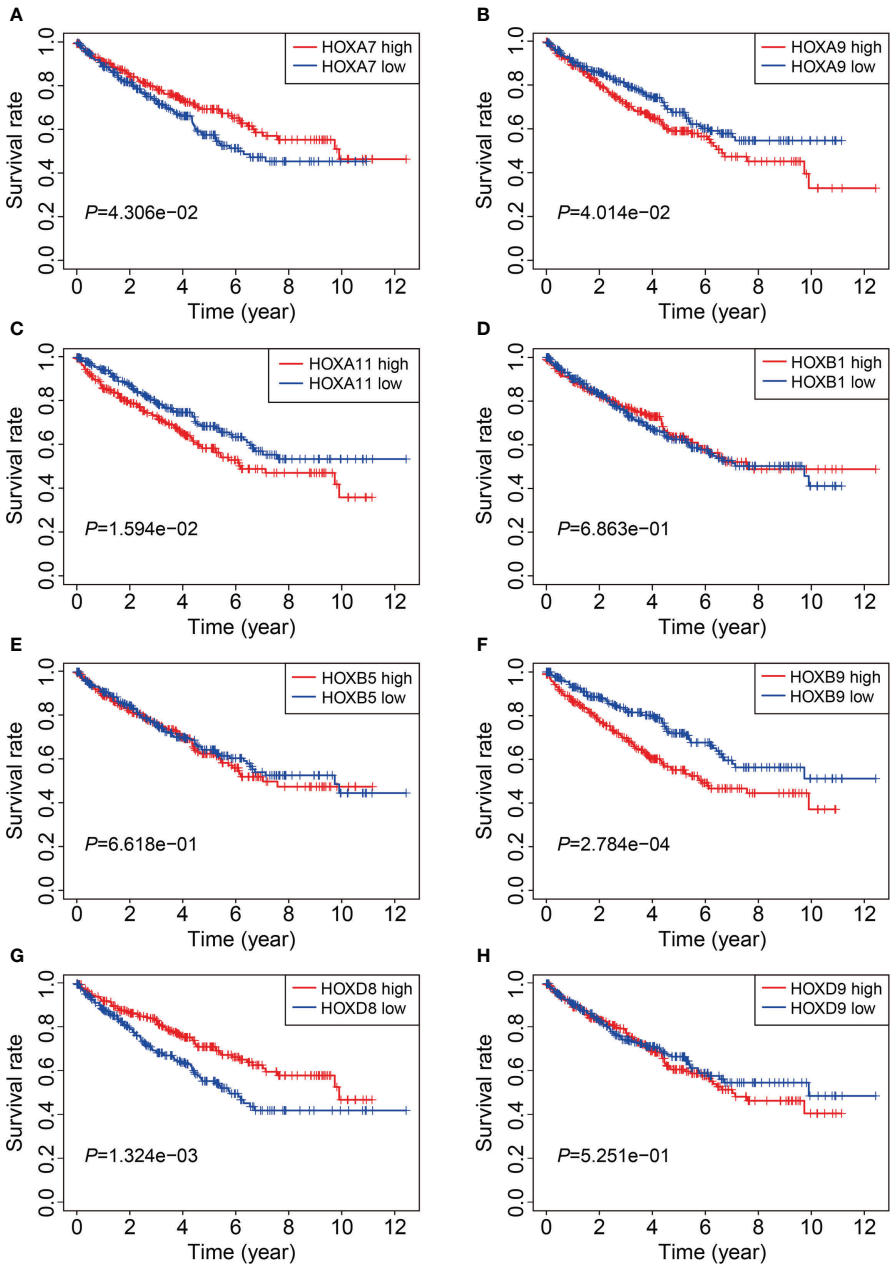

FIGURE 11
Kaplan-Meier survival analysis of *HOXA7* **(A)**, *HOXA9* **(B)**, *HOXA11* **(C)**, *HOXB1* **(D)**, *HOXB5* **(E)**, *HOXB9* **(F)**, *HOXD8* **(G)**, and *HOXD9* **(H)** in TCGA cohort.

that these DEGs were mainly enriched in PI3K-Akt, MAPK, Ras, Rap1, and HIF-1 signaling pathways, and these enriched pathways had been previously demonstrated to be critical for ccRCC development and progression (32–35). For example, the modestly mutated genes in PI3K/AKT pathway leads to its highly activated in ccRCC and represents promising drug targets (36). Isoform-specific AKT inhibitors are being tested in ccRCC clinical trials (37). Thus, we could speculate that the two risk groups stratified by our signature might exhibit distinct activation of these signaling pathways.

Tumor microenvironment consists of two major categories of components, including cellular components (e.g., tumor cell, vascular endothelial cells, immune cells, and mesenchymal stem cells) and surrounding acellular components (e.g., cytokines, adhesion molecules, growth factors). These non-tumor components provide a scaffold, barrier and environment for

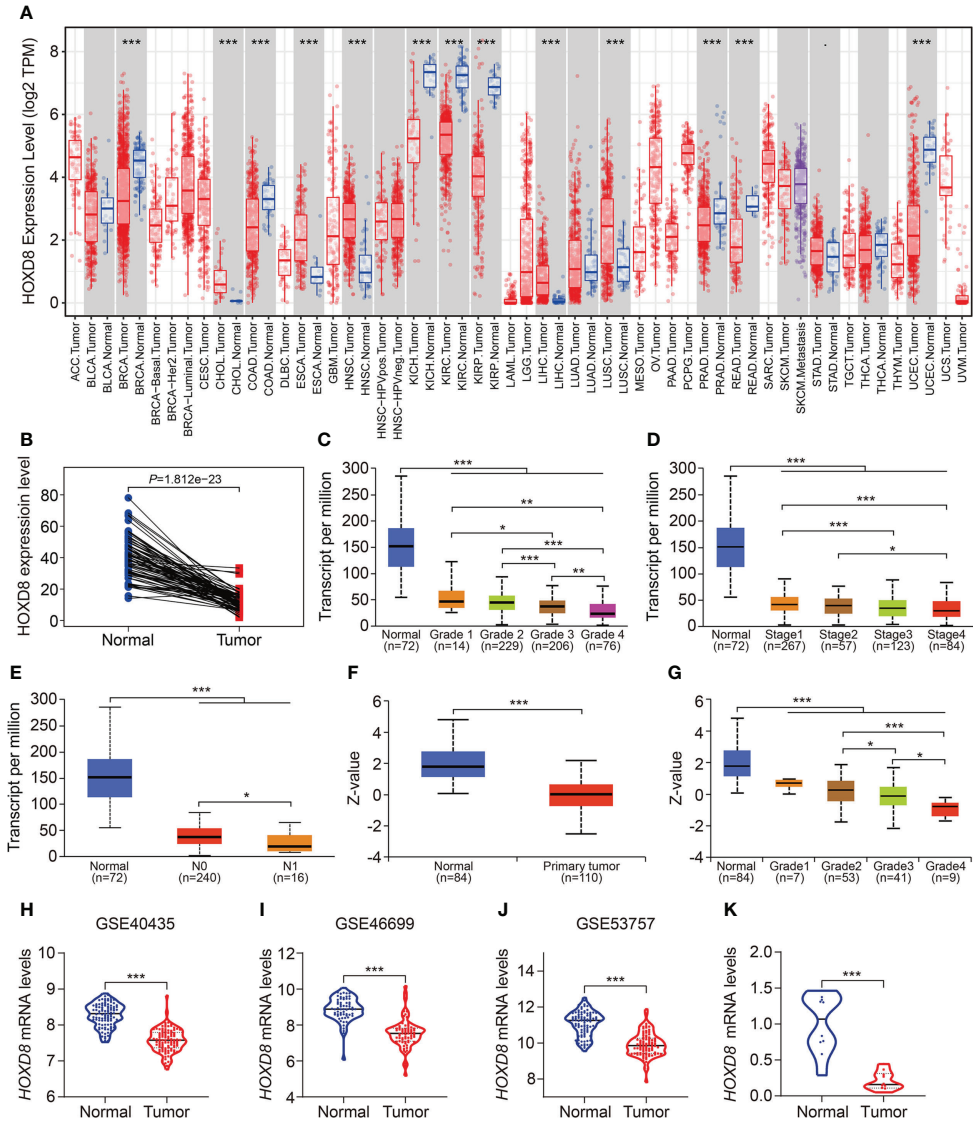

FIGURE 12
HOXD8 was downregulated in KIRC and correlated with tumor progression. **(A)** The expression profiles of HOXD8 in various types of tumors. **(B)** Comparison of the expression of HOXD8 in KIRC tissues and match non-tumor tissues. **(C-E)** The expression of HOXD8 in KIRC tissues with different tumor grade, stage, and N status. **(F)** The protein level of HOXD8 in KIRC tissues and normal tissues. **(G)** The protein level of HOXD8 in KIRC tissues with different tumor grade. **(H-J)** Comparison of the expression of HOXD8 in normal and tumor tissues in GSE40435, GSE46699, and GSE53757 database. **(K)** qRT-PCR was used to detect HOXD8 expression in clinical samples *$P < 0.05$; **$P < 0.01$; ***$P < 0.001$.

tumor occurrence and growth. Recent studies revealed that ccRCC is one of the most immune and vascularly infiltrated cancer types and the immune microenvironment played crucial role in ccRCC progression, and was associated with immune therapy response and patients' prognosis (38, 39). Thus, we further explored the association of the signature with immune microenvironment and immune cell infiltration in ccRCC. CIBERSORT algorithm revealed that CD8 T cells, M2 macrophages, and resting memory CD4 T cells were the three most abundant immune cell types in ccRCC tissues. Moreover, a higher level of immune infiltration by regulatory T cells (Tregs), and a lower level of M1 macrophages and resting dendritic cell were associated with higher risk score. The regulatory T cells in tumor microenvironment hindered protective immunosurveillance of tumor and suppress anticancer immunity, thereby leading to tumor progression (40–42). A higher proportion of infiltrated regulatory T cells in tumor tissues was regarded to be associated with worse prognosis (43). Treg-cell targeting therapy was shown to evoke and enhance anti-tumor immune response (44). The M1 macrophages, developed from M0 macrophages, exert tumor

inhibiting role by mediating cytotoxicity and antibody-dependent cell-mediated cytotoxicity (ADCC) to kill tumor cells (45, 46). The abundance of infiltrating M1 macrophages was positively correlated with clinical outcome in diverse tumor types (47). By combining our findings with those of previous studies, we were able to conclude that our HOX gene-based signature was closely associated with distinct immune status and different patterns of infiltrating immune cells, which might contribute to diverse clinical outcome in the two risk groups. Our signature might offer prominent therapy guidance and could be useful in determining which patients would benefit from immune therapy.

Of the eight HOX genes (*HOXB1*, *HOXA7*, *HOXB5*, *HOXD8*, *HOXD9*, *HOXB9*, *HOXA9*, and *HOXA11*) comprised in our signature, their transcript levels were consistently lower in ccRCC tissues compared to adjacent normal tissues (except for *HOXD9*). Survival analysis indicated that lower expression of *HOXA9*, *HOXA11*, and *HOXB9* were associated with favorable clinical outcome in ccRCC patients, thus the prognostic prediction performance of *HOXA9*, *HOXA11*, and *HOXB9* might be controversial with their expression level in ccRCC. *HOXA9* had been extensively studied in various types of tumors and it could act in opposite ways when it was dysregulated in tumors. Lower expression of *HOXA9*, accompanied by hypermethylation of its promoter region, was diagnostic or prognostic biomarker in tumors such as non-small cell lung cancer, ovarian cancer, and head and neck squamous cell carcinoma (48–50). Modulating HOXA9 expression could either promote or inhibit tumor progression through different mechanism, depending on context (51, 52). In renal cell tumors (RCT), promoter methylation of HOX9A was disclosed in 73% of RCTs, and the two-gene (HOX9A and OXR1) methylation panel led to 90% sensitivity and 98% specificity in the identification of ccRCC (53). However, up to now, little is known about the role of HOXA9 in ccRCC, further experiments should be carried out to detect the effect of HOXA9 knockdown or overexpression on malignant behaviors of ccRCC cells and unearth the underlying mechanism. *HOXA11* was a putative tumor suppressor in a number of solid tumors and it was frequently epigenetic inactivated (54, 55). HOXA11 antisense LncRNA (HOXA11-AS) was shown to be associated with advanced tumor stage and metastasis in RCC. Functionally, overexpression of HOXA11-AS promoted tumor growth and invasion through regulating miR-146b-5p-MMP16 axis (56). *HOXB9* was also reported to play a dual role in different types of tumors (57). The aberrant expression of *HOXB9* in tumors was not only prognostic predictor but also indicator of response to target therapy. Protein encoded by *HOXB9* functioned as oncoprotein and could accelerate cell proliferation and invasion in endometrial cancer, colorectal cancer, and hepatocellular carcinoma cells (58–60). However, HOXB9 could also delay tumor progression in other kinds of tumors such as gastric cancer and pancreatic cancer (61, 62). Nevertheless, the functional role of HOXB9 in ccRCC remains largely unknown and deserves further investigation. *HOXB1* is a well-defined tumor suppressor gene in diverse tumors (63, 64) and it was dramatically downregulated in ccRCC. However, *HOXB1* expression is extremely low in ccRCC tissues, which might limit its biological roles in ccRCC. Whether *HOXB1* had an effect on malignant behavior of ccRCC cells should be further explored *in vitro* and *in vivo*. The downregulated expression of *HOXA7* in ccRCC and its lower expression being associated with poorer patients' prognosis indicated that it might be a tumor suppressor in ccRCC. However, *HOXA7* was recently more reported to be oncogene and promoted oncogenic characteristics in many kinds of tumors such as liver cancer, cervical cancer, ovarian cancer, colorectal cancer and breast cancer (65–69). The role of *HOXA7* in ccRCC had not been reported until now and exploring its effect on malignant characteristics of ccRCC might lead to the understanding of its diverse biological role and the complicated intracellular regulatory network. *HOXB5* and *HOXD9* were suspected to be oncogenes in tumors and their translation products were reported to aggravate malignant development of tumors (70–72). Though our bioinformatic analysis suggested that *HOXB5* and *HOXD9* were markedly downregulated in ccRCC, the detailed role of them in ccRCC should be further experimentally investigated. Protein encoded by *HOXD8* gene is a conserved transcription factor that exert a tumor-suppressing role in various tumors through diverse mechanism. Overexpression of HOXD8 in colorectal cancer cells impaired cell proliferation and migration *via* inducing apoptotic event (73). Enforced expression of HOXD8 in breast cancer repressed tumor growth by inactivating AKT/mTOR pathway (74). Up to now, the role of HOXD8 in ccRCC had not been elucidated. Intriguingly, we found that the mRNA and protein levels of HOXD8 were downregulated in ccRCC than that in normal tissues, and decreased expression of HOXD8 was associated with increased tumor grade and stage, and lymph node metastasis. Survival analysis revealed that lower expression of *HOXD8* predicted worse overall survival in ccRCC. Taken together, it is reasonable to speculate that HOXD8 might be a tumor suppressor gene in ccRCC and a potential predictor of tumor progression.

Inevitably, there are several shortcomings in our study. First, we should endeavor to collect prospective cohort to verify the reliability of our signature. Second, we need to examine the protein levels of the HOX family genes, especially *HOXD8*, in ccRCC though immunoblotting or immunohistochemistry staining. Third, the role of HOX family genes, especially *HOXD8*, are warrant to be experimentally explored in ccRCC.

In all, we here systemically analyzed HOX family genes in ccRCC using bioinformatic method, and successfully constructed a prognostic signature based on eight HOX genes. Our signature was a favorable indicator to predict the prognosis of ccRCC cases and associated with tumor immune microenvironment and immune cell infiltration. *HOXD8*, one

of the eight HOX genes, might be a tumor suppressor gene in ccRCC and a potential predictor of tumor progression.

Data availability statement

The original contributions presented in the study are included in the article/Supplementary Material. Further inquiries can be directed to the corresponding author/s.

Ethics statement

The studies involving human participants were reviewed and approved by Ethics Committee of Renmin Hospital of Wuhan University. The patients/participants provided their written informed consent to participate in this study.

Author contributions

FC and YR designed the study. DZ and JN conducted bioinformatic analysis, wrote the manuscript and responsible for language revisions. All authors contributed to the article and approved the submitted version.

Funding

This study was funded by grants from National Natural Science Foundation of China (81870471 and 81800617) and Science and Technology Major Project of Hubei Province(2019AEA170).

Acknowledgments

We sincerely thank the TCGA project for using their data.

Conflict of interest

The authors declare that the research was conducted in the absence of any commercial or financial relationships that could be construed as a potential conflict of interest.

Publisher's note

Supplementary material

The Supplementary Material for this article can be found online at: https://www.frontiersin.org/articles/10.3389/fonc.2022.1008714/full#supplementary-material

References

1. Ljungberg B, Albiges L, Abu-Ghanem Y, Bensalah K, Dabestani S, Fernández-Pello S, et al. European Association of urology guidelines on renal cell carcinoma: The 2019 update. *Eur Urol* (2019) 75:799–810. doi: 10.1016/j.eururo.2019.02.011

2. Zhang MX, Wang JL, Mo CQ, Mao XP, Feng ZH, Li JY, et al. CircME1 promotes aerobic glycolysis and sunitinib resistance of clear cell renal cell carcinoma through cis-regulation of ME1. *Oncogene* (2022) 41(33):3979–90. doi: 10.1038/s41388-022-02386-8

3. Bray F, Ferlay J, Soerjomataram I, Siegel RL, Torre LA, Jemal A. Global cancer statistics 2018: GLOBOCAN estimates of incidence and mortality worldwide for 36 cancers in 185 countries. *CA Cancer J Clin* (2018) 68:394–424. doi: 10.3322/caac.21492

4. Li QK, Pavlovich CP, Zhang H, Kinsinger CR, Chan DW. Challenges and opportunities in the proteomic characterization of clear cell renal cell carcinoma (ccRCC): A critical step towards the personalized care of renal cancers. *Semin Cancer Biol* (2019) 55:8–15. doi: 10.1016/j.semcancer.2018.06.004

5. Yu M, Liu X, Xu H, Shen S, Wang F, Chen D, et al. Comprehensive evaluation of the m(6)A regulator prognostic risk score in the prediction of immunotherapy response in clear cell renal cell carcinoma. *Front Immunol* (2022) 13:818120. doi: 10.3389/fimmu.2022.818120

6. Hu J, Chen Z, Bao L, Zhou L, Hou Y, Liu L, et al. Single-cell transcriptome analysis reveals intratumoral heterogeneity in ccRCC, which results in different clinical outcomes. *Mol Ther* (2020) 28:1658–72. doi: 10.1016/j.ymthe.2020.04.023

7. Motzer RJ, Jonasch E, Agarwal N, Alva A, Baine M, Beckermann K, et al. Kidney cancer, version 3.2022, NCCN clinical practice guidelines in oncology. *J Natl Compr Canc Netw* (2022) 20:71–90. doi: 10.6004/jnccn.2022.0001

8. Lai Y, Tang F, Huang Y, He C, Chen C, Zhao J, et al. The tumour microenvironment and metabolism in renal cell carcinoma targeted or immune therapy. *J Cell Physiol* (2021) 236:1616–27. doi: 10.1002/jcp.29969

9. Mallo M. Reassessing the role of hox genes during vertebrate development and evolution. *Trends Genet* (2018) 34:209–17. doi: 10.1016/j.tig.2017.11.007

10. Feng Y, Zhang T, Wang Y, Xie M, Ji X, Luo X, et al. Homeobox genes in cancers: From carcinogenesis to recent therapeutic intervention. *Front Oncol* (2021) 11:770428. doi: 10.3389/fonc.2021.770428

11. Gonçalves CS, Le Boiteux E, Arnaud P, Costa BM. HOX gene cluster (de) regulation in brain: from neurodevelopment to malignant glial tumours. *Cell Mol Life Sci* (2020) 77:3797–821. doi: 10.1007/s00018-020-03508-9

12. Shah N, Sukumar S. The hox genes and their roles in oncogenesis. *Nat Rev Cancer* (2010) 10:361–71. doi: 10.1038/nrc2826

13. Miller KR, Patel JN, Ganapathi MK, Tait DL, Ganapathi RN. Biological role and clinical implications of homeobox genes in serous epithelial ovarian cancer. *Gynecol Oncol* (2016) 141:608–15. doi: 10.1016/j.ygyno.2016.03.004

14. De Bessa Garcia SA, Araújo M, Pereira T, Mouta J, Freitas R. HOX genes function in breast cancer development. *Biochim Biophys Acta Rev Cancer* (2020) 1873:188358. doi: 10.1016/j.bbcan.2020.188358

15. Tan Z, Chen K, Wu W, Zhou Y, Zhu J, Wu G, et al. Overexpression of HOXC10 promotes angiogenesis in human glioma *via* interaction with PRMT5 and upregulation of VEGFA expression. *Theranostics* (2018) 8:5143–58. doi: 10.7150/thno.27310

16. Dai L, Hu W, Yang Z, Chen D, He B, Chen Y, et al. Upregulated expression of HOXB7 in intrahepatic cholangiocarcinoma is associated with tumor cell metastasis and poor prognosis. *Lab Invest* (2019) 99:736–48. doi: 10.1038/s41374-018-0150-4

17. Shenoy US, Adiga D, Kabekkodu SP, Hunter KD, Radhakrishnan R. Molecular implications of HOX genes targeting multiple signaling pathways in cancer. *Cell Biol Toxicol* (2022) 38:1–30. doi: 10.1007/s10565-021-09657-2

18. Francis JC, Gardiner JR, Renaud Y, Chauhan R, Weinstein Y, Gomez-Sanchez C, et al. HOX genes promote cell proliferation and are potential therapeutic targets in adrenocortical tumours. *Br J Cancer* (2021) 124:805–16. doi: 10.1038/s41416-020-01166-z

19. Song C, Zhou C. HOXA10 mediates epithelial-mesenchymal transition to promote gastric cancer metastasis partly *via* modulation of TGFB2/Smad/METTL3 signaling axis. *J Exp Clin Cancer Res* (2021) 40:62. doi: 10.1186/s13046-021-01859-0

20. Reuter JA, Spacek DV, Snyder MP. High-throughput sequencing technologies. *Mol Cell* (2015) 58:586–97. doi: 10.1016/j.molcel.2015.05.004

21. Hong M, Tao S, Zhang L, Diao LT, Huang X, Huang S, et al. RNA Sequencing: new technologies and applications in cancer research. *J Hematol Oncol* (2020) 13:166. doi: 10.1186/s13045-020-01005-x

22. Zhang C, Zhang G, Sun N, Zhang Z, Zhang Z, Luo Y, et al. Comprehensive molecular analyses of a TNF family-based signature with regard to prognosis, immune features, and biomarkers for immunotherapy in lung adenocarcinoma. *EBioMedicine* (2020) 59:102959. doi: 10.1016/j.ebiom.2020.102959

23. Dong B, Liang J, Li D, Song W, Song J, Zhu M, et al. Identification of a prognostic signature associated with the homeobox gene family for bladder cancer. *Front Mol Biosci* (2021) 8:688298. doi: 10.3389/fmolb.2021.688298

24. Newman AM, Liu CL, Green MR, Gentles AJ, Feng W, Xu Y, et al. Robust enumeration of cell subsets from tissue expression profiles. *Nat Methods* (2015) 12:453–7. doi: 10.1038/nmeth.3337

25. Pan Q, Wang L, Chai S, Zhang H, Li B. The immune infiltration in clear cell renal cell carcinoma and their clinical implications: A study based on TCGA and GEO databases. *J Cancer* (2020) 11:3207–15. doi: 10.7150/jca.37285

26. Wu DM, Zhang T, Liu YB, Deng SH, Han R, Liu T, et al. The PAX6-ZEB2 axis promotes metastasis and cisplatin resistance in non-small cell lung cancer through PI3K/AKT signaling. *Cell Death Dis* (2019) 10:349. doi: 10.1038/s41419-019-1591-4

27. Cui Y, Yan M, Zhang C, Xue J, Zhang Q, Ma S, et al. Comprehensive analysis of the HOXA gene family identifies HOXA13 as a novel oncogenic gene in kidney renal clear cell carcinoma. *J Cancer Res Clin Oncol* (2020) 146:1993–2006. doi: 10.1007/s00432-020-03259-x

28. Cui Y, Zhang C, Wang Y, Ma S, Cao W, Guan F. HOXC11 functions as a novel oncogene in human colon adenocarcinoma and kidney renal clear cell carcinoma. *Life Sci* (2020) 243:117230. doi: 10.1016/j.lfs.2019.117230

29. Cui Y, Zhang C, Li Y, Ma S, Cao W, Guan F. HOXD1 functions as a novel tumor suppressor in kidney renal clear cell carcinoma. *Cell Biol Int* (2021) 45:1246–59. doi: 10.1002/cbin.11568

30. Ning XH, Li NY, Qi YY, Li SC, Jia ZK, Yang JJ. Identification of a hypoxia-related gene model for predicting the prognosis and formulating the treatment strategies in kidney renal clear cell carcinoma. *Front Oncol* (2021) 11:806264. doi: 10.3389/fonc.2021.806264

31. Zhan C, Wang Z, Xu C, Huang X, Su J, Chen B, et al. Development and validation of a prognostic gene signature in clear cell renal cell carcinoma. *Front Mol Biosci* (2021) 8:609865. doi: 10.3389/fmolb.2021.609865

32. Zhang Y, Jiang X, Qin X, Ye D, Yi Z, Liu M, et al. RKTG inhibits angiogenesis by suppressing MAPK-mediated autocrine VEGF signaling and is downregulated in clear-cell renal cell carcinoma. *Oncogene* (2010) 29:5404–15. doi: 10.1038/onc.2010.270

33. Sato Y, Yoshizato T, Shiraishi Y, Maekawa S, Okuno Y, Kamura T, et al. Integrated molecular analysis of clear-cell renal cell carcinoma. *Nat Genet* (2013) 45:860–7. doi: 10.1038/ng.2699

34. Schödel J, Grampp S, Maher ER, Moch H, Ratcliffe PJ, Russo P, et al. Hypoxia, hypoxia-inducible transcription factors, and renal cancer. *Eur Urol* (2016) 69:646–57. doi: 10.1016/j.eururo.2015.08.007

35. Rao H, Li X, Liu M, Liu J, Li X, Xu J, et al. Di-Ras2 promotes renal cell carcinoma formation by activating the mitogen-activated protein kinase pathway in the absence of von hippel-lindau protein. *Oncogene* (2020) 39:3853–66. doi: 10.1038/s41388-020-1247-y

36. Guo H, German P, Bai S, Barnes S, Guo W, Qi X, et al. The PI3K/AKT pathway and renal cell carcinoma. *J Genet Genomics* (2015) 42:343–53. doi: 10.1016/j.jgg.2015.03.003

37. Fruman DA, Rommel C. PI3K and cancer: lessons, challenges and opportunities. *Nat Rev Drug Discovery* (2014) 13:140–56. doi: 10.1038/nrd4204

38. Lei X, Lei Y, Li JK, Du WX, Li RG, Yang J, et al. Immune cells within the tumor microenvironment: Biological functions and roles in cancer immunotherapy. *Cancer Lett* (2020) 470:126–33. doi: 10.1016/j.canlet.2019.11.009

39. Simonaggio A, Epaillard N, Pobel C, Moreira M, Oudard S, Vano YA. Tumor microenvironment features as predictive biomarkers of response to immune checkpoint inhibitors (ICI) in metastatic clear cell renal cell carcinoma (mccRCC). *Cancers (Basel)* (2021) 13(2):231. doi: 10.3390/cancers13020231

40. Ohue Y, Nishikawa H. Regulatory T (Treg) cells in cancer: Can treg cells be a new therapeutic target? *Cancer Sci* (2019) 110:2080–9. doi: 10.1111/cas.14069

41. Li C, Jiang P, Wei S, Xu X, Wang J. Regulatory T cells in tumor microenvironment: new mechanisms, potential therapeutic strategies and future prospects. *Mol Cancer* (2020) 19:116. doi: 10.1186/s12943-020-01234-1

42. Nishikawa H, Koyama S. Mechanisms of regulatory T cell infiltration in tumors: implications for innovative immune precision therapies. *J Immunother Cancer* (2021) 9(7):e002591. doi: 10.1136/jitc-2021-002591

43. Shang B, Liu Y, Jiang SJ, Liu Y. Prognostic value of tumor-infiltrating FoxP3 + regulatory T cells in cancers: a systematic review and meta-analysis. *Sci Rep* (2015) 5:15179. doi: 10.1038/srep15179

44. Nishikawa H, Sakaguchi S. Regulatory T cells in tumor immunity. *Int J Cancer* (2010) 127:759–67. doi: 10.1002/ijc.25429

45. Pan Y, Yu Y, Wang X, Zhang T. Tumor-associated macrophages in tumor immunity. *Front Immunol* (2020) 11:583084. doi: 10.3389/fimmu.2020.583084

46. Tan Y, Sun R, Liu L, Yang D, Xiang Q, Li L, et al. Tumor suppressor DRD2 facilitates M1 macrophages and restricts NF-κB signaling to trigger pyroptosis in breast cancer. *Theranostics* (2021) 11:5214–31. doi: 10.7150/thno.58322

47. Boutilier AJ, Elsawa SF. Macrophage polarization states in the tumor microenvironment. *Int J Mol Sci* (2021) 22(13):6995. doi: 10.3390/ijms22136995

48. Hwang JA, Lee BB, Kim Y, Hong SH, Kim YH, Han J, et al. HOXA9 inhibits migration of lung cancer cells and its hypermethylation is associated with recurrence in non-small cell lung cancer. *Mol Carcinog* (2015) 54 Suppl 1:E72–80. doi: 10.1002/mc.22180

49. Zhou C, Li J, Li Q, Liu H, Ye D, Wu Z, et al. The clinical significance of HOXA9 promoter hypermethylation in head and neck squamous cell carcinoma. *J Clin Lab Anal* (2019) 33:e22873. doi: 10.1002/jcla.22873

50. Faaborg L, Jakobsen A, Waldstrøm M, Petersen CB, Andersen RF, Steffensen KD. HOXA9-methylated DNA as a diagnostic biomarker of ovarian malignancy. *biomark Med* (2021) 15:1309–17. doi: 10.2217/bmm-2021-0144

51. Han S, Li X, Liang X, Zhou L. HOXA9 transcriptionally promotes apoptosis and represses autophagy by targeting NF-κB in cutaneous squamous cell carcinoma. *Cells* (2019) 8(11):1360. doi: 10.3390/cells8111360

52. Miyamoto R, Kanai A, Okuda H, Komata Y, Takahashi S, Matsui H, et al. HOXA9 promotes MYC-mediated leukemogenesis by maintaining gene expression for multiple anti-apoptotic pathways. *Elife* (2021) 10:e64148. doi: 10.7554/eLife.64148

53. Pires-Luís AS, Costa-Pinheiro P, Ferreira MJ, Antunes L, Lobo F, Oliveira J, et al. Identification of clear cell renal cell carcinoma and oncocytoma using a three-gene promoter methylation panel. *J Transl Med* (2017) 15:149. doi: 10.1186/s12967-017-1248-y

54. Bai Y, Fang N, Gu T, Kang Y, Wu J, Yang D, et al. HOXA11 gene is hypermethylation and aberrant expression in gastric cancer. *Cancer Cell Int* (2014) 14:79. doi: 10.1186/s12935-014-0079-7

55. Kong C, Zhu Z, Li Y, Xue P, Chen L. Downregulation of HOXA11 enhances endometrial cancer malignancy and cisplatin resistance *via* activating PTEN/AKT signaling pathway. *Clin Transl Oncol* (2021) 23:1334–41. doi: 10.1007/s12094-020-02520-6

56. Yang FQ, Zhang JQ, Jin JJ, Yang CY, Zhang WJ, Zhang HM, et al. HOXA11-AS promotes the growth and invasion of renal cancer by sponging miR-146b-5p to upregulate MMP16 expression. *J Cell Physiol* (2018) 233:9611–9. doi: 10.1002/jcp.26864

57. Song J, Wang T, Xu W, Wang P, Wan J, Wang Y, et al. HOXB9 acetylation at K27 is responsible for its suppression of colon cancer progression. *Cancer Lett* (2018) 426:63–72. doi: 10.1016/j.canlet.2018.04.002

58. Sha L, Dong L, Lv L, Bai L, Ji X. HOXB9 promotes epithelial-to-mesenchymal transition *via* transforming growth factor-β1 pathway in hepatocellular carcinoma cells. *Clin Exp Med* (2015) 15:55–64. doi: 10.1007/s10238-014-0276-7

59. Wan J, Liu H, Feng Q, Liu J, Ming L. HOXB9 promotes endometrial cancer progression by targeting E2F3. *Cell Death Dis* (2018) 9:509. doi: 10.1038/s41419-018-0556-3

60. Martinou E, Moller-Levet C, Karamanis D, Bagwan I, Angelidi AM. HOXB9 overexpression promotes colorectal cancer progression and is associated with worse survival in liver resection patients for colorectal liver metastases. *Int J Mol Sci* (2022) 23(4):2281. doi: 10.3390/ijms23042281

61. Zhang L, Wu Q, He C, Liang D, Yi Q, Shi J, et al. HOXB9 inhibits proliferation in gastric carcinoma cells *via* suppression of phosphorylated-akt and NF-κB-dependent snail expression. *Dig Liver Dis* (2019) 51:157–65. doi: 10.1016/j.dld.2018.08.018

62. Yao Y, Liu C, Wang B, Guan X, Fang L, Zhan F, et al. HOXB9 blocks cell cycle progression to inhibit pancreatic cancer cell proliferation through the DNMT1/RBL2/c-myc axis. *Cancer Lett* (2022) 533:215595. doi: 10.1016/j.canlet.2022.215595

63. Petrini M, Felicetti F, Bottero L, Errico MC, Morsilli O, Boe A, et al. HOXB1 restored expression promotes apoptosis and differentiation in the HL60 leukemic cell line. *Cancer Cell Int* (2013) 13:101. doi: 10.1186/1475-2867-13-101

64. Han L, Liu D, Li Z, Tian N, Han Z, Wang G, et al. HOXB1 is a tumor suppressor gene regulated by miR-3175 in glioma. *PloS One* (2015) 10:e0142387. doi: 10.1371/journal.pone.0142387

65. Zhang Y, Cheng JC, Huang HF, Leung PC. Homeobox A7 stimulates breast cancer cell proliferation by up-regulating estrogen receptor-alpha. *Biochem Biophys Res Commun* (2013) 440:652–7. doi: 10.1016/j.bbrc.2013.09.121

66. Tang B, Qi G, Sun X, Tang F, Yuan S, Wang Z, et al. HOXA7 plays a critical role in metastasis of liver cancer associated with activation of snail. *Mol Cancer* (2016) 15:57. doi: 10.1186/s12943-016-0540-4

67. Ji F, Du R, Chen T, Zhang M, Zhu Y, Luo X, et al. Circular RNA circSLC26A4 accelerates cervical cancer progression *via* miR-1287-5p/HOXA7 axis. *Mol Ther Nucleic Acids* (2020) 19:413–20. doi: 10.1016/j.omtn.2019.11.032

68. Wang S, Diao YJ, Zhu BB. MiR-193a-5p suppresses cell proliferation and induces cell apoptosis by regulating HOXA7 in human ovarian cancer. *Neoplasma* (2020) 67:825–33. doi: 10.4149/neo_2020_190730N687

69. Dang Y, Yu J, Zhao S, Cao X, Wang Q. HOXA7 promotes the metastasis of KRAS mutant colorectal cancer by regulating myeloid-derived suppressor cells. *Cancer Cell Int* (2022) 22:88. doi: 10.1186/s12935-022-02519-9

70. Lee JY, Hur H, Yun HJ, Kim Y, Yang S, Kim SI, et al. HOXB5 promotes the proliferation and invasion of breast cancer cells. *Int J Biol Sci* (2015) 11:701–11. doi: 10.7150/ijbs.11431

71. Li ZX, Wu G, Jiang WJ, Li J, Wang YY, Ju XM, et al. HOXB5 promotes malignant progression in pancreatic cancer *via* the miR-6732 pathway. *Cell Cycle* (2020) 19:233–45. doi: 10.1080/15384101.2019.1707456

72. Liu M, Xiao Y, Tang W, Li J, Hong L, Dai W, et al. HOXD9 promote epithelial-mesenchymal transition and metastasis in colorectal carcinoma. *Cancer Med* (2020) 9:3932–43. doi: 10.1002/cam4.2967

73. Mansour MA, Senga T. HOXD8 exerts a tumor-suppressing role in colorectal cancer as an apoptotic inducer. *Int J Biochem Cell Biol* (2017) 88:1–13. doi: 10.1016/j.biocel.2017.04.011

74. Zhang Y, Yu Y, Su X, Lu Y. HOXD8 inhibits the proliferation and migration of triple-negative breast cancer cells and induces apoptosis in them through regulation of AKT/mTOR pathway. *Reprod Biol* (2021) 21:100544. doi: 10.1016/j.repbio.2021.100544

frontiers | Frontiers in Oncology

TYPE Original Research
PUBLISHED 05 December 2022
DOI 10.3389/fonc.2022.1079446

OPEN ACCESS

EDITED BY
Linhui Wang,
Second Military Medical University, China

REVIEWED BY
Yu-Yan Chen,
Affiliated Hospital of Nantong University, China
Jianfeng Yang,
Shanghai University of Traditional Chinese Medicine, China
Guiming Zhang,
The Affiliated Hospital of Qingdao University, China

*CORRESPONDENCE
Dingwei Ye
dwyelie@163.com
Hailiang Zhang
zhanghl918@163.com

†These authors have contributed equally to this work

SPECIALTY SECTION
This article was submitted to Genitourinary Oncology, a section of the journal Frontiers in Oncology

RECEIVED 25 October 2022
ACCEPTED 11 November 2022
PUBLISHED 05 December 2022

CITATION
Chang K, Su J, Li C, Anwaier A, Liu W, Xu W, Qu Y, Zhang H and Ye D (2022) Multi-omics profiles refine L-dopa decarboxylase (DDC) as a reliable biomarker for prognosis and immune microenvironment of clear cell renal cell carcinoma. *Front. Oncol.* 12:1079446. doi: 10.3389/fonc.2022.1079446

Multi-omics profiles refine L-dopa decarboxylase (DDC) as a reliable biomarker for prognosis and immune microenvironment of clear cell renal cell carcinoma

Kun Chang[1,2,3†], Jiaqi Su[1,2,3†], Chuanyu Li[4†], Aihetaimujiang Anwaier[1,2,3], Wangrui Liu[4], Wenhao Xu[1,2,3], Yuanyuan Qu[1,2,3], Hailiang Zhang[1,2,3*] and Dingwei Ye[1,2,3*]

[1]Department of Urology, Fudan University Shanghai Cancer Center, Shanghai, China, [2]Department of Oncology, Shanghai Medical College, Fudan University, Shanghai, China, [3]Shanghai Genitourinary Cancer Institute, Shanghai, China, [4]Department of Neurosurgery, Affiliated Hospital of Youjiang Medical University for Nationalities, Baise, China

Background: Increasing evidence indicates that L-dopa decarboxylase (DDC), which mediates aberrant amino acid metabolism, is significantly associated with tumor progression. However, the impacts of DDC are not elucidated clearly in clear cell renal cell carcinoma (ccRCC). This study aimed to evaluate DDC prognostic value and potential mechanisms for ccRCC patients.

Methods: Transcriptomic and proteomic expressions of and clinical data including 532 patients with ccRCC (The Cancer Genome Atlas RNA-seq data), 226 ccRCC samples (Gene Expression Omnibus), 101 ccRCC patients from the E-MTAB-1980 cohort, and 232 patients with ccRCC with proteogenomic data (Fudan University Shanghai Cancer Center) were downloaded and analyzed to investigate the prognostic implications of DDC expression. Cox regression analyses were implemented to explore the effect of DDC expression on the prognosis of pan-cancer. The "limma" package identified the differentially expressed genes (DEGs) between high DDC subgroups and low DDC groups. Functional enrichments were performed based DEGs between DDC subgroups. The differences of immune cell infiltrations and immune checkpoint genes between DDC subgroups were analyzed to identify potential influence on immune microenvironment.

Results: We found significantly decreased DDC expression in ccRCC tissues compared with normal tissues from multiple independent cohorts based on multi-omics data. We also found that DDC expression was correlated with

tumor grades and stages.The following findings revealed that lower DDC expression levels significantly correlated with shorter overall survival (P <0.001) of patients with ccRCC. Moreover, we found that DDC expression significantly correlated with an immunosuppressive tumor microenvironment, higher intra-tumoral heterogeneity, elevated expression of immune checkpoint CD274, and possibly mediated malignant behaviors of ccRCC cells via the PI3k/Akt signaling pathway.

Conclusion: The present study is the first to our knowledge to indicate that decreased DDC expression is significantly associated with poor survival and an immune-suppressive tumor microenvironment in ccRCC. These findings suggest that DDC could serve as a biomarker for guiding molecular diagnosis and facilitating the development of novel individual therapeutic strategies for patients with advanced ccRCC.

KEYWORDS

l-DOPA decarboxylase, amino acids metabolism, tumor microenvironment, clear cell renal cell carcinoma (ccRCC), prognosis, biomarker

Introduction

Renal cell carcinoma (RCC) is the third most common genitourinary malignancy worldwide (1, 2). In 2022, it is estimated that 79,000 new cases are diagnosed as RCC and 13,920 related deaths in the United States (3). Pathologically, RCC incorporates three main subtypes, including clear cell RCC (ccRCC), papillary RCC, and chromophobe RCC (4). Clear-cell RCC is the most common type of RCC with high aggressiveness, accounting for approximately 80% of all RCC pathology types (5). Around 30% of RCC patients are diagnosed as having advanced RCC, and the five-year survival rate is 23% (6). Hence, there is an urgent need to discover the underlying mechanisms of high invasiveness and high metastatic potential to find more reliable biomarkers that could assist in diagnosing and predicting prognosis.

Metabolic reprogramming is widespread in malignant tumors, the most well-known of which is glucose metabolic reprogramming that is termed the "Warburg effect" (7). This inefficient form of energy metabolism supplies the need for new proliferating cancer cells and enables the use of intermediate products to yield biomolecules, such as amino acids, and nucleotides (8). Previous studies revealed that amino acids could have impacts on cell proliferation, the tumor microenvironment, epigenetic modification, and drug resistance (9–14). Previous studies also revealed that amino acid aberrant metabolism was associated with tumor progression and immune infiltration in ccRCC and other cancers (15–18). Therefore, to better understand the profound mechanisms, studies are in demand to identify key amino acid metabolism-related genes and transfer them to drug targets.

L-dopa decarboxylase (DDC) locates at chromosome 7p and encodes a protein that catalyzes the decarboxylation process of L-3,4-dihydroxyphenylalanine (DOPA), L-5-hydroxytryptophan, and L-tryptophan to dopamine, serotonin, and tryptamine, respectively (19). Our previous proteomic analysis demonstrated that L-dopa decarboxylase was significantly downregulated in ccRCC (15). The regional dopamine of the kidney plays a potential role in regulating blood pressure, and the dysregulation of DDC might lead to hypertension, which is a common symptom of RCC (20). Tremmel et al. found that DDC was a favorable prognostic factor in breast cancer (21). However, in prostate cancer, the higher expression of DDC was associated with advanced stages, higher Gleason scores, biochemical recurrence, and short disease-free survival (DFS) (22). Also, the role of DDC has been investigated in the development of colorectal cancer (23), small cell lung cancer (24), and gastric cancer (25). However, the prognostic value and underlying mechanism caused by aberrant L-dopa decarboxylase expression have not been systematically elucidated in ccRCC.

In this study, we thoroughly performed DDC-related bioinformatics analysis in ccRCC and validated conclusions using external cohorts from multi-omics data. We found the downregulation of DDC in ccRCC was significantly associated with worse outcomes. Furthermore, DDC expression showed close relationships with clinicopathologic features and prognosis. We also revealed that DDC was correlated with immune cell

infiltration and expressions of immune checkpoint genes. In order to boost the knowledge of basic cancer biology, our study sought to identify the underlying mechanisms of DDC in carcinogenesis and provided a new therapeutic target for ccRCC patients.

Materials and methods

Patients' inclusion and data preprocessing

Proteogenomic expression data of 232 Chinese paired ccRCC and normal samples and 93 ccRCC tumors were included from our institute, the Fudan University Shanghai Cancer Center (FUSCC-ccRCC cohort) (15), and the Clinical Proteomic Tumor Analysis Consortium (CPTAC) (https://proteomics.cancer.gov/programs/cptac). Transcriptomic expression profiles, tumor somatic mutations, and corresponding clinical information of 532 patients with ccRCC and patients across 33 cancers were obtained from The Cancer Genome Atlas (TCGA) database. Transcriptomics data of 226 ccRCC and 196 normal kidney samples were also enrolled from the Gene Expression Omnibus (GEO) database, including GSE36895 (53 ccRCC and 23 normal samples), GSE40435 (101 ccRCC and 101 normal renal samples), and GSE53757 (72 ccRCC and 72 normal samples) cohorts. Additionally, RNA sequences and clinicopathological data of 101 ccRCC patients from the E-MTAB-1980 cohort were available from the ArrayExpress (https://www.ebi.ac.uk/arrayexpress/) database as a transcriptomics validation cohort. Besides, we also included 232 ccRCC samples with proteomics information and available clinical and pathologic data from the FUSCC-ccRCC cohort as a proteomics validation cohort. The details about the FUSCC-ccRCC cohort and how amino acid metabolism clusters are defined were discussed in the previous study (15).

DDC expression and correlations with clinicopathological features

The DDC expressions of two proteomic cohorts and three transcriptomic cohorts were used to determine whether DDC expression was dysregulated in ccRCC using the Wilcox test. Statistical analyses were conducted on the relationship between DDC expression and clinicopathological features using ggplot2 (v3.3.2) in R software. The Sankey plot of clinicopathological features was conducted in R software.

Differentially expressed genes identification and functional enrichment analysis

We divided the TCGA cohort into two subgroups based on the median value of DDC expression in order to keep the classification model simple and ensure universality. Then the DEGs between two subgroups were identified with the threshold of $|\log2(\text{Fold Change})| > 1.5$ and adjusted $P < 0.05$ using the R package "limma" (26) in the TCGA cohort. The Cluster Profiler package (version: 3.18.0) in R software was employed to analyze the Gene Ontology (GO)-identified functions of potential targets and perform Kyoto Encyclopedia of Genes and Genomes (KEGG) pathway enrichment analysis between subgroups. For pathway analysis, the R software GSVA package was used, choosing parameter as method = 'ssgsea' (27). The correlation between DDC expression and pathway score was assessed using Spearman's correlation analysis.

Evaluation of immune cells abundance in the TME and immunological response of ccRCC

To evaluate the absolute proportion of tumor-infiltrating lymphocytes (TILs) in ccRCC, we conducted the CIBERSORT and assessed the proportion of all TILs using support vector regression. Besides, to assess the reliability of the algorithms, we used the "immuneeconv" and "pheatmap" R packages that provide an integrated P-value from the six latest algorithms, including TIMER, xCell, MCP-counter, CIBERSORT, EPIC, and quanTIseq for individuals (28). We also explored the TIL differences between two DDC subgroups. The potential therapeutic response to immune checkpoint inhibitors (ICIs) was predicted with the TIDE algorithm, as described previously (29).

Survival analysis

The primary endpoint was overall survival (OS), and the secondary endpoint was progression-free survival (PFS) in ccRCC patients. Survival curves were performed to assess the prognostic significance using the Kaplan–Meier method and log-rank test with 95% confidence intervals (95% CI). The cut-off value was defined *via* the "survminer" R package or median threshold according to samples assigned to the TCGA cohort. To detect the independent prognostic indicators, we assessed the hazard ratio (HR) and 95% CI using univariate and multivariate Cox logistic regression analysis and visualized the results in the forest plots. We utilized two external validation cohorts, including E-MTAB-1980 and the FUSCC-ccRCC cohort, to confirm the prognostic value of DDC in ccRCC.

Immunohistochemical analysis

Samples were embedded in paraffin at a thickness of 4 nm. Deparaffinization and rehydration were performed on each slide.

Immunohistochemical (IHC) assay was conducted with anti-DOPA Decarboxylase/DDC antibody (1:1,000, ab211535, Abcam) diluted 1:1,000. After incubating the HRP-labeled secondary antibody for 2 h, we performed immunodetection the next day, following the manufacturer's protocols. Based on the integration of the degree of intensity and density of staining, two independent pathologists evaluated the overall IHC score (from 0 to 12) as follows: negative staining, 0 to 3; positive staining, 4 to 12, as previously described (30).

Statistical analysis

For statistical analyses, the SPSS software (version 23.0), GraphPad Prism software (version 8.0), or R software (version 3.3.2) were employed. The relationships between DDC expression and clinicopathological characteristics were evaluated using the Chi-square test. The Student's t-test was used to compare the differences between the two groups. A one-way ANOVA was performed to compare the differences among multiple groups. All hypothesis tests were two-sided, and P-values below 0.05 were regarded as significant.

Results

Identification of DDC expression in regulating amino acids metabolism of ccRCC

Our previous study found that tumor and adjacent normal tissue had significant differences in amino acid metabolism-related pathways in the FUSCC proteomic ccRCC cohort (Figure 1A). The amino acid metabolism-related proteins, including SHMT1, BHMT, AHCY, ALDH1L1, DDC, AOX1, AFMID, KYNU, and HAAO, were downregulated in ccRCC compared to adjacent normal tissue, while NNMT was upregulated in ccRCC compared to adjacent normal tissue (Figure 1A). Thus, we found that DDC was significantly downregulated compared to other downregulated amino acid metabolism-related genes. The immunohistochemistry staining demonstrated a similar phenomenon (Figure 1B). To determine whether DDC is aberrantly expressed in ccRCC, we utilized two proteomic cohorts (FUSCC and CPTAC) and three transcriptomic cohorts (GSE36859, GSE40435, and GSE53757) to verify DDC expression at the transcription and translation level. The results demonstrated that both the protein and mRNA levels of DDC were lower in the ccRCC specimen compared to adjacent normal tissue (P <0.001) (Figures 1C, D). We next explored DDC expression in human cancers and found that DDC is widely differentially expressed in pan-cancer analysis using the TCGA expression profiling (Figure 1E), which indicated that DDC is expressed differently in different human cancers. The aberrant DDC expressions deserved further investigation to determine whether DDC could serve as a therapeutic target.

Associations between DDC and clinicopathological features in ccRCC from the TCGA cohort

To explore whether DDC expression altered in the process of tumor progression, we divided TCGA cohort into two subgroups based on the median value of DDC expression (DDC^{High} vs. DDC^{Low}). We found that different DDC subgroups had different compositions of clinicopathological features, indicating that DDC expression had potential associations with clinicopathological features, including gender, T stage, N stage, and M stage, as well as the American Joint Committee on Cancer (AJCC) stage and tumor grade (P <0.05) (Figure 2A). Then, the distribution of clinical phenotypes and DDC expression of the TCGA cohort was presented in Figure 2B. Patients diagnosed as stages III–IV were more likely to have lower DDC expression, and the DDC^{Low} group showed a worse prognosis compared to the DDC^{High} group (Figure 2B). We then found that DDC expression demonstrated weak but statistically significant correlations with tumor AJCC stage (R = −0.126, P = 0.0036) and tumor grade (R = −0.134, P = 0.00214) (Figure 2C). The results indicated the indispensable role of DDC expression in the ccRCC progression process.

Low DDC expression in ccRCC is associated with worse prognosis

Due to DDC expression dysregulation in human cancers, we first explored the prognostic value of DDC in pan-cancer analysis. We found that, among all the cancers in the TCGA database, the prognostic implications of DDC expression showed the most significant value in the ccRCC (Figure 3A). The following analyses performed in ccRCC cohort demonstrated similar results: lower DDC expression was associated with shorter OS and progression-free survival (PFS) (P <0.001) (Figure 3B). We next employed univariate and multivariate Cox analyses to identify the independent prognostic factor. In univariate Cox analysis, the gender, T stage, N stage, M stage, and tumor grade was correlated with worse outcome, while DDC expression was correlated with better outcome (P <0.001). After adjusting for the confounding factors, only DDC expression (HR: 0.828, 95% CI: 0.754–0.909) and M stage (HR: 5.194, 95% CI: 3.080–8.759) could serve as independent prognostic factors (P <0.001) (Figure 3C). To confirm the prognostic ability of DDC expression, we performed survival analysis in two external cohorts. The results revealed that the lower level of DDC expression was correlated with a worse prognosis in the E-MTAB-1980 cohort (P = 0.030) and in the FUSCC-proteomic-ccRCC cohort (P = 0.003), respectively (Figure 3D). The findings above indicated the stable prognostic

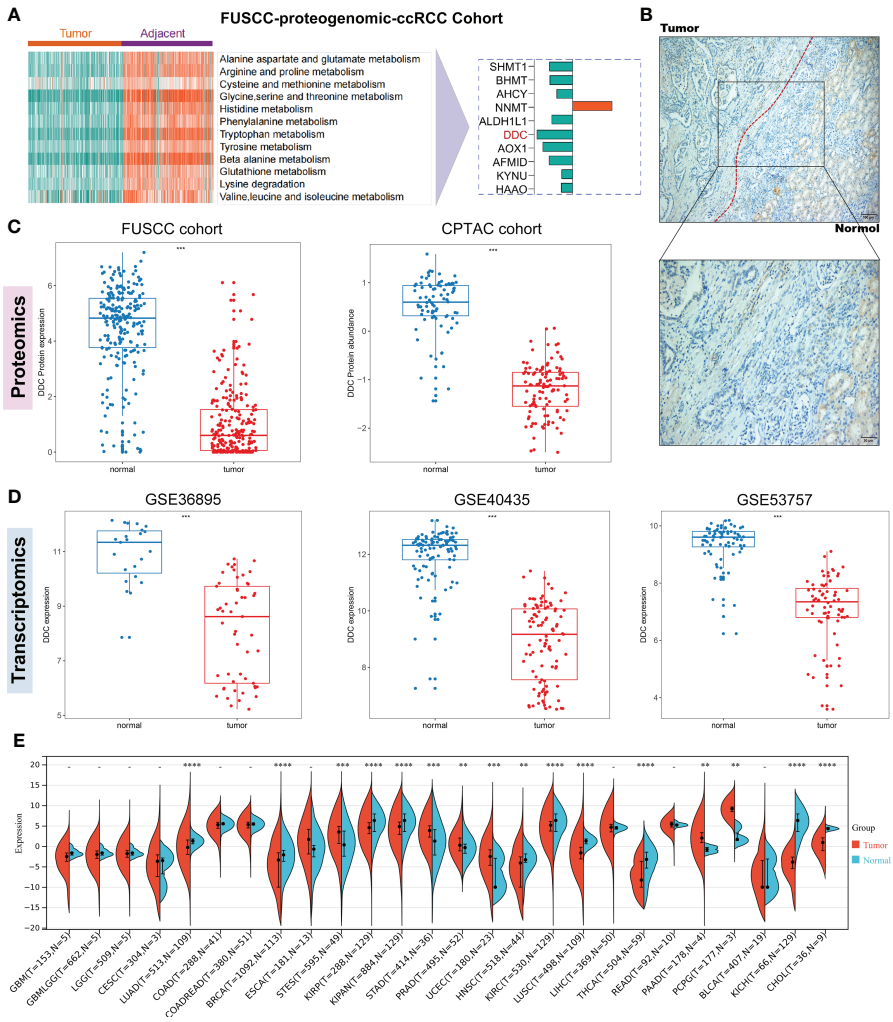

FIGURE 1
Identification of DDC expression in regulating amino acid metabolism of ccRCC. **(A)** The FUSCC proteomic ccRCC cohort demonstrates that amino acid metabolism is extensively dysregulated between tumor and normal tissue and the DDC protein is significantly downregulated in ccRCC. **(B)** Representative immunohistochemical (IHC) staining of DDC protein in normal kidney and ccRCC tissues. **(C)** Proteomic cohorts (FUSCC and CPTAC) showed DDC protein is lower in tumors than in normal tissue. **(D)** Transcriptomic cohorts (GSE36859, GSE40435, and GSE53757) showed DDC mRNA is lower in tumors than in normal tissue. **(E)** Pan-cancer analysis of DDC mRNA expression in human cancers. CPTAC, Clinical Proteomic Tumor Analysis Consortium; ccRCC, clear cell renal cell carcinoma; DDC, L-dopa decarboxylase; mRNA, messenger RNA (**P <.01; ***P <.001; ****P <.0001).

value of DDC expression, suggesting that DDC expression could be an independent biomarker in predicting outcomes.

Functional enrichments of DDC expression subgroups

Based on the above results that DDC expression was lower in ccRCC specimens and correlated with a worse prognosis, we tried to undermine the potential mechanisms that might contribute to the differential prognosis. The differentially expressed genes (DEGs) between the DDC^{Low} and DDC^{High} subgroups are presented in Figure 4A. With the exception of DDC, other genes such as PKLR, AGX12, HAO2, TMEM174, LRP2, CYP4A11, CUBN, SLC22A6, SLC22A12, SLC6A19, ALDOB, and SLC17A3 also showed significant low expression in the DDC^{Low} group (Figure 4A). The DEGs were used to perform the following functional enrichment analysis: The upregulated DEGs are mainly enriched in the PI3K-Akt signaling pathway, while the downregulated DEGs are mainly enriched in valine, leucine, and isoleucine degradation, the PPAR signaling pathway, drug metabolism-cytochrome P450, bile secretion, and arginine and proline metabolism (Figure 4B). The GO results demonstrated that upregulated DEGs were mainly enriched in

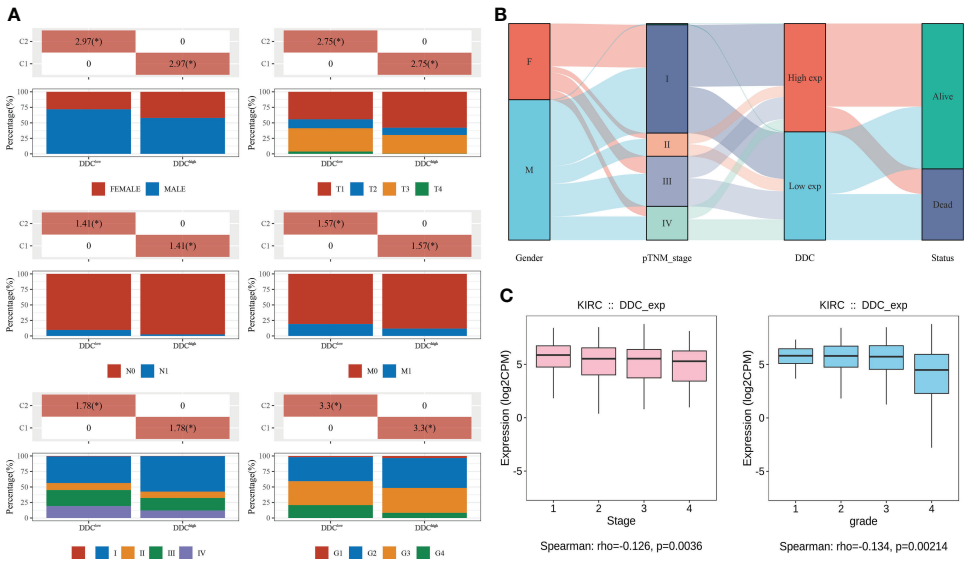

FIGURE 2
Associations between DDC and clinicopathological features in ccRCC from the TCGA cohort. **(A)** The differences between clinicopathological features and DDC subgroups. **(B)** The distribution of clinicopathological features, DDC subgroups, and live status in KIRC. **(C)** The Spearman correlation between DDC mRNA expression and tumor stage (left) and tumor grade (right) in KIRC. DDC, L-dopa decarboxylase; mRNA, messenger RNA; KIRC, Kidney renal clear cell carcinoma (*P <.05).

extracellular structure organization, extracellular matrix organization, and so on. The downregulated DEGs were mainly enriched in small molecule catabolic processes, organic acid transport, organic acid catabolic processes, cellular amino acid metabolic processes, carboxylic acid transport, carboxylic acid catabolic processes, and so on (Figure 4B). Because the KEGG pathway is enriched in the PI3K-Akt signaling pathway, we explored the correlation between the tumor proliferation signature and DDC expression. The Spearman's correlation test indicated potential correlations between DDC and cancer cell proliferation (R = −0.15, P <0.001) (Figure 4C). These results revealed the biological differences between the DDC^{Low} and DDC^{High} subgroups and the potential correlation of DDC on proliferation.

Differential immune microenvironment between DDC expression subgroups

Based on the above subgroups, we wondered whether DDC could exert a potential influence on immune cell infiltrations and expressions of ICP genes. The immune cell infiltrations analyzed by the "CIBERSORT" package showed that the proportions of monocytes and M1 macrophages were higher in the DDC^{High} subgroup, while the proportions of Tregs, follicular helper T cells, M0 macrophages, and memory B cells were higher in the DDC^{Low} subgroup (Figure 5A). This might partly explain the survival difference in that the prognosis of the DDC^{Low} subgroup was better than that of the DDC^{Low} subgroup. Next, we found that the ICP genes, including SIGLEC15, HAVCR2, and CD274 (PD-L1), expressed differently in DDC subgroups (Figure 5B). The SIGLEC15 expression was lower in the DDC^{High} subgroup, while HAVCR2 and CD274 were higher in the DDC^{High} subgroup (P <0.001), which suggested the potential capability in immune regulation. The tumor immune dysfunction and exclusion (TIDE) score has confirmed its ability to predict the immune checkpoint inhibitor (ICI) response (31). In our study, we found that the DDC^{High} subgroup had a lower level of TIDE score than the DDC^{Low} subgroup (P <0.0001) (Figure 5C), which meant that the DDC^{Low} subgroup seemed to have a worse immunotherapy response and worse prognosis. To investigate the impacts of DDC protein on immune cell infiltrations, we explored the pan-cancer analysis and found that DDC expression was closely correlated with immune cell infiltrations in the ccRCC cohort (Figure 5D). Consistent with the above results, DDC demonstrated significant correlations with M0 and M1 macrophages in ccRCC, and the underlying regulatory mechanisms need to be elucidated in the future.

Discussion

Kidney cancer is a highly genetically heterogeneous malignant tumor, which may cause patients from different races and regions to carry different gene mutations and genetic phenotypes, which in turn cause the biological behavior of tumor cells and different

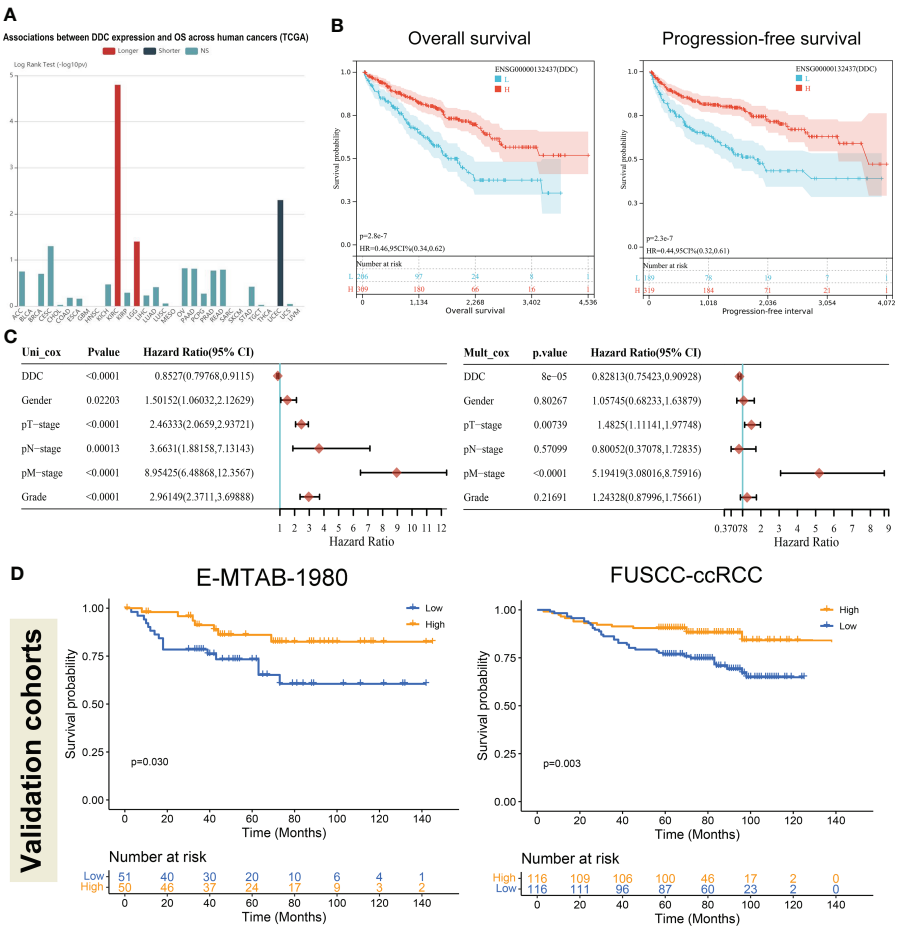

FIGURE 3
Low DDC expression in ccRCC correlated with a worse prognosis. **(A)** The pan-cancer associations between DDC expression and OS in human cancers. **(B)** Kaplan–Meier survival analysis of the relationships between DDC mRNA expression and OS (P <.001) and PFS (P <.001) in the KIRC cohort. **(C)** Univariate and multivariate Cox logistic regression analysis of OS in the TCGA cohort. **(D)** External Kaplan–Meier survival analysis of the relationships between DDC expression and OS in the E-MTAB-1980 cohort (P = .030) and FUSCC-ccRCC cohort (P = .003). DDC, L-dopa decarboxylase; mRNA, messenger RNA; OS, Overall Survival; PFS, Progression-free Survival; KIRC, Kidney renal clear cell carcinoma.

sensitivity to treatment (32, 33). Therefore, molecular characteristics and subtypes based on multi-omics data are essential for improving treatment efficacy and promoting the achievement of precision medicine in cancer (34, 35). Although there is a growing interest in the function of amino acid metabolism-related genes in cancer, little is known about how DDC proteins work in ccRCC, and it is uncertain whether DDC expression may be used as diagnostic or prognostic markers. Here, we assessed the diagnostic and prognostic value of DDC mRNA and protein expression in external ccRCC cohorts and found potential associations between DDC expression and clinicopathological features. We also explored functional analysis and found aberrant enrichment in the PI3K-Akt signaling pathway. Analysis of immune cell infiltration and ICP expression revealed the underlying regulatory effects of DDC on the tumor microenvironment (TME) and immune system.

In our study, we discovered that DDC mRNA and protein expression were downregulated in ccRCC compared to adjacent normal tissue. There were potential correlations between DDC expression and higher grade, advanced stages. The survival analysis from external validation cohorts revealed that low DDC expression correlated with worse OS. The results above indicate that DDC expression level might be a reliable biomarker assisting in diagnosis and predicting prognosis in ccRCC. To further investigate the potential functions of DDC, we employed KEGG and GO analyses. The findings reveal that DDC protein could possibly enrich the PI3K-Akt signaling pathway, amino acid metabolism, extracellular matrix organization, and so on. The following subgroup analysis identified Treg as being significantly upregulated in the DDC^{High} subgroup, while M1 macrophage was significantly upregulated in the DDC^{Low} subgroup. There were significant

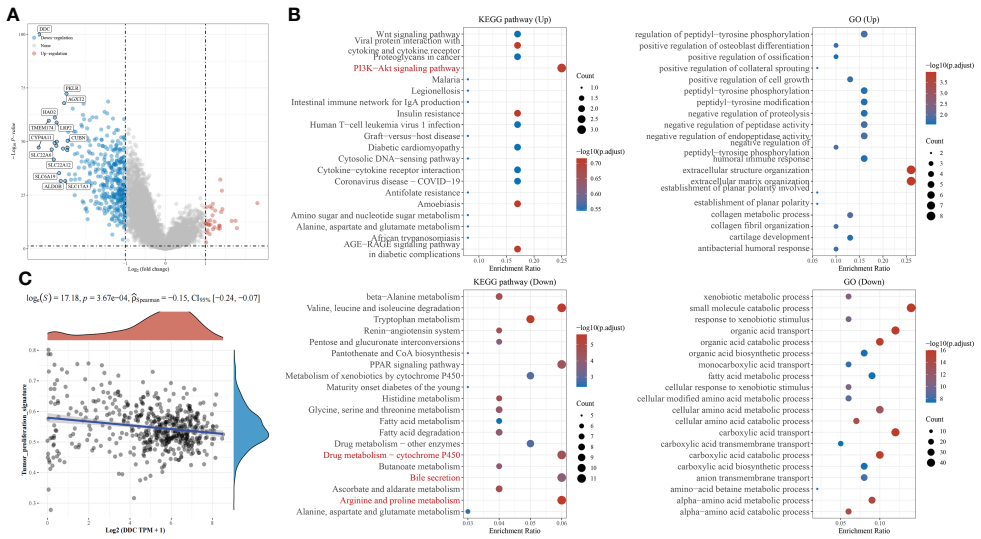

FIGURE 4
Functional enrichment analysis of DEGs between DDC subgroups. **(A)** The volcano plot of DEGs between DDC subgroups in KIRC. **(B)** The KEGG pathways and GO functional enrichment analysis of DEGs between DDC subgroups. **(C)** The Spearman correlation between DDC expression and tumor proliferation signature (R = −0.15; P <.001). DDC, L-dopa decarboxylase; KIRC, Kidney renal clear cell carcinoma; GO, Gene Ontology; KEGG, Kyoto Encyclopedia of Genes and Genomes.

differences in ICP gene expressions between the two DDC subgroups, which might eventually contribute to the different TIDE scores and prognosis.

DDC expression has been investigated in several malignant tumors. But in contrast, high DDC expressions are found more frequently in high Gleason's score and advanced stage, and the underlying mechanism could be attributed to that DDC could co-activate androgen receptor (AR)–ligand transcriptional activity without affecting AR protein expression (36, 37). The following research tested whether the DDC enzymatic inhibitor, carbidopa, would suppress prostate cancer cell proliferation (38). Carbidopa could significantly restrict AR transactivation and PSA upregulation. The cell and castrated mice experiments demonstrated significant tumor growth suppression and decreased serum PSA effects of carbidopa. However, in ccRCC, the opposite strategy should be taken into consideration because of the unique genetic backgrounds between prostate cancer and ccRCC. In breast cancer, DDC upregulation was associated with a longer OS. The two breast cancer cells treated with epinephrine demonstrated contrary results in DDC expression and cell viability (21). Although the previous studies provided a novel insight that antitumor treatments could be combined with endocrine-related therapy strategies, targeted therapy combined with immunotherapy has become the first line of treatment for advanced ccRCC patients and ccRCC patients usually demonstrate relatively fixed types of mutations unlike prostate cancer or breast cancer. The underlying correlations between DDC and mutations such as VHL, BAP1, SETD2, and PBRM1 and whether DDC could serve as a new drug target for treating ccRCC patients or boosting immunotherapy response should be investigated in future studies to better guide treatments.

Dopamine (DA), catalyzed by the DDC protein, plays a role in the normal activities of human lives. It is also an important ingredient in orepinephrine and epinephrine (39). Previous studies found that dopamine receptors could be a biomarker for several malignant tumors (40), which highlights the important role of dopamine that depends on DDC activity in carcinogenesis. Chakroborty et al. found that a low dosage of DDC could restrict tumor angiogenesis *via* inhibiting VEGFR phosphorylation and was correlated with growth restriction *in vitro* (41). Dopamine could significantly promote the efficacy of anti-cancer drugs. The replenishments caused a low proliferation rate and metastatic potential that might be attributed to decreased phosphorylation levels of VEGF receptor-2, mitogen-activated protein kinase, and focal adhesion kinase. Angiogenesis is also one of the major characteristics of ccRCC, and several targeted therapies such as sunitinib, axitinib, and other drugs inhibit ccRCC progression by targeting VEGF targets. Supplementation with dopamine or increasing the activity of DDC enzymes may have a synergistic effect in combination with targeted therapy, significantly inhibiting tumor growth and progression. Moreover, a previous study found that mice with daily stress contributed to increased tumor growth compared to those without daily stress, which could be blocked by dopamine replenishment (42). This study also highlighted the importance of the tumor

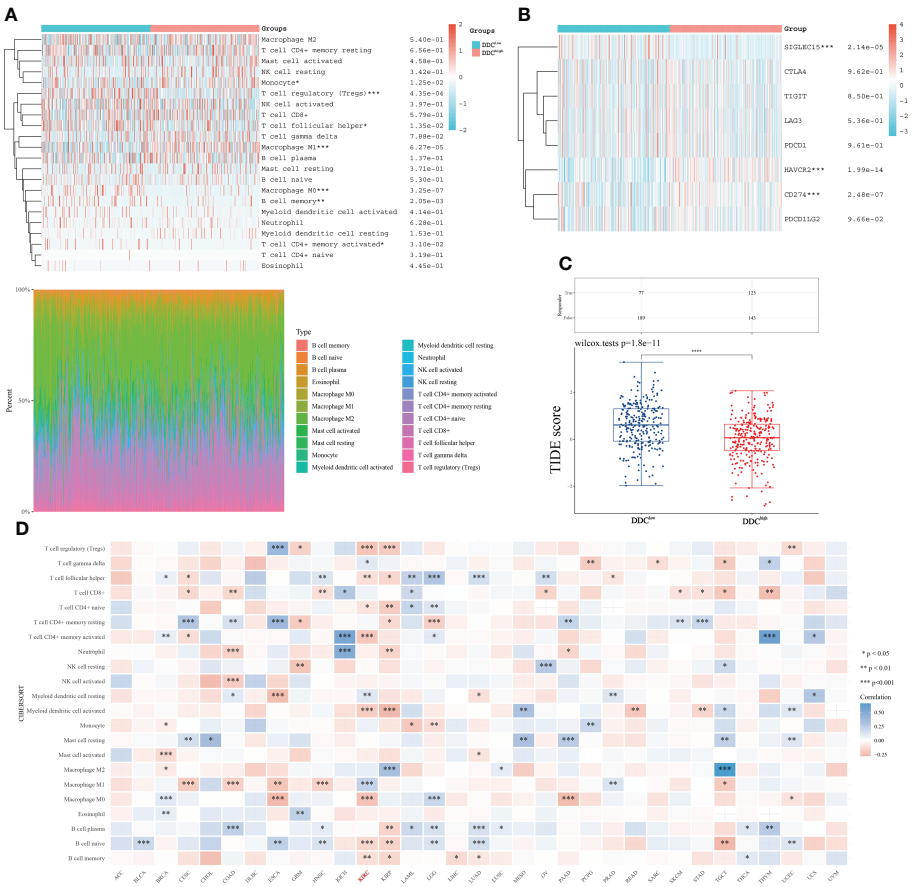

FIGURE 5
DDC expression correlated with immune microenvironment regulation in ccRCC. **(A)** The differences in immune cell infiltration between DDC subgroups. **(B)** The differences of ICP genes between DDC subgroups. **(C)** The differences in TIDE scores between DDC subgroups. The TIDE score is significantly higher in the DDC^{Low} group (P <.0001). **(D)** The pan-cancer correlations between immune cell infiltrations and DDC expression. DDC, L-dopa decarboxylase; ICP, immune checkpoint; TIDE, Tumor Immune Dysfunction and Exclusion (*P <.05; **P <.01; ***P <.001; ****P <.0001).

microenvironment in dopamine deletion and high-stress conditions. Dopamine could activate resting effector T cells (Teffs) and suppress regulatory T cells (Tregs) (43, 44). It also affects helper T-cell differentiation, inhibits Treg activation, takes part in antigen presentation processes, and modulates intracellular signaling pathways, suggesting that dopamine plays an important regulatory role in affecting the tumor microenvironment (45). Dopamine improved the efficacy of chemotherapy *in vivo* and *in vitro* experiments by inhibiting the M2 characteristics of tumor-associated macrophages (TAMs) (46). Qin et al. attempted to re-polarize M2 macrophages to M1 macrophages, and they found that dopamine could upregulate M1-polarized markers and downregulate M2-polarized markers, which could transfer the tumor microenvironment from “cold” to “hot” (47, 48). The M1 macrophage exerted anti-tumor effects and correlated with the immunotherapy response (49, 50). PD-L1 expression (CD274) was previously approved by the FDA as a predictive biomarker for ICI (50, 51). Thus, the differentially expressed PD-L1 and different proportions of M1 macrophages may influence the efficacy of immunotherapy. Future studies should focus on the effects of dopamine catalyzed by the DDC protein on the TME and the underlying mechanisms.

The findings of this study contribute to our knowledge of the function of DDC and recognize it as a potential diagnostic and prognostic factor in ccRCC. However, our study has certain limitations. First, although we utilize several external cohorts to validate DDC expression, large cohorts are needed to validate our conclusions. Second, the diagnostic and prognostic significance of DDC expression has been defined, although the underlying processes regulating its expression levels are still unknown. This will be made clearer by additional functional enrichment and annotation analysis. Third, the DDC protein could influence the percentage of M1 macrophages within the

tumor microenvironment, and the underlying mechanisms are needed to be explored in future studies.

In conclusion, our study first systematically identified and assessed DDC expression and its potential functions in the regulation of metabolism and tumor microenvironment of ccRCC. DDC might function as a tumor suppressor protein and has been markedly linked to cancer progression and a worse prognosis in ccRCC.

Data availability statement

The original contributions presented in the study are included in the article/Supplementary Material. Further inquiries can be directed to the corresponding authors.

Author contributions

Conceptualization: KC, JS, CL, and AA. Data curation and formal analysis: KC, WX, JS, AA, WL, and YQ. Funding acquisition: WX, YQ, HZ, and DY. Investigation and methodology: KC, WX, JS, AA, and WL. Resources and software: WL, WX, YQ, HZ, and DY. Supervision: YQ, HZ, and DY. Validation and visualization: WX, WL, KC, and AA. Original draft: KC, JS, and CL. Editing: YQ, HZ, and DY. All authors listed have made a substantial, direct, and intellectual contribution to the work and approved it for publication.

Funding

This work was supported by grants from the National Natural Science Foundation of China (nos. 81802525 and 82172817), the Natural Science Foundation of Shanghai (no. 20ZR1413100), the Beijing Xisike Clinical Oncology Research Foundation (no. Y-HR2020MS-0948), the National Key Research and Development Project (no. 2019YFC1316005), the Shanghai "Science and Technology Innovation Action Plan" Medical Innovation Research Project (no. 22Y11905100), and the Shanghai Anti-Cancer Association Eyas Project (nos. SACA-CY21A06 and SACA-CY21B01).

Acknowledgments

We thank all the writers who gave precious advice to this article.

Conflict of interest

The authors declare that the research was conducted in the absence of any commercial or financial relationships that could be construed as a potential conflict of interest.

Publisher's note

All claims expressed in this article are solely those of the authors and do not necessarily represent those of their affiliated organizations, or those of the publisher, the editors and the reviewers. Any product that may be evaluated in this article, or claim that may be made by its manufacturer, is not guaranteed or endorsed by the publisher.

Supplementary material

The Supplementary Material for this article can be found online at: https://www.frontiersin.org/articles/10.3389/fonc.2022.1079446/full#supplementary-material

References

1. Sung H, Ferlay J, Siegel RL, Laversanne M, Soerjomataram I, Jemal A, et al. Global Cancer Statistics 2020: GLOBOCAN Estimates of Incidence and Mortality Worldwide for 36 Cancers in 185 Countries. *CA: Cancer J Clin* (2021) 71(3):209–49. doi: 10.3322/caac.21660

2. Zheng R, Zhang S, Zeng H, Wang S, Sun K, Chen R, et al. Cancer incidence and mortality in China, 2016. *J Natl Cancer Center* (2022) 2(1):1–9. doi: 10.1016/j.jncc.2022.02.002

3. Siegel RL, Miller KD, Fuchs HE, Jemal A. Cancer statistics, 2022. *CA: Cancer J Clin* (2022) 72(1):7–33. doi: 10.3322/caac.21708

4. Moch H, Cubilla AL, Humphrey PA, Reuter VE, Ulbright TM. The 2016 WHO Classification of Tumours of the Urinary System and Male Genital Organs-Part A: Renal, Penile, and Testicular Tumours. *Eur Urol* (2016) 70(1):93–105. doi: 10.1016/j.eururo.2016.02.029

5. Rini BI, Campbell SC, Escudier B. Renal cell carcinoma. *Lancet (London England)* (2009) 373(9669):1119–32. doi: 10.1016/s0140-6736(09)60229-4

6. Motzer RJ, Jonasch E, Agarwal N, Bhayani S, Bro WP, Chang SS, et al. Kidney Cancer, Version 2.2017, NCCN Clinical Practice Guidelines in Oncology. *J Natl Compr Cancer Network JNCCN* (2017) 15(6):804–34. doi: 10.6004/jnccn.2017.0100

7. Vander Heiden MG, Cantley LC, Thompson CB. Understanding the Warburg effect: the metabolic requirements of cell proliferation. *Sci (New York NY)* (2009) 324(5930):1029–33. doi: 10.1126/science.1160809

8. Tian X, Wang Y, Xu W, Tang H, Zhu S, Anwaier A, et al. Special issue "The advance of solid tumor research in China": Multi-omics analysis based on 1311 clear cell renal cell carcinoma samples identifies a glycolysis signature associated with prognosis and treatment response. *Int J Cancer* (2023) 152(1):66–78. doi: 10.1002/ijc.34121

9. Li Z, Zhang H. Reprogramming of glucose, fatty acid and amino acid metabolism for cancer progression. *Cell Mol Life Sci CMLS* (2016) 73(2):377–92. doi: 10.1007/s00018-015-2070-4

10. Yoo HC, Han JM. Amino Acid Metabolism in Cancer Drug Resistance. *Cells* (2022) 11(1):140. doi: 10.3390/cells11010140

11. Johnson C, Warmoes MO, Shen X, Locasale JW. Epigenetics and cancer metabolism. *Cancer Lett* (2015) 356(2 Pt A):309–14. doi: 10.1016/j.canlet.2013.09.043

12. Xu W, Anwaier A, Liu W, Tian X, Zhu W-K, Wang J, et al. Systematic Genome-Wide Profiles Reveal Alternative Splicing Landscape and Implications of Splicing Regulator DExD-Box Helicase 21 in Aggressive Progression of Adrenocortical Carcinoma. *Phenomics* (2021) 1(6):243–56. doi: 10.1007/s43657-021-00026-x

13. Zhao J, Xu H, Su Y, Pan J, Xie S, Xu J, et al. Emerging Regulatory Mechanisms of N6-Methyladenosine Modification in Cancer Metastasis. *Phenomics* (2022). doi: 10.1007/s43657-021-00043-w

14. Du Y, Zhang P, Liu W, Tian J. Optical Imaging of Epigenetic Modifications in Cancer: A Systematic Review. *Phenomics* (2022) 2(2):88–101. doi: 10.1007/s43657-021-00041-y

15. Qu Y, Feng J, Wu X, Bai L, Xu W, Zhu L, et al. A proteogenomic analysis of clear cell renal cell carcinoma in a Chinese population. *Nat Commun* (2022) 13 (1):2052. doi: 10.1038/s41467-022-29577-x

16. Su J, Tian X, Zhang Z, Xu W, Anwaier A, Ye S, et al. A novel amino acid metabolism-related gene risk signature for predicting prognosis in clear cell renal cell carcinoma. *Original Res* (2022) 12:1019949. doi: 10.3389/fonc.2022.1019949

17. Feng F, Pan L, Wu J, Li L, Xu H, Yang L, et al. Cepharanthine inhibits hepatocellular carcinoma cell growth and proliferation by regulating amino acid metabolism and suppresses tumorigenesis *in vivo*. *Int J Biol Sci* (2021) 17(15):4340–52. doi: 10.7150/ijbs.64675

18. Yang J, Dai X, Xu H, Tang Q, Bi F. Regulation of Ferroptosis by Amino Acid Metabolism in Cancer. *Int J Biol Sci* (2022) 18(4):1695–705. doi: 10.7150/ijbs.64982

19. Mappouras DG, Stiakakis J, Fragoulis EG. Purification and characterization of L-dopa decarboxylase from human kidney. *Mol Cell Biochem* (1990) 94(2):147–56. doi: 10.1007/bf00214121

20. Carey RM. The intrarenal renin-angiotensin and dopaminergic systems: control of renal sodium excretion and blood pressure. *Hypertension (Dallas Tex 1979)* (2013) 61(3):673–80. doi: 10.1161/hypertensionaha.111.00241

21. Tremmel E, Kuhn C, Kaltofen T, Vilsmaier T, Mayr D, Mahner S, et al. L-Dopa-Decarboxylase (DDC) Is a Positive Prognosticator for Breast Cancer Patients and Epinephrine Regulates Breast Cancer Cell (MCF7 and T47D) Growth In Vitro According to Their Different Expression of G(i)- Protein- Coupled Receptors. *Int J Mol Sci* (2020) 21(24):9565. doi: 10.3390/ijms21249565

22. Koutalellis G, Stravodimos K, Avgeris M, Mavridis K, Scorilas A, Lazaris A, et al. L-dopa decarboxylase (DDC) gene expression is related to outcome in patients with prostate cancer. *BJU Int* (2012) 110(6 Pt B):E267–73. doi: 10.1111/j.1464-410X.2012.11152.x

23. Artemaki PI, Papatsirou M, Boti MA, Adamopoulos PG, Christodoulou S, Vassilacopoulou D, et al. Revised Exon Structure of l-DOPA Decarboxylase (DDC) Reveals Novel Splice Variants Associated with Colorectal Cancer Progression. *Int J Mol Sci* (2020) 21(22):8568. doi: 10.3390/ijms21228568

24. Kim JH, Lee SY, Choi JE, Do SK, Lee JH, Hong MJ, et al. Polymorphism in ASCL1 target gene DDC is associated with clinical outcomes of small cell lung cancer patients. *Thorac Cancer* (2020) 11(1):19–28. doi: 10.1111/1759-7714.13212

25. Sakakura C, Takemura M, Hagiwara A, Shimomura K, Miyagawa K, Nakashima S, et al. Overexpression of dopa decarboxylase in peritoneal dissemination of gastric cancer and its potential as a novel marker for the detection of peritoneal micrometastases with real-time RT-PCR. *Br J Cancer* (2004) 90(3):665–71. doi: 10.1038/sj.bjc.6601544

26. Xu W, Liu W, Anwaier A, Tian X, Su J, Shi G, et al. Deciphering the role of miR-187-3p/LRFN1 axis in modulating progression, aerobic glycolysis and immune microenvironment of clear cell renal cell carcinoma. *Discovery Oncol* (2022) 13(1):59. doi: 10.1007/s12672-022-00523-z

27. Hänzelmann S, Castelo R, Guinney J. GSVA: gene set variation analysis for microarray and RNA-seq data. *BMC Bioinf* (2013) 14:7. doi: 10.1186/1471-2105-14-7

28. Xu W, Anwaier A, Ma C, Liu W, Tian X, Su J, et al. Prognostic Immunophenotyping Clusters of Clear Cell Renal Cell Carcinoma Defined by the Unique Tumor Immune Microenvironment. *Front Cell Dev Biol* (2021) 9:785410. doi: 10.3389/fcell.2021.785410

29. Jiang P, Gu S, Pan D, Fu J, Sahu A, Hu X, et al. Signatures of T cell dysfunction and exclusion predict cancer immunotherapy response. *Nat Med* (2018) 24(10):1550–8. doi: 10.1038/s41591-018-0136-1

30. Xu W, Wu Y, Liu W, Anwaier A, Tian X, Su J, et al. Tumor-associated macrophage-derived chemokine CCL5 facilitates the progression and immunosuppressive tumor microenvironment of clear cell renal cell carcinoma. *Int J Biol Sci* (2022) 18(13):4884–900. doi: 10.7150/ijbs.74647

31. Fu J, Li K, Zhang W, Wan C, Zhang J, Jiang P, et al. Large-scale public data reuse to model immunotherapy response and resistance. *Genome Med* (2020) 12 (1):21. doi: 10.1186/s13073-020-0721-z

32. Xu W, Anwaier A, Liu W, Tian X, Su J, Shi G, et al. The unique genomic landscape and prognostic mutational signature of Chinese clear cell renal cell carcinoma. *J Natl Cancer Center* (2022) 2(3):162–70. doi: 10.1016/j.jncc.2022.07.001

33. Xu WH, Shi SN, Xu Y, Wang J, Wang HK, Cao DL, et al. Prognostic implications of Aquaporin 9 expression in clear cell renal cell carcinoma. *J Trans Med* (2019) 17(1):363. doi: 10.1186/s12967-019-2113-y

34. Anwaier A, Zhu S-X, Tian X, Xu W-H, Wang Y, Palihati M, et al. Large-Scale Proteomics Data Reveal Integrated Prognosis-Related Protein Signatures and Role of SMAD4 and RAD50 in Prognosis and Immune Infiltrations of Prostate Cancer Microenvironment. *Phenomics* (2022). doi: 10.1007/s43657-022-00070-1

35. Wang F, Yang M, Luo W, Zhou Q. Characteristics of tumor microenvironment and novel immunotherapeutic strategies for non-small cell lung cancer. *J Natl Cancer Center* (2022). doi: 10.1016/j.jncc.2022.10.002

36. Wafa LA, Cheng H, Rao MA, Nelson CC, Cox M, Hirst M, et al. Isolation and identification of L-dopa decarboxylase as a protein that binds to and enhances transcriptional activity of the androgen receptor using the repressed transactivator yeast two-hybrid system. *Biochem J* (2003) 375(Pt 2):373–83. doi: 10.1042/bj20030689

37. Avgeris M, Koutalellis G, Fragoulis EG, Scorilas A. Expression analysis and clinical utility of L-Dopa decarboxylase (DDC) in prostate cancer. *Clin Biochem* (2008) 41(14-15):1140–9. doi: 10.1016/j.clinbiochem.2008.04.026

38. Wafa LA, Cheng H, Plaa N, Ghaidi F, Fukumoto T, Fazli L, et al. Carbidopa abrogates L-dopa decarboxylase coactivation of the androgen receptor and delays prostate tumor progression. *Int J Cancer* (2012) 130(12):2835–44. doi: 10.1002/ijc.26287

39. Beaulieu JM, Espinoza S, Gainetdinov RR. Dopamine receptors - IUPHAR Review 13. *Br J Pharmacol* (2015) 172(1):1–23. doi: 10.1111/bph.12906

40. Sachlos E, Risueño RM, Laronde S, Shapovalova Z, Lee JH, Russell J, et al. Identification of drugs including a dopamine receptor antagonist that selectively target cancer stem cells. *Cell* (2012) 149(6):1284–97. doi: 10.1016/j.cell.2012.03.049

41. Chakroborty D, Sarkar C, Mitra RB, Banerjee S, Dasgupta PS, Basu S. Depleted dopamine in gastric cancer tissues: dopamine treatment retards growth of gastric cancer by inhibiting angiogenesis. *Clin Cancer Res an Off J Am Assoc Cancer Res* (2004) 10(13):4349–56. doi: 10.1158/1078-0432.Ccr-04-0059

42. Moreno-Smith M, Lu C, Shahzad MM, Pena GN, Allen JK, Stone RL, et al. Dopamine blocks stress-mediated ovarian carcinoma growth. *Clin Cancer Res an Off J Am Assoc Cancer Res* (2011) 17(11):3649–59. doi: 10.1158/1078-0432.Ccr-10-2441

43. Levite M. Dopamine and T cells: dopamine receptors and potent effects on T cells, dopamine production in T cells, and abnormalities in the dopaminergic system in T cells in autoimmune, neurological and psychiatric diseases. *Acta physiologica (Oxford England)* (2016) 216(1):42–89. doi: 10.1111/apha.12476

44. Nasi G, Ahmed T, Rasini E, Fenoglio D, Marino F, Filaci G, et al. Dopamine inhibits human CD8+ Treg function through D(1)-like dopaminergic receptors. *J neuroimmunology* (2019) 332:233–41. doi: 10.1016/j.jneuroim.2019.02.007

45. Zhang T. Immune checkpoint inhibitors in extensive-stage small cell lung cancer. *J Natl Cancer Center* (2022) 2(3):130–1. doi: 10.1016/j.jncc.2022.07.003

46. Liu Q, Zhang R, Zhang X, Liu J, Wu H, Li Y, et al. Dopamine improves chemotherapeutic efficacy for pancreatic cancer by regulating macrophage-derived inflammations. *Cancer immunology immunotherapy CII* (2021) 70(8):2165–77. doi: 10.1007/s00262-020-02816-0

47. Qin T, Wang C, Chen X, Duan C, Zhang X, Zhang J, et al. Dopamine induces growth inhibition and vascular normalization through reprogramming M2-polarized macrophages in rat C6 glioma. *Toxicol Appl Pharmacol* (2015) 286 (2):112–23. doi: 10.1016/j.taap.2015.03.021

48. Demaria S, Coleman CN, Formenti SC. Radiotherapy: Changing the Game in Immunotherapy. *Trends cancer.* (2016) 2(6):286–94. doi: 10.1016/j.trecan.2016.05.002

49. Epelman S, Lavine KJ, Randolph GJ. Origin and functions of tissue macrophages. *Immunity* (2014) 41(1):21–35. doi: 10.1016/j.immuni.2014.06.013

50. Li W, Wu F, Zhao S, Shi P, Wang S, Cui D. Correlation between PD-1/PD-L1 expression and polarization in tumor-associated macrophages: A key player in tumor immunotherapy. *Cytokine Growth factor Rev* (2022) 67:49–57. doi: 10.1016/j.cytogfr.2022.07.004

51. Davis AA, Patel VG. The role of PD-L1 expression as a predictive biomarker: an analysis of all US Food and Drug Administration (FDA) approvals of immune checkpoint inhibitors. *J immunotherapy cancer.* (2019) 7 (1):278. doi: 10.1186/s40425-019-0768-9

frontiers | Frontiers in Oncology

TYPE Original Research
PUBLISHED 09 December 2022
DOI 10.3389/fonc.2022.1094657

OPEN ACCESS

EDITED BY
Le Qu,
Nanjing University, China

REVIEWED BY
Xun Shangguan,
Shanghai Jiao Tong University, China
Jian Zou,
Nanjing Medical University, China
Dalong Cao,
Fudan University, China

*CORRESPONDENCE
Hongbin Yuan
jfjczyy@aliyun.com

†These authors have contributed equally to this work

SPECIALTY SECTION
This article was submitted to Genitourinary Oncology, a section of the journal Frontiers in Oncology

RECEIVED 10 November 2022
ACCEPTED 23 November 2022
PUBLISHED 09 December 2022

CITATION
Ding R, Wei H, Jiang X, Wei L, Deng M and Yuan H (2022) Prognosis and pain dissection of novel signatures in kidney renal clear cell carcinoma based on fatty acid metabolism-related genes.
Front. Oncol. 12:1094657.
doi: 10.3389/fonc.2022.1094657

Prognosis and pain dissection of novel signatures in kidney renal clear cell carcinoma based on fatty acid metabolism-related genes

Ruifeng Ding[1†], Huawei Wei[1†], Xin Jiang[1†], Liangtian Wei[2], Mengqiu Deng[1] and Hongbin Yuan[1*]

[1]Department of Anesthesiology, Changzheng Hospital, Second Affiliated Hospital of Naval Medical University, Shanghai, China, [2]Jiangsu Province Key Laboratory of Anesthesiology, Xuzhou Medical University, Xuzhou, China

Renal cell carcinoma (RCC) is a malignant tumor that is characterized by the accumulation of intracellular lipid droplets. The prognostic value of fatty acid metabolism-related genes (FMGs) in RCC remains unclear. Alongside this insight, we collected data from three RCC cohorts, namely, The Cancer Genome Atlas (TCGA), E-MTAB-1980, and GSE22541 cohorts, and identified a total of 309 FMGs that could be associated with RCC prognosis. First, we determined the copy number variation and expression levels of these FMGs, and identified 52 overall survival (OS)-related FMGs of the TCGA-KIRC and the E-MTAB-1980 cohort data. Next, 10 of these genes—FASN, ACOT9, MID1IP1, CYP2C9, ABCD1, CPT2, CRAT, TP53INP2, FAAH2, and PTPRG—were identified as pivotal OS-related FMGs based on least absolute shrinkage and selection operator and Cox regression analyses. The expression of some of these genes was confirmed in patients with RCC by immunohistochemical analyses. Kaplan–Meier analysis showed that the identified FMGs were effective in predicting the prognosis of RCC. Moreover, an optimal nomogram was constructed based on FMG-based risk scores and clinical factors, and its robustness was verified by time-dependent receiver operating characteristic analysis, calibration curve analysis, and decision curve analysis. We have also described the biological processes and the tumor immune microenvironment based on FMG-based risk score classification. Given the close association between fatty acid metabolism and cancer-related pain, our 10-FMG signature may also serve as a potential therapeutic target with dual effects on ccRCC prognosis and cancer pain and, therefore, warrants further investigation.

KEYWORDS

kidney renal clear cell carcinoma, fatty acid metabolism, prognostic signature, nomogram, tumor microenvironment, cancer pain

Introduction

Renal cell carcinoma (RCC) originates in tubular epithelial cells, occupying approximately 2%–3% of adult malignancies (1). For several decades, the incidence and mortality of RCC have been on the rise. According to the International Agency for Research on Cancer, 431,288 new cases of clear-cell RCC (ccRCC) were diagnosed and 179,368 deaths related to this cancer were recorded worldwide in 2020 (2). The majority of deaths associated with kidney cancer are caused by ccRCC, which is the most common subtype (3). The survival rate after treatment for early-stage RCC is 60–70%, while advanced RCC usually has a poor prognosis, of which the 5-year survival is<10% (4). Therefore, it is clinically significant to predict prognosis and provide guidance for personalized treatment by exploring potential markers to improve overall survival of patients.

More and more evidence shows that metabolic changes play an explanatory role in tumor progression (5). Although increased lipid synthesis has received less attention than aerobic glycolysis, it has recently been recognized as another important metabolic abnormality required for carcinogenesis (6). There is growing evidence to suggest that upregulation of several enzymes involved in fatty acid metabolism is a universal metabolic marker in cancer cells (7). In many cancers, lipids are ingested and stored to meet the energy needs of tumor cells, which are supplied with energy by fatty acids through the process of β-oxidation (8). ccRCC is characterized by a high rate of mutation of genes that control metabolism; therefore, this cancer is also thought to be driven by metabolic changes (9). In fact, it is known that ccRCC cells accumulate a large amount of lipids and exhibit abnormal fatty acid metabolism, which is correlated with clinical outcomes (10).

Pain is one of the most common and bothersome symptoms in cancer patients. Across all stages of cancer, 50.7% of patients experience pain; in particular, 66.4% of cancer patients in the advanced stage experience pain (11). Uncontrolled pain can contribute to poor physical and emotional well-being. It is widely accepted that cancer pain is caused by nociceptive, inflammatory, and neuropathic mechanisms (12). It is essential to note that fatty acid metabolism not only has an impact on cancer development but also has an effect on pain development. As shown in the study by Koundouros et al., an increase in the levels of arachidonic acid and eicosanoids can promote cell proliferation (13). Furthermore, the role of arachidonic acid and its metabolite prostaglandin in inflammation and pain has been demonstrated (14). Both anandamide hydrolase and monoacylglycerol lipase are endocannabinoid-degrading enzymes, and inhibitors of these enzymes can reduce pain by blocking the metabolism of anandamide and 2-arachidonic glycerol, while increasing endogenous levels of fatty acid amides. Interestingly, inhibitors of these enzymes, on their own or in combination with other drugs, have shown therapeutic potential in a variety of cancers (15, 16). Thus, further investigation of the role of fatty acid metabolism-related genes (FMGs) in ccRCC might be useful for better prediction of patient prognosis and pain management.

In this study, we constructed a fatty acid-related signature to evaluate the prognosis of RCC. Potential relationships between this signature and the immune microenvironment were investigated. Moreover, we attempted to determine the potential association between these genes and cancer pain, as this could provide new insights into personalized cancer therapy.

Materials and methods

Data source

Transcriptome sequencing (mRNA) data, along with detailed clinical information about RCC patients, were acquired from The Cancer Genome Atlas (TCGA) database, the E-MTAB-1980 cohort (17) in the EMBL-EBI database, and the GSE22541 cohort in the Gene Expression Omnibus (GEO) database. Altogether, we obtained data for 535 samples from the TCGA-KIRC database, 101 samples from the E-MTAB-1980 cohort, and 68 samples from the GSE22541 cohort.

Screening of FMG-associated genes

A predefined set of FMGs was obtained from the Molecular Signature Database (MSigDB, v7.4) (18). We identified three relevant sets of FMGs, namely, KEGG fatty acid metabolism pathway genes, hallmark fatty acid metabolism genes, and reactome fatty acid metabolism genes. After deleting duplicates from these three sets of genes, 309 reliable records were obtained. Furthermore, we performed intersection analysis of these 309 genes with three ccRCC cohorts, and finally obtained 291 genes for follow-up studies (Supplementary Figure 1, Supplementary Table 1).

Identification of mutated and differentially expressed genes

The UCSC Xena database (19) was used to obtain the copy number variation (CNV) information of the TCGA-KIRC patients. Then, we calculated and summarized the most significant results of CNV frequencies for these FMGs. Differential expression genes (DEGs) between normal kidney group and KIRC group were analyzed by "limma" package in R, and genes with fold change > 1.50 and $P< 0.05$ were considered to be differentially expressed.

Construction and validation of risk scores

Univariate Cox regression analysis was used to identify FMGs associated with overall survival (OS) in the TCGA-KIRC and E-MTAB-1980 datasets ($P< 0.01$), and the least absolute shrinkage and selector operation (LASSO) analysis was used to analyze overlapping gene sets with the "glmnet" package in R (20). The prognostic genes were determined by the best penalty parameter λ, and 10 optimal FMGs were screened out. The expression levels between normal kidney group and KIRC group and Kaplan-Meier (K-M) analysis results were also respectively shown base on TCGA-KIRC cohort. Furthermore, the fatty acid metabolic index (FMI) was calculated by adding the expression and corresponding coefficients of the FMGs for each RCC patient. In order to make the results more intuitive, MinMax variation was used to adjust FMI by using the following formula.

$$\textbf{Adjust FMI} = \frac{\boldsymbol{x}_i - \boldsymbol{min}(\boldsymbol{x}_i)}{\boldsymbol{max}(\boldsymbol{x}_i) - \boldsymbol{min}(\boldsymbol{x}_i)}$$

The median cut-off value of FMI was used to classify patients, and prognostic performance was evaluated by K-M analysis and time-dependent receiver operating characteristic (ROC) analysis.

Comprehensive assessment of FMI in patients

The association of FMG-based risk scores with clinical features was analyzed based on adjusted FMI values to assess the clinical usability of FMGs. The factors included age, T/N/M stage, and tumor grade.

Construction and evaluation of an FMG-based clinicopathologic nomogram

Univariate and multivariate Cox regression analyses were performed to explore the prognostic value of FMI. A nomogram combining the clinical features of RCC and FMG-based risk score was developed. To evaluate the performance of nomogram, calibration curve, ROC curve and decision curve analysis (DCA) were performed.

Functional enrichment analysis of the FMI groups

To further characterize the biological processes in different FMI groups, gene set enrichment analysis (GSEA) was performed. Enrichment results with $P< 0.05$ as well as FDR< 0.1 were considered statistically significant.

Evaluation of the immunogenomic landscape of RCC

Immune checkpoints are new target molecules in immunotherapy for RCC. In this study, the immune checkpoints were compared between the FMI groups in the three cohorts to evaluate the potential application of these immune checkpoints for FMI-based immunotherapy. The candidate checkpoints identified were PDCD1, IL2RA, MICB, SELP, CX3CL1 and EDNRB.

Since the tissue samples used in transcriptome sequencing are not composed of single cells, the heterogeneity of these samples is inevitable. Therefore, the gene expression profile data may also reflect changes in the cell components in the tissue. In this study, xCell tool was used to predict the immune microenvironment typing of gene expression profile data, and further compared the expression differences of cell subsets between different groups.

Analysis of sensitivity to chemotherapy

Based on the Genomics of Drug Sensitivity in Cancer (GDSC) database, we performed the "pRRophetic" package in R to predict semi-inhibitory concentrations (IC50) of ccRCC chemotherapeutic drugs between different groups.

Validation of genes included in the risk model

Immunohistochemical (IHC) staining was performed with antibodies against FASN (D162701, BBI), ACOT9 (D121491, BBI), FAAH2 (D122328, BBI), and PTPRG (GB114422, Servicebio) to validate the expression of risk model-related genes in 10 paired tumor and normal tissues from the Naval Medical University cohort. The procedure for IHC was based on a previous protocol (21). Three independent blind observers analyzed the images by using ImageJ Software (ImageJ, Marlyand, USA), and sum of area and integrated option density (IOD) were measured. The mean integrated option density was calculated by dividing the IOD sum by the area sum.

Statistical analysis

Unless otherwise stated, statistical significance was considered significant at $P< 0.05$ and two-sided tests.

Results

Construction of the FMG-related signature for ccRCC

The CNVs and DEGs from the 309 FMGs were detected in the TCGA-KIRC cohort. As a result of exploring the incidence of CNVs, FMGs were found have massive CNV alterations. We have listed the top 10 genes with amplified or deleted CNVs (Figure 1A). A total of 34 DEGs were detected in 535 ccRCC samples when compared to 72 normal renal samples. The 10 significantly augmented FMGs were among the DEGs identified in the ccRCC samples, while 24 have been attenuated essentially (Figures 1B, C). The OS-related FMGs were screened in TCGA-KIRC and E-MTAB-1980 datasets (Figures 1D, E). In total, 160 and 67 significant OS-related FMGs were retrieved respectively. Further analysis of 52 overlapping OS-related FMGs was conducted by combining the results of the two cohorts (Figure 1F). Partial likelihood deviation analysis was performed on the results of

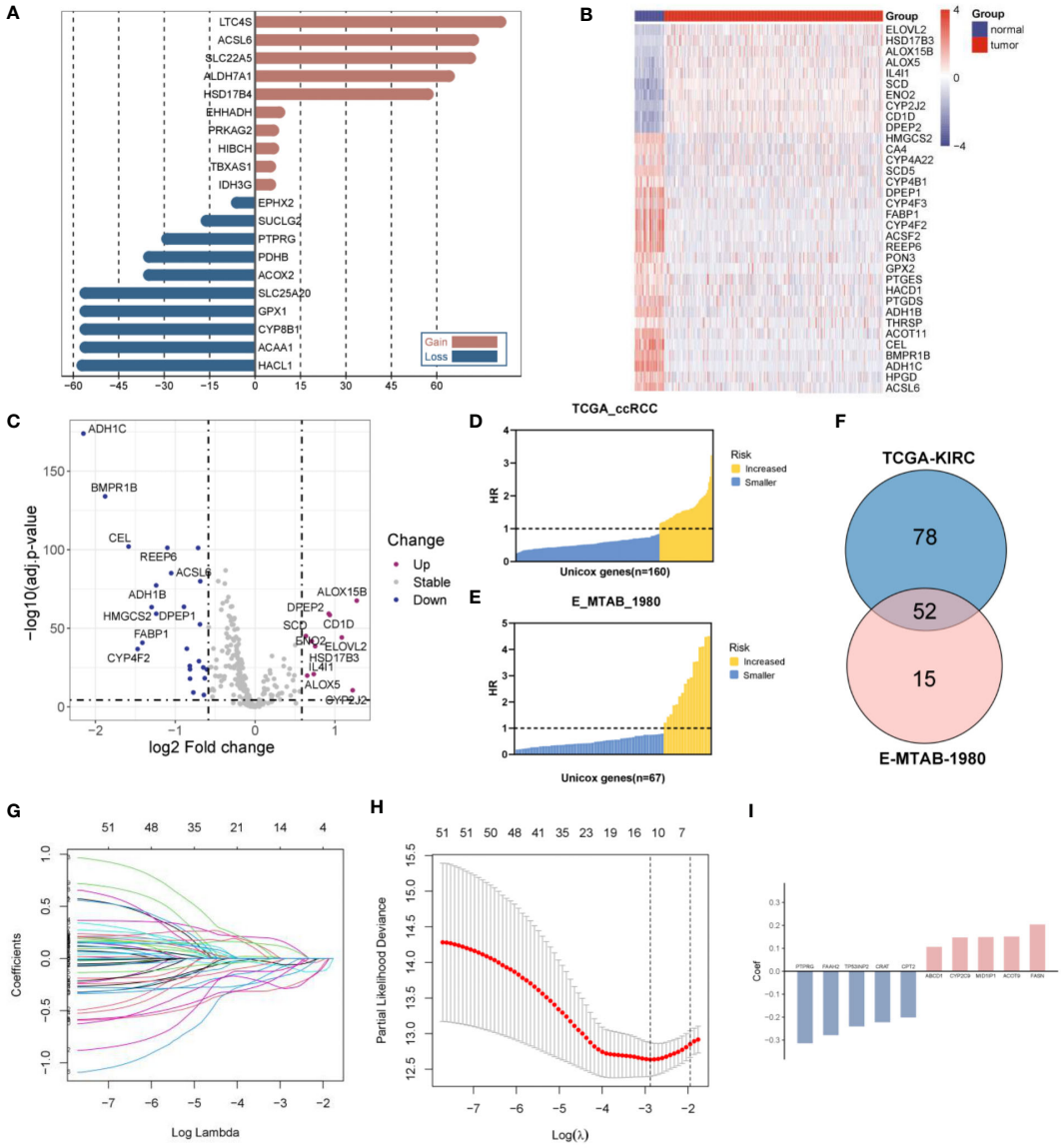

FIGURE 1
Construction of a fatty acid metabolism-related signature in ccRCC patients. **(A)** The frequency of the top 10 genes with amplified or deleted CNVs of FMGs in the TCGA-KIRC cohort. **(B)** Heatmap analysis of 34 DEGs among FMGs. **(C)** Volcano plot depicting the distribution of DEGs. **(D)** 160 prognostic FMGs in the TCGA-KIRC dataset. **(E)** 67 prognostic FMGs in the MTAB dataset. **(F)** Venn plot identifying 52 overlapping prognostic FMGs. **(G)** LASSO Cox regression analysis of the 52 prognostic FMGs. **(H)** Plot depicting partial likelihood deviance of the LASSO regression. **(I)** Corresponding coefficients of the 10 FMGs.

LASSO regression (Figures 1G, H). We calculated the coefficient for the prediction of the prognosis of ccRCC by the OS-related FMGs (Figure 1I).

Effect of expression levels of each of the 10 FMGs in the signature on prognosis of RCC

A prognostic gene signature was constructed by identifying 10 pivotal OS-related FMGs, namely, FASN, ACOT9, MID1IP1, CYP2C9, ABCD1, CPT2, CRAT, TP53INP2, FAAH2, and PTPRG. The expression level and prognostic potential of the 10 selected genes were evaluated individually. Boxplots were used to depict the expression level of the 10 prognostic FMGs in tumors and normal tissues (Figure 2A), and K-M curves were drawn for analysis of OS (Figure 2B). As shown in the figures, a significant decrease was observed in the expression of MID1IP1, CYP2C9, CPT2, CRAT, TP53INP2, FAAH2, and PTPRG, while a moderate increase in the expression of ABCD1 was observed in the ccRCC samples. As noted in the separate K-M analyses of OS, high expression of FASN, ACOT9, MID1IP1, CYP2C9, and ABCD1 and low expression of CPT2, CRAT, TP53INP2, FAAH2, and PTPRG were associated with more impaired OS.

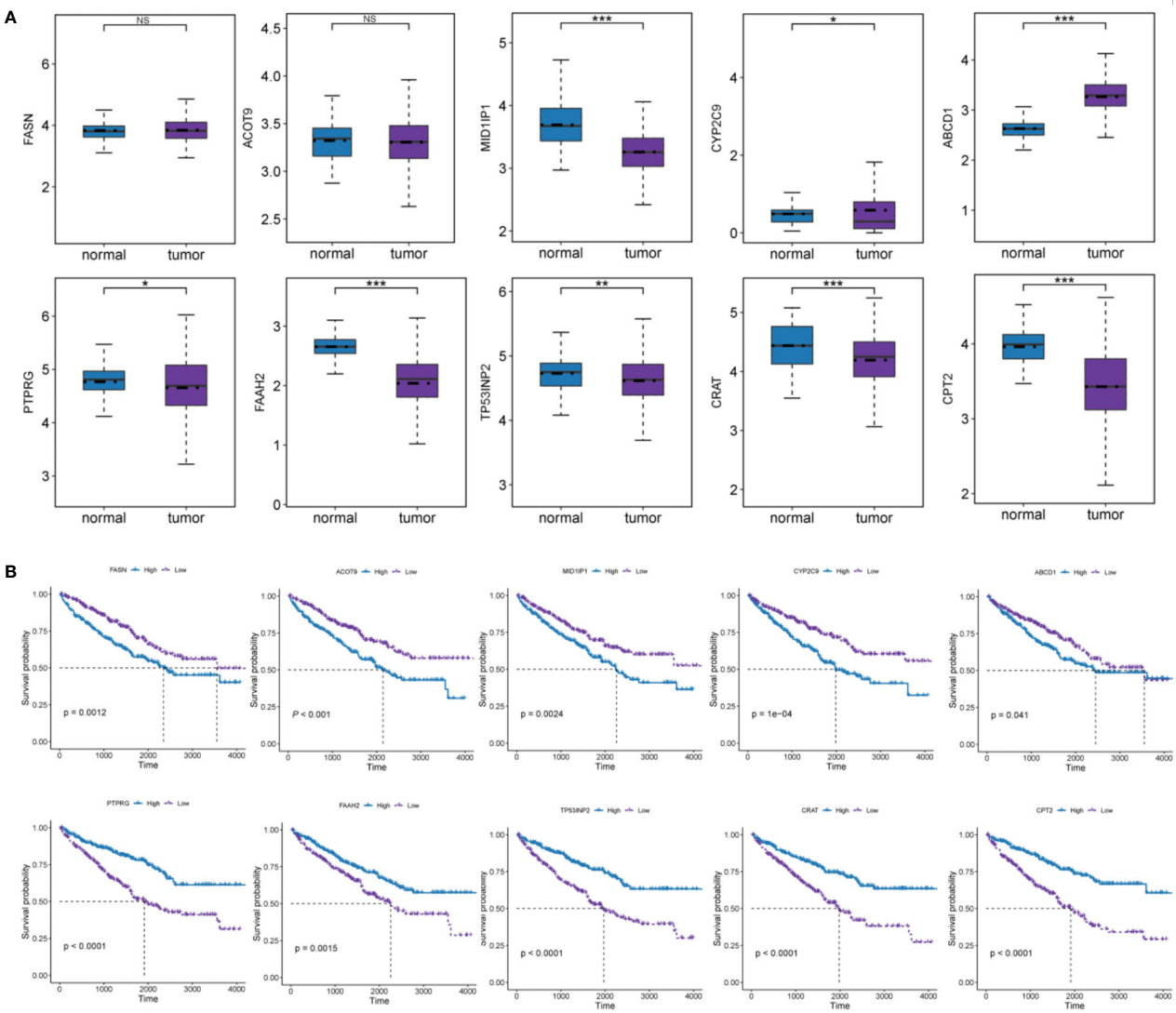

FIGURE 2
Analyses of the effect of expression levels of each of the 10 FMGs in the signature on prognosis. **(A)** Expression level of the 10 prognostic FMGs in tumor and normal samples. **(B)** K-M overall survival curves of ccRCC patients according to relative expression of the 10 FMGs. *P< 0.05; **P< 0.01; ***P< 0.001; ns means no significance.

Evaluation and validation of the 10-FMG signature

Based on the expression level of the 10 FMGs, the FMI was calculated using the following formula. FMI = Sum of the expression of each gene × coefficients = FASN × 0.204117 + ACOT9 × 0.151747 + MID1IP1 × 0.149099 + CYP2C9 × 0.147525 + ABCD1 × 0.106468 − CPT2 × 0.20157 − CRAT × 0.222481 − TP53INP2 × 0.240641 − FAAH2 × 0.278899 − PTPRG × 0.314233.

According to their median FMI values, ccRCC patients could be classified as low-risk or high-risk group. Further, FMI was normalized for easy visual representation of the data. According to the data for the TCGA-KIRC cohort, patients in the high-risk group were more likely to die than those in the low-risk group (Figure 3A). The prognostic significance of FMI was confirmed in two additional cohorts (Figures 3B, C). K-M analyses revealed that the high-risk group had significantly worse OS and disease-free survival (DFS) than the low-risk group in TCGA-ccRCC cohort (Figures 3D, E). The two additional cohorts showed that

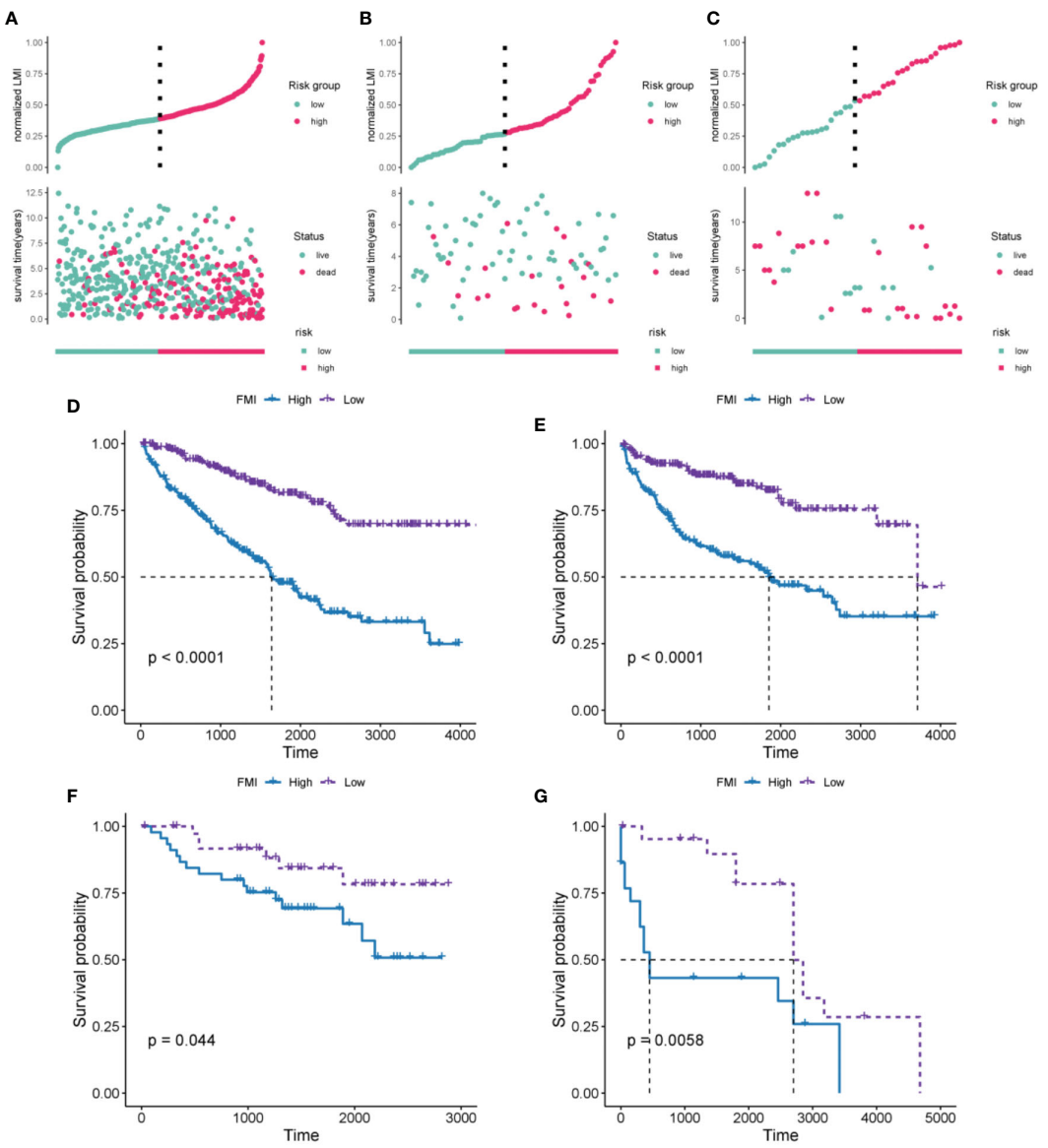

FIGURE 3
Evaluation and validation of the 10-FMG signature. Distribution plots of the patients' normalized FMI and OS status TCGA-KIRC **(A)**, E-MTAB-1980 **(B)**, and GSE22541 cohorts **(C)**. K-M analyses of OS **(D)** and DFS **(E)** in the TCGA-KIRC cohorts. K-M analyses of OS **(F)** and DFS **(G)** in the E-MTAB-1980 and GSE22541 cohorts respectively.

OS deteriorated more among those at high risk than those at low risk, consistent with the TCGA-ccRCC cohort (Figures 3F, G).

Correlation between FMI and clinical features of ccRCC

The clinical parameters survival status and clinicopathologic T/N/M were correlated with FMI to varying degrees (Figure 4A, $P< 0.05$ for all). That is, higher FMI was associated with greater severity of these clinical characteristics. The E-MTAB-1980 cohort also showed conspicuous differences in various clinical parameters, including tumor stage and grade (Figure 4B). In addition, FMI was found to be associated with gender and age: specifically, male patients and patients older than 65 years had higher FMI than female patients and patients younger than 65 years in the E-MTAB-1980 and GSE22541 cohorts (except for age in the GSE22541 dataset) (Figures 4B, C). Figure 4D presents a heatmap of the overall distribution of the 10 FMGs with clinical parameters in the TCGA-KIRC cohort.

Establishment and assessment of an FMG-based clinicopathologic nomogram

According to univariate Cox analysis, age, T/N/M stage, tumor grade, AJCC stage, and FMI showed a remarkable association with OS (Figure 5A, $P< 0.001$ for all). Multivariate Cox analysis of these variables showed that only age, N, M, and FMI were independent predictors (Figure 5B, $P< 0.01$ for all).

According to the above results, an individual OS prediction nomogram was developed using FMI and the six clinical features that were associated with prognosis according to univariate Cox regression analysis (Figure 5C). In the calibration plot, the nomogram was similar to an ideal curve in terms of predictive value, and this was indicative of perfect stability (Figure 5D). According to the results of DCA, the nomogram had a better predictive effect than any individual clinical feature (Figure 5E). Additionally, the area under the ROC curve values for the nomogram for 2-year, 4-year, and 5-year survival were 0.853, 0.851, and 0.844, respectively, and it had better efficiency than each of the other clinical factors in predicting OS (Figures 4F, G, H). Thus, the predictive nomogram for OS appears to be fairly accurate, and it could be used to assist decision-making in the clinical setting.

GSEA analysis based on FMI grouping

The GSEA analysis results from the GO database, demonstrated in Figures 6A and B, indicate that B-cell-mediated immunity, interferon–gamma production, NIK/NF–kappaB signaling, phagocytosis, engulfment, and regulation of tumor necrosis factor superfamily cytokine production were considerably enriched in the group with high FMI (Figure 6A). In addition, the results from the KEGG database showed that antigen processing and presentation, the B cell receptor signaling pathway, the cell cycle, PD–L1 expression and PD–1 checkpoint pathway, and the TNF signaling pathway were enriched in the high-FMI group (Figure 6B).

Immune microenvironment of ccRCC

In TCGA cohort, the immune score and tumor microenvironment score were higher in the high-FMI group, whereas the stroma score was markedly lower (Figures 6C, D, E, $P< 0.05$ for all). The tumor microenvironment analysis results demonstrated that the number of B cells, plasma B cells, M1 and M2 macrophages, monocytes, central and effector memory CD4+ T cells, naive CD4+ T cells, Th1 and Th2 CD4+ T cells, CD8+ T cells, central and effector memory CD8+ T cells, naive CD8+ T cells, and natural killer (NK) T cells was significantly higher in the high-FMI group (Figures 6F, G). Additionally, the immune microenvironment analysis results of E-MTAB-1980 and GSE22541 cohorts are shown in Supplementary Figure 2. The results revealed that B cells, plasma B cells, M1 macrophages, Th2 CD4+ T cells, and NK T cells were notably strengthened in the high-FMI group in all three cohorts.

Immunotherapy has shown great promise in cancer treatment, and immune checkpoint blockade is a promising anti-tumor strategy. Accordingly, the expression of six candidate immune checkpoints were assessed. The results revealed that PDCD1, IL2RA and MICB exhibited significant augmentation in the high-FMI group, whereas SELP, CX3CL1 and EDNRB exhibited significant augmentation in the low-FMI group. All results were consistent across all three datasets (Figures 7A, B, C). These findings indicate that the efficacy of immunotherapy against different targets for patients with ccRCC may differ according to whether they have high or low FMI.

Prediction of chemotherapeutic drug sensitivity

According to the predicted results of the "pRRophetic", we observed differences in drug sensitivity between different groups (Figures 8A-F). The results showed that there were no difference in response for pazopanib and axitinib ($P > 0.05$ for all), and the low-FMI group was more sensitive to sorafenib ($P< 0.05$), while the high-FMI group were more sensitive to paditaxel, rapamycin, and temsirolimus ($P< 0.05$ for all).

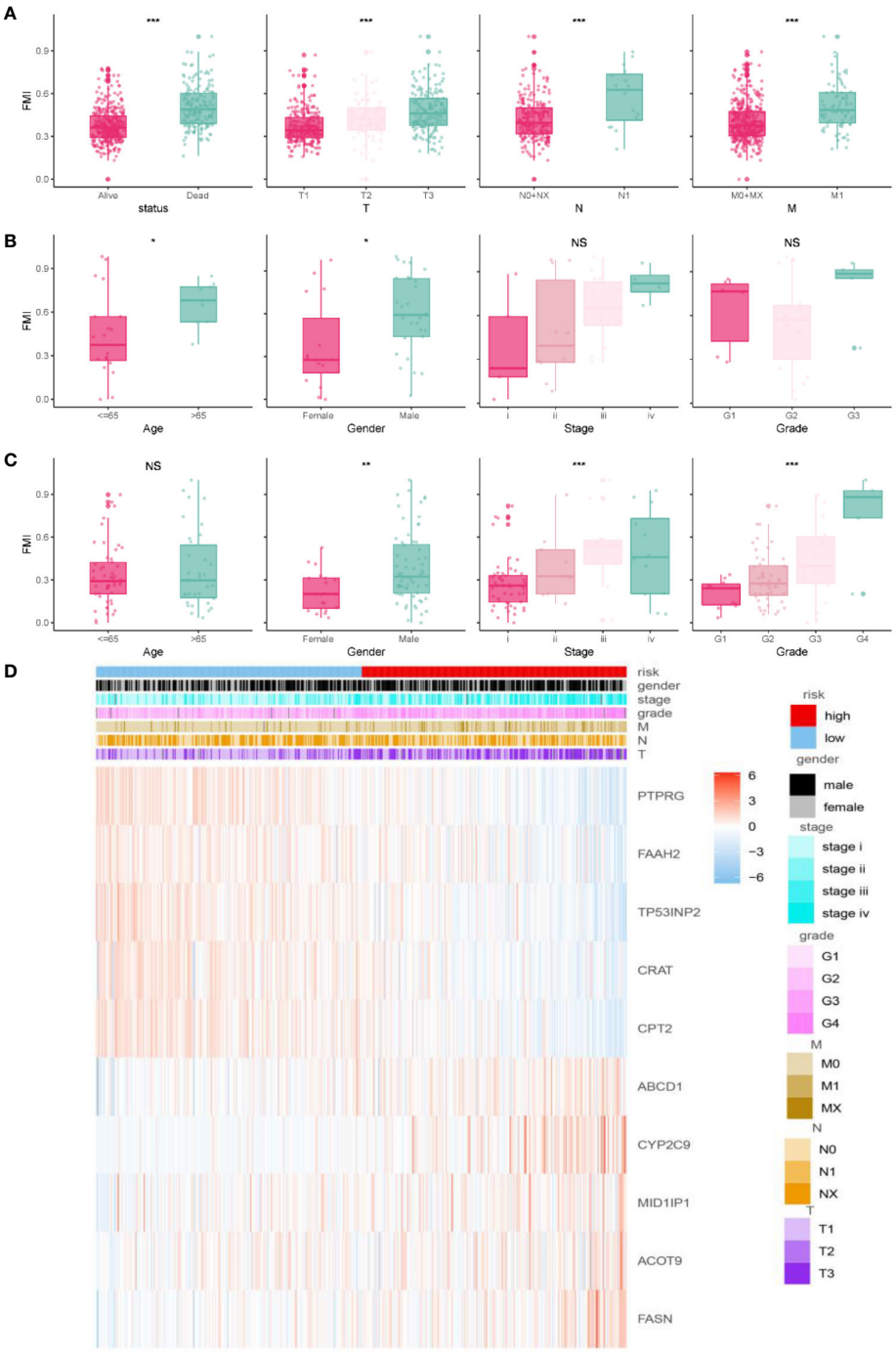

FIGURE 4
Correlation analysis of clinical features and FMI. Association between adjusted FMI and different clinical parameters in the TGCA-KIRC. **(A)**, E-MTAB-1980 **(B)**, and GSE22541 **(C)** cohorts. Heatmaps of the correlations between FMI and clinical parameters in the TGCA-ccRCC cohort **(D)**. *$P < 0.05$; **$P < 0.01$; ***$P < 0.001$; ns means no significance.

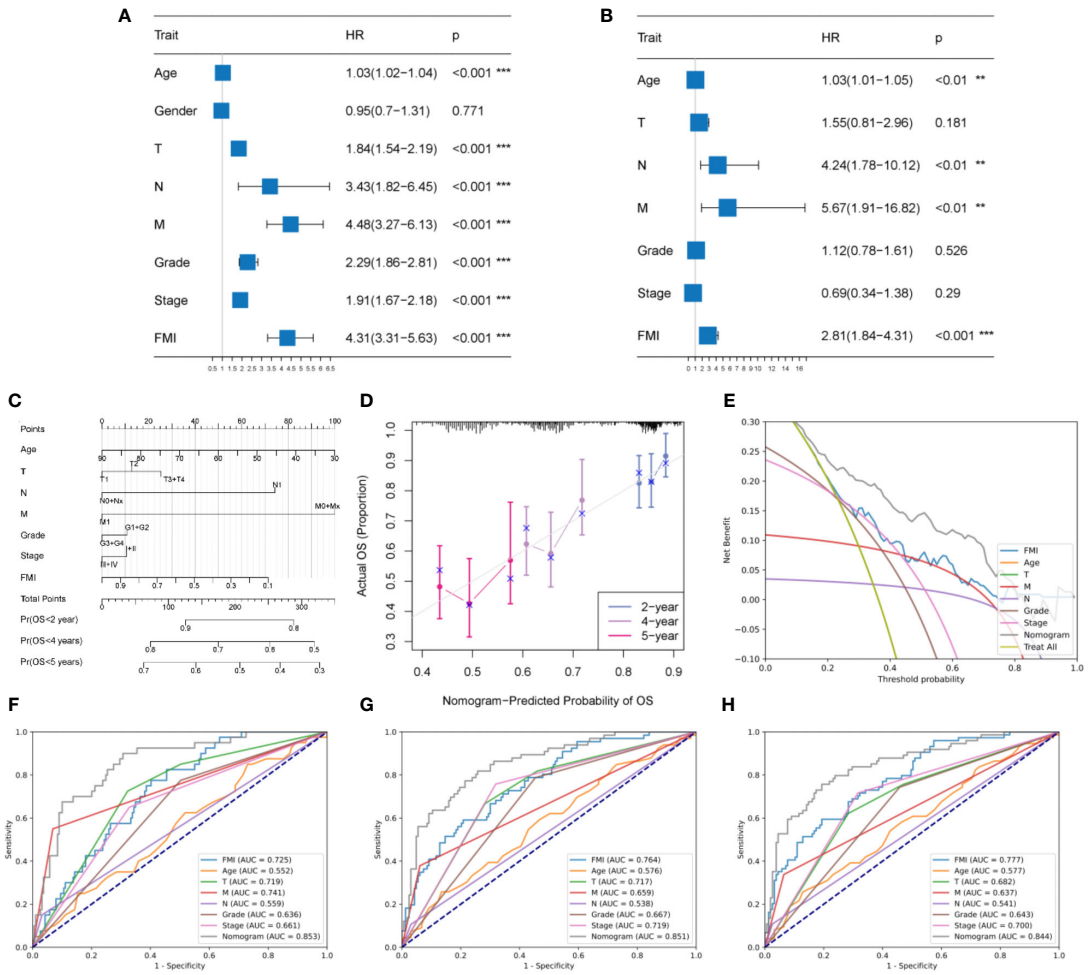

FIGURE 5
Development and evaluation of a clinicopathologic nomogram based on the identified FMGs. **(A, B)** Univariate and multivariate Cox regression analyses. **(C)** Development of a prognostic nomogram based on age, T stage, N stage, M stage, tumor grade, AJCC stage, and FMI. **(D)** Calibration curve showing the predicted OS versus actual OS. **(E)** DCA of the clinical usefulness of the constructed nomogram. **(F, G, H)** Receiver operating characteristic (ROC) analysis of the nomogram for predicting 2-, 4-, and 5-year OS in the TCGA-KIRC cohorts. $^{**}P < 0.01$; $^{***}P < 0.001$.

Clinical validation of the expression of genes

The protein expression of four genes (FASN, ACOT9, FAAH2, and PTPRG) in the identified FMG signature was validated with IHC in 10 ccRCC samples and 10 paired normal samples. The results showed that all the four genes expressed in higher amounts in normal samples than in tumor samples (Figures 9A, B). In particular, to our knowledge we evaluated the immunohistochemical expression of FAAH2 in ccRCC for the first time. The protein expression of other 4 genes (ABCD1, CPT2, CRAT and MID1IP1) in the identified FMG signature could be assessed using the Human Protein Atlas (http://www.proteinatlas.org/) database, and we summarized the representative images of these genes in Supplementary Figure 3.

Pain dissection of the FMGs signature

Considering that the majority of cancer patients experience pain during cancer progression or treatment, we further dissected the association of FMGs signature with cancer pain. As shown in Table 1, we first provided literature evidence for 10 signatures associated with fatty acids, and further we summarized the literature-reported evidence for pain-related genes, including gene FASN, CYP2C9, ABCD1, CPT2, and FAAH2.

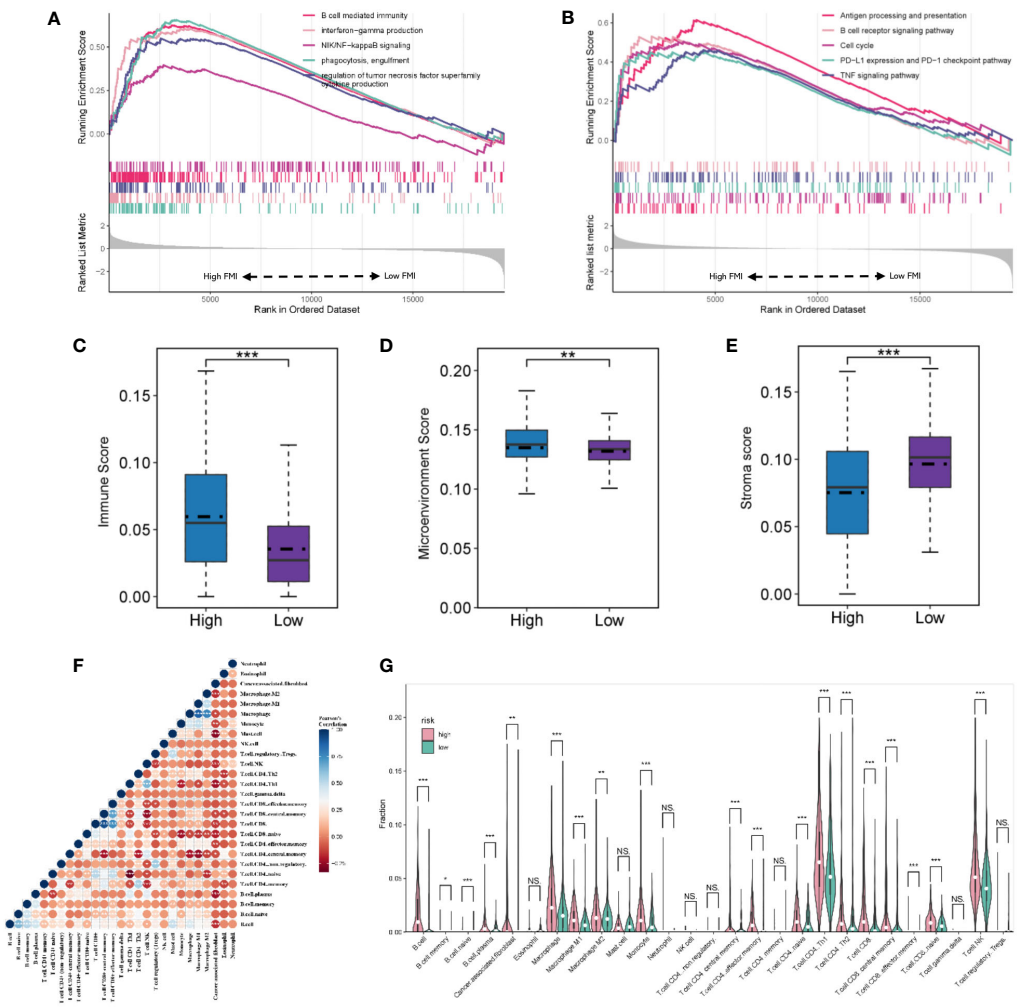

FIGURE 6
Gene set enrichment analysis and landscape of the immune microenvironment in the TGCA-KIRC. GO **(A)** and KEGG pathway **(B)** analyses of the high- and low-FMI groups. **(C, D, E)** Evaluation of the tumor microenvironment of ccRCC. **(F)** The correlation of infiltrating immune cells. **(G)** Violin diagram of the proportions of different tumor-infiltrating cells in the high- and low-FMI group. *$P < 0.05$; **$P < 0.01$; ***$P < 0.001$. ns means no significance.

Discussion

There is considerable evidence that fatty acid metabolism is severely disrupted in ccRCC; further, the dysregulation of various lipid metabolism pathways that drive lipid deposition is closely related to ccRCC (22). For example, it has been appreciated that elevated lipid storage levels can maintain cell membrane fluidity, thereby enhancing metastatic capacity (23). Timely intervention with therapeutic approaches, such as tyrosine kinase inhibition with sunitinib, pazopanib, and nivolumab, has been found to significantly improve survival in patients with advanced RCC (24). However, the complexity of the tumor microenvironment in ccRCC and the high heterogeneity of individual gene regulation are associated with inadequate treatment response and drug resistance. Given the close association between ccRCC and fatty acid metabolism, a systematic analysis of the role of FMGs in RCC could be helpful for understanding the mechanism of disease progression and for treatment decision-making.

In this study, we first identified FMGs and later confirmed the significant role of FMGs in RCC based on the identification of DEGs with CNV alterations. Based on data from the TCGA-KIRC and E-MTAB-1980 cohorts, univariate Cox analysis along with LASSO Cox regression analysis were used to identify a novel robust prognostic signature of FMGs. Subsequently, the signature was used to classify RCC patients into low- and high-FMI groups and was validated in the three cohorts. Further, each ccRCC patient was further stratified by constructing a risk score

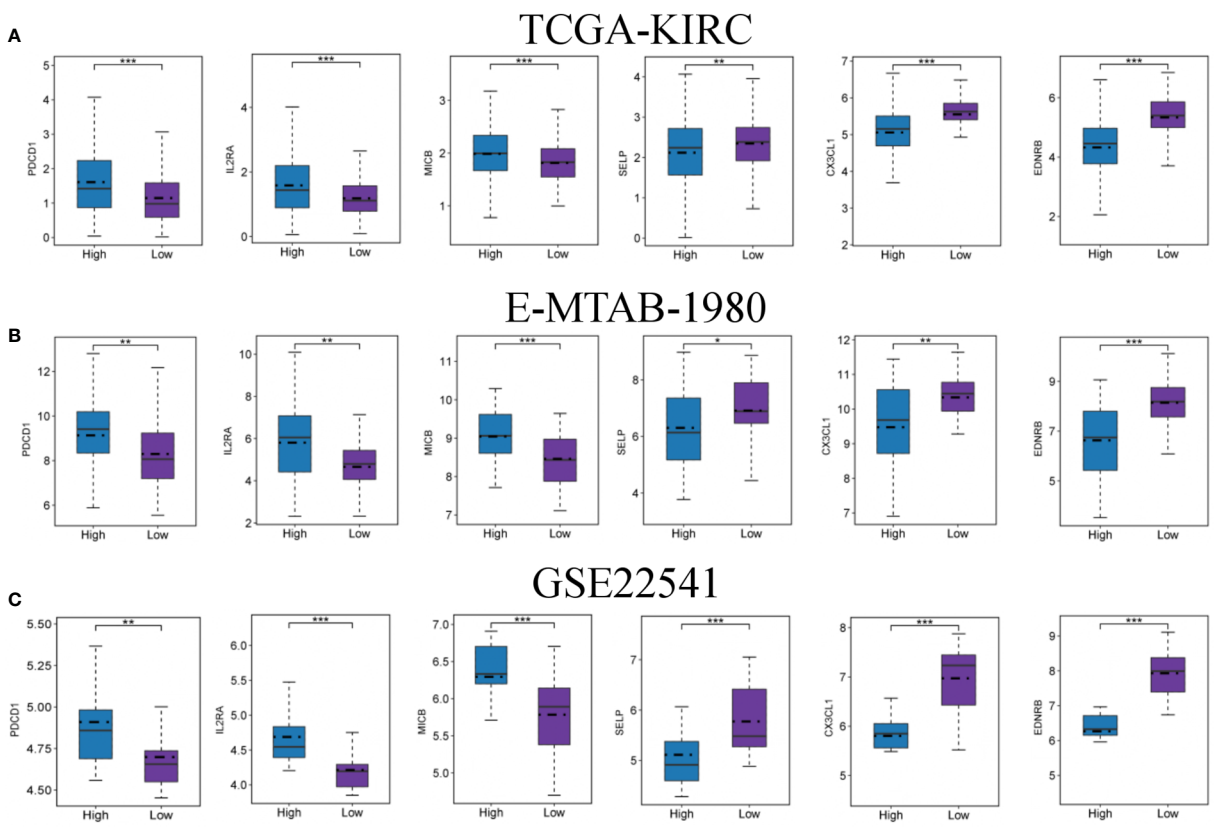

FIGURE 7
Expression levels of immune checkpoints in the high- and low-FMI group. Expression level of PDCD1, IL2RA, MICB, SELP, CX3CL1 and EDNRB in TCGA-KIRC **(A)**, E-NTAB-1980 **(B)**, and GSE22541 **(C)** cohorts. *$P < 0.05$; **$P < 0.01$; ***$P < 0.001$.

model, and the groups showed significant differences in survival and various clinicopathological parameters. In addition, ROC analysis demonstrated the superior performance of our model and indicated that it might be useful for formulating follow-up treatments. We further used xCell to construct the immunogenomic landscape of RCC and explore differences in the distribution of immune cells. Altogether, the results above revealed the prognostic signature of our FMGs has a great promise in ccRCC.

The signature we constructed contains 10 fatty acid metabolism genes, some of which have previously been reported to be associated with multiple cancers. FASN encodes fatty acid synthase, which primarily regulates the deposition of animal liposomes by synthesizing long-chain fatty acids from acetyl-coenzyme A (CoA) and malonyl-CoA. All esterified fatty acids in most tumor cells are synthesized *de novo*. FASN is dysregulated in a variety of cancers, including kidney, liver, lung, and colorectal cancer, and this dysregulation is thought to be associated with the aggressiveness and poor prognosis of cancers (25, 26). The ACOT9 gene encodes acyl-CoA thioesterase 9, which is a well-known key regulator of cellular utilization and regulates intracellular acyl-CoA/fatty acid levels. A recent study found that ACOT9 promoted tumor metastasis and growth by reprogramming lipid metabolism pathways in hepatocellular carcinoma (27). Interestingly, we found that the FASN and ACOT9 genes were significantly downregulated in RCC patients. In the future, we will further study its potential mechanisms in ccRCC. Protein tyrosine phosphatase receptor gamma (PTPRG) is a well-known tumor suppressor in various neoplasms (28). For example, Shu et al. found that PTPRG may play an inhibitory role in breast tumorigenesis by upregulating the p21(cip) and p27(kip) proteins through the ERK1/2 pathway (29). In line with this finding, PTRPG expression was significantly reduced in ccRCC according to the IHC results of this study. In addition, the results of this study revealed that low expression of PTRPG could predict poor prognosis. According to recent reports, other genes, such as MID1IP1 (30), ABCD1 (31), CPT2 (32), and TP53INP2 (33), are closely associated with the progression of ccRCC. However, our study is the first to demonstrate that FAAH2 is inhibited in ccRCC and is an indicator of poor prognosis. In general, the above results confirm the reliability of our signature to a certain extent, but

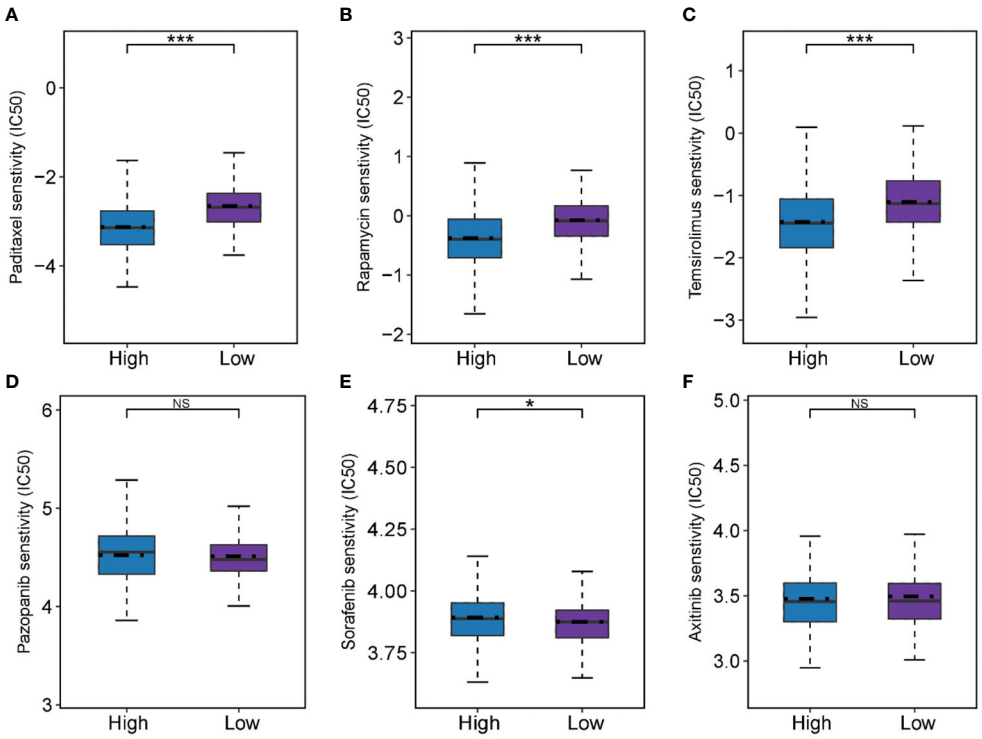

FIGURE 8
Predictive results of chemotherapeutic responses. **(A–F)** The differences of chemotherapeutic response in the high- and low-FMI group. *P < 0.05; ***P <0.001.

the specific influencing mechanism and prognostic value in clinical practice need to be further studied.

In order to further investigate the role of the signature genes, GSEA analyses were conducted in two FMI groups. Noticeable NIK/NF-κB signaling enrichment was observed in the high-FMI patients. Growing body of research suggests that dysregulation of NF-κB signaling pathway activity can lead to inflammatory diseases as well as cancer and NF-κB has long been proposed as a potential therapeutic target (34). Meteoglu et al. reported that NF-κB was associated with markers of angiogenesis and apoptosis in ccRCC, including VEGF, EGFR, and p53 (35). In addition, it has also been reported that activation of the NF-κB pathway is associated with ccRCC cell migration and invasion (36). Further, drugs that target NF-κB have been found to have therapeutic and preventive effects in a variety of cancers (37, 38). The results of our study suggest that patients with high FMI could benefit more from NF-κB-targeted therapy than patients with low FMI. Similarly, it is now widely accepted that immunotherapy is an effective method for treating cancer, and an increasing number of immunotherapy drugs are being evaluated in clinical trials (39). As an indispensable strategy in immunotherapy, immune checkpoint inhibitors have gained attention for their potential to improve the long-term outcomes of cancer patients (40). However, the effectiveness of this treatment varies, as it is only effective in certain subsets of cancer patients (41). Therefore, we compared six immune checkpoint genes to explore potential immune therapeutic targets in different FMI groups. In the high-FMI group, PDCD1, IL2RA and MICB were significantly elevated, whereas in the low-FMI group, SELP, CX3CL1 and EDNRB were significantly elevated. These results indicate that FMI should be considered when making decisions about immune checkpoint inhibitor therapy for ccRCC patients. Brahmer et al. has reported that PD-L1 inhibitors could promote tumor regression and prolong survival in patients with advanced cancers including ccRCC (42). Accordingly, ccRCC patients with higher FMI might be more likely to benefit from anti-PD-L1 therapy, since they have higher expression levels of PDCD1.

Notably, the majority of cancer patients experience pain during cancer treatment and after curative treatment (55% and 40%, respectively) (43). For cancer survivors, the long-term sequelae of pain after cancer treatment should not be ignored, as cumulative reports have found that opioid abuse is associated with increased mortality (44). Therefore, there is an urgent need to explore other effective pain management options. Basically, cancer cells are abnormal cell growth and proliferation, and fatty acid metabolism changes significantly in the rapid proliferation of cancer cells. Accordingly, interventions to prevent fatty acid

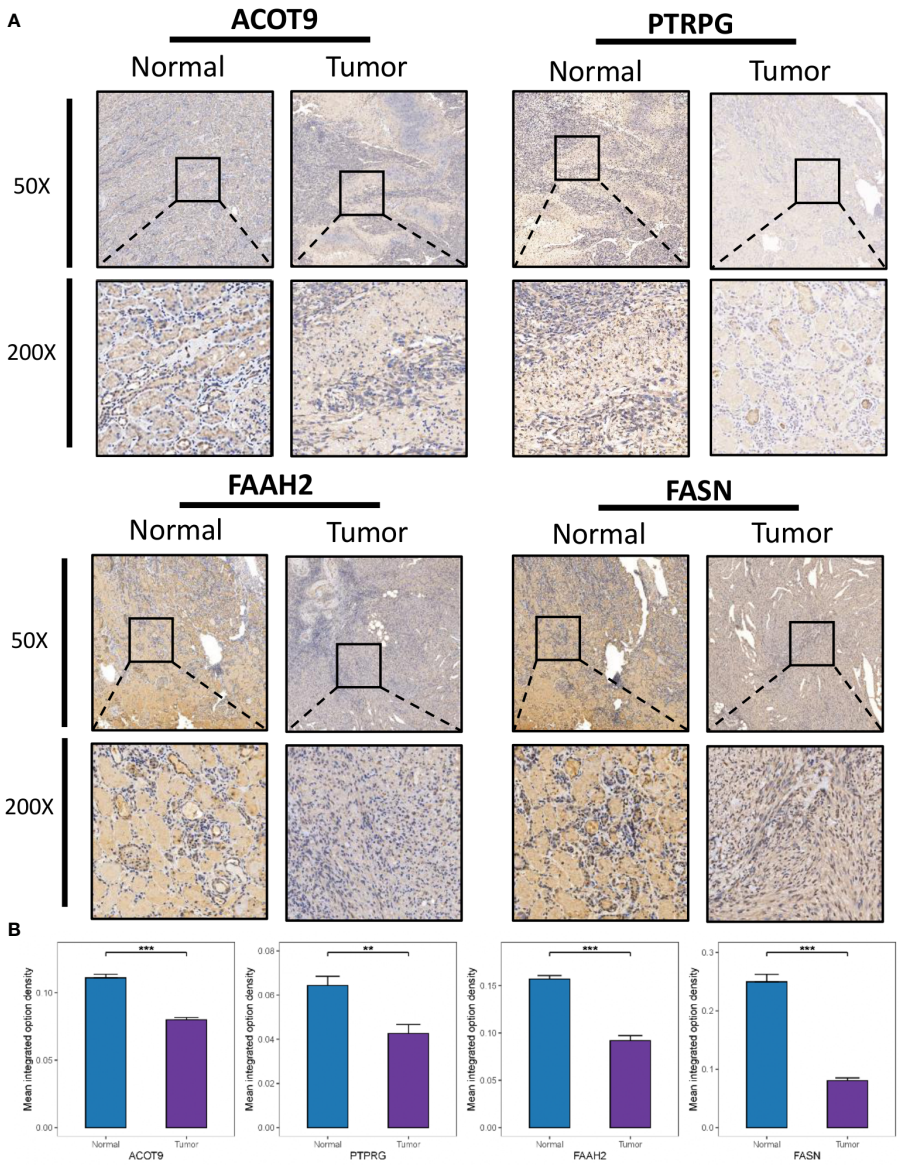

FIGURE 9
Clinical Validation of the risk model based on IHC. **(A)** Representative IHC images of the four selected gene. **(B)** The quantitative expression levels of each gene. $^{**}P < 0.01$; $^{***}P < 0.001$.

synthesis, increase fatty acid degradation through oxidation, and decrease fatty acid release from storage are commonly used to manage the abnormal proliferation of lipids and arrest cancer progression (45). Among the 10 fatty acid metabolism genes associated with prognosis that were identified in this study, FASN has been previously reported as a therapeutic target. That is, studies have confirmed that inhibition of FASN reduced triacylglycerol and phospholipid levels and inhibited lymph node metastasis of prostate carcinoma (46). Similarly, down-regulation of CPT2 also inhibited fatty acid β-oxidation in the tumor microenvironment and promoted cancer progression through acylcarnitine accumulation (47). Interestingly, fatty acid metabolism interventions may not only alter cancer cell proliferation but also help reduce pain during the disease. Recent studies have found that specialized pro-resolving lipid mediators (SPMs) can reduce fatty acid levels and effectively relieve chronic pain, and this mechanism of pain regulation is currently believed to be associated with the activation of immune cell receptors in the lipid environment, changes in pro-/anti-inflammatory pathways, and changes in peripheral nociceptor sensitivity (48). For example, SPMs can activate the immune cell receptor N-formyl peptide receptor 2 (ALX/FPR2), induce cell cycle

TABLE 1 The summary of the pain dissection of the FMGs signature.

Gene	Association with fatty acid	Association with pain
FASN	FASN is a key enzyme regulating the *de novo* synthesis of fatty acids, which can catalyze acetyl-CoA and malonyl-CoA to produce palmitate. (PMID: 26519059)	Palmitate can activate NF-κB transcription factors and regulate the expression of NMDA receptor subunits. FASN can be used as a therapeutic target to reduce neuropathic pain. (PMID: 25855977)
ACOT9	ACOT9 regulates fatty acid synthesis by catalyzing the hydrolysis of fatty acyl-coenzyme A to form free fatty acid (FFA) and coenzyme A (CoA). (PMID: 36004563)	NA
MID1IP1	The change of MID1IP1 expression can affect the expression of fatty acid synthase (FASN) and induce phosphorylation of Acetyl-CoA carboxylase (ACC), thereby affecting the biosynthesis of fatty acids and triglycerides. (PMID: 34153683, 35916211)	NA
CYP2C9	CYP2C9 is a cytochrome P450 enzyme that has cyclooxygenase activity and catalyzes the oxidation of polyunsaturated fatty acid arachidonic acid to eicosatrienoic acids. (PMID: 30012669)	CYP2C9 can predict the analgesic effect of tramadol and ketorolac. (PMID: 34246203)
ABCD1	ABCD1 gene encodes peroxisome transport protein, which is involved in transporting saturated very long chain fatty acids to peroxidase for β-oxidation. (PMID: 32017990)	Absence of ABCD1 will lead to mechanical allodynia mediated by mechanosensitive ion channels and dysfunction of satellite glial cells. (PMID: 35681537)
CPT2	Fatty acid oxidation (FAO) is a process in which carnitine palmitoyltransferase 1 and 2 (CPT1 and CPT2) transport long-chain fatty acids to the mitochondrial matrix, and then oxidize them to acetyl-CoA, NADH and FADH2 and generate energy. (PMID: 33027638)	CPT2 deficiency may lead to metabolic disorder in the body, causing patients to have diffuse muscle pain symptoms. (PMID: 27034144)
CRAT	Carnitine acetyltransferase (CRAT) is the basic enzyme in carnitine metabolism, which regulates the metabolic flexibility of muscle and increases exercise ability. Carnitine can promote fatty acids to enter mitochondria for oxidative decomposition during fat metabolism, which is helpful to promote the balance of fat metabolism. (PMID: 29444428)	NA
TP53INP2	TP53INP2 mediates peroxisome proliferator-activated receptor gamma (PPARG) regulates macroautophagic/autophagic-dependent mechanism that induce brown fat differentiation and thermogenesis. (PMID: 35947488)	NA
FAAH2	Fatty acid amide hydrolase (FAAH1 and FAAH2) can inactivate endogenous cannabinoid, and monoacylglycerol lipase can hydrolyze to 2-arachidonic glycerol. (PMID: 30070030)	Fatty acid amide hydrolase (FAAH) plays an important role in the hydrolysis and inactivation of endogenous arachidonic ethanolamide (AEA). AEA can protect neurons from inflammatory injury by activating cannabinoid receptors (CB1R and CB2R) and transient receptor TRPV1. FAAH inhibitors may become a safe and reliable new analgesic. (PMID: 34364309, 29017758)
PTPRG	PTPRG is a negative regulator of insulin signal transduction, and insulin can promote the synthesis and storage of fat and reduce free fatty acids in blood. (PMID: 29180649)	NA

NA, missing references.

arrest, and prevent phosphorylation of the nuclear factor kappa B (NF-κB) pathway (49). Moreover, altered fatty acid metabolism may also prevent the formation of neutrophil extracellular traps, thus promoting inflammation resolution and exerting an analgesic effect (48). In a nutshell, our results and the aforementioned studies might indicate that interventions targeting fatty acid metabolism-related genes may have a dual effect on improving prognosis and pain that warrants further investigation.

Conclusions

In summary, we integrated multiple bioinformatic analysis methods to construct a reliable 10-gene prognostic signature of ccRCC based on fatty acid metabolism and established a nomogram that can be used in clinical practice. The signature may also serve as a potential therapeutic target with dual effects on both ccRCC prognosis and cancer pain, but further studies are needed to support the conclusions.

Data availability statement

The original contributions presented in the study are included in the article/Supplementary Material. Further inquiries can be directed to the corresponding author.

Author contributions

RD, HW and XJ designed the study and wrote original draft. RD and LW analyzed the data and performed the bioinformatics analysis. MD and HY reviewed the conclusions. RD, HW and XJ

edited and revised the manuscript. All authors contributed to the article and approved the submitted version.

Funding

This work was supported by National Natural Science Foundation of China (Grant No. 82171220).

Conflict of interest

The authors declare that the research was conducted in the absence of any commercial or financial relationships that could be construed as a potential conflict of interest.

Publisher's note

All claims expressed in this article are solely those of the authors and do not necessarily represent those of their affiliated organizations, or those of the publisher, the editors and the reviewers. Any product that may be evaluated in this article, or claim that may be made by its manufacturer, is not guaranteed or endorsed by the publisher.

Supplementary material

The Supplementary Material for this article can be found online at: https://www.frontiersin.org/articles/10.3389/fonc.2022.1094657/full#supplementary-material

References

1. Znaor A, Lortet-Tieulent J, Laversanne M, Jemal A, Bray F. International variations and trends in renal cell carcinoma incidence and mortality. *Eur Urol* (2015) 67(3):519–30. doi: 10.1016/j.eururo.2014.10.002

2. Sung H, Ferlay J, Siegel RL, Laversanne M, Soerjomataram I, Jemal A, et al. Global cancer statistics 2020: GLOBOCAN estimates of incidence and mortality worldwide for 36 cancers in 185 countries. *CA Cancer J Clin* (2021) 71(3):209–49. doi: 10.3322/caac.21660

3. Rini BI, Campbell SC, Escudier B. Renal cell carcinoma. *Lancet* (2009) 373 (9669):1119–32. doi: 10.1016/S0140-6736(09)60229-4

4. Dimitrieva S, Schlapbach R, Rehrauer H. Prognostic value of cross-omics screening for kidney clear cell renal cancer survival. *Biol Direct* (2016) 11(1):68. doi: 10.1186/s13062-016-0170-1

5. Warburg O. On respiratory impairment in cancer cells. *Science* (1956) 124 (3215):269–70. doi: 10.1126/science.124.3215.269

6. Swierczynski J, Hebanowska A, Sledzinski T. Role of abnormal lipid metabolism in development, progression, diagnosis and therapy of pancreatic cancer. *World J Gastroenterol* (2014) 20(9):2279–303. doi: 10.3748/wjg.v20.i9.2279

7. von Roemeling CA, Marlow LA, Wei JJ, Cooper SJ, Caulfield TR, Wu K, et al. Stearoyl-CoA desaturase 1 is a novel molecular therapeutic target for clear cell renal cell carcinoma. *Clin Cancer Res* (2013) 19(9):2368–80. doi: 10.1158/1078-0432.CCR-12-3249

8. Akhtar M, Al-Bozom IA, Al Hussain T. Molecular and metabolic basis of clear cell carcinoma of the kidney. *Adv Anat Pathol* (2018) 25(3):189–96. doi: 10.1097/PAP.0000000000000185

9. Qi X, Li Q, Che X, Wang Q, Wu G. The uniqueness of clear cell renal cell carcinoma: Summary of the process and abnormality of glucose metabolism and lipid metabolism in ccRCC. *Front Oncol* (2021) 11:727778. doi: 10.3389/fonc.2021.727778

10. Weiss RH. Metabolomics and metabolic reprogramming in kidney cancer. *Semin Nephrol* (2018) 38(2):175–82. doi: 10.1016/j.semnephrol.2018.01.006

11. van den Beuken-van Everdingen MH, Hochstenbach LM, Joosten EA, Tjan-Heijnen VC, Janssen DJ. Update on prevalence of pain in patients with cancer: Systematic review and meta-analysis. *J Pain Symptom Manage* (2016 51(6):1070–1090 e9. doi: 10.1016/j.jpainsymman.2015.12.340

12. Falk S, Dickenson AH. Pain and nociception: mechanisms of cancer-induced bone pain. *J Clin Oncol* (2014) 32(16):1647–54. doi: 10.1200/JCO.2013.51.7219

13. Koundouros N, Karali E, Tripp A, Valle A, Inglese P, Perry NJS, et al. Metabolic fingerprinting links oncogenic PIK3CA with enhanced arachidonic acid-derived eicosanoids. *Cell* (2020) 181(7):1596–1611 e27. doi: 10.1016/j.cell.2020.05.053

14. Funk CD. Prostaglandins and leukotrienes: advances in eicosanoid biology. *Science* (2001) 294(5548):1871–5. doi: 10.1126/science.294.5548.1871

15. Jaiswal S, Ayyannan SR. Anticancer potential of small-molecule inhibitors of fatty acid amide hydrolase and monoacylglycerol lipase. *ChemMedChem* (2021) 16(14):2172–87. doi: 10.1002/cmdc.202100120

16. Charrua A, Matos R, Oliveira R, Marczylo T, Nagy I, Cruz F. Fatty acid amide hydrolase inhibition normalises bladder function and reduces pain through normalising the anandamide/palmitoylethanolamine ratio in the inflamed bladder of rats. *Naunyn Schmiedebergs Arch Pharmacol* (2020) 393(2):263–72. doi: 10.1007/s00210-019-01729-9

17. Yang T, Santisteban MM, Rodriguez V, Li E, Ahmari N, Carvajal JM, et al. Gut dysbiosis is linked to hypertension. *Hypertension* (2015) 65(6):1331–40. doi: 10.1161/HYPERTENSIONAHA.115.05315

18. Rohrig F, Schulze A. The multifaceted roles of fatty acid synthesis in cancer. *Nat Rev Cancer* (2016) 16(11):732–49. doi: 10.1038/nrc.2016.89

19. Hoy AJ, Nagarajan SR, Butler LM. Tumour fatty acid metabolism in the context of therapy resistance and obesity. *Nat Rev Cancer* (2021) 21(12):753–66. doi: 10.1038/s41568-021-00388-4

20. Gui J, Li H. Penalized cox regression analysis in the high-dimensional and low-sample size settings, with applications to microarray gene expression data. *Bioinformatics* (2005) 21(13):3001–8. doi: 10.1093/bioinformatics/bti422

21. Ramos-Vara JA. Technical aspects of immunohistochemistry. *Vet Pathol* (2005) 42(4):405–26. doi: 10.1354/vp.42-4-405

22. Corn KC, Windham MA, Rafat M. Lipids in the tumor microenvironment: From cancer progression to treatment. *Prog Lipid Res* (2020) 80:101055. doi: 10.1016/j.plipres.2020.101055

23. Du Y, Wang Q, Zhang X, Wang X, Qin C, Sheng Z, et al. Lysophosphatidylcholine acyltransferase 1 upregulation and concomitant phospholipid alterations in clear cell renal cell carcinoma. *J Exp Clin Cancer Res* (2017) 36(1):66. doi: 10.1186/s13046-017-0525-1

24. Tan SK, Hougen HY, Merchan JR, Gonzalgo ML, Welford SM. Fatty acid metabolism reprogramming in ccRCC: mechanisms and potential targets. *Nat Rev Urol* (2022). doi: 10.1038/s41585-022-00654-6

25. Yuan Y, Yang X, Li Y, Liu Q, Wu F, Qu H, et al. Expression and prognostic significance of fatty acid synthase in clear cell renal cell carcinoma. *Pathol Res Pract* (2020) 216(11):153227. doi: 10.1016/j.prp.2020.153227

26. Xu W, Hu X, Anwaier A, Wang J, Liu W, Tian X, et al. Fatty acid synthase correlates with prognosis-related abdominal adipose distribution and metabolic disorders of clear cell renal cell carcinoma. *Front Mol Biosci* (2020) 7:610229. doi: 10.3389/fmolb.2020.610229

27. Wang B, Zhang H, Chen YF, Hu LQ, Tian YY, Tong HW, et al. Acyl-CoA thioesterase 9 promotes tumour growth and metastasis through reprogramming of fatty acid metabolism in hepatocellular carcinoma. *Liver Int* (2022) 42(11):2548–61. doi: 10.1111/liv.15409

28. Zeng X, Li L, Hu Z, Peng D. Integrated multi-omics analysis identified PTPRG and CHL1 as key regulators of immunophenotypes in clear cell renal cell Carcinoma(ccRCC). *Front Oncol* (2022) 12:832027. doi: 10.3389/fonc.2022.832027

29. Shu ST, Sugimoto Y, Liu S, Chang HL, Ye W, Wang LS, et al. Function and regulatory mechanisms of the candidate tumor suppressor receptor protein tyrosine phosphatase gamma (PTPRG) in breast cancer cells. *Anticancer Res* (2010) 30(6):1937–46.

30. Yang W, Zhou J, Zhang K, Li L, Xu Y, Ma K, et al. Identification and validation of the clinical roles of the VHL-related LncRNAs in clear cell renal cell carcinoma. *J Cancer* (2021) 12(9):2702–14. doi: 10.7150/jca.55113

31. Shi Y, Dou Y, Zhang J, Qi J, Xin Z, Zhang M, et al. The RNA N6-methyladenosine methyltransferase METTL3 promotes the progression of kidney cancer via N6-Methyladenosine-Dependent translational enhancement of ABCD1. *Front Cell Dev Biol* (2021) 9:737498. doi: 10.3389/fcell.2021.737498

32. Zhao Y, Tao Z, Chen X. A three-Metabolic-Genes risk score model predicts overall survival in clear cell renal cell carcinoma patients. *Front Oncol* (2020) 10:570281. doi: 10.3389/fonc.2020.570281

33. Li X, Hu D, Li Y, Luo Y, Liang B, Yu K, et al. Overexpression of TP53INP2 promotes apoptosis in clear cell renal cell cancer via caspase-8/TRAF6 signaling pathway. *J Immunol Res 2022* (2022) p:1260423. doi: 10.1155/2022/1260423

34. Yu H, Lin L, Zhang Z, Zhang H, Hu H. Targeting NF-kappaB pathway for the therapy of diseases: mechanism and clinical study. *Signal Transduct Target Ther* (2020) 5(1):209. doi: 10.1038/s41392-020-00312-6

35. Meteoglu I, Erdogdu IH, Meydan N, Erkus M, Barutca S. NF-KappaB expression correlates with apoptosis and angiogenesis in clear cell renal cell carcinoma tissues. *J Exp Clin Cancer Res* (2008) 27:53. doi: 10.1186/1756-9966-27-53

36. Pei X, Li M, Zhan J, Yu Y, Wei X, Guan L, et al. Enhanced IMP3 expression activates NF-small ka, CyrillicB pathway and promotes renal cell carcinoma progression. *PloS One* (2015) 10(4):e0124338. doi: 10.1371/journal.pone.0124338

37. Rasmi RR, Sakthivel KM, Guruvayoorappan C. NF-κB inhibitors in treatment and prevention of lung cancer. *Biomed Pharmacother* (2020) 130:110569. doi: 10.1016/j.biopha.2020.110569

38. Liu B, Sun L, Liu Q, Gong C, Yao Y, Lv X, et al. A cytoplasmic NF-kappaB interacting long noncoding RNA blocks IkappaB phosphorylation and suppresses breast cancer metastasis. *Cancer Cell* (2015) 27(3):370–81. doi: 10.1016/j.ccell.2015.02.004

39. Riley RS, June CH, Langer R, Mitchell MJ. Delivery technologies for cancer immunotherapy. *Nat Rev Drug Discovery* (2019) 18(3):175–96. doi: 10.1038/s41573-018-0006-z

40. Sharma P, Allison JP. The future of immune checkpoint therapy. *Science* (2015) 348(6230):56–61. doi: 10.1126/science.aaa8172

41. Zhang Y, Zhang Z. The history and advances in cancer immunotherapy: understanding the characteristics of tumor-infiltrating immune cells and their therapeutic implications. *Cell Mol Immunol* (2020) 17(8):807–21. doi: 10.1038/s41423-020-0488-6

42. Brahmer JR, et al. Safety and activity of anti-PD-L1 antibody in patients with advanced cancer. *N Engl J Med* (2012) 366(26):2455–65. doi: 10.1056/NEJMoa1200694

43. Sheinfeld Gorin S, Krebs P, Badr H, Janke EA, Jim HS, Spring B. Meta-analysis of psychosocial interventions to reduce pain in patients with cancer. *J Clin Oncol* (2012) 30(5):539–47. doi: 10.1200/JCO.2011.37.0437

44. Deng G. Integrative medicine therapies for pain management in cancer patients. *Cancer J* (2019) 25(5):343–8. doi: 10.1097/PPO.0000000000000399

45. Currie E, Schulze A, Zechner R, Walther TC, Farese RV Jr. Cellular fatty acid metabolism and cancer. *Cell Metab* (2013) 18(2):153–61. doi: 10.1016/j.cmet.2013.05.017

46. De Schrijver E, Brusselmans K, Heyns W, Verhoeven G, Swinnen JV. RNA Interference-mediated silencing of the fatty acid synthase gene attenuates growth and induces morphological changes and apoptosis of LNCaP prostate cancer cells. *Cancer Res* (2003) 63(13):3799–804.

47. Fujiwara N, Nakagawa H, Enooku K, Kudo Y, Hayata Y, Nakatsuka T, et al. CPT2 downregulation adapts HCC to lipid-rich environment and promotes carcinogenesis via acylcarnitine accumulation in obesity. *Gut* (2018) 67(8):1493–504. doi: 10.1136/gutjnl-2017-315193

48. Chavez-Castillo M, Ortega Á, Cudris-Torres L, Duran P, Rojas M, Manzano A, et al. Specialized pro-resolving lipid mediators: The future of chronic pain therapy? *Int J Mol Sci* (2021) 22(19):10370. doi: 10.3390/ijms221910370

49. Serhan CN, Chiang N, Van Dyke TE. Resolving inflammation: dual anti-inflammatory and pro-resolution lipid mediators. *Nat Rev Immunol* (2008) 8 (5):349–61. doi: 10.1038/nri2294

frontiers | Frontiers in Oncology

TYPE Original Research
PUBLISHED 22 December 2022
DOI 10.3389/fonc.2022.1094248

OPEN ACCESS

EDITED BY
Linhui Wang,
Second Military Medical University, China

REVIEWED BY
Lifeng Zhang,
Changzhou No. 2 People's Hospital, China
Haiwei Zhang,
University of Nevada Reno, United States

*CORRESPONDENCE
Yan-Ping Zhang
zyphbmu@126.com

SPECIALTY SECTION
This article was submitted to Genitourinary Oncology, a section of the journal Frontiers in Oncology

RECEIVED 09 November 2022
ACCEPTED 05 December 2022
PUBLISHED 22 December 2022

CITATION
Teng Z-H, Li W-C, Li Z-C, Wang Y-X, Han Z-W and Zhang Y-P (2022) Neutrophil extracellular traps-associated modification patterns depict the tumor microenvironment, precision immunotherapy, and prognosis of clear cell renal cell carcinoma.
Front. Oncol. 12:1094248.
doi: 10.3389/fonc.2022.1094248

Neutrophil extracellular traps-associated modification patterns depict the tumor microenvironment, precision immunotherapy, and prognosis of clear cell renal cell carcinoma

Zhi-Hai Teng, Wen-Ce Li, Zhi-Chao Li, Ya-Xuan Wang, Zhen-Wei Han and Yan-Ping Zhang*

Department of Urology, The Second Hospital of Hebei Medical University, Shijiazhuang, China

Background: Neutrophil extracellular traps (NETs) are web-like structures formed by neutrophils, and their main function is antimicrobial defense. Moreover, NETs have numerous roles in the pathogenesis and progression of cancers. However, the potential roles of NET-related genes in renal cell carcinoma remain unclear. In this study, we comprehensively investigated the NETs patterns and their relationships with tumor environment (TME), clinicopathological features, prognosis, and prediction of therapeutic benefits in the clear cell renal cell carcinoma (ccRCC) cohort.

Methods: We obtained the gene expression profiles, clinical characteristics, and somatic mutations of patients with ccRCC from The Cancer Genome Atlas database (TCGA), Gene Expression Omnibus (GEO), and ArrayExpress datasets, respectively. ConsensusCluster was performed to identify the NET clusters. The tumor environment scores were evaluated by the "ESTIMATE," "CIBERSORT," and ssGSEA methods. The differential analysis was performed by the "limma" R package. The NET-scores were constructed based on the differentially expressed genes (DEGs) among the three cluster patterns using the ssGSEA method. The roles of NET scores in the prediction of immunotherapy were investigated by Immunophenoscores (TCIA database) and validated in two independent cohorts (GSE135222 and IMvigor210). The prediction of targeted drug benefits was implemented using the "pRRophetic" and Gene Set Cancer Analysis (GSCA) datasets. Real-time quantitative reverse transcription polymerase chain reaction (RT-PCR) was performed to identify the reliability of the core genes' expression in kidney cancer cells.

Results: Three NET-related clusters were identified in the ccRCC cohort. The patients in Cluster A had more metabolism-associated pathways and better overall survival outcomes, whereas the patients in Cluster C had more

immune-related pathways, a higher immune score, and a poorer prognosis than those in Cluster B. Based on the DEGs among different subtypes, patients with ccRCC were divided into two gene clusters. These gene clusters demonstrated significantly different immune statuses and clinical features. The NET scores were calculated based on the ten core genes by the Gene Set Variation Analysis (GSVA) package and then divided ccRCC patients into two risk groups. We observed that high NET scores were associated with favorable survival outcomes, which were validated in the E-MTAB-1980 dataset. Moreover, the NET scores were significantly associated with immune cell infiltration, targeted drug response, and immunotherapy benefits. Subsequently, we explored the expression profiles, methylation, mutation, and survival prediction of the 10 core genes in TCGA-KIRC. Though all of them were associated with survival information, only four out of the 10 core genes were differentially expressed genes in tumor samples compared to normal tissues. Finally, RT-PCR showed that MAP7, SLC16A12, and SLC27A2 decreased, while SLC3A1 increased, in cancer cells.

Conclusion: NETs play significant roles in the tumor immune microenvironment of ccRCC. Identifying NET clusters and scores could enhance our understanding of the heterogeneity of ccRCC, thus providing novel insights for precise individual treatment.

KEYWORDS

neutrophil extracellular traps, ccRCC, subtypes, prognosis, immune tumor environment

Introduction

Renal cell carcinoma (RCC) is one of the most common urological carcinomas (1). In 2022, the number of tumor cases and cancer-associated deaths in China are expected to reach 7,410 and 46,345, respectively (2). Although the diagnosis and management of RCC have improved (3), its incidence is expected to increase globally. Moreover, approximately 30% of patients are diagnosed with advanced ccRCC, develop distant metastases, and have a poor prognosis due to the atypical symptoms in the early stage of ccRCC (1). ccRCC is the most common subtype of RCC (4). Thus, for better personal precision therapy and management, investigating novel biomarkers is an urgent necessity.

Neutrophils are one type of affluent inflammatory cell in the tumor microenvironment (TME). They could activate cancer cells and desorb modified DNA structures coated with cytoplasmic and granular proteins (5). The web-like structures released by neutrophils to trap microorganisms are termed neutrophil extracellular traps (NETs) (6, 7). Commonly, NETs play critical roles in infectious and non-infectious conditions, such as bacterial and viral infections (5), cystic fibrosis (8), and psoriasis (9). Recently, NETs have been reported to be involved in tumor growth, metastatic spread (10, 11), and immunomodulatory (12). Moreover, NET extrusion exerts a protective effect on the tumor from NK cells and T cells (13). NETs can increase the metastatic potential of circulating tumor cells through augmentation of cell cycle progression (14). Hu et al. reported that NETs could promote the dysfunction of glomerular endothelial cells and pyroptosis in diabetic kidney disease (15). NETs are closely associated with dirty necrosis in RCC (16). Several recent studies have documented the scrutiny of NET-related genes for head and neck squamous cell carcinomas (6), non-small-cell lung cancer (17), and breast cancer (18); however, few studies have focused on the functions of NETs in kidney diseases, particularly kidney cancers. Therefore, it is meaningful to explore new NET-related biomarkers to identify the molecular characteristics of NETs in patients with kidney cancer.

Considering the previous findings, we performed a systemic study on NET-related genes to investigate their roles in the ccRCC cohort. In this study, we first screened the expression, protein–protein network, and prognostic values in the TCGA-KIRC dataset. Based on the expression of NET-related genes, we classified ccRCC patients into three clusters. Patients were further stratified into two gene clusters based on the differentially expressed genes (DEGs) among the three NET subtypes. We further constructed a scoring system to predict overall survival (OS), which may form the basis for research on ccRCC precision treatment.

Methods

Data collection and processing

The RNA-sequencing dataset of 534 kidney renal clear cell carcinoma (KIRC) samples, which contained mRNA and clinical and survival data, were acquired from UCSC Xena (http://xena.ucsc.edu/). The GSE29609 dataset, which contained 39 KIRC samples, were downloaded from the GEO database. The mRNA expression levels were transformed from counts to transcripts per kilobase million (TPM) values. The batch effects of the two datasets were eliminated by "ComBat" from the "sva" R package, and principal component analysis (PCA) was performed to demonstrate the before and aftereffects. Finally, 573 samples, 14,074 genes were enrolled into our after-batched cohort. The E-MTAB-1980 dataset, which contained 101 patients with ccRCC, was downloaded from ArrayExpress (https://www.ebi.ac.uk/arrayexpress/).

Exploration of the genetics and biological significance of NET genes in KIRC

According to previous studies (19–22), we acquired a list of published NET gene sets, which had 69 genes with NET initial biomarkers. The mRNA expression and prognostic values of NETs were based on the TCGA-KIRC dataset. The network of 69 genes was explored based on the GeneMANIA (http://genemania.org/) website.

Unsupervised clustering analysis

The unsupervised consensus clustering algorithm was applied to assess the variability and stability of clusters based on NET-related and NET subtype-related genes from the ConsensusClusterPlus (23) R package. Then Kaplan–Meier survival analysis was performed to explore the prognosis among different clusters based on the survival (24) and survivor (25) R packages.

Gene set variation analysis

The 50 terms of the HALLMARK pathway, the Kyoto Encyclopedia of Genes and Genomes (KEGG) pathway, and the Reactome pathway were downloaded from the Molecular Signatures Database (MsigDB, http://software.broadinstitute.org/gsea/msigdb/). Then, function enrichments for different subtypes were performed using the GSVA (26) and ClusterProfiler (27) R packages.

The immune infiltration landscape of the ccRCC cohort

The StromaScore, ImmuneScore, and ESTIMATEScore were calculated with the "ESTIMATE" R package. The ImmuneScore and StromalScore were the abundance of immune and stromal components, respectively. The ESTIMATEScore was the total values of ImmuneScore and StromalScore. The abundance of 23 kinds of infiltrating immune cells (28) was evaluated using the ssGSEA method from the GSVA (26) R package.

Calculation of NET score (NET-scores)

According to the mRNA expression of NET subtype-related genes, 94 DEGs were used for further univariate Cox regression analysis. Then the NET score was calculated as an enrichment score (ES) by the ssGSEA method from the GSVA R package based on the top ten genes with $P < 0.05$ samples. The ccRCC cohort was divided into high and low NET score groups based on the optimal cutoff value.

Prognosis, enrichment analysis, genetic alterations, chemokines, immune exploration, and clinical feature analysis based on NET-scores

The prognosis analysis between the high- and low-NET score groups was tested using the log-rank method. The correspondence among different groups, subtypes, and survival outcomes was shown as Sankey diagrams by the "ggalluvial" R package. The hallmark enrichment analysis between different NET score groups was done using the GSVA R package and genetic alterations by the "maftools" (29) R package. The mRNA expression of chemokines between different NET score groups was displayed using a heatmap. The clinical characteristics of "survival outcomes," "clinical grade," "TNM," and "clinical stage" were selected to demonstrate the discrepancy in the different NET score groups.

Expression levels of immune checkpoints, immunotherapy response, and drug sensitivity of patients in different NET-score groups

Two immunotherapy-treated cohorts, the IMvigor210 cohort (288 urological tumor patients treated with anti-PDL1) and the GSE135222 cohort (27 lung carcinoma patients treated with anti-PD-1/PD-L1), were collected to explore the immunotherapy response ability of NET scores. The pRRophetic (30) package

was implemented to predict the half-maximal inhibitory concentration (IC50) of 138 antitumor agents.

Online analysis

mRNA expression, single nucleotide variation (SNV), copy number variation (CNV), drug sensitivity, and methylation of genes were analyzed by the GSCA database (http://bioinfo.life.hust.edu.cn/GSCA/#/). The protein levels of core genes in human tumor and non-tumor samples were acquired from the Human Protein Atlas (HPA; https://www.proteinatlas.org/). The oncoplot of genes was explored from cBioportal (https://www.cbioportal.org/).

Cell culture and RT-PCR

Human normal renal tubular epithelial cells (HK-2) and kidney cells (Caki-1 and 786-O) were purchased from the ATCC company. All cells were cultured in RPMI 1640 as previously described (28). Total RNA from the cultured cells was extracted using the Faster reagent (Invitrogen). Relative gene expression was calculated by Eq. $2^{-\Delta\Delta CT}$, with GAPDH as an internal control. The primers are as follows:

MAP7 gene 5'-TCATCATGCCCTACAAAGCTG-3'(sense) and 5'-TGCCAGATGTGAGGAAGAGTA-3'(antisense).

SLC16A12 gene 5'-TGCTTGCATCTACTGGACTCA-3'(sense) and 5'-TGGCAATAGCTGGAGAGTAACA-3' (antisense).

SLC27A2 gene 5'-TGGCGCTCCTTATGGGTAACG-3'(sense) and 5'-CTTGGCAGTATCTCTTCGACAG-3' (antisense).

SLC3A1 gene 5'-CAGGAGCCCGACTTCAAGG-3'(sense) and 5'-GAGGGCAATGATGGCTATGGT-3' (antisense).

Statistical analysis

All data were analyzed using R software (v4.1.1); a P-value less than 0.05 was considered statistically significant. The "limma" (31) R package was used to perform a difference analysis. The Wilcoxon test was used for data that did not accord with a normal distribution. A t-test was used for normally distributed data. Univariate Cox regression analysis and the Kaplan–Meier method were used to assess the prognostic value of DEGs. The forest plot was achieved by "forestplot" (32) R package. All heatmaps were performed *via* the R "pheatmap" package.

Results

Expression and prognostic values of NET-related genes in the TCGA-KIRC

We identified 43 differential expression NET-related genes in the TCGA-KIRC dataset, of which 20 are upregulated genes and 23 are downregulated genes with a false discovery rate <0.05 and |log2FoldChange| >0.5 (Figures 1A, B, Supplementary Table 1). Figure 1C shows the locations of the NET-related genes. We then submitted the NET-related genes to GeneMANIA for exploring their interaction network. The results revealed the co-expression to be high (62.39%) and the physical interaction to be 15.79% (Figure 1D).

Identification of NET-related gene subtypes in the ccRCC cohort

The TCGA-KIRC and GSE29609 datasets were merged, and PCA demonstrated the before and after batch effects (Figure S1A). In the merged ccRCC cohort, we performed unsupervised clustering and classification based on these NET-related genes. Our results showed that k = 3 appeared to be an optimal selection (Figures 2A–C). The Kaplan–Meier survival analysis demonstrated that the prognoses of patients were significantly different among these subtypes (log-rank test, P <0.001, Figure 2D). Cluster A exhibited better survival better survival advantage than other clusters. The PCA results showed significant differences in NET-related gene expression among the three clusters (Figure 2E). The clinicopathological features among the different clusters also revealed significant differences (Figure 2F). Moreover, most of the NET-related genes were differentially expressed (Figure 2G).

Characteristics of TME in different subtypes

Cluster A was significantly associated with cancer-related and metabolism pathways, such as pancreatic cancer, renal cell carcinoma, butanoate metabolism, histidine metabolism, fatty acid metabolism, tryptophan metabolism, and beta-alanine metabolism (Figure 3A). Cluster C was significantly enriched in immune-activated pathways, including NK cell-mediated cytotoxicity, antigen processing and presentation, allograft rejection, autoimmune thyroid disease, T and B cell receptor signaling pathways, and Toll-like and NOD-like receptor signaling pathways (Figure 3A). To explore the roles of NET-related genes in the TME of ccRCC, we calculated the TME score using the ESTIMATE method. The results revealed that Cluster C had higher stromal and immune scores than the other two

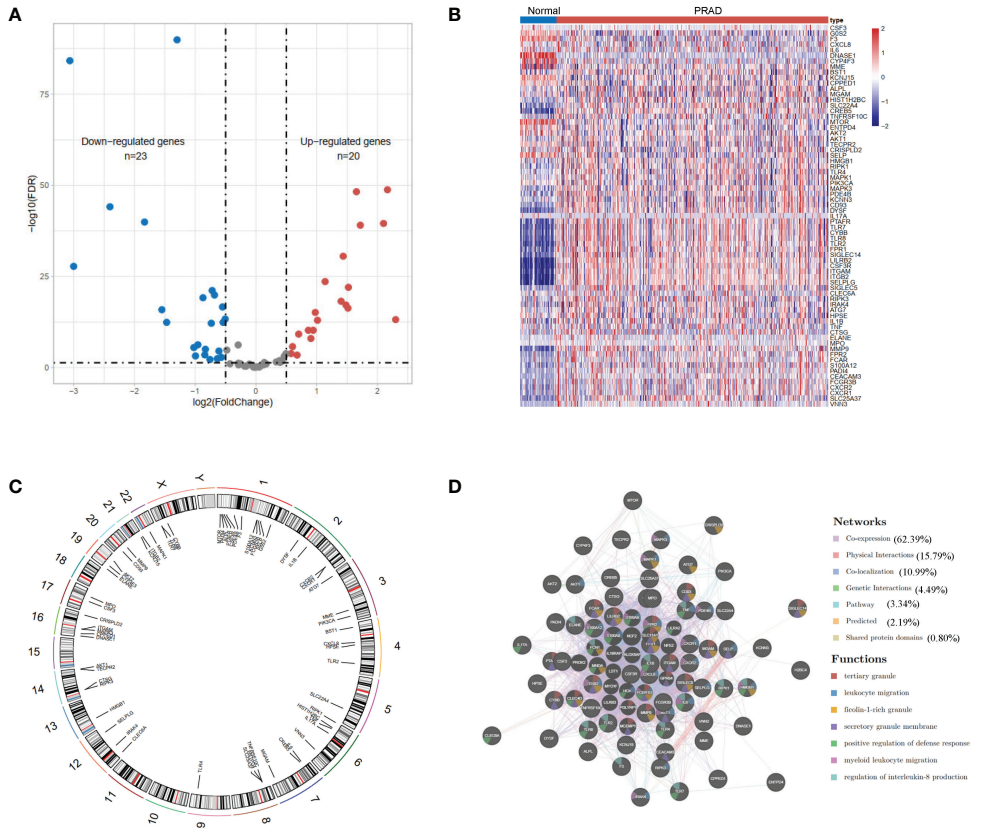

FIGURE 1
The landscape of neutrophil extracellular trap-associated genes in the TCGA-KIRC. **(A)** Volcano plot and **(B)** heatmap of 69 NET-associated genes in ccRCC and non-tumor samples. **(C)** The location of the NET-associated genes on different chromosomes. **(D)** GeneMANIA gene–gene interaction network showed the correlation among different genes.

clusters (Figure 3B). Analysis of three critical immune checkpoints showed significance among three subtypes (Figure 3C). Then, the ssGSEA method was applied to calculate the infiltrating status of immune cells and explore the differential patterns. The results revealed that the infiltration levels of several cells, such as activated B cells, CD4 T cells, and CD8 T cells, were significantly higher in Cluster C than in other clusters (P <0.05, Figure 3D), which agreed with the results of the TME score.

Identification of gene clusters based on DEGs

To explore genes associated with our NET-related clusters, differential gene analyses were performed to select the DEGs among clusters A–C by using "limma" R packages (|logFC| >1.5 and P-value <0.05, Figure S1B). The DEGs of these results were then combined, and 94 genes were enrolled for further analysis. The GO enrichment of DEGs demonstrated that the NET subtype-related genes were significantly enriched in transmembrane transport and transporter activity (Figure 4A). The KEGG analysis revealed enrichment of immune response-related diseases (such as coronavirus disease 2019 and systemic lupus erythematosus) and cancer-related pathways (Figure 4B), which indicated that NETs may play a critical role in immunomodulation. Then, the univariate Cox method was used to explore the prognostic values, and 89 genes were found to be related to OS time (Supplementary Table 2). The top ten genes (SLCA16A12, SLC3A1, TMEM27, GFPT2, NPR3, MAP7, BBOX1, PDK4, SLC27A2, and CUBN) with the smallest P-value were selected for further analysis (Figure 4C). Based on these 10 prognostic genes, patients were divided into two clusters, namely gene clusters A and B (Figure 4D). The Kaplan–Meier curves demonstrated that patients in gene cluster B had poor OS, whereas those in gene cluster A had favorable OS (P-value <0.001, Figure 4E). In addition, the gene cluster A patterns were closely related to the late TNM stage (Figure 4F). The expression profiles of 10 hub genes were significantly different, consistent with the expected gene clusters (Figure 4G).

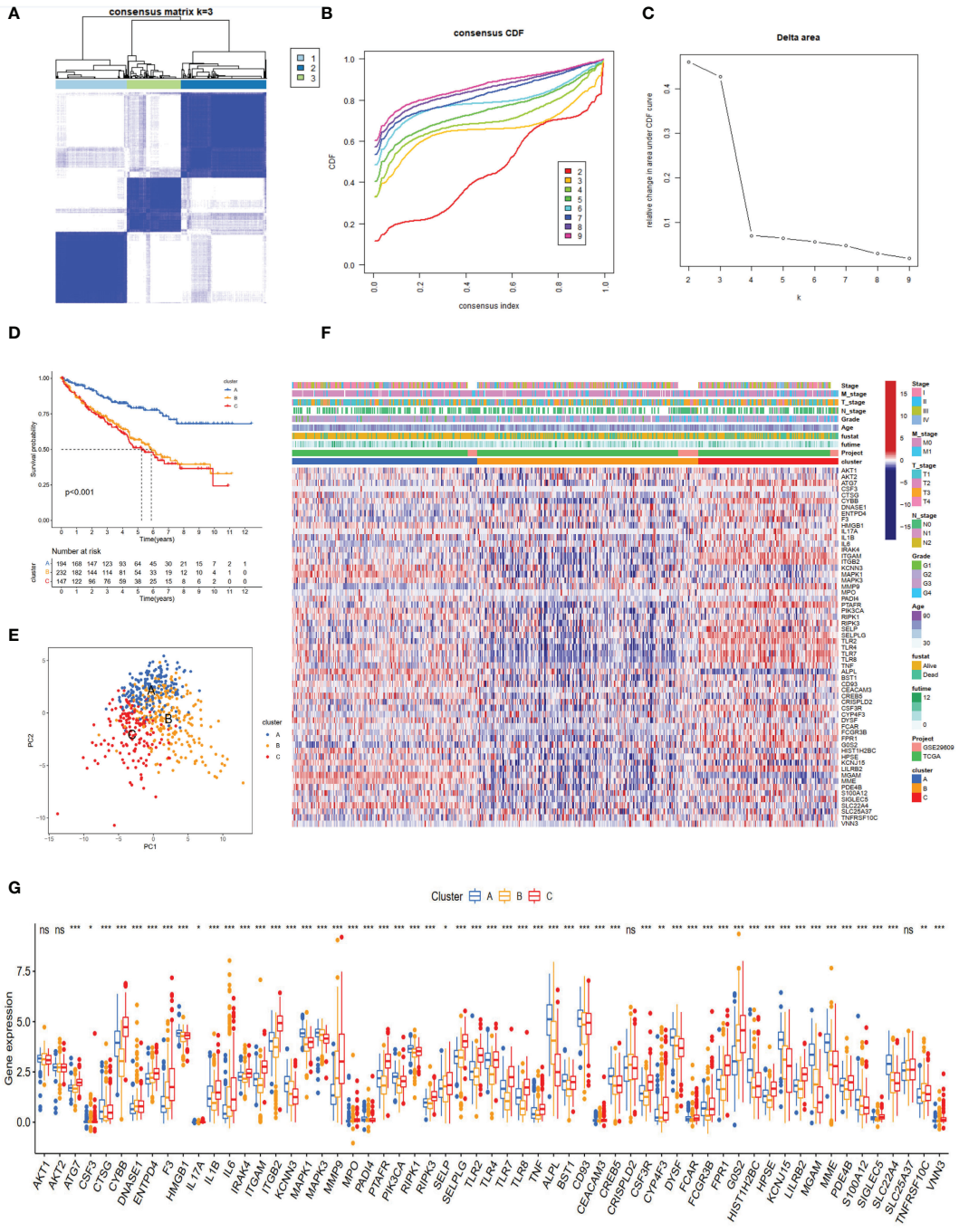

FIGURE 2
NET subtypes and clinicopathological features of three clusters. **(A)** Consensus matrix of ccRCC samples' co-occurrence proportion for k = 3. **(B, C)** Consensus clustering CDF for k from 2 to 9. **(D)** The Kaplan–Meier plot showed the overall survival differences among the three subtypes in the ccRCC cohorts. **(E)** Principal component analysis of ccRCC samples grouped by clusters. **(F)** Heatmap showing the association of subtypes with clinical characteristics and expression of neutrophil extracellular trap-associated genes. **(G)** The boxplot of neutrophil extracellular trap-associated genes among different clusters. ns, no significance. *p < 0.05, **p < 0.01, ***p < 0.001.

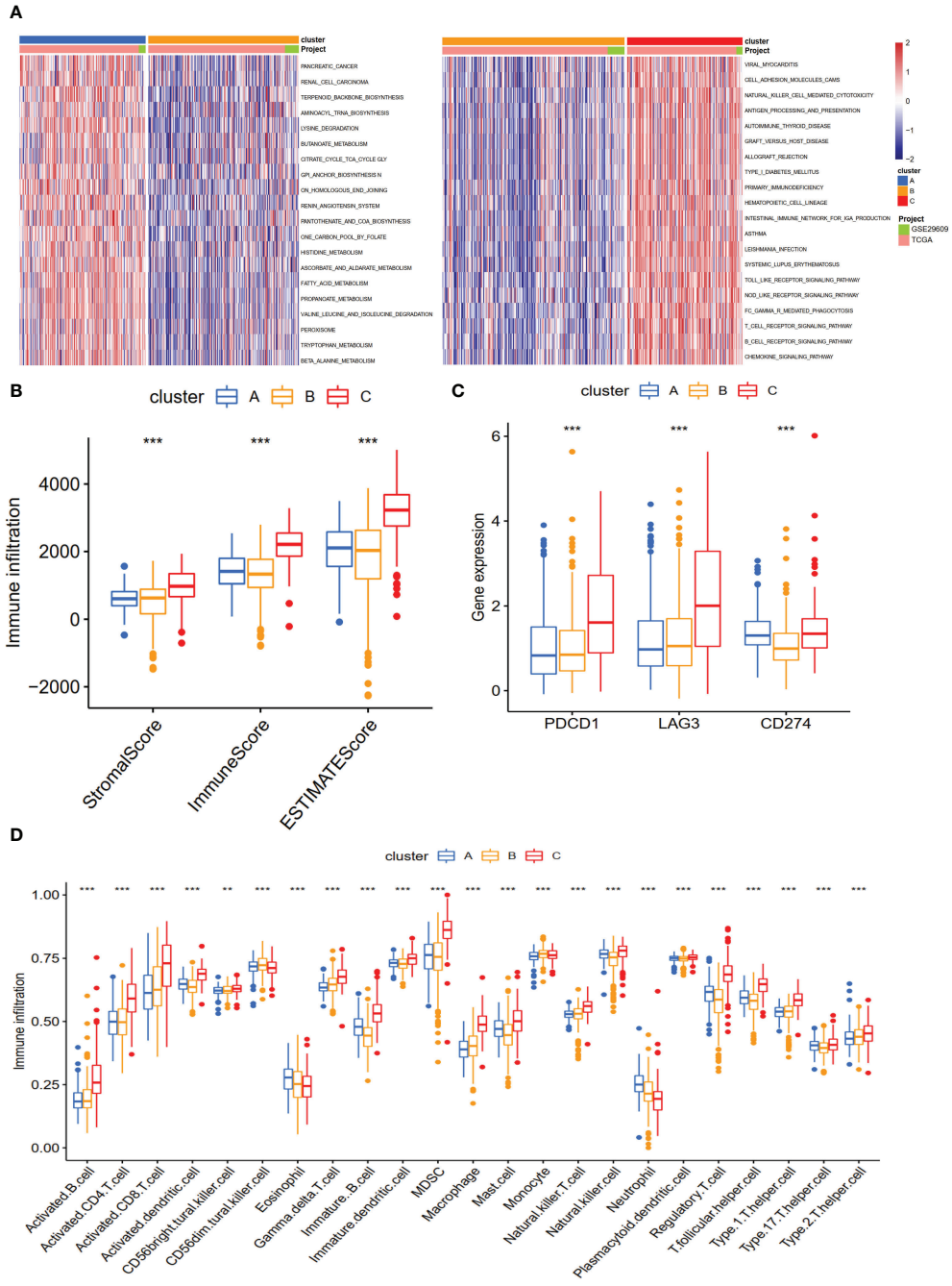

FIGURE 3
The biological characteristics and landscape of immune status among different subtypes. **(A)** KEGG enrichment analysis of three NET subtypes. **(B)** The ESTIMATE proportion of stromal score, immune score, and ESTIMATE score among the three clusters. **(C)** The gene expression profiles of three common immune checkpoint genes, PDCD1, LAG3, and CD274. **(D)** The infiltration levels of 23 immune cell types among three subtypes. **p < 0.01, ***p < 0.001.

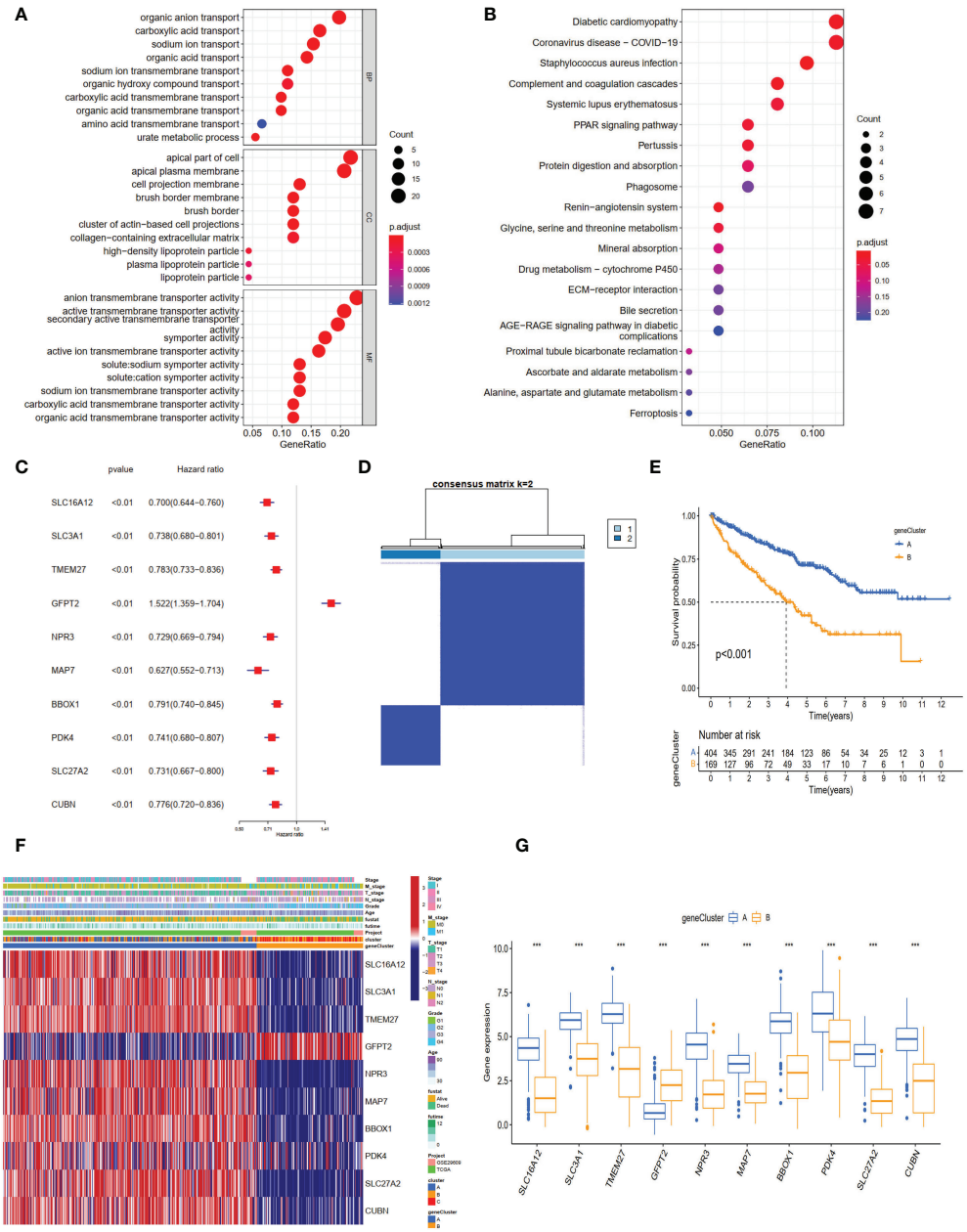

FIGURE 4
The different expression genes (DEGs), enrichment pathways among different clusters, and consensus clustering based on DEGs. **(A)** The GO and **(B)** KEGG enrichment of different subtypes. **(C)** The forest plot for ten core DEGs based on univariate Cox regression analysis. **(D)** Consensus matrix of ccRCC samples' co-occurrence proportion for k = 2. **(E)** Kaplan–Meier curves for the two gene clusters of ccRCC patients. The log-rank test shows an overall p <0.001. **(F)** Heatmap showing the relationship among the clinicopathological characteristics of the gene clusters. **(G)** The boxplot of gene expression of ten core genes between the two subtypes. ***p < 0.001.

Calculation of the NET scores, and evaluation of TME and chemokines in different risk groups

Based on the 10 core genes, we used the ssGSEA method to calculate the NET scores of each patient in the ccRCC cohort. The patients were then divided into high (n = 337) and low (n = 236) risk score groups based on the NET scores. Moreover, compared with the low NET-score group, the high NET-score group had a favorable OS (Figure 5A), which was also validated in E-MTAB-1980 (Figures S1D–G). We observed a significant difference in the NET scores among different subtypes, which are displayed in

Figures 5B, C. Cluster C had the lowest NET scores, whereas Cluster A had the highest, revealing that NET scores may be closely associated with immune-infiltration status (Figure 3B). Figure 5D shows the plots displaying the distribution of patients in three clusters: two gene clusters and two risk score groups.

To investigate the relationship between the abundance of immune cells and NET-scores, we performed the CIBERSORT algorithm to assess. As shown in the correlation matrix, the NET-scores were positive for NK cells and neutrophils, and negative for type 2 helper T cells (Figure 5E). The heatmap showed that several chemokines, interleukins, interferons, and their receptors were significantly overexpressed in the high NET-score group (Figure 5F), indicating that NET scores may provide novel targets for anti-tumor immunity.

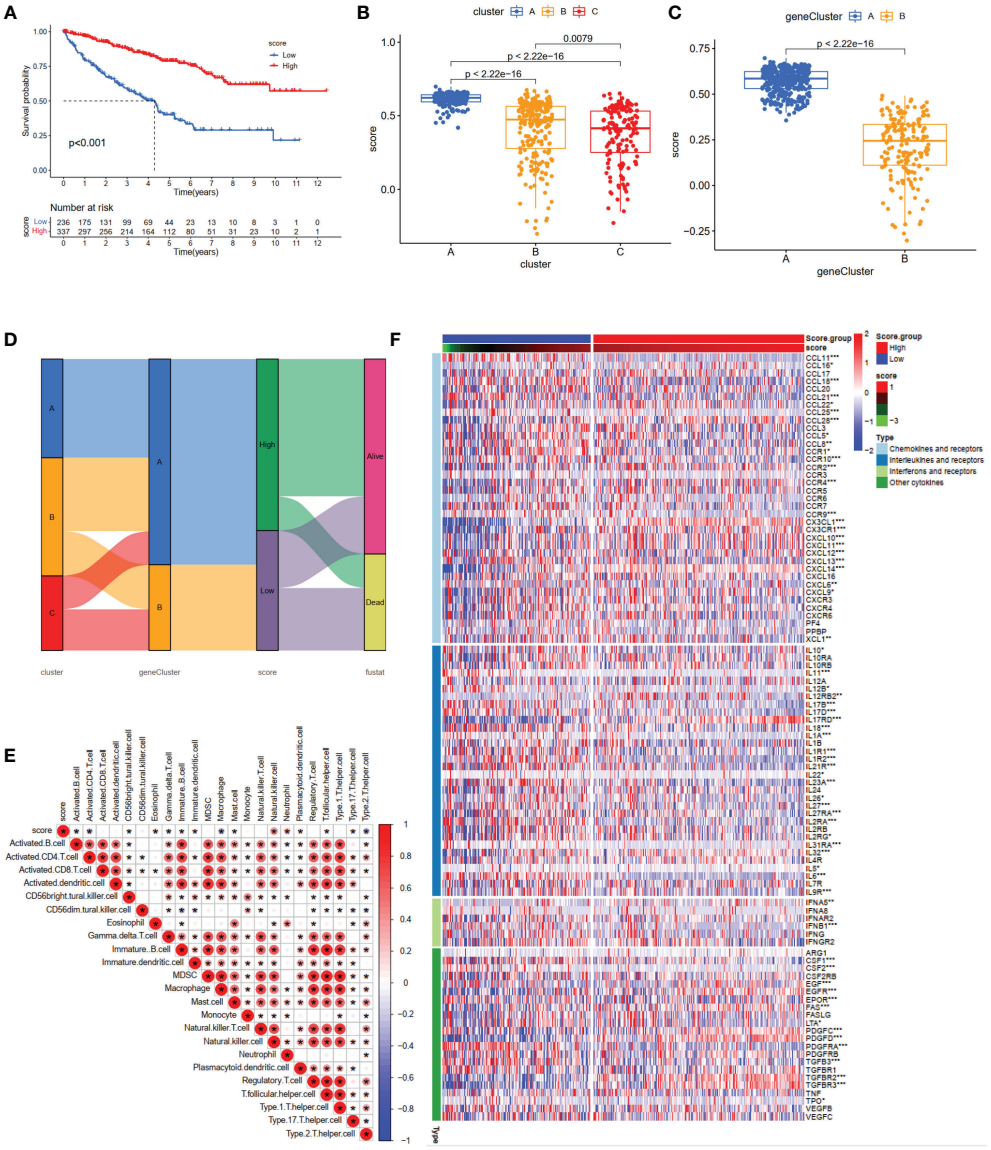

FIGURE 5
Construction of the NET-score system and clinical prognosis analysis in ccRCC patients. **(A)** Kaplan–Meier curves for high and low NET-score ccRCC patient groups (log-rank test, *P* <0.001). Differences in NET scores among the three clusters **(B)** (P <0.001) and two gene clusters **(C)** (P <0.001). **(D)** Alluvial diagram of NET-associated gene clusters in groups with different gene clusters, NET-score groups, and survival outcomes. **(E)** The correlation matrix of all infiltrating immune cells. Some fractions of immune cells were positively related and are represented in red, whereas others were negatively related and are represented in blue. p <0.05 was the cut-off. **(F)** Heatmap showing the relationship between scoring groups and chemokines, interferons, and cytokines. *p < 0.05, **p < 0.01, ***p < 0.001.

Clinical characteristics of the NET-scores and functional enrichment between different subtypes

To assess the effect of the NET scores on clinical characteristics, we investigated the association between the NTE scores and several critical features (overall survival status, grade, stage, and TNM stage). The results demonstrated that patients with higher NET scores were associated with a better survival status (Figure 6A). Moreover, advanced tumor stages (Grades 3–4, Stages III–IV) also displayed low NET scores (Figures 6B, C), which were also observed in tumor size (Figure 6D), regional lymph node status (Figure 6E), and metastasis (Figure 6F).

To further analyze the specific mechanism, common functional enrichments were performed between the high and low NET-score groups using the GSVA method. The hallmark results indicated that high NET scores were associated with several metabolisms and oxidative phosphorylation pathways, such as fatty acid metabolism and xenobiotic metabolism (Figure 6G), which were also identified in the KEGG enrichment results (Figure 6H). Furthermore, the hallmark and KEGG enrichment showed that the high NET-score group was associated with a series of immune-related pathways, such as allograft rejection and autoimmune thyroid disease (Figures 6G, H).

Evaluation of checkpoints and immunotherapeutic benefit between the high- and low-NET-score groups

We next investigated the expression profiles of three checkpoints (PDCD1, LAG3, and CD274), immunophenoscores (IPS), and immune-checkpoint therapy response. The results demonstrated that PD-1 (PDCD1) and LAG3 were significantly higher in the low NET-score group than the high NET-score group, whereas the PD-L1 (CD274) level displayed a reverse discrepant trend (Figures 7A–C). According to the above results, we speculated that the PD-1 inhibitor is more reactive in the low NET-score group and the PDL-1 inhibitor is more effective in the high NET scores. IPS, as the novel method for evaluating the potential clinical efficacy of immunotherapy, was calculated to predict the immunotherapeutic benefit. The results revealed that the high IPS with a positive CTLA-4 signature was associated with high NET-scores (Figure 7D).

In the subsequent analysis, we included two public datasets, GSE135222 and IMvigor210 to predict the immunotherapeutic efficacy. Patients with low NET scores were more likely to benefit from immunotherapy (Figures 7E, H). Compared to the high-risk group, there was an increase in patients with responses in the low-risk group (Figures 7F, I). Patients with low NET scores showed significant immunotherapeutic benefits and favorable survival (Figures 7G, J).

Pathway activity and drug sensitivity analysis

As chemotherapy is still a traditional therapy method for ccRCC, particularly for advanced ccRCC, we investigated the response of the two NET-score groups to common chemo-drugs. As shown in Figures 8A–H, compared with the high NET-score group, sunitinib (P-value = 3.6e−08) and rapamycin (P-value <0.001) showed lower IC50 values in the low NET-score group, whereas sorafenib (P-value = 1.2e−14), lapatinib (P-value= 0.038), erotinib (P-value = 3e−09) and axitinib (P-value =0.081) showed higher values in the low NET-score group, suggesting that patients in the low NET-score group were more likely to respond well to sunitinib, and poorly to sorafenib and axitinib than those in the high NET-score group. Based on the GSCA dataset, we first explored the activity pathways in the TCGA-KIRC. As shown in Figure 8I, the NET scores were negatively associated with apoptosis, cell cycle, and DNA damage and positively associated with PI3K/AKT and RTX pathways. This indicated that the NET scores were more likely to play roles in apoptosis and cell cycle by regulating PI3K/AKT and RTX pathways. The drug sensitivity in the pan-cancer analysis of GDSCs and CTRP is shown in Figures 8J–K. The results demonstrated that BRD-A96377914, tubastatin A, BRD-K85133207, WZ8040, afatinib, canertinib, ibrutinib, cetuximab, gefitinib, TGX221, CCT007093, and RO-3306 were more likely to function well.

Genetic mutations of two NET-score groups, landscape, and validation of core genes

To investigate the mutation status between the two NET-score groups, genetic mutations were analyzed using the maftools (29) R package. The results revealed that the high NET-score group had a higher mutation rate than the low NET-score group (70.05% *vs* 58.4%). The top 10 most frequently mutated genes are displayed in Figure S1C. Subsequently, the landscape of 10 core genes was explored in the TCGA-KIRC. The results demonstrated that only four genes (MAP7, SLC16A12, SLC27A2, and SLC3A1) were DEGs in ccRCC compared to normal samples (Figure S2A). Four genes had more than a 1% mutation rate (Figure S2B). The 10 core genes were significantly associated with DSS, OS, and PFS (Figure S2C). Several genes were positively correlated with methylation levels, whereas CUBN, MAP7, and SLC16A12 were closely associated with copy number variation (CNV) levels (Figure S2D). Most of the genes (9/10) were positively associated with PI3K/AKT, RTK, and hormone AR activity and negatively associated with apoptosis, cell cycle, and DNA damage (Figure S2E). Considering only four genes were DEGs, we explored these four genes in the CCLE dataset. The results revealed that the

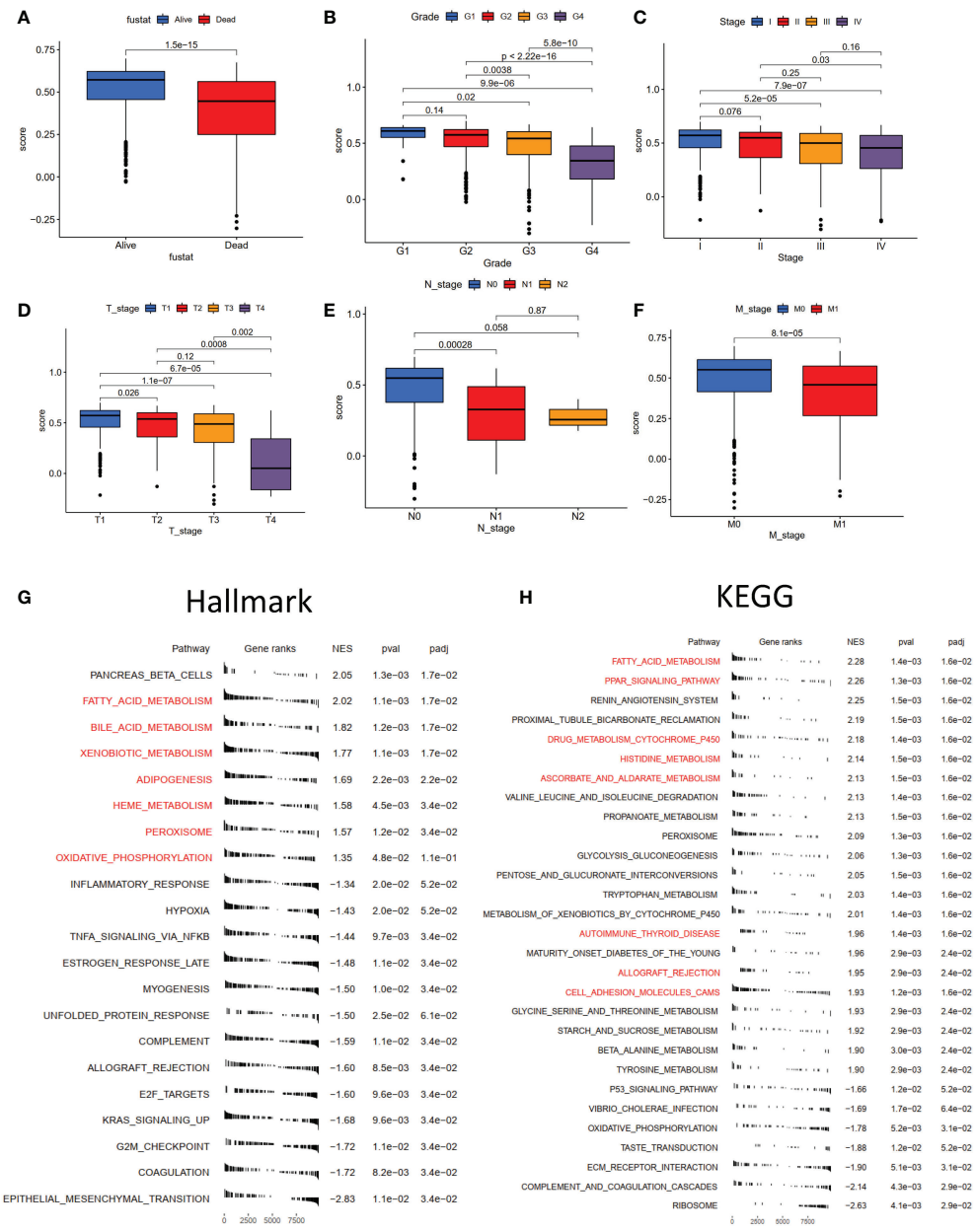

FIGURE 6
The correlation of NET-scores with clinic-pathological characteristics, hallmark and KEGG enrichment between high- and low-NET-score groups. The boxplot of different survival status **(A)**, clinical grade **(B)**, clinical stage **(C)**, tumor stage **(D)**, regional lymph node status **(E)**, and distant metastasis **(F)**. The hallmark **(G)** and **(H)** KEGG enrichment between high- and low-NET-score groups.

basal expression profiles of MAP7, SLC16A12, and SLC3A1 were high in kidney cancer cells (Figure S2F). The RT-PCR showed that MAP7, SLC16A12, and SLC27A2 were decreased in 786-0 and Caki-1 compared with HK2, while SLC3A1 increased (Figure S2G), which was consistent with the results of the TCGA-KIRC (Figure S2A). The protein levels of HPA demonstrated that MAP7 and SLC27A2 levels were lower, and SLC3A1 levels were higher, in tumor tissues than in normal samples (Figure S2H), in accordance with the results of the TCGA-KIRC and RT-PCR.

Discussion

ccRCC, the most common subtype of RCC, is highly associated with poor clinical outcomes (33). Emerging

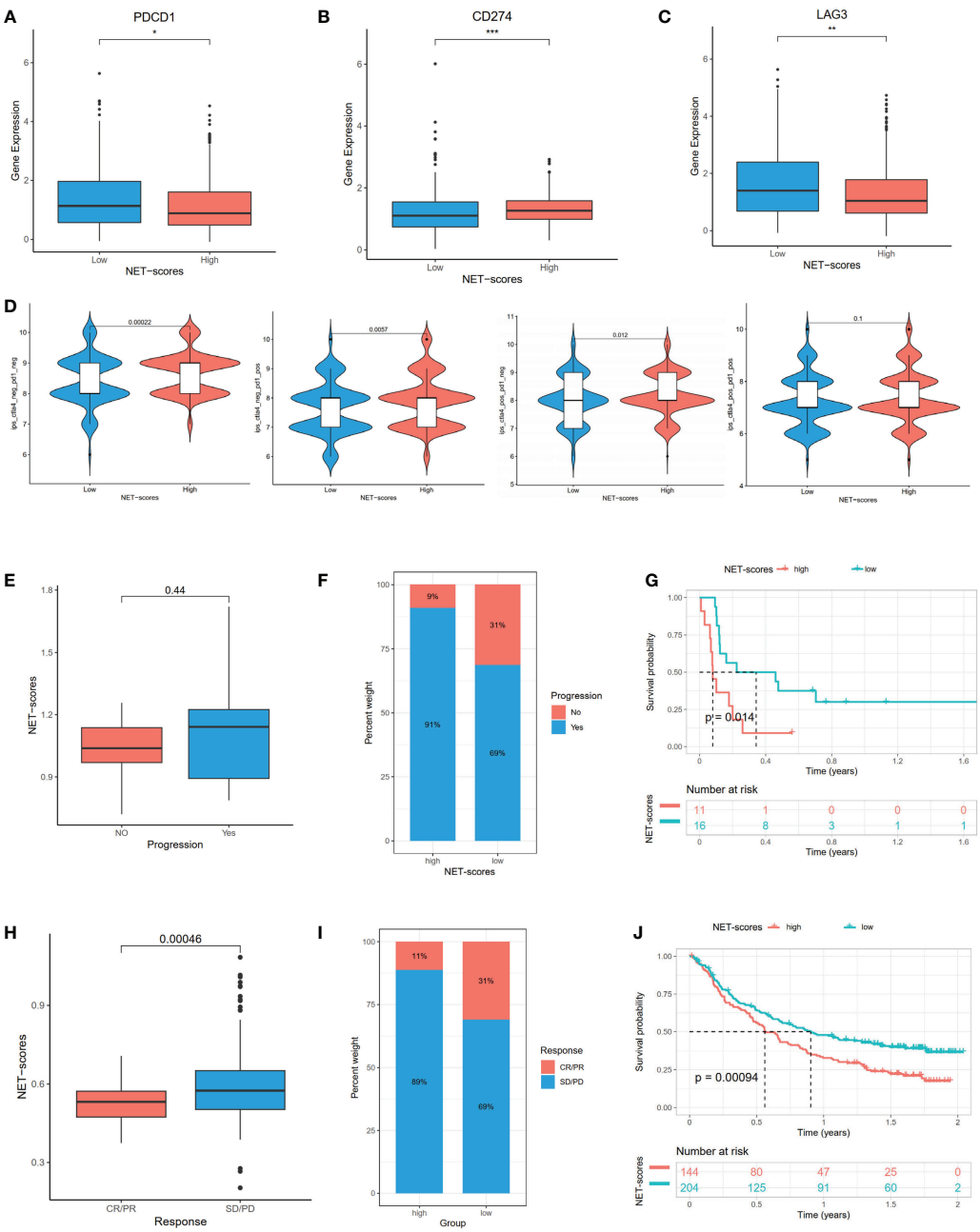

FIGURE 7
The mRNA expression of immune checkpoint genes and immunotherapeutic benefits. The PDCD1 **(A)**, LAG3 **(B)**, and CD274 **(C)** expression between different NET-score groups. The association between IPS and NET scores **(D)**. The different immunotherapy responses between high- and low-NET-score groups in GSE135222 **(E–G)** and IMvigor210 **(H–J)** datasets. *p < 0.05, **p < 0.01, ***p < 0.001.

treatments such as targeted drugs and immunotherapy have significantly enhanced the prognosis of patients with advanced ccRCC; however, the effectiveness of these treatment strategies still needs to be improved (34). Moreover, ccRCC has strong immune-associated characteristics (35). Thus, reliable biomarkers are urgently required to predict recurrence risk and guide treatments. NETs and immune cell infiltrations have been reported to have critical roles in tumor progression (36). Sivan et al. first described the association between NETs and cancer (Ewing sarcoma) (12). Subsequently, there are increasing studies on NETs and cancer. For example, NETs drive the process of endothelial-to-mesenchymal transition (37). Aldabbous et al. identified that NETs promote angiogenesis (38). Moreover, NETs promote cancer-associated thrombosis *via*

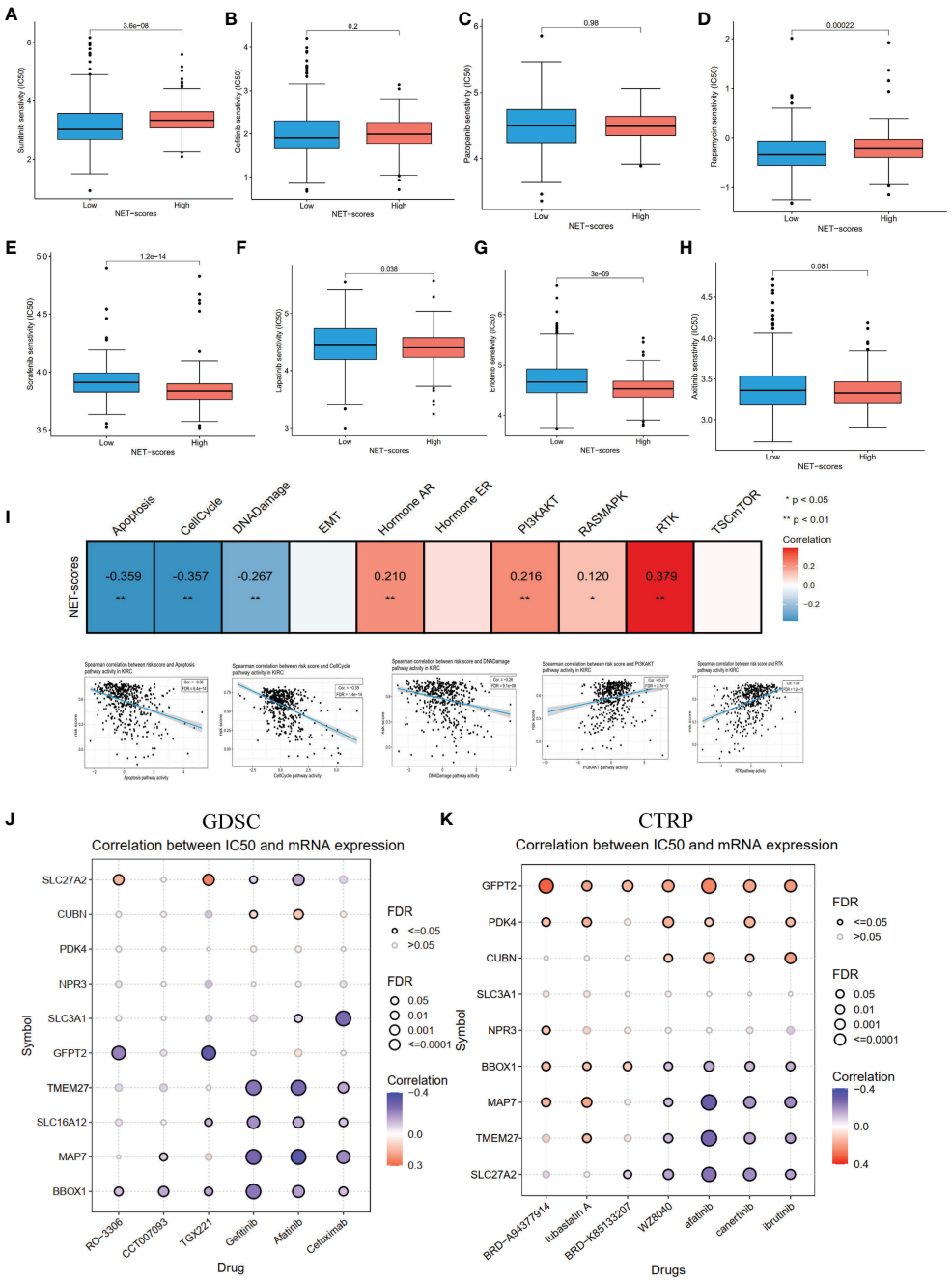

FIGURE 8
The pathway activity, drug sensitivity in ccRCC cohorts and pan cancer. **(A–H)** The drug sensitivity of eight common targeted compounds. **(I)** The associations of NET scores with activity pathways in the TCGA-KIRC dataset. **(J)** The correlation between gene expression and the sensitivity of GDSC drugs in pan-cancer. **(K)** The correlation between gene expression and the sensitivity of CTRP drugs in pan-cancer.

thrombin generation and the conversion of fibrinogen to fibrin (39). Additionally, many prognostic signatures based on NETs have been reported in human cancers (19, 20). However, whether NETs are also involved in tumor prognosis and play prognostic values in ccRCC has not been explored. Therefore, we collected the expression profiles of NET-related genes and clinical characteristics from the TCGA, GEO, and ArrayExpress datasets and comprehensively explored the NET-related genes in the ccRCC cohort.

In the current study, we first examined the roles of NET-related genes in the TCGA-KIRC and found that 43 of 69 genes were significantly differentially expressed in the tumor samples

compared to non-tumor tissues. Moreover, most of the genes were prognostic genes. Then, three NET-related subtypes (Clusters A–C) were identified in the ccRCC cohort by consensus cluster algorithms. It was found Cluster B had low levels of NET-related genes and low abundance of immune cells infiltration, whereas Cluster C had high levels of NET-related genes and immune cell infiltration. Moreover, the three subtypes had significantly different overall survival outcomes. The differences in mRNA expression profiles among the three subtypes were dramatically correlated with metabolism- and immune-related biological pathways. We identified two gene clusters, A and B, based on the DEGs among the three NET-related subtypes. Our findings suggested that NETs act as a predictor for clinical survival outcomes, targeted drugs, and the immunotherapy response of ccRCC. Therefore, we established the NET scores based on 10 hub genes by using the ssGSEA method. Patients with low and high NET scores showed significant discrepancies in clinical characteristics, prognosis, immune cell infiltrations, immune checkpoints, and activity signal pathways.

As for the 10 core genes, MAP7, SLC16A12, SLC27A2, and SLC3A1 were significantly different in patients with ccRCC when compared to non-tumor samples. MAP7, Microtubule-associated protein 7, functions as a regulator of microtubule bundling and dynamics. Several studies had reported MAP7 involved in cell cycle progression (40) and autophagy pathway in cancers (41). SLC16A12, SLC27A2, and SLC3A1 belonged to the solute carrier group of membrane transport proteins (42). Liu et al. reported that decreased expression of SLC16A12 mRNA levels was associated with a poor prognosis for ccRCC (43). Upregulation of SLC27A2 could inhibit the proliferation and invasion of RCC *via* a CDK3-mediated pathway (44). SLC3A1, the cysteine carrier, has been reported to promote breast cancer tumorigenesis *via* AKT signaling (45). In our study, we found MAP7, SLC16A12, and SLC27A2 in kidney cancer cells when compared with normal kidney cells, which agreed with the results of the TCGA-KIRC. Generally, the results indicated that MAP7, SLC16A12, SLC27A2, and SLC3A1 could be the biomarkers for the complement system of ccRCC.

Immunotherapies, particularly immune checkpoint inhibitors (ICIs), have transformed the treatment of several advanced carcinomas (46–49). Although clinical benefits have been achieved when patients with ccRCC receive ICIs, the responses demonstrated personal heterogeneity (50). Thus, looking for markers to predict the responses of ICI treatment is highly important. In our study, we observed higher expression levels of PD1 and LAG3 in Cluster C and low NET scores. Moreover, we found that the NET scores were significantly lower in patients responding to ICIs, which identified their predictive effects. These results suggested that patients with low NET scores and higher expression levels of PD1 and LAG3 are more likely to respond to ICI treatment. Considering that targeted therapy remains the recommended treatment for patients with advanced ccRCC, we evaluated eight common drugs based on the GDSC dataset. The results showed that a low-NET-score group might be likely to acquire benefits from sorafenib, axitinib, gemcitabine, and lapatinib treatments. The above results indirectly suggested the use of NET modifications for predicting clinical benefits from ICI and targeted therapy.

Although in the present study we identified three NET clusters, established a NET-score system, and provided a novel perspective for precise immunotherapy and targeted therapy for ccRCC, several limitations should be addressed. First, all analyses were performed on data obtained from public datasets; thus, the analysis results might be influenced by an intrinsic case selection bias. Large-scale prospective studies and cell and animal experimental research are necessary to confirm our findings.

In conclusion, our study expansively displayed the relationship between NET modification patterns and TME, clinical characteristics, and prognosis. We also assessed the treatment sensitivity prediction of NETs in ICI and targeted treatments. Finally, we constructed a NET-score system for quantifying the NET patterns of patients with ccRCC and validated the expression of core genes. Thus, the findings of the present study might facilitate our understanding of ccRCC and provide ideal strategies for individual treatment.

Data availability statement

The original contributions presented in the study are included in the article/Supplementary Material. Further inquiries can be directed to the corresponding author.

Author contributions

Y-PZ and Z-HT designed the study. Z-HT and W-CL performed the experiment and data analysis. Z-CL, Y-XW, and Z-WH conducted the Q-PCR. Z-WH and Z-HT contributed to manuscript writing, reviewing, and revision. Y-PZ and Z-HT supervised the study. All authors contributed to the article and approved the submitted version.

Conflict of interest

The authors declare that the research was conducted in the absence of any commercial or financial relationships that could be construed as a potential conflict of interest.

Publisher's note

Supplementary material

The Supplementary Material for this article can be found online at: https://www.frontiersin.org/articles/10.3389/fonc.2022.1094248/full#supplementary-material

SUPPLEMENTARY FIGURE 1
The PCA differential, mutation analysis in different groups, and validation of E-MTAB-1980. **(A)** Principal component analysis of before and after removing batch effects in TCGA-KIRC and GSE29609 cohorts. **(B)** The volcano plot for differential analysis between different clusters. **(C)** The waterfall plot for high and low NET-scores in TCGA-KIRC. **(D)** Consensus matrix, **(E)** consensus clustering CDF, and **(F-G)** Kaplan–Meier curves for different clusters, and NET scores for ccRCC samples in E-MTAB-1980.

SUPPLEMENTARY FIGURE 2
The expression profiles, mutation, and survival analysis of cores genes. The differential analysis **(A)**, mutation **(B)**, survival analysis **(C)**, correlations between mRNA expression and CNV, methylation **(D)**, pathways activity **(E)** based on TCGA-KIRC dataset. The mRNA expression of four differential expressed cores in CCLE dataset (F). RT-PCR validated the mRNA expression of four differential expressed cores **(G)**. The expression profiles of differential expressed cores in HPA dataset. Notes: SLC16A12 cannot be found in HPA.

SUPPLEMENTARY TABLE 1
The differential expression results of NET-related genes in TCGA-KIRC dataset.

SUPPLEMENTARY TABLE 2
The results of univariate Cox regression for 94 DEGs in ccRCC cohort.

References

1. Siegel RL, Miller KD, Fuchs HE, Jemal A. Cancer statistics, 2022. *CA Cancer J Clin* (2022) 72(1):7–33. doi: 10.3322/caac.21708

2. Xia C, Dong X, Li H, Cao M, Sun D, He S, et al. Cancer statistics in China and united states, 2022: Profiles, trends, and determinants. *Chin Med J (Engl)* (2022) 135(5):584–90. doi: 10.1097/cm9.0000000000002108

3. Capitanio U, Montorsi F. Renal cancer. *Lancet* (2016) 387(10021):894–906. doi: 10.1016/s0140-6736(15)00046-x

4. Jonasch E, Gao J, Rathmell WK. Renal cell carcinoma. *BMJ* (2014) 349:g4797. doi: 10.1136/bmj.g4797

5. Jorch SK, Kubes P. An emerging role for neutrophil extracellular traps in noninfectious disease. *Nat Med* (2017) 23(3):279–87. doi: 10.1038/nm.4294

6. He X, Xiao Y, Liu S, Deng R, Li Z, Zhu X. Predicting the immune microenvironment and prognosis with a NETosis-related lncRNA signature in head and neck squamous cell carcinoma. *BioMed Res Int* (2022) 2022:3191474. doi: 10.1155/2022/3191474

7. Brinkmann V, Reichard U, Goosmann C, Fauler B, Uhlemann Y, Weiss DS, et al. Neutrophil extracellular traps kill bacteria. *Science* (2004) 303(5663):1532–5. doi: 10.1126/science.1092385

8. Gray RD, Hardisty G, Regan KH, Smith M, Robb CT, Duffin R, et al. Delayed neutrophil apoptosis enhances NET formation in cystic fibrosis. *Thorax* (2018) 73 (2):134–44. doi: 10.1136/thoraxjnl-2017-210134

9. Hoffmann JH, Enk AH. Neutrophil extracellular traps in dermatology: Caught in the NET. *J Dermatol Sci* (2016) 84(1):3–10. doi: 10.1016/j.jdermsci.2016.07.001

10. Wang W, Zhang J, Zheng N, Li L, Wang X, Zeng Y. The role of neutrophil extracellular traps in cancer metastasis. *Clin Trans Med* (2020) 10(6):e126. doi: 10.1002/ctm2.126

11. Yang L, Liu Q, Zhang X, Liu X, Zhou B, Chen J, et al. DNA Of neutrophil extracellular traps promotes cancer metastasis *via* CCDC25. *Nature* (2020) 583 (7814):133–8. doi: 10.1038/s41586-020-2394-6

12. Berger-Achituv S, Brinkmann V, Abed UA, Kühn LI, Ben-Ezra J, Elhasid R, et al. A proposed role for neutrophil extracellular traps in cancer immunoediting. *Front Immunol* (2013) 4:48. doi: 10.3389/fimmu.2013.00048

13. Teijeira Á, Garasa S, Gato M, Alfaro C, Migueliz I, Cirella A, et al. CXCR1 and CXCR2 chemokine receptor agonists produced by tumors induce neutrophil extracellular traps that interfere with immune cytotoxicity. *Immunity* (2020) 52 (5):856–71.e8. doi: 10.1016/j.immuni.2020.03.001

14. Szczerba BM, Castro-Giner F, Vetter M, Krol I, Gkountela S, Landin J, et al. Neutrophils escort circulating tumour cells to enable cell cycle progression. *Nature* (2019) 566(7745):553–7. doi: 10.1038/s41586-019-0915-y

15. Zheng F, Ma L, Li X, Gao R, Peng C, Kang B, et al. Neutrophil extracellular traps induce glomerular endothelial cell dysfunction and pyroptosis in diabetic kidney disease. *Diabetes* (2022) 71(12):2739–50. doi: 10.2337/db22-0153

16. Kuroe T, Watanabe R, Morisue R, Miyazaki S, Kojima M, Murata SC, et al. Dirty necrosis in renal cell carcinoma is associated with NETosis and systemic inflammation. *Cancer Med* (2022) 00:1-11. doi: 10.1002/cam4.5249

17. Fang C, Liu F, Wang Y, Yuan S, Chen R, Qiu X, et al. A innovative prognostic symbol based on neutrophil extracellular traps (NETs)-related lncRNA signature in non-small-cell lung cancer. *Aging (Albany N Y)* (2021) 13(13):17864–79. doi: 10.18632/aging.203289

18. Martins-Cardoso K, Almeida VH, Bagri KM, Rossi MID, Mermelstein CS, König S, et al. Neutrophil extracellular traps (NETs) promote pro-metastatic phenotype in human breast cancer cells through epithelial-mesenchymal transition. *Cancers (Basel)* (2020) 12(6):1542. doi: 10.3390/cancers12061542

19. Li Q, Chen W, Li Q, Mao J, Chen X. A novel neutrophil extracellular trap signature to predict prognosis and immunotherapy response in head and neck squamous cell carcinoma. *Front Immunol* (2022) 13:1019967. doi: 10.3389/fimmu.2022.1019967

20. Zhang Y, Guo L, Dai Q, Shang B, Xiao T, Di X, et al. A signature for pan-cancer prognosis based on neutrophil extracellular traps. *J Immunother Cancer* (2022) 10(6):e004210. doi: 10.1136/jitc-2021-004210

21. Şenbabaoğlu Y, Gejman RS, Winer AG, Liu M, Van Allen EM, de Velasco G, et al. Tumor immune microenvironment characterization in clear cell renal cell carcinoma identifies prognostic and immunotherapeutically relevant messenger RNA signatures. *Genome Biol* (2016) 17(1):231. doi: 10.1186/s13059-016-1092-z

22. Papayannopoulos V. Neutrophil extracellular traps in immunity and disease. *Nat Rev Immunol* (2018) 18(2):134–47. doi: 10.1038/nri.2017.105

23. Wilkerson MD, Hayes DN. ConsensusClusterPlus: a class discovery tool with confidence assessments and item tracking. *Bioinformatics* (2010) 26 (12):1572–3. doi: 10.1093/bioinformatics/btq170

24. Therneau T, Grambsch P. Modeling Survival Data: Extending the Cox Model. New York, NY: Springer. (2000). doi: 10.1007/978-1-4757-3294-8

25. Kassambara A, Kosinski M, Przemyslaw B, Scheipl F. *Survminer: Drawing survival curves using "ggplot2"*; (2021). Available from: https://CRAN.R-project.org/package=survminer.

26. Hänzelmann S, Castelo R, Guinney J. GSVA: gene set variation analysis for microarray and RNA-seq data. *BMC Bioinf* (2013) 14:7. doi: 10.1186/1471-2105-14-7

27. Wu T, Hu E, Xu S, Chen M, Guo P, Dai Z, et al. clusterProfiler 4.0: A universal enrichment tool for interpreting omics data. *Innovation (Cambridge (Mass))* (2021) 2(3):100141. doi: 10.1016/j.xinn.2021.100141

28. Zhang G, Chen X, Fang J, Tai P, Chen A, Cao K. Cuproptosis status affects treatment options about immunotherapy and targeted therapy for patients with kidney renal clear cell carcinoma. *Front Immunol* (2022) 13:954440. doi: 10.3389/fimmu.2022.954440

29. Mayakonda A, Lin DC, Assenov Y, Plass C, Koeffler HP. Maftools: efficient and comprehensive analysis of somatic variants in cancer. *Genome Res* (2018) 28 (11):1747–56. doi: 10.1101/gr.239244.118

30. Geeleher P, Cox N, Huang RS. pRRophetic: an r package for prediction of clinical chemotherapeutic response from tumor gene expression levels. *PloS One* (2014) 9(9):e107468. doi: 10.1371/journal.pone.0107468

31. Ritchie ME, Phipson B, Wu D, Hu Y, Law CW, Shi W, et al. Limma powers differential expression analyses for RNA-sequencing and microarray studies. *Nucleic Acids Res* (2015) 43(7):e47. doi: 10.1093/nar/gkv007

32. Gordon M, Lumley T. *Lumley MGaT. Forestplot: Advanced forest plot using 'grid' graphics. Vienna: The R Foundation* (2022). https://CRAN.R-project.org/package=forestplot.

33. Linehan WM, Ricketts CJ. The cancer genome atlas of renal cell carcinoma: findings and clinical implications. *Nat Rev Urol* (2019) 16(9):539–52. doi: 10.1038/s41585-019-0211-5

34. Atkins MB, Tannir NM. Current and emerging therapies for first-line treatment of metastatic clear cell renal cell carcinoma. *Cancer Treat Rev* (2018) 70:127–37. doi: 10.1016/j.ctrv.2018.07.009

35. Krishna C, DiNatale RG, Kuo F, Srivastava RM, Vuong L, Chowell D, et al. Single-cell sequencing links multiregional immune landscapes and tissue-resident T cells in ccRCC to tumor topology and therapy efficacy. *Cancer Cell* (2021) 39 (5):662–77.e6. doi: 10.1016/j.ccell.2021.03.007

36. Chen X, Ma H, Mo S, Yu S, Lu Z, Chen J. Intratumoral neutrophil extracellular traps are associated with unfavorable clinical outcomes and immunogenic context in pancreatic ductal adenocarcinoma. *Front Immunol* (2022) 13:1027459. doi: 10.3389/fimmu.2022.1027459

37. Pieterse E, Rother N, Garsen M, Hofstra JM, Satchell SC, Hoffmann M, et al. Neutrophil extracellular traps drive endothelial-to-Mesenchymal transition. *Arterioscler Thromb Vasc Biol* (2017) 37(7):1371–9. doi: 10.1161/atvbaha.117.309002

38. Aldabbous L, Abdul-Salam V, McKinnon T, Duluc L, Pepke-Zaba J, Southwood M, et al. Neutrophil extracellular traps promote angiogenesis: Evidence from vascular pathology in pulmonary hypertension. *Arterioscler Thromb Vasc Biol* (2016) 36(10):2078–87. doi: 10.1161/atvbaha.116.307634

39. Yang C, Sun W, Cui W, Li X, Yao J, Jia X, et al. Procoagulant role of neutrophil extracellular traps in patients with gastric cancer. *Int J Clin Exp Pathol* (2015) 8(11):14075–86.

40. Zhang R, Li L, Chen L, Suo Y, Fan J, Zhang S, et al. MAP7 interacts with RC3H1 and cooperatively regulate cell-cycle progression of cervical cancer cells *via* activating the NF-κB signaling. *Biochem Biophys Res Commun* (2020) 527(1):56–63. doi: 10.1016/j.bbrc.2020.04.008

41. Zhang L, Liu X, Song L, Zhai H, Chang C. MAP7 promotes migration and invasion and progression of human cervical cancer through modulating the autophagy. *Cancer Cell Int* (2020) 20:17. doi: 10.1186/s12935-020-1095-4

42. Lin L, Yee SW, Kim RB, Giacomini KM. SLC transporters as therapeutic targets: emerging opportunities. *Nat Rev Drug Discovery* (2015) 14(8):543–60. doi: 10.1038/nrd4626

43. Mei J, Hu K, Peng X, Wang H, Liu C. Decreased expression of SLC16A12 mRNA predicts poor prognosis of patients with clear cell renal cell carcinoma. *Med (Baltimore)* (2019) 98(30):e16624. doi: 10.1097/md.0000000000016624

44. Xu N, Xiao W, Meng X, Li W, Wang X, Zhang X, et al. Up-regulation of SLC27A2 suppresses the proliferation and invasion of renal cancer by down-regulating CDK3-mediated EMT. *Cell Death Discovery* (2022) 8(1):351. doi: 10.1038/s41420-022-01145-8

45. Jiang Y, Cao Y, Wang Y, Li W, Liu X, Lv Y, et al. Cysteine transporter SLC3A1 promotes breast cancer tumorigenesis. *Theranostics* (2017) 7(4):1036–46. doi: 10.7150/thno.18005

46. Yaghoubi N, Soltani A, Ghazvini K, Hassanian SM, Hashemy SI. PD-1/PD-L1 blockade as a novel treatment for colorectal cancer. *BioMed Pharmacother* (2019) 110:312–8. doi: 10.1016/j.biopha.2018.11.105

47. Carlino MS, Larkin J, Long GV. Immune checkpoint inhibitors in melanoma. *Lancet* (2021) 398(10304):1002–14. doi: 10.1016/s0140-6736(21)01206-x

48. Braun DA, Hou Y, Bakouny Z, Ficial M, Sant' Angelo M, Forman J, et al. Interplay of somatic alterations and immune infiltration modulates response to PD-1 blockade in advanced clear cell renal cell carcinoma. *Nat Med* (2020) 26 (6):909–18. doi: 10.1038/s41591-020-0839-y

49. Rotte A. Combination of CTLA-4 and PD-1 blockers for treatment of cancer. *J Exp Clin Cancer Res* (2019) 38(1):255. doi: 10.1186/s13046-019-1259-z

50. Roviello G, Corona SP, Nesi G, Mini E. Results from a meta-analysis of immune checkpoint inhibitors in first-line renal cancer patients: does PD-L1 matter? *Ther Adv Med Oncol* (2019) 11:1758835919861905. doi: 10.1177/1758835919861905

frontiers | Frontiers in Oncology

TYPE Original Research
PUBLISHED 19 January 2023
DOI 10.3389/fonc.2022.1118472

OPEN ACCESS

EDITED BY
Le Qu,
Nanjing University, China

REVIEWED BY
Jianfeng Chen,
University of Texas MD Anderson Cancer Center, United States
Can Liu,
Fujian Medical University, China

*CORRESPONDENCE
Hua-Guo Xu
huaguoxu@njmu.edu.cn
Jie-Xin Zhang
jiexinzhang@njmu.edu.cn
Peng-Fei Shao
spf032@hotmail.com

†These authors have contributed equally to this work

SPECIALTY SECTION
This article was submitted to Genitourinary Oncology, a section of the journal Frontiers in Oncology

RECEIVED 07 December 2022
ACCEPTED 29 December 2022
PUBLISHED 19 January 2023

CITATION
Chen C, Chen L-Y, Yang R-X, Zhang J-X, Shao P-F and Xu H-G (2023) Identification of IRF-associated molecular subtypes in clear cell renal cell carcinoma to characterize immunological characteristics and guide therapy.
Front. Oncol. 12:1118472.
doi: 10.3389/fonc.2022.1118472

Identification of IRF-associated molecular subtypes in clear cell renal cell carcinoma to characterize immunological characteristics and guide therapy

Can Chen[1,2†], Lin-Yuan Chen[1,2†], Rui-Xia Yang[1,2†], Jie-Xin Zhang[1,2*], Peng-Fei Shao[3*] and Hua-Guo Xu[1,2*]

[1]Department of Laboratory Medicine, The First Affiliated Hospital of Nanjing Medical University, Nanjing, Jiangsu, China, [2]Branch of National Clinical Research Center for Laboratory Medicine, Nanjing, Jiangsu, China, [3]Department of Urology, The First Affiliated Hospital of Nanjing Medical University, Nanjing, Jiangsu, China

Background: Recently studies have identified a critical role for interferon regulatory factor (IRF) in modulating tumour immune microenvironment (TME) infiltration and tumorigenesis.

Methods: Based on IRF1-9 expression profiles, we classified all ccRCC samples into three molecular subtypes (clusters A-C) and characterized the prognosis and immune infiltration of these clusters. IRFscore constructed by principal component analysis was performed to quantify IRF-related subtypes in individual patients.

Results: We proved that IRFscore predicted multiple patient characteristics, with high IRFscore group having poorer prognosis, suppressed TME, increased T-cell exhaustion, increased TMB and greater sensitivity to anti- PD-1/CTLA-4 therapies. Furthermore, analysis of metastatic ccRCC (mccRCC) molecular subtypes and drug sensitivity proved that low IRFscore was more sensitive to targeted therapies. Moreover, IRFscore grouping can be well matched to the immunological and molecular typing of ccRCC. qRT-PCR showed differential expression of IRFs in different cell lines.

Conclusions: Evaluating IRF-related molecular subtypes in individual ccRCC patients not only facilitates our understanding of tumour immune infiltration, but also provides more effective clinical ideas for personalised treatment.

KEYWORDS

ccRCC, IRF family, tumour microenvironment, t cell exhaustion, immunotherapy, targeted therapy

Introduction

As the most common pathological subtype of kidney cancer, clear cell renal cell carcinoma (ccRCC) is the least malignant but has a high metastatic rate of up to 60% (1). Patients with advanced metastatic kidney cancer are mostly treated with drug therapy, including targeted therapy and immunotherapy (2, 3). Targeted therapies specifically target certain mutated genes or abnormal proteins, which cause less damage to normal cells (4, 5). Some immunotherapeutic drugs are widely used and achieve significant efficacy (2). Actually, researchers found that immunotherapeutic drugs combined with targeted drugs were more effective than monotherapy, which represents a gradual shift in treatment options for kidney cancer towards targeted combination immunotherapy (6).

Interferon regulatory factors (IRFs), can regulate interferons transcriptional modification to fight pathogenic infections (7). Multiple studies confirmed that IRFs regulate tumour immune activity and tumorigenesis. For example, IRF7 high expression potently induces CD8+ T cell responses and strengthens host immune surveillance to fight viral infection and restrict tumour metastasis (8); IRF9 effectively prevents CD8+ T cell exhaustion caused by over-exposure to antigens (9). These results provide a theoretical basis for future studies on tumour immune mechanism and therapeutic applications of IRFs.

In this work, three IRF-related clusters were constructed in ccRCC, and clinical and immune characteristics were assessed between three clusters. Furthermore, we proposed to calculate IRFscore to quantify IRF subtypes in individual patients and proved that IRFscore is highly correlated with patient prognosis, immune infiltration, T-cell exhaustion and treatment. This work will assist clinicians to better understand and differentiate ccRCC immunological and molecular subtypes, and formulate individualised treatment.

Materials and methods

Data sources and pre-processing

Figure S1 illustrated the workflow for this study. We searched and downloaded ccRCC expression datasets with complete clinical annotation and mutations from The Cancer Genome Atlas (TCGA) and Gene Expression Omnibus (GEO) databases. Two datasets (TCGA-KIRC and GSE36895 datasets) were analysed in this work. For TCGA-KIRC dataset, we obtained gene expression data from UCSC website (https://xenabrowser.net/datapages/) and converted them to kilobase per million values. GSE36895 dataset were downloaded from GEO (http://www.ncbi.nlm.nih.gov/geo/). "Sva" package was performed for correcting batch effects in two datasets (10). Samples lacking complete clinical information and mutation data were excluded. Clinical information was summarised in Table S1.

Cell culture

Human renal tubular epithelial cells (HK-2) and ccRCC cell lines (786-O and Caki-1) were obtained from the Cell Bank of the Chinese Academy of Sciences (Shanghai, China). These cells were cultured in DMEM or RPMI-1640 medium containing 10% fetal bovine serum and 1% streptomycin-penicillin. All cells were incubated in a sterile incubator at 5% CO2 and 37°C.

RNA isolation and quantitative real-time PCR

TRIzol reagent (Invitrogen, USA) was applied to isolate and extract total RNA from the cells. NanoDrop 2000 spectrophotometer (Thermo Scientific, USA) was applied for evaluating of RNA quantity control and concentration. Reverse Transcription Kit (Takara, China) was applied to reverse transcribe total cellular RNA into cDNA. ABI 7500 real-time fluorescence quantitative PCR instrument was designed for carrying out qRT-PCR process. The cycling threshold (Ct) for each gene was recorded and 2-ΔΔCt method was applied to calculate gene mRNA expression. All experiments were repeated 3 times and procedures were carried out according to reagent instructions. Primer sequences were listed in Table S2.

Unsupervised clustering of IRF1-9

Unsupervised clustering analysis were applied to identify IRF-related molecular subtypes. Consensus clustering algorithm was performed for determining the number of clusters. "ConsensusClusterPlus" package was employed to perform consistency clustering analysis (11). The process was repeated a thousand times to ensure consistency of classification.

Gene set variance analysis

GSVA is a non-parametric unsupervised analysis method that transforms gene expression matrices into gene set expression matrices to evaluate gene set enrichment results of transcriptome (12). Based on the "c2.cp.kegg.v6.2.symbols" gene set obtained from MSigDB database, GSVA analysis was conducted using "GSVA" package.

Estimation of immune infiltration

Single sample gene set enrichment analysis (ssGSEA) was performed to assess immune infiltration levels based on immune cell-specific gene expression. The immune gene set file is derived from Charoentong et al (13, 14). ESTIMATE algorithm calculates immune and stroma score to estimate the amount of stroma and immune cells and compute tumour purity (15). CIBERSORT is designed to calculate the composition ratio of the 22 immune cells. 22 immune cell expression data are taken from CIBERSORT website (https://cibersort.stanford.edu/) (16). Considering that CD4 naive T cells was 0 in all ccRCC samples, CIBERSORT algorithm only analysed remaining 21 immune cells.

Identification of DEGs and functional annotation

"limma" package is applied to filter differentially expressed genes (DEGs) between clusters (17). Genes with adjusted P-value<0.001 were recognized as DEGs. "ClusterProfiler" package is intended for GO (Gene Ontology) and KEGG (Kyoto Encyclopedia of Genes and Genomes) enrichment analysis of DEGs (18).

Construction of IRFscore

Univariate COX regression screened for prognosis-related DEGs. Principal component analysis (PCA) was performed for constructing IRF gene signature. PC1 and PC2 were used as feature scores to calculate IRFscore for individual samples (19). IRFscore = ∑ (PC1i + PC2i), where i represented DEGs' expression.

Validation of the clinical value of IRFscore

The TCGA-KIRP and TCGA-KICH cohorts were used to validate the clinical performance of the IRFscore. Information on both queues can be downloaded from the online website (https://portal.gdc.cancer.gov/).

IPS analysis

The four different immunophenotypic scores (antigen-presenting, effector, suppressor, checkpoint) are calculated separately by immunophenoscore (IPS), IPS z-score is the integration of the four, and the higher the IPS z-score, the more immunogenic the sample (20). IPS was obtained from The Cancer Immunome Atlas (https://tcia.at/home).

Drug sensitivity analysis

GDSC (https://www.cancerrxgene.org/) database contains massive genomic data on tumour therapeutics and drug sensitivity data (21). We predicted the response of ccRCC patients to five chemotherapeutic agents, including sunitinib, sorafenib, nilotinib, temsirolimus and pazopanib. "pRRophetic" package was performed for quantifying the half maximal inhibitory concentration (IC50).

Statistics analysis

Protein-protein interaction (PPI) network maps between IRFs was obtained from STRING database (22). Wilcoxon rank sum test was designed to comparative analysis of two groups, Kruskal-Wallis and one-way ANOVA was designed to calculate differences between three and more groups. Spearman correlation analysis was designed to determine correlation coefficient. Kaplan-Meier and log-rank test were performed for plotting survival curves and calculating statistical differences. Multivariate COX regression analysis was conducted to detect independent prognostic factors. "maftools" package was conducted to describe mutations. Statistical analyses were all two-sided and P<0.05 was considered statistically different. All data were analysed by R software (version 4.1.1).

Results

Expression pattern and clinical relevance of IRFs in ccRCC

IRF1-9 were included in this work. First, we analysed mRNA expression levels of IRFs in TCGA and GSE36895 cohort, respectively. IRFs were severely imbalanced in expression and the results of both databases remained largely consistent (Figures 1A, B). All genes were up-regulated in ccRCC except IRF6. ROC and PCA analysis indicated that IRFs can distinguish well between ccRCC and normal samples (Figures 1C-E). We then used two databases, CTPAC and HPA, to compare differential protein expression. CTPAC database results were consistent with the above database (Figure S2A). Figure S2B illustrated that in HPA database, IRF1, IRF3, IRF7-9 were upregulated in tumour, while the opposite is true for IRF6. IRF2 was highly expressed in both tissues. IRF4 and IRF5 were low or undetectable in both tissues. Furthermore, we observed that IRFs were highly correlated in expression (Figure 1F) and interacted with each other in PPI network (Figure 1G).

To validate IRFs mRNA expression, we performed qRT-PCR analysis in three cell lines. Most IRFs were more highly expressed in tumour cells (Figure 2), which is generally consistent with the results above. Furthermore, we noted that IRFs were expressed with cell specificity in different cells (Figure S2C).

We then discussed clinical relevance of IRFs. We found that most IRFs were correlated with prognosis (Figure 1F and S2D). IRF6 exhibited a tumour suppressive profile and its expression was positively correlated with prognosis. In contrast, the higher the expression of other IRFs, the worse the prognosis of patients.

Identification of IRF-related subtypes in ccRCC

Using an unsupervised clustering approach, we classified ccRCC patients into different subtypes. We ultimately identified three IRF-associated molecular subtypes, termed IRF Cluster A-C (Figure 3A and S3A-C). Heat maps illustrated the relationship between three subtypes and clinicopathological features (Figure S3D). Prognostic analysis pointed to a much higher survival advantage for cluster B (Figure 3B). By analysing IRF expression profiles, we observed higher expression of protective factors (IRF6) in cluster B, while the opposite was true for risk factors (e.g. IRF3 and IRF7) (Figure 3C). This laterally explained why cluster B had a better prognosis.

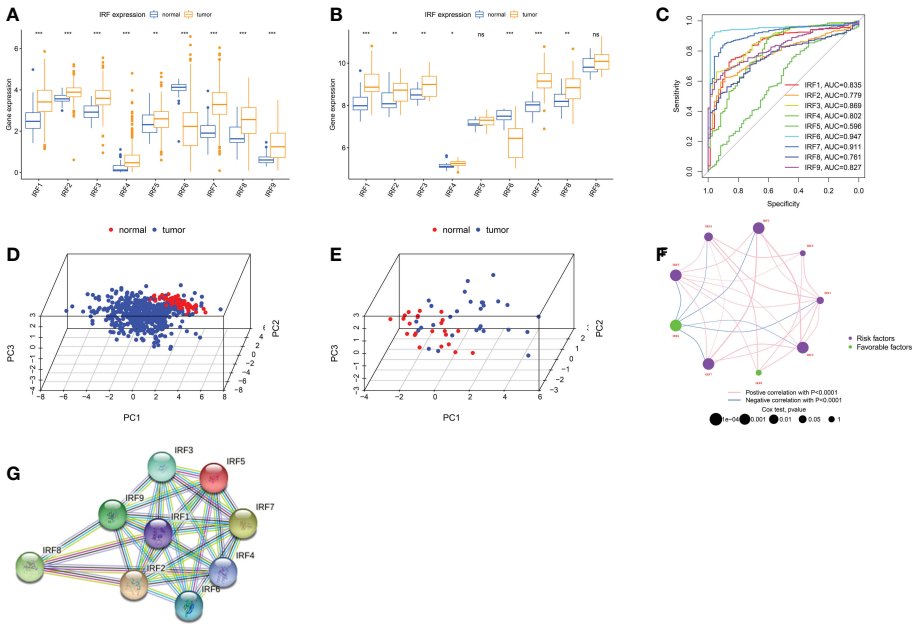

FIGURE 1
Landscape of IRFs expression in ccRCC. **(A-B)** Boxplot of IRFs expression in ccRCC and normal tissues from TCGA database **(A)** and GSE36895 **(B)**. **(C)** ROC curves demonstrate IRF family ability to differentiate between tumour and normal tissue. **(D-E)** Principal component analysis for the expression profiles of IRFs to distinguish tumours from normal samples in TCGA database **(D)** and GSE36895 **(E)**. **(F)** The interaction between IRFs in ccRCC. **(G)** The PPI network of IRFs. ns, not significant; *p < 0.05; **p < 0.01; ***p < 0.001.

Immune characteristics of different IRF-related subtypes

GSVA analysis was performed to characterise different biological properties. Multiple immune activation-related pathways, including T and B cell receptor signalling pathways accumulated in cluster C (Figures 3D, E and S3E). Cluster B enriched for some matrix activation pathways, whereas cluster A was mainly associated with immunosuppression and base excision repair. We then proceeded to analyse TME immune infiltration. First, we evaluated 23 immune cell infiltrations using ssGSEA, and almost all immune cells were heavily infiltrated in cluster C (Figure 3F). We then ran ESTIMATE algorithm to calculate stromal and immune cell content. Apparently, cluster C had much higher immune and stromal scores, signifying that cluster C had lowest tumour purity (Figure 3G). However, no matching survival advantage was found for cluster C with this immune profile. Therefore, we counted the relative proportions of cell subpopulations *via* CIBERSORT. CD8+ T cells and M2 macrophages were more predominant (Figures S3F-G). Typically, the higher the expression of CD8+ T cells, the more positive the prognosis (23). Interestingly, we observed the greatest proportion of CD8+ T cells in cluster C and the lowest in cluster B, which is opposite to the prognosis. Researches have revealed that CD8+ T cells are exhausted in ccRCC and secrete numerous immune checkpoints, including PD-1 and CTLA-4. At this point, the higher the intensity of CD8+ T cell infiltration, the worse the prognosis of ccRCC (24). Here, we analysed T cell exhaustion-related immune checkpoint expression. Most checkpoints were highest in cluster C (Figure 3H). Combining with previous studies, we speculated IRFs may regulate T-cell exhaustion.

Comprehensive analysis of IRFs-related DEGs

To further characterise biological functions of IRF-related subtypes, we filtered 547 DEGs from three subtypes and performed functional enrichment analysis (Figure 4A). These DEGs participated in many immune cell activation and proliferation-related pathways (Figures 4B, C). This implied that IRF-associated DEGs are actively engaged in immune processes and modulating immune infiltration. Subsequently, univariate COX regression analysis was performed to identify 426 prognosis-related DEGs (Table S3). Similarly, we ran unsupervised cluster analysis on 426 DEGs and identified three gene clusters, termed IRF gene Cluster A-C (Figures S4A-D). Similarly, we compared clinicopathological characteristics and immune infiltration between different gene clusters and found that gene cluster A had superior prognostic prospects (p<0.001, Figures 4D and S4E). Except for IRF6 and IRF8, the remaining risk genes were expressed in gene clusters in the order C, B and A (Figure 4E). CD8+ T cells and MDSC had lowest infiltration intensity in Cluster A (Figure 4F). This accounted for the greatest survival advantage of gene cluster A. Overall, the concordance of prognostic and immune infiltration characteristics among gene clusters justified this classification.

Establishment of IRF gene signature and its clinical characteristics

PCA analysis was conducted on 426 DEGs and IRFscore were calculated to accurately quantify individual IRF-related molecular subtypes. The samples were divided into high and low IRFscore

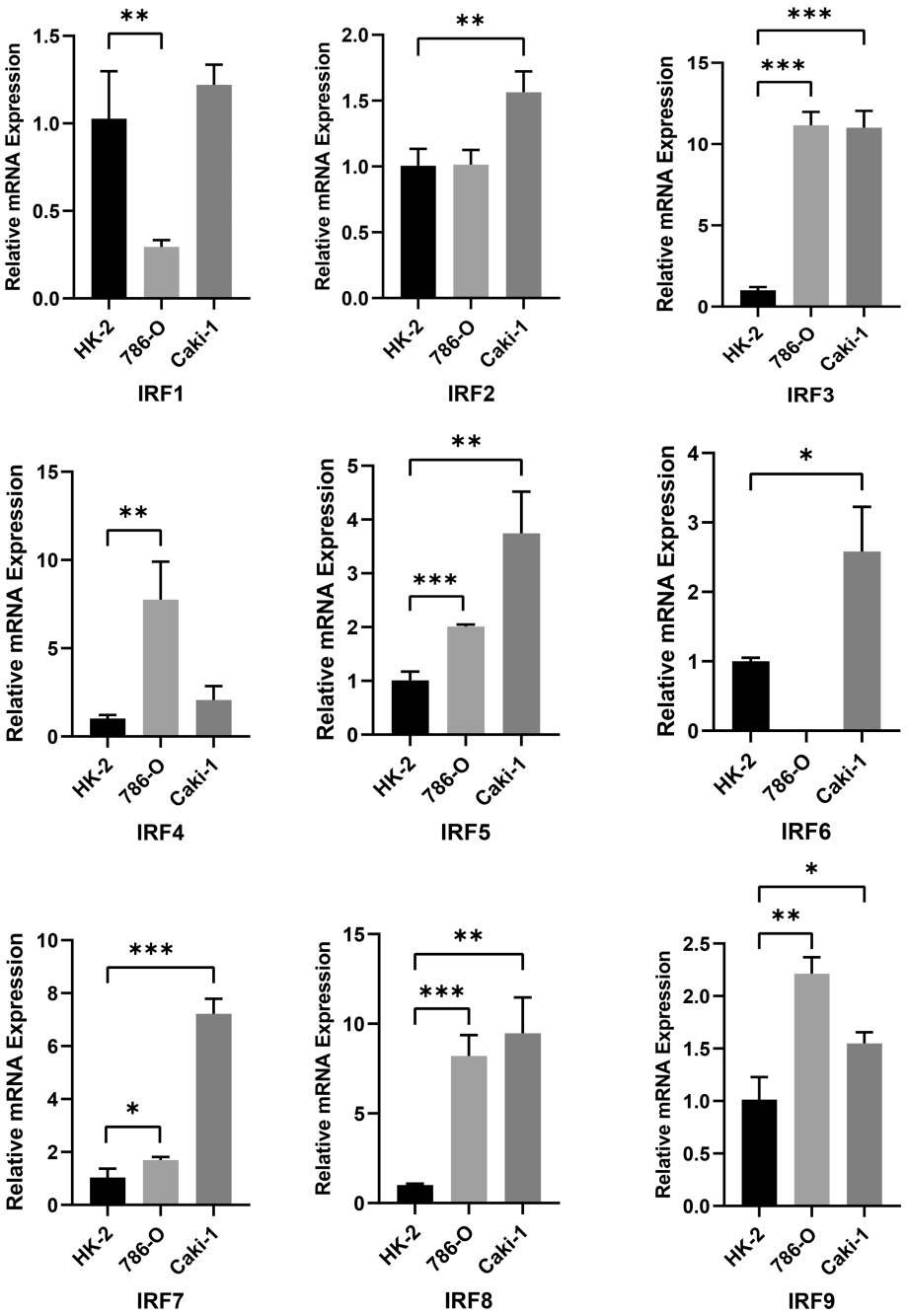

FIGURE 2
RT-PCR analysis of IRF1-9 expression levels in 786-O, Caki-1 and HK-2 cells. *P < 0.05, **P < 0.01, ***P < 0.001.

groups following the threshold values determined by "survminer" package. Figures 5A-C exhibited the variation in attributes of individual patients in different clusters. Figure 5D demonstrated IRFs expression profiles in two groups. Prognostic analysis revealed that the higher the IRFscore, the worse the prognosis (p<0.001, Figure 5E).

Next, we proceeded with a stratified prognostic analysis by different clinical characteristics. First, we observed a higher proportion of patients with advanced tumours were in high-IRFscore group (p<0.05, Figure S5A). Patients with VHL, PBRM1 and BAP1 mutations also had higher IRFscore, although not statistically different (Figure S5B). Stratified prognostic analysis revealed that low IRFscore consistently showed marked survival advantages (p<0.05, Figure S5C). Multivariate Cox regression analysis proved that IRFscore could be independent prognostic factor (Table S4). ROC curves and nomograms demonstrated the performance of IRF scores in predicting patients' rates at 1, 3, 5 and 7 years (AUC≥0.666, Figures 5F, G).

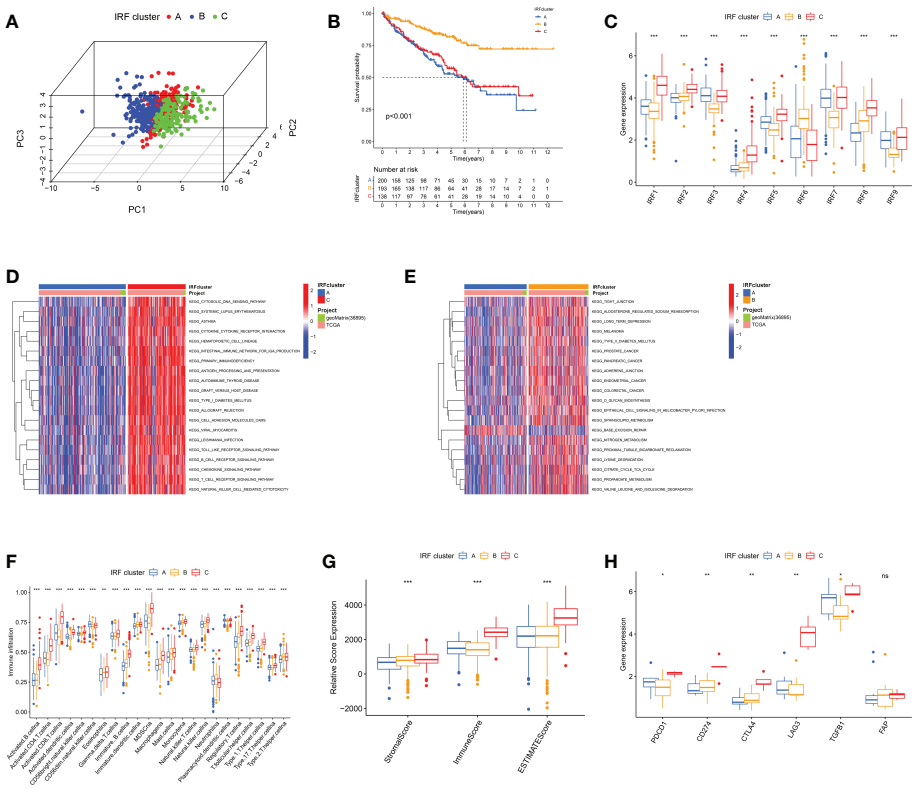

FIGURE 3
The IRF-related molecular subtypes in ccRCC and biological and immune characteristic of each pattern. **(A)** PCA for the transcriptome profiles of three IRF clusters. **(B)** Survival analyses of three IRF clusters. **(C)** The expression of IRF1-9 in three IRF clusters. **(D-E)** GSVA enrichment analysis showing the activation states of biological pathways in distinct clusters. **(F)** The abundance of each TME infiltrating cell in three clusters. **(G)** Box plot indicated the correlation between IRF clusters and immune scores, stromal scores and estimate scores. **(H)** The expression of most immune checkpoints among distinct IRF clusters. ns, not significant; *p < 0.05; **p < 0.01; ***p < 0.001.

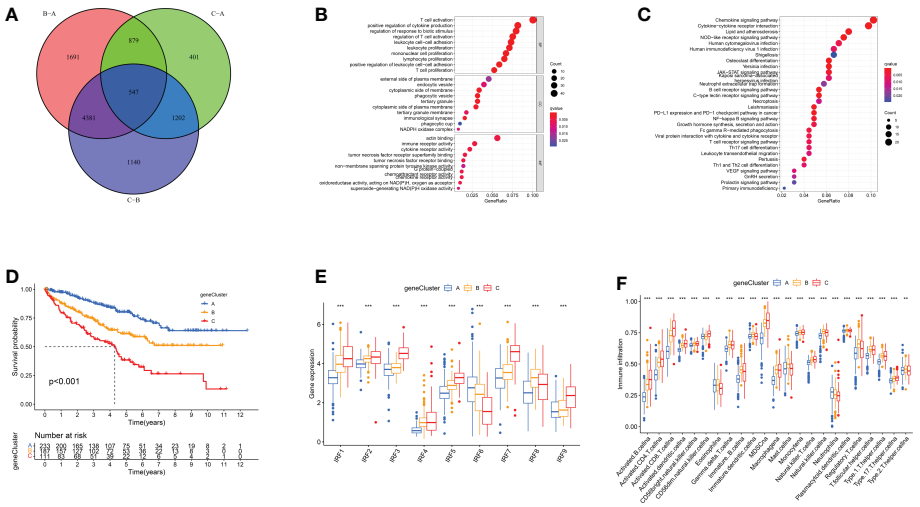

FIGURE 4
IRF gene clusters in ccRCC and biological characteristics of each gene cluster. **(A)** 547 IRF-associated DEGs shown in venn diagram. **(B-C)** GO **(B)** and KEGG **(C)** enrichment analysis on these DEGs. **(D)** Survival analyses of three IRF gene clusters. **(E)** The expression of IRFs in three gene clusters. **(F)** The abundance of each TME infiltrating cell in three gene clusters. **p < 0.01; ***p < 0.001

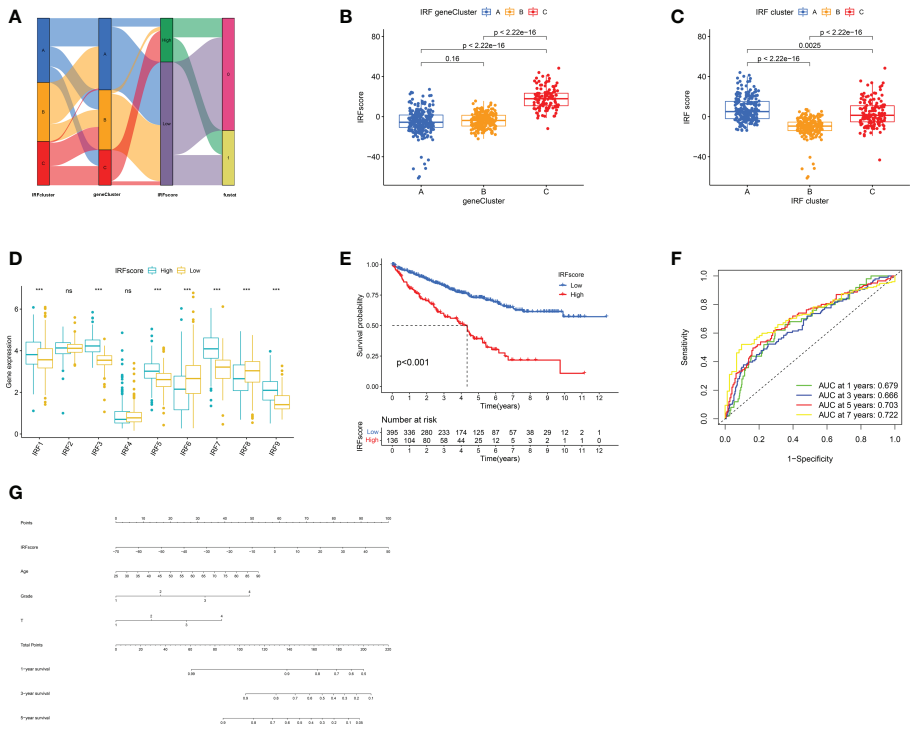

FIGURE 5
Construction of IRF signatures. **(A)** Alluvial diagram showing the changes of IRF cluster, gene cluster, IRFscore and patient survival status. **(B-C)** Differences in IRFscore among three gene clusters **(B)** and IRF clusters **(C)**. **(D)** The expression of IRF1-9 in two IRFscore groups. **(E)** Kaplan-Meier survival analysis for two IRFscore groups. **(F)** ROCs for 1-, 3-, 5-, and 7-year survival time based on IRFscore. **(G)** Nomograms incorporating IRFscore and clinical characteristics for predicting patient 1-, 3-, 5-year survival. ns, not significant; ***p < 0.001.

Further validation of IRFscore's prognostic performance using two independent cohorts

To gain insight into IRFscore's prognostic value, we further validated the effectiveness of IRFscore in predicting papillary renal cell carcinoma (KIRP) and kidney chromophobe (KICH) prognosis. Based on previous PCA results obtained from 426 DEGs, IRFscore was re-established and survival analyses were performed. In KICH, the prognosis was significantly better in low IRFscore group, while the opposite was true in KIRP (P<0.05, Figures S5D, E). This suggested that IRFs are responsible for renal cancer progression, but for specific efficacy, it depended on cancer type.

Association between IRFscore and CD8+ T cell exhaustion

To uncover how IRFscore works in regulating TME, we examined immune infiltration in two groups. High IRFscore group had a more significant immune infiltration (Figures 6A, B). Furthermore, we found that CD8+ T cells and M2 macrophages accounted for largest proportion in both groups (Figure 6C). Therefore, we speculated that these cells probably function primarily in ccRCC progression. Previous studies demonstrated that immune dysregulation occurs in advanced ccRCC (25), when massive exhausted T cells and M2 macrophages are simultaneously enriched in TME and substantial receptor-ligand interactions exist between two cells leading to worse prognosis (26). Table S5 listed receptors or ligands expressed by two cells. Expression analysis revealed that most co-stimulatory receptors, except for HAVCR2 and BTLA, were significantly overexpressed in high IRFscore group (Figure 6D). This suggested that CD8+ T cells in high IRFscore were mostly in exhausted state. However, a matching profile of M2 macrophages was not observed in high IRFscore group (Figure S6A). These results indicated that IRFs may not participate in interaction of exhausted T cells with M2 macrophages.

Tertiary lymphoid structures (TLS) are ectopic lymphoid tissues that surround the tumour. The higher the density of its presence, the better the patient's prognosis (27). In ccRCC, TLS not only occurs significantly less frequently than other cancers, but also becomes dysfunctional (28). Interestingly, when TLS density and mature DCs are increased in ccRCC, a group of patients with high CD8+ T-cell infiltration and good prognosis emerges (29). This contradicted previous findings that CD8+ T cells cause worse prognosis in ccRCC (23). Therefore, scientists assumed that the emergence of TLS and mature DCs could be one reason for reduced T-cell exhaustion (30). We extracted TLS-related markers from published literatures, including three chemokines (CCL19, CCL21 and CXCL13) and two TLS-DC-related markers (HLA-DR and CD83). HLA-DR, CD83 and CCL13 were significantly upregulated in low IRFscore, while only CCL19 was downregulated (Figure 6E). Thus, we hypothesized that increased presence of TLS and mature DCs in low IRFscore may enhance ccRCC prognosis by reducing T-cell exhaustion.

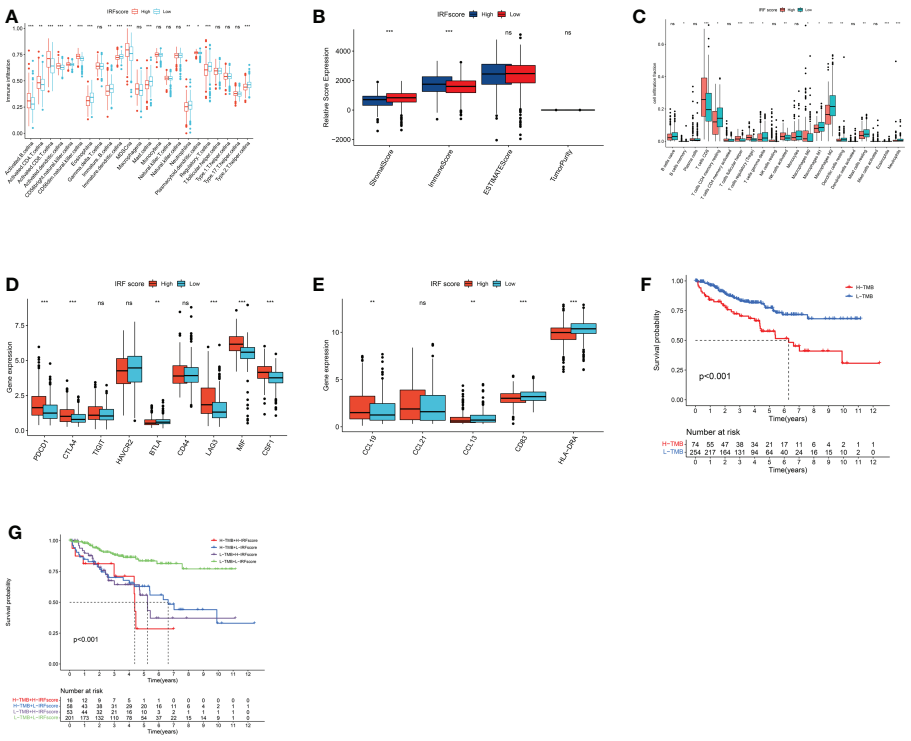

FIGURE 6
immune characteristics and somatic variants in IRFscore groups. **(A)** The abundance of each TME infiltrating cell in two IRFscore groups. **(B)** The immune scores, stromal scores and estimate score difference in high and low IRFscore groups. **(C)** The relative fraction of each TME-infiltrated cell in two IRFscore groups. **(D)** The differences in the receptors or ligands expressed by exhausted T cells between two IRFscore groups. **(E)** The differences in TLS-related markers between two IRFscore groups. **(F)** Kaplan-Meier survival analysis for two TMB score groups. **(G)** Kaplan-Meier survival analysis for patients stratified by IRFscore and TMB score. ns, not significant; *p < 0.05; **p < 0.01; ***p < 0.001.

The role of IRFs in TMB and therapy

Many studies proved that the more genetic mutations a tumour has, the more abnormal proteins it produces and the more likely the immune system is to be activated. This implied that tumour mutational burden (TMB) is somewhat predictive of immunotherapy effects (31). Furthermore, TMB can accurately predict multiple targeted and chemotherapeutic drug effects (32). Generally, the higher the TMB, the better the treatment effect. In this work, quantitative analysis and correlation analysis confirmed a positive correlation between IRFscore and TMB (Figures S6B-C). Survival analysis proved that lower TMB predicts a good prognosis (p<0.001, Figure 6F). We further assessed the synergistic effect of these two scores in prognosis. Stratified survival analysis indicated that TMB and IRFscore did not interfere with each other, with IRFscore showing significant survival differences in two TMB subgroups (p<0.001, Figure 6G). This meant that IRFscore could serve as a prognostic indicator independent of TMB.

Next, we discussed the performance of IRFscore in predicting targeted therapy efficacy. We compared estimated IC50 of five drugs (Figures 7A-E). Except for pazopanib, IC50 levels for remaining drugs

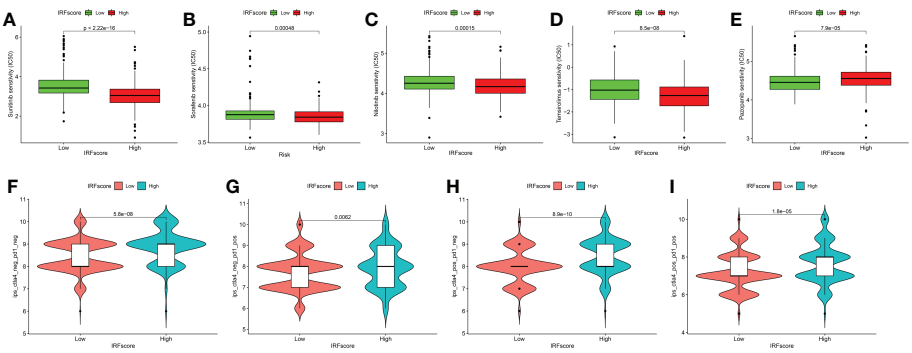

FIGURE 7
IRFscore in the role of ccRCC clinical therapies. **(A-E)** Box plot showing the sensitivity of patients with high and low IRFscore subgroups to chemotherapy drugs, including sunitinib **(A)**, sorafenib **(B)**, nilotinib **(C)**, temsirolimus **(D)** and pazopanib **(E)**. **(F-I)** The association between IPS and immune checkpoints in ccRCC patients with different IRFscore.

were significantly higher in low IRFscore, meaning that low IRFscore was more sensitive to these drugs ($p < 0.001$). We then investigated the association between IRFscore and immune checkpoint inhibitor (ICI) therapy by IPS. Figures 7F-I depicted that four IPS scores were significantly higher in high IRFscore ($p<0.001$), signifying that higher IRFscore may have higher immunogenic phenotypes and be more sensitive to ICIs. Additionally, the higher the frequency of PBRM1 mutations, the better the outcome of anti-PD-1 treatment was found (26). Figure S5B demonstrated that PBRM1 mutations were more frequent in high IRFscore. Above results indicated that low IRFscore group may be more sensitive to targeted therapies, while high IRFscore subgroup were more sensitive to immunotherapy.

Degree of matching of IRFscore groups to ccRCC immunological and molecular subtypes

Numerous studies indicated that patient response to treatment options can be predicted by different tumour subtypes (33). We therefore sought to understand whether ccRCC-related phenotypes could explain why IRFs influence treatment outcome and analysed the extent to which IRFscore-related subgroups matched these tumour phenotypes. First, combining immune infiltration characteristics (Figures 6A-C), we hypothesized that high IRFscore group matched immune-inflamed phenotype, whereas low IRFscore group matched immune-desert phenotype. Generally, immune-inflamed phenotype was more responsive to anti-PD-L1/PD-1 therapies. In contrast, immune-desert phenotypes had no or the weakest response (34). This was consistent with our previous prediction that high IRFscore group was more sensitive to ICI therapies (Figures 7F-I).

Generally, targeted therapies are more effective in metastatic ccRCC (mccRCC) than other treatments (2, 3). To accurately predict the effectiveness of tyrosine kinase inhibitor (TKI) therapy in mccRCC, Benoit et al. identified four mccRCC molecular subtypes with different therapeutic effects on sunitinib based on tumour gene mutations, copy number variants (CNV) and methylation status (35). To determine whether this typing was applicable to our work, we collated the distribution of these features across two groups and summarised in Table S6 and Figures S6D-L. We considered that high IRFscore group may correspond to mccRCC 1/4 group, characterised by poor prognosis, low sunitinib sensitivity, increased methylation levels, slightly higher VHL and PBRM1 mutations, higher CNV, highly inflammatory immunosuppressive environment and low stem cell differentiation (Figures S6D-L). In contrast, low IRFscore group corresponded to mccRCC 2/3 group, which has the opposite characteristics. Although not all features match exactly, in general we assume that mccRCC subtypes can be applied to describe IRFscore grouping. These results pointed that IRFscore groupings can be well matched to ccRCC immunological and molecular typing, indicating that optimal treatment can be selected according to each patient's tumour subtype.

Discussion

Numerous studies highlight the important role of IRFs in regulating host immune responses and tumorigenesis. To date, most studies focused on single IRF and still lack a comprehensive understanding of how entire IRF family integrally regulates cancer development and TME. In our research, we focus on the value of IRF1-9 in modifying ccRCC TME and treatment.

Different ccRCC molecular subtypes and their characteristics have been identified through transcriptome analysis. In our study, we identified three distinct IRF-related subtypes, each with different prognostic and immune characteristics. Combining with previous studies, we hypothesized that cluster C corresponded to immune-inflamed phenotype characterised by massive immune cell infiltration (33). Unlike three immune phenotypes (immune-inflamed, immune-excluded and immune-desert phenotype) that are widely recognised in other tumours (33), David et al. argued that immune-excluded phenotype is rare in ccRCC (25). Thus, combining immune infiltration, we hypothesized that clusters A and B correspond to immune-desert phenotype with low immune infiltration (33). Previous studies demonstrated that CD8+ T cells are exhausted in ccRCC, when the greater the cellular infiltration, the worse the prognosis (28). By analysing the proportion and degree of immune cell infiltration, we observed that Cluster C exhibited significant CD8 + T cell exhaustion characteristics, while Cluster B had relatively few. Comprehensive analysis of prognostic and immunological features plausibly explained why Cluster C had the worst prognosis despite being immunologically activated, while the opposite was true for Cluster B. This meant that immunophenotypic classification of different IRF-related subtypes was reasonable and valid.

According to these DEGs, we classified ccRCC into three distinct gene subtypes, which also have different clinical and immunological profiles. This reaffirmed IRFs' potential value in predicting survival and shaping different TMEs. Given individual heterogeneity in IRFs expression, we quantified IRF-related molecular subtypes in individual ccRCC patients accurately by IRFscore. Comprehensive analysis suggested that IRFscore not only correlated significantly with clinical features, but also served as an independent prognostic factor. Besides, several mutation-prone genes in ccRCC, including PBRM1, VHL and BAP1, were mutated more frequently in high IRFscore group. It has been well established that these mutations indicate a poor prognosis for patients (36) and PBRM1 mutations substantially increase patient susceptibility to targeted therapies and immunotherapy (37). These results indirectly indicated potential value of IRFscore in predicting patient prognosis, suggesting that IRFs may be critical factors in affecting ccRCC treatment efficacy.

During chronic infection or cancer with continuous antigen stimulation, T cells fail to differentiate effectively into effector and memory T cells, at which point they gradually lose their original effect and become exhausted. This process is accompanied by massive inhibitory receptors (IRS) expression (24). In ccRCC TME, interactions between exhausted CD8+ T cells and M2-like macrophages cause immune dysfunctional circuits (25, 26). However, by analysing two cell infiltrations and corresponding receptor (ligand) expression in IRFscore groups, we did not find significant interactions between two cells. This indicated that IRFs may not regulate this interaction. TLS, existing around the tumour, consists of a B-cell follicular zone with a germinal centre and a T-cell zone with DC-Lamp+ mature DCs (27). During TLS formation, CCL19 and CCL21 recruit immune cells in vicinity of high endothelial vein to form T, B cell areas. CXCL13 recruits lymphoid

tissue-inducing factors and initial B cells to inflammatory site and TLS-B cell area, respectively. A reduced risk of death and recurrence of ccRCC has been found when increased frequency of TLS is accompanied by increased CD8+ T-cell infiltration, contradicting the previous belief that CD8+ T cells cause poorer prognosis (29). Therefore, researchers pointed that increased mature TLS in ccRCC may be relevant to reduced T-cell exhaustion (30). In our study, TLS and mature DCs were more frequent in low IRFscore group (high prognosis) and accompanied by reduced CD8+ T-cell exhaustion. We speculated that IRF may improve patient prognosis by influencing TLS frequency.

Targeted therapy is preferred for mccRCC as it is not effective against conventional chemotherapy and radiotherapy (3). Widely recognised kidney cancer targeted agents fall into two categories, TKI and mTOR inhibitors, acting through VHL/HIF/VEGF and PI3K/AKT/mTOR signalling pathways respectively (4). Some TKI drugs, including sorafenib and sunitinib, can slow down neo-angiogenesis by blocking VEGF (38). Temsirolimus and everolimus, as mTOR pathway inhibitors, can block mTOR proteins to exert therapeutic effects (4). Benoit et al. constructed mccRCC-related molecular markers to predict patient response to treatment with sunitinib and identified four different molecular subtypes (mccRCC1-4) (35). Interestingly, we found that high IRFscore matched mccRCC1/4, while low IRFscore matched mccRCC2/3. Therefore, we proposed that IRFscore not only serves as a marker for mccRCC typing, but also predicts targeted therapeutic efficacy. ICIs restore T-cell anti-tumour activity by blocking intra-tumour immunosuppressive signalling (6). PBRM1 mutations, TMB and tumour immunophenotypes influence ICI efficacy to some extent. In this work, we revealed significant associations between IRFscore and PBRM1 mutations, TMB and immunotype and confirmed the predictive value of IRFscore in immunotherapy efficacy.

Due to technical limitations, most conclusions in this paper were based on information from public databases. In future, appropriate clinical cohorts and basic trials will be required to address these issues.

Conclusion

The IRFscore, constructed based on the transcriptomic expression of the IRF family, has independent prognostic value and can provide accurate survival prediction for ccRCC patients. Furthermore, IRFscore can help us to comprehensively assess the IRF-related immune and molecular subtypes in individual patients and guide more effective individualised clinical treatment.

Data availability statement

The original contributions presented in the study are included in the article/Supplementary Material. Further inquiries can be directed to the corresponding authors.

Author contributions

All authors are contributors to the article. H-GX, J-XZ and P-FS proposed the idea and participated in research design and execution. CC and L-YC performed bioinformatics analysis, paper writing and experimental manipulation. R-XY modified the manuscript. All authors contributed to the article and approved the submitted version.

Funding

This study was supported by the Natural Science Foundation of Jiangsu Province of China (BK20181492), the National Key Clinical Department of Laboratory Medicine of China in Nanjing, Key laboratory for Laboratory Medicine of Jiangsu Province (ZDXKB2016005) and by the Priority Academic Program Development of Jiangsu Higher Education Institutions.

Conflict of interest

The authors declare that the research was conducted in the absence of any commercial or financial relationships that could be construed as a potential conflict of interest.

Publisher's note

Supplementary material

The Supplementary Material for this article can be found online at: https://www.frontiersin.org/articles/10.3389/fonc.2022.1118472/full#supplementary-material

References

1. Motzer RJ, Bacik J, Schwartz LH, Reuter V, Russo P, Marion S, et al. Prognostic factors for survival in previously treated patients with metastatic renal cell carcinoma. *J Clin Oncol* (2004) 22:454–63. doi: 10.1200/jco.2004.06.132

2. Choueiri TK, Escudier B, Powles T, Tannir NM, Mainwaring PN, Rini BI, et al. Cabozantinib versus everolimus in advanced renal cell carcinoma (METEOR): final results from a randomised, open-label, phase 3 trial. *Lancet Oncol* (2016) 17:917–27. doi: 10.1016/s1470-2045(16)30107-3

3. Escudier B, Porta C, Schmidinger M, Rioux-Leclercq N, Bex A, Khoo V, et al. Renal cell carcinoma: ESMO clinical practice guidelines for diagnosis, treatment and follow-up. *Ann Oncol* (2016) 27:v58–68. doi: 10.1093/annonc/mdw328

4. Hsieh JJ, Purdue MP, Signoretti S, Swanton C, Albiges L, Schmidinger M, et al. Renal cell carcinoma. *Nat Rev Dis Primers* (2017) 3:17009. doi: 10.1038/nrdp.2017.9

5. Motzer RJ, Jonasch E, Michaelson MD, Nandagopal L, Gore JL, George S, et al. NCCN guidelines insights: Kidney cancer, version 2.2020. *J Natl Compr Canc Netw* (2019) 17:1278–85. doi: 10.6004/jnccn.2019.0054

6. Rini BI, Plimack ER, Stus V, Gafanov R, Hawkins R, Nosov D, et al. Pembrolizumab plus axitinib versus sunitinib for advanced renal-cell carcinoma. *N Engl J Med* (2019) 380:1116–27. doi: 10.1056/NEJMoa1816714

7. Honda K, Takaoka A, Taniguchi T. Type I interferon [corrected] gene induction by the interferon regulatory factor family of transcription factors. *Immunity* (2006) 25:349–60. doi: 10.1016/j.immuni.2006.08.009

8. Bidwell BN, Slaney CY, Withana NP, Forster S, Cao Y, Loi S, et al. Silencing of Irf7 pathways in breast cancer cells promotes bone metastasis through immune escape. *Nat Med* (2012) 18:1224–31. doi: 10.1038/nm.2830

9. Huber M, Suprunenko T, Ashhurst T, Marbach F, Raifer H, Wolff S, et al. IRF9 prevents CD8(+) T cell exhaustion in an extrinsic manner during acute lymphocytic choriomeningitis virus infection. *J Virol* (2017) 91(22):e01219-17. doi: 10.1128/jvi.01219-17

10. Johnson WE, Li C, Rabinovic A. Adjusting batch effects in microarray expression data using empirical bayes methods. *Biostatistics* (2007) 8:118–27. doi: 10.1093/biostatistics/kxj037

11. Wilkerson MD, Hayes DN. ConsensusClusterPlus: a class discovery tool with confidence assessments and item tracking. *Bioinformatics* (2010) 26:1572–3. doi: 10.1093/bioinformatics/btq170

12. Hänzelmann S, Castelo R, Guinney J. GSVA: gene set variation analysis for microarray and RNA-seq data. *BMC Bioinf* (2013) 14:7. doi: 10.1186/1471-2105-14-7

13. Charoentong P, Finotello F, Angelova M, Mayer C, Efremova M, Rieder D, et al. Pan-cancer immunogenomic analyses reveal genotype-immunophenotype relationships and predictors of response to checkpoint blockade. *Cell Rep* (2017) 18:248–62. doi: 10.1016/j.celrep.2016.12.019

14. Barbie DA, Tamayo P, Boehm JS, Kim SY, Moody SE, Dunn IF, et al. Systematic RNA interference reveals that oncogenic KRAS-driven cancers require TBK1. *Nature* (2009) 462:108–12. doi: 10.1038/nature08460

15. Yoshihara K, Shahmoradgoli M, Martínez E, Vegesna R, Kim H, Torres-Garcia W, et al. Inferring tumour purity and stromal and immune cell admixture from expression data. *Nat Commun* (2013) 4:2612. doi: 10.1038/ncomms3612

16. Newman AM, Liu CL, Green MR, Gentles AJ, Feng W, Xu Y, et al. Robust enumeration of cell subsets from tissue expression profiles. *Nat Methods* (2015) 12:453–7. doi: 10.1038/nmeth.3337

17. Ritchie ME, Phipson B, Wu D, Hu Y, Law CW, Shi W, et al. Limma powers differential expression analyses for RNA-sequencing and microarray studies. *Nucleic Acids Res* (2015) 43:e47. doi: 10.1093/nar/gkv007

18. Yu G, Wang LG, Han Y, He QY. clusterProfiler: an r package for comparing biological themes among gene clusters. *Omics* (2012) 16:284–7. doi: 10.1089/omi.2011.0118

19. Sotiriou C, Wirapati P, Loi S, Harris A, Fox S, Smeds J, et al. Gene expression profiling in breast cancer: understanding the molecular basis of histologic grade to improve prognosis. *J Natl Cancer Inst* (2006) 98:262–72. doi: 10.1093/jnci/djj052

20. Geeleher P, Cox N, Huang RS. pRRophetic: an r package for prediction of clinical chemotherapeutic response from tumor gene expression levels. *PloS One* (2014) 9: e107468. doi: 10.1371/journal.pone.0107468

21. Yang W, Soares J, Greninger P, Edelman EJ, Lightfoot H, Forbes S, et al. Genomics of drug sensitivity in cancer (GDSC): a resource for therapeutic biomarker discovery in cancer cells. *Nucleic Acids Res* (2013) 41:D955–961. doi: 10.1093/nar/gks1111

22. Szklarczyk D, Franceschini A, Wyder S, Forslund K, Heller D, Huerta-Cepas J, et al. STRING v10: protein-protein interaction networks, integrated over the tree of life. *Nucleic Acids Res* (2015) 43:D447–452. doi: 10.1093/nar/gku1003

23. Bindea G, Mlecnik B, Tosolini M, Kirilovsky A, Waldner M, Obenauf AC, et al. Spatiotemporal dynamics of intratumoral immune cells reveal the immune landscape in human cancer. *Immunity* (2013) 39:782–95. doi: 10.1016/j.immuni.2013.10.003

24. Wherry EJ. T Cell exhaustion. *Nat Immunol* (2011) 12:492–9. doi: 10.1038/ni.2035

25. Braun DA, Hou Y, Bakouny Z, Ficial M, Sant' Angelo M, Forman J, et al. Interplay of somatic alterations and immune infiltration modulates response to PD-1 blockade in advanced clear cell renal cell carcinoma. *Nat Med* (2020) 26:909–18. doi: 10.1038/s41591-020-0839-y

26. Braun DA, Street K, Burke KP, Cookmeyer DL, Denize T, Pedersen CB, et al. Progressive immune dysfunction with advancing disease stage in renal cell carcinoma. *Cancer Cell* (2021) 39:632–648.e638. doi: 10.1016/j.ccell.2021.02.013

27. Germain C, Gnjatic S, Tamzalit F, Knockaert S, Remark R, Goc J, et al. Presence of b cells in tertiary lymphoid structures is associated with a protective immunity in patients with lung cancer. *Am J Respir Crit Care Med* (2014) 189:832–44. doi: 10.1164/rccm.201309-1611OC

28. Giraldo NA, Becht E, Vano Y, Petitprez F, Lacroix L, Validire P, et al. Tumor-infiltrating and peripheral blood T-cell immunophenotypes predict early relapse in localized clear cell renal cell carcinoma. *Clin Cancer Res* (2017) 23:4416–28. doi: 10.1158/1078-0432.Ccr-16-2848

29. Giraldo NA, Becht E, Pagès F, Skliris G, Verkarre V, Vano Y, et al. Orchestration and prognostic significance of immune checkpoints in the microenvironment of primary and metastatic renal cell cancer. *Clin Cancer Res* (2015) 21:3031–40. doi: 10.1158/1078-0432.Ccr-14-2926

30. Dieu-Nosjean MC, Giraldo NA, Kaplon H, Germain C, Fridman WH, Sautès-Fridman C. Tertiary lymphoid structures, drivers of the anti-tumor responses in human cancers. *Immunol Rev* (2016) 271:260–75. doi: 10.1111/imr.12405

31. Samstein RM, Lee CH, Shoushtari AN, Hellmann MD, Shen R, Janjigian YY, et al. Tumor mutational load predicts survival after immunotherapy across multiple cancer types. *Nat Genet* (2019) 51:202–6. doi: 10.1038/s41588-018-0312-8

32. Offin M, Rizvi H, Tenet M, Ni A, Sanchez-Vega F, Li BT, et al. Tumor mutation burden and efficacy of EGFR-tyrosine kinase inhibitors in patients with EGFR-mutant lung cancers. *Clin Cancer Res* (2019) 25:1063–9. doi: 10.1158/1078-0432.Ccr-18-1102

33. Chen DS, Mellman I. Elements of cancer immunity and the cancer-immune set point. *Nature* (2017) 541:321–30. doi: 10.1038/nature21349

34. Herbst RS, Soria JC, Kowanetz M, Fine GD, Hamid O, Gordon MS, et al. Predictive correlates of response to the anti-PD-L1 antibody MPDL3280A in cancer patients. *Nature* (2014) 515:563–7. doi: 10.1038/nature14011

35. Beuselinck B, Job S, Becht E, Karadimou A, Verkarre V, Couchy G, et al. Molecular subtypes of clear cell renal cell carcinoma are associated with sunitinib response in the metastatic setting. *Clin Cancer Res* (2015) 21:1329–39. doi: 10.1158/1078-0432.Ccr-14-1128

36. Cancer Genome Atlas Research Network. Comprehensive molecular characterization of clear cell renal cell carcinoma. *Nature* (2013) 499:43–9. doi: 10.1038/nature12222

37. Miao D, Margolis CA, Gao W, Voss MH, Li W, Martini DJ, et al. Genomic correlates of response to immune checkpoint therapies in clear cell renal cell carcinoma. *Science* (2018) 359:801–6. doi: 10.1126/science.aan5951

38. Nadal R, Amin A, Geynisman DM, Voss MH, Weinstock M, Doyle J, et al. Safety and clinical activity of vascular endothelial growth factor receptor (VEGFR)-tyrosine kinase inhibitors after programmed cell death 1 inhibitor treatment in patients with metastatic clear cell renal cell carcinoma. *Ann Oncol* (2016) 27:1304–11. doi: 10.1093/annonc/mdw160

frontiers | Frontiers in Oncology

TYPE Original Research
PUBLISHED 15 February 2023
DOI 10.3389/fonc.2023.1071816

OPEN ACCESS

EDITED BY
Linhui Wang,
Second Military Medical University, China

REVIEWED BY
Zeyan Li,
Shandong University, China
Cai Jiarong,
Third Affiliated Hospital of Sun Yat-sen University, China

*CORRESPONDENCE
Jianming Guo
guo.jianming@zs-hospital.sh.cn
Xiaoyi Hu
hu.xiaoyi@zs-hospital.sh.cn

†These authors have contributed equally to this work and share first authorship

SPECIALTY SECTION
This article was submitted to Genitourinary Oncology, a section of the journal Frontiers in Oncology

RECEIVED 17 October 2022
ACCEPTED 31 January 2023
PUBLISHED 15 February 2023

CITATION
Lin D, Lai P, Zhang W, Lin J, Wang H, Hu X and Guo J (2023) Development and validation of a nomogram to evaluate the therapeutic effects of second-line axitinib in patients with metastatic renal cell carcinoma. *Front. Oncol.* 13:1071816. doi: 10.3389/fonc.2023.1071816

Development and validation of a nomogram to evaluate the therapeutic effects of second-line axitinib in patients with metastatic renal cell carcinoma

Dengqiang Lin[1†], Peng Lai[1†], Wen Zhang[2†], Jinglai Lin[1], Hang Wang[3], Xiaoyi Hu[3*] and Jianming Guo[1,3*]

[1]Department of Urology, Zhongshan Hospital (Xiamen Branch), Fudan University, Xiamen, China, [2]Department of Traditional Chinese Medicine, Zhongshan Hospital, Fudan University, Shanghai, China, [3]Department of Urology, Zhongshan Hospital, Fudan University, Shanghai, China

The unpredictable biological behavior and tumor heterogeneity of metastatic renal cell carcinoma (mRCC) cause significant differences in axitinib efficacy. The aim of this study is to establish a predictive model based on clinicopathological features to screen patients with mRCC who can benefit from axitinib treatment. A total of 44 patients with mRCC were enrolled and divided into the training set and validation set. In the training set, variables related with the therapeutic efficacy of second-line treatment with axitinib were screened through univariate Cox proportional hazards regression and least absolute shrinkage and selection operator analyses. A predictive model was subsequently established to assess the therapeutic efficacy of second-line treatment with axitinib. The predictive performance of the model was evaluated by analyzing the concordance index and time-dependent receiver operating characteristic, calibration, and decision curves. The accuracy of the model was similarly verified in the validation set. The International Metastatic RCC Database Consortium (IMDC) grade, albumin, calcium, and adverse reaction grade were identified as the best predictors of the efficacy of second-line axitinib treatment. Adverse reaction grade was an independent prognostic index that correlated with the therapeutic effects of second-line treatment with axitinib. Concordance index value of the model was 0.84. Area under curve values for the prediction of 3-, 6-, and 12-month progression-free survival after axitinib treatment were 0.975, 0.909, and 0.911, respectively. The calibration curve showed a good fit between the predicted and actual probabilities of progression-free survival at 3, 6, and 12 months. The results were verified in the validation set. Decision curve analysis revealed that the nomogram based on a combination of four clinical parameters (IMDC grade, albumin, calcium, and adverse reaction grade) had more net benefit than adverse reaction grade alone. Our predictive model can be useful for clinicians to identify patients with mRCC who can benefit from second-line treatment with axitinib.

KEYWORDS

renal cell carcinoma, tyrosine kinase inhibitor, axitinib, nomogram, receiver operating characteristic

1 Introduction

Globally, approximately 85% of renal tumors were renal cell carcinoma (RCC), which is one of the ten most common cancer types and characterized by unpredictable biological behavior and heterogeneity (1, 2). Until recently, surgical resection was the standard of care, with a favorable overall prognosis for patients with localized RCC. The 5-year survival rate for patients with early stage I and II/III RCC are 93% and 72.5%, respectively, whereas those for patients with stage IV metastatic RCC is 12% (3). Moreover, 17%–30% of patients present with advanced stage of the disease at primary diagnosis, and 20%–40% of patients with localized disease eventually develop advanced disease (4, 5), which requires systemic therapies. In the past decades, the therapeutic strategy for locally advanced and metastatic RCC (mRCC) has broadened remarkably—from the use of cytokines (interferon-alpha and interleukin-2) to the administration of molecular-targeted therapies, such as tyrosine kinase inhibitors (TKIs) (6). Although treatment with molecular-targeted therapies has improved the prognosis of patients with mRCC, first-line therapies fail in most patients because of disease progression or unacceptable side effects (7).

After first-line therapies fail, a second-line therapeutic strategy is selected to improve patient prognosis. According to the NCCN guidelines, axitinib is recommended as a second-line treatment option. Compared with sorafenib as second-line treatment, axitinib significantly increased median progression-free survival (PFS) time and provided a better objective response rate for patients with mRCC who received sunitinib or cytokine treatment as a first-line therapy in a randomized phase III study (AXIS trial) (8). Moreover, the results of subgroup analyses of the AXIS study attested to the efficacy of axitinib in the Asian population, further supporting the registration of axitinib in China (8). Axitinib is more cost-effective than sorafenib (9). By contrast, a retrospective and noncomparative phase II trial indicated that the 5-year survival rate of patients who received axitinib was 20.6% after failure of prior systemic treatment (10). The differences in PFS and overall survival were insignificant in patients with mRCC who received axitinib or everolimus as second-line treatment (11); however, axitinib had a manageable tolerability profile.

Genomic studies have reported intratumoral and intertumoral heterogeneity in RCC (8, 12, 13), which leads to differential prognosis and response to targeted treatment. Consequently, it is imperative to screen patients with mRCC who can benefit from axitinib therapy after failure of first-line therapies and improve the cost-effectiveness of therapy. This study aimed to retrospectively evaluate the prognostic clinicopathological parameters associated with the therapeutic effects of second-line treatment with axitinib.

Abbreviations: mRCC, Metastatic renal cell carcinoma; IMDC, The International Metastatic RCC Database Consortium; RCC, Renal cell carcinoma; TKI, Tyrosine kinase inhibitor; PFS, Progression-free survival; CPHR, Cox proportional-hazards regression; ROC, Receiver operating characteristic curve; AUC, Area under the curve; C-index, Concordance index; DCA, Decision curve analysis; HR, Hazard rate; VHL, The von Hippel–Lindau; PDGF, Platelet-derived growth factor (PDGF); CCRCC, Clear cell renal cell carcinoma; nCCRCC, Non-clear cell renal cell carcinoma; PD, Progressive disease; PR, Partial response; SD, Stable disease; KPS score, Karnofsky score.

2 Methods

2.1 Patients and inclusion criteria

The study was conducted in accordance with the Declaration of Helsinki (revised in 2013). Study approval was given by the Ethics Committee of Zhongshan Hospital, affiliated to Fudan University, China (B2016-030). Data from 44 patients with advanced RCC, who received axitinib as second-line targeted therapy between December 2014 and December 2021 at the Department of Urology, Zhongshan Hospital, Fudan University, were retrospectively collected and analyzed. The inclusion criteria were as follows: (1) advanced RCC or mRCC verified histopathologically with surgery or biopsy, (2) advanced RCC irrespective of pathological type, (3) advanced RCC irrespective of first-line treatment, and (4) advanced RCC with axitinib as second-line targeted therapy. Because 14 patients lacked complete clinicopathological data, 30 patients were finally enrolled in the study as the training set to evaluate factors related to the therapeutic effects of second-line treatment with axitinib and construct a predictive model. Four clinical parameters, namely albumin, calcium, International Metastatic RCC Database Consortium (IMDC) grade, and adverse reaction grade, were further identified. Because complete data were available for the four candidate factors for 14 patients, they were included in the validation set to verify the model (Figure 1). Biochemical parameters were collected before patients received axitinib.

2.2 Statistical analysis

Statistical analysis was performed using SPSS v23 and R v4.20. Continuous variables are presented as the mean and standard deviation, and categorical variables are presented as frequency or percentage. Comparisons of continuous variables between two groups were performed with the *t* test, and categorical variables were compared using the chi-square test or Fisher's exact test. p-Value < 0.05, two-tailed, was considered statistically significant. Kaplan–Meier survival plots were generated with the log-rank statistic using the survival package of R.

We first screened the clinicopathological parameters associated with the therapeutic effects of second-line treatment with axitinib using univariate Cox proportional-hazards regression (CPHR) analysis. Because CPHR is not used to analyze multidimensional survival datasets, the least absolute shrinkage and selection operator (LASSO) technique was subsequently performed for variable selection and shrinkage from many clinical variables identified by univariate CPHR, using the glmnet package of R (8, 14). Finally, we identified and then established a predictive model based on four clinical parameters (albumin, calcium, IMDC grade, and adverse reaction grade) through multivariate CPHR.

To evaluate the predictive accuracy of the model, time-dependent receiver operating characteristic curve (ROC) and area under curve (AUC) at 3-, 6-, and 12-month PFS after axitinib treatment were constructed using the survival package of R. Concordance index (C-index) is used to evaluate predictive accuracy (15). The consistence between predicted PFS probability and actual PFS probability was confirmed using a calibration curve after 1000 bootstrap resampling. The ROC curve and AUC are not used to make clinical decisions. In clinical practice, decision curve analysis (DCA) was used to estimate the net benefit for patients based on threshold from the predictive model.

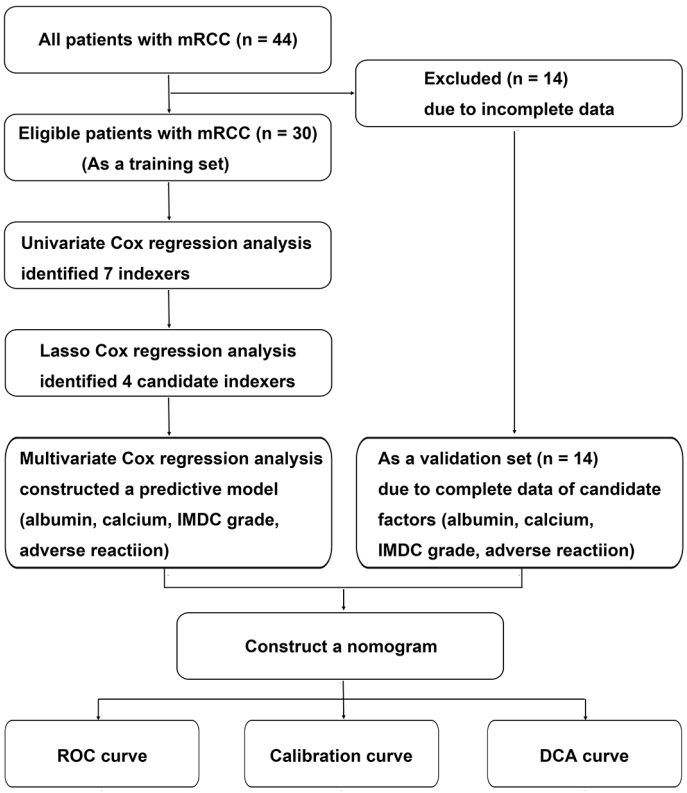

FIGURE 1
Flow chart of the data selection and process. IMDC, International Metastatic Renal Cell Carcinoma Database Consortium classification; LASSO, least absolute shrinkage and selection operator; RCC, renal cell carcinoma.

3 Results

3.1 General characteristics

Based on the inclusion criteria, 44 patients with advanced RCC received axitinib as a second-line targeted therapy. Thirty patients were included in the training set and 14 in the validation set. The clinicopathological features of patients are shown in Table 1. Mean age at initial diagnosis was 60.25 ± 10.02 years. Most of the patients were men (79.55%, 35/44) and had received nephrectomy (86.36%, 38/44). The pathologic type of 35 patients (79.55%) was clear cell carcinoma, of which two tissue samples were associated with sarcomatous degeneration. The maximum tumor diameter was 2.5–15.0 cm. The most common metastatic sites were the lungs (63.64%, 28/44), bones (34.10%, 15/44), and liver (15.91%, 7/44). In addition, the lymph node was a common distant site (40.91%, 18/44). In some patients, the tumor metastasized to the brain (4.55%, 2/44), adrenal gland (4.55%, 2/44), and pancreas (9.10%, 4/44). Mean overall follow-up time was 1485.44 ± 1150.61 days and median survival time was 2071 days for the whole cohort.

Axitinib was introduced as a second-line targeted therapy after the failure of first-line treatment with drugs, including sorafenib (n = 5), sunitinib (n = 33), and pazopanib (n = 6). Failure of first-line therapy was a result of progression (25/44, 56.82%) or intolerable adverse effects (19/44, 43.18%). Mean therapeutic time and median PFS time of first-line treatment were 841.68 ± 695.15 days and 1058 days, respectively, for the whole cohort. Time of disease progression during second-line treatment with axitinib was defined as the time from the start of axitinib treatment to the first documentation of progression. Patients during treatment comprised the progression (Pro) group (n = 20) or the progression-free (ProFree) group (n = 24). The mean therapeutic time of second-line treatment was 446.02 ± 350.21 days for the whole cohort and 486.30 ± 372.28 days and 359.71 ± 291.11 days for the training and validation sets, respectively (p = 0.2690).

Statistically significant differences were present between the training and validation sets within the cohort, including hemoglobin level (120.77 ± 20.67 vs. 104.33 ± 28.28 g/L, p = 0.0429), C-reactive protein level (4.69 ± 10.72 vs. 38.04 ± 33.40 mg/L, p = 0.0002), and other metastatic sites (14/30 vs. 11/14, $P = 0.0466$). The differences were not statistically significant for the other clinicopathological features. However, hemoglobin level, C-reactive protein level, and other metastatic sites were unrelated to the therapeutic effects of second-line treatment with axitinib.

3.2 Subtype analysis

Results of subtype analysis are shown in Table 2. Albumin concentration was higher in the Pro group than in the ProFree group (41.13 ± 4.64 vs. 35.75 ± 6.39 g/L, p = 0.0024), and patients with mRCC who were malnourished (albumin ≤35 g/L) were more likely to have disease progression (8/10 vs. 12/34, p = 0.0270). Patients who were younger (<75 years old) did not benefit more from second-line treatment with axitinib than patients who were older (≥75 years

10.3389/fonc.2023.1071816

TABLE 1 Patient demographics and clinicopathological features.

Variable	All patients (n = 44)	Training set (n = 30)	Validation set (n = 14)	p-Value
Age (years)	60.25 ± 10.02	59.37 ± 10.91	62.14 ± 7.77	0.3990
Gender				0.2471
Male (n)	34	25	9	
Female (n)	10	5	5	
Tumor location				0.5206
Left	21	13	8	
Right	23	17	6	
Nephrectomy	38/44	25/30	13/14	0.6467
Pathologic type				0.6951
CCRCC	36	25	11	
nCCRCC	8	5	3	
Sarcomatous change	2/44	1/30	1/14	0.5720
Primary tumor size (cm)	6.91 ± 2.94	6.87 ± 3.13	7.00 ± 2.59	0.8932
Metastasis				
Liver	7/44	3/30	4/14	0.1167
Lung	28/44	20/30	8/14	0.5408
Bone	15/44	9/30	6/14	0.4020
Brain	2/44	2/30	0/14	0.3227
Lymph node	18/44	12/30	6/14	0.8575
Other	25/44	14/30	11/14	0.0466
First-line drug				0.5009
Sorafenib	5	3	2	
Sunitinib	33	24	9	
Pazopanib	6	3	3	
Time from first- to second-line treatment (days)	841.68 ± 695.15	647.43 ± 593.93	662.57 ± 712.80	0.9419
Results of first-line treatment				0.7530
PD	25	18	7	
SD	17	11	6	
PR	2	1	1	
Time from second-line treatment (days)	446.02 ± 350.21	486.30 ± 372.28	359.71 ± 291.11	0.2690
Results of second-line treatment				0.5881
PD	21	15	6	
SD	17	12	5	
PR	6	3	3	
KPS score >80	31	21	10	>0.9999
Hemoglobin	116.07 ± 23.94	120.77 ± 20.67	104.33 ± 28.28	0.0429
Platelet	237.31 ± 117.35	241.30 ± 119.25	226.45 ± 116.90	0.7244
Lymphocyte	1.53 ± 0.80	1.59 ± 1.06	1.53 ± 1.12	0.8712
Neutrophil	3.62 ± 2.26	3.22 ± 1.53	4.70 ± 3.46	0.0629

(Continued)

TABLE 1 Continued

Variable	All patients (n = 44)	Training set (n = 30)	Validation set (n = 14)	p-Value
C-reactive protein	9.59 ± 22.87	4.69 ± 10.72	38.04 ± 33.40	0.0002
Creatinine	127.21 ± 34.43	132.43 ± 35.31	114.17 ± 29.52	0.1218
Albumin	28.68 ± 6.07	38.60 ± 5.57	40.17 ± 5.87	0.3967
Calcium	2.45 ± 0.25	2.47 ± 0.16	2.44 ± 0.43	0.7366
IMDC grade				0.6824
I	6	5	1	
II	30	20	10	
III	8	6	2	
Largest adverse reaction grade				0.8266
0	5	3	2	
I	16	12	4	
II	22	15	7	
III	1	1	0	
Follow-up time (days)	1485.44 ± 1150.61	1623.83 ± 1268.75	1166.08 ± 764.94	0.2353
Alive at last follow-up	22/44	16/30	6/14	0.5174

CCRCC, Clear cell renal cell carcinoma; nCCRCC, non-clear cell renal cell carcinoma; PD, Progressive disease; PR, Partial response; SD, Stable disease; KPS score, Karnofsky score; IMDC, International Metastatic Renal Cell Carcinoma Database Consortium classification.

old, p = 0.5832). Age distribution between the Pro and ProFree groups was not different (58.10 ± 11.14 vs. 62.04 ± 8.81 years, p = 0.1972). Higher levels of calcium (≥ 2.55 mmol/L) were related to worse prognosis than lower levels (<2.55 mmol/L) (9/12 vs. 11/32, p = 0.0212). Nephrectomy in patients with RCC did not affect the therapeutic effect of second-line treatment with axitinib. Consistently, significant differences between first-line treatment settings or metastatic sites and efficacy of second-line treatment with axitinib were not verified.

3.3 Prognostic model construction

To evaluate the therapeutic effects of second-line treatment with axitinib, univariate CPHR analysis was used to identify potentially important factors. Seven parameters were screened, namely, IMDC grade [hazard rate (HR) = 5.26, p < 0.0001], albumin (HR = 0.82, p < 0.0001), calcium (HR = 172.34, p = 0.0005), adverse reaction grade (HR = 0.31, p = 0.0169), Karnofsky score (KPS score, HR = 0.92, p = 0.0442), bone metastasis (HR = 2.85, p = 0.0462), and hemoglobin (HR = 0.97, p = 0.0124) (Table 3). These parameters were incorporated into LASSO regression analysis to avoid bias from collinearity between factors (Figure 2). IMDC grade, albumin, calcium, and adverse reaction grade, with non-zero coefficients, were further enrolled in multivariate CPHR analysis to construct a prognostic model. IMDC grade had the highest hazard ratio (HR) (3.21, p = 0.1370), followed by calcium (2.55, p = 0.6833) (Figure 3 and Table 2). Adverse reaction grade was an independent prognostic index that correlated with the therapeutic effects of second-line treatment with axitinib. To construct a quantitative and more intuitive tool for the individualized prediction of the therapeutic effects of second-line treatment with axitinib in patients with advanced RCC, a novel prognostic nomogram was established based on the four parameters, and the probability of 3-, 6-, and 12-month PFS was predicted (Figure 4).

3.4 Predictive performance of the model

The C-index value of the model was 0.84, suggesting that the predictive model had excellent predictive performance. Time-dependent ROC curve analysis verified the accuracy of the model; AUC values for the prediction of 3-, 6-, and 12-month PFS were 0.975, 0.909, and 0.911, respectively (Figure 5A). After 1000 bootstrap resampling was complete, the predictive model showed excellent consistency between predicted PFS probability and actual PFS probability at 3, 6, and 12 months, confirmed by the calibration curve (Figure 5B). The results were verified in the validation set, which had a C-index value of 0.776 (Figure 5C). Moreover, DCA was used to evaluate net benefit and make clinical decisions at 3, 6, and 12 months (Figure 5D). A nomogram (green) based on a combination of IMDC grade, albumin, calcium, and adverse reaction grade showed more area than adverse reaction grade alone (purple) (Figure 5D).

4 Discussion

Two primary signaling pathways are involved in RCC pathogenesis—vascular endothelial growth factor (VEGF) and mammalian target of rapamycin (mTOR) signaling pathways (16, 17). Loss mutation of the von Hippel–Lindau (VHL) is a common event in many RCCs, and then causes the abnormal activation of the

10.3389/fonc.2023.1071816

TABLE 2 Subtype analysis.

Variable	Difference of axitinib efficacy		p-Value
	Progression	Progression-Free	
Age (years)	58.10 ± 11.14	62.04 ± 8.81	0.1972
Age ≥75 years			0.5832
Yes	2	1	
No	18	23	
Gender			0.7344
Male	16	18	
Female	4	6	
Tumor location			>0.9999
Left	10	11	
Right	10	13	
Nephrectomy			>0.9999
Yes	17	21	
No	3	3	
Pathologic type			0.4361
CCRCC	15	21	
nCCRCC	5	3	
Sarcomatous change			0.4926
Yes	0	2	
No	20	22	
Primary tumor size ≤7 cm			0.5385
Yes	11	16	
No	9	8	
Liver metastasis			0.2172
Yes	5	2	
No	15	22	
Lung metastasis			>0.9999
Yes	13	15	
No	7	9	
Bone metastasis			0.2097
Yes	9	6	
No	11	18	
Brain metastasis			>0.9999
Yes	1	1	
No	19	23	
Lymph node metastasis			0.2268
Yes	6	12	
No	14	12	
Other metastasis sites			0.1151

(Continued)

10.3389/fonc.2023.1071816

TABLE 2 Continued

Variable	Difference of axitinib efficacy		p-Value
	Progression	Progression-Free	
Yes	9	16	
No	11	6	
First-line drug			
Sorafenib			0.1605
Yes	4	1	
No	16	23	
Sunitinib			0.4728
Yes	14	19	
No	6	4	
Pazopanib			0.6731
Yes	2	4	
No	18	20	
KPS score >80			0.5220
Yes	13	18	
No	7	6	
Albumin (g/L)	35.75 ± 6.39	41.13 ± 4.64	0.0024
Albumin ≤35 g/L			0.0270
Yes	8	2	
No	12	22	
Calcium	2.49 ± 0.22	2.41 ± 0.28	0.3053
Calcium ≥2.55 mmol/L			0.0212
Yes	9	3	
No	11	21	
IMDC grade I			0.1977
Yes	1	5	
No	19	19	
Largest adverse reaction grade ≤I			>0.9999
Yes	10	11	
No	10	13	

CCRCC, Clear cell renal cell carcinoma; nCCRCC, Non-clear cell renal cell carcinoma; PD, Progressive disease; PR, Partial response; SD, Stable disease; KPS score, Karnofsky score; IMDC, International Metastatic Renal Cell Carcinoma Database Consortium classification.

above pathways, which is linked to cancer progression and poor prognosis (18). Currently, many TKIs targeting to VEGF-induced angiogenesis, including sunitinib, pazopanib, and axitinib, have been developed and are integral to the treatment (6, 16). However, RCC is characterized by a wide range of molecular and clinicopathological heterogeneity. Although considerable efforts have been made in the past decades to treat mRCC, targeted agents offer limited benefits to most patients. Compared with 8–9 months in the first-line treatment setting, the average time of stable disease is 5–6 months in the second-line treatment setting (19). At second-line treatment setting, axitinib significantly increased PFS time and improved objective response rate compared with sorafenib (8). Compared to first-line treatment with TKIs, axitinib not only showed fewer side effects, such as hepatotoxicity, hematological toxicity, and hypertension (20–22), but also immunomodulatory effects, where it downregulated the expression of the immune-suppressor signal transducer and activator of transcription 3 in patients with RCC (23), indicating that axitinib is relatively potent and must be further explored in combination therapy, first- or second-line setting.

However, fewer studies have identified biomarkers, including clinicopathological features and biochemical indices, to guide treatment. Biomarkers related to the therapeutic effects of second-

TABLE 3 Results of the Cox proportional-hazards regression analysis.

Variable	Univariate CPHR		Multivariate CPHR	
	HR	p-Value	HR	p-Value
IMDC grade	5.26	<0.0001	3.21	0.1370
Albumin	0.82	<0.0001	0.91	0.1814
Calcium	172.34	0.0005	2.55	0.6833
Adverse reaction	0.31	0.0169	0.28	0.0152
KPS score	0.92	0.044		
Bone metastasis	2.85	0.046		
Hemoglobin	0.97	0.0124		

CPHR, Cox proportional-hazards regression; HR, hazard ratio; KPS score: Karnofsky score; IMDC: International Metastatic Renal Cell Carcinoma Database Consortium classification.

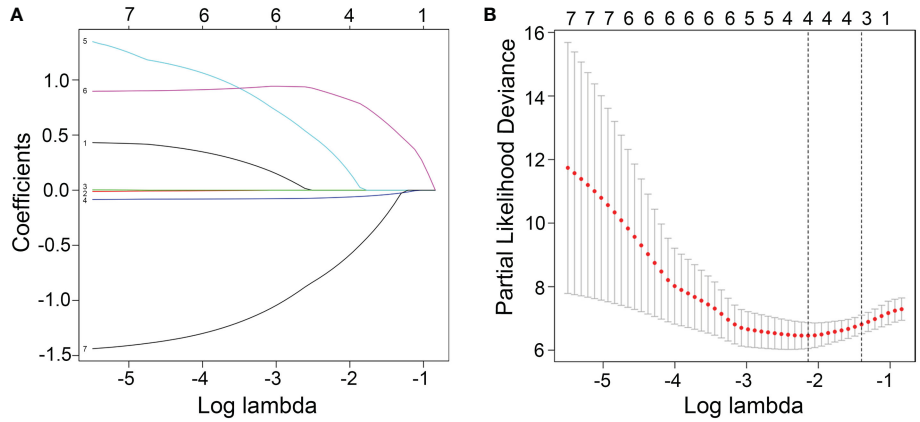

FIGURE 2
(A) Screening path of the least absolute shrinkage and selection operator (LASSO) regression model. **(B)** Penalty parameter (log lambda) in the LASSO regression model.

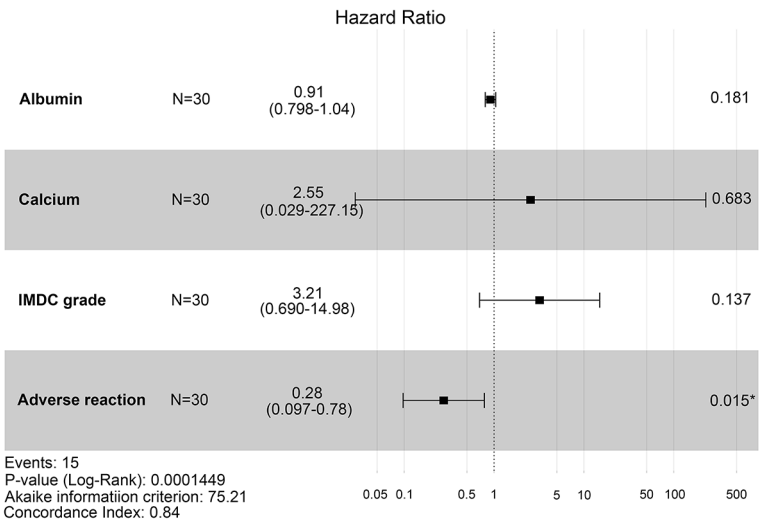

FIGURE 3
Forest plot of hazard ratios for four clinicopathological features (IMDC grade, albumin, calcium, and adverse reaction) using multivariate Cox proportional-hazards regression analysis. IMDC: International Metastatic Renal Cell Carcinoma Database Consortium classification.

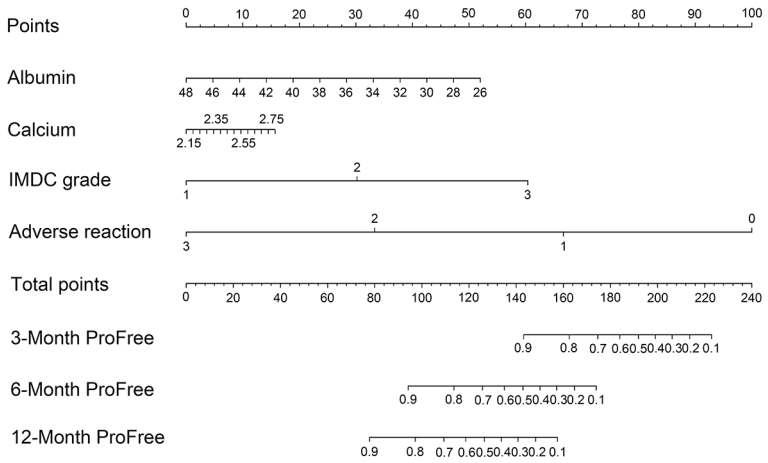

FIGURE 4
Nomogram based on the logarithm of four clinicopathological features (IMDC grade, albumin, calcium, and adverse reaction) predicting the efficacy of second-line treatment with axitinib in patients with metastatic renal cell carcinoma after failure of prior systemic treatment. IMDC: International Metastatic Renal Cell Carcinoma Database Consortium classification, ProFree: progression-free.

line treatment with axitinib should be identified based on precision medicine or individual treatment.

In this study, a nomogram (C-index value = 0.84) was developed based on four variables (IMDC grade, albumin, calcium, and adverse reaction grade) in the test set. AUC values of the model for the prediction of 3-, 6-, and 12-month PFS were 0.975, 0.909, and 0.911, respectively. In addition, the model was internally validated after 1000-bootstrap resampling and externally validated in the validation set. But neither the ROC curve nor the calibration curve guides clinical decision. The DCA method was used to first evaluate the benefit of the predictive model and then help make a rational clinical decision. To our knowledge, DCA has never been used to evaluate the therapeutic effects of axitinib. Therefore, the performance of this prognostic model is reliable and accurate. Of course, small sample size is a limitation of this study. Moreover, independent validation sets from other centers were not enrolled in this study. Thus, further studies must verify the conclusion made using this prognostic model.

Hypertension is the most frequently documented adverse reaction in patients who received second-line treatment with axitinib (8); therefore, hypertension can be an effective predictor of axitinib efficacy. For instance, diastolic blood pressure ≥ 90 mmHg (23–26) and systolic blood pressure ≥ 140 mmHg (25, 27) were related to improved outcome of axitinib. Consistently, the findings of this study indicated that more adverse reaction grade was as an independent protective biomarker of axitinib efficacy. Compared with variable hypertension alone, the adverse

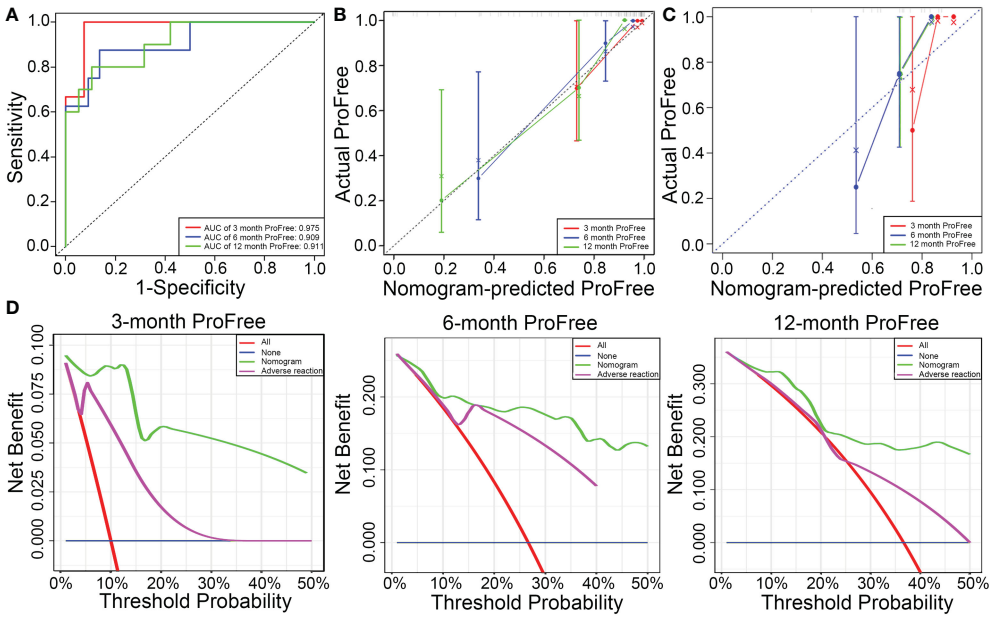

FIGURE 5
(A) Predictive performance of the model is evaluated using receiver operating characteristic curve. **(B)** Consistency of the model is evaluated using a calibration curve in the training set. **(C)** Consistence of the model is evaluated using a calibration curve in the validation set. **(D)** Decision curve analysis to evaluate the clinical benefit of 3-, 6-, and 12-month PFS and compare the clinical benefit of the model based on four parameters (IMDC grade, albumin, calcium, and adverse reaction) with adverse reaction grade.

reaction grade in this study reflected more information about the kinds of side effects, such as hypertension, fatigue, diarrhea, myelosuppression, hypothyroidism, and stomatitis. Moreover, blood pressure may be affected by many factors. In other words, its specificity is worse compared to our indexer that consists of all adverse reaction grades. However, it is still unclear for us and other researchers whether the adverse reaction, when it occurs, should be included into our nomogram, which must be further explored in prospective studies. Generally, 4 weeks is optimal for evaluating the efficacy and adverse reaction grade of second-line treatment with axitinib. Irrespective of the Memorial Sloan Kettering Cancer Center risk score or IMDC risk score, hypercalcemia in patients with mRCC was considered a risk factor for poor outcome, such as advanced stages and bone metastasis (28, 29). Consistently, in this study, IMDC grade and calcium level are included in the nomogram, confirming that higher IMDC grade and hypercalcemia are associated with lesser efficacy of axitinib. Albumin is sensitive to the nutritional state. Many studies have demonstrated that albumin is a risk parameter for the prognosis of some diseases, such as gastrointestinal stromal tumors, human immunodeficiency virus, lymphoma, and cutaneous malignant melanoma (30–35). For example, Datta et al. (31) reported that low albumin level was common in patients with stage IV cutaneous malignant melanoma. However, to our knowledge, the relationship between the prognosis of RCC or efficacy of TKIs and albumin concentration remains unclear. The findings of this study demonstrated that second-line axitinib treatment had worse efficacy in patients with RCC who were malnourished. Thus, improved nutrition may benefit more during targeted, second-line treatment with axitinib.

Older patients with RCC have often been excluded from receiving axitinib treatment, owing to safety concerns. According to Hideaki et al. (36), axitinib therapy was not only effective but also safe in patients aged >75 years. The results of this study revealed that patients aged <75 years old did not benefit more than patients aged ≥75 years ($p = 0.5832$). Patients in the ProFree group may be older than those in the Pro group (62.04 ± 8.81 vs. 58.10 ± 11.14 years, $p = 0.1972$), further suggesting that treatment with axitinib in older patients is worthy of attention. According to a phase III AXIS study, there was a significant difference for the effect size of the PFS benefit in different prior first-line treatments (37). In this study, differences in axitinib efficacy were not statistically significant between prior first-line treatment types.

This study has limitations. First, the sample size was small ($n = 44$), and the study was retrospective. Although the patients were divided into the training set and validation set, which was used to validate the performance of the model, the relatively small sample size and retrospective nature of the study significantly affected the accuracy and predictive performance of the study. Second, although patients were enrolled regardless of the type of first-line therapy, including sorafenib ($n = 5$), sunitinib ($n = 33$), and pazopanib ($n = 6$), patients who received a combination of TKI and immunotherapy as a first-line therapy were not included in the nomogram. Combined treatment with lenvatinib and pembrolizumab was related to significantly longer PFS and overall survival than that with sunitinib (38). Therefore, it is unclear whether the combination of TKI and immunotherapy as a first-line therapy could affect the efficacy of second-line treatment with axitinib. In addition, results from KEYNOTE 426 indicated that patients who received pembrolizumab–axitinib showed better ORR (59.3% vs. 35.7%) and median PFS (15.1 vs. 11.1 months) compared with patients who received sunitinib (39). Similarly, whether the model can be used to evaluate the efficacy of first-line treatment with axitinib, with a combination of pembrolizumab (39) or avelumab (20), is unclear.

Although the included parameters in the model may not only indirectly reflect plasma exposure of the drug by distinguishing adverse grade (23, 40) but also directly reflect individualized status, such as nutrition (albumin) and biochemical level (calcium), those parameters don't reflect altered signaling pathways such as VHL, VEGF, mTOR, platelet-derived growth factor (PDGF), cell cycle, p53 Related Signaling, Ferroptosis, and so on (17, 41, 42). Additionally, imaging features of tumor during targeted therapy should be considered. The predictive performance and scope of applicability of the model to evaluate the efficacy of second-line axitinib treatment should be further verified in large-sample, multicenter, prospective studies in the future.

Data availability statement

The original contributions presented in the study are included in the article/supplementary material. Further inquiries can be directed to the corresponding authors.

Ethics statement

The studies involving human participants were reviewed and approved by the Ethics Committee of Zhongshan Hospital, affiliated to Fudan University. The patients/participants provided their written informed consent to participate in this study.

Author contributions

DL, PL, and WZ contributed equally to this work and share first authorship. DL, PL, and WZ conceived and designed the study. DL and PL analyzed the data. DL, PL, and WZ prepared the figures and wrote the main manuscript. JL,HW, and XH provided technical guidance. XH and JG revised the manuscript. DL, PL, and XH provided funding support. All authors reviewed the manuscript and approved the final version for publication.

Funding

This study was supported by the Hospital Science Foundation (grant number: KYYJ201921), Medical Project of Xiamen (grant number: 3502Z20209045 and 3502Z20194029), Scientific Research Project of Fujian for Youth (grant number: 2020QNB061), and Special project of Integrated Traditional Chinese and Western medicine of the Shanghai Municipal Health Commission (grant number: ZHYY-ZXYJHZX-202017).

Conflict of interest

The authors declare that the research was conducted in the absence of any commercial or financial relationships that could be construed as a potential conflict of interest.

Publisher's note

References

1. Motzer RJ, Jonasch E, Agarwal N, Alva A, Baine M, Beckermann K, et al. Kidney cancer, version 3.2022, NCCN clinical practice guidelines in oncology. *J Natl Compr Canc Netw* (2022) 20:71–90. doi: 10.6004/jnccn.2022.0001

2. Li Z, Zhao S, Zhu S, Fan Y. MicroRNA-153-5p promotes the proliferation and metastasis of renal cell carcinoma *via* direct targeting of AGO1. *Cell Death Dis* (2021) 12:33. doi: 10.1038/s41419-020-03306-y

3. Padala SA, Barsouk A, Thandra KC, Saginala K, Mohammed A, Vakiti A, et al. Epidemiology of renal cell carcinoma. *World J Oncol* (2020) 11:79–87. doi: 10.14740/wjon1279

4. Garcia-Roig M, Ortiz N, Lokeshwar V. Molecular marker for predicting treatment response in advanced renal cell carcinoma: Does the promise fulfill clinical need? *Curr Urol Rep* (2014) 15:375. doi: 10.1007/s11934-013-0375-0

5. Capitanio U, Montorsi F. Renal cancer. *Lancet* (2016) 387:894–906. doi: 10.1016/s0140-6736(15)00046-x

6. Calvo E, Schmidinger M, Heng DY, Grünwald V, Escudier B. Improvement in survival end points of patients with metastatic renal cell carcinoma through sequential targeted therapy. *Cancer Treat Rev* (2016) 50:109–17. doi: 10.1016/j.ctrv.2016.09.002

7. Vento JA, Rini BI. Treatment of refractory metastatic renal cell carcinoma. *Cancers (Basel)* (2022) 14. doi: 10.3390/cancers14205005

8. Rini BI, Escudier B, Tomczak P, Kaprin A, Szczylik C, Hutson TE, et al. Comparative effectiveness of axitinib versus sorafenib in advanced renal cell carcinoma (AXIS): A randomised phase 3 trial. *Lancet* (2011) 378:1931–9. doi: 10.1016/S0140-6736(11)61613-9

9. Petrou P. Cost-effectiveness analysis of axitinib through a probabilistic decision model. *Expert Opin Pharmacother* (2015) 16:1233–43. doi: 10.1517/14656566.2015.1039982

10. Rini BI, de la Motte Rouge T, Harzstark AL, Michaelson MD, Liu G, Grünwald V, et al. Five-year survival in patients with cytokine-refractory metastatic renal cell carcinoma treated with axitinib. *Clin Genitourin Cancer* (2013) 11:107–14. doi: 10.1016/j.clgc.2012.12.004

11. Vogelzang NJ, Pal SK, Signorovitch JE, Reichmann WM, Li N, Yang C, et al. Comparative effectiveness of everolimus and axitinib as second targeted therapies for metastatic renal cell carcinoma in the US: A retrospective chart review. *Curr Med Res Opin* (2016) 32:741–7. doi: 10.1185/03007995.2016.1140028

12. Ueda K, Suekane S, Nishihara K, Ogasawara N, Kurose H, Hayashi S, et al. Duration of first-line treatment with molecular targeted-therapy is a prognostic factor in metastatic renal cell carcinoma. *Anticancer Res* (2015) 35:3415–21.

13. Ueda K, Suekane S, Ogasawara N, Chikui K, Suyama S, Nakiri M, et al. Long-term response of over ten years with sorafenib monotherapy in metastatic renal cell carcinoma: A case report. *J Med Case Rep* (2016) 10:177. doi: 10.1186/s13256-016-0961-0

14. Zhang J, Zhang H, Wang Y, Wang Q. MCM2-7 in clear cell renal cell carcinoma: MCM7 promotes tumor cell proliferation. *Front Oncol* (2021) 11:782755. doi: 10.3389/fonc.2021.782755

15. Wolbers M, Koller MT, Witteman JC, Steyerberg EW. Prognostic models with competing risks: Methods and application to coronary risk prediction. *Epidemiology* (2009) 20:555–61. doi: 10.1097/EDE.0b013e3181a39056

16. Barata PC, Rini BI. Treatment of renal cell carcinoma: Current status and future directions. *CA Cancer J Clin* (2017) 67:507–24. doi: 10.3322/caac.21411

17. Dell'Atti L, Bianchi N, Aguiari G. New therapeutic interventions for kidney carcinoma: Looking to the future. *Cancers (Basel)* (2022) 14:3616–38. doi: 10.3390/cancers14153616

18. Ganner A, Gehrke C, Klein M, Thegtmeier L, Matulenski T, Wingendorf L, et al. VHL suppresses RAPTOR and inhibits mTORC1 signaling in clear cell renal cell carcinoma. *Sci Rep* (2021) 11:14827. doi: 10.1038/s41598-021-94132-5

19. Hsieh JJ, Purdue MP, Signoretti S, Swanton C, Albiges L, Schmidinger M, et al. Renal cell carcinoma. *Nat Rev Dis Primers* (2017) 3:17009. doi: 10.1038/nrdp.2017.9

20. Motzer RJ, Penkov K, Haanen J, Rini B, Albiges L, Campbell MT, et al. Avelumab plus axitinib versus sunitinib for advanced renal-cell carcinoma. *N Engl J Med* (2019) 380:1103–15. doi: 10.1056/NEJMoa1816047

21. Qi WX, He AN, Shen Z, Yao Y. Incidence and risk of hypertension with a novel multi-targeted kinase inhibitor axitinib in cancer patients: A systematic review and meta-analysis. *Br J Clin Pharmacol* (2013) 76:348–57. doi: 10.1111/bcp.12149

22. Wood LS, Gornell S, Rini BI. Maximizing clinical outcomes with axitinib therapy in advanced renal cell carcinoma through proactive side-effect management. *Community Oncol* (2012) 9:46–55. doi: 10.1016/j.cmonc.2011.11.002

23. Rini BI, Melichar B, Fishman MN, Oya M, Pithavala YK, Chen Y, et al. Axitinib dose titration: analyses of exposure, blood pressure and clinical response from a randomized phase II study in metastatic renal cell carcinoma. *Ann Oncol* (2015) 26:1372–7. doi: 10.1093/annonc/mdv103

24. Rini BI, Schiller JH, Fruehauf JP, Cohen EE, Tarazi JC, Rosbrook B, et al. Diastolic blood pressure as a biomarker of axitinib efficacy in solid tumors. *Clin Cancer Res* (2011) 17:3841–9. doi: 10.1158/1078-0432.CCR-10-2806

25. Motzer RJ, Escudier B, Tomczak P, Hutson TE, Michaelson MD, Negrier S, et al. Axitinib versus sorafenib as second-line treatment for advanced renal cell carcinoma: Overall survival analysis and updated results from a randomised phase 3 trial. *Lancet Oncol* (2013) 14:552–62. doi: 10.1016/S1470-2045(13)70093-7

26. Rini BI, Garrett M, Poland B, Dutcher JP, Rixe O, Wilding G, et al. Axitinib in metastatic renal cell carcinoma: Results of a pharmacokinetic and pharmacodynamic analysis. *J Clin Pharmacol* (2013) 53:491–504. doi: 10.1002/jcph.73

27. Donskov F, Michaelson MD, Puzanov I, Davis MP, Bjarnason GA, Motzer RJ, et al. Sunitinib-associated hypertension and neutropenia as efficacy biomarkers in metastatic renal cell carcinoma patients. *Br J Cancer* (2015) 113:1571–80. doi: 10.1038/bjc.2015.368

28. Teishima J, Murata D, Inoue S, Hayashi T, Mita K, Hasegawa Y, et al. Prediction of early progression of metastatic renal cell carcinoma treated with first-line tyrosine kinase inhibitor. *Curr Urol* (2021) 15:187–92. doi: 10.1097/cu9.0000000000000042

29. Heng DY, Xie W, Regan MM, Warren MA, Golshayan AR, Sahi C, et al. Prognostic factors for overall survival in patients with metastatic renal cell carcinoma treated with vascular endothelial growth factor-targeted agents: Results from a large, multicenter study. *J Clin Oncol* (2009) 27:5794–9. doi: 10.1200/JCO.2008.21.4809

30. Ding P, Guo H, Yang P, Sun C, Tian Y, Liu Y, et al. Association between the nutritional risk and the survival rate in newly diagnosed GIST patients. *Front Nutr* (2021) 8:743475. doi: 10.3389/fnut.2021.743475

31. Datta M, Savage P, Lovato J, Schwartz GG. Serum calcium, albumin and tumor stage in cutaneous malignant melanoma. *Future Oncol* (2016) 12:2205–14. doi: 10.2217/fon-2016-0046

32. Hashimoto N, Ueda T, Hiraiwa S, Tajiri T, Nakamura N, Yokoyama K. Clonally related plasmablastic lymphoma simultaneously occurring with diffuse large b-cell lymphoma. *Case Rep Hematol* (2020) 2020:8876567. doi: 10.1155/2020/8876567

33. Zhou Q, Wei Y, Huang F, Wei X, Wei Q, Hao X, et al. Low prognostic nutritional index predicts poor outcome in diffuse large b-cell lymphoma treated with r-CHOP. *Int J Hematol* (2016) 104:485–90. doi: 10.1007/s12185-016-2052-9

34. Hao X, Wei Y, Wei X, Zhou L, Wei Q, Zhang Y, et al. Glasgow Prognostic score is superior to other inflammation-based scores in predicting survival of diffuse large b-cell lymphoma. *Oncotarget* (2017) 8:76740–8. doi: 10.18632/oncotarget.20832

35. Park S, Han B, Cho JW, Woo SY, Kim S, Kim SJ, et al. Effect of nutritional status on survival outcome of diffuse large b-cell lymphoma patients treated with rituximab-CHOP. *Nutr Cancer* (2014) 66:225–33. doi: 10.1080/01635581.2014.867065

36. Miyake H, Harada K, Ozono S, Fujisawa M. Efficacy and safety of axitinib in elderly patients with metastatic renal cell carcinoma. *Med Oncol* (2016) 33:95. doi: 10.1007/s12032-016-0813-1

37. Escudier B, Pluzanska A, Koralewski P, Ravaud A, Bracarda S, Szczylik C, et al. Bevacizumab plus interferon alfa-2a for treatment of metastatic renal cell carcinoma: A randomised, double-blind phase III trial. *Lancet* (2007) 370:2103–11. doi: 10.1016/S0140-6736(07)61904-7

38. Motzer R, Alekseev B, Rha SY, Porta C, Eto M, Powles T, et al. Lenvatinib plus pembrolizumab or everolimus for advanced renal cell carcinoma. *N Engl J Med* (2021) 384:1289–300. doi: 10.1056/NEJMoa2035716

39. Rini BI, Plimack ER, Stus V, Gafanov R, Hawkins R, Nosov D, et al. Pembrolizumab plus axitinib versus sunitinib for advanced renal-cell carcinoma. *N Engl J Med* (2019) 380:1116–27. doi: 10.1056/NEJMoa1816714

40. Tortorici MA, Cohen EE, Pithavala YK, Garrett M, Ruiz-Garcia A, Kim S, et al. Pharmacokinetics of single-agent axitinib across multiple solid tumor types. *Cancer Chemother Pharmacol* (2014) 74:1279–89. doi: 10.1007/s00280-014-2606-6

41. Li Z, Liu J, Zhang X, Fang L, Zhang C, Zhang Z, et al. Prognostic significance of cyclin D1 expression in renal cell carcinoma: A systematic review and meta-analysis. *Pathol Oncol Res* (2020) 26:1401–09. doi: 10.1007/s12253-019-00776-0

42. Rini BI, Pal SK, Escudier BJ, Atkins MB, Hutson TE, Porta C, et al. Tivozanib versus sorafenib in patients with advanced renal cell carcinoma (TIVO-3): A phase 3, multicentre, randomised, controlled, open-label study. *Lancet Oncol* (2020) 21:95–104. doi: 10.1016/s1470-2045(19)30735-1

frontiers | Frontiers in Oncology

TYPE Original Research
PUBLISHED 10 March 2023
DOI 10.3389/fonc.2023.1077309

OPEN ACCESS

EDITED BY
Le Qu,
Nanjing University, China

REVIEWED BY
Tiezheng Qi,
Xiangya School of Medicine, Central South University, China
Anca Maria Cimpean,
Victor Babes University of Medicine and Pharmacy, Romania

*CORRESPONDENCE
Qinghua Xia
xqhgege@hotmail.com

†These authors have contributed equally to this work and share first authorship

SPECIALTY SECTION
This article was submitted to Genitourinary Oncology, a section of the journal Frontiers in Oncology

RECEIVED 22 October 2022
ACCEPTED 27 February 2023
PUBLISHED 10 March 2023

CITATION
Zhang P, Li J, Wang Z, Zhao L, Qiu J, Xu Y, Wu G and Xia Q (2023) Establishment of a new prognostic risk model of MAPK pathway-related molecules in kidney renal clear cell carcinoma based on genomes and transcriptomes analysis.
Front. Oncol. 13:1077309.
doi: 10.3389/fonc.2023.1077309

Establishment of a new prognostic risk model of MAPK pathway-related molecules in kidney renal clear cell carcinoma based on genomes and transcriptomes analysis

Peizhi Zhang[1†], Jiayi Li[2†], Zicheng Wang[3], Leizuo Zhao[1,4], Jiechuan Qiu[3], Yingkun Xu[5], Guangzhen Wu[6] and Qinghua Xia[1*]

[1]Department of Urology, Shandong Provincial Hospital, Cheeloo College of Medicine, Shandong University, Jinan, China, [2]School of Business, Hanyang University, Seoul, Republic of Korea, [3]Department of Urology, Shandong Provincial Hospital Affiliated to Shandong First Medical University, Jinan, China, [4]Department of Urology, Dongying People's Hospital, Dongying, China, [5]Department of Breast and Thyroid Surgery, The First Affiliated Hospital of Chongqing Medical University, Chongqing, China, [6]Department of Urology, The First Affiliated Hospital of Dalian Medical University, Dalian, China

Purpose: The mitogen-activated protein kinase (MAPK) signaling pathway is often studied in oncology as the most easily mentioned signaling pathway. This study aims to establish a new prognostic risk model of MAPK pathway related molecules in kidney renal clear cell carcinoma (KIRC) based on genome and transcriptome analysis.

Methods: In our study, RNA-seq data were acquired from the KIRC dataset of The Cancer Genome Atlas (TCGA) database. MAPK signaling pathway-related genes were obtained from the gene enrichment analysis (GSEA) database. We used "glmnet" and the "survival" extension package for LASSO (Least absolute shrinkage and selection operator) regression curve analysis and constructed a prognosis-related risk model. The survival curve and the COX regression analysis were used the "survival" expansion packages. The ROC curve was plotted using the "survival ROC" extension package. We then used the "rms" expansion package to construct a nomogram plot. We performed a pan-cancer analysis of CNV (copy number variation), SNV (single nucleotide variant), drug sensitivity, immune infiltration, and overall survival (OS) of 14 MAPK signaling pathway-related genes using several analysis websites, such as GEPIA website and TIMER

database. Besides, the immunohistochemistry and pathway enrichment analysis used The Human Protein Atlas (THPA) database and the GSEA method. Finally, the mRNA expression of risk model genes in clinical renal cancer tissues versus adjacent normal tissues was further verified by real-time quantitative reverse transcription (qRT-PCR).

Results: We performed Lasso regression analysis using 14 genes and created a new KIRC prognosis-related risk model. High-risk scores suggested that KIRC patients with lower-risk scores had a significantly worse prognosis. Based on the multivariate Cox analysis, we found that the risk score of this model could serve as an independent risk factor for KIRC patients. In addition, we used the THPA database to verify the differential expression of proteins between normal kidney tissues and KIRC tumor tissues. Finally, the results of qRT-PCR experiments suggested large differences in the mRNA expression of risk model genes.

Conclusions: This study constructs a KIRC prognosis prediction model involving 14 MAPK signaling pathway-related genes, which is essential for exploring potential biomarkers for KIRC diagnosis.

KEYWORDS

KIRC, tumor biomarkers, MAPK pathway, TCGA, prognostic model

1 Introduction

The mortality rate of kidney cancer ranks first among all urological malignancies (1). Renal cell carcinoma (RCC) is the most common type of primary renal malignancy, and about 70% of RCC patients are diagnosed with KIRC (2). More than one-fifth of patients with advanced kidney cancer will relapse even after radical nephrectomy. Besides, kidney cancer patients with distant metastases have a 1-year survival rate of only 50% and a 5-year survival rate of only 10% (3, 4). Early diagnosis and treatment are of great importance to improve the prognosis of kidney cancer. A growing number of studies confirm that cancer is a human genomic disease (5, 6). Tumor progression is caused by coordinated genetic changes in multiple signaling pathways (7). Therefore, it is important to explore the relevant cancer-causing genes and pathways and construct risk models based on them for early detection and treatment of KIRC.

MAPK (mitogen-activated protein kinase) signaling pathway is one of the most extensive pathways in tumor pathway research. Related studies in human cancers have confirmed that most of cancers are associated with changes in the MAPK pathway. Since the recognition of Ras small GTPases as the first oncogenes of sarcoma viruses, research on the MAPK pathway has intensified over the past 40 years (8). The internal signaling of the MAPK signaling pathway is complex. Besides, this signaling pathway is often regulated by related genes or by crosstalk with other signaling pathways. In the physiological state, intracellular MAPK signaling is tightly controlled. Growth factors (GFs) bind to and activate receptor tyrosine kinases (RTKs) on the cell membrane, a critical first step in initiating the classical MAPK signaling pathway (9). Activation of RTKs drives phosphorylation of RAS superfamily proteins represented by HRAS, KRAS, and NRAS, thereby transducing extracellular signals to the cytoplasm (10). The subsequent activation of intracellular cascade reactions is also caused by the phosphorylation of molecules. Activated RAS further activates MAPKKK (mitogen-activated protein kinase kinase, represented by RAF and its variants), followed by MAPK kinase (MAPKK: MEK1/2/3/4/5/6/7), and finally MAPK, resulting in a cascade activation reaction of the intracellular MAPK signaling pathway (11). The MAPKs mainly include the following: ERKs (extracellular signal-regulated kinases, represented by ERK1/2/5), JNKs(c-Jun N-terminal kinases, represented by JNK1/2/3), and p38 MAPKs(represented by p38α/β/γ/δ) (12–14). Numerous studies have confirmed that the progression of most solid tumors is associated with gene mutations in the RAS/RAF/MEK/ERK signaling pathway (15). Approximately 30% of human solid tumors are associated with mutations in the RAS gene (16). Activation of Ras not only drives the MAPK cascade, but also acts as an initiator of the PI3k/AKT/mTOR cascade to regulate cell growth (11). In addition, ERK1/2 can regulate the activation of transcriptional factors such as c-Myc (transcriptional regulator Myc-like) through phosphorylation, which has received much attention in the research of tumor-targeted therapy (12).

In recent years, studies have demonstrated that the MAPK signaling pathway influences the prognosis of KIRC through the regulation of HIF-1α (17). In addition, the MAPK signaling pathway also influences the sensitivity of KIRC patients to

targeted drugs such as sunitinib and sorafenib (17, 18). The construction of predictive models based on genes related to the MAPK signaling pathway and the exploration of the mechanisms by which the MAPK signaling pathway affects prognosis and targeted therapy resistance will be of great significance in the future for the diagnosis and treatment of KIRC.

2 Materials and methods

2.1 Data acquisition

The mRNA expression data and clinical datasets of KIRC patients used in this study were obtained from the TCGA database (https://portal.gdc.cancer.gov/). The dataset we downloaded included 539 tumor tissues and 72 normal tissues. We then downloaded and analyzed the MAPK pathway-related genes using the GSEA analysis website (https://www.gsea-msigdb.org/gsea/index.jsp).

2.2 Data processing and analysis

The R language operating platform (https://www.rstudio.com/) is one of the most influential and widely used bioinformatics operating platforms. We used Perl and several R packages to analyze and process data. The "heatmaps" expansion package was used to make the heatmap. Then we used tbtools (https://github.com/CJ-Chen/TBtools) to further beautify and process the heatmap to better display the data. Statistical data analysis was performed using the "limma" software package to analyze variance. Lasso regression analysis was mainly performed using "glmnet" expansion packages. The survival curve was plotted using the "survival" expansion packages, and the ROC curve was analyzed and plotted using the "survival ROC" extension package. Finally, based on the risk model, we validated it with clinical characteristics by univariate Cox analysis and multivariate Cox analysis using the "survival" and "forestplot" expansion packages. Finally, we combined the predictive risk model with various clinical features as independent risk factors to draw a nomogram using the "rms" expansion package. $P < 0.05$ was considered a statistically significant difference. We used the "plyr", "ggplot2", "grid" and "gridExtra" extension packages for multi-GSEA analysis, to explore the biological pathways that risk model genes may affect in KIRC, and to explore the correlation of the MAPK pathway with other pathways.

2.3 GEPIA website

GEPIA (http://gepia.cancer-pku.cn/) has a robust data aggregation function. The analysis tool includes RNA-seq expression data from more than 9,000 tumors and 8,000 tumor genome maps based on the TCGA database (19). Based on the website's online tool, the CNV and SNV of model genes were differentially analyzed in different tumors.

2.4 ImmuCellAI website

We analyzed the infiltration of 24 types of immune cells in pan-cancer based on the ImmuCellAI website (http://bioinfo.life.hust.edu.cn/ImmuCel lAI/). We used the "pheatmap" R language to draw and visualize the analysis results in the form of heat maps. Statistical analysis was performed using the Spearman's correlation coefficient.

2.5 Generation of PPI networks

We draw the PPI network based on the online analysis tool STRING (https://www.string-db.org/). To make the PPI network more beautiful, we used the visualization software of Cystoscope. The data in PPI were used to construct a quantization table.

2.6 TIMER website

The Tumor Immune Estimation Resource (TIMER) 2.0s (http://cistrome.org/TIMER/) has recently been used to analyze immune cell infiltration in the environment of tumors. This study further judged the infiltration of immune cells in 14 genes by analyzing the correlation between 14 genes and immune cells. Heatmaps were drawn and visualized using the "heatmaps" expansion package.

2.7 GDSC database

Two hundred sixty-six drugs are included in the GDSC database (20). In this study, we analyzed the relationship between related drugs and the mRNA expression of MAPK pathway-related genes based on the GDSC database, and then we drew a heatmap to visualize the correlation.

2.8 The Human Protein Atlas database

The Human Protein Atlas database (http://www.proteinatlas.org/) was a proteome analysis website of 27173 antibodies targeting 17268 unique proteins (21). In our study, we used this website to explore the protein expression of MAPK pathway-related genes in normal kidney tissues and ccRCC tumor tissues.

2.9 Collection of clinical tissue samples

From March to May 2022, we collected tumor and adjacent normal kidney samples of 8 KIRC patients from Shandong Provincial Hospital. This study was approved by the Ethics Committee of Shandong Affiliated Hospital. Patients provided written informed consent for all samples and information collected. The research adhered to the principles of the Declaration of Helsinki and those of the World Medical Association.

2.10 Total RNA extraction and qRT-PCR experiments

We extracted total RNA from collected KIRC tumor tissues and paracancerous normal tissues using TRIzol reagent (Thermo Fisher Scientific, Waltham, MA, USA). Next, we reverse-transcribed the pre-extracted RNA into cDNA using EvoM-MLVRT master mix (Accurate Biotechnology). We then mixed the reagents for qRT-PCR detection according to the manufacturer's instructions of the SYBR® Green Premix Pro Taq HS qPCR Kit (Accurate Biotechnology). The above process was carried out in strict accordance with the manufacturer's instructions.

2.11 Statistical analyses

Expression of MAPK pathway-related genes in tumor tissues and adjacent tissues using One-way ANOVA. T-test was used to compare the expression of MAPK pathway-related genes of different gender, age, stage, node (N), tumor (T) and metastasis (M) in KIRC data set. The "survminer" package was used to determine the cut-off value of each risk score in the tumor group, and we divided patients into a high-risk group and a low-risk group. R Studio software package was used for all statistical analysis. $P < 0.05$ meant statistically significant.

3 Results

3.1 The expression of MAPK signaling pathway-related genes in KIRC and univariate Cox analysis

We first drew the flowchart to more conveniently show this research process (Figure 1). Then, We constructed a heat map of the mRNA data of the 81 MAPK signaling pathway-related genes in the KIRC patient dataset based on the TCGA database (Figure 2A). Among the 81 MAPK signaling pathway-related genes, nearly 80% of the genes have statistically significant differences in expression between normal kidney tissue and KIRC tissue, further confirming that the MAPK signaling pathway plays an essential role in the occurrence and development of KIRC. We then performed the univariate Cox analysis of MAPK signaling pathway-related genes in KIRC patients, and drew a forest plot (Figure 2B). The potential role of each signaling pathway-related gene in the occurrence and development of KIRC was determined. Using the HR value of 1 as a cutoff, there are 16 genes with HR values >1, including STAT1(signal transducer and activator of transcription 1), MAP3K8(mitogen-activated protein kinase kinase 8), SHC1(SHC adaptor protein 1), MAP3K9(mitogen-activated protein kinase kinase kinase 9), TRAF2(TNF receptor associated factor 2), RAC1(Rac family small GTPase 1), MAP3K12(mitogen-activated protein kinase kinase kinase 12), RPS6KA4(ribosomal protein S6 kinase A4), meaning that these genes are risk factors in disease progression. whereas 23 genes, including MAPK3(MAPK3: mitogen-activated protein kinase 3), MAP2K6(MAP2K6: mitogen-activated protein kinase kinase 6), MAPK13, MAP3K5(mitogen-activated protein kinase kinase 5), RPS6KA2(ribosomal protein S6 kinase A2), RPS6KA5(ribosomal protein S6 kinase A5), NFKB1(nuclear factor kappa B subunit 1), whose HR values are less than 1, are protective factors. Finally, we used the String database to analyze the PPI protein interaction to verify the interaction and connection between the proteins in the MAPK pathway (Figure 2C).

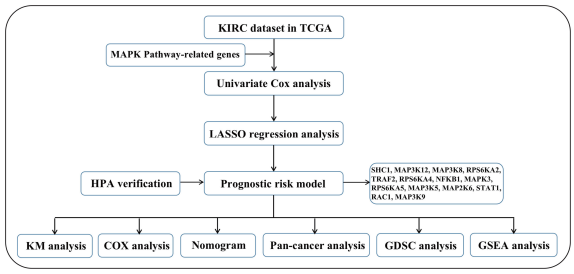

FIGURE 1
The flow chart of this research.

3.2 Construct a novel prognostic-related survival model in KIRC

After univariate cox analysis of genes related to the MAPK signaling pathway, we screened out genes with a P value < 0.05 for LASSO regression analysis, and screened out 14 model genes, including RPS6KA2, MAPK3, RPS6KA5, MAP2K6, MAP3K5, NFKB1, STAT1, RAC1, MAP3K9, TRAF2, RPS6KA4, SHC1, MAP3K12, and MAP3K8 (Figures 3A, B). A prognostic risk model was established based on these model genes. KIRC patients were divided into high-risk and low-risk groups with the median level of risk score as the optimal cutoff value. After plotting the survival curves, we found a significant difference in survival between the two groups (Figure 3C). Subsequently, we validated this prognostic-related risk model using the ROC curve. The results showed that the 5-year AUC value was 0.744 (Figure 3D) and the 10-year AUC value was 0.825 (Figure 3E), suggesting that the risk model is suitable for prognosis prediction of KIRC patients with high accuracy.

3.3 The relationship between the risk model and clinicopathological characteristics, and draw the corresponding nomogram in KIRC

We verified the relationship between the prognostic risk model and the clinical characteristics of patients (Figure 3F). The prognostic risk model was correlated with clinical characteristics including tumor volume (T), lymph nodes (N) distant metastasis (M), stage, grade, gender, and fustat, suggesting that the predictive model has good clinical prognosis and diagnostic and therapeutic efficacy. Univariate Cox analysis found that age, stage, grade tumor volume (T), distant

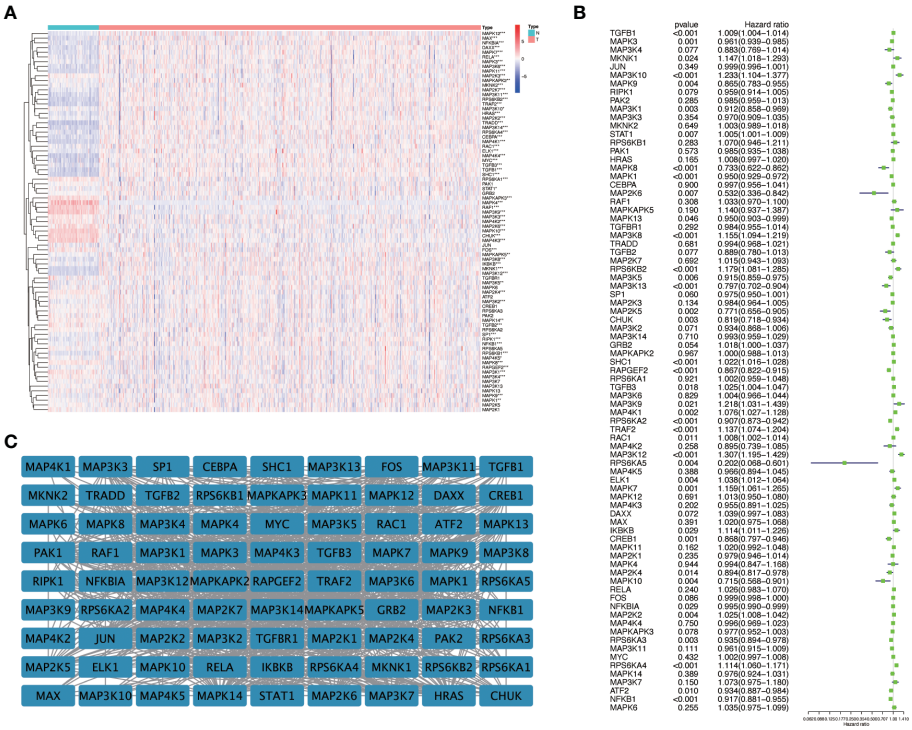

FIGURE 2
The expression of genes related to the MAPK signaling pathway in KIRC and univariate Cox regression analysis. **(A)** The differential expression of 81 MAPK signaling pathway-related genes in cancer and normal tissue in KIRC patients. Red represents the gene that is highly expressed in the tumor. The darker the color, the higher the expression level; blue represents the gene that is lowly expressed in the tumor, and the color the deeper it is, the lower the expression level. **(B)** Perform univariate Cox regression analysis on genes related to the MAPK signaling pathway. **(C)** The String database was used to analyze the protein interaction of 81 genes related to the MAPK signaling pathway, and the Cytoscope software platform was used to visualize the analysis results. *P<0.05, **P<0.01, and ***P<0.001.

metastasis (M), and risk score were statistically significant (Figure 4A). Multivariate Cox analysis showed that age, stage, grade, and risk score were independent risk factors for KIRC (Figure 4B). Subsequently, we established a new nomogram based on the four independent risk factors verified by multivariate Cox analysis (Figure 4C). In this nomogram, the quantified values of each variable correspond to the scale axis to obtain a score. Finally, the total score is obtained by summing the scores corresponding to the four variables, so that the 5-, 7-, or 10-year survival of KIRC patients can be intuitively obtained.

3.4 OS and variation of model genes in pan-cancer

We mapped the mRNA expression, CNV and SNV of these genes in 33 different tumors. First, we observed the extent to which these 14 model genes affect survival and prognosis in pan-cancer (Figure 5A). When we explored the role of genes in different tumors, we found that genes such as RAC1 and SHC1 were elevated in most cancers, suggesting their role as prognostic risk factors in most tumors. For a specific tumor pathological type, we can observe that most MAPK signaling pathway model genes are highly expressed in KICH and LGG, suggesting that they are associated with poor prognosis. Notably, we found that high expression of MAP2K6, MAP3K5, RPS6KA5, MAPK3, NFKB1, and RPS6KA4 in KIRC tumors suggested a better prognosis. In contrast, high expression of MAP3K8 and MAP3K12 suggested a poorer prognosis for KIRC. The SNV percentage heatmap (Figure 5B) and CNV percentage (Figure 5C) heatmap show the single nucleotide variation and copy number variation of different model genes in pan-cancer, respectively. The SNV percentage heatmap found that MAP3K5, STAT1, and MAP3K9 have the highest single-nucleotide mutation rates in pan-cancer. When we explored the single-nucleotide mutations of pathway-related genes in various pathological types of tumors, we found that the MAPK signaling pathway prognostic model genes had the most obvious SNV in uterine corpus endometrial carcinoma (UCEC), skin cutaneous melanoma (SKCM), and colon adenocarcinoma (COAD). In particular, the single-nucleotide mutation rate of MAP3K5 in UCEC and SKCM tumors was as high as 45% and 46%, respectively, while the single-nucleotide mutation rate of MAP3K9 in SKCM tumors was 46%. Nucleotide mutations played an essential role in the development of these tumors. Next, we found copy number variations of MAP2K6, SHC1, and RAC1 in most cancer tissues. RPS6KA2, MAP3K5, MAP3K9, RPS6KA5, and TRAF2 had higher rates of heterozygous deletion mutations in KIRC tissue, while STAT1, MAPK3, MAP3K12, SHC1, and RAC1 heterozygous amplification mutations were more prevalent. Notably, the MAPK pathway model genes had a

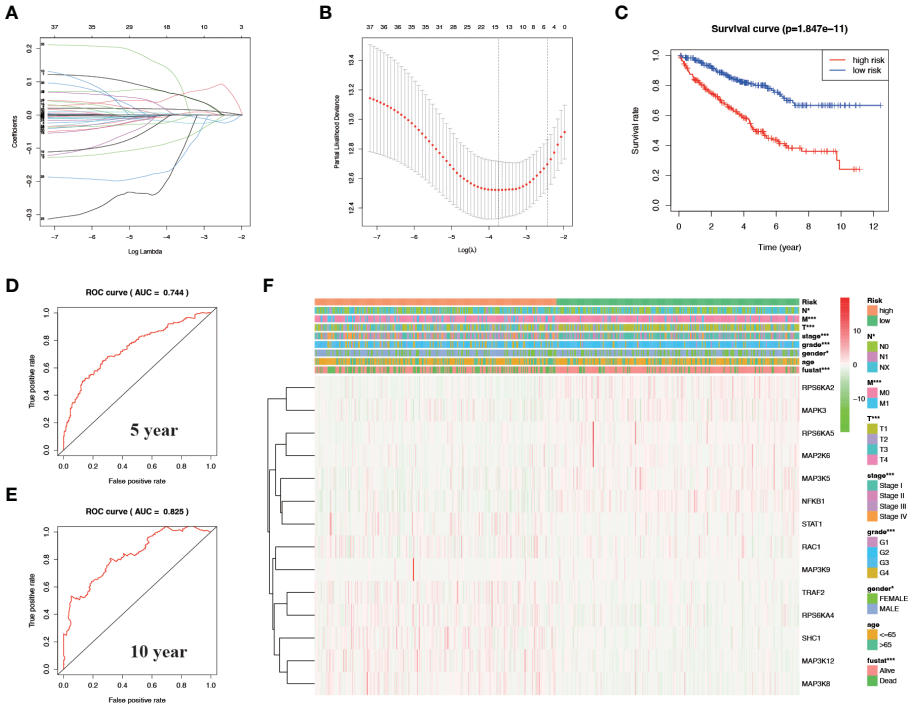

FIGURE 3
Construct a prognostic-related risk model in KIRC through LASSO regression analysis. **(A, B)** Results of LASSO regression analysis and cross-validation. **(C)** Kaplan–Meier survival analysis between high-risk and low-risk groups according to the optimal cut-off value; **(D)** ROC curve for predicting 5-year survival time; **(E)** ROC curve for predicting 10-year survival time; **(F)** Heat map based on the correlation of this risk feature with clinical features. *P<0.05 and ***P<0.001.

significantly increased mutation rate in KICH, which was one of the most common pathological types of RCC.

3.5 Immune infiltration and drug sensitivity of model genes in pan-cancer

We verified the correlation of the risk model genes with the infiltration of various immune cells in different types of tumors (Figure 5D). DC, NKT, Tr1, NK, Macrophage, CD4_T, nTreg, Th1, Tfh, and iTreg show high expression in most types of tumors, suggesting that their infiltration potentially contributes to tumor progression. On the contrary, Neutrophil and CD8_naive were lowly expressed in most types of tumors. Notably, immune cells such as NKT, Tr1, NK, macrophages, CD4_T, nTreg, Th1, Tfh, and iTreg were more infiltrated in KIRC tissues, while neutrophils, CD8_naive, CD4_naive, Th2, and Th17 were less infiltrated. Based on the establishment of the previous prediction model, we analyzed the correlation between the mRNA expression of 14 model genes and drug sensitivity (Figure 5E). Drug sensitivity analysis showed that MAPK3, RPS6KA4, STAT1, RAC1, RPS6KA2, SHC1 and other model genes, especially RAC1 and SHC1 genes, were significantly positively correlated with drug sensitivity. On the contrary, the higher the expression of RPS6KA5, MAP2K6 and other genes, the worse the drug sensitivity and the worse the curative effect.

3.6 Verify the protein expression of model genes between KIRC tissues and normal tissues

To further understand the protein expression of 14 model genes in KIRC tumor and normal tissues, we used the HPA website for further analysis (Figures 6A–N). We found that MAP2K6, MAP3K5, MAP3K9, MAP3K12, RPS6KA2, RPS6KA5, and STAT1 were lowly expressed in tumor tissues; However, NFKB1, RAC1, SHC1, and TRAF2 are highly expressed compared to normal tissues. The above results are consistent with our previous verification results.

3.7 GSEA analysis in KIRC for risk model genes

We performed GSEA pathway analysis on these risk model genes to explore the role of MAPK-related genes in other pathways and to establish the connection between the MAPK pathway and other pathways (Figures 7A–N). We found that risk model genes play different roles in different pathways, and each gene is also involved in different signaling pathways. For example, MAP2K6 is elevated in focal adhesion, adhesion, long-term potentiation, vascular smooth muscle contraction, GnRH signaling pathway, pathways in cancer, but its expression

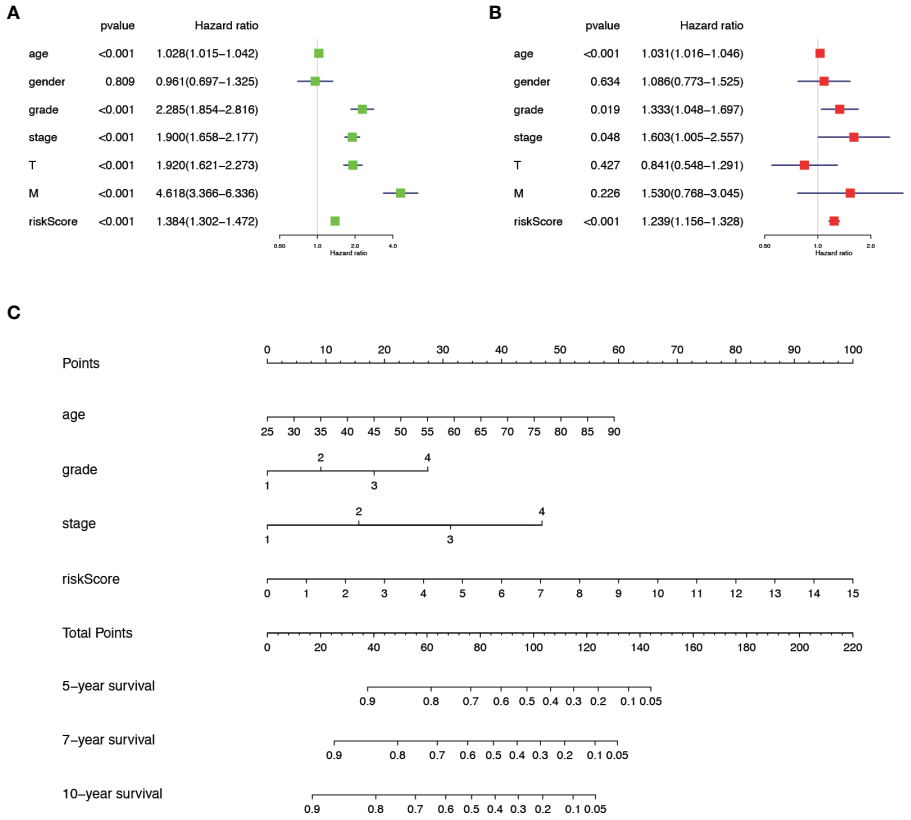

FIGURE 4
The comprehensive analysis is based on the clinical information of KIRC patients. **(A)** Univariate Cox analysis. **(B)** Multivariate Cox analysis. **(C)** A new nomogram was drawn based on this prognostic risk signature. The value of each variable gets a score on the dot scale axis. The total score can be easily calculated by adding each score and projecting the total score to a lower total score system. We can estimate the risk for predicting 5-, 7- or 10-year survival in KIRC.

decreased in Parkinson disease, oxidative phosphorylation, phenylalanine metabolism.

3.8 Validation of mRNA differential expression of risk model genes in KIRC clinical samples based on qRT-PCR

Based on the analysis of public databases, we successfully screened out 14 risk model genes. To further verify the reliability of the previous experimental results and evaluate the clinical application value, we collected 8 pairs of KIRC pathological tissues and normal control tissues. Based on qRT-PCR experiments, we verified the samples' relative mRNA expression levels of 14 risk model genes (Figures 8A–N). We found that most genes (including MAP3K5, MAP3K8, MAP3K12, MAPK3, NFKB1, RAC1, RPS6KA4, SHC1, STAT1 and TRAF2) were increased in KIRC pathological tissues. In contrast, the mRNA expression levels of MAP2K6, MAP3K9 and RPS6KA5 in KIRC pathological tissues were reduced to varying degrees compared with normal control tissues. The mRNA expression of RPS6KA2 was not statistically significant in the difference analysis.

4 Discussion

In 2020, experts estimated 431,288 new kidney tumors worldwide, and 179,368 patients worldwide died from kidney cancer in the same year (22). Renal cell carcinoma (RCC) originates from renal cortical or tubular epithelial cells, of which KIRC is the most common subtype. The current treatment methods for early KIRC are mainly limited to surgery, and patients often have a good prognosis after surgery (23). However, although the targeted therapies has brought the light of treatment to advanced stage KIRC patients who are ineligible for surgery, drug resistance and side effects have resulted in a median survival of less than 3 years (24). Precision medicine has always been the development trend of current medical diagnosis and treatment, and the establishment of new predictive models will have a positive effect on the early diagnosis of cancers. To this end, we comprehensively

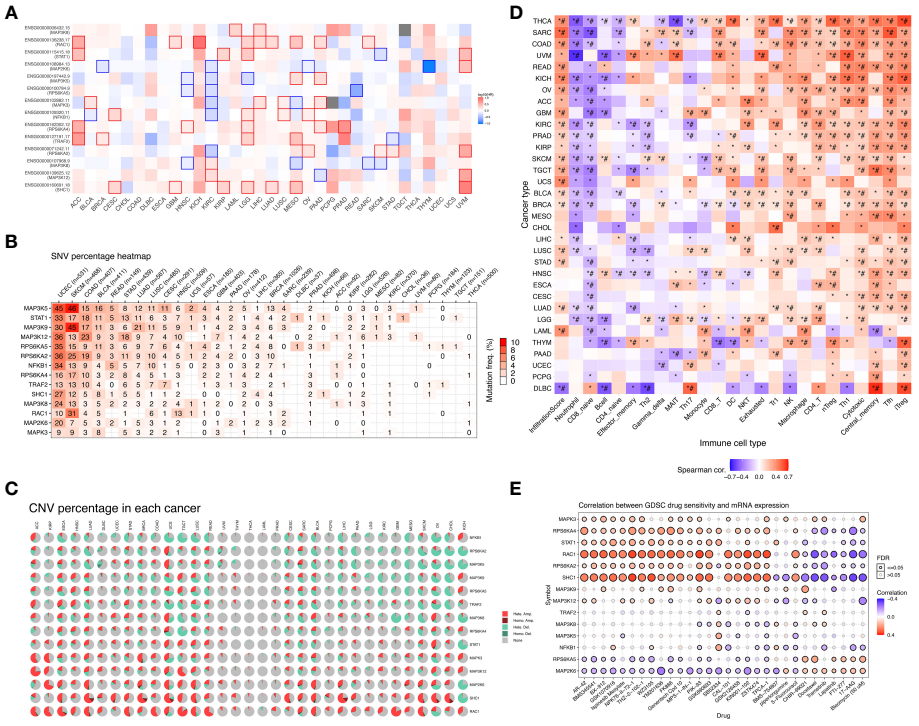

FIGURE 5
Overall survival analysis and variation analysis of this risk model gene in pan-cancer. **(A)** Overall survival analysis of this risk model gene in pan-cancer. Red represents this risk model gene as a risk factor, and blue represents this risk model gene as a protective factor. **(B)** SNV levels of 14 model genes in pan-cancer, where the darker the red color, the higher the probability of SNV. **(C)** CNV ratio of 14 model genes in pan-cancer, Light red hete amp represents heterozygous amplification, light green hete del represents heterozygous deletion, dark red Homo amp represents homozygous amplification, dark green Homo del represents homozygous deletion, and gray represents no CNV. **(D)** The GSVA method was used to analyze the level of immune cell infiltration in 33 different types of tumors, and the Spearman correlation coefficient was used to evaluate its correlation. Red indicates that the level of immune cell infiltration is positively correlated with the tumor. On the contrary, blue indicates a negative correlation. (*P-value $\leq$ 0.05; $^{\#}$FDR $\leq$ 0.05). **(E)** In a sensitivity analysis of prognostic risk model gene mRNA expression and mainstream anticancer drugs, red represents a positive correlation, while blue represents a negative correlation.

used bioinformatics analysis tools and websites to analyze MAPK pathway-related genes in pan-cancer and establish a predictive model in KIRC. In addition, we validated these prognostic genes in KIRC tissues. We hope that this study will provide guidance for the early diagnosis and targeted treatment of KIRC.

We used 14 risk model genes in pan-cancer for CNV, SNV, drug sensitivity, immune infiltration, and overall survival analysis, and predicted other biological pathways that these 14 MAPK pathway-related genes may be involved in. Since the main area of focus of this study is KIRC, we discuss KIRC in more depth. Our study first analyzed the mRNA expression of 81 MAPK pathway-related genes in KIRC patients and normal kidney tissues. The results indicated that nearly 80% of the genes were differentially expressed. Research statistics show that over 85% of cancers have overactive MAPK signaling, which is directly caused by genetic changes in its upstream activators or key molecules (including RTK, RAS, and BRAF) or affected by changes in other regulatory genes (25). These results also demonstrate that altered expression of MAPK pathway-related genes may influence KIRC progression by affecting MAPK signaling pathway transduction. Precision medicine has always been the development trend of current medical diagnosis and treatment, and the establishment of new predictive models has led the way in the diagnosis and treatment of cancers. After univariate COX and LASSO regression analysis, we established a risk model consisting of 14 MAPK pathway-related genes, including RAC1, SHC1, NFKB1, MAPK3, RPS6KA2, RPS6KA4, RPS6KA5, MAP3K5, MAP3K8, MAP3K9, MAP3K12, STAT1, TRAF2, MAP2K6.

RAC1 belongs to the RAS superfamily of small GTP-binding proteins. This molecule often acts as an upstream of the MAPK signaling pathway and is often used as a target for tumor therapy (26). RAC1 inhibitors, such as the compound GYS32661 proved to be effective in tumor therapy. Our investigation further confirmed that RAC1 is highly expressed in ccRCC at the mRNA and protein levels. Further investigation of RAC1 may provide a basis for the therapeutic application of RAC1 inhibitors in ccRCC. The role of SHC1 in the MAPK signaling pathway is mainly to link activated receptor tyrosine kinases to the Ras, which in turn participates in the MAPK signaling cascade. Recent studies have confirmed that SHC1 interacts to form protein complexes to promote the progression of lung cancer (27). This is consistent with the trend

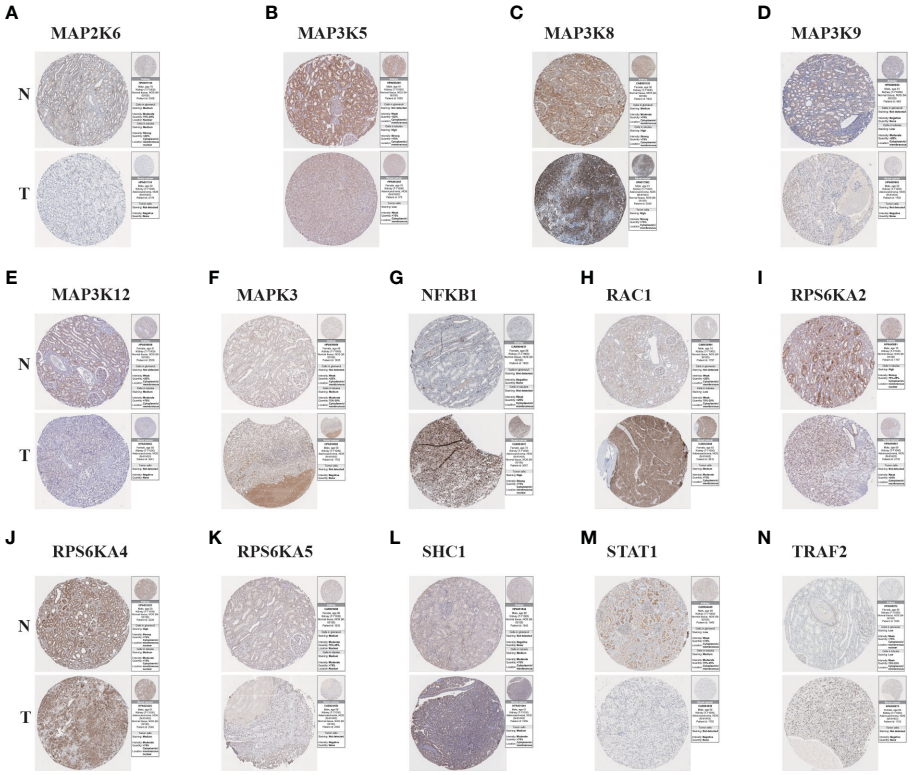

FIGURE 6
The Results of immunohistochemistry. **(A–N)** The Human Protein Atlas database was used to verify the proteins' differential expression of 14 model genes (MAP2K6, MAP3K5, MAP3K8, MAP3K9, MAP3K12, MAPK3, NFKB1, RAC1, RPS6KA2, RPS6KA4, RPS6KA5, SHC1, STAT1, TRAF2) in KIRC tumor tissues (T) and adjacent normal tissues (N).

of elevated expression of SHC1 in ccRCC in our study. NFKB1, a common transcription regulator, acts as a transcriptional regulator and contributes to the infiltration of inflammatory cells by moving to the nucleus when it is activated. The present study demonstrated that NFKB1 mRNA was highly expressed in ccRCC. A related study confirmed that the expression of HIF-1α decreased dramatically in ccRCC cells due to the reduced movement of NF-kB1 to the nucleus, which also inhibited the progression of ccRCC (28). The above results also confirm that the decreased expression of NFKB1 in ccRCC may be associated with the inhibition of tumor progression. MAPK3 encodes a protein that is an important member of the MAP kinase family. MAPK3/ERK1 plays a critical role in the MAPK/ERK cascade. As a recognized oncogene, its role in promoting cancer progression and influencing drug resistance to targeted drugs has been demonstrated in a variety of cancers (29, 30). Mutations in BRCA1-associated protein-1 (BAP1) are very common in ccRCC, and Jin S et al. used PPI network analysis to confirm that mutations in MAPK3, one of the core genes, regulated BAP1 (31). Our study also confirmed the increased mRNA expression of MAPK3 in ccRCC, and whether it could regulate BAP1 to affect the prognosis of ccRCC needs to be further investigated. RPS6KA2, RPS6KA4, and RPS6KA5 belong to the RSK (ribosomal S6 kinase) family of serine/threonine kinases. The common characteristics of this family are that they all have kinase catalytic domains, which can phosphorylate various MAPK signaling pathway-related molecules. Milosevic N et al. showed that RPS6KA2 acts downstream of EGFR/RAS/MEK/ERK signaling and is activated by EGF. Inhibition of its activity could synergize with erlotinib against pancreatic cancer cell survival (32). RPS6KA5 regulates lung tumor growth by activating the MAPK classical signaling pathway through phosphorylation, which in turn phosphorylates TRIM7 protein (33). RPS6KA4 is activated by the RAS-MAPK or p38-MAPK pathway and activates histone H3 by phosphorylation, leading to increased transcription of genes such as proto-oncogene c-fos/FOS and c-jun/JUN (34). MAP3K5, MAP3K8, MAP3K9, and MAP3K8 all belong to the serine/threonine protein kinase family. The above four kinases have been extensively studied in different types. MAP3K8 is a common oncogene in most tumors. Our study likewise confirmed the high expression of MAP3K8 in ccRCC. This molecule can mediate the MAPK signaling pathway by activating MAP kinase and JNK kinase pathways. Many studies have shown that some striking features of the tumor microenvironment can promote immunosuppression and limit the anticancer immune response. Among them, immune cells infiltrating the physical barrier and causing local inflammation play an essential role in forming and developing

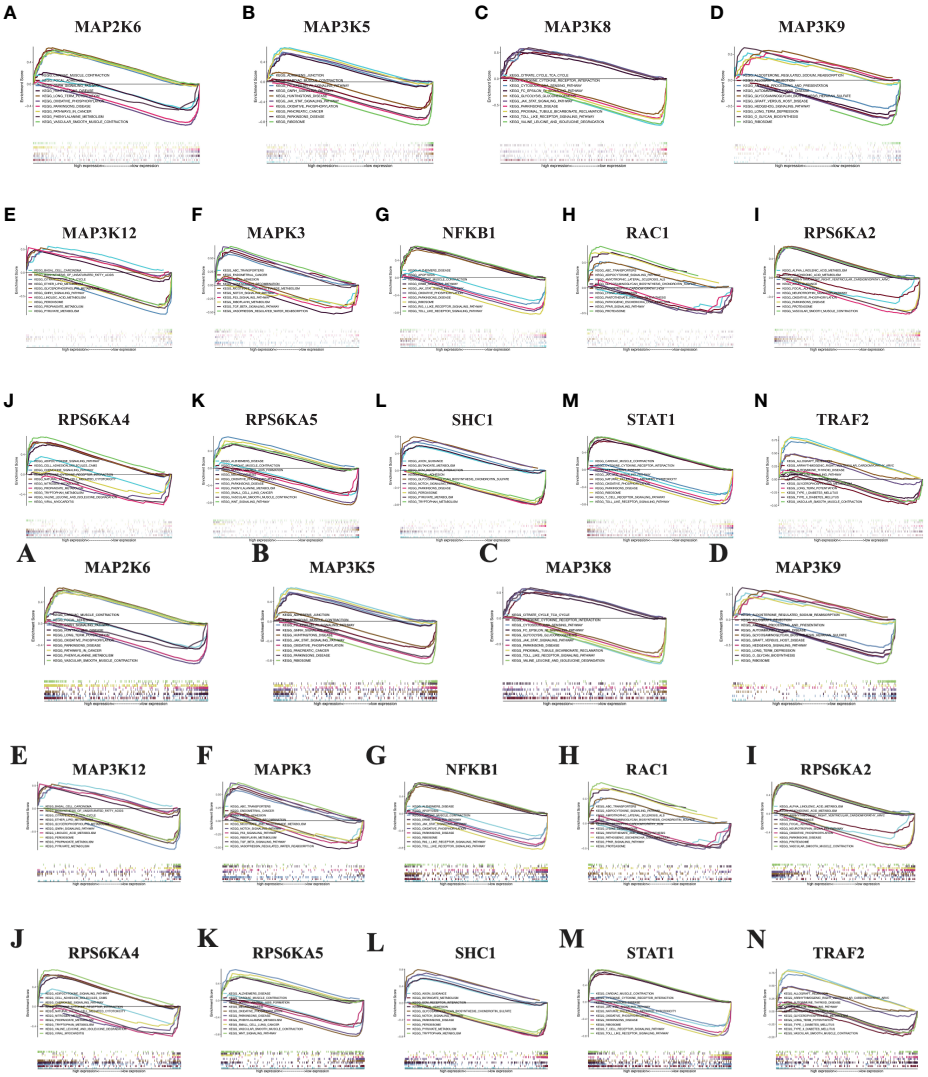

FIGURE 7
GSEA in KIRC. **(A)** MAP2K6. **(B)** MAP3K5. **(C)** MAP3K8. **(D)** MAP3K9. **(E)** MAP3K12. **(F)** MAPK3. **(G)** NFKB1. **(H)** RAC1. **(I)** RPS6KA2. **(J)** RPS6KA4. **(K)** RPS6KA5. **(L)** SHC1. **(M)** STAT1. **(N)** TRAF2.

tumors (35). MAP3K8 also promotes the production of TNF-alpha and IL-2 during T-lymphocyte activation, which also links the MAPK signaling pathway to immune cell infiltration (36–38). STAT1 can be activated by EGF phosphorylation, thus forming a dimer that is transferred to the nucleus to act as a transcriptional activator. Most evidence suggests that STAT1 plays an oncogenic role in tumor cells. However, results from several experimental and clinical studies suggest that STAT1 also functions as a tumor promoter under specific conditions. In ccRCC, STAT1 activation of JAK2/STAT1/IRF-1 signaling drives the expression of PD-L1 in ccRCC (39). TRAF2 interaction with TNF receptors is required for TNF-alpha-mediated JNK MAP kinase signaling and NF-kappaB activation (40). In addition, TRAF2 regulates inflammatory signaling, thereby affecting the immune response to tumors (41, 42). MAP2K6 is one of the important mitogen-activated protein (MAP) kinase kinases in the MAPK signaling pathway. This protein is involved in cell growth or apoptosis by activating p38 MAP kinase in response to immune stimulation or stress. Our study confirmed the differential expression of MAP2K6 in KIRC, which suggests its possible involvement in the biological processes of ccRCC. Recent study confirms MAP2K6 as senescence-related genes in ccRCC may influence the efficacy of anti-PD-1 therapy and Sunitinib/Everolimus treatment (43). Related studies have confirmed that activation of the Ras-MAPK pathway promotes immune evasion of tumor cells, proving that many associated molecules of the MAPK signaling pathway are significantly correlated with immune cell infiltration. MAPK pathway-targeting inhibitors combined with immune drugs can enhance anti-tumor immunity (44). Meanwhile, this study confirmed the alteration of multiple immune cell infiltrations including CD4_T,

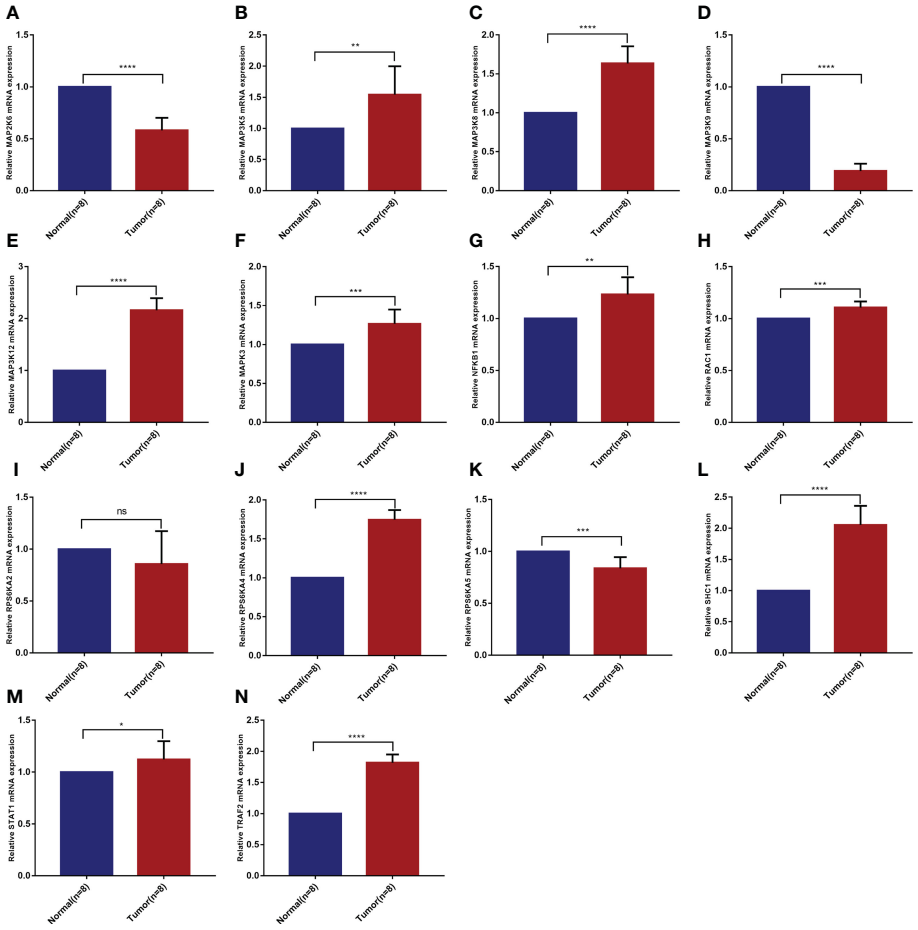

FIGURE 8
Validation of mRNA differential expression of risk model genes between KIRC pathological tissues and normal control tissues based on qRT-PCR. **(A)** MAP2K6. **(B)** MAP3K5. **(C)** MAP3K8. **(D)** MAP3K9. **(E)** MAP3K12. **(F)** MAPK3. **(G)** NFKB1. **(H)** RAC1. **(I)** RPS6KA2. **(J)** RPS6KA4. **(K)** RPS6KA5. **(L)** SHC1. **(M)** STAT1. **(N)** TRAF2. *p < 0.05, **p < 0.01, ***p < 0.001, ****p < 0.0001, ns means no significance.

CD4_naive, and CD8_naive in the immune microenvironment of KIRC. The above studies on the regulation of MAPK signaling-related genes in different tumors for inflammatory cell infiltration and for PD-1/PD-L1 expression seem to explain the changes in immune cell infiltration in ccRCC.

We divided KIRC patients into high-risk and low-risk groups based on this risk model, and KIRC patients in the high-risk group had a lower survival rate than KIRC patients in the low-risk group. The ROC curve calculation results proved the high accuracy of the risk model. We validated the relationship between the risk model and the clinical characteristics of the patients and the results suggest that prognostic model genes influence the tumor volume (T), lymph node (N) distant metastasis (M) of KIRC patients. After identifying age, stage, grading and risk score as the four independent risk factors for KIRC, we drew a nomogram based on these independent risk factors. We could judge the 5-, 7- or 10-year survival of the KIRC patients based on this new nomogram. Numerous studies have investigated the role of MAPK pathway-related genes in different cancers.

In summary, the pathogenesis of KIRC and various cancers are related to the signal changes of the MAPK signaling pathway. The development of drugs acting on this pathway may provide new ideas for treating KIRC and cancer. Research in this field has confirmed that abnormal activation of MAPK is related to tumor cell invasion, migration, proliferation, apoptosis and degradation of extracellular matrix (45). A deeper understanding of the mechanism of action of the MAPK pathway on cancer, especially KIRC, may become the direction of future basic research.

5 Conclusions

In our research, we used 14 genes related to the MAPK signaling pathway to establish a new KIRC predictive risk model, and the role of the ROC curve is to predict the accuracy of the model (5-year AUC value of 0.744, 10-year AUC value of 0.825), suggesting that the model has good predictive performance. However, it must be acknowledged that the specific mechanism of how these 14 genes function in KIRC is not yet clear. In addition, this prognostic risk model needs to be further validated using large-scale multi-center clinical data. However, we firmly believe our study can provide valuable consultation for future scientific diagnosis and clinical treatment of KIRC.

Data availability statement

The original contributions presented in the study are included in the article/supplementary material. Further inquiries can be directed to the corresponding author.

Author contributions

QX and GW designed the research methods. PZ and JL participated in data collection and analyzed the data. ZW, LZ and PZ drafted the manuscript. YX and JL revised the manuscript. PZ and JQ participated in the execution of the experiments. All authors contributed to the article and approved the submitted version.

Funding

This project is supported by grants from the National Natural Science Foundation of China (Grant no. 82072816).

Acknowledgments

PZ is particularly grateful to Yanjie Wang for her assistance in the progress of this research.

Conflict of interest

The authors declare that the research was conducted in the absence of any commercial or financial relationships that could be construed as a potential conflict of interest.

Publisher's note

Supplementary material

The Supplementary Material for this article can be found online at: https://www.frontiersin.org/articles/10.3389/fonc.2023.1077309/full#supplementary-material

References

1. Dy GW, Gore JL, Forouzanfar MH, Naghavi M, Fitzmaurice C. Global burden of urologic cancers, 1990-2013. *Eur Urol* (2017) 71:437–46. doi: 10.1016/j.eururo.2016.10.008

2. Hsieh JJ, Le V, Cao D, Cheng EH, Creighton CJ. Genomic classifications of renal cell carcinoma: a critical step towards the future application of personalized kidney cancer care with pan-omics precision. *J Pathol* (2018) 244:525–37. doi: 10.1002/path.5022

3. Barata PC, Rini BI. Treatment of renal cell carcinoma: Current status and future directions. *CA Cancer J Clin* (2017) 67:507–24. doi: 10.3322/caac.21411

4. Berquist SW, Yim K, Ryan ST, Patel SH, Eldefrawy A, Cotta BH, et al. Systemic therapy in the management of localized and locally advanced renal cell carcinoma: Current state and future perspectives. *Int J Urol* (2019) 26:532–42. doi: 10.1111/iju.13943

5. Hanahan D, Weinberg RA. Hallmarks of cancer: the next generation. *Cell* (2011) 144:646–74. doi: 10.1016/j.cell.2011.02.013

6. Hanahan D, Weinberg RA. The hallmarks of cancer. *Cell* (2000) 100:57–70. doi: 10.1016/S0092-8674(00)81683-9

7. Yuan J, Dong X, Yap J, Hu J. The MAPK and AMPK signalings: interplay and implication in targeted cancer therapy. *J Hematol Oncol* (2020) 13:113. doi: 10.1186/s13045-020-00949-4

8. Rapp UR, Todaro C. Generation of new mouse sarcoma viruses in cell culture. *Science* (1978) 201:821–4. doi: 10.1126/science.210501

9. Cargnello M, Roux PP. Activation and function of the MAPKs and their substrates, the MAPK-activated protein kinases. *Microbiol Mol Biol Rev* (2011) 75:50–83. doi: 10.1128/MMBR.00031-10

10. Johnson DS, Chen YH. Ras family of small GTPases in immunity and inflammation. *Curr Opin Pharmacol* (2012) 12:458–63. doi: 10.1016/j.coph.2012.02.003

11. Braicu C, Buse M, Busuioc C, Drula R, Gulei D, Raduly L, et al. A comprehensive review on MAPK: A promising therapeutic target in cancer. *Cancers (Basel)* (2019) 11 (10):1618. doi: 10.3390/cancers11101618

12. McCain J. The MAPK (ERK) pathway: Investigational combinations for the treatment of BRAF-mutated metastatic melanoma. *P T* (2013) 38(2):96–108.

13. Fanger GR, Johnson NL, Johnson GL. MEK kinases are regulated by EGF and selectively interact with Rac/Cdc42. *EMBO J* (1997) 16:4961–72. doi: 10.1093/emboj/16.16.4961

14. Lavoie H, Therrien M. Regulation of RAF protein kinases in ERK signalling. *Nat Rev Mol Cell Biol* (2015) 16:281–98. doi: 10.1038/nrm3979

15. Stern DF. Keeping tumors out of the MAPK fitness zone. *Cancer Discovery* (2018) 8:20–3. doi: 10.1158/2159-8290.CD-17-1243

16. Tate JG, Bamford S, Jubb HC, Sondka Z, Beare DM, Bindal N, et al. COSMIC: the catalogue of somatic mutations in cancer. *Nucleic Acids Res* (2019) 47:D941–d947. doi: 10.1093/nar/gky1015

17. Salinas-Sánchez AS, Giménez-Bachs JM, Serrano-Oviedo L, Nam Cha S, Sánchez-Prieto R. [Role of mitogen-activated protein kinase (MAPK) in the sporadic renal cell carcinoma]. *Actas Urol Esp* (2012) 36:99–103. doi: 10.1016/j.acuro.2011.07.013

18. Li W, Ye K, Li X, Liu X, Peng M, Chen F, et al. YTHDC1 is downregulated by the YY1/HDAC2 complex and controls the sensitivity of ccRCC to sunitinib by targeting the ANXA1-MAPK pathway. *J Exp Clin Cancer Res* (2022) 41:250. doi: 10.1186/s13046-022-02460-9

19. Tang Z, Li C, Kang B, Gao G, Li C, Zhang Z. GEPIA: a web server for cancer and normal gene expression profiling and interactive analyses. *Nucleic Acids Res* (2017) 45 (W1):W98–w102. doi: 10.1093/nar/gkx247

20. Gui CP, Wei JH, Chen YH, Fu LM, Tang YM, Cao JZ, et al. A new thinking: extended application of genomic selection to screen multiomics data for development of novel hypoxia-immune biomarkers and target therapy of clear cell renal cell carcinoma. *Brief Bioinform* (2021) 22(6):bbab173. doi: 10.1093/bib/bbab173

21. Wang K, Guan C, Shang X, Ying X, Mei S, Zhu H, et al. A bioinformatic analysis: the overexpression and clinical significance of FCGBP in ovarian cancer. *Aging (Albany NY)* (2021) 13:7416–29. doi: 10.18632/aging.202601

22. Sung H, Ferlay J, Siegel RL, Laversanne M, Soerjomataram I, Jemal A, et al. Global cancer statistics 2020: GLOBOCAN estimates of incidence and mortality worldwide for 36 cancers in 185 countries. *CA Cancer J Clin* (2021) 71:209–49. doi: 10.3322/caac.21660

23. Xu Y, Li X, Han Y, Wang Z, Han C, Ruan N, et al. A new prognostic risk model based on PPAR pathway-related genes in kidney renal clear cell carcinoma. *PPAR Res* (2020) 2020:6937475. doi: 10.1155/2020/6937475

24. Greef B, Eisen T. Medical treatment of renal cancer: new horizons. *Br J Cancer* (2016) 115:505–16. doi: 10.1038/bjc.2016.230

25. Degirmenci U, Wang M, Hu J. Targeting aberrant RAS/RAF/MEK/ERK signaling for cancer therapy. *Cells* (2020) 9(1):198. doi: 10.3390/cells9010198

26. Bailly C, Beignet J, Loirand G, Sauzeau V. Rac1 as a therapeutic anticancer target: Promises and limitations. *Biochem Pharmacol* (2022) 203:115180. doi: 10.1016/j.bcp.2022.115180

27. Yang P, Li W, Li X. SHC1 promotes lung cancer metastasis by interacting with EGFR. *J Oncol* (2022) 2022:3599832. doi: 10.1155/2022/3599832

28. Zhan B, Dong X, Yuan Y, Gong Z, Li B. hZIP1 inhibits progression of clear cell renal cell carcinoma by suppressing NF-kB/HIF-1α pathway. *Front Oncol* (2021) 11:759818. doi: 10.3389/fonc.2021.759818

29. Deng R, Zhang HL, Huang JH, Cai RZ, Wang Y, Chen YH, et al. MAPK1/3 kinase-dependent ULK1 degradation attenuates mitophagy and promotes breast cancer bone metastasis. *Autophagy* (2021) 17:3011–29. doi: 10.1080/15548627.2020.1850609

30. Cao HY, Xiao CH, Lu HJ, Yu HZ, Hong H, Guo CY, et al. MiR-129 reduces CDDP resistance in gastric cancer cells by inhibiting MAPK3. *Eur Rev Med Pharmacol Sci* (2020) 24:11468. doi: 10.26355/eurrev_202011_23759

31. Jin S, Wu J, Zhu Y, Gu W, Wan F, Xiao W, et al. Comprehensive analysis of BAP1 somatic mutation in clear cell renal cell carcinoma to explore potential mechanisms in silico. *J Cancer* (2018) 9:4108–16. doi: 10.7150/jca.27281

32. Milosevic N, Kühnemuth B, Mühlberg L, Ripka S, Griesmann H, Lölkes C, et al. Synthetic lethality screen identifies RPS6KA2 as modifier of epidermal growth factor receptor activity in pancreatic cancer. *Neoplasia* (2013) 15:1354–62. doi: 10.1593/neo.131660

33. Chakraborty A, Diefenbacher ME, Mylona A, Kassel O, Behrens A. The E3 ubiquitin ligase Trim7 mediates c-Jun/AP-1 activation by ras signalling. *Nat Commun* (2015) 6:6782. doi: 10.1038/ncomms7782

34. Healy S, Khan P, He S, Davie JR. Histone H3 phosphorylation, immediate-early gene expression, and the nucleosomal response: a historical perspective. *Biochem Cell Biol* (2012) 90:39–54. doi: 10.1139/o11-092

35. DePeaux K, Delgoffe GM. Metabolic barriers to cancer immunotherapy. *Nat Rev Immunol* (2021) 21:785–97. doi: 10.1038/s41577-021-00541-y

36. You Y, Wen D, Zeng L, Lu J, Xiao X, Chen Y, et al. ALKBH5/MAP3K8 axis regulates PD-L1+ macrophage infiltration and promotes hepatocellular carcinoma progression. *Int J Biol Sci* (2022) 18:5001–18. doi: 10.7150/ijbs.70149

37. Ren J, Xu Y, Liu J, Wu S, Zhang R, Cao H, et al. MAP3K8 is a prognostic biomarker and correlated with immune response in glioma. *Front Mol Biosci* (2021) 8:779290. doi: 10.3389/fmolb.2021.779290

38. Zhang H, Deng J, Huang K, He Y, Cai Z, He Y. circNup188/miR-760-3p/Map3k8 axis regulates inflammation in cerebral ischemia. *Mol Cell Probes* (2022) 64:101830. doi: 10.1016/j.mcp.2022.101830

39. Ye S, Li S, Qin L, Zheng W, Liu B, Li X, et al. GBP2 promotes clear cell renal cell carcinoma progression through immune infiltration and regulation of PD−L1 expression *via* STAT1 signaling. *Oncol Rep* (2023) 49(3):49. doi: 10.3892/or.2023.8486

40. Borghi A, Verstrepen L, Beyaert R. TRAF2 multitasking in TNF receptor-induced signaling to NF-κB, MAP kinases and cell death. *Biochem Pharmacol* (2016) 116:1–10. doi: 10.1016/j.bcp.2016.03.009

41. Kreckel J, Anany MA, Siegmund D, Wajant H. TRAF2 controls death receptor-induced caspase-8 processing and facilitates proinflammatory signaling. *Front Immunol* (2019) 10:2024. doi: 10.3389/fimmu.2019.02024

42. Xie X, Zhu L, Jie Z, Li Y, Gu M, Zhou X, et al. TRAF2 regulates T cell immunity by maintaining a Tpl2-ERK survival signaling axis in effector and memory CD8 T cells. *Cell Mol Immunol* (2021) 18:2262–74. doi: 10.1038/s41423-020-00583-7

43. Zhou P, Liu Z, Hu H, Lu Y, Xiao J, Wang Y, et al. Comprehensive analysis of senescence characteristics defines a novel prognostic signature to guide personalized treatment for clear cell renal cell carcinoma. *Front Immunol* (2022) 13:901671. doi: 10.3389/fimmu.2022.901671

44. Loi S, Dushyanthen S, Beavis PA, Salgado R, Denkert C, Savas P, et al. RAS/MAPK activation is associated with reduced tumor-infiltrating lymphocytes in triple-negative breast cancer: Therapeutic cooperation between MEK and PD-1/PD-L1 immune checkpoint inhibitors. *Clin Cancer Res* (2016) 22:1499–509. doi: 10.1158/1078-0432.CCR-15-1125

45. Guo YJ, Pan WW, Liu SB, Shen ZF, Xu Y, Hu LL. ERK/MAPK signalling pathway and tumorigenesis. *Exp Ther Med* (2020) 19:1997–2007. doi: 10.3892/etm.2020.8454

10.3389/fonc.2023.1077309

Glossary

RTKs	receptor tyrosine kinases
GEFs	GTP/GDP exchange factors
CTRP	The Cancer Therapeutics Response Portal
GTEx	Genotype-Tissue Expression
PPI	Protein-protein interaction
ERK	extracellular regulated protein kinases
TGFB1	transforming growth factor-beta 1
MKNK1	MAPK interacting serine/threonine kinase 1
MAP3K10	mitogen-activated protein kinase kinase kinase 10
STAT1	signal transducer and activator of transcription 1
MAP3K8	mitogen-activated protein kinase kinase kinase 8
RPS6KB2	ribosomal protein S6 kinase B2
SHC1	SHC adaptor protein 1
TGFB3	transforming growth factor-beta 3
MAP3K9	mitogen-activated protein kinase kinase kinase 9
MAP4K1	mitogen-activated protein kinase kinase kinase kinase 1
TRAF2	TNF receptor associated factor 2
RAC1	Rac family small GTPase 1)
MAP3K12	mitogen-activated protein kinase kinase kinase 12
IKBKB	inhibitor of nuclear factor kappa B kinase subunit beta
MAP2K2	mitogen-activated protein kinase kinase 2
RPS6KA4	ribosomal protein S6 kinase A4
MAPK3	mitogen-activated protein kinase 3
MAPK9	mitogen-activated protein kinase 9
MAP3K1	mitogen-activated protein kinase kinase 1
MAPK8	mitogen-activated protein kinase 8
MAPK1	mitogen-activated protein kinase 1
MAP2K6	mitogen-activated protein kinase kinase 6
MAPK13	mitogen-activated protein kinase 13
MAP3K5	mitogen-activated protein kinase kinase 5
MAP3K13	mitogen-activated protein kinase kinase kinase 13
MAP2K5	mitogen-activated protein kinase kinase 5
CHUK	component of inhibitor of nuclear factor kappa B kinase complex
RAPGEF2	Rap guanine nucleotide exchange factor 2
RPS6KA2	ribosomal protein S6 kinase A2
RPS6KA5	ribosomal protein S6 kinase A5
MAP2K4	mitogen-activated protein kinase kinase 4
MAP4K1	mitogen-activated protein kinase kinase kinase kinase 1
RPS6KA3	ribosomal protein S6 kinase A3

(Continued)

Continued

MAPK5	mitogen-activated protein kinase 5
MAPK7	mitogen-activated protein kinase 7
MAPK10	mitogen-activated protein kinase 10
ELK1	ETS transcription factor ELK1
CREB1	cAMP responsive element binding protein 1
NFKBIA	NFKB inhibitor alpha
ATF2	activating transcription factor 2
NFKB1	nuclear factor kappa B subunit 1
ACC	Adrenocortical carcinoma
BRCA	Breast invasive carcinoma
BLCA	Bladder Urothelial Carcinoma
KICH	Kidney Chromophobe
KIRP	Kidney renal papillary cell carcinoma

frontiers | Frontiers in Oncology

TYPE Review
PUBLISHED 21 March 2023
DOI 10.3389/fonc.2023.1114461

OPEN ACCESS

EDITED BY
Linhui Wang,
Second Military Medical University, China

REVIEWED BY
Wei Huang,
Capital Medical University, China
Haifeng Yang,
Thomas Jefferson University, United States

*CORRESPONDENCE
Yuan Zhu
zhuyuan1990@whu.edu.cn
Lingao Ju
julingao1990@whu.edu.cn

SPECIALTY SECTION
This article was submitted to Genitourinary Oncology, a section of the journal Frontiers in Oncology

RECEIVED 02 December 2022
ACCEPTED 09 March 2023
PUBLISHED 21 March 2023

CITATION
Yu M, Qian K, Wang G, Xiao Y, Zhu Y and Ju L (2023) Histone methyltransferase SETD2: An epigenetic driver in clear cell renal cell carcinoma.
Front. Oncol. 13:1114461.
doi: 10.3389/fonc.2023.1114461

Histone methyltransferase SETD2: An epigenetic driver in clear cell renal cell carcinoma

Mengxue Yu[1], Kaiyu Qian[2], Gang Wang[1,3], Yu Xiao[3,4], Yuan Zhu[3]* and Lingao Ju[1,5]*

[1]Department of Biological Repositories, Zhongnan Hospital of Wuhan University, Wuhan, China, [2]Department of Urology, Zhongnan Hospital of Wuhan University, Wuhan, China, [3]Human Genetic Resources Preservation Center of Hubei Province, Wuhan, China, [4]Wuhan Research Center for Infectious Diseases and Cancer, Chinese Academy of Medical Sciences, Wuhan, China, [5]Medical Research Institute, Wuhan University, Wuhan, China

SET domain-containing 2 (SETD2) is a lysine methyltransferase that catalyzes histone H3 lysine36 trimethylation (H3K36me3) and has been revealed to play important roles in the regulation of transcriptional elongation, RNA splicing, and DNA damage repair. *SETD2* mutations have been documented in several cancers, including clear cell renal cell carcinoma (ccRCC). *SETD2* deficiency is associated with cancer occurrence and progression by regulating autophagy flux, general metabolic activity, and replication fork speed. Therefore, SETD2 is considered a potential epigenetic therapeutic target and is the subject of ongoing research on cancer-related diagnosis and treatment. This review presents an overview of the molecular functions of SETD2 in H3K36me3 regulation and its relationship with ccRCC, providing a theoretical basis for subsequent antitumor therapy based on SETD2 or H3K36me3 targets.

KEYWORDS

SETD2, clear cell renal cell carcinoma (ccRCC), H3K36me3, epigenetic regulation, mutation

Abbreviations: AWS, associated with SET; AID, auto-inhibitory domain; ATG, autophagy-related genes; ATR, Ataxia telangiectasia and Rad3 related; CTD, C terminal domain; ccRCC, clear cell renal cell carcinoma; CC: coiled-coil; CtIP, C-terminal binding protein interacting protein; DAC, 5-aza-2'-deoxycytidine; DDR, DNA damage response; DSBs, DNA double-strand breaks; DNMT3B, DNA-methyltransferase 3B; emRNA, exosomal mRNA; FH, Fumarate hydratase; GSEA, Gene set enrichment analysis; hnRNP L, heterogeneous nuclear ribonucleoprotein L; H3K36me3: histone H3 lysine36 trimethylation; HR, homologous recombination; HIP1R, HTT-interacting protein 1-related protein; HTT, Huntingtin; LEDGF, Lens epithelium-derived growth factor; MSI, microsatellite instability; MMR, mismatch repair; MRG15, MORF4-related gene on chromosome 15; MDSC, myeloid-derived immune suppressive cell; NHEJ, non-homologous end-joining; PHD, plant homeodomain; PKD, polycystic kidney disease; PTB, polypyrimidine tract-binding protein; PRR, proline-rich region; PWWP, Pro-Trp-Trp-Pro; RCC, renal cell carcinoma; PTECs, renal primary tubular epithelial cells; RPA, replication protein A; PHRF1, ring finger domains 1; RNAPII, RNA polymerase II; RRM2, RNA-recognition motif 2; SAM, S-adenosylmethionine; SDH, Succinate dehydrogenase; SETD2, SET domain-containing 2; SRI, Set2-Rpb1 interacting; SHI, SETD2-hnRNP interaction; ssDNA, single-stranded DNA; VHL, von Hippel-Lindau; ZMYND11, zinc finger MYND-domain containing 11.

1 Introduction

Renal cell carcinoma (RCC) is one of the most prevalent malignancies with a case-fatality rate among urinary tract tumors (1, 2). There are several pathological types of renal cancer, such as clear cell RCC (ccRCC), papillary RCC (pRCC), and chromophobe RCC (chRCC). In the WHO classification, with a list of RCC defined molecularly, including TFE3-rearranged RCC, TFEB-rearranged RCC, ELOC (TCEB1)-mutated RCC, Fumarate hydratase (FH)-deficient RCC, Succinate dehydrogenase (SDH)-deficient RCC, ALK-rearranged RCC, SMARCB1-deficient RCC, and so on (3), a molecular perspective to define RCC is necessary. ccRCC is the major type with a high incidence rate and poor prognosis. Remarkably, several secondary mutations of tumor suppressor genes and chromatin regulators have been identified near von Hippel-Lindau (*VHL*), including *PBRM1*, *BAP1*, and *SETD2* (4). Furthermore, metastatic ccRCC occurs in about 30% of patients, and there are few effective treatment options available (5). Despite advances in chemotherapeutic drugs, chemotherapy resistance remains a problem in ccRCC treatment; therefore, there is an urgent need to understand the regulatory mechanism underlying the recurrence and metastasis of ccRCC, identify possible therapeutic targets and develop new therapeutic options.

Epigenetic regulation, including histone modification, plays a crucial role in maintaining eukaryotic genome stability, gene expression regulation, and chromatin structure. Histone H3 lysine 36 trimethylation (H3K36me3) is involved in the regulation of transcriptional activation and RNA splicing, as well as DNA repair and recombination (6). In mammalian cells, SETD2 is the main H3K36me3 methyltransferase (7), and genomic profiling of ccRCC clinical samples revealed high-frequency *SETD2* mutations. SETD2 has been reported to accelerate ccRCC progression (4, 8) and is a potential prognostic and predictive marker in both localized and metastatic RCC (9). This paper reviews the multiple roles and functions of SETD2 in the occurrence and progression of ccRCC.

2 Protein structure of SETD2

The human SETD2 gene is located in the p21.31 region of chromosome 3, where the copy number is frequently lost in many tumors. Thus, SETD2 is generally considered a tumor suppressor. The human SETD2 protein consists of several conserved functional domains, containing the AWS (associated with SET)-SET-PS (post-SET) domains, WW domains, SRI (Set2-Rpb1 Interacting domain), SETD2-hnRNP interaction (SHI) domains, and a large unstructured N-terminal domain (Figure 1).

2.1 The AWS-SET-PS domains

The AWS-SET-PS domains are essential as a catalytic methyltransferase domain for H3K36me3; the AWS and post-SET domains are flanked onto the SET domain at the N- and C-terminally, respectively. All methylation of H3K36me2 to H3K36me3 depends on the SET domain, with S-adenosylmethionine (SAM) as the cofactor, providing an additional methyl (10). It is reported that the H3K36M oncohistone mutation inhibits SETD2 methyltransferase activity; the structure of the SETD2-H3K36M-SAM complex suggests that SAM indirectly affects the SETD2-H3K36M interaction and maintains the SET domain in the proper fold state (11). The AWS-SET-PS domains of SETD2 recognize the α-N helix of histone H3 and bind to the nucleosome DNA by cryo-EM analyses (12).

2.2 The Set2-Rpb1 interacting domain

The SRI domain of 108 amino acids at the C-terminal end is the main region that interacts with RNA polymerase II (RNAPII), entering a transcription elongation phase. The SRI domain binds to RNAPII-C terminal domain (RNAPII-CTD) Ser5P and Ser2P (13) and promotes SETD2 activity to modify H3K36me3, particularly along the 3' end of the coding sequences of long genes (Figure 2). This association is crucial for SETD2 activity and stability. In addition, the SRI domain of SETD2 is also required for microtubule lysine 40 trimethylation (α-TubK40me3) (14, 15) (Figure 2). Molenaar et al. recently reported that overexpression of the SRI domain significantly inhibited H3K36me3 and enlarged cell size (16).

2.3 The WW domain

The WW domain comprises two conserved tryptophan (W) residues in the SETD2 C-terminus. The WW domain interacts with

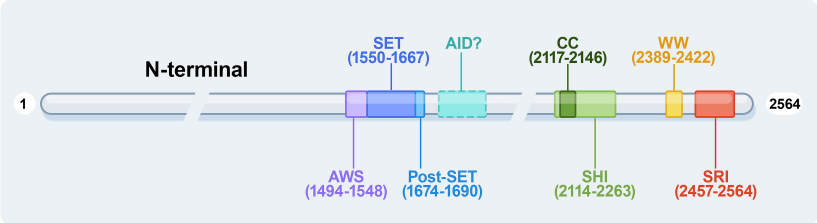

FIGURE 1
The protein domains of human SETD2. AWS, associated with-SET domain; AID, auto-inhibitory domain; WW, tryptophan-tryptophan domain; CC, coiled-coil domain; SHI, SETD2-hnRNP interaction domain; SRI, Set2-Rpb1 interacting domain.

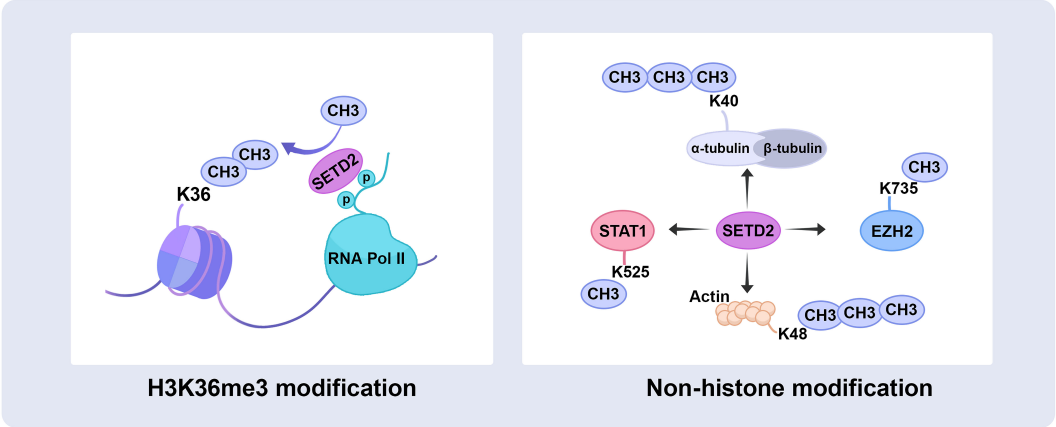

FIGURE 2
SETD2 catalyzes histone and non-histone substrate methylation. SETD2 has initially identified a methyltransferase that trimethylates H3 histones on lysine 36, also occurs on the non-histone substrate, trimethylates α-tubulin at lysine 40 and actin at lysine 68, as well as methylates STAT1 at lysine 525 and EZH2 at lysine 735. RNA Pol II, RNA polymerase II; STAT1, signal transducer and activator of transcription 1; EZH2, enhancer of zeste homolog 2.

proline-rich or proline-containing motifs of other proteins mediating protein-protein interactions (17). For example, the WW domain interacts with the Huntingtin (HTT) proline-rich region (PRR) and the actin-binding adaptor HTT-interacting protein 1-related protein (HIP1R), leading to SETD2 tri-methylating actin at lysine 68 (ActK68me3) (Figure 2). The SETD2-HTT-HIP1R axis modifies actin, which increases actin polymerization and promotes cell migration (18).

2.4 The SHI domain

The structure of the coiled-coil (CC) domain has been predicted by in-silico calculations to be a conserved motif that participates in protein-protein interactions in yeast and promotes protein homodimerization. In human SETD2, the predicted structure of the CC domain is much shorter (19). The SHI domain contains the CC domain and adjacent unstructured sequences in a recently identified region. The histone mark H3K36me3 is known to regulate splicing (8). The SHI region interacts with heterogeneous nuclear ribonucleoprotein L (hnRNP L), RNA-recognition motif 2 (RRM2), as well as other splicing-related factors associated with RNA processing (20). Crystallographic analysis revealed that the Leu-Leu in the SHI domain is important for the interaction (21). Moreover, the double mutant that lacks both the SHI and SRI domains lost practically all catalyzing H3K36me3 activity, indicating that these domains are regulators of SETD2 activity. SETD2 activity toward H3K36me3 modification is similarly influenced by the SHI domain (20).

2.5 Auto-inhibitory domain

The AID domain in the middle region of Set2 (a yeast ortholog of human SETD2) suppresses SET domain activity, and the AID domain suppresses its catalytic activity when the SRI domain is lost. AID mutations usually lead to excessive activity of Set2 *in vivo* and promote the abnormal methylation of Set2 to histones (22). The AID and SRI domains synergistically control the catalytic SET domain, with AID mutations resulting in changes in Set2 protein stability and binding to RNAPII-CTD and variable H3K36me3 levels. In summary, Set2 AID exerts repressive effects requiring the presence of the SRI domain and Set2 SRI to interact with RNAPII and histones, ensuring that H3K36 methylation occurs explicitly on the active transcript chromatin. Therefore, under specific growth conditions, the Set2 autoinhibitory domain may serve as a target for other regulators (23). It would be intriguing to ascertain whether the Set2 AID interacts with any proteins and whether this interaction infuses Set2 activity *via* the AID-SRI axis (19). All the above studies are implemented in yeast, but there are no reports about the structure and function of human AID as yet.

2.6 The large unstructured N–terminal domain

Human SETD2 has an extended N-terminal region with unknown function (~1400 amino acids) and is unstructured. SETD2 is an unstable protein that depends on the degradation of the proteasome (24). It was recently reported that the N-terminal region regulates its half-life by the proteasome system, and removal of the N-terminal region leads to SETD2 stabilization (25), and a segment (aa 1104-1403) of the N-terminal region contributes to SETD2 degradation by the proteasome (24). SETD2 is an intrinsically aggregation-prone protein, and the N-terminal region contributes to SETD2 droplet formation *in vivo*, a property that is enhanced by its reduced degradation. The N-terminal region is conducive to the liquid-liquid phase separation of the protein, and the phase separation behavior of SETD2 intensifies with the removal of the N-terminal fragment (26). Thus, the N-terminal

fragment of SETD2 regulates the amount of SETD2 protein required in the cell and may contribute to its role in regulating transcription and splicing.

3 SETD2 and clear cell renal cell carcinomas

3.1 *SETD2* mutation and ccRCC

VHL inactivation occurs in 90% of all ccRCCs, and several mutations in tumor suppressor genes on chromosome 3p have been identified: *PBRM1*, *BAP1*, and *SETD2* (4, 27). *SETD2* mutations occur in about 15% of ccRCC (4). Mono-allelic and bi-allelic mutations in *SETD2* are observed in many cancers, including ccRCC (28–30). Bi-allelic mutations in *SETD2* cause loss of H3K36me3 in ccRCC (31). *SETD2* gene inactivation mutations are a prevalent molecular feature, and *SETD2* deficiency is associated with ccRCC recurrence and poor prognosis (Tables 1, 2). Moreover, *SETD2* mutations are more frequently found in late-stage ccRCC tumors, which is related to a higher and earlier risk of relapse and poor survival outcomes (9, 50).

Referenced by cBioPortal database and reported research (31, 32, 34, 36–38, 42), *SETD2* mutations were identified in ccRCC predominantly inactivating, containing nonsense mutations, missense mutations, frame shift, and fusion, which lead to loss of function, such as mutations R1625C or R1625G, resulting in a complete loss of SETD2 enzymatic activity (31, 33) (Table 1). The presence of intratumor heterogeneity was confirmed in metastatic renal-cell carcinoma tumors, which demonstrated independent and different *SETD2* mutations in different sections of an individual tumor (51). Thus, SETD2 plays a critical role in the development and progression of ccRCC.

3.2 SETD2 serves as a tumor-suppressor gene in ccRCC

3.2.1 Cryptic transcription

Cryptic transcription initiates transcription from a downstream "promoter-like" region and produces short and meaningless transcripts in gene bodies. Previous studies have demonstrated that SETD2 suppresses cryptic transcription initiation from within several active gene bodies (52, 53). The histone chaperone FACT and its subunits SPT16 and SPT6 promote transcriptional elongation through nucleosome recombination, and deletion of *SETD2* reduces recruitment to FACT and plays a critical role in repressing cryptic intragenic transcriptional initiation (52). In yeast, Set2-mediated prevention of cryptic intragenic transcription is independent on histone deacetylation (54). In mammalian cells, SETD2-mediated H3K36me3 recruits DNA-methyltransferase 3B (DNMT3B), resulting in a high density of DNA methylation, and thus represses transcription from alternate intragenic promoters or initiation of cryptic transcription (55), protecting RNAPII from inappropriate transcription re-initiation and enforced silence intragenic transcription (53, 56). In conclusion, SETD2 is crucial in maintaining active gene bodies dormant in mammalian cells (Figure 3).

3.2.2 RNA splicing

SETD2 is linked to the RNA splicing process. Compared to controls, SHI domain deletion mutation lost interaction with hnRNP L and did not affect splicing events (21). *SETD2*-deficient ccRCC is susceptible to mis-splicing. Gene set enrichment analysis (GSEA) shows that *SETD2*-deficient negatively enriched the gene related to the mRNA splicing pathway (57). A genome-wide transcript profile for *SETD2*-deficient primary ccRCC tumors demonstrated that altered splicing patterns or splicing defects, including intron retention and variation in exon utilization, are widely present in *SETD2*-deficient cancers. Notably, active genes also revealed increased chromatin accessibility (39). The increased chromatin accessibility of upstream abnormally spliced exons and decreased occupancy of nearby nucleosomes significantly contribute to the splicing defect in tumors with H3K36me3 deficiency (58).

Proteins containing the Pro-Trp-Trp-Pro (PWWP) domain play an important role in recognizing H3K36me3. MORF4-related gene on chromosome 15 (MRG15) can bind to H3K36me3 (59, 60) and recruit polypyrimidine tract-binding protein (PTB) to its target alternatively spliced exon sites (61). Lens epithelium-derived growth factor (LEDGF) binds to H3K36me3 (62), as well as to both chromatin and multiple regulators, to modulate alternative splicing events and influence transcription elongation (63, 64). Zinc finger MYND-domain containing 11 (ZMYND11) directly binds to H3K36me3 and H3K36me3-modified chromatin to regulate RNA splicing and Pol II elongation (65, 66). Furthermore, the deficiency of SETD2-mediated H3K36me3 reduces the recruitment of readers, resulting in splicing defects (Figure 3).

3.2.3 DNA damage and repair signaling

SETD2 is vital in the DNA damage response (DDR) by generating H3K36me3. Cell death occurs if DNA repair fails, and tumor development may arise from incorrect DNA repair. SETD2 facilitates DNA double-strand breaks (DSBs) repair by homologous recombination (HR), activating replication protein A (RPA) single-stranded DNA (ssDNA)-binding protein complex loading and the formation of RAD51 presynaptic filaments (35, 62, 67, 68). ATM is activated in DSB, then phosphorylates a variety of downstream effector proteins, such as p53. *SETD2*-deficient cancer cells failed to activate p53 and displayed lower cell survival in DNA damage (62, 67, 68). Ectopic expression of demethylase KDM4A decreased H3K36me3 levels and resulted in HR (62). Consistent with this, LEDGF recruits and binds C-terminal binding protein interacting protein (CtIP), promoting HR by CtIP-dependent DNA end resection (69). Accordingly, the loss of SETD2 obstructs HR repair (70, 71). Also, SETD2 promotes DSB repair *via* combination with plant homeodomain (PHD) of Ring finger domains 1 (PHRF1), modulating non-homologous end-joining (NHEJ) and stabilizing genomic integrity (72). SETD2 has also

TABLE 1 List of *SETD2* mutations reported in ccRCC.

Site	Mutation type	Domain	Function	Ref.
R1625C, R1625H	Missense Mutation	SET	Oncogenic, inactivate SETD2 enzymatic activity	(31–33)
X2413_splice	Splice Site	WW	Oncogenic	(32, 34, 35)
X2478_splice	Splice Site	SRI	Oncogenic, lose the interaction with RNA polymerase II	(32, 34–36)
K2545*	Frame Shift Ins	SRI	Oncogenic, lose the interaction with RNA polymerase II	(32, 34, 35)
T2540Sfs*22, D2504*	Frame Shift Del	SRI	Oncogenic, lose the interaction with RNA polymerase II	(32, 34, 35)
K2511=	Splice Region	SRI	Oncogenic, lose the interaction with RNA polymerase II	(32, 34, 35)
Y2489*	Nonsense Mutation	SRI	Oncogenic, lose the interaction with RNA polymerase II	(32, 34, 35)
X2477_splice	Splice Site	SRI	Oncogenic, lose the interaction with RNA polymerase II	(32, 34, 35)
X2475_splice	Splice Site	SRI	Oncogenic, lose the interaction with RNA polymerase II	(32, 34, 35, 37)
Q2207*	Nonsense Mutation	SHI	Oncogenic	(32, 34, 35)
Y1666H	Missense Mutation	SET	Oncogenic, SETD2 Y1666 interact with H3K36M	(38)
Y1666*	Nonsense Mutation	SET	Oncogenic	(32, 34, 35)
X1572_splice	Splice Site	SET	Oncogenic	(32, 34, 35)
V1656Efs*11	Frame Shift Ins	SET	Oncogenic	(32, 34, 35)
X1640_splice	Splice Site	SET	Oncogenic	(32, 34, 35)
X1672_splice	Splice Region	SET	Oncogenic	(32, 34, 35)
Y1688_L1689delins*	Nonsense Mutation	Post-SET	Oncogenic	(32, 34, 35)

(Continued)

TABLE 1 Continued

Site	Mutation type	Domain	Function	Ref.
L2124*	Nonsense Mutation	CC	Oncogenic	(32, 34, 35)
X1529_splice	Splice Site	AWS	Oncogenic	(32, 34, 35)
S203Ifs*33, K1969Nfs*2, P1973Lfs*33, K941Rfs*41, T2372Sfs*54, S708Hfs*54, S595Kfs*3, Y1286Sfs*12, L1778Cfs*9, R1994Nfs*9, P1822Qfs*16 (Germline), R1694Sfs*17, L2364Cfs*8, K1863Sfs*2 (Germline), I669*, D289Mfs*12, P1873Nfs*10, D2004Ifs*2, I1194Yfs*42, Y2296Lfs*72, P2380Tfs*31	Frame Shift Del	–	Oncogenic	(32, 34, 35)
Q109*, S185*, Q256*, R368*, R400*, K466*, E505*, K528*, G538*, S543*, Y545*, S560*, S618*, C727*, E777*, R973*, S996*, Y1113*, W1217*, R1322*, Q1368*, Y1472*, R1492*, E1720*, L1748*, W1782*, E1964*, Q2277*	Nonsense Mutation	–	Oncogenic	(32, 34, 35)
S2382Lfs*47, S546Ffs*2, D1456Gfs*28, T2443Nfs*3, P2288Ifs*22, P230Tfs*7 (Germline)	Frame Shift Ins	–	Oncogenic	(32, 34, 35)
X1485_splice, X2450_splice, X2037_splice	Splice Site	–	Oncogenic	(32, 34, 35)
X2037_splice	Splice Region	–	Oncogenic	(32, 34, 35)
R2510H	Missense Mutation	SRI	Globally restore H3K36me3; loss of both tubulin binding and methylation	(15, 31)
G1681fs, Q320fs	Frame Shift Del	SET	Reduce SETD2 enzymatic activity	(39)
R2510L	Missense Mutation	SRI	Reduce SETD2 enzymatic activity	(39)
E978*, Q1409*	Nonsense Mutation	–	Inactivate SETD2 enzymatic activity	(39)
N1734D, S1769P	Missense Mutation	–	Facilitate localization of hMSH6 (hMutSα) to chromatin	(40)
R2132fsX13	Frame Shift Del	–	Result in a PTC 42 nucleotides downstream	(41)
D1616N	Missense Mutation	SET	Influence methyltransferase activity of SETD2	(41)
T2354A	Missense Mutation	–	Affect transcriptional activation activity	(41)
K2541fs	Frame Shift Ins	SRI	Oncogenic, lose the interaction with RNA polymerase II	(37)
E2120fs	Frame Shift Del	CC	Unknown	(37)
F1651Lfs*12	Frame Shift Del	SET	Unknown	(42)
Q2131*	Nonsense Mutation	CC	Unknown	(42)

(Continued)

TABLE 1 Continued

Site	Mutation type	Domain	Function	Ref.
E2128*	Nonsense Mutation	SHI	Unknown	(42)
T2513I	Missense Mutation	SRI	Unknown	(42)
W2417Lfs*7	Frame Shift Del	WW	Unknown	(42)
C1516S	Missense Mutation	AWS	Unknown	(42)
SETD2-QRICH1	Fusion	–	Oncogenic	(32, 34, 35)

Frame Shift Ins, Frame Shift Insertion; Frame Shift Del, Frame Shift Deletion; PTC, Premature Termination Codons. The asterisk (*) indicates the stop codon.

been proven to trigger DNA mismatch repair (MMR). Specifically, the mismatch recognition protein hMutSα (hMSH2-hMSH6), hMSH6 contains a PWWP domain that recruits and interacts with H3K36me3 like many other H3K36me3 effector proteins. hMSH6 foci are reduced in *SETD2* knockdown cancer cells (40). The crystal structure modeling revealed that H3G34R/V mutations block the SETD2 catalytic activity and inhibit H3K36me3-MSH6 interaction from inducing tumorigenesis (73). *SETD2*-deficient cells exhibit microsatellite instability (MSI) with a high frequency of spontaneous mutations (40). Compared to introns and non-transcribed regions, H3K36me3 and MutS are more enriched in exons as well as active transcriptional regions and transcriptionally protect against actively transcribed genes (74). Recent studies suggest that targeting DDR is feasible to achieve immunotherapy in ccRCC (75, 76) (Figure 3).

3.2.4 Autophagy

Autophagy is involved in physiological and pathological processes and tightly regulated by a network of autophagy-related genes (ATG). Also, the actin cytoskeleton regulates autophagy dynamics (77). Autophagy is an intracellular degradation system procedure associated with cytoplasmic events, and key epigenetic events are recognized to be significant for this progression. De facto, histone post-translational modification plays a central role in regulating transcriptional programs and epigenetic networks during autophagy (78–83).

Autophagy is an important regulatory process in ccRCC (84–86). The deficiency of *SETD2* in ccRCC cells reduces LC3-II expression, which is linked with abnormal cumulative ATG12 in free and complexes containing ATG12, except for the ATG5-ATG12 complex. Furthermore, *SETD2*-loss deregulates alternative splicing, which is related to increased *ATG12* short isoform and reduced conventional *ATG12* long isoform (43). Another research confirms that *SETD2* knockdown causes a decreased expression of *ATG14* long isoform in HeLa cells (87). Whether *ATG14* long isoforms expression is down-regulated in ccRCC cells with a high-frequency mutation in SETD2 remains to be further investigated.

Autophagy also involves the actin cytoskeleton. As mentioned before, SETD2 trimethylates actin (ActK68me3), cells lacking SETD2 have decreased interaction of the actin nucleation-promoting factor WHAMM with its target actin, actin filaments are required for initiation of autophagy in ccRCC, and autophagy markers LC3-II and p62 are decreased (44).

Recent studies display that the components of the autophagic system play a central role in regulating the innate immune system (88, 89). In pancreatic ductal adenocarcinoma cells, autophagy deficiency results in increased MHC-I expression and increased infiltration of $CD8^+$ T cells. Inhibition of autophagy or lysosomal

TABLE 2 Effects and mechanisms of *SETD2* deficiency in ccRCC.

Effect	Mechanism	Cell type	Ref.
Decreased autophagic flux	Increase ATG12 short isoform	ACHN, Caki-1	(43)
	Inhibit the actin-WHAMM interaction	786-O	(44)
Metabolic alterations	Enhance oxidative phosphorylation	786-O	(45)
	Inhibit multiple metabolic-related genes	293T	(46)
Promotes metastases	Induce the recruitment of histone chaperone ASF1A/B and SPT16, increase MMP1 chromatin accessibility	JHRCC12, Caki-2	(47)
Cell cycle arrest	RRM2 expression reduction, dNTP depletion, S-phase arrest	A498	(48)
PKD conversion to ccRCC	Activate the Wnt/β-catenin signaling pathway	PETC, 293T	(49)

ATG12, autophagy-related gene 12; WHAMM, WAS Protein Homolog Associated with Actin, Golgi Membranes, and Microtubules; ASF1A/B, anti-silencing function 1 A/B; SPT16, suppressor of Ty 16; MMP1, matrix metalloproteinase-1; RRM2, Ribonucleotide reductase (RNR) small subunit M2; PKD, Polycystic Kidney Disease.

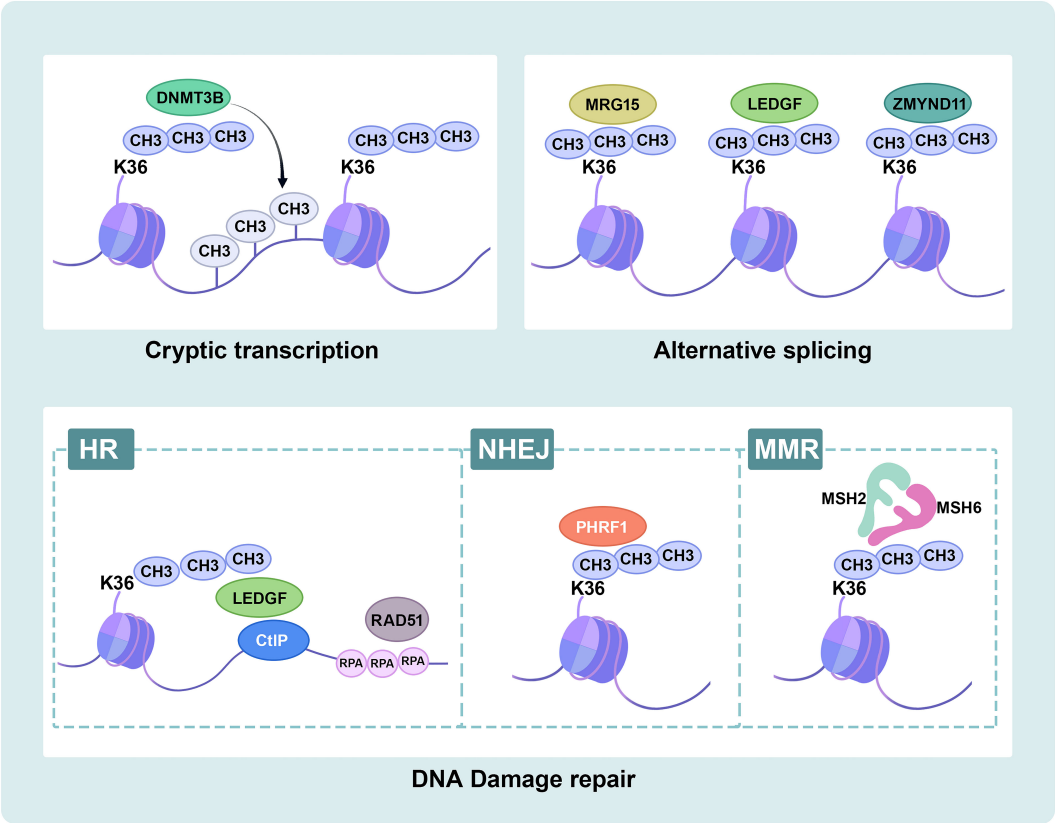

FIGURE 3
Schematic overview of SETD2 functions. SETD2-mediated H3K36me3 plays important biological roles in ccRCC. Cryptic transcription: SETD2-mediated H3K36me3 recruits DNMT3B to target intragenic DNA methylation. RNA splicing: SETD2-mediated H3K36me3 recruits splice factors MRG15, LEDGF and ZMYND11 to modulate alternative splicing events. DNA damage repair: SETD2-mediated H3K36me3 recruits LEDGF, and LEDGF binds CtIP at the break site to promote HR repair. SETD2-mediated H3K36me3 recruits PHRF1 to modulate NHEJ repair. SETD2-mediated H3K36me3 recruits hMutSα (hMSH2-hMSH6) to MMR repair. DNMT3B, DNA-methyltransferase 3B; MRG15, MORF4-related gene on chromosome 15; LEDGF, lens epithelium-derived growth factor; ZMYND11, Zinc finger MYND-domain containing 11; HR, Homologous recombination; CtIP, C-terminal binding protein interacting protein; RPA, replication protein A; NHEJ, non-homologous end-joining; PHRF1, plant homeodomain of Ring finger domains 1; MMR, mismatch repair; MSH2, MutSα homolog 2; MSH6, MutSα homolog 6.

production increases MHC-I expression, enhances the adaptive immune response, and inhibits the generation of tumors (90). Thus, tumor-autonomous autophagy can alter tumor growth by regulating immune responses. SETD2 promotes autophagy flux. Therefore, further understanding the pathways inhibited by *SETD2* deficiency in ccRCC may help identify immunotherapy targets.

3.2.5 Cancer metabolism

ccRCC is considered a metabolic disease and involves several inactivated genes (91), such as *VHL*, controlled tumor energetics and biosynthesis, and the hypoxia pathway (92). The KEGG pathway-based study identified compounds that were present in varied abundance in tumor and normal kidney tissues. Remarkably, most of the upregulated pathways in tumor tissues were engaged in carbohydrate metabolism, whereas the deregulated pathways involved amino acid metabolism (93).

However, the influence of inactivated SETD2 on metabolic reprogramming is unclear. Compared to parental 786-O cells, *SETD2*-deficient cells promote PGC1α, increase oxidative phosphorylation, and elevate mitochondrial oxidative metabolism. Acetyl-CoA is a pivotal substance in biochemical metabolism, which enters the TCA cycle for oxidation and catabolism, and also as a source of fatty acid synthesis, given fatty acid metabolism is always associated with metastasis. Liu et al., hypothesized that enhanced TCA metabolite acetyl-CoA may shunt fatty acid synthesis, resulting in cancer metastasis (45). Compared to wild-type cells, *SETD2* knockout cells inhibit multiple metabolic-related genes in the various metabolic pathways (46). Therefore, tumor metastasis accompanied by metabolic alterations and further metabolic pathways analysis of SETD2 inactivated in ccRCC will have the potential to discover new therapeutics for precision medicine.

3.2.6 Metastases

Previous studies identified an association between SETD2 mutations and the prognosis of patients with localized ccRCC. The mono-allelic mutant of *SETD2* is insignificant in H3K36me3 modification. *SETD2* loss-of-function mutations were revealed in 10%~20% of primary ccRCC tumors, increasing to 30%~60% of metastatic ccRCC tumors. A significant reduction in H3K36

methylation was also found in both ccRCC cell lines and patient samples, suggesting the potential involvement of SETD2 in driving ccRCC metastatic progression (8, 9). In the TCGA cohort, *SETD2* mutations were correlated with poorer cancer-specific survival in ccRCC patients (50). Immunohistochemical staining displayed a gradually decreasing H3K36me3 modification with distant metastases from primary ccRCC tumors. During the progression of ccRCC, H3K36me3 is reduced in distant metastases, and regional H3K36me3 alterations influence alternative splicing in ccRCC (94–97). The H3K36me3 dysregulation axis is linked to an increased risk of death from RCC. Specifically, this connection is substantial, especially for patients with low-risk malignancies (98); however, the mechanism by which SETD2 causes cell metastasis has not been fully elucidated.

The activation of enhancer elements that promote metastatic carcinoma progression has been proven in several cancers, including ccRCC (99–101). Increased chromatin accessibility containing activating enhancers is regulated by aberrant histone chaperone recruitment and activity (102, 103). A recent study has shown that *SETD2* deficiency mediated reduction of H3K36me3 induced the recruitment of histone chaperone ASF1A/B and SPT16, increased MMP1 chromatin accessibility, and activated enhancers to drive genes involved in metastasis, promoted ccRCC metastasis (47).

3.2.7 Cell proliferation and cell cycle regulation

SETD2 stabilization increases cell proliferation contrary to its canonical role as a tumor suppressor (25). According to Li et al., decreased *SETD2* reduces cell proliferation and can be restored by *CDK1* knockdown. Multiple SETD2-regulated cellular pathways suppress cancer development and uncover mechanisms underlying aberrant cell cycle regulation in *SETD2*-depleted cells (46). SETD2 is a tumor suppressor in renal primary tubular epithelial cells (PTECs). The proliferative capacity of SETD2-knockdown PTECs was higher than that of SETD2 wild-type PTECs, indicating that SETD2 inactivation enables PTECs to facilitate a malignant transformation toward ccRCC (67).

Generally, DNA damage could cause cell cycle arrest. The abundance of H3K36me3 ensures the recruitment of DNA damage repair key proteins during DNA replication to restore genome integrity in G1 and early S phase (40, 104). Replication fork speed is also decreased in ccRCC cells when *SETD2* is depleted (35). Throughout the cell cycle, the SETD2 protein level is minimal in G1 and maximal in G2/M. Both H3K36me3 and WEE1 are critical in DNA replication and promote ribonucleotide reductase subunit (RRM2) expression, respectively. In *SETD2*-deficient cells, WEE1 inhibition reduces dNTP and RRM2 with higher sensitivity, resulting in S-phase arrest (48).

In recent studies, Helena et al. and Zhu et al. found SETD2 can also catalyze H3K37me1 and H3K14me3, H3K14me3 recruits the RPA complex to active Ataxia telangiectasia and Rad3 related (ATR) during replication stress, which plays a crucial role in the DNA replication stress response and negatively regulates replication initiation, the deletion of *SETD2* reduces replication stress in the absence of H3K37me1 and H3K14me3 (105, 106). In conclusion, SETD2 controls the proper course of the S-phase, and catalyzes H3K37me1 and H3K14me3 to regulate the replication progress. However, the detailed correlation between SETD2 and cell cycle regulation is still incomplete and requires further exploration.

3.2.8 Non-histone substrates of SETD2

SETD2 is the main H3K36me3 methyltransferase in mammalian cells. Recent studies have suggested that SETD2 could also catalyze non-histone substrate methylation. During ccRCC mitosis, SETD2 trimethylates α-TubK40me3 and maintains genomic stability. Mono-allelic mutation of SETD2 results in α-TubK40me3 deficiency, leading to chromosome abnormalities and genomic instability exhibiting multipolar spindle formation, chromosome bridges, micronuclei, polyploidy, and multiple nuclei (14). SETD2, as a chromatocytoskeletal remodeler, trimethylates ActK68me3. The SETD2-HTT-HIP1R axis modifies actin, which increases actin polymerization and promotes ccRCC migration (18). In addition, SETD2 methylates STAT1 on lysine 525 promotes IFNα-dependent antiviral immunity (107), and methylates EZH2 on lysine 735 inhibits prostate cancer metastasis (33). Since SETD2 and EZH2 commonly occur abnormally in urological cancers, the SETD2-EZH2 axis may also be promising targets for pharmacological intervention in ccRCC. In order to search the specificity substrate sequence of SETD2, the amino acid specificity profile of the SETD2 substrate sequence was determined by the peptide SPOT arrays and find the super-matching methylation site on K666 of FBN-1 (108). Further cytological work is still needed to demonstrate that FBN1 is a methylated substrate of SETD2.

A recent study reported that SETD2 could indirectly methylate non-histone substrates, loss of *SETD2* increases protein translation-related gene expression and decreases eEF1A1 K165me3 and K318me1 in ccRCC, but SETD2 is associated with eEF1A1 methylation indirectly, SET domain of SETD2 regulated the expression of EEF1AKMT2 and EEF1AKMT3, EEF1AKMT3 methylates eEF1A1 on lysine 165 and EEF1AKMT2 methylates eEF1A1 on lysine 318 (109). Finally, the discovery of SETD2 for non-histone substrates is particularly crucial for a more in-depth understanding of its biological role (Figure 2).

3.2.9 Other functions

Recent research has depicted that multiple chromatin remodeling enzymes are genetically inactive in ccRCC. Even though there is emerging evidence that epigenetic changes are important in cancer, only DNA methylation changes have been identified (92). Widespread DNA hypomethylation correlates to the mutation of the H3K36 methyltransferase SETD2 (94).

Patients with polycystic kidney disease (PKD) have a high probability of converting to RCC. However, there is a paucity of knowledge regarding how PKD can develop into RCC, necessitating further research into genetic alterations or the regulation of signaling pathways. Li et al. found that SETD2 deletion can lead to increased activation of the Wnt/β-catenin signaling pathway and promote epithelial-mesenchymal transition and tumor formation.

SETD2 plays an essential role in the process of the conversion of PKD to ccRCC (49).

Emerging evidence suggests that exosomal circRNAs might be potential cancer biomarkers (110–112). He et al. reported that circulating exosomal mRNA (emRNA) is a potential diagnostic biomarker of ccRCC; thus, an emRNA-based screening signature could be developed to provide noninvasive indicators for ccRCC (113).

4 Conclusion

SETD2-mediated H3K36me3 enhances transcriptional elongation and is also involved in DNA damage repair and alternative splicing (Figures 2, 3). *SETD2* mutations have been identified in ccRCC (41), but further research should focus on the association with the function of SETD2 and ccRCC. Loss of SETD2 in ccRCC is related to decreased autophagy processing, greater levels of general metabolic activity, poorer cancer-specific survival in ccRCC patients, and slower replication fork speed.

As a tumor suppressor, *SETD2* may serve as a biomarker to reduce drug resistance to targeted therapy and as a potential therapeutic target to promote individualized treatment and improve patient survival. The TCGA pan-cancer cohort shows that patients with *SETD2* mutations have a higher immune-related gene expression and MSI. Clinical data analysis of cancer patients treated with immune checkpoint inhibitors demonstrated that *SETD2* mutation is a potential biomarker (114). 5-aza-2'-deoxycytidine (DAC) is used clinically to treat tumors with mutations in chromatin regulators, which competitively inhibits DNA methyltransferase activity and demethylates DNA. H3K36me3 is reduced in *SETD2*-deficient tumor cells, decreasing the recruitment of DNMT3B and the methylation of DNA, increasing interferon immune responses and the expression of transposable elements, therefore improving the sensitivity to DAC. In wild-type tumors, the number of myeloid-derived immune suppressive cell (MDSC) increased with DAC treatment. In the SETD2-knockdown tumor model, increased $CD8^+$ T cell infiltration and fewer MDSC following combined treatment with DAC and anti-PD-L1. ccRCC with altered *SETD2* gene provides preclinical support for a therapeutic target for DAC and anti-PD-L1 (57). A case report about advanced HCC showed that immunotherapy could be effective, leading to long-term survival, and they focused on two mutated genes, *SETD2* and *LRP1B*, to further explore (115). Thus, the hypermutated *SETD2* in ccRCC is worthy of attention.

With current innovations in genome engineering and proteomics, the role of SETD2 in normal cells and cancer will be better understood at the molecular level. Nonetheless, it is urgent to explore whether and how SETD2 regulates the molecular mechanisms of recurrence and ccRCC metastasis.

Furthermore, SMYD5 and SETD5 were also demonstrated to catalyze H3K36me3 (7, 116). A growing number of enzymes were initially discovered for methylating additional amino acid residues of histones and other proteins (117), so a reanalysis of known histone methyltransferases is necessary.

In conclusion, the in-depth study of SETD2 during tumor formation and development is warranted for diagnosing, treating, and preventing tumors. It is anticipated that further epigenetics studies will reveal the regulatory pathway of SETD2 expression.

Author contributions

YZ and LJ supervised the review study. MY, YZ, and LJ reviewed the literature and drafted the first draft. GW and KQ provided suggestions to improve the draft. MY, YX, and LJ edited the figures and tables. All authors contributed to the article and approved the submitted version.

Funding

This study was supported by the National Natural Science Foundation of China (31900902), Hubei Province health and family planning scientific research project (WJ2023M063), and Non-profit Central Research Institute Fund of Chinese Academy of Medical Sciences (2020-PT320-004).

Acknowledgments

We gratefully acknowledge the exceptional assistance in editing diagram by Dr. Yuruo Chen, and we would like to thank Freescience Editorial Team for English language editing.

Conflict of interest

The authors declare that the research was conducted in the absence of any commercial or financial relationships that could be construed as a potential conflict of interest.

Publisher's note

References

1. Sung H, Ferlay J, Siegel RL, Laversanne M, Soerjomataram I, Jemal A, et al. Global cancer statistics 2020: GLOBOCAN estimates of incidence and mortality worldwide for 36 cancers in 185 countries. *CA Cancer J Clin* (2021) 71(3):209–49. doi: 10.3322/caac.21660

2. Siegel RL, Miller KD, Fuchs HE, Jemal A. Cancer statistics, 2022. *CA Cancer J Clin* (2022) 72(1):7–33. doi: 10.3322/caac.21708

3. WHO. *Classification of tumours, urinary and Male genital tumours*. Lyon (France: IARC Press (2022).

4. Walton J, Lawson K, Prinos P, Finelli A, Arrowsmith C, Ailles L. PBRM1, SETD2 and BAP1 - the trinity of 3p in clear cell renal cell carcinoma. *Nat Rev Urol* (2022) 20 (2):96–115. doi: 10.1038/s41585-022-00659-1

5. Patard JJ, Pignot G, Escudier B, Eisen T, Bex A, Sternberg C, et al. ICUD-EAU international consultation on kidney cancer 2010: treatment of metastatic disease. *Eur Urol* (2011) 60(4):684–90. doi: 10.1016/j.eururo.2011.06.017

6. Wagner EJ, Carpenter PB. Understanding the language of Lys36 methylation at histone H3. *Nat Rev Mol Cell Biol* (2012) 13(2):115–26. doi: 10.1038/nrm3274

7. Zhang Y, Fang Y, Tang Y, Han S, Jia J, Wan X, et al. SMYD5 catalyzes histone H3 lysine 36 trimethylation at promoters. *Nat Commun* (2022) 13(1):3190. doi: 10.1038/s41467-022-30940-1

8. Ho TH, Park IY, Zhao H, Tong P, Champion MD, Yan H, et al. High-resolution profiling of histone h3 lysine 36 trimethylation in metastatic renal cell carcinoma. *Oncogene.* (2016) 35(12):1565–74. doi: 10.1038/onc.2015.221

9. Wang J, Liu L, Qu Y, Xi W, Xia Y, Bai Q, et al. Prognostic value of SETD2 expression in patients with metastatic renal cell carcinoma treated with tyrosine kinase inhibitors. *J Urol* (2016) 196(5):1363–70. doi: 10.1016/j.juro.2016.06.010

10. Lam UTF, Tan BKY, Poh JJX, Chen ES. Structural and functional specificity of H3K36 methylation. *Epigenet Chromatin* (2022) 15(1):17. doi: 10.1186/s13072-022-00446-7

11. Zhang Y, Shan CM, Wang J, Bao K, Tong L, Jia S. Molecular basis for the role of oncogenic histone mutations in modulating H3K36 methylation. *Sci Rep* (2017) 7:43906. doi: 10.1038/srep43906

12. Liu Y, Zhang Y, Xue H, Cao M, Bai G, Mu Z, et al. Cryo-EM structure of SETD2/Set2 methyltransferase bound to a nucleosome containing oncohistone mutations. *Cell Discovery* (2021) 7(1):32. doi: 10.1038/s41421-021-00261-6

13. Li M, Phatnani HP, Guan Z, Sage H, Greenleaf AL, Zhou P. Solution structure of the Set2-Rpb1 interacting domain of human Set2 and its interaction with the hyperphosphorylated c-terminal domain of Rpb1. *Proc Natl Acad Sci U S A* (2005) 102(49):17636–41. doi: 10.1073/pnas.0506350102

14. Chiang YC, Park IY, Terzo EA, Tripathi DN, Mason FM, Fahey CC, et al. SETD2 haploinsufficiency for microtubule methylation is an early driver of genomic instability in renal cell carcinoma. *Cancer Res* (2018) 78(12):3135–46. doi: 10.1158/0008-5472.CAN-17-3460

15. Kearns S, Mason FM, Rathmell WK, Park IY, Walker C, Verhey KJ, et al. Molecular determinants for alpha-tubulin methylation by SETD2. *J Biol Chem* (2021) 297(1):100898. doi: 10.1016/j.jbc.2021.100898

16. Molenaar TM, Malik M, Silva J, Liu NQ, Haarhuis JHI, Ambrosi C, et al. The histone methyltransferase SETD2 negatively regulates cell size. *J Cell Sci* (2022) 135(19): jcs259856. doi: 10.1242/jcs.259856

17. Gao YG, Yang H, Zhao J, Jiang YJ, Hu HY. Autoinhibitory structure of the WW domain of HYPB/SETD2 regulates its interaction with the proline-rich region of huntingtin. *Structure.* (2014) 22(3):378–86. doi: 10.1016/j.str.2013.12.005

18. Seervai RNH, Jangid RK, Karki M, Tripathi DN, Jung SY, Kearns SE, et al. The huntingtin-interacting protein SETD2/HYPB is an actin lysine methyltransferase. *Sci Adv* (2020) 6(40):eabb7854. doi: 10.1126/sciadv.abb7854

19. Molenaar TM, van Leeuwen F. SETD2: from chromatin modifier to multipronged regulator of the genome and beyond. *Cell Mol Life Sci* (2022) 79 (6):346. doi: 10.1007/s00018-022-04352-9

20. Bhattacharya S, Levy MJ, Zhang N, Li H, Florens L, Washburn MP, et al. The methyltransferase SETD2 couples transcription and splicing by engaging mRNA processing factors through its SHI domain. *Nat Commun* (2021) 12(1):1443. doi: 10.1038/s41467-021-21663-w

21. Bhattacharya S, Wang S, Reddy D, Shen S, Zhang Y, Zhang N, et al. Structural basis of the interaction between SETD2 methyltransferase and hnRNP l paralogs for governing co-transcriptional splicing. *Nat Commun* (2021) 12(1):6452. doi: 10.1038/s41467-021-26799-3

22. Wang Y, Niu Y, Li B. Balancing acts of SRI and an auto-inhibitory domain specify Set2 function at transcribed chromatin. *Nucleic Acids Res* (2015) 43(10):4881–92. doi: 10.1093/nar/gkv393

23. Gopalakrishnan R, Marr SK, Kingston RE, Winston F. A conserved genetic interaction between Spt6 and Set2 regulates H3K36 methylation. *Nucleic Acids Res* (2019) 47(8):3888–903. doi: 10.1093/nar/gkz119

24. Zhu K, Lei PJ, Ju LG, Wang X, Huang K, Yang B, et al. SPOP-containing complex regulates SETD2 stability and H3K36me3-coupled alternative splicing. *Nucleic Acids Res* (2017) 45(1):92–105. doi: 10.1093/nar/gkw814

25. Bhattacharya S, Workman JL. Regulation of SETD2 stability is important for the fidelity of H3K36me3 deposition. *Epigenet Chromatin* (2020) 13(1):40. doi: 10.1186/s13072-020-00362-8

26. Bhattacharya S, Lange JJ, Levy M, Florens L, Washburn MP, Workman JL. The disordered regions of the methyltransferase SETD2 govern its function by regulating its proteolysis and phase separation. *J Biol Chem* (2021) 297(3):101075. doi: 10.1016/j.jbc.2021.101075

27. Kim H, Shim BY, Lee SJ, Lee JY, Lee HJ, Kim IH. Loss of Von hippel-lindau (VHL) tumor suppressor gene function: VHL-HIF pathway and advances in treatments for metastatic renal cell carcinoma (RCC). *Int J Mol Sci* (2021) 22(18):9795. doi: 10.3390/ijms22189795

28. Li J, Ahn JH, Wang GG. Understanding histone H3 lysine 36 methylation and its deregulation in disease. *Cell Mol Life Sci* (2019) 76(15):2899–916. doi: 10.1007/s00018-019-03144-y

29. Skucha A, Ebner J, Grebien F. Roles of SETD2 in leukemia-transcription, DNA-damage, and beyond. *Int J Mol Sci* (2019) 20(5):1029. doi: 10.3390/ijms20051029

30. Xiao C, Fan T, Tian H, Zheng Y, Zhou Z, Li S, et al. H3K36 trimethylation-mediated biological functions in cancer. *Clin Epigenetics* (2021) 13(1):199. doi: 10.1186/s13148-021-01187-2

31. Hacker KE, Fahey CC, Shinsky SA, Chiang YJ, DiFiore JV, Jha DK, et al. Structure/Function analysis of recurrent mutations in SETD2 protein reveals a critical and conserved role for a SET domain residue in maintaining protein stability and histone H3 lys-36 trimethylation. *J Biol Chem* (2016) 291(40):21283–95. doi: 10.1074/jbc.M116.739375

32. Fontebasso AM, Schwartzentruber J, Khuong-Quang DA, Liu XY, Sturm D, Korshunov A, et al. Mutations in SETD2 and genes affecting histone H3K36 methylation target hemispheric high-grade gliomas. *Acta Neuropathol* (2013) 125 (5):659–69. doi: 10.1007/s00401-013-1095-8

33. Yuan H, Han Y, Wang X, Li N, Liu Q, Yin Y, et al. SETD2 restricts prostate cancer metastasis by integrating EZH2 and AMPK signaling pathways. *Cancer Cell* (2020) 38(3):350–65.e7. doi: 10.1016/j.ccell.2020.05.022

34. Zhu X, He F, Zeng H, Ling S, Chen A, Wang Y, et al. Identification of functional cooperative mutations of SETD2 in human acute leukemia. *Nat Genet* (2014) 46 (3):287–93. doi: 10.1038/ng.2894

35. Kanu N, Gronroos E, Martinez P, Burrell RA, Yi Goh X, Bartkova J, et al. SETD2 loss-of-function promotes renal cancer branched evolution through replication stress and impaired DNA repair. *Oncogene.* (2015) 34(46):5699–708. doi: 10.1038/onc.2015.24

36. Dong Y, Zhao X, Feng X, Zhou Y, Yan X, Zhang Y, et al. SETD2 mutations confer chemoresistance in acute myeloid leukemia partly through altered cell cycle checkpoints. *Leukemia.* (2019) 33(11):2585–98. doi: 10.1038/s41375-019-0456-2

37. Hakimi AA, Chen YB, Wren J, Gonen M, Abdel-Wahab O, Heguy A, et al. Clinical and pathologic impact of select chromatin-modulating tumor suppressors in clear cell renal cell carcinoma. *Eur Urol* (2013) 63(5):848–54. doi: 10.1016/j.eururo.2012.09.005

38. Yang S, Zheng X, Lu C, Li GM, Allis CD, Li H. Molecular basis for oncohistone H3 recognition by SETD2 methyltransferase. *Genes Dev* (2016) 30(14):1611–6. doi: 10.1101/gad.284323.116

39. Simon JM, Hacker KE, Singh D, Brannon AR, Parker JS, Weiser M, et al. Variation in chromatin accessibility in human kidney cancer links H3K36 methyltransferase loss with widespread RNA processing defects. *Genome Res* (2014) 24(2):241–50. doi: 10.1101/gr.158253.113

40. Li F, Mao G, Tong D, Huang J, Gu L, Yang W, et al. The histone mark H3K36me3 regulates human DNA mismatch repair through its interaction with MutSalpha. *Cell.* (2013) 153(3):590–600. doi: 10.1016/j.cell.2013.03.025

41. Duns G, van den Berg E, van Duivenbode I, Osinga J, Hollema H, Hofstra RM, et al. Histone methyltransferase gene SETD2 is a novel tumor suppressor gene in clear cell renal cell carcinoma. *Cancer Res* (2010) 70(11):4287–91. doi: 10.1158/0008-5472.CAN-10-0120

42. Scelo G, Riazalhosseini Y, Greger L, Letourneau L, Gonzalez-Porta M, Wozniak MB, et al. Variation in genomic landscape of clear cell renal cell carcinoma across Europe. *Nat Commun* (2014) 5:5135. doi: 10.1038/ncomms6135

43. Gonzalez-Rodriguez P, Engskog-Vlachos P, Zhang H, Murgoci AN, Zerdes I, Joseph B. SETD2 mutation in renal clear cell carcinoma suppress autophagy *via* regulation of ATG12. *Cell Death Dis* (2020) 11(1):69. doi: 10.1038/s41419-020-2266-x

44. Seervai RNH, Grimm SL, Jangid RK, Tripathi DN, Coarfa C, Walker CL. An actin-WHAMM interaction linking SETD2 and autophagy. *Biochem Biophys Res Commun* (2021) 558:202–8. doi: 10.1016/j.bbrc.2020.09.025

45. Liu J, Hanavan PD, Kras K, Ruiz YW, Castle EP, Lake DF, et al. Loss of SETD2 induces a metabolic switch in renal cell carcinoma cell lines toward enhanced oxidative phosphorylation. *J Proteome Res* (2019) 18(1):331–40. doi: 10.1021/acs.jproteome.8b00628

46. Li L, Miao W, Huang M, Williams P, Wang Y. Integrated genomic and proteomic analyses reveal novel mechanisms of the methyltransferase SETD2 in renal cell carcinoma development. *Mol Cell Proteomics* (2019) 18(3):437–47. doi: 10.1074/mcp.RA118.000957

47. Xie Y, Sahin M, Sinha S, Wang Y, Nargund AM, Lyu Y, et al. SETD2 loss perturbs the kidney cancer epigenetic landscape to promote metastasis and engenders actionable dependencies on histone chaperone complexes. *Nat Cancer* (2022) 3(2):188–202. doi: 10.1038/s43018-021-00316-3

48. Pfister SX, Markkanen E, Jiang Y, Sarkar S, Woodcock M, Orlando G, et al. Inhibiting WEE1 selectively kills histone H3K36me3-deficient cancers by dNTP starvation. *Cancer Cell* (2015) 28(5):557–68. doi: 10.1016/j.ccell.2015.09.015

49. Rao H, Li X, Liu M, Liu J, Feng W, Tang H, et al. Multilevel regulation of beta-catenin activity by SETD2 suppresses the transition from polycystic kidney disease to clear cell renal cell carcinoma. *Cancer Res* (2021) 81(13):3554–67. doi: 10.1158/0008-5472.CAN-20-3960

50. Hakimi AA, Ostrovnaya I, Reva B, Schultz N, Chen YB, Gonen M, et al. Adverse outcomes in clear cell renal cell carcinoma with mutations of 3p21 epigenetic regulators BAP1 and SETD2: a report by MSKCC and the KIRC TCGA research network. *Clin Cancer Res* (2013) 19(12):3259–67. doi: 10.1158/1078-0432.CCR-12-3886

51. Gerlinger M, Rowan AJ, Horswell S, Math M, Larkin J, Endesfelder D, et al. Intratumor heterogeneity and branched evolution revealed by multiregion sequencing. *N Engl J Med* (2012) 366(10):883–92. doi: 10.1056/NEJMoa1113205

52. Carvalho S, Raposo AC, Martins FB, Grosso AR, Sridhara SC, Rino J, et al. Histone methyltransferase SETD2 coordinates FACT recruitment with nucleosome dynamics during transcription. *Nucleic Acids Res* (2013) 41(5):2881–93. doi: 10.1093/nar/gks1472

53. Neri F, Rapelli S, Krepelova A, Incarnato D, Parlato C, Basile G, et al. Intragenic DNA methylation prevents spurious transcription initiation. *Nature.* (2017) 543 (7643):72–7. doi: 10.1038/nature21373

54. Ha SD, Ham S, Kim MY, Kim JH, Jang I, Lee BB, et al. Transcription-dependent targeting of Hda1C to hyperactive genes mediates H4-specific deacetylation in yeast. *Nat Commun* (2019) 10(1):4270. doi: 10.1038/s41467-019-12077-w

55. Baubec T, Colombo DF, Wirbelauer C, Schmidt J, Burger L, Krebs AR, et al. Genomic profiling of DNA methyltransferases reveals a role for DNMT3B in genic methylation. *Nature.* (2015) 520(7546):243–7. doi: 10.1038/nature14176

56. Ball MP, Li JB, Gao Y, Lee JH, LeProust EM, Park IH, et al. Targeted and genome-scale strategies reveal gene-body methylation signatures in human cells. *Nat Biotechnol* (2009) 27(4):361–8. doi: 10.1038/nbt.1533

57. Li HT, Jang HJ, Rohena-Rivera K, Liu M, Gujar H, Kulchycki J, et al. RNA Mis-splicing drives viral mimicry response after DNMTi therapy in SETD2-mutant kidney cancer. *Cell Rep* (2023) 42(1):112016. doi: 10.1016/j.celrep.2023.112016

58. Jimeno-Gonzalez S, Payan-Bravo L, Munoz-Cabello AM, Guijo M, Gutierrez G, Prado F, et al. Defective histone supply causes changes in RNA polymerase II elongation rate and cotranscriptional pre-mRNA splicing. *Proc Natl Acad Sci U S A* (2015) 112(48):14840–5. doi: 10.1073/pnas.1506760112

59. Zhang P, Du J, Sun B, Dong X, Xu G, Zhou J, et al. Structure of human MRG15 chromo domain and its binding to Lys36-methylated histone H3. *Nucleic Acids Res* (2006) 34(22):6621–8. doi: 10.1093/nar/gkl989

60. Fang D, Gan H, Lee JH, Han J, Wang Z, Riester SM, et al. The histone H3.3K36M mutation reprograms the epigenome of chondroblastomas. *Science* (2016) 352(6291):1344–8. doi: 10.1126/science.aae0065

61. Luco RF, Pan Q, Tominaga K, Blencowe BJ, Pereira-Smith OM, Misteli T. Regulation of alternative splicing by histone modifications. *Science.* (2010) 327 (5968):996–1000. doi: 10.1126/science.1184208

62. Pfister SX, Ahrabi S, Zalmas LP, Sarkar S, Aymard F, Bachrati CZ, et al. SETD2-dependent histone H3K36 trimethylation is required for homologous recombination repair and genome stability. *Cell Rep* (2014) 7(6):2006–18. doi: 10.1016/j.celrep.2014.05.026

63. Pradeepa MM, Sutherland HG, Ule J, Grimes GR, Bickmore WA. Psip1/Ledgf p52 binds methylated histone H3K36 and splicing factors and contributes to the regulation of alternative splicing. *PloS Genet* (2012) 8(5):e1002717. doi: 10.1371/journal.pgen.1002717

64. LeRoy G, Oksuz O, Descostes N, Aoi Y, Ganai RA, Kara HO, et al. LEDGF and HDGF2 relieve the nucleosome-induced barrier to transcription in differentiated cells. *Sci Adv* (2019) 5(10):eaay3068. doi: 10.1126/sciadv.aay3068

65. Guo R, Zheng L, Park JW, Lv R, Chen H, Jiao F, et al. BS69/ZMYND11 reads and connects histone H3.3 lysine 36 trimethylation-decorated chromatin to regulated pre-mRNA processing. *Mol Cell* (2014) 56(2):298–310. doi: 10.1016/j.molcel.2014.08.022

66. Wen H, Li Y, Xi Y, Jiang S, Stratton S, Peng D, et al. ZMYND11 links histone H3.3K36me3 to transcription elongation and tumour suppression. *Nature* (2014) 508 (7495):263–8. doi: 10.1038/nature13045

67. Li J, Kluiver J, Osinga J, Westers H, van Werkhoven MB, Seelen MA, et al. Functional studies on primary tubular epithelial cells indicate a tumor suppressor role of SETD2 in clear cell renal cell carcinoma. *Neoplasia.* (2016) 18(6):339–46. doi: 10.1016/j.neo.2016.04.005

68. Carvalho S, Vitor AC, Sridhara SC, Martins FB, Raposo AC, Desterro JM, et al. SETD2 is required for DNA double-strand break repair and activation of the p53-mediated checkpoint. *Elife.* (2014) 3:e02482. doi: 10.7554/eLife.02482.016

69. Daugaard M, Baude A, Fugger K, Povlsen LK, Beck H, Sorensen CS, et al. LEDGF (p75) promotes DNA-end resection and homologous recombination. *Nat Struct Mol Biol* (2012) 19(8):803–10. doi: 10.1038/nsmb.2314

70. Marnef A, Cohen S, Legube G. Transcription-coupled DNA double-strand break repair: Active genes need special care. *J Mol Biol* (2017) 429(9):1277–88. doi: 10.1016/j.jmb.2017.03.024

71. Aymard F, Bugler B, Schmidt CK, Guillou E, Caron P, Briois S, et al. Transcriptionally active chromatin recruits homologous recombination at DNA double-strand breaks. *Nat Struct Mol Biol* (2014) 21(4):366–74. doi: 10.1038/nsmb.2796

72. Chang CF, Chu PC, Wu PY, Yu MY, Lee JY, Tsai MD, et al. PHRF1 promotes genome integrity by modulating non-homologous end-joining. *Cell Death Dis* (2015) 6: e1716. doi: 10.1038/cddis.2015.81

73. Fang J, Huang Y, Mao G, Yang S, Rennert G, Gu L, et al. Cancer-driving H3G34V/R/D mutations block H3K36 methylation and H3K36me3-MutSα interaction. *Proc Natl Acad Sci U S A* (2018) 115(38):9598–603. doi: 10.1073/pnas.1806355115

74. Huang Y, Gu L, Li GM. H3K36me3-mediated mismatch repair preferentially protects actively transcribed genes from mutation. *J Biol Chem* (2018) 293(20):7811–23. doi: 10.1074/jbc.RA118.002839

75. Jiang A, Song J, Fang X, Fang Y, Wang Z, Liu B, et al. A novel thinking: DDR axis refines the classification of ccRCC with distinctive prognosis, multi omics landscape and management strategy. *Front Public Health* (2022) 10:1029509. doi: 10.3389/fpubh.2022.1029509

76. Chabanon RM, Rouanne M, Lord CJ, Soria JC, Pasero P, Postel-Vinay S. Targeting the DNA damage response in immuno-oncology: Developments and opportunities. *Nat Rev Cancer* (2021) 21(11):701–17. doi: 10.1038/s41568-021-00386-6

77. Coutts AS, La Thangue NB. Actin nucleation by WH2 domains at the autophagosome. *Nat Commun* (2015) 6:7888. doi: 10.1038/ncomms8888

78. Fullgrabe J, Lynch-Day MA, Heldring N, Li W, Struijk RB, Ma Q, et al. The histone H4 lysine 16 acetyltransferase hMOF regulates the outcome of autophagy. *Nature.* (2013) 500(7463):468–71. doi: 10.1038/nature12313

79. Artal-Martinez de Narvajas A, Gomez TS, Zhang JS, Mann AO, Taoda Y, Gorman JA, et al. Epigenetic regulation of autophagy by the methyltransferase G9a. *Mol Cell Biol* (2013) 33(20):3983–93. doi: 10.1128/MCB.00813-13

80. Fullgrabe J, Klionsky DJ, Joseph B. The return of the nucleus: transcriptional and epigenetic control of autophagy. *Nat Rev Mol Cell Biol* (2014) 15(1):65–74. doi: 10.1038/nrm3716

81. Wei FZ, Cao Z, Wang X, Wang H, Cai MY, Li T, et al. Epigenetic regulation of autophagy by the methyltransferase EZH2 through an MTOR-dependent pathway. *Autophagy.* (2015) 11(12):2309–22. doi: 10.1080/15548627.2015.1117734

82. Shin HJ, Kim H, Oh S, Lee JG, Kee M, Ko HJ, et al. AMPK-SKP2-CARM1 signalling cascade in transcriptional regulation of autophagy. *Nature.* (2016) 534 (7608):553–7. doi: 10.1038/nature18014

83. Baek SH, Kim KI. Epigenetic control of autophagy: Nuclear events gain more attention. *Mol Cell* (2017) 65(5):781–5. doi: 10.1016/j.molcel.2016.12.027

84. Zhu L, Ding R, Yan H, Zhang J, Lin Z. ZHX2 drives cell growth and migration *via* activating MEK/ERK signal and induces sunitinib resistance by regulating the autophagy in clear cell renal cell carcinoma. *Cell Death Dis* (2020) 11(5):337. doi: 10.1038/s41419-020-2541-x

85. Xiao W, Xiong Z, Xiong W, Yuan C, Xiao H, Ruan H, et al. Melatonin/PGC1A/UCP1 promotes tumor slimming and represses tumor progression by initiating autophagy and lipid browning. *J Pineal Res* (2019) 67(4):e12607. doi: 10.1111/jpi.12607

86. Xu Y, Zhou J, Li L, Yang W, Zhang Z, Zhang K, et al. FTO-mediated autophagy promotes progression of clear cell renal cell carcinoma *via* regulating SIK2 mRNA stability. *Int J Biol Sci* (2022) 18(15):5943–62. doi: 10.7150/ijbs.77774

87. González-Rodríguez P, Delorme-Axford E, Bernard A, Keane L, Stratoulias V, Grabert K, et al. SETD2 transcriptional control of ATG14L/S isoforms regulates autophagosome-lysosome fusion. *Cell Death Dis* (2022) 13(11):953. doi: 10.1038/s41419-022-05381-9

88. White J, Suklabaidya S, Vo MT, Choi YB, Harhaj EW. Multifaceted roles of TAX1BP1 in autophagy. *Autophagy.* (2023) 19(1):44–53. doi: 10.1080/15548627.2022.2070331

89. Pan M, Yin Y, Hu T, Wang X, Jia T, Sun J, et al. UXT attenuates the CGAS-STING1 signaling by targeting STING1 for autophagic degradation. *Autophagy.* (2023) 19(2):440–56. doi: 10.1080/15548627.2022.2076192

90. Yamamoto K, Venida A, Perera RM, Kimmelman AC. Selective autophagy of MHC-I promotes immune evasion of pancreatic cancer. *Autophagy.* (2020) 16 (8):1524–5. doi: 10.1080/15548627.2020.1769973

91. Wettersten HI, Aboud OA, Lara PNJr., Weiss RH. Metabolic reprogramming in clear cell renal cell carcinoma. *Nat Rev Nephrol* (2017) 13(7):410–9. doi: 10.1038/nrneph.2017.59

92. Linehan WM, Srinivasan R, Schmidt LS. The genetic basis of kidney cancer: A metabolic disease. *Nat Rev Urol* (2010) 7(5):277–85. doi: 10.1038/nrurol.2010.47

93. Hakimi AA, Reznik E, Lee CH, Creighton CJ, Brannon AR, Luna A, et al. An integrated metabolic atlas of clear cell renal cell carcinoma. *Cancer Cell* (2016) 29 (1):104–16. doi: 10.1016/j.ccell.2015.12.004

94. Cancer Genome Atlas Research N. Comprehensive molecular characterization of clear cell renal cell carcinoma. *Nature* (2013) 499(7456):43–9. doi: 10.1038/nature12222

95. Sato Y, Yoshizato T, Shiraishi Y, Maekawa S, Okuno Y, Kamura T, et al. Integrated molecular analysis of clear-cell renal cell carcinoma. *Nat Genet* (2013) 45 (8):860–7. doi: 10.1038/ng.2699

96. Gerlinger M, Horswell S, Larkin J, Rowan AJ, Salm MP, Varela I, et al. Genomic architecture and evolution of clear cell renal cell carcinomas defined by multiregion sequencing. *Nat Genet* (2014) 46(3):225–33. doi: 10.1038/ng.2891

97. Hsieh JJ, Chen D, Wang PI, Marker M, Redzematovic A, Chen YB, et al. Genomic biomarkers of a randomized trial comparing first-line everolimus and sunitinib in patients with metastatic renal cell carcinoma. *Eur Urol* (2017) 71 (3):405–14. doi: 10.1016/j.eururo.2016.10.007

98. Ho TH, Kapur P, Joseph RW, Serie DJ, Eckel-Passow JE, Tong P, et al. Loss of histone H3 lysine 36 trimethylation is associated with an increased risk of renal cell carcinoma-specific death. *Mod Pathol* (2016) 29(1):34–42. doi: 10.1038/modpathol.2015.123

99. Denny SK, Yang D, Chuang CH, Brady JJ, Lim JS, Gruner BM, et al. Nfib promotes metastasis through a widespread increase in chromatin accessibility. *Cell.* (2016) 166(2):328–42. doi: 10.1016/j.cell.2016.05.052

100. Morrow JJ, Bayles I, Funnell APW, Miller TE, Saiakhova A, Lizardo MM, et al. Positively selected enhancer elements endow osteosarcoma cells with metastatic competence. *Nat Med* (2018) 24(2):176–85. doi: 10.1038/nm.4475

101. Rodrigues P, Patel SA, Harewood L, Olan I, Vojtasova E, Syafruddin SE, et al. NF-kappaB-Dependent lymphoid enhancer Co-option promotes renal carcinoma metastasis. *Cancer Discovery* (2018) 8(7):850–65. doi: 10.1158/2159-8290.CD-17-1211

102. Burgess RJ, Zhang Z. Histone chaperones in nucleosome assembly and human disease. *Nat Struct Mol Biol* (2013) 20(1):14–22. doi: 10.1038/nsmb.2461

103. Venkatesh S, Workman JL. Histone exchange, chromatin structure and the regulation of transcription. *Nat Rev Mol Cell Biol* (2015) 16(3):178–89. doi: 10.1038/nrm3941

104. Sharda A, Humphrey TC. The role of histone H3K36me3 writers, readers and erasers in maintaining genome stability. *DNA repair* (2022) 119:103407. doi: 10.1016/j.dnarep.2022.103407

105. Zhu Q, Yang Q, Lu X, Wang H, Tong L, Li Z, et al. SETD2-mediated H3K14 trimethylation promotes ATR activation and stalled replication fork restart in response to DNA replication stress. *Proc Natl Acad Sci U.S.A.* (2021) 118(23):e2011278118. doi: 10.1073/pnas.2011278118

106. Santos-Rosa H, Millan-Zambrano G, Han N, Leonardi T, Klimontova M, Nasiscionyte S, et al. Methylation of histone H3 at lysine 37 by Set1 and Set2 prevents spurious DNA replication. *Mol Cell* (2021) 81(13):2793–807.e8. doi: 10.1016/j.molcel.2021.04.021

107. Chen K, Liu J, Liu S, Xia M, Zhang X, Han D, et al. Methyltransferase SETD2-mediated methylation of STAT1 is critical for interferon antiviral activity. *Cell.* (2017) 170(3):492–506.e14. doi: 10.1016/j.cell.2017.06.042

108. Schuhmacher MK, Beldar S, Khella MS, Bröhm A, Ludwig J, Tempel W, et al. Sequence specificity analysis of the SETD2 protein lysine methyltransferase and discovery of a SETD2 super-substrate. *Commun Biol* (2020) 3(1):511. doi: 10.1038/s42003-020-01223-6

109. Hapke R, Venton L, Rose KL, Sheng Q, Reddy A, Prather R, et al. SETD2 regulates the methylation of translation elongation factor eEF1A1 in clear cell renal cell carcinoma. *Kidney Cancer J Off J Kidney Cancer Assoc* (2022) 6(3):179–93. doi: 10.3233/kca-220009

110. Kalluri R, LeBleu VS. The biology, function, and biomedical applications of exosomes. *Science.* (2020) 367(6478):eaau6977. doi: 10.1126/science.aau6977

111. Dai J, Su Y, Zhong S, Cong L, Liu B, Yang J, et al. Exosomes: key players in cancer and potential therapeutic strategy. *Signal Transduct Target Ther* (2020) 5(1):145. doi: 10.1038/s41392-020-00261-0

112. Hu W, Liu C, Bi ZY, Zhou Q, Zhang H, Li LL, et al. Comprehensive landscape of extracellular vesicle-derived RNAs in cancer initiation, progression, metastasis and cancer immunology. *Mol Cancer* (2020) 19(1):102. doi: 10.1186/s12943-020-01199-1

113. He X, Tian F, Guo F, Zhang F, Zhang H, Ji J, et al. Circulating exosomal mRNA signatures for the early diagnosis of clear cell renal cell carcinoma. *BMC Med* (2022) 20 (1):270. doi: 10.1186/s12916-022-02467-1

114. Lu M, Zhao B, Liu M, Wu L, Li Y, Zhai Y, et al. Pan-cancer analysis of SETD2 mutation and its association with the efficacy of immunotherapy. *NPJ Precis Oncol* (2021) 5(1):51. doi: 10.1038/s41698-021-00193-0

115. Reiter FP, Rau M, Kunzmann V, Kickuth R, Klein I, Neumann O, et al. Profound tumor response to combined CTLA-4 and PD-1 inhibition in systemic fourth line therapy observed in a patient with hepatocellular carcinoma harboring SETD2 and LRP1B mutations. *Z Gastroenterol* (2023) 61(1):71–5. doi: 10.1055/a-1952-1233

116. Sessa A, Fagnocchi L, Mastrototaro G, Massimino L, Zaghi M, Indrigo M, et al. SETD5 regulates chromatin methylation state and preserves global transcriptional fidelity during brain development and neuronal wiring. *Neuron.* (2019) 104(2):271–89.e13. doi: 10.1016/j.neuron.2019.07.013

117. Husmann D, Gozani O. Histone lysine methyltransferases in biology and disease. *Nat Struct Mol Biol* (2019) 26(10):880–9. doi: 10.1038/s41594-019-0298-7

frontiers | Frontiers in Oncology

TYPE Original Research
PUBLISHED 24 March 2023
DOI 10.3389/fonc.2023.1102623

OPEN ACCESS

EDITED BY
Łukasz Zapała,
Medical University of Warsaw, Poland

REVIEWED BY
Rossana Franzin,
University of Bari Aldo Moro, Italy
Andrew Mallett,
Townsville University Hospital, Australia

*CORRESPONDENCE
Xiaolei Shi
neilsxl@foxmail.com
Meimian Hua
huamm19@163.com

†These authors have contributed equally to this work

SPECIALTY SECTION
This article was submitted to Genitourinary Oncology, a section of the journal Frontiers in Oncology

RECEIVED 19 November 2022
ACCEPTED 14 March 2023
PUBLISHED 24 March 2023

CITATION
Zhang W, Liu W, Yang Y, Xiao C, Xiao Y, Tan X, Pang Q, Wu H, Hua M and Shi X (2023) Integrative analysis of transcriptomic landscape and urinary signature reveals prognostic biomarkers for clear cell renal cell carcinoma. *Front. Oncol.* 13:1102623. doi: 10.3389/fonc.2023.1102623

Integrative analysis of transcriptomic landscape and urinary signature reveals prognostic biomarkers for clear cell renal cell carcinoma

Wei Zhang[1†], Wenqiang Liu[1†], Yiren Yang[1†], Chengwu Xiao[1], Yutian Xiao[1], Xiaojie Tan[2], Qingyang Pang[1], Han Wu[1], Meimian Hua[1*] and Xiaolei Shi[1*]

[1]Department of Urology, Changhai Hospital, Naval Medical University, Shanghai, China, [2]Department of Epidemiology, Naval Medical University, Shanghai, China

Background: Clear cell renal cell carcinoma (ccRCC) patients with venous tumor thrombus (VTT) have poor prognosis. We aimed to reveal features of ccRCC with VTT and develop a urine-based prognostic classifier to predict ccRCC prognosis through integrative analyses of transcriptomic landscape and urinary signature.

Methods: RNA sequencing was performed in five patients with ccRCC thrombus-tumor-normal tissue triples, while mass spectrometry was performed for urine samples from 12 ccRCC and 11 healthy controls. A urine-based classifier consisting of three proteins was developed to predict patients' survival and validated in an independent cohort.

Results: Transcriptomic analysis identified 856 invasion-associated differentially expressed genes (DEGs). Furthermore, proteomic analysis showed 133 differentially expressed proteins (DEPs). Integration of transcriptomic landscape and urinary signature reveals 6 urinary detectable proteins (VSIG4, C3, GAL3ST1, TGFBI, AKR1C3, P4HB) displaying abundance changes consistent with corresponding genes in transcriptomic profiling. According to TCGA database, VSIG4, TGFBI, and P4HB were significantly overexpressed in patients with shorter survival and might be independent prognostic factors for ccRCC (all $p<0.05$). A prognostic classifier consisting of the three DEPs highly associated with survival performed satisfactorily in predicting overall survival (HR=2.0, $p<0.01$) and disease-free survival (HR=1.6, $p<0.001$) of ccRCC patients. The ELISA analysis of urine samples from an independent cohort confirmed the satisfied predictive power of the classifier for pathological grade (AUC=0.795, $p<0.001$) and stage (AUC=0.894, $p<0.001$).

Conclusion: Based on integrative analyses of transcriptomic landscape and urinary signature, the urine-based prognostic classifier consisting of VSIG4, TGFBI, and P4HB has satisfied predictive power of ccRCC prognosis and may facilitate ccRCC molecular subtyping and treatment.

KEYWORDS

clear cell renal cell carcinoma, venous tumor thrombus, prognosis, urine, biomarker

Introduction

Renal cell carcinoma (RCC) is a frequently diagnosed cancer originating from the renal epithelium, with an estimated 431,280 new incidences globally in 2020 (1). RCC comprises a heterogeneous group of malignant tumors, of which the most common (~70%) and aggressive histological subtype is clear cell RCC (ccRCC) (2). ccRCC is prone to metastasis, as about 30% of the patients have metastasis at the first visit, and one-third of the remaining patients have recurrence and metastasis after surgery (3, 4). In addition, 4%-15% of the patients have their primary tumor invading the venous system to form venous tumor thrombus (VTT). The ccRCC patients with VTT exhibit poor prognosis if left untreated, with a 5-year disease-specific survival rate of 10% (2, 5). The current first-line regimen for metastatic and locally advanced ccRCC is immune checkpoint inhibitor combined with tyrosine kinase inhibitor (6). Although it has greatly improved the survival of ccRCC patients, the acquired resistance after receiving treatment or even original drug resistance are still challenges (7–9). Timely identification of these cases would improve the overall survival (OS) of ccRCC patients.

At present, the risk stratification and prognosis prediction models in current clinical practice are mainly pathological characteristics including WHO/ISUP grades and TNM stages (6). However, patients with similar clinical and pathological features may have different prognosis in that ccRCC exhibited extensive functional and genomic intratumoral heterogeneity (10, 11). Therefore, it is urgent to discover those molecular markers related to prognosis, so as to develop a prognostic classifier to facilitate ccRCC molecular subtyping and treatment. As an important method of liquid biopsy, urine is the ideal biological matrix for discovery of cancer biomarkers, in particular for kidney-related diagnostics (12). In addition, its non-invasive and cost-effective natures make it suitable for providing a personalized snapshot of disease during active surveillance or postoperative follow-up (13).

In the study, we first reveal features of ccRCC with VTT through integrative analyses of transcriptomic landscape and urinary signature. Second, a urine-based prognostic classifier consisting of the prognosis-related proteins was developed to predict ccRCC prognosis. Finally, the predictive efficiency of this prognostic classifier was further validated by ELISA analysis of urine samples from an independent cohort to facilitate ccRCC molecular subtyping.

Materials and methods

Patient selection and sample collection

For RNA sequencing, patients were included if they had histologically confirmed ccRCC with VTT. The ccRCC thrombus-tumor-normal tissue triples of 5 cases were obtained following nephrectomy and tumor thrombus resection (Supplementary Table 1). For mass spectrometry, 12 patients with histological-type ccRCC undergoing nephrectomy and 11 healthy donor volunteers from the same period were included (Supplementary Table 2). Their samples of the second urine in the morning were collected before surgery in sterile tubes containing 1 mM of phenylmethanesulfonyl fluoride (Sigma, St. Louis, MO) to inhibit proteases. In addition, 54 urine samples from an independent cohort of consecutive ccRCC patients were also collected for ELISA analysis (Supplementary Table 3). Figure 1 shows a

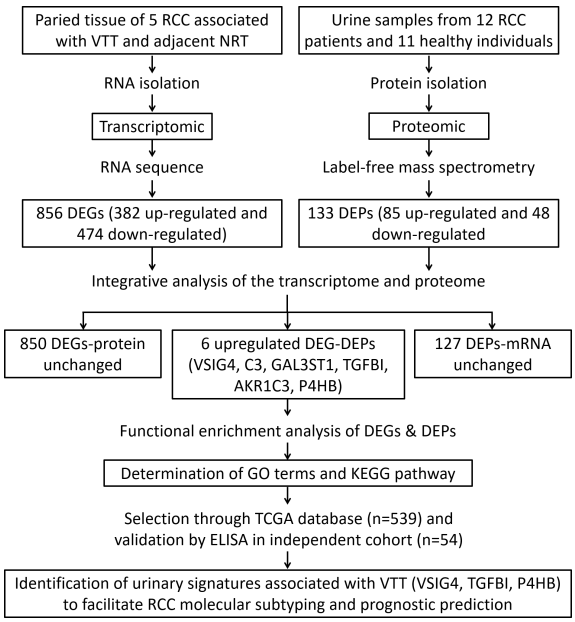

FIGURE 1
Flowchart of RNA sequencing in ccRCC patients with thrombus-tumor-normal tissue triples and mass spectrometry in urine samples from ccRCC patients and healthy controls to develop a urine-based prognostic classifier for predicting ccRCC prognosis.

workflow summary of the transcriptomic and proteomic research that revealed characteristics of ccRCC with VTT and developed a urine-based prognostic classifier to predict ccRCC prognosis. The study was approved by the ethics committee of Changhai Hospital, Naval Medical University, and written informed consent was obtained from all participants prior to study enrollment.

RNA sequencing

Total RNA of thrombus, tumor and normal tissue from ccRCC patients was extracted using the mirVana miRNA Isolation Kit (Ambion, TX, USA) following the manufacturer's instructions. RNA purity was checked using a NanoPhotometer spectrophotometer (IMPLEN, CA, USA). The TruSeq Stranded mRNA LTSample Prep Kit (Illumina, CA, USA) was used to build the libraries. Then these libraries were sequenced on the Illumina sequencing platform (HiSeqTM 2500 or Illumina HiSeq X Ten) and 150 bp paired-end reads were generated.

Mass spectrometry

The urine samples were centrifugated to collect the supernatant, and then the protein extract in urine supernatant was digested into peptides with trypsin. The peptides were subjected to capillary source followed by the timsTOF Pro (Bruker Daltonics) mass spectrometry. The electrospray voltage applied was 1.60 kV. Precursors and fragments were analyzed at the TOF detector, with a MS/MS scan range from 100-1700 m/z. The timsTOF Pro was operated in parallel accumulation serial fragmentation (PASEF) mode. Precursors with charge states 0 to 5 were selected for fragmentation, and 10 PASEF-MS/MS scans were acquired per cycle. The dynamic exclusion was set to 30s.

Analyses of differentially expressed genes/proteins

The analyses of differentially expressed genes (DEGs) and differentially expressed proteins (DEPs) were performed using the "limma" package of R statistical software.

DEGs were divided among three groups: RCC vs. normal renal tissue (NRT), VTT vs. NRT, VTT vs. RCC. The DEGs which co-expressed in RCC vs. NRT and VTT vs. NRT and those in VTT vs. RCC were defined as thrombus invasion-associated genes. Furthermore, DEPs were selected based on their different levels between urinary samples of ccRCC patients and healthy controls. DEGs/DEPs were defined by $|\log2\ FC|>2$ and $P<0.05$. For the public single-cell RNA sequencing data, the transcriptional profiles from all ccRCC patients and samples were visualized *via* uniform manifold approximation and projection. Then, the normalized expressions of DEGs were presented in all single-cell clusters and compared among tissues of ccRCC tumor, adjacent normal kidney, and lymph node. Gene Ontology (GO) functional annotation and Kyoto Encyclopedia of Genes and Genomes (KEGG) pathway enrichment were performed using the "clusterProfiler" package of R statistical software.

Screening of prognostic proteins for survival

Using the survival package, the univariate Cox regression analysis was carried out to targeted proteins linked to OS. (version 3.3.1; https://github.com/therneau/survival). The optimal prognostic protein set for OS was further screened on the basis of SVM-RFE method using the e1071 (version 1.7.1; https://cran.r-project.org/web/packages/e1071) and caret packages (version 6.0.76; https://cran.r-project.org/web/packages/caret). The SVM classifier was then built to predict OS according to the expression levels of optimal prognostic protein set. Additionally, the results of the SVM classification analysis were validated using data from The Cancer Genome Atlas-Kidney Renal Clear Cell Carcinoma (TCGA-KIRC) dataset.

Development and validation of prognostic classifier for survival

The multivariate Cox regression analysis was performed to extract independent prognostic genes for OS using survival package (version 3.3.1; https://github.com/therneau/survival). Afterwards, a risk score model of prognostic makers was established according to following formula: risk score = $\sum\beta$DEPs × ExpDEPs. The βDEPs represented the estimated contribution coefficient of independent prognostic proteins in multivariate Cox regression analysis and ExpDEPs denoted the level of independent prognostic genes. Then, all patients were divided into high- or low-risk groups with the median of risk scores as the cutoff.

Statistical analysis

All data processing and statistical tests were performed using R 4.1.2 and further visualized using GraphPad Prism 6. The continuous parametric variables were displayed as mean ± standard deviation and compared using Student's t-Test. The hazard ratios (ORs) and corresponding 95% confidence intervals (CIs) of the selected predictors of survival were also presented. The difference in survival between two groups was shown with Kaplan-Meier curves, and the receiver operating characteristic curve (ROC) for pathological grades and stages were drawn to obtain the area under the curve (AUC) values. Statistically significant P value was set at 0.05 with two sides.

Results

Transcriptomic landscape and urinary signature of ccRCC patients with VTT

The transcriptomic analysis of 5 matched RCC, VTT and NRT tissues found 1131, 1258, and 63 transcripts differentially expressed

in RCC vs. NRT, VTT vs. NRT, and VTT vs. RCC groups, respectively. Among them, 856 DEGs were obtained as thrombus invasion-associated genes, of which there were 382 up-regulated and 474 down-regulated genes (Figure 2A). In addition, mass spectrometry analysis of urinary samples between 12 ccRCC patients and 11 healthy subjects showed 133 DEPs, with 85 up-regulated and 48 down-regulated proteins (Figure 2B).

The integrative analysis of transcriptomic landscape and urinary signature reveals six urinary detectable proteins (VSIG4, C3, GAL3ST1, TGFBI, AKR1C3, P4HB) displaying upregulated abundance changes consistent with corresponding genes in transcriptomic profiling (Figure 2C). Among them, expressions of TGFBI, AKR1C3, and P4HB increased consecutively from NRT to RCC and then to VTT, indicating that they had a consistent promoting effect in the processes of tumorigenesis and thrombus invasion (Figure 2D). The expressions of the targeted proteins in urine samples of ccRCC patients were over 1.5-time higher than those of healthy controls. However, only the expressions of C3, GAL3ST1, TGFBI, and P4HB achieved statistically significant difference between two groups (Figure 2E).

The upregulated DEPs indicate poor survival in ccRCC patients

We obtained the transcriptional and follow-up data from TCGA and evaluated the correlation between expressions of targeted proteins and prognosis of ccRCC patients. First, the significant higher mRNA levels of all the six proteins in tumor compared to matched normal renal tissue were verified (Figure 3A; Supplementary Figure 1A). Second, in the TCGA cohort of ccRCC patients, increased mRNA levels of VSIG4, TGFBI, P4HB were associated with higher pathological grades (all $p<0.01$) and later pathological stages (all $p<0.05$) (Figures 3B-E). While mRNA levels of C3, AKR1C3, GAL3ST1 were not completely correlated with tumor pathological grades and stages (Supplementary Figures 1B-E). Third, significant expression differences of VSIG4, TGFBI, and P4HB could be seen between patients with different OS events (366 alive vs. 173 dead). They were significantly overexpressed in patients with shorter survival and might be independent prognostic factors for ccRCC patients (all $p<0.05$) (Figure 3F). However, the expression differences of C3, AKR1C3, and GAL3ST1 were not seen in ccRCC patients with different prognosis (Supplementary Figure 1F).

A urine-based prognostic classifier to predict ccRCC prognosis

The qRT-PCR and immunohistochemistry (IHC) experiments were respectively conducted to evaluate the mRNA and protein expression levels of VSIG4, TGFBI, and P4HB in ccRCC thrombus-tumor-normal tissue triples. The qRT-PCR analysis showed that mRNA levels of these three molecules were the highest in VTT, and then their levels in RCC were significantly higher than those in NRT (Figure 4A). The IHC assay further confirmed that protein expressions of VSIG4, TGFBI, and P4HB increased consecutively from normal kidney to renal tumor and then to tumor thrombus (Figure 4B).

The three proteins highly associated with survival (VSIG4, TGFBI, and P4HB) were used to establish a prognostic classifier (Figure 4C). We calculated the risk score of survival in each case from TCGA database according to expression levels of these three proteins, and then divided patients into high- or low-risk groups (Figure 4D). It demonstrated that ccRCC patients in high-risk group had shorter OS time (HR=2.0, $p<0.01$) and disease-free survival (DFS) time (HR=1.6, $p<0.001$) (Figure 4E).

The ELISA analysis was conducted in 54 urine samples from an independent cohort of ccRCC patients. As for the tumor pathological characteristics, the WHO/ISUP grade was I in two cases, II in 41 cases, III in nine cases, and IV in two cases. Urinary detectable TGFBI and P4HB, but not VSIG4, were demonstrated to be higher expressed in patients with III-IV grade tumor than those with I-II grade tumor (Figure 4F). The T stage was T1a in 36 cases, T1b in nine cases, T2 in three cases, and T3-4 in six cases. Urinary detectable VSIG4 and TGFBI, but not P4HB, were demonstrated to be higher expressed in patients with pathological T2-4 stage than those with pathological T1 stage (Figure 4G). Finally, it confirmed the satisfactory predictive power of the prognostic classifier for pathological grade (AUC=0.795, $p<0.001$) (Figure 4H) and stage (AUC=0.894, $p<0.001$) (Figure 4I) in ccRCC patients.

Effects of DEPs on tumor microenvironment and thrombus invasion

To determine the key roles of selected proteins in processes of tumorigenesis and thrombus invasion, we analyze the single-cell RNA-sequencing data obtained from research by Krishna et al (14). Louvain clustering revealed 31 clusters across tissues spanning lymphoid, myeloid, epithelial cells, and cancer cells based on the single-cell RNA-sequencing of 167,283 cells from multiple tumor regions, lymph node, normal kidney of ccRCC patients (Figure 5A). VSIG4 was indicated to be a characteristic marker for tumor-associated macrophage populations, while TGFBI and P4HB were showed to be broadly expressed in ccRCC tumor and its immune microenvironment. Furthermore, the average expression level of P4HB in ccRCC tumor and renal epithelium was the highest among 31 single-cell clusters (Figure 5B). After dividing single-cell transcriptomes into ccRCC tumor, adjacent normal kidney, and lymph node subgroup according to the different sources of each cell. As we can see, the macrophage-expressed VSIG4 in lymph node was higher than that in ccRCC tumor and adjacent normal kidney (Figure 5C), whereas the epithelium-expressed TGFBI and P4HB in ccRCC tumor were higher than those in adjacent normal kidney (Figures 5D, E). In addition, the GO and KEGG enrichment analyses disclosed that those selected proteins were predominantly related to the central carbon metabolism, ferroptosis, ECM-receptor interaction, and platinum drug resistance (Supplementary Figure 2).

10.3389/fonc.2023.1102623

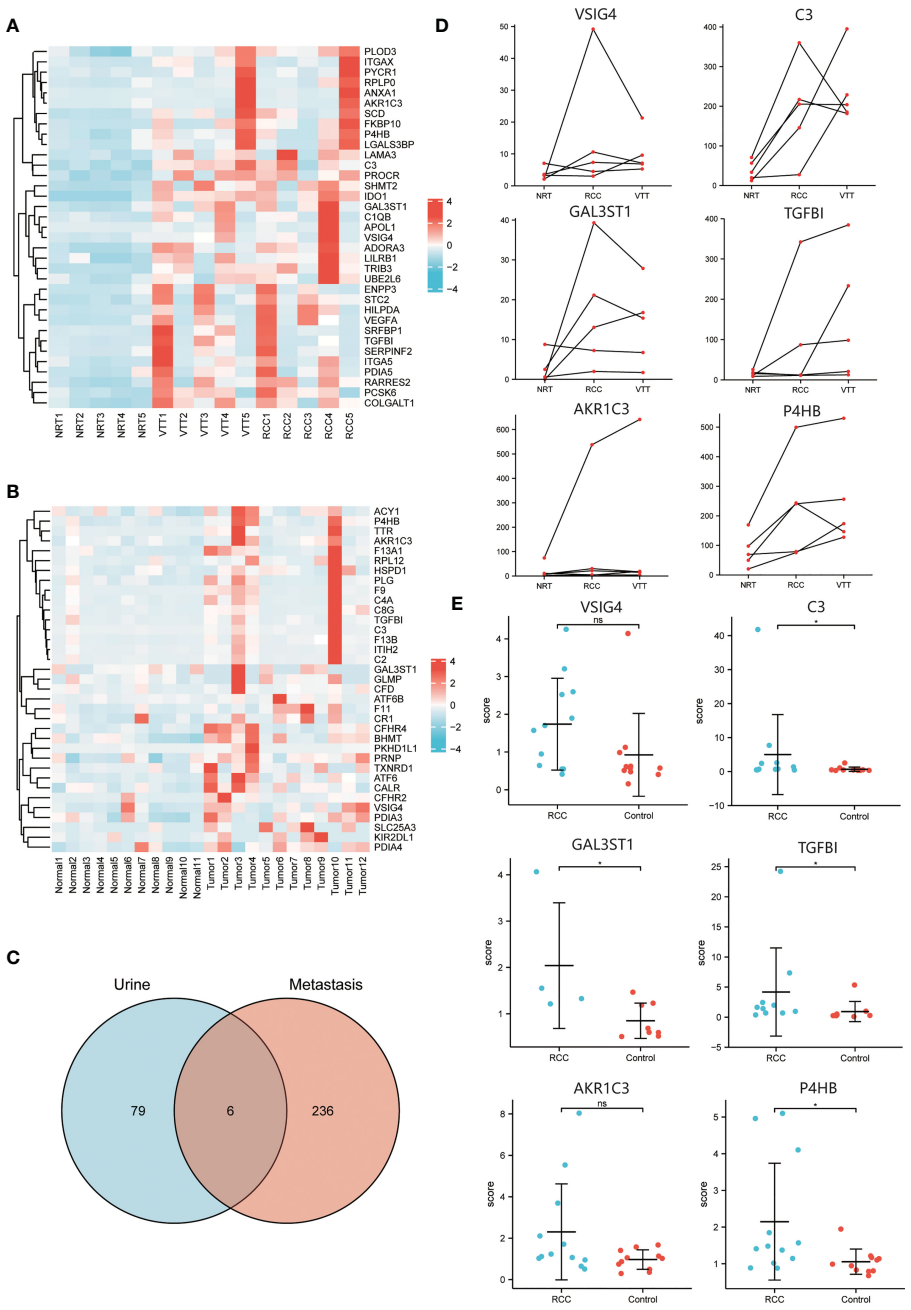

FIGURE 2
The integrative analysis data of transcriptomic landscape and urinary signature in ccRCC patients. **(A)** Heatmap of DEGs in transcriptome analysis of normal, tumor and thrombus tissue showing the top up-regulated thrombus invasion-associated genes. **(B)** Heatmap of DEPs in proteome analysis of urine samples from ccRCC patients and healthy controls showing the top up-regulated proteins. **(C)** Venn diagram to illustrate the six urinary detectable proteins (VSIG4, C3, GAL3ST1, TGFBI, AKR1C3, P4HB) displaying abundance changes consistent with corresponding genes in transcriptomic profiling. **(D)** Regulative expression trends of DEGs among normal, tumor and thrombus tissue indicating expressions of TGFBI, AKR1C3, P4HB increase consecutively from NRT to RCC and then to VTT. **(E)** Different expressions of DEPs in urine between ccRCC patients and healthy controls indicating expressions of VSIG4, C3, GAL3ST1, TGFBI, AKR1C3, P4HB in ccRCC patients are over 1.5-time higher than those in healthy controls. *p < 0.05, ns, no significance.

Discussion

The omics-based analytical approaches are becoming available to enhance the understanding of the tumor pathophysiology (15, 16). Transcriptomic technique focuses on coding and noncoding sequences to identify differentially expressed genes. While proteomic approach makes it an ideal strategy to study the molecular mechanism of RCC. However, given the complexity and variability of the pathophysiological processes involved in RCC, independent analysis from each omics level may miss crosstalk between different molecular entities and biological relevant information (17, 18). In this context, integrated analysis

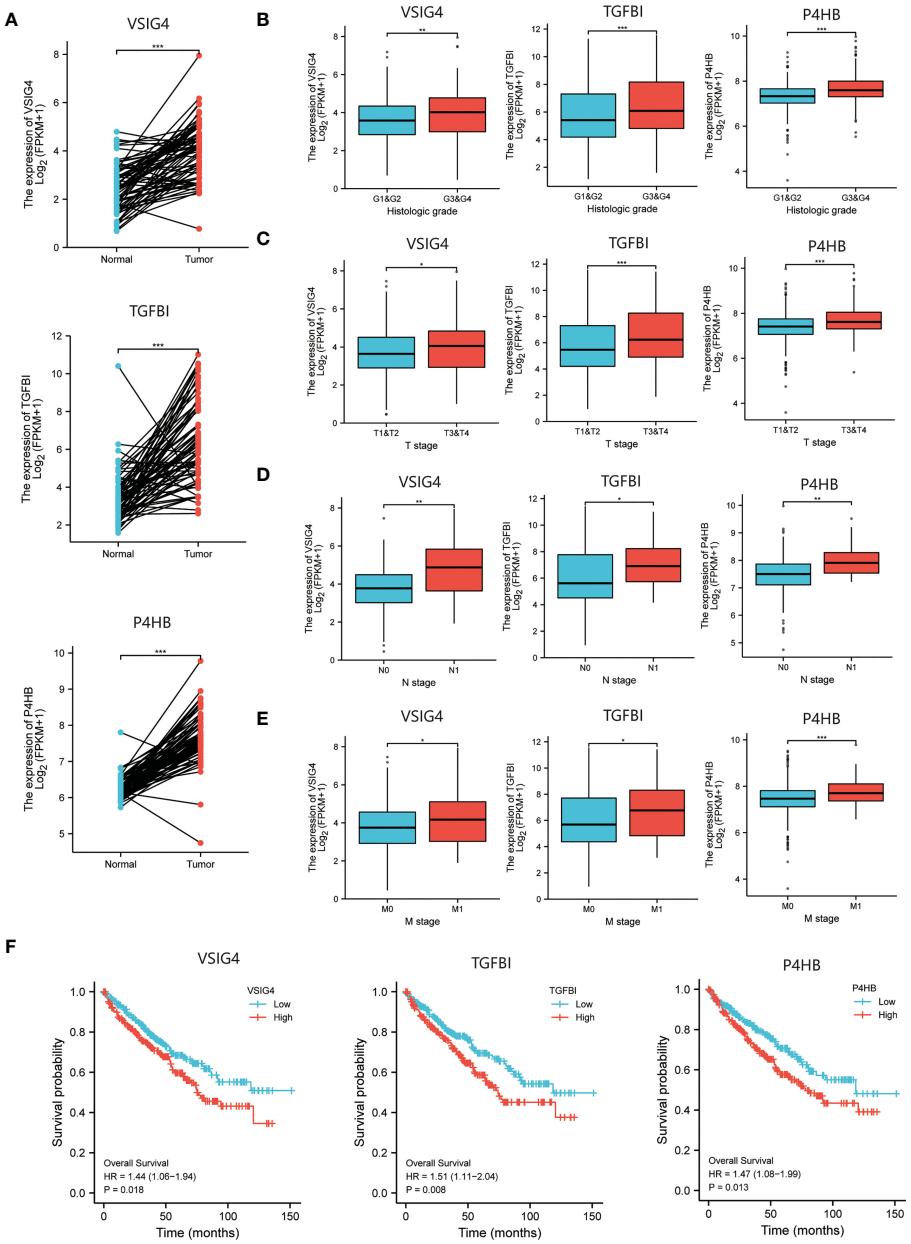

FIGURE 3
The selection of prognosis-related molecules based on TCGA database. **(A)** Different expressions of the prognosis-related genes between ccRCC tumor and normal renal tissue indicating higher mRNA levels of VSIG4, TGFBI, P4HB in tumor compared to matched normal tissue. **(B–E)** Different expressions of the prognosis-related genes between ccRCC patients with different pathological characteristics including WHO/ISUP grades and TNM stages indicating increased mRNA levels of VSIG4, TGFBI, P4HB are associated with higher pathological grades and later pathological stages. **(F)** The Kaplan-Meier curves of OS for ccRCC patients with different expressions of the prognosis-related genes showing VSIG4, TGFBI, P4HB are overexpressed in patients with shorter survival. *p < 0.05, **p < 0.01, ***p < 0.001.

has emerged as a novel approach that facilitate interpretation of multidimensional data and insights into extensive functional and genomic intratumoral heterogeneity in RCC. The ccRCC patients with/without VTT show distinct molecular characteristics in that tumors from ccRCC patients with VTT showed a higher mutational burden and genomic instability (19). Furthermore, macrophages, malignant cells, endothelial cells and myofibroblasts in VTT exhibited enhanced remodeling of the extracellular matrix pathways compared to matched primary cancer cells, providing evidence of phenotypic heterogeneity between primary tumors and tumor thrombus (20). To our knowledge, there have been few studies depicting RCC infiltration into the renal vein by tumor thrombus-related multi-omics analysis (21).

As the number of prognostic biomarkers for ccRCC has been increasing regularly over the last decade, Petitprez et al. (22) performed a review of the relevant studies and found that the predictive methods have evolved from single markers to multiple-marker models. Interestingly, the main genes involved in ccRCC carcinogenesis such as VHL, PBRM1, BAP1, and SETD2, were not the most relevant for predicting survival. Our results suggest that in

10.3389/fonc.2023.1102623

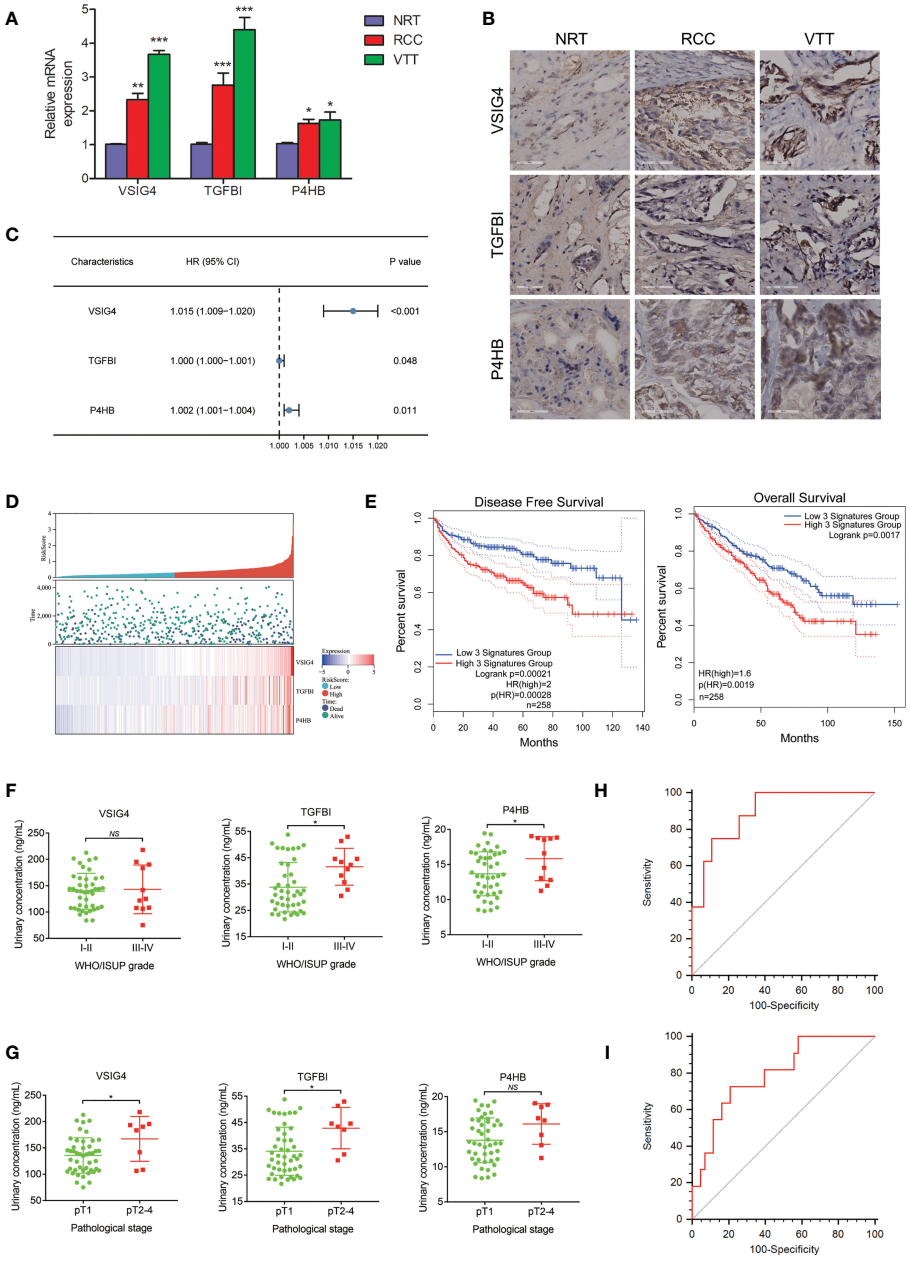

FIGURE 4
The development and validation of a urine-based prognostic classifier for survival. **(A)** qRT-PCR analysis of the selected prognosis-related molecules in ccRCC thrombus-tumor-normal tissue triples showing mRNA levels of VSIG4, TGFBI, P4HB are the highest in VTT, followed by those in RCC and NRT. **(B)** IHC analysis of the selected prognosis-related molecules in ccRCC thrombus-tumor-normal tissue triples showing protein expressions of VSIG4, TGFBI, P4HB increase consecutively from NRT to RCC and then to VTT. **(C)** Forest plot of hazard ratios for the genes in prognostic classifier showing expressions of VSIG4, TGFBI, P4HB are highly associated with survival. **(D)** Distributions of risk score and expression profile of the genes in prognostic classifier in patients with different survival time and status. **(E)** The Kaplan-Meier curves of OS and DFS for ccRCC patients in high-risk and low-risk groups by prognostic classifier in TCGA database showing patients in high-risk group had shorter OS and DFS time. **(F, G)** Different urinary expressions of the proteins in prognostic classifier between ccRCC patients with different pathological grades and stages indicating urinary TGFBI and P4HB are overexpressed in patients with higher grade tumors while urinary VSIG4 and TGFBI are overexpressed in patients with later pathological stages. **(H, I)** The ROCs for the prognostic classifier predicting pathological grade and stage of ccRCC patients by ELISA showing AUC value of 0.795 for pathological grade and AUC value of 0.894 for pathological stage. *p < 0.05, **p < 0.01, ***p < 0.001, NS, no significance.

addition to body biofluid samples including plasma and urine, thrombosis may also contain biomarker information related to the prognosis of ccRCC patients, which can provide new ideas for the discovery of biomarkers. In addition, the constructed prognostic classifier in our study can be detected in urinary specimens. The urine carries a variety of set of soluble proteins and peptides that are primarily derived from kidney, bladder and prostate (23). Chinello et al. (24) conducted integrative proteomic analyses of the urine and blood in ccRCC patients and found that urine carried specific "biofluid functional signature", which provided a landscape of RCC dynamic system of processes in venous infiltration. One major advantage of urinary biomarkers is that the detection of

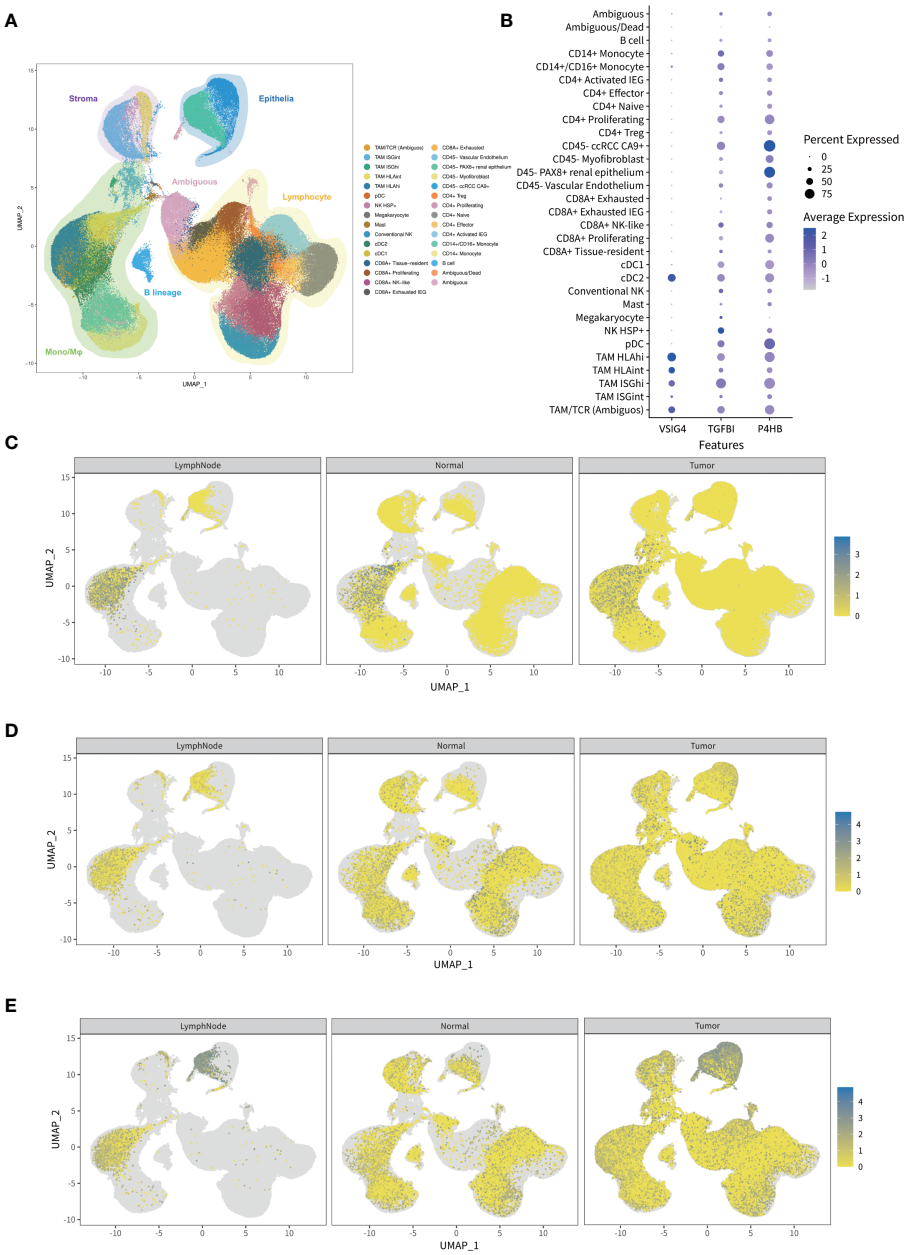

FIGURE 5
The expression analysis of the genes in prognostic classifier through single-cell RNA sequencing public database. **(A)** Visualized map of transcriptional profiles from all ccRCC patients and samples showing 31 single-cell clusters including lymphoid, myeloid, epithelial cells, and cancer cells. **(B)** Normalized expressions of the genes in prognostic classifier among 31 single-cell clusters indicating VSIG4 is uniquely expressed in tumor-associated macrophages while TGFBI and P4HB are broadly expressed. **(C–E)** Comparison of gene expressions among ccRCC tumor, adjacent normal kidney, and lymph node indicating macrophage-expressed VSIG4 is higher in lymph node than tumor while epithelium-expressed TGFBI and P4HB are higher in tumor than normal kidney.

these markers is noninvasive, convenient, high-volume, and easy to evaluate. Thus, this liquid biopsy method can be scheduled frequently to provide a personalized snapshot of disease to actively monitor disease progression. Such narrow control also allows a rapid switch in the case for therapy by any changes (13). In our study, satisfactory predictive power of the urine-based prognostic classifier for pathological grade and stage of ccRCC was finally verified through ELISA analysis of 54 urine samples from an independent cohort.

The review of 341 reported prognostic biomarkers in ccRCC found that 20% of these biomarkers were involved in four biological pathways: hypoxia, angiogenesis, cell cycle, and immune response (22). In terms of the biological activities of the dysregulated thrombus invasion-associated genes in our study, several *in vitro* experiments showed that TGFBI promoted adhesion, migration, and invasion in ccRCC cells (25, 26). Recent study further showed that TGFBI were ubiquitinated and downregulated by VHL restoration and upregulated in human ccRCC (27). M2-related

factor frequencies were regarded as robust biomarkers for predicting the renal clear cell carcinoma patient clinical phenotype and immune microenvironment. Wang et al. explored M2 macrophage-related factors of ccRCC and found that VSIG4, as a co-expressed gene of M2 macrophages, was correlated with infiltration of M2 macrophages and predicted outcomes of ccRCC (28). As an autophagy-related gene, P4HB was proposed to be one potential novel ccRCC diagnostic and prognostic biomarker at both mRNA and protein levels (29, 30). Furthermore, P4HB could be used to construct prognostic models with other autophagy-related genes or clinicopathological parameters (31). However, the role of P4HB in occurrence and invasion processes of ccRCC has not been reported. Further studies on biological processes associated with these molecules would expand applications of our prognostic classifier including prediction of patient response to targeted therapy or immunotherapy and discovery of novel therapeutic targets.

We do acknowledge some limitations of the study. First, the independent cohort applied to validate the performance of our prognostic classifier lacked survival information of patients. Second, the study was conducted in a single-center with limited sample size, further multicenter studies for validation are needed. Last, the biological functions of these proteins in tumorigenesis and invasion processes of ccRCC need to be revealed in the future.

Conclusion

Based on integrative analyses of transcriptomic landscape and urinary signature, the urine-based prognostic classifier consisting of VSIG4, TGFBI, and P4HB has satisfied predictive power of survival time, pathological grade and stage in ccRCC patients, which facilitate ccRCC molecular subtyping and treatment.

Data availability statement

The data presented in the study are deposited in the Genome Sequence Archive (Genomics, Proteomics & Bioinformatics 2021) in National Genomics Data Center (Nucleic Acids Res 2022), China National Center for Bioinformation / Beijing Institute of Genomics, Chinese Academy of Sciences repository, accession number PRJCA012759.

Ethics statement

Written informed consent was obtained from the individual(s) for the publication of any potentially identifiable images or data included in this article.

Author contributions

Study concept and design: WZ, MH, XS. Acquisition of data: WZ, WL, YY, CX, XS. Analysis and interpretation of data: WZ, WL, YY, YX, QP, XS Drafting of the manuscript: WZ, WL Critical revision of the manuscript for important intellectual content: MH, XS. Statistical analysis: YY, XT, HW. Administrative, technical, or material support: XT, HW. Supervision: MH, XS. All authors contributed to the article and approved the submitted version.

Funding

This work was sponsored by National Natural Science Foundation of China (XS 82203134, WZ 81802581), Naval Medical University Sailing Program (WZ 2021), Changhai Hospital Basic Medical Research Program (WZ 2021JCMS04), Shanghai Research Center of Genitourinary System Diseases Program (2022ZZ01011). The funders had no role in study design, data collection and analysis, decision to publish, or preparation of the manuscript.

Conflict of interest

The authors declare that the research was conducted in the absence of any commercial or financial relationships that could be construed as a potential conflict of interest.

Publisher's note

Supplementary material

The Supplementary Material for this article can be found online at: https://www.frontiersin.org/articles/10.3389/fonc.2023.1102623/full#supplementary-material

SUPPLEMENTARY FIGURE 1
The exclusion of prognosis-unrelated molecules based on TCGA database. **(A)** Different expressions of the prognosis-unrelated genes between ccRCC tumor and normal renal tissue indicating higher mRNA levels of C3, AKR1C3, GAL3ST1 in tumor compared to matched normal tissue. **(B-E)** Different expressions of the prognosis-unrelated genes between ccRCC patients with different pathological characteristics including WHO/ISUP grades and TNM stages indicating mRNA levels of C3, AKR1C3, GAL3ST1 are not completely correlated with tumor pathological grades and stages. **(F)** The Kaplan-Meier curves of OS for ccRCC patients with different expressions of the prognosis-unrelated genes showing no difference exists in expressions of C3, AKR1C3, GAL3ST1 between ccRCC patients with different survivals. *p < 0.05, **p < 0.01, ***p < 0.001.

SUPPLEMENTARY FIGURE 2
GO and KEGG analyses of the transcriptome. **(A)** The GO functional annotation of the genes in prognostic classifier. **(B)** KEGG pathway annotation of the genes in prognostic classifier.

References

1. Sung H, Ferlay J, Siegel RL, Laversanne M, Soerjomataram I, Jemal A, et al. Global cancer statistics 2020: Globocan estimates of incidence and mortality worldwide for 36 cancers in 185 countries. *CA Cancer J Clin* (2021) 71(3):209–49. doi: 10.3322/caac.21660

2. Hsieh JJ, Purdue MP, Signoretti S, Swanton C, Albiges L, Schmidinger M, et al. Renal cell carcinoma. *Nat Rev Dis Primers* (2017) 3:17009. doi: 10.1038/nrdp.2017.9

3. Gupta K, Miller JD, Li JZ, Russell MW, Charbonneau C. Epidemiologic and socioeconomic burden of metastatic renal cell carcinoma (Mrcc): A literature review. *Cancer Treat Rev* (2008) 34(3):193–205. doi: 10.1016/j.ctrv.2007.12.001

4. Kotecha RR, Motzer RJ, Voss MH. Towards individualized therapy for metastatic renal cell carcinoma. *Nat Rev Clin Oncol* (2019) 16(10):621–33. doi: 10.1038/s41571-019-0209-1

5. Makhov P, Joshi S, Ghatalia P, Kutikov A, Uzzo RG, Kolenko VM. Resistance to systemic therapies in clear cell renal cell carcinoma: Mechanisms and management strategies. *Mol Cancer Ther* (2018) 17(7):1355–64. doi: 10.1158/1535-7163.MCT-17-1299

6. Bedke J, Albiges L, Capitanio U, Giles RH, Hora M, Lam TB, et al. 2021 Updated European association of urology guidelines on the use of adjuvant pembrolizumab for renal cell carcinoma. *Eur Urol* (2022) 81(2):134–7. doi: 10.1016/j.eururo.2021.11.022

7. Motzer RJ, Penkov K, Haanen J, Rini B, Albiges L, Campbell MT, et al. Avelumab plus axitinib versus sunitinib for advanced renal-cell carcinoma. *N Engl J Med* (2019) 380(12):1103–15. doi: 10.1056/NEJMoa1816047

8. Braun DA, Bakouny Z, Hirsch L, Flippot R, Van Allen EM, Wu CJ, et al. Beyond conventional immune-checkpoint inhibition - novel immunotherapies for renal cell carcinoma. *Nat Rev Clin Oncol* (2021) 18(4):199–214. doi: 10.1038/s41571-020-00455-z

9. Haddad AF, Young JS, Gill S, Aghi MK. Resistance to immune checkpoint blockade: Mechanisms, counter-acting approaches, and future directions. *Semin Cancer Biol* (2022) 86(Pt 3):532–41. doi: 10.1016/j.semcancer.2022.02.019

10. Gerlinger M, Rowan AJ, Horswell S, Math M, Larkin J, Endesfelder D, et al. Intratumor heterogeneity and branched evolution revealed by multiregion sequencing. *N Engl J Med* (2012) 366(10):883–92. doi: 10.1056/NEJMoa1113205

11. Gerlinger M, Horswell S, Larkin J, Rowan AJ, Salm MP, Varela I, et al. Genomic architecture and evolution of clear cell renal cell carcinomas defined by multiregion sequencing. *Nat Genet* (2014) 46(3):225–33. doi: 10.1038/ng.2891

12. Di Meo A, Bartlett J, Cheng Y, Pasic MD, Yousef GM. Liquid biopsy: A step forward towards precision medicine in urologic malignancies. *Mol Cancer* (2017) 16(1):80. doi: 10.1186/s12943-017-0644-5

13. Di Meo A, Batruch I, Brown MD, Yang C, Finelli A, Jewett MA, et al. Searching for prognostic biomarkers for small renal masses in the urinary proteome. *Int J Cancer* (2020) 146(8):2315–25. doi: 10.1002/ijc.32650

14. Krishna C, DiNatale RG, Kuo F, Srivastava RM, Vuong L, Chowell D, et al. Single-cell sequencing links multiregional immune landscapes and tissue-resident T cells in ccrcc to tumor topology and therapy efficacy. *Cancer Cell* (2021) 39(5):662–77.e6. doi: 10.1016/j.ccell.2021.03.007

15. Ng S, Strunk T, Jiang P, Muk T, Sangild PT, Currie A. Precision medicine for neonatal sepsis. *Front Mol Biosci* (2018) 5:70. doi: 10.3389/fmolb.2018.00070

16. Liu L, Zhuang M, Tu XH, Li CC, Liu HH, Wang J. Bioinformatics analysis of markers based on M(6) a related to prognosis combined with immune invasion of renal clear cell carcinoma. *Cell Biol Int* (2022) 47(1):260–72. doi: 10.1002/cbin.11929

17. Brown LC, Zhu J, Desai K, Kinsey E, Kao C, Lee YH, et al. Evaluation of tumor microenvironment and biomarkers of immune checkpoint inhibitor response in metastatic renal cell carcinoma. *J Immunother Cancer* (2022) 10(10):e005249. doi: 10.1136/jitc-2022-005249

18. Brown LC, Desai K, Wei W, Kinsey EN, Kao C, George DJ, et al. Clinical outcomes in patients with metastatic renal cell carcinoma and brain metastasis treated with ipilimumab and nivolumab. *J Immunother Cancer* (2021) 9(9):e003281. doi: 10.1136/jitc-2021-003281

19. Wang XM, Lu Y, Song YM, Dong J, Li RY, Wang GL, et al. Integrative genomic study of Chinese clear cell renal cell carcinoma reveals features associated with thrombus. *Nat Commun* (2020) 11(1):739. doi: 10.1038/s41467-020-14601-9

20. Shi Y, Zhang Q, Bi H, Lu M, Tan Y, Zou D, et al. Decoding the multicellular ecosystem of vena caval tumor thrombus in clear cell renal cell carcinoma by single-cell rna sequencing. *Genome Biol* (2022) 23(1):87. doi: 10.1186/s13059-022-02651-9

21. Matthaei S, Baly DL, Horuk R. Rapid and effective transfer of integral membrane proteins from isoelectric focusing gels to nitrocellulose membranes. *Anal Biochem* (1986) 157(1):123–8. doi: 10.1016/0003-2697(86)90205-8

22. Petitprez F, Ayadi M, de Reynies A, Fridman WH, Sautes-Fridman C, Job S. Review of prognostic expression markers for clear cell renal cell carcinoma. *Front Oncol* (2021) 11:643065. doi: 10.3389/fonc.2021.643065

23. Chinello C, L'Imperio V, Stella M, Smith AJ, Bovo G, Grasso A, et al. The proteomic landscape of renal tumors. *Expert Rev Proteomics* (2016) 13(12):1103–20. doi: 10.1080/14789450.2016.1248415

24. Chinello C, Stella M, Piga I, Smith AJ, Bovo G, Varallo M, et al. Proteomics of liquid biopsies: Depicting rcc infiltration into the renal vein by Ms analysis of urine and plasma. *J Proteomics* (2019) 191:29–37. doi: 10.1016/j.jprot.2018.04.029

25. Shang D, Liu Y, Yang P, Chen Y, Tian Y. Tgfbi-promoted adhesion, migration and invasion of human renal cell carcinoma depends on inactivation of Von hippel-lindau tumor suppressor. *Urology* (2012) 79(4):966.e1–7. doi: 10.1016/j.urology.2011.12.011

26. Corona A, Blobe GC. The role of the extracellular matrix protein tgfbi in cancer. *Cell Signal* (2021) 84:110028. doi: 10.1016/j.cellsig.2021.110028

27. Wang X, Hu J, Fang Y, Fu Y, Liu B, Zhang C, et al. Multi-omics profiling to assess signaling changes upon vhl restoration and identify putative vhl substrates in clear cell renal cell carcinoma cell lines. *Cells* (2022) 11(3):472. doi: 10.3390/cells11030472

28. Wang Y, Yan K, Lin J, Li J, Bi J. Macrophage M2 Co-expression factors correlate with the immune microenvironment and predict outcome of renal clear cell carcinoma. *Front Genet* (2021) 12:615655. doi: 10.3389/fgene.2021.615655

29. Xie L, Li H, Zhang L, Ma X, Dang Y, Guo J, et al. Autophagy-related gene P4hb: A novel diagnosis and prognosis marker for kidney renal clear cell carcinoma. *Aging* (2020) 12(2):1828–42. doi: 10.18632/aging.102715

30. Zhu Z, He A, Lv T, Xu C, Lin L, Lin J. Overexpression of P4hb is correlated with poor prognosis in human clear cell renal cell carcinoma. *Cancer biomark* (2019) 26(4):431–9. doi: 10.3233/CBM-190450

31. Fei H, Chen S, Xu C. Construction autophagy-related prognostic risk signature combined with clinicopathological validation analysis for survival prediction of kidney renal papillary cell carcinoma patients. *BMC Cancer* (2021) 21(1):411. doi: 10.1186/s12885-021-08139-2

frontiers | Frontiers in Oncology

TYPE Original Research
PUBLISHED 24 March 2023
DOI 10.3389/fonc.2023.1096341

OPEN ACCESS

EDITED BY
Linhui Wang,
Second Military Medical University, China

REVIEWED BY
Yingkun Xu,
Chongqing Medical University, China
Dengxiong Li,
Sichuan University, China

*CORRESPONDENCE
Wei Guan
deniskwan@gmail.com
Heng Li
lihengtjmu@163.com
Shao-Gang Wang
sgwangtjm@163.com

†These authors have contributed equally to this work and share first authorship

SPECIALTY SECTION
This article was submitted to Genitourinary Oncology, a section of the journal Frontiers in Oncology

RECEIVED 12 November 2022
ACCEPTED 14 February 2023
PUBLISHED 24 March 2023

CITATION
Xia Q-D, Li B, Sun J-X, Liu C-Q, Xu J-Z, An Y, Xu M-Y, Zhang S-H, Zhong X-Y, Zeng N, Ma S-Y, He H-D, Zhang Y-C, Guan W, Li H and Wang S-G (2023) Integrated bioinformatic analysis and cell line experiments reveal the significant role of the novel immune checkpoint TIGIT in kidney renal clear cell carcinoma. *Front. Oncol.* 13:1096341. doi: 10.3389/fonc.2023.1096341

Integrated bioinformatic analysis and cell line experiments reveal the significant role of the novel immune checkpoint TIGIT in kidney renal clear cell carcinoma

Qi-Dong Xia†, Bo Li†, Jian-Xuan Sun, Chen-Qian Liu, Jin-Zhou Xu, Ye An, Meng-Yao Xu, Si-Han Zhang, Xing-Yu Zhong, Na Zeng, Si-Yang Ma, Hao-Dong He, Yu-Cong Zhang, Wei Guan*, Heng Li* and Shao-Gang Wang*

Department and Institute of Urology, Tongji Hospital, Tongji Medical College, Huazhong University of Science and Technology, Wuhan, China

Background: T cell immunoglobulin and ITIM domain (TIGIT) is a widely concerned immune checkpoint, which plays an essential role in immunosuppression and immune evasion. However, the role of TIGIT in normal organ tissues and renal clear cell carcinoma is unclear. We aim to identify the critical role of TIGIT in renal clear cell carcinoma and find potential targeted TIGIT drugs.

Materials and methods: Data retrieved from the GTEX database and TCGA database was used to investigate the expression of TIGIT in normal whole-body tissues and abnormal pan-cancer, then the transcriptome atlas of patients with kidney renal clear cell carcinoma (KIRC) in the TCGA database were applied to distinguish the TIGIT related features, including differential expression status, prognostic value, immune infiltration, co-expression, and drug response of sunitinib an anti-PD1/CTLA4 immunotherapy in KIRC. Furthermore, we constructed a gene-drug network to discover a potential drug targeting TIGIT and verified it by performing molecular docking. Finally, we conducted real-time polymerase chain reaction (PCR) and assays for Transwell migration and CCK-8 to explore the potential roles of TIGIT.

Results: TIGIT showed a moderate expression in normal kidney tissues and was confirmed as an essential prognostic factor that was significantly higher expressed in KIRC tissues, and high expression of TIGIT is associated with poor OS, PFS, and DSS in KIRC. Also, the expression of TIGIT was closely associated with the pathological characteristics of the tumor, high expression of TIGIT in KIRC was observed with several critical functions or pathways such as apoptosis, BCR signaling, TCR signaling et al. Moreover, the expression of TIGIT showed a strong positive correlation with infiltration of CD8+ T cells and Tregs and a positive correlation with the drug sensitivity of sunitinib simultaneously. Further Tide ips score analysis and submap analysis reveal that patients with high TIGIT expression significantly show a better response to anti-PD1 immunotherapy. Following this, we discovered Selumetinib and PD0325901 as potential drugs

targeting TIGIT and verified the interaction between these two drugs and TIGIT protein by molecular docking. Finally, we verified the essential role of TIGIT in the proliferation and migration functions by using KIRC cell lines.

Conclusions: TIGIT plays an essential role in tumorigenesis and progression in KIRC. High expression of TIGIT results in poor survival of KIRC and high drug sensitivity to sunitinib. Besides, Selumetinib and PD0325901 may be potential drugs targeting TIGIT, and combined therapy of anti-TIGIT and other treatments show great potential in treating KIRC.

KEYWORDS

KIRC, TIGIT, targeted therapy, immunotherapy, molecular docking

Introduction

T cell immunoglobulin and ITIM domain (TIGIT), first introduced by Yu et al. (1), is a member of the poliovirus receptor (PVR)/nectin family and a subset of the immunoglobulin superfamily. The protein encoded by TIGIT contained an extracellular immunoglobulin variable-set (IgV) domain, a type I transmembrane domain, an intracellular immune receptor tyrosine inhibitory motif (ITIM), and an Immunoglobulin tyrosine tail (ITT) motif (1, 2). Interestingly, once introduced, TIGIT was discovered to inhibit T cell activity (1, 3, 4). Moreover, the expression level of TIGIT on the surface of tumor-infiltrating T cells was discovered to increase fourfold than that on peripheral blood mononuclear cells (PBMC), and further studies reveal that only the expression of TIGIT in $CD8^+$ T cell exhaustion increased significantly, and changed synchronously with that of PD-1 (5), indicating that TIGIT and PD1/PD-Ll pathway had a synergistic inhibitory effect on tumor-infiltrating T cells. Furthermore, compared with $CD8^+$ T cells that less expressed TIGIT, $CD8^+$ T cells expressing TIGIT showed a significantly low expression of TNF α, IFN γ, and IL-2. However, the expression of Annexin V and CD95, which represent apoptosis markers, was significantly increased simultaneously (6). Also, when knocked down the expression of TIGIT in $CD8^+$ T cells by siRNA, the expression of Annexin V and CD95 decreased significantly, and the level of TNF α, IFN γ, and IL-2 increased significantly (6). Thus, the expression of TIGIT was considered closely related to the apoptosis of $CD8^+$ T cells, and once blocking TIGIT signaling pathway, the apoptosis of $CD8^+$ T cells can be reversed to some extent. More importantly, it not only plays a significant inhibitory role in $CD8^+$ T cells, but TIGIT was also found combating anti-tumor immunity by influencing nature kill cells (7, 8), antigen-presenting dendritic cells (1, 9), and T regulatory cells (Tregs) (10, 11). Thus, TIGIT has been considered one of the most critical immune checkpoints that more and more researchers and scientists devoted to investigating and developing a novel drug for TIGIT, such as TIGIT monoclonal antibody tiragolumab (12). However, our standing of the TIGIT expression in normal organs and tissues is still unclear because we only focused on the immune cell's expression in TIGIT.

Kidney cancer is the 6th most common cancer in both sexes and the most common urogenital tumor, accounting for approximately 2-3% of all malignancies and 90% of all diagnosed renal parenchymal malignancies1 (13, 14), claiming 14,830 lives with 73,750 new confirmed cases in the USA in 2020 (13). Kidney renal clear cell carcinoma (KIRC) is the predominant pathological subtype of all kidney cancer, accounting for approximately 85% of renal cancer (15, 16), also considered to be one of the most invasive diseases, which is associated with a high mortality rate in the form of metastasis (17). Although surgical intervention is still the main treatment considering that it is not sensitive to radiation, hormone, and cytotoxic therapy. Besides, tyrosine kinase inhibitors (TKIs) such as sunitinib targeting vascular endothelial growth factor (VEGF) pathway also play an essential role in the current clinical treatment as the first-line targeted therapy (18, 19). Moreover, immunotherapy consisting of anti-PD1/PDL1 or anti-CTLA4 therapy have also shown great performance in the therapy of KIRC (20), especially in combination with VEGF-directed therapy (21). Interestingly, immunotherapy combined therapy has replaced TKI's first-line targeted therapy as a first-line treatment in the latest 2020 European Association of Urology (EAU) guidelines for clear cell metastatic renal cell carcinoma (cc-mRCC) (22).

KIRC has long been categorized as an immunotherapy-responsive cancer type that belongs to 'hot tumor' (18). However, the efficacy of Nivolumab monotherapy in advanced renal cell carcinoma was reported as 16% to 29% (23, 24), and the effective rate of Atezolizumab monotherapy was 15% (25–27). It seems only a small part of patients can benefit from immunotherapy,

Abbreviations: TIGIT, T cell immunoglobulin and ITIM domain; PVR, poliovirus receptor; IgV, immunoglobulin variable-set; ITIM, immune receptor tyrosine inhibitory motif; ITT, Immunoglobulin tyrosine tail; PBMC, peripheral blood mononuclear cells; ICIS, immune checkpoint inhibitors; KIRC, Kidney renal clear cell carcinoma; TKIs, tyrosine kinase inhibitors; VEGF, vascular endothelial growth factor; EAU, European Association of Urology; cc-mRCC, clear cell metastatic renal cell carcinoma; AML, acute myelogenous leukemia; RCC, renal cell carcinoma; AFP, α-fetoprotein; HCC, human hepatocellular carcinoma.

suggesting that other mechanisms must limit anti-tumor immunity. Whether the TIGIT signaling pathway is the significant immunosuppression and immune evasion mechanism in KIRC is unclear. Thus, we wonder what role TIGIT plays in KIRC and whether it could be a potential therapeutic target in the future. In this study, we first systematically explored the expression of TIGIT in various normal organs of the body, especially in the kidney, and then investigated the differential expression of TIGIT between normal tissues and KIRC tissues, explored the prognostic value and clinical correlation of TIGIT in KIRC, further focused on the TIGIT related functions and pathways, investigate the correlation between TIGIT and tumor-infiltrating immune cells, as well as drug sensitivity, and considered TIGIT as a novel therapeutic target and discovered two potential drugs targeting TIGIT by applying molecular docking technology, which referred to the process that a small molecular is spatially docked into a macromolecular and can evaluate the complementary energy at the binding sites, used for structure-based drug design (28) and finally performed a series of *in vitro* experiments to validate our results.

Materials and methods

Data acquisition and sources

The transcriptional expression data of normal tissues from the whole-body's organs and systems, including both male and female, were retrieved from the GTEX database (29). The expression status of TIGIT between the tumor and normal tissues of whole-body was acquired from the GEPIA database (30). The transcriptional data and corresponding survival information of pan-cancer were downloaded from the UCSC Xena (http://xena.ucsc.edu/). The transcriptome profiles of kidney clear cell carcinoma patients and their corresponding clinical characteristics were downloaded from the TCGA database (https://portal.gdc.cancer.gov/) (31). The different expression status of TIGIT in pan-cancer and the corresponding immune infiltration of each sample emphasized by multiple acknowledged methods was acquired from TIMER 2.0 database (http://timer.cistrome.org/) (32).

TIGIT in normal tissues between organs and genders or between tumor and normal tissues

The expression of TIGIT in normal tissues from the whole-body was extracted and sorted according to the expression value. Then we visualized it as a boxplot to show the ranking of TIGIT's expression. Besides, we compared the expression of TIGIT in the same organ tissues but between different genders by performing Wilcoxon rank-sum test. Following this, we visualized the expression of TIGIT in whole-body including male and female by applying R program package 'gganatogram'. We would also like to investigate the expression status of TIGIT between tumor and normal tissues in the whole-body, especially in the kidney. Thus, we searched TIGIT in pan-cancer from the GEPIA database and acquired the differential expression plot.

TIGIT in KIRC: Differential expression, prognostic value, and clinical correlation

The fragments per kilobase of per million formats (FPKM) of kidney clear cell carcinoma (KIRC) transcriptome profiles were sorted and normalized. The expression of TIGIT in the KIRC tumor and normal adjacent tumor tissues was extracted. Wilcoxon rank-sum test was performed to compare the differential expression of TIGIT between tumor and normal tissues in KIRC (including both paired and non-paired samples). Following this, samples were divided into high or low TIGIT expression groups by the expression of TIGIT that was higher/lower than the medium value was considered high/low TIGIT expression groups. Then Kaplan-Meier methods survival curves were plotted that including overall survival (OS), progression-free survival (PFS), disease-specific survival (DSS), and disease-free survival (DFS). The log-rank test was also carried out to examine these survival interval differences between high and low TIGIT expression patients. Further univariate and multivariate cox regression was applied to check whether TIGIT could serve as an independent prognostic factor and the differential expression status of TIGIT between different clinicopathological subgroups containing age (<=65 or >65). gender (male or female), grade (G1, G2, G3, G4), grade (G1-2 or G3-4), stage (stage I, stage II, stage III, stage IV), stage (stage I-II or stage III-IV), pathological T stage (T1, T2, T3, T4), pathological N stage (N0 or N1), and pathological M stage (M0 or M1) were compared by Wilcoxon rank-sum test.

TIGIT in KIRC: Differential enhanced pathways, differential immune infiltration, and differential drug response

Same as above, samples were grouped as high or low TIGIT expression, and the transcriptome profiles were merged, proceeded, and exported as 'gct' and 'cls' format files prepared for the following gene set enrichment analysis (GSEA). The GSEA version 4.0.3 was applied to perform the enrichment analysis, and here we focused on the HALLMARK gene sets and KEGG pathway gene sets. Discovered the enhanced pathways were associated with immunity, and as TIGIT was an immune checkpoint, we were interested in the association between TIGIT and immune infiltration in KIRC. However, there were several acknowledged methods to estimate the immune infiltration of samples according to their transcriptional expression atlas. Thus, here we performed seven different methods to precisely investigate the immune infiltration status of KIRC patients, including XCELL, TIMER, QUANTISEQ, MCPCOUNTER, EPIC, CIBERSORT-ABS, and CIBERSORT. We then applied the SPEARMAN correlation test to explore the significant TIGIT-related immune cells with $p < 0.05$, we explored the differential immune infiltration between the high-/low-TIGIT group by the Wilcox test. Besides, we were also

interested in the drug response of the first-line targeted therapy for renal clear cell carcinoma, applying R program package 'pRRophetic' to predict each sample's drug sensitivity to the targeted therapy of sunitinib. Then compared the different drug sensitivity between high-TIGIT and low-TIGIT patients by using Wilcoxon signed-rank test and explored the correlation between TIGIT and the drug sensitivity by applying the SPEARMAN correlation test to discover the association between expression of TIGIT and drug sensitivity of the targeted therapy. Furthermore, Tide ips scores analysis and submap algorithm were applied to predict the treatment response to anti-PD1 or anti-CTLA4 immunotherapy between KIRC patients with high-/low-TIGIT expression.

TIGIT in KIRC: Novel potential targeted drug and molecular docking

Interested in the TIGIT and targeted therapy, we searched TIGIT in the IGMDR database (33), acquired the gene-drug network, and discovered two potential targeted therapy drugs for TIGIT. Subsequently, molecular docking was applied to verify the interaction between these two drugs and TIGIT. The 2D structure of these two drugs was acquired from the PubChem database (34), and ChemBio 3D software was used to calculate the 3D structure with minimizing energy. The receptor protein encoded by TIGIT was searched in the Uniprot database (35), and then the 3D structure of the protein was downloaded from the RCSB PDB database (36). PyMOL 2.4.0 software was applied to conduct the dehydration of the receptor protein, and Autodock software was used to carry out further hydrogenation and charge calculation of proteins. Parameters of the receptor protein docking site were set to include the active pocket sites where small-molecule drugs bind. Finally, Autodock Vina was used to conduct docking the receptor protein encoded by TIGIT with the small molecule drugs.

Cell culture

The human ccRCC cell lines (786-O), the human embryonic kidney 293T (HEK-293T) cell and the human renal tubular epithelial cell lines (HK_2) were purchased from the Shanghai Cell Bank Type Culture Collection Committee (Shanghai, China). The 786-O and HK_2 cells were cultured in RPMI-1640 (Gibco, Thermo Fisher Scientific, Waltham, MA, United States) supplemented with 10% FBS and 100 U/mL Penicillin/Streptomycin in a 5% CO2 incubator. While the HEK-293T cells were cultured in high-glucose DMEM media supplemented with 10% FBS. Cells were collected at 90% confluence, and the medium was changed every 48–72 h.

Cell transfection

Relative target fragments were inserted into lentiviral vectors PCDH-CMV-MCS-EF1-copGFP. Together with pGC-LV, pHelper1.0, pHelper2.0, pHelper3.0, and recombinant lentiviral vectors, plasmids were co-transfected into HEK-293T cells using Lipofectamine 3,000 (Invitrogen, United States).

RNA extraction and quantitative real-time polymerase chain reaction

Total RNAs of cells or tissues were extracted using the TRIzol reagent (Vazyme, R401-01), and then cDNA was synthesized by reverse transcription using the HiScript III RT SuperMix for qPCR (Vazyme, R323-01). RT-PCR was conducted using Taq Pro Universal SYBR qPCR Master Mix (Vazyme, Q712-02). GAPDH was used as an internal control. Supplementary Table S1 displayed the sequences of all primers.

CCK-8 assay

1,500 of 786-O cells were seeded into 96-well plates per well for the CCK-8 assay. Then 10 μL CCK-8 (MCE, HY-K0301) was added to each well for 1-h incubation, and the absorbance of each well was measured at 450 nm every day for 5 times.

Transwell migration assay

For migration assays, about 5×10^4 of 786-O cells were suspended and seeded in the upper chambers of 24-well transwell plates (Corning, United States) with 250μl FBS-free medium. Then, 500μl RPMI-1640 with 10% FBS was added to the lower chamber. After 12h incubation, the chambers were fixed and stained with crystal violet for 30 min. Finally, imaging was performed under an inverted microscope

Results

Basic characteristics

The study flow was displayed in the Figure 1. A total of 611 transcriptome profile (72 normal tissue and 539 tumor tissue) from 530 TCGA_KIRC patients were downloaded and sorted, for those samples sequenced multiple time, we took the average of them as their transcriptional data. and the characteristic of the samples were shown in Table 1, χ^2 test or Fisher's exact test were performed to explore the heterogeneity between high or low expression of TIGIT.

TIGIT in normal tissues and tumor tissues

We first systematically analyze the relationship between TIGIT and a variety of cancers, especially kidney cancer, and discovered that the expression of TIGIT was quite high in KIRC, but not KICH and KIRP, and was associated with poor prognosis (Figures 2A–C). We also found that there is a positive correlation between the expression level of TIGIT and objective response rate (ORR) in

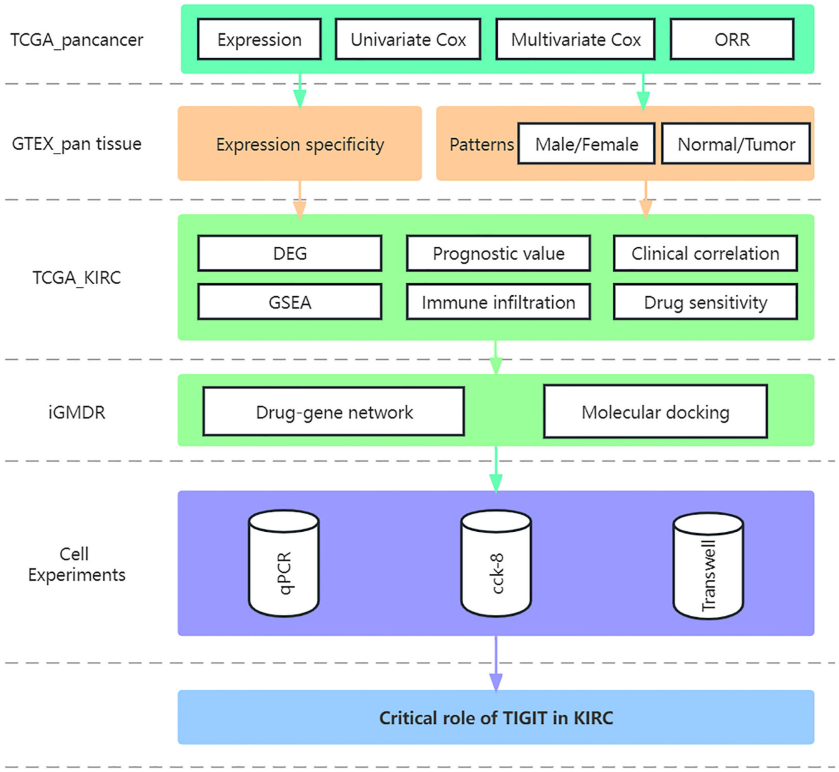

FIGURE 1
The study flow.

TABLE 1 Detailed clinicopathological characteristics of the KIRC patients.

	Overall	High TIGIT	Low TIGIT	P-value
Number	530	265	265	
Age (mean (SD))	60.56 (12.14)	60.42 (11.81)	60.71 (12.47)	0.789
Gender = FEMALE/MALE (%)	186/344 (35.1/64.9)	81/184 (30.6/69.4)	105/160 (39.6/60.4)	0.036
Grade (%)				<0.001
G1	14 (2.6)	4 (1.5)	10 (3.8)	
G2	227 (42.8)	91 (34.3)	136 (51.3)	
G3	206 (38.9)	117 (44.2)	89 (33.6)	
G4	75 (14.2)	52 (19.6)	23 (8.7)	
GX	5 (0.9)	0 (0.0)	5 (1.9)	
unknow	3 (0.6)	1 (0.4)	2 (0.8)	
Stage (%)				<0.001
Stage I	265 (50.0)	106 (40.0)	159 (60.0)	
Stage II	57 (10.8)	34 (12.8)	23 (8.7)	
Stage III	123 (23.2)	73 (27.5)	50 (18.9)	
Stage IV	82 (15.5)	50 (18.9)	32 (12.1)	
unknow	3 (0.6)	2 (0.8)	1 (0.4)	
T (%)				<0.001
T1	21 (4.0)	6 (2.3)	15 (5.7)	

(Continued)

TABLE 1 Continued

	Overall	High TIGIT	Low TIGIT	P-value
T1a	140 (26.4)	45 (17.0)	95 (35.8)	
T1b	110 (20.8)	60 (22.6)	50 (18.9)	
T2	55 (10.4)	29 (10.9)	26 (9.8)	
T2a	10 (1.9)	7 (2.6)	3 (1.1)	
	4 (0.8)	4 (1.5)	0 (0.0)	
T3	5 (0.9)	4 (1.5)	1 (0.4)	
T3a	120 (22.6)	68 (25.7)	52 (19.6)	
T3b	52 (9.8)	35 (13.2)	17 (6.4)	
T3c	2 (0.4)	0 (0.0)	2 (0.8)	
T4	11 (2.1)	7 (2.6)	4 (1.5)	
M (%)				0.002
M0	420 (79.2)	206 (77.7)	214 (80.8)	
M1	78 (14.7)	50 (18.9)	28 (10.6)	
MX	30 (5.7)	8 (3.0)	22 (8.3)	
unknow	2 (0.4)	1 (0.4)	1 (0.4)	
N (%)				0.107
N0	239 (45.1)	121 (45.7)	118 (44.5)	
N1	16 (3.0)	12 (4.5)	4 (1.5)	
NX	275 (51.9)	132 (49.8)	143 (54.0)	

various cancers (Figure 2D). And the first three organs with the highest expression of TIGIT were the spleen, blood, and small intestine. The lowest three were pancreas, skeletal muscle, and bone marrow, and TIGIT showed a moderate expression in normal kidney (Figure 3A). Interestingly, the expression of TIGIT in females' brains, lungs, breasts, and small intestine was significantly higher than that in males (Figure 3B). TIGIT was the highest expression in the spleen in males and females (Figures 3C, D). Here we focused on the kidney and discovered a higher expression of TIGIT in kidney tumor with a mean expression of 0.24 in normal kidney and that of 1.47 in kidney tumor (Figure 3E).

TIGIT in KIRC: Differential expression, prognostic value, and clinical correlations

TIGIT showed a significantly higher expression in KIRC tissues than normal tissues in both non-paired and paired samples (Figures 4A, B). Following this, we wondered whether high expression of TIGIT resulted in poor clinical outcomes and discovered the high expression of TIGIT was associated with poor overall survival (Figure 4C), poor progression survival (Figure 3D), and poor disease-specific survival (Figure 4E). There was no difference in disease-free survival (Figure 4F). This showed that TIGIT played an essential role in the tumorigenesis, progression, and clinical outcomes of KIRC. Besides, we performed univariate and multivariate cox regression and found TIGIT as a significant risk factor with a hazard ratio (HR) of 1.344 (1.098 to 1.646) for KIRC patients in univariate Cox regression (Figure 4G). Subsequently, after correction from other clinical features, the HR of TIGIT was 1.009 (0.822 to 1.238), showing no significant difference (Figure 4H). This suggested that the expression of TIGIT was significant associated with clinical characteristics, so we conducted further exploration about the clinical correlation of TIGIT. There were no significant differences between age (Figure 5A) and gender (Figure 5B). However, TIGIT showed great association with pathological characteristics as expected. TIGIT showed a gradually increasing trend from G1 to G4 (Figure 5C), and significantly higher expressed in G3-4 than G1-2 (Figure 5D). Also showed the same trend from Stage I to Stage IV (Figure 5E), and significantly higher expressed in Stage III-IV than Stage I-II (Figure 5F). Besides, TIGIT was significantly lowest expressed in T1 than T2 to T4 (Figure 5G), and significantly higher expressed in N1 than N0 (Figure 5H), in M1 than M0 (Figure 5I), which showed the significant role of TIGIT in the tumor metastasis.

TIGIT in KIRC: Differential enhanced pathways, differential immune infiltration, and differential drug response

Having identified TIGIT as an essential prognostic factor and explored its association between expression and clinical

10.3389/fonc.2023.1096341

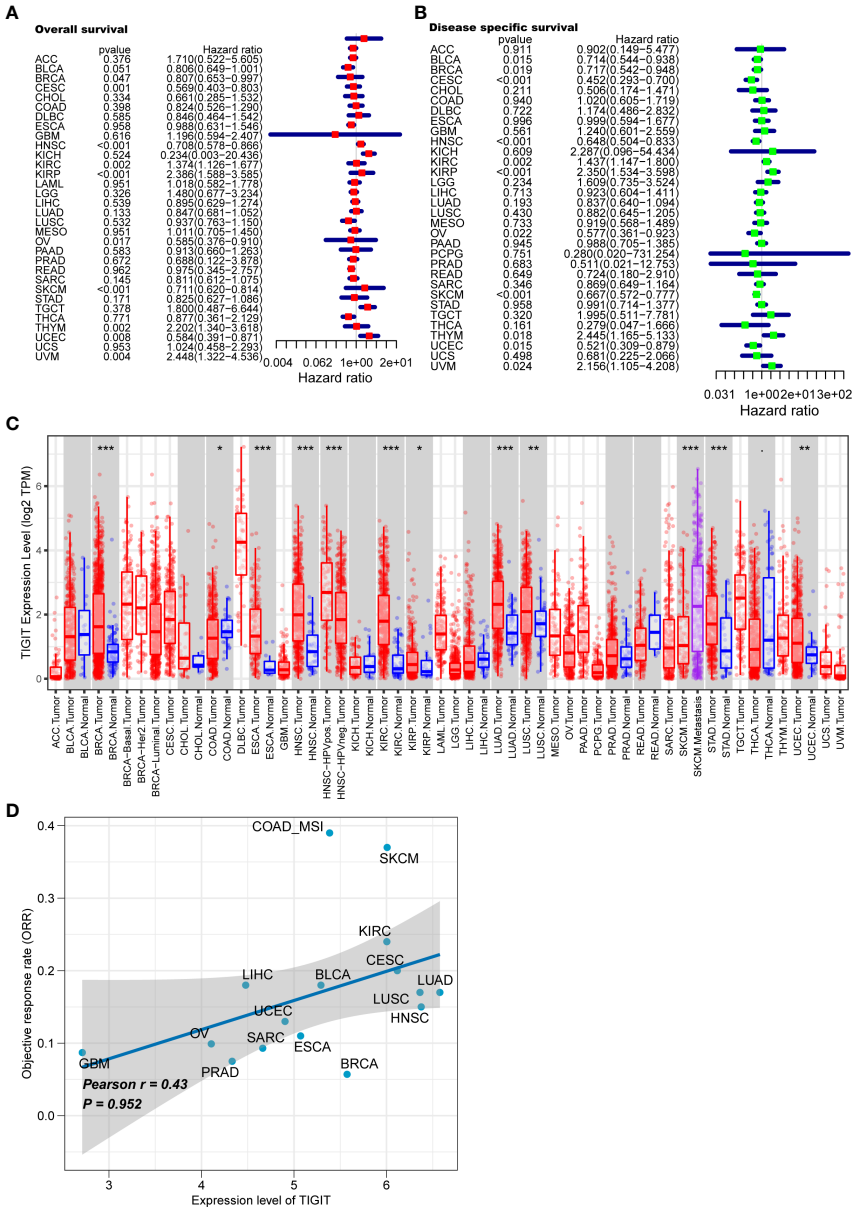

FIGURE 2
Analysis of TIGIT in pan-cancer. **(A)** Univariate Cox regression showed the OS of TIGIT in pan-cancer. **(B)** Univariate Cox regression showed the disease specific survival of TIGIT in pan-cancer. **(C)** Differential expression status of TIGIT in pan-cancer. **(D)** The potiential association between the expression level of TIGIT and objective response rate in various cancers. *: p<0.05, **: p<0.01, ***: p<0.001

characteristics, we were interested in the functions and pathways influenced by TIGIT. Subsequent KEGG enrichment analysis showed high expression of TIGIT was associated with significantly enhanced pathways such as B cell receptor signaling pathway, cell adhesion molecular cams, cytokine-cytokine receptor interaction, JAK-STAT signaling pathway, nature kill cell-mediated cytotoxicity, T cell receptor signaling pathway, and Toll-like receptor signaling pathway, also associated with significantly attenuated functions such as glutathione metabolism and glycerolipid metabolism (Figure 6A). HALLMARK gene set enrichment analysis suggested high expression of TIGIT was associated with significantly enhanced functions and pathways such as apoptosis, IL2-STAT5 signaling pathways, IL6-JAK-STAT3 signaling, inflammatory response, interferon-α response, interferon-Λ response, P53 pathway, PI3K-AKT-mTOR signaling, and TNF-α signaling *via* NF-κB, and significantly attenuated functions such as estrogen response and TGF beta signaling (Figure 6B). It was interesting that TIGIT was associated with so many essential pathways and functions in KIRC.

As TIGIT is one of the most important immune checkpoints associated with so many immunity-related functions and pathways, we further investigated the association between its expression and patients' immune infiltration. The SPEARMAN correlation test suggested the expression of TIGIT was significant negative correlated with NK resting cell, endothelial cell, neutrophil, M2 macrophages, and significant positive correlated with M1

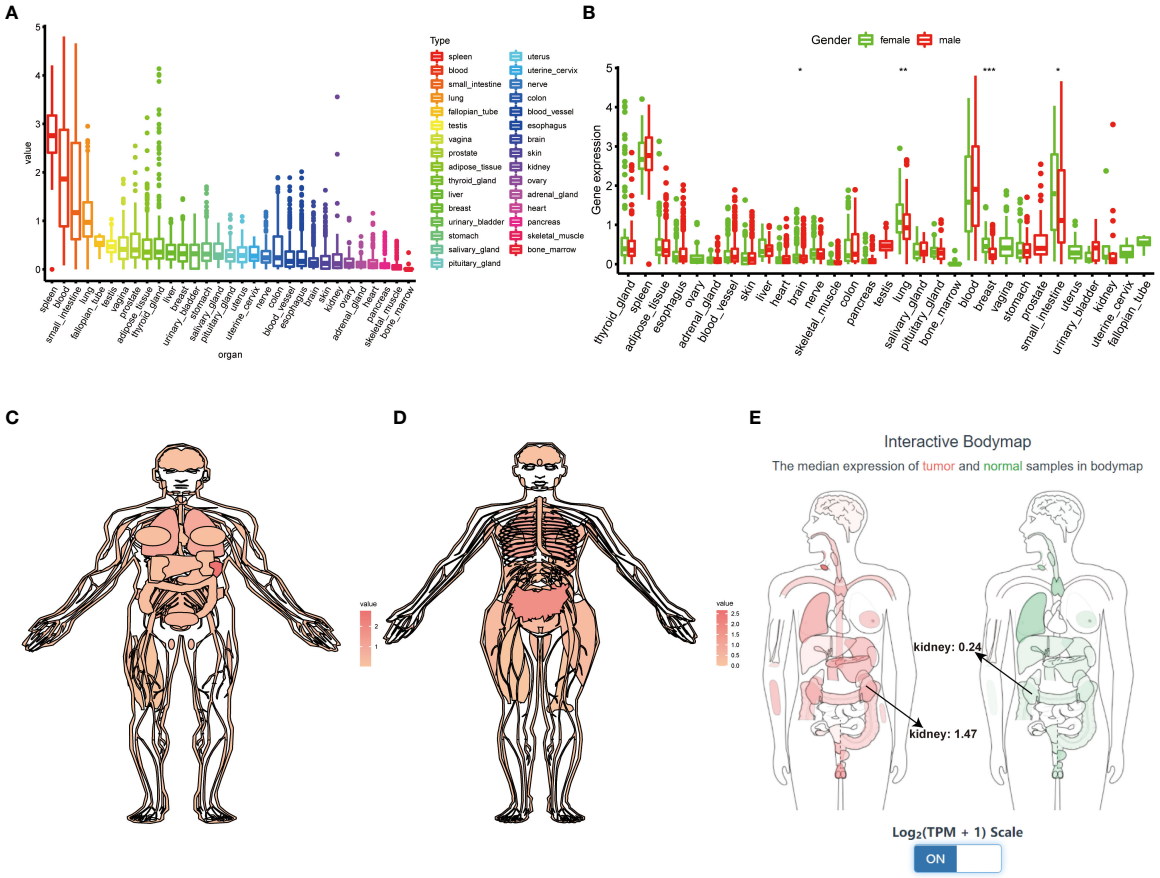

FIGURE 3
Comprehensive analysis of TIGIT in whole-body's normal tissues. **(A)** The expression status of TIGIT in normal organs sorted by the expression value. **(B)** The differential expression status of TIGIT between males and females. **(C)** The expression atlas of TIGIT in males. **(D)** The expression atlas of TIGIT in females. **(E)** The expression of TIGIT in tumor organ tissues (red) and normal organ tissues (green). *: p<0.05, **: p<0.01, ***: p<0.001

macrophages, $CD8^+$ T cells, T regulatory cells (Tregs), Th1 cells, Th2 cells et al. (Figure 7A). All these seven emphasized methods suggested TIGIT a strong positive correlation with $CD8^+$ T cells, which should have resulted in a great clinical outcome. So, we focused on the Tregs, and discovered TIGIT was significantly positively correlated with the infiltration of Tregs (Figure 7A), and significant-high infiltration with Tregs was observed in high TIGIT expression samples emphasized by CIBESORT (Figure 7B), CIBESORT-ABS (Figure 7C), and QUANTISEQ (Figure 7D).

Observed TIGIT as a significant correlation with immune infiltration in KIRC, we were interested in the correlation between TIGIT and other common immune checkpoints such as PD1(PDCD1), PD-L1 (CD274), and CTLA4. As expected, we found TIGIT significant positive correlated with PDCD1 (R =0.87, p< 0.001), CD274 (R=0.38, p< 0.001), CTLA4 (R=0.81, p< 0.001) as Figures 8A–C. This may explain the poor response for the existing immunotherapy in KIRC that although we inhibit some immune checkpoints like PD1, PD-L1, or CTLA4, their associated expression of TIGIT still plays a role in immunosuppression and immune evasion. Besides, we further explored the correlation between the expression of TIGIT and the drug response of sunitinib, the most used targeted therapy drug in KIRC. Discovered high expression of TIGIT was associated with a significantly higher response for sunitinib (Figure 8D), and TIGIT showed a significant positive correlation with the drug sensitivity of sunitinib (R= -0.31, p< 0.001) as Figure 8E. Further Tide ips scores analysis showed that KIRC patients with high TIGIT expression may response better to anti-PD1 immunotherapy (Figure 9A), anti-CTLA4 immunotherapy (Figure 9B), and combined immunotherapy (Figure 9C). Also, the submap analysis reaches a consistent result that KIRC patients with high TIGIT expression showed a significant better response to anti-PD1 immunotherapy (p=0.001, Bonferroni corrected p=0.008, Figure 9D).

TIGIT in KIRC: Novel potential targeted drug and molecular docking

After revealing the important role of TIGIT in immunotherapy and targeted therapy of KIRC, we believe that TIGIT is an important therapeutic target for KIRC and intend to discover a new drug or a new use targeting TIGIT in conventional drugs. Thus, we constructed the gene-drug network (Figure 10A) and found two potential therapeutic drugs targeting TIGIT, and they were Selumetinib and PD0325901. To verify our discovery, we performed molecular docking technology to examine the

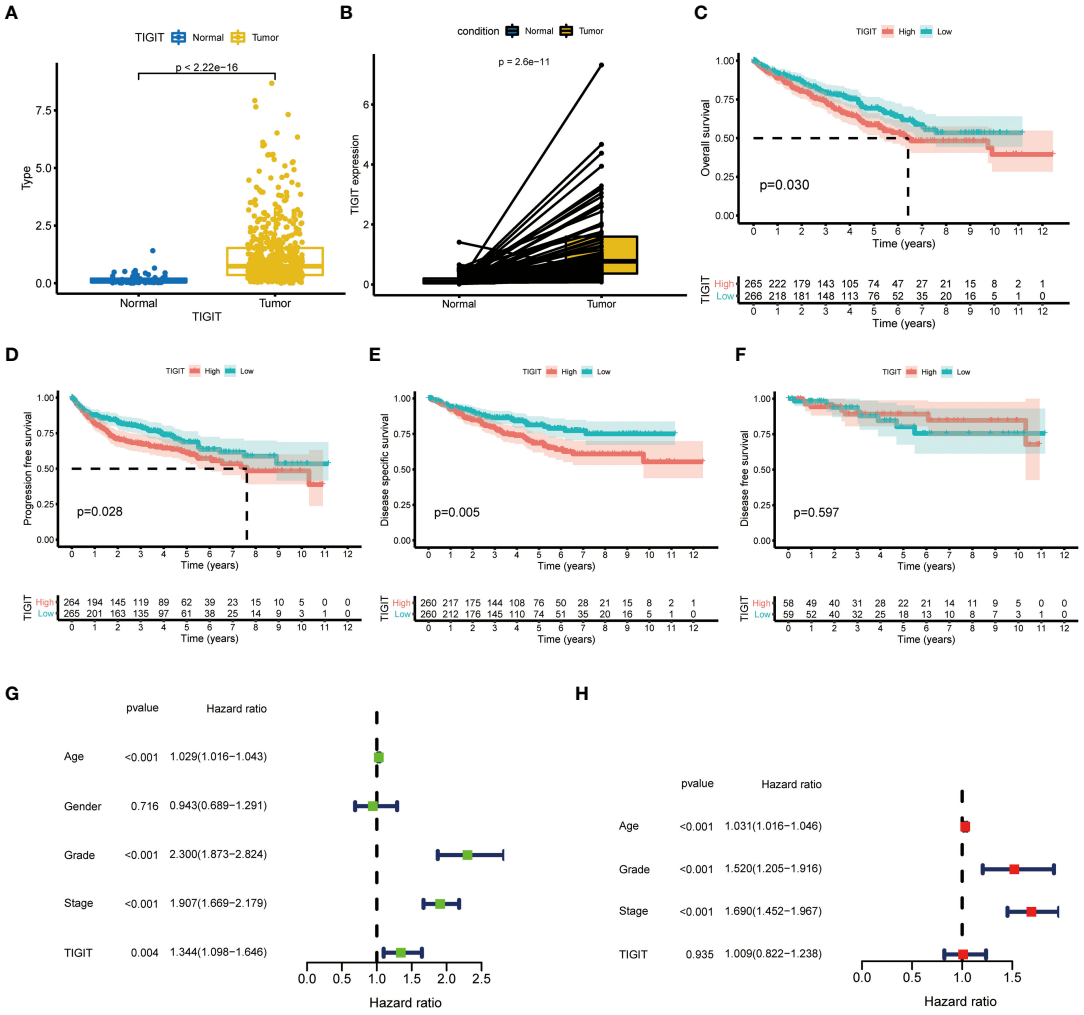

FIGURE 4
Differential expression and prognostic value of TIGIT in KIRC. **(A)** TIGIT shows a significantly higher expression in non-paired KIRC tissues compared to the normal tissues. **(B)** TIGIT shows a significantly higher expression in paired KIRC tissues compared to the normal tissues. **(C)** High expression of TIGIT was associated with significantly poor overall survival in KIRC. **(D)** High expression of TIGIT was associated with significantly poor progression-free survival in KIRC. **(E)** High expression of TIGIT was associated with significantly poor disease-specific survival in KIRC. **(F)** There were no significant differences between patients with high or low expression of TIGIT in disease-free survival in KIRC. **(G)** Univariate Cox regression showed TIGIT a significant prognostic factor in KIRC. **(H)** Multivariate Cox regression of TIGIT in KIRC.

interaction between these two drugs and TIGIT protein. The 3D structure of the TIGIT protein was shown in Figure 10B, the 2D structure and 3D structure of Selumetinib were shown in Figures 10C, D, that of PD0325901 was shown in Figures 10F, G. Both molecular dockings for Selumetinib and PD0325901 showed that these two drugs could enter into the active pocket of TIGIT (Figures 10E, H), which suggested they could serve as potential drugs targeting TIGIT.

TIGIT enhanced the progression of 786-O clear cell renal carcinoma cells

Finally, we validated the potential physiological role of TIGIT in *in vitro* experiments. We explored the expression of TIGIT in renal carcinoma cells (786-O) and normal cells (HK_2) and found that the level of TIGIT in tumor cells was significantly increased compared to normal cells (Figure 11A). To investigate the biological functions of TIGIT in renal carcinoma, TIGIT was overexpressed in 786-O cells by lentiviral infection, and its expression was validated by qRT-PCR (Figure 11B). CCK8 assay demonstrated that TIGIT promoted cellular viability of 786-O cells by contrast with control groups (Figure 11C). Furthermore, we explored whether TIGIT was involved in cell metastasis and discovered that the overexpression of TIGIT remarkably increased migration ability in 786-O cells (Figure 11D). Taken together, these findings indicated that TIGIT enhanced carcinogenesis of renal carcinoma cells *in vitro*.

Discussion

The present study conducted a comprehensive analysis of TIGIT in KIRC, confirmed TIGIT as an essential prognostic factor significantly higher expressed in KIRC tissues, and high

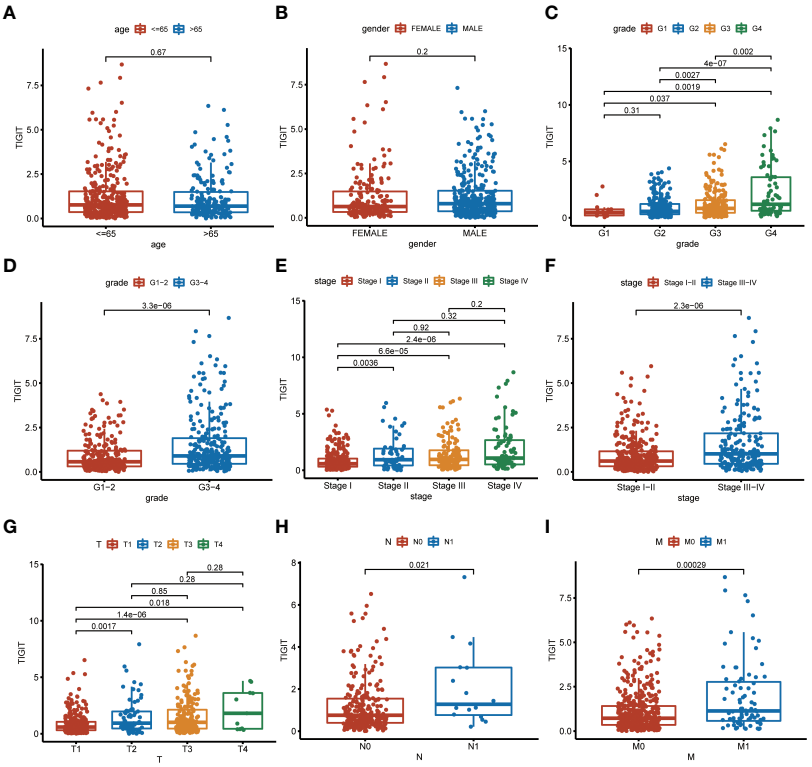

FIGURE 5
Clinical correlation of TIGIT expression. **(A)** clinical correlation between age and TIGIT. **(B)** clinical correlation between gender and TIGIT. **(C)** clinical correlation between grade and TIGIT. **(D)** clinical correlation between grade and TIGIT. **(E)** clinical correlation between stage and TIGIT. **(F)** clinical correlation between stage and TIGIT. **(G)** clinical correlation between T stage and TIGIT. **(H)** clinical correlation between N stage and TIGIT. **(I)** clinical correlation between M stage and TIGIT.

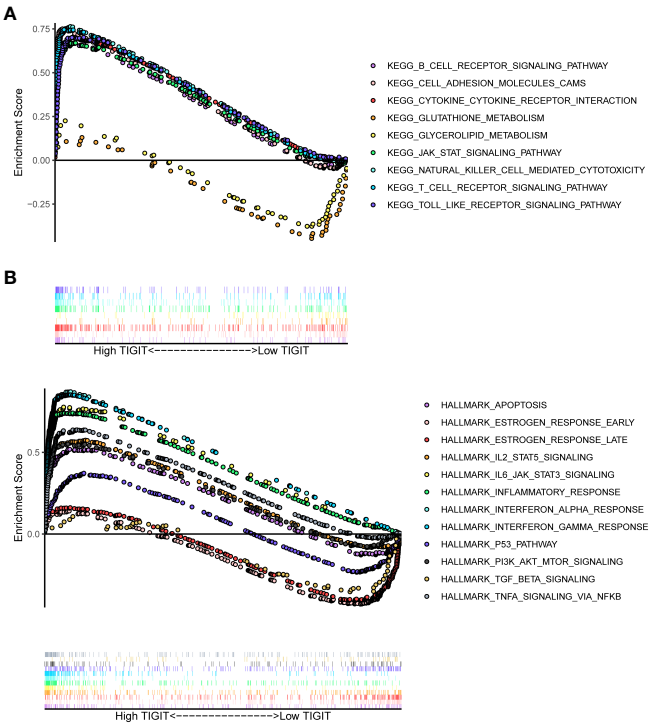

FIGURE 6
Differential enriched functions or pathways correlated with the expression of TIGIT. **(A)** Differential enriched KEGG pathways associated with the expression of TIGIT in KIRC. **(B)** Differential enriched HALLMARK pathways associated with the expression of TIGIT in KIRC.

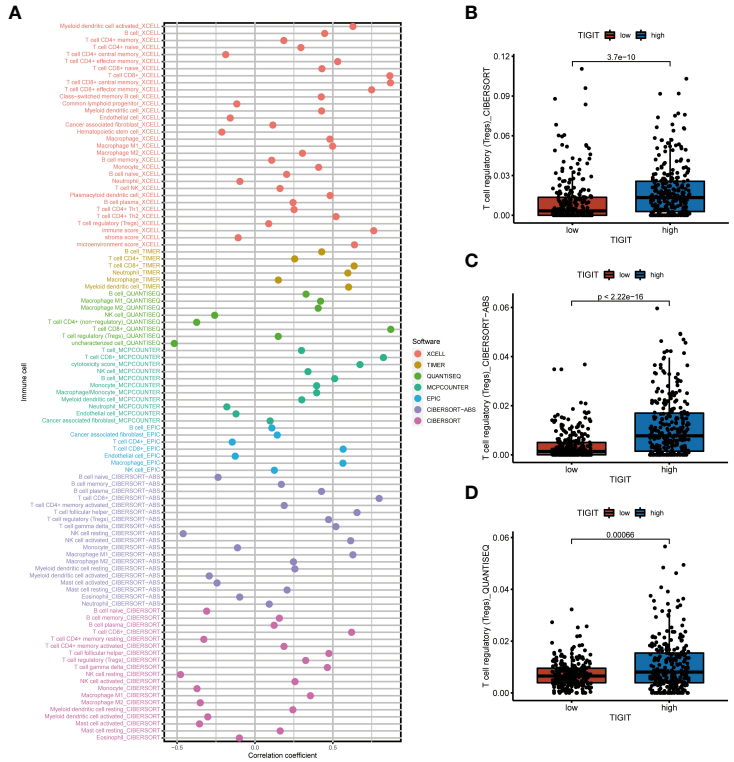

FIGURE 7
The correlation between immune infiltration and the expression of TIGIT in KIRC. **(A)** Spearman correlation test showed TIGIT was significantly associated with several types of immune infiltration cells. **(B)** Differential infiltration of Tregs between high or low TIGIT expression patients calculated by the CIBESORT. **(C)** Differential infiltration of Tregs between high or low TIGIT expression patients calculated by the CIBESORT-ABS. **(D)** Differential infiltration of Tregs between high or low TIGIT expression patients calculated by the QUANTISEQ.

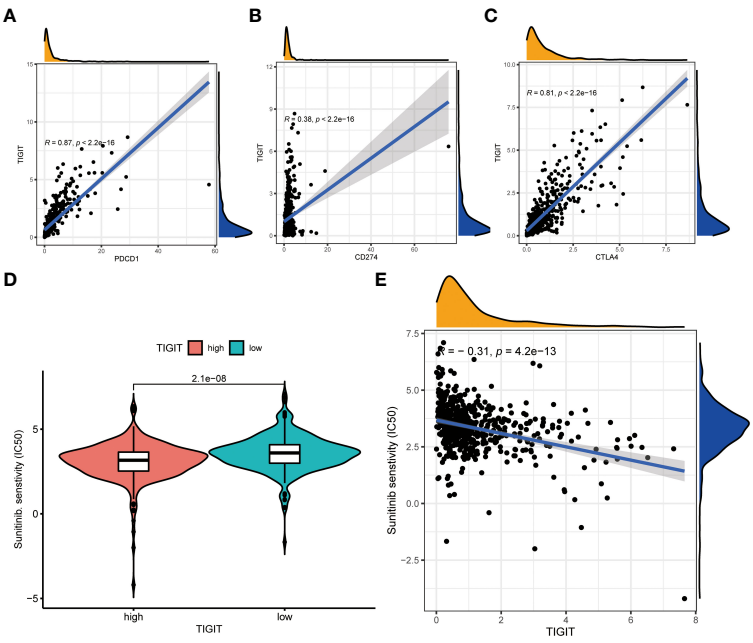

FIGURE 8
The co-expression between TIGIT and other common immune checkpoints and the drug response of sunitinib between high or low TIGIT expression patients. **(A)** TIGIT was significantly positive co-expression with PDCD1. **(B)** TIGIT was significantly positive co-expression with CD247. **(C)** TIGIT was significantly positive co-expression with CTLA4. **(D)** High expression of TIGIT was associated with a significantly higher drug sensitivity of sunitinib in KIRC. **(E)** TIGIT was significantly positively correlated with the drug sensitivity of sunitinib in KIRC.

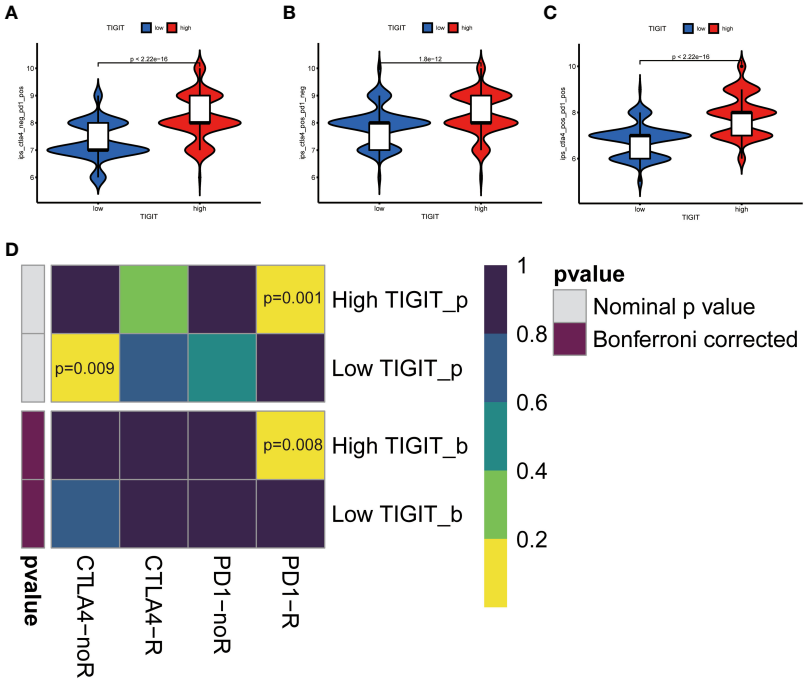

FIGURE 9
TIGIT and response of immunotherapy. **(A)** Prediction of immunotherapy in CTLA4 negative PD1 positive patients with high/low TIGIT expression. **(B)** Prediction of immunotherapy in CTLA4 positive PD1 negative patients with high/low TIGIT expression. **(C)** Prediction of immunotherapy in CTLA4 positive PD1 positive patients with high/low TIGIT expression. **(D)** Prediction of response to anti-PD1 or anti-CTLA4 immunotherapy by submap in KIRC patients with high/low TIGIT expression.

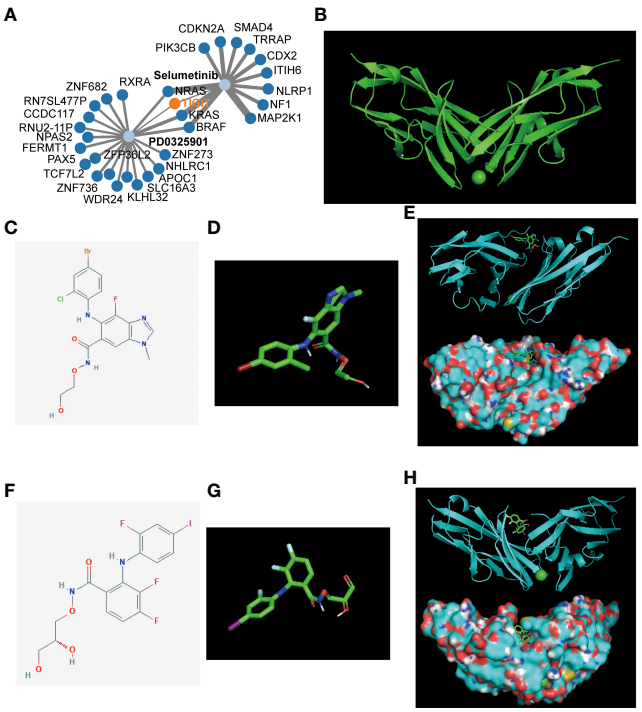

FIGURE 10
Gene-drug network and molecular docking. **(A)** The potential gene-drug networks target TIGIT. **(B)** The 3D structure of the TIGIT protein. **(C)** The 2D structure of Selumetinib. **(D)** The 3D structure of Selumetinib. **(E)** The molecular docking between Selumetinib and TIGIT showed Selumetinib could enter into the active pocket of TIGIT protein. **(F)** The 2D structure of PD0325901. **(G)** The 3D structure of PD0325901. **(H)** The molecular docking between PD0325901and TIGIT showed PD0325901could enter into the active pocket of TIGIT protein.

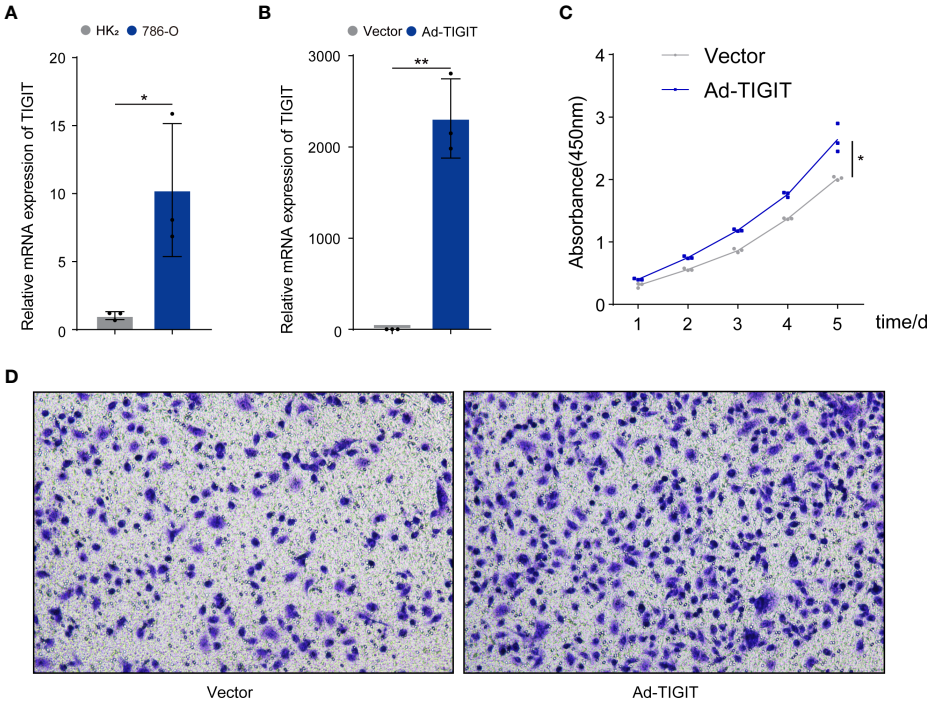

FIGURE 11
TIGIT affected the proliferation and migration of cells in renal carcinoma. **(A)** qRT-PCR was used to detect expression levels of TIGIT in tumor cells and normal cells. **(B)** The overexpression of TIGIT in 786-O cells was confirmed by qRT-PCR. **(C)** CCK8 assay: TIGIT could increase the viability of 786-O cells. **(D)** Transwell migration assay: TIGIT could promote the migration of 786-O cells. *p < 0.05; **p < 0.01.

expression of TIGIT is associated with a poor OS, PFS, and DSS in KIRC. Also, the expression of TIGIT was closely associated with the pathological characteristics of the tumor, high expression of TIGIT in KIRC was observed with several critical functions or pathways such as apoptosis, BCR signaling, TCR signaling et al. Moreover, the expression of TIGIT shows a strong positive correlation with infiltration of $CD8^+$ T cells and Tregs, and shows a positive correlation with the drug sensitivity to sunitinib and anti-PD1 immunotherapy at the same time. Furthermore, we constructed a gene-drug network, discovered Selumetinib and PD0325901 as potential drugs targeting TIGIT, and verified the interaction between these drugs and TIGIT protein by molecular docking. Finally, *in-vitro* experiments verified the essential role of TIGIT in KIRC.

Hong et al. reported a significant positive observation of TIGIT expression in renal cell carcinoma (RCC) tissues than adjacent normal tissues by immunohistochemistry in their cohorts (37), which was consistent with our results TIGIT showed a significantly higher expression in KIRC tissues than normal tissues. Also, Yin et al. reported the prognostic value of TIGIT in KIRC and constructed a survival-predicting model based on this (38). All these studies confirmed the significant role TIGIT played in tumorigenesis, progression, and clinical outcomes of KIRC. Interestingly, not only KIRC, Duan et al. reported TIGIT as an effective tumor biomarker in human hepatocellular carcinoma (HCC) that the expression levels of TIGIT were upregulated in the cancerous tissues with the degree of cancerous differentiation from high to low from patients with HCC, and TIGIT showed positive correlation with the level of α-fetoprotein (AFP), which reveals the potential of TIGIT as a cancer biomarker in HCC (39). Thus, Whether TIGIT is differentially expressed in the pan-cancer spectrum and whether TIGIT can be used as a tumor marker of pan-cancer is still questionable and needs more exploration in the future.

Another interesting result is the TIGIT-related functions and pathways. Our work shows that high TIGIT was associated with an enhanced function of apoptosis. This is consistent with the previous study. Kong et al. focused on TIGIT expression in T cells in patients with acute myelogenous leukemia (AML) (6). They confirmed the correct correlations between apoptosis and exhaustion of $CD8^+$ T cells and the TIGIT, and the enhanced apoptosis or exhaustion could be reversed after the knockdown of TIGIT (6). Also, Song et al. demonstrated the significant role of TIGIT in aging $CD8^+$ cells in aged mice (40), found that TIGIT was associated with high levels of expression of other inhibitory receptors, including PD-1 and showed features of exhaustion such as downregulation of the key costimulatory receptor CD28, the representative internal transcriptional regulation, the low production of cytokines, and high susceptibility to apoptosis. Importantly, their functional defects associated with aging could be reversed by TIGIT knockdown (40). Thus, TIGIT has great potential as a therapeutic target that several significant functions, such as apoptosis, could be reversed after targeting TIGIT.

Studies of TIGIT in NK cells can better show the important role of TIGIT in inhibiting anti-tumor immunity. Previous studies have shown that PVR molecules expressed on the surface of tumor cells

can bind to TIGIT on the surface of NK cells, which lead to inhibitory signals in NK cells, and then reduce the function of NK cells to kill tumor cells (8, 41, 42). These results indicate that TIGIT is also an inhibitory molecule on the surface of NK cells. Moreover, exhaustion NK cells highly express TIGIT rather than PD1, and whether it is to knock out the TIGIT gene or to inhibit TIGIT with anti TIGIT antibody can increase the expression of CD107a, tumor necrosis factor (TNF), and other tumor suppressor factors in NK cells, enhance the tumor-killing ability of NK cells and prolong the survival time of tumor-bearing mice (8). Also, it is surprising that the specific knockout of the TIGIT gene in NK cells can reverse the depletion of NK cells and significantly reduce the expression of PD1 in tumor-infiltrating cytotoxic T cells (8). Manieri et al. systematically summarized the important mechanisms of TIGIT in inhibiting anti-tumor immunity (43), which mainly includes the following three mechanisms: first, the PVR of tumor cells or dendritic cells binds to the TIGIT on the surface of tumor-infiltrating $CD8^+$T cells or NK cells, directly inhibiting the activity of these two immune cells. Second, TIGIT can also be used as a ligand. TIGIT ligands on the surface of tumor-infiltrating $CD8^+$T cells or Tregs can bind to PVR receptors of tumor cells or dendritic cells, promote the production of anti-inflammatory cytokines such as IL-10 and inhibit the immune response. Third, the TIGIT on the surface of tumor-infiltrating $CD8^+$T cells competitively binds to the PVR on the surface of tumor cells or dendritic cells, resulting in the failure of T cell-activated receptor CD226 to bind to PVR, thus inhibiting the activity of T cells (43).

These results indicate that targeting TIGIT can play a role in multiple ways and relieve the immunosuppression. This also inspires the combination therapy of PD1/PD-L1 and TIGIT monoclonal antibody. Johnston et al. reported that the combined use of TIGIT antibody and PD-L1 antibody at the same time is far better than blocking TIGIT or PD1/PD-L1 pathway alone, which can more significantly reduce the tumor volume and the survival time of tumor-bearing mice (5). Besides, CITYSCAPE (44), a randomized, double-blind, placebo-controlled phase II clinical trial of anti-TIGIT antibody tiragolumab combined with atezolizumab in the first-line treatment of patients with PD-L1 positive non-small cell lung cancer, demonstrated that the objective response rate (ORR) of combination therapy was 31.3%. In comparison, that of PD-L1 antibody monotherapy combined with placebo was 16.2%. Besides, in patients with high expression of PD-L1, ORR of combination therapy was 55.2%, while ORR of PD-L1 antibody monotherapy combined with placebo group was 17.2% (44). This is quite encouraging. As a result, Roche TIGIT monoclonal antibody tiragolumab has been recognized by FDA as a breakthrough therapy designation and combined with PD-L1 monoclonal antibody atezolizumab for the first-line treatment of metastatic non-small cell lung cancer with high expression of PD-L1 and non-EGFR nor ALK mutation patients.

TIGIT antibody showed huge potential in futural immunotherapy, and our works also identified TIGIT as an essential prognosis related and immune suppressive factor in KIRC. We discovered a significant correlation between PD1, PD-L1, and CTLA4 expression and TIGIT expression, which might give the explanation on the low response for the common immune monotherapy and might contribute to the combined therapy of PD1/PD-L1 or CTLA4 antibody therapy with TIGIT antibody in KIRC in the future. Besides, we found the expression of TIGIT was positive associated with the drug sensitivity of sunitinib, which might contribute to the combined therapy of the TIGIT antibody with sunitinib in KIRC in the future. More importantly, we discovered two potential drugs targeting TIGIT: Selumetinib and PD0325901. Interestingly, Selumetinib, a selective MEK1 inhibitor, was reported to enhance the antitumor activity of everolimusa against renal cell carcinoma by decreasing p-RPS6 and p-4E-BP1 dramatically, which caused G1 cell cycle arrest and preventing reactivation of AKT and ERK (45). Besides, Zeng et al. reported everolimus-induced autophagy involves activation of the ERK, which could impair the cytotoxicity of everolimus in RCC cells and inhibit the activation of ERK pathway-mediated autophagy like combined use of Selumetinib, which contributed to overcoming chemoresistance to everolimus (46). As for PD0325901, Diaz-Montero has claimed the combined use of PD0325901 contributes to abrogating the sunitinib resistance and leading to improved anti-tumour efficacy renal cell carcinoma (47). Thus, based on these studies and our discoveries, combined therapy of TKIs with Selumetinib or PD0325901 also shows great potential in treating KIRC in the future. More in-depth cohort studies were urgently needed in the future.

There are several limitations in this study. Firstly, our analysis were based on the bulk RNA-seq. However, the results would be more precise if the data were acquired by single-cell sequencing, which could contribute to our understanding of TIGIT in different cell types. Secondly, we suggested several novel therapeutic strategies for KIRC in this research, such as the application of Selumetinib or PD0325901 monotherapy as targeting TIGIT, combined therapy of PD1/PD-L1 antibody with TIGIT antibody, combined therapy of sunitinib with Selumetinib or PD0325901, et al. They were all hypotheses, and we need carrying out further studies including laboratory experiments and real-world cohort studies in the future.

Conclusion

TIGIT plays an essential role in tumorigenesis, progression in KIRC. High expression of TIGIT results in poor survival of KIRC and higher drug sensitivity to sunitinib and anti-PD1 immunotherapy. Besides, Selumetinib and PD0325901 may be potential drugs targeting TIGIT, and combined therapy of anti-TIGIT and other treatments show great potential in treating KIRC.

Data availability statement

The original contributions presented in the study are included in the article/Supplementary Material. Further inquiries can be directed to the corresponding authors.

Author contributions

Conception and design: Q-DX, BL, WG, HL, and S-GW. Acquisition of data: Q-DX and BL. Analysis of data: Q-DX and BL. Interpretation of data: Q-DX, BL, Drafting the manuscript: Q-DX and BL. Revising the manuscript: All authors. All authors contributed to the article and approved the submitted version.

Conflict of interest

The authors declare that the research was conducted in the absence of any commercial or financial relationships that could be construed as a potential conflict of interest.

Publisher's note

Supplementary material

The Supplementary Material for this article can be found online at: https://www.frontiersin.org/articles/10.3389/fonc.2023.1096341/full#supplementary-material

References

1. Yu X, Harden K, Gonzalez LC, Francesco M, Chiang E, Irving B, et al. The surface protein TIGIT suppresses T cell activation by promoting the generation of mature immunoregulatory dendritic cells. *Nat Immunol* (2009) 10:48–57. doi: 10.1038/ni.1674

2. Abbas AR, Baldwin D, Ma Y, Ouyang W, Gurney A, Martin F, et al. Immune response in silico (IRIS): Immune-specific genes identified from a compendium of microarray expression data. *Genes Immun* (2005) 6:319–31. doi: 10.1038/sj.gene.6364173

3. Lozano E, Dominguez-Villar M, Kuchroo V, Hafler DA. The TIGIT/CD226 axis regulates human T cell function. *J Immunol Am Assoc Immunologists* (2012) 188:3869–75. doi: 10.4049/jimmunol.1103627

4. Pauken KE, Wherry EJ. TIGIT and CD226: Tipping the balance between costimulatory and coinhibitory molecules to augment the cancer immunotherapy toolkit. *Cancer Cell Cell Press* (2014) p:785–7. doi: 10.1016/j.ccell.2014.11.016

5. Johnston RJ, Comps-Agrar L, Hackney J, Yu X, Huseni M, Yang Y, et al. The immunoreceptor TIGIT regulates antitumor and antiviral CD8+ T cell effector function. *Cancer Cell* (2014) 26:923–37. doi: 10.1016/j.ccell.2014.10.018

6. Kong Y, Zhu L, Schell TD, Zhang J, Claxton DF, Ehmann WC, et al. T-Cell immunoglobulin and ITIM domain (TIGIT) associates with CD8+ T-cell exhaustion and poor clinical outcome in AML patients. *Clin Cancer Res* (2016) 22:3057–66. doi: 10.1158/1078-0432.CCR-15-2626

7. Harjunpää H, Guillerey C. TIGIT as an emerging immune checkpoint. *Clin Exp Immunol* (2020) p:108–19. doi: 10.1111/cei.13407

8. Zhang Q, Bi J, Zheng X, Chen Y, Wang H, Wu W, et al. Blockade of the checkpoint receptor TIGIT prevents NK cell exhaustion and elicits potent anti-tumor immunity. *Nat Immunol Nat* (2018) 19:723–32. doi: 10.1038/s41590-018-0132-0

9. Chauvin JM, Pagliano O, Fourcade J, Sun Z, Wang H, Sander C, et al. TIGIT and PD-1 impair tumor antigen-specific CD8+ T cells in melanoma patients. *J Clin Invest* (2015) 125:2046–58. doi: 10.1172/JCI80445

10. Fourcade J, Sun Z, Chauvin JM, Ka M, Davar D, Pagliano O, et al. CD226 opposes TIGIT to disrupt tregs in melanoma. *JCI Insight NLM (Medline)* (2018) 3:1–13. doi: 10.1172/jci.insight.121157

11. Josefsson SE, Huse K, Kolstad A, Beiske K, Pende D, Steen CB, et al. T Cells expressing checkpoint receptor TIGIT are enriched in follicular lymphoma tumors and characterized by reversible suppression of T-cell receptor signaling. *Clin Cancer Res* (2018) 24:870–81. doi: 10.1158/1078-0432.CCR-17-2337

12. Tiragolumab impresses in multiple trials. *Cancer Discov* (2020) 10:1086–7. doi: 10.1158/2159-8290.CD-NB2020-063

13. Siegel RL, Miller KD, Jemal A. Cancer statistics, 2019. *CA Cancer J Clin* (2019) 69:7–34. doi: 10.3322/caac.21551

14. Motzer RJ, Jonasch E, Agarwal N, Bhayani S, Bro WP, Chang SS, et al. Kidney cancer, version 2.2017: Clinical practice guidelines in oncology. *JNCCN J Natl Compr* (2017) 15(6):804–34. doi: 10.6004/jnccn.2017.0100

15. Linehan WM, Ricketts CJ. The cancer genome atlas of renal cell carcinoma: Findings and clinical implications. *Nat Rev Urol* (2019) 16(9):539–52. doi: 10.1038/s41585-019-0211-5

16. Barata PC, Rini BI. Treatment of renal cell carcinoma: Current status and future directions. *CA Cancer J Clin* (2017) 67:507–24. doi: 10.3322/caac.21411

17. Motzer RJ, Bacik J, Mazumdar M, Atkins M, Linehan WM, Gordon M. Prognostic factors for survival of patients with stage IV renal cell carcinoma: Memorial Sloan-Kettering cancer center experience. *Clin Cancer Res* (2004) 10(18 Pt 2):6302S–3S. doi: 10.1158/1078-0432.CCR-040031

18. Vugrin D. Systemic therapy of metastatic renal cell carcinoma. *Semin Nephrol. N Engl J Med* (1987) 7(2):152–62.

19. Beroukhim R, Brunet JP, Di Napoli A, Mertz KD, Seeley A, Pires MM, et al. Patterns of gene expression and copy-number alterations in von-hippel lindau disease-associated and sporadic clear cell carcinoma of the kidney. *Cancer Res* (2009) 69:4674–81. doi: 10.1158/0008-5472.CAN-09-0146

20. Motzer RJ, Tannir NM, McDermott DF, Arén Frontera O, Melichar B, Choueiri TK, et al. Nivolumab plus ipilimumab versus sunitinib in advanced renal-cell carcinoma. *N Engl J Med* (2018) 378:1277–90. doi: 10.1056/NEJMoa1712126

21. Motzer RJ, Penkov K, Haanen J, Rini B, Albiges L, Campbell MT, et al. Avelumab plus axitinib versus sunitinib for advanced renal-cell carcinoma. *N Engl J Med* (2019) 380:1103–15. doi: 10.1056/NEJMoa1816047

22. Ljungberg B, Albiges L, Bensalah K, Bex A, Giles RH, Hora M, et al. EAU guidelines. edn. presented at the EAU annual congress Amsterdam 2020. *Eur Urol.* (2020) 67:913–24. doi: 10.1016/j.eururo.2015.01.005

23. Motzer RJ, Escudier B, McDermott DF, George S, Hammers HJ, Srinivas S, et al. Nivolumab versus everolimus in advanced renal-cell carcinoma. *N Engl J Med New Engl J Med (NEJM/MMS);* (2015) 373:1803–13. doi: 10.1056/NEJMoa1510665

24. Topalian SL, Hodi FS, Brahmer JR, Gettinger SN, Smith DC, McDermott DF, et al. Five-year survival and correlates among patients with advanced melanoma, renal cell carcinoma, or non-small cell lung cancer treated with nivolumab. *JAMA Oncol Am Med Association;* (2019) 5:1411–20. doi: 10.1001/jamaoncol.2019.2187

25. Rini BI, Motzer RJ, Powles T, McDermott DF, Escudier B, Donskov F, et al. Atezolizumab plus bevacizumab versus sunitinib for patients with untreated metastatic renal cell carcinoma and sarcomatoid features: A prespecified subgroup analysis of the IMmotion151 clinical trial. *Eur Urol* (2020) 79(5):659–62. doi: 10.1016/j.eururo.2020.06.021

26. McGregor BA, McKay RR, Braun DA, Werner L, Gray K, Flaifel A, et al. Results of a multicenter phase II study of atezolizumab and bevacizumab for patients with metastatic renal cell carcinoma with variant histology and/or sarcomatoid features. *J Clin Oncol* (2020) 38:63–70. doi: 10.1200/JCO.19.01882

27. Rini BI, Powles T, Atkins MB, Escudier B, McDermott DF, Suarez C, et al. Atezolizumab plus bevacizumab versus sunitinib in patients with previously untreated metastatic renal cell carcinoma (IMmotion151): A multicentre, open-label, phase 3, randomised controlled trial. *Lancet* (2019) 393:2404–15. doi: 10.1016/S0140-6736(19)30723-8

28. Xia QD, Xun Y, Lu JL, Lu YC, Yang YY, Zhou P, et al. Network pharmacology and molecular docking analyses on lianhua qingwen capsule indicate Akt1 is a potential target to treat and prevent COVID-19. *Cell Prolif* (2020) 53:1–13. doi: 10.1111/cpr.12949

29. Lonsdale J, Thomas J, Salvatore M, Phillips R, Lo E, Shad S, et al. The genotype-tissue expression (GTEx) project. *Nat Genet* (2013) p:580–5. doi: 10.1038/ng.2653

30. Tang Z, Li C, Kang B, Gao G, Li C, Zhang Z. GEPIA: A web server for cancer and normal gene expression profiling and interactive analyses. *Nucleic Acids Res* (2017) 45:W98–102. doi: 10.1093/nar/gkx247

31. Blum A, Wang P, Zenklusen JC. SnapShot: TCGA-analyzed tumors. *Cell* (2018) 173(2):530. doi: 10.1016/j.cell.2018.03.059

32. Li T, Fan J, Wang B, Traugh N, Chen Q, Liu JS, et al. TIMER: A web server for comprehensive analysis of tumor-infiltrating immune cells. *Cancer Res* (2017) 77:e108–10. doi: 10.1158/1538-7445.AM2017-108

33. Chen X, Guo Y, Chen X. iGMDR: Integrated pharmacogenetic resource guide to cancer therapy and research. *Genomics Proteomics Bioinforma* (2020) 18:150–60. doi: 10.1016/j.gpb.2019.11.011

34. Wang Y, Xiao J, Suzek TO, Zhang J, Wang J, Zhou Z, et al. PubChem's BioAssay database. *Nucleic Acids Res* (2012) 40:D400–12. doi: 10.1093/nar/gkr1132

35. Bateman A, Martin MJ, O'Donovan C, Magrane M, Alpi E, Antunes R, et al. UniProt: The universal protein knowledgebase. *Nucleic Acids Res* (2017) 45:D158–69. doi: 10.1093/nar/gkw1099

36. Berman HM, Westbrook J, Feng Z, Gilliland G, Bhat TN, Weissig H, et al. The protein data bank. *Nucleic Acids Res* (2000) 28(1):235–42. doi: 10.1093/nar/28.1.235

37. Hong X, Wang X, Wang T, Zhang X. Correlation of T cell immunoglobulin and ITIM domain (TIGIT) and programmed death 1 (PD-1) with clinicopathological characteristics of renal cell carcinoma may indicate potential targets for treatment. *Med Sci Monit* (2018) 24:6861–72. doi: 10.12659/MSM.910388

38. Yin X, Zhang X, Liu Z, Sun G, Zhu X, Zhang H, et al. Assessment for prognostic value of differentially expressed genes in immune microenvironment of clear cell renal cell carcinoma. *Am J Transl Res* (2020) 12:5416–32.

39. Duan X, Liu J, Cui J, Ma B, Zhou Q, Yang X, et al. Expression of TIGIT/CD155 and correlations with clinical pathological features in human hepatocellular carcinoma. *Mol Med Rep* (2019) 20:3773–81. doi: 10.3892/mmr.2019.10641

40. Song Y, Wang B, Song R, Hao Y, Wang D, Li Y, et al. T-Cell immunoglobulin and ITIM domain contributes to CD8 + T-cell immunosenescence. *Aging Cell* (2018) 17:1–12. doi: 10.1111/acel.12716

41. Li M, Xia P, Du Y, Liu S, Huang G, Chen J, et al. T-Cell immunoglobulin and ITIM domain (TIGIT) receptor/poliovirus receptor (PVR) ligand engagement suppresses interferon-γ production of natural killer cells *via* β-arrestin 2-mediated negative signaling. *J Biol Chem* (2014) 289:17647–57. doi: 10.1074/jbc.M114.572420

42. Stanietsky N, Rovis TL, Glasner A, Seidel E, Tsukerman P, Yamin R, et al. Mouse TIGIT inhibits NK-cell cytotoxicity upon interaction with PVR. *Eur J Immunol* (2013) 43:2138–50. doi: 10.1002/eji.201243072

43. Manieri NA, Chiang EY, Grogan JL. TIGIT: A key inhibitor of the cancer immunity cycle. *Trends Immunol* 38(1):20–8. doi: 10.1016/j.it.2016.10.002

44. Rodriguez-Abreu D, Johnson ML, Hussein MA, Cobo M, Patel AJ, Secen NM, et al. Primary analysis of a randomized, double-blind, phase II study of the anti-TIGIT antibody tiragolumab (tira) plus atezolizumab (atezo) versus placebo plus atezo as first-line (1L) treatment in patients with PD-L1-selected NSCLC (CITYSCAPE). *J Clin Oncol* (2020) 38(Suppl. 15):9503–3. doi: 10.1200/JCO.2020.38.15_suppl.9503

45. Zou Y, Wang J, Leng X, Huang J, Xue W, Zhang J, et al. The selective MEK1 inhibitor selumetinib enhances the antitumor activity of everolimus against renal cell carcinoma in vitro and *in vivo*. *Oncotarget* (2017) 8:20825–33. doi: 10.18632/oncotarget.15346

46. Zeng Y, Tian X, Wang Q, He W, Fan J, Gou X. Attenuation of everolimus-induced cytotoxicity by a protective autophagic pathway involving ERK activation in renal cell carcinoma cells. *Drug Des Devel Ther* (2018) 12:911–20. doi: 10.2147/DDDT.S160557

47. Diaz-Montero CM, Mao FJ, Barnard J, Parker Y, Zamanian-Daryoush M, Pink JJ, et al. MEK inhibition abrogates sunitinib resistance in a renal cell carcinoma patient-derived xenograft model. *Br J Cancer* (201) 115:920–8. doi: 10.1038/bjc.2016.263

frontiers | Frontiers in Oncology

TYPE Original Research
PUBLISHED 30 March 2023
DOI 10.3389/fonc.2023.1131473

OPEN ACCESS

EDITED BY
Linhui Wang,
Second Military Medical University, China

REVIEWED BY
Jinxiang Wang,
Precision Medicine Center, Sun Yat-sen University, China
Fangdie Ye,
Fudan University, China

*CORRESPONDENCE
Yue Wu
wuyuetjm@163.com

SPECIALTY SECTION
This article was submitted to Genitourinary Oncology, a section of the journal Frontiers in Oncology

RECEIVED 25 December 2022
ACCEPTED 20 March 2023
PUBLISHED 30 March 2023

CITATION
Lin D, Hu B, Zhu S and Wu Y (2023) Exploring a ferroptosis and oxidative stress-based prognostic model for clear cell renal cell carcinoma.
Front. Oncol. 13:1131473.
doi: 10.3389/fonc.2023.1131473

Exploring a ferroptosis and oxidative stress-based prognostic model for clear cell renal cell carcinoma

Dongxu Lin[1,2], Bintao Hu[1,2], Shiqing Zhu[1,2] and Yue Wu[1,2]*

[1]Department of Urology, Tongji Hospital, Tongji Medical College, Huazhong University of Science and Technology, Wuhan, Hubei, China, [2]Institute of Urology, Tongji Hospital, Tongji Medical College, Huazhong University of Science and Technology, Wuhan, Hubei, China

Background: Ferroptosis is a newly defined cell death process triggered by increased iron load and tremendous lipid reactive oxygen species (ROS). Oxidative stress-related ferroptosis is of great important to the occurrence and progression of clear cell renal cell carcinoma (ccRCC), which is particularly susceptibility to ferroptosis agonist. Therefore, exploring the molecular features of ferroptosis and oxidative stress might guide the clinical treatment and prognosis prediction for ccRCC patients.

Methods: The differentially expressed ferroptosis and oxidative stress-associated genes (FPTOSs) between normal renal and ccRCC tissues were identified based on The Cancer Genome Atlas (TCGA) database, and those with prognostic significances were applied to develop a prognostic model and a risk scoring system (FPTOS_score). The clinical parameter, miRNA regulation, tumor mutation burden (TMB), immune cell infiltration, immunotherapy response, and drug susceptibility between two FPTOS-based risk stratifications were determined.

Results: We have identified 5 prognosis-associated FPTOSs (*ACADSB*, *CDCA3*, *CHAC1*, *MYCN*, and *TFAP2A*), and developed a reliable FPTOS_socre system to distinguish patients into low- and high-risk groups. The findings implied that patients from the high-risk group performed poor prognoses, even after stratified analysis of various clinical parameters. A total of 30 miRNA-FPTOS regulatory pairs were recognized to identify the possible molecular mechanisms. Meanwhile, patients from the high-risk group exhibited higher TMB levels than those from the low-risk groups, and the predominant mutated driver genes were *VHL*, *PBRM1* and *TTN* in both groups. The main infiltrating immune cells of high- and low-risk groups were $CD8^+$ T cells and resting mast cells, respectively, and patients from the high-risk groups showed preferable drug responsiveness to anti-PD-1 immunotherapy. Eventually, potential sensitive drugs (cisplatin, BI-D1870, and docetaxel) and their enrichment pathways were identified to guide the treatment of ccRCC patients with high-risk.

Conclusion: Our study comprehensively analyzed the expression profiles of FPTOSs and constructed a scoring system with considerable prognostic value, which would supply novel insights into the personalized treatment strategies and prognostic evaluation of ccRCC patient.

KEYWORDS

clear cell renal cell carcinoma, ferroptosis, oxidative stress, prognostic model, bioinformatics

1 Introduction

Renal cell carcinoma (RCC) is one of the most common malignant genitourinary tumors. There are 431,288 newly diagnosed cases and 179,368 newly dead cases worldwide in 2020 (1), and it is estimated that there are 81,800 new cases and 14,890 dead cases in the United States in 2023 (2). The incidence of RCC continued increasing at a rate of approximately 1% annually, while mortality rates have decreased by about 2% annually from 2016 to 2020, which might be attributed to advancements in diagnostic tools and early treatment (2). Clear cell renal cell carcinoma (ccRCC) represents the predominant pathological subtype, accounting for almost 70% of all RCC (3). Although 70% of early localized RCC tumor can be completely surgery resection by radical nephrectomy, there is still up to 30% of patients will eventually progress to distant metastasis (3, 4). The ccRCC patients with advanced stage are likely to experience poor outcomes, and the 5-year overall survival (OS) rate is only 11.7% (5). Despite there are occasional reports of durable responses, most advanced RCC patients will develop resistance to targeted drugs such as first-line VEGFR inhibitor (sunitinib, pazopanib) and second-line mTOR inhibitor (everolimus) (6, 7). Therefore, seeking for molecular biomarkers with accurate predictive capacity and therapeutical potential has attract the concerns of many scholars.

Crosstalk between ferroptosis and oxidative stress has been demonstrated in many diseases, such as ischemic stroke (8), inflammation (9), and cancer (10). Ferroptosis is a newly defined nonapoptotic programmed cell death type, characterized by active iron overload, excessive lipid reactive oxygen species (ROS) generation and membrane phospholipid peroxidation (11). In brief, when the redox homeostasis is impaired, iron generates active hydroxyl radical (·OH) *via* Fenton reaction, which then promotes the production of phospholipid hydroperoxides (PLOOH). Meanwhile, blocking of cystine/glutamate antiporter system Xc^- decreases the synthesis of glutathione (GSH) and the only intracellular PLOOH-neutralizing enzyme glutathione peroxidase 4 (GPX4), and eventually contributes to the accumulation of ROS and ferroptosis (12). Oxidative stress is occurred due to the breakdown of the redox homeostasis, characterized by an increase of ROS and a decrease of antioxidant enzymes (13). ROS at physiological level is essential to maintain the function of cellular biology, however, excessive ROS generation under oxidative stress condition is a double-edged sword for cancer (14). For one thing, ROS-caused oxidative damage promotes cell death (apoptosis, ferroptosis) and triggers anti-tumor immune cells (M1 macrophages, T cells) infiltration to function as a tumor suppressor (15). Besides, high level of ROS causes detrimental damages of DNA, protein, and lipid, and induces genomic instability to function as a tumor promoter (16). In general, exacerbating ROS generation and undermining antioxidant system are sufficient to trigger oxidative stress and ferroptosis in tumor cells (17).

Sensitivity analysis of ferroptosis agonist erastin on 177 cancer cell lines indicated that RCC and diffuse large B cell lymphoma were extremely susceptible to GPX4-dependent ferroptosis (18). Hence, targeting ferroptosis and oxidative stress may challenge the current treatment paradigm of RCC. Previous studies usually consider the impact of a single gene or variable on the ccRCC development. However, a widely accepted consensus is that tumorigenesis and progression were affected by the interaction of multiple factors in a sequential and coordinated manner. Thus, it is urgent to develop an integrative and efficient utility to reflect the features of ferroptosis and oxidative stress in ccRCC. With the advances in multiomic sequencing, it is possible to comprehensively explore the genomic profiles of ccRCC. Here, we had identified differentially expressed ferroptosis and oxidative stress-associated genes (FPTOSs), and 5 genes with independent prognostic values were incorporated into the prognostic model. Subsequently, all ccRCC patients were allocated into low- and high-risk groups according to the FPTOS_score, and the prognostic significance of FPTOS-based risk stratification was assessed in both the TCGA-KIRC and E-MTAB-1980 cohorts. The miRNA regulation, mutation pattern, immune cell population, immunotherapy responsiveness, and drug susceptibility were also examined.

2 Materials and methods

2.1 Data collection and preprocessing

Transcriptome data, clinical parameters and prognosis data, miRNA sequencing data, and somatic mutation data of ccRCC patients were extracted from The Cancer Genome Atlas (TCGA) database (https://portal.gdc.cancer.gov/). E-MTAB-1980 cohort was acquired from ArrayExpress database (https://www.ebi.ac.uk/arrayexpress/) and served as the external validation dataset. The raw

data from TCGA-KIRC cohort were preprocessed through averaging the expression levels of same genes, removing the genes with low expression levels below 1, and normalizing the expression profiles using trimmed mean of M-values (TMM) method based on the edgeR package. As for the microarray data from E-MTAB-1980 cohort, we performed background adjustment and normalization using the robust multiarray analysis (RMA) method based on Affy package. Furthermore, the expression values were log2 transformed, and the probes were converted into corresponding gene symbols.

2.2 Preparation of ferroptosis and oxidative stress-associated gene set

Ferroptosis-associated genes were gained from the FerrDb database (http://www.zhounan.org/ferrdb/current/). To obtain oxidative stress-associated genes, we applied "oxidative stress" as search term to acquire genes that were involved in the process of oxidative stress from the OMIN database (https://www.oncomine.org/resource/), NCBI gene function module (https://www.ncbi.nlm.nih.gov/gene/) and GeneCard database (https://www.genecards.org/). We then acquired the integrative gene set from the TCGA-KIRC cohort. After that, ferroptosis and oxidative stress-associated gene set was prepared by selecting the intersecting genes among above gene sets using Venn diagram.

2.3 Development and validation of a FPTOS-based prognostic model

Differentially expressed FPTOSs of ccRCC patients were identified through R package "EdgeR" referring to screening criteria of |log2 fold change (FC)| > 1 and adjusted $P < 0.05$. Subsequently, univariate Cox regression, least absolute shrinkage and selection operator (LASSO) regression, and multivariate Cox regression analyses were utilized to investigate the FPTOSs with prognostic significance of ccRCC. The individualized risk score of each ccRCC patient, named FPTOS_score, was measured using the formula: $FPTOS\_score = \sum_{i=1}^{n} Expi\beta i$. Of that, *Exp* denoted the expression level of specific gene, while β represented the corresponding regression coefficient. On basis of the median value of FPTOS_score, all ccRCC patients were allocated into low- and high-risk groups. Subsequently, Kaplan-Meier method was used to explore the prognosis difference between two risk groups, and receiver operating characteristic (ROC) curve was plotted to estimate the power and accuracy of FPTOS-based prognostic model. The external validation cohort (E-MTAB-1980) was applied to assess the predictive performance and stability of the prognostic model. Meanwhile, the prognostic values of the FPTOSs were verified separately based on the GEPIA database (http://gepia.cancer-pku.cn/index.html).

We first compared the difference in the number of deaths between two risk stratifications, and calculated the FPTOS_score of alive and dead patients, so as to reveal whether FPTOS-based risk stratification could distinguish patients with poor prognosis. In order to discover independent prognostic factors of ccRCC, FPTOS_score and various clinical parameters including age, gender, grade, stage, T stage, N stage, M stage were subjected to univariate and multivariate Cox regression analyses. Furthermore, stratified analyses of various clinical parameters were conducted to determine whether FPTOS-based risk stratification still performed a considerable prognostic value.

2.4 Construction of miRNA-FPTOS regulatory network

miRNA sequencing data were extracted from TCGA-KIRC cohort, and the differentially expressed miRNAs were determined *via* comparing the expression differences between the normal and tumor samples with the setting criteria of |log2 FC| > 1 and $P < 0.05$. Then we investigated the co-expression patterns between miRNAs and prognostic-associated FPTOSs, and mapped miRNA-FPTOS regulatory pairs on the basis of filtering criteria (|cor| > 0.25, $P < 0.001$).

2.5 Tumor mutation burden (TMB) analysis

R package "Maftool" was applied to determine the TMB levels using somatic mutation data from the TCGA database. Survival analysis was applied to determine the influence of TMB on the outcome of ccRCC patients. The TMB levels in two risk stratifications and their correlations with FPTOS_score were also measured. TMB was estimated *via* counting the overall number of mutations per coding in the tumor sample. Moreover, waterfall diagrams were plotted to display the landscape of gene mutation profiles in two risk stratifications. We then evaluated the predictive capacities of risk stratification on the ccRCC patients' prognosis when the mutation of driver genes such as *VHL*, *PBRM1* and *TNN* were considered.

2.6 Exploration of immune microenvironment and response to immunotherapy

The abundances of immune cell types between two risk stratifications was evaluated by the CIBERSORT approach and LM22 signature matrix (19). We performed 1000 permutation tests to ensure the stability of the outputs. The immune microenvironment was investigated using ESTIMATE algorithm according to the predictive results of immune score, estimate score and tumor purity (20).

In order to determine the immunotherapy responsiveness, we subsequent analyzed the expression profiles of immune checkpoint inhibitor (ICI)-targeted genes (*PD-1*, *CTLA-4*) between two risk stratifications. Taken the mutation profiles of ICI-targeted genes into account, the influence of FPTOS_score on the patients' prognosis was explored. Since the lack of available ccRCC cohorts

receiving immunotherapy, we employed the Tumor Immune Dysfunction and Exclusion (TIDE) algorithm to predict the responsiveness towards immunotherapy (21). Applying an open-access immunotherapy-treated melanoma cohorts, unsupervised subclass mapping (SubMap) method was utilized to indirectly predict the immunotherapy responsiveness in the two risk stratifications according to the similarity of gene expression profile (22). Additionally, adopting expression and survival data from a metastatic melanoma cohort who receiving PD-1 immunotherapy, we further conducted survival analysis to evaluate the progression-free survival (PFS) rates of different risk groups.

2.7 Identification of sensitive drugs based on FPTOS_score

The transcriptional data, drug susceptibility data, and corresponding drug targets or pathways of various tumor cell lines were extracted from a pharmacogenomic dataset Genomics of Drug Sensitivity in Cancer (GDSC, https://www.cancerrxgene.org/). The relationship between the drug susceptibility and the FPTOS_score was evaluated by Person correlation analysis according to the criteria (|correlation coefficient (R) | > 0.15 and $P < 0.05$). The targets or pathways of these drugs were also screened out to estimate the underlying mechanisms.

2.8 Real-time PCR (RT-PCR) analysis

To examine the expression level of the identified FPTOSs in ccRCC sample, we further carried out RT-PCR experiments to compare the mRNA expression difference between human ccRCC tumor specimen and adjacent normal specimen. Moreover, the mRNA expression of FPTOSs in human normal renal proximal tubular cell line (HK2), human renal clear cell carcinoma cell lines (786-O, OS-RC-2) were also evaluated. Cells was purchased from Shanghai Cell Bank Type Culture Collection Committee (Shanghai, China) and incubated in RPMI-1640 medium containing 10% fetal bovine serum (FBS). The total RNA was extracted using Trizol reagent and then transcribed into cDNA using 1st Strand cDNA Synthesis Kit (Vazyme, China). RT-PCR method was performed *via* qPCR SYBR Green Master Mix (Vazyme, China) in a QuantStudio™ 6 Flex Real-Time PCR System. The result was normalized to housekeeping gene GAPDH, and the selected primers for the FPTOSs were listed in Table S1.

2.9 Statistical analysis

The statistical analysis and result presentation were realized *via* R version 4.0.5 and GraphPad Prism version 8.0. Unpaired student's *t* test or Mann-Whitney *U* test was utilized to investigate the differences between two groups with or without normally distributed variables, respectively. Log-rank test was applied to compare different survival outcomes between two groups. Correlation analysis between two continuous variables was realized by either Pearson or Spearman test as appropriate. Contingency table variables were processed with Chi-squared (χ^2) test or Fisher's exact test. Unless otherwise stated, $P < 0.05$ was regarded as statistically significant for all analysis.

3 Results

3.1 Identification of FPTOS gene signature

Figure 1 depicted the selection procedures of FPTOS-based prognostic signature. Specifically, we first obtained transcriptome data of ccRCC patients from the TCGA-KIRC cohort, which included 72 normal renal specimens and 539 ccRCC tumor specimens. A Venn diagram was plotted to identify all genes of interest that was closely associated with ferroptosis and oxidative stress, and a total of 437 FPTOSs were output for further analysis (Figure 2A). Subsequently, the differentially expressed FPTOSs between normal and tumor specimens were screened out based on the filtering criteria (|log2 FC| > 1.0, $P < 0.05$), and 50 downregulated genes and 81 upregulated genes met the requirement. The expression and distribution profiles of these FPTOSs were presented in Figures 2B, C.

We then carried out GO and KEGG enrichment analyses to determine the biological functions and involved pathways of the FPTOSs. The biological processes were enriched in the responses to hypoxia, oxygen levels, chemical stress and oxidative stress. The cell components lied in apical part of cell, apical plasma membrane, and basolateral plasma membrane. With regard to molecular functions, these genes were involved in iron ion binding, oxidoreductase activity, acting on single donors with incorporation of molecular oxygen, and dioxygenase activity (Figure 2D). Additionally, KEGG analysis indicated that the identified genes were related with miRNAs in cancer, HIF-1 signaling pathway, carcinogenesis-reactive oxygen species, human cytomegalovirus infection, and ferroptosis (Figure 2E). The findings revealed that the

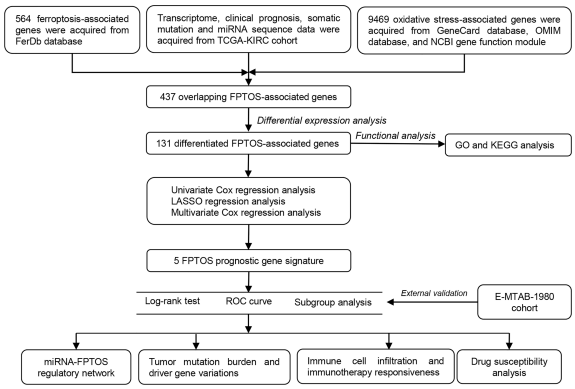

FIGURE 1
Flowchart depicts the searching procedures to develop a FPTOS-based prognostic model in ccRCC.

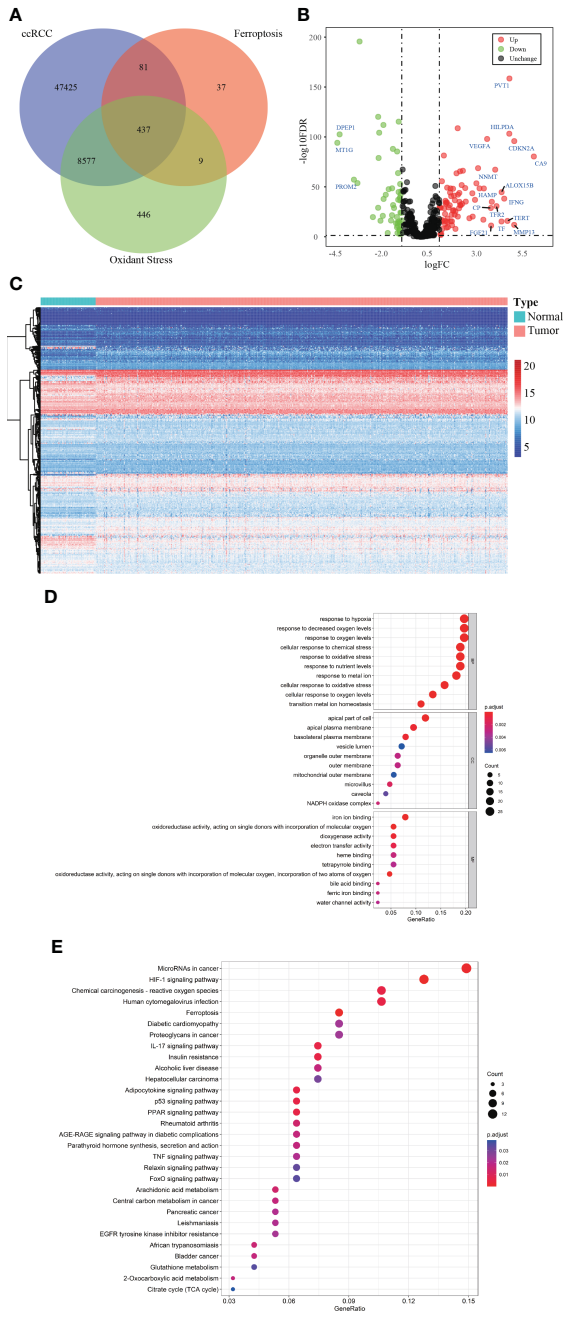

FIGURE 2
Identification of the differentially expressed FPTOSs of ccRCC in TCGA database. **(A)** Searching for FPTOS-associated genes in ccRCC patients using Venn diagram. **(B)** Visualization of differentially expressed FPTOSs between normal renal tissues (N = 72) and ccRCC tissues (N = 539) using volcano plot based on the transcriptional data in TCGA-KIRC cohort. **(C)** Visualization of differentially expressed FPTOSs using heatmap based on transcriptional data in TCGA-KIRC cohort. **(D)** GO enrichment analysis of differentially expressed FPTOSs to determine involved gene function. **(E)** KEGG enrichment analysis of differentially expressed FPTOSs to determine involved pathway.

differentially expressed FPTOSs were primarily implicated in hypoxia, oxidative stress, ferroptosis and oxygen level regulation, confirming that the filtering criteria could accurately recognize the FPTOSs of interest.

3.2 Development and validation of a FPTOS-based prognostic model

We identified 131 FPTOS-related prognostic genes by univariate Cox regression analysis (Table S2). LASSO regression analysis was carried out to search the predominant prognostic FPTOSs. The trajectory variations in regression coefficients of above 131 genes were presented in Figure S1A, and the cross-validation results of LASSO model construction were presented in Figures S1B. Finally, 6 output genes (*ACADSB*, *BID*, *CDCA3*, *CHAC1*, *MYCN* and *TFAP2A*) were identified and subjected for further study. Applying multivariate Cox regression analysis, 5 genes (*ACADSB*, *CDCA3*, *CHAC1*, *MYCN*, *TFAP2A*) with independent prognostic significances were incorporated into the prognostic model (Table 1; Figure 3A). Among them, *ACADSB* and *MYCN* were considered as the protective factors, while *CDCA3*, *CHAC1*, and *TFAP2A* were considered as the detrimental factors. Furthermore, we examined the prognostic values of the identified FPTOSs in the ccRCC patients. Based on the expression profiles and outcome data in the GEPIA database, we found that *ACADSB* and *MYCN* are the favorable prognostic marker of ccRCC, while *CDCA3*, *CHAC1*, and *TFAP2A* are the unfavorable prognostic marker of ccRCC (Figure S2). The above findings further highlighted the considerable prognostic capacities of the FPTOSs in monitoring ccRCC progression.

The FPTOS_score of each ccRCC patient was computed applying the following formula: FPTOS_score = (-0.2832 × Exp *ACADSB*) + (0.2549 × Exp *CDCA3*) + (0.1523 × Exp *CHAC1*) + (-0.1508 × Exp *MYCN*) + (0.0672 × Exp *TFAP2A*). To assess the model applicability, the ccRCC patients were allocated into the low- and high-risk groups on the basis of the median value of FPTOS_score. The difference of OS between two risk stratifications from the TCGA-KIRC cohorts was measured by Kaplan-Meier method, and the results suggested that patients from the high-risk group performed a worse prognosis than those from the low-risk group (P = 4.432e-12, Figure 3B). The ROC curve was also plotted to evaluate the prediction power and accuracy of FPTOS-based risk stratification. As presented in Figure 3C, the area under the ROC curve (AUC) values were 0.751 at 1-year, 0.724 at 3-year, and 0.734 at 5-year. Furthermore, external validation was applied to evaluate whether the prognostic model showed stable performance in the E-MTAB-1980 cohort. As a result, a poor prognosis was observed in the high-risk group (P = 0.003, Figure 3D), and the AUC values of 1-year, 3-year, and 5-year OS rates were 0.807, 0.797, and 0.804 (Figure 3E). Generally, these findings indicated a preferable predictive power and stability of the FPTOS-based prognostic model.

3.3 Independence of the FPTOS_score from clinical parameters of ccRCC

We then investigated the survival outcomes between two FPTOS-based risk stratifications, and it is shown that ccRCC patients with high-risk exhibited lower OS rates than those with low-risk (χ^2= 84.130, P < 0.001) (Figure 4A). Similarly, the dead

TABLE 1 Multivariate Cox regression analysis to identify prognosis-related FPTOSs.

Gene	Coef	Exp (coef)	se (coef)	z	Pr (>|z|)
ACADSB	-0.2832	0.7534	0.1130	-2.5057	0.0122
CDCA3	0.2549	1.2904	0.0868	2.9370	0.0033
CHAC1	0.1523	1.1645	0.0603	2.5261	0.0115
MYCN	-0.1508	0.8600	0.0587	-2.5688	0.0102
TFAP2A	0.0672	1.0695	0.0405	1.6575	0.0974

Coef, coefficient.

patients performed a higher FPTOS_score than the alive patients ($P \leq$ 2e-16) (Figure 4B), indicating a positive correlation between FPTOS_score and poor prognosis. To further confirm the independence of FPTOS_score on the prognostic evaluation of ccRCC, the crucial clinical parameters (age, gender, grade, stage, T stage, N stage, M stage) and FPTOS_score were subjected to univariate and multivariate Cox regression analyses (Table S3; Figures 4C, D). The findings suggested that FPTOS_score could serve as an independent prognostic variable of ccRCC patients (HR = 2.028, 95% CI: 1.640-2.507, $P < 0.001$).

We next investigated the feasibility of the FPTOS-based risk stratification in predicting the prognosis of ccRCC patient subgroups stratified by above clinical parameters. As the results acquired from the Kaplan-Meier survival analyses, the survival prognosis of ccRCC patients with high-risk were significantly worse than those with low-risk, regardless of the clinical variable stratifications (All $P < 0.001$) (Figures S3A–S3N). Such results implied that FPTOS-based risk stratification could distinguish patients with poor outcomes without considering the influence of other clinical parameters.

3.4 Construction of miRNA-FPTOS regulatory network

miRNAs are implicated in multiple cellular processes including redox homeostasis regulation (23). Therefore, it is valuable to map the miRNA-FPTOS regulatory network, which may underlie the upstream regulatory mechanism of FPTOSs. We first extracted the miRNA sequencing data from the TCGA database. Abnormally expressed miRNAs were identified according to filtering criteria ($|\log2 FC| > 1.0$, $P < 0.05$), and were displayed in heatmap (Figure 5A). Then the co-expression analysis between prognostic FPTOSs and abnormally expressed miRNAs was conducted in reference to the inclusion criteria ($|cor| > 0.25$, $P < 0.001$). A total of 30 miRNA-FPTOS regulatory pairs were screened out (Table S4), and a Sankey diagram was plotted to exhibit the regulatory network (Figure 5B).

3.5 Association between FPTOS_score and mutation profiles

The occurrence and progression of ccRCC were partially attributed to the mutation of driver genes. At present, we extracted the somatic mutation data of ccRCC patients from TCGA-KIRC cohort to reveal the association between FPTOS_score and mutation profiles. We found that patients with high TMB levels experienced worse outcomes than patients with low levels ($P = 0.002$) (Figure 6A), and elevated TMB levels were observed in the patients from high-risk group (Figure 6B). Moreover, correlation analysis suggested that FPTOS_score was positively correlated with TMB level ($R = 0.20$, $P =$ 3e-4) (Figure 6C).

Subsequently, the genes mutated in at least 5% of the tumor specimens from two risk stratifications were illustrated *via* waterfall plot. A significant abundant mutation events was existed in the specimens from high-risk group, accompanying by an increased dead population (Figures 6D, E). We employed the top 3 mutated driver genes (*VHL*, *PRBM1*, *TNN*) to investigate whether the FPTOS_score still had prognostic value when the driver gene mutations were taken into account. The results revealed that *VHL*-mutated patients with low-risk performed significant survival advantages than those with high-risk, meanwhile, *VHL*-wild patients with low-risk also performed significant survival advantages than those with high-risk (Figure 6F). Consistent with the performance of different *VHL* phenotype groups, patients with low-risk still experienced better outcomes than those with high-risk, no matter whether the mutation of *PRBM1* and *TNN* occurred (Figures 6G, H). Collectively, these findings implied that FPTOS-based risk stratification was positively correlated with TMB level and gene mutation frequency, and patients with relatively low FPTOS_score exhibited favorable prognosis even when the mutation of driver genes were considered.

3.6 Determination of immune cell infiltration and immune microenvironment

RCC is recently regarded as an immunogenic tumor, which is partly caused by the immune dysfunction with the infiltration of suppressive immune cell subtypes such as regulatory T cells (Tregs) and myeloid-derived suppressor cells (MDSCs) (24). Currently, the components of immune cells were measured using CIBERSORT method. Correlation matrix was plotted to depict all the 22 immune cell proportions, and a strong relevance was existed between $CD8^+$ T cells and Tregs in the TCGA-KIRC cohort (Figure 7A). It was shown that abundant populations of $CD8^+$ T cells, M0

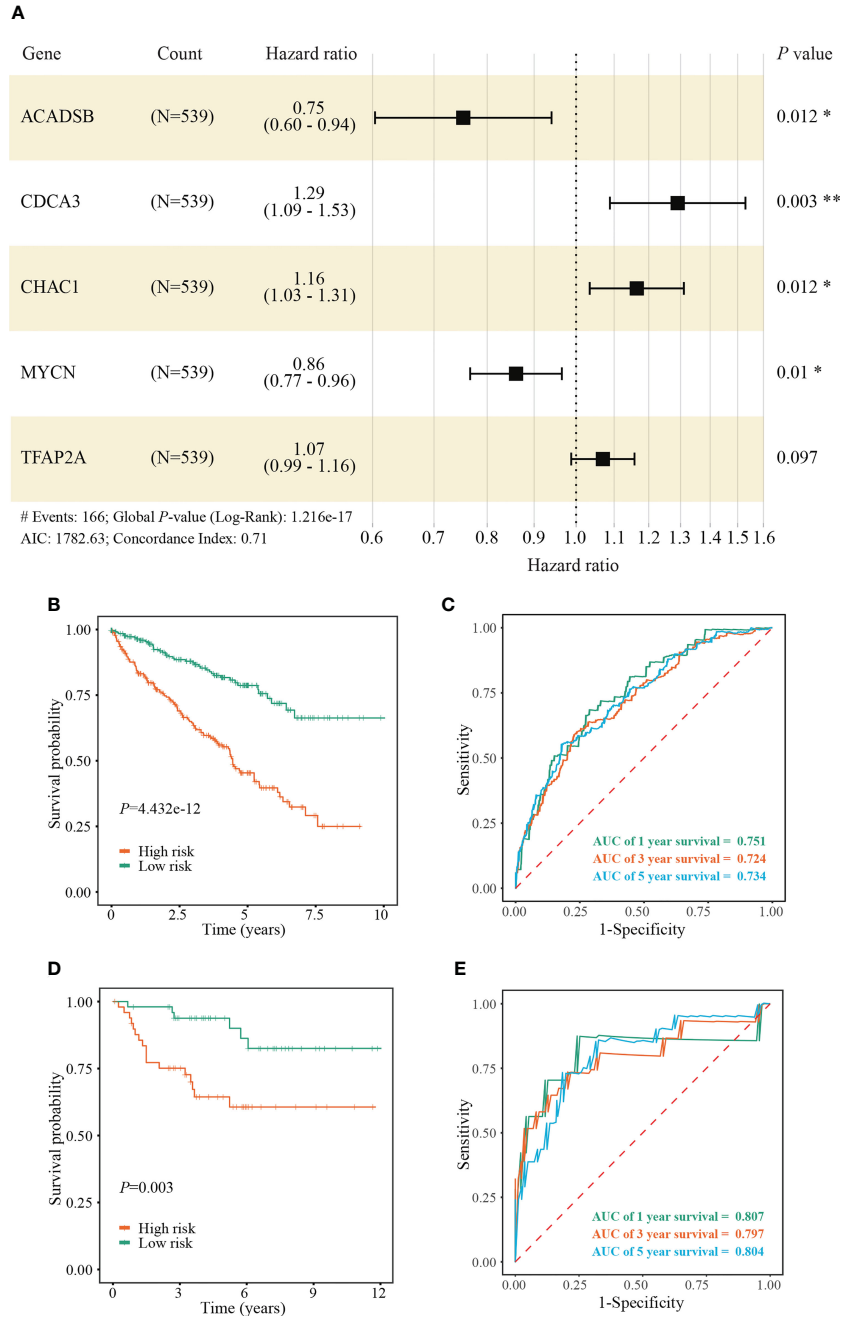

FIGURE 3
Construction and validation of a FPTOS-based prognostic model. **(A)** Multivariate Cox regression analysis to evaluate the prognostic values of 5 FPTOSs. **(B)** Kaplan-Meier survival curve analysis to compare overall survival (OS) difference between low- and high-risk groups in the TCGA-KIRC cohort. **(C)** Time-dependent ROC curve analysis to evaluate the predictive power of the FPTOS-based risk stratification in the TCGA-KIRC cohort. **(D)** Kaplan-Meier survival curve analysis to compare OS difference between low and high-risk groups in the validated E-MTAB-1980 cohort. **(E)** Time-dependent ROC curve analysis to evaluate the predictive power of the FPTOS-based risk stratification in the validated E-MTAB-1980 cohort. Log-rank test was applied to compare the statistical differences in the Kaplan-Meier curves.

macrophages, and Tregs existed in the patient specimens from high-risk group, while predominant populations of resting mast cells, M2 macrophages, and monocytes accumulated in the specimens from low-risk group (Figure 7B).

What else, the immune microenvironment properties of ccRCC specimens were quantified, and the output values of immune score and estimate score in the high-risk group (1152.85 ± 793.65, 1796.53 ± 1239.89, respectively) were significantly higher than those in the low-risk group (860.65 ± 565.16, 1504.52 ± 943.08, respectively), while the output values of tumor purity in the high-risk group (0.6348 ± 0.1311) were significantly lower than those in the low-risk group (0.6712 ± 0.0956) (Figures 7C–E).

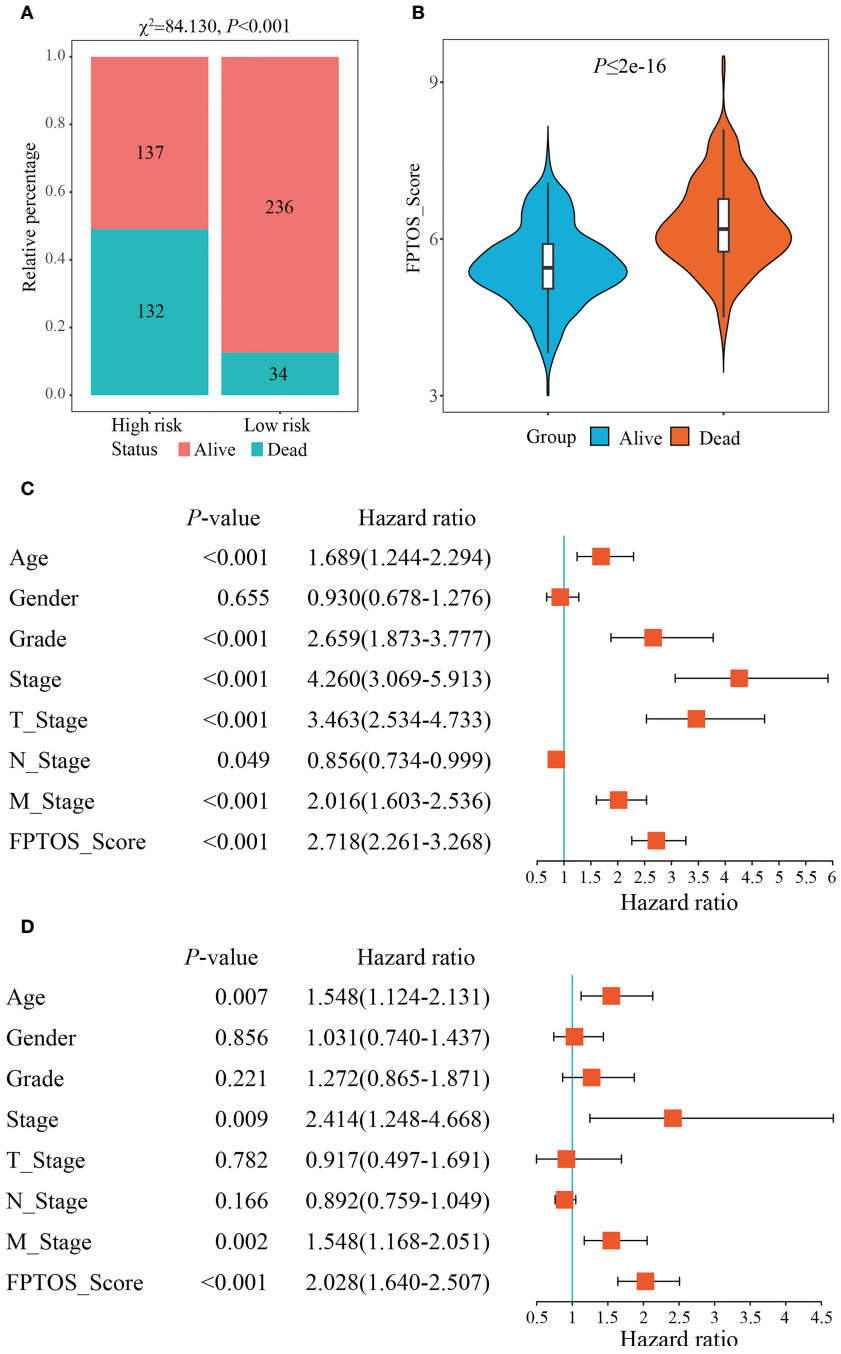

FIGURE 4
Independence of the FPTOS_score from clinical parameters of ccRCC. **(A)** Survival status of low- and high-risk groups stratified by FPTOS_score in ccRCC patients. The categorical variables were analyzed with the Chi-squared (χ^2) test. **(B)** FPTOS_score of ccRCC patients stratified by survival status. **(C, D)** Univariate or multivariate Cox regression analysis to confirm the independent prognostic significance of FPTOS_score and clinical parameters for ccRCC patients.

3.7 Evaluation of immunotherapy responsiveness based on FPTOS risk stratification

Immunotherapy, especially immune checkpoint inhibitor (ICI), has witnessed a tremendous development and revolutionized the treatment of various tumors (25). Therefore, we next measured the changes of ICI targeted genes (*PD-1, CTLA-4*) in different risk stratifications. Compared with the low-risk patients, the expression of *PD-1* and *CTLA-4* in the high-risk patients were dramatically upregulated (all $P < 0.001$) (Figures 8A, B). Subsequently, we measured the survival prognosis of ccRCC patients between two

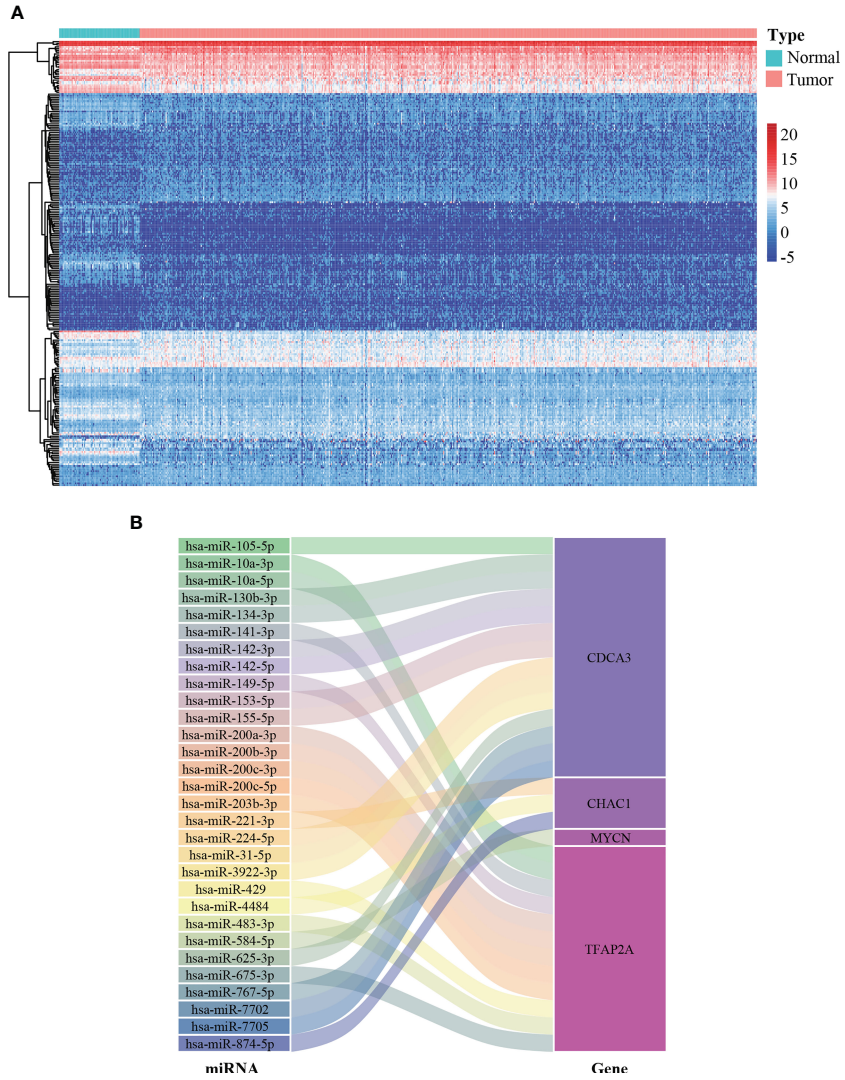

FIGURE 5
Construction of miRNA-FPTOS regulatory network for ccRCC patients. **(A)** Heatmap of differentially expressed miRNAs between normal renal samples and ccRCC tumor samples. **(B)** Sankey plot to visualize the potential regulatory relationship between differentially expressed miRNAs and prognostic FPTOSs.

risk stratifications when the expression of ICI-targeted genes was taken into consideration. As a result, patients with high-risk and high *PD-1/CTLA-4* expression experienced worse outcomes when compared with patients with low risk and high *PD-1/CTLA-4* level, and patients with high-risk and low *PD-1/CTLA-4* level experienced worse outcomes when compared with patients with low-risk and low *PD-1/CTLA-4* level (Figures 8C, D).

Since the absence of easily-accessible ccRCC cohort treated with immunotherapy, the TIDE algorithm, which integrated T cell dysfunction and exclusion on the basis of the expression profiles, was applied to predict the response to immunotherapy. When compared with the low-risk group, the high-risk group presented significantly elevated TIDE prediction scores (P = 0.00047) (Figure 8E). Meanwhile, patients in different risk stratifications exhibited different immunotherapy responsiveness, while the response ratio of high-risk to low risk was 46.77% to 35.21% (χ^2 = 7.325, P = 0.007) (Figure 8F).

Subsequently, the SubMap analysis was conducted to compare the expression characteristics of FPTOS_score acquired from the TCGA and GEO databases with an open-access metastatic melanoma cohort who receiving anti-PD-1 or anti-CTLA-4 treatment. The results revealed that patients with high-risk might respond positively to anti-PD-1 immunotherapy in both TCGA and GEO cohorts (adjusted P = 0.049 and 0.012, respectively), conversely, patients with low-risk might respond poorly to anti-CTLA-4 immunotherapy (adjusted P = 0.0033 and 0.011, respectively) (Figures 8G, H). Furthermore, we evaluated the predictive efficacy of FPTOS_score in the Riaz's cohort who receiving anti-PD-1 immunotherapy, and discovered that patients with high-risk experienced worse outcomes in PFS when compared with those with low-risk (P = 0.015) (Figure 8I). These results had provided guidance for the immunotherapy strategy of ccRCC patients, for instance, a feasibility of anti-PD-1 treatment for high-risk patients.

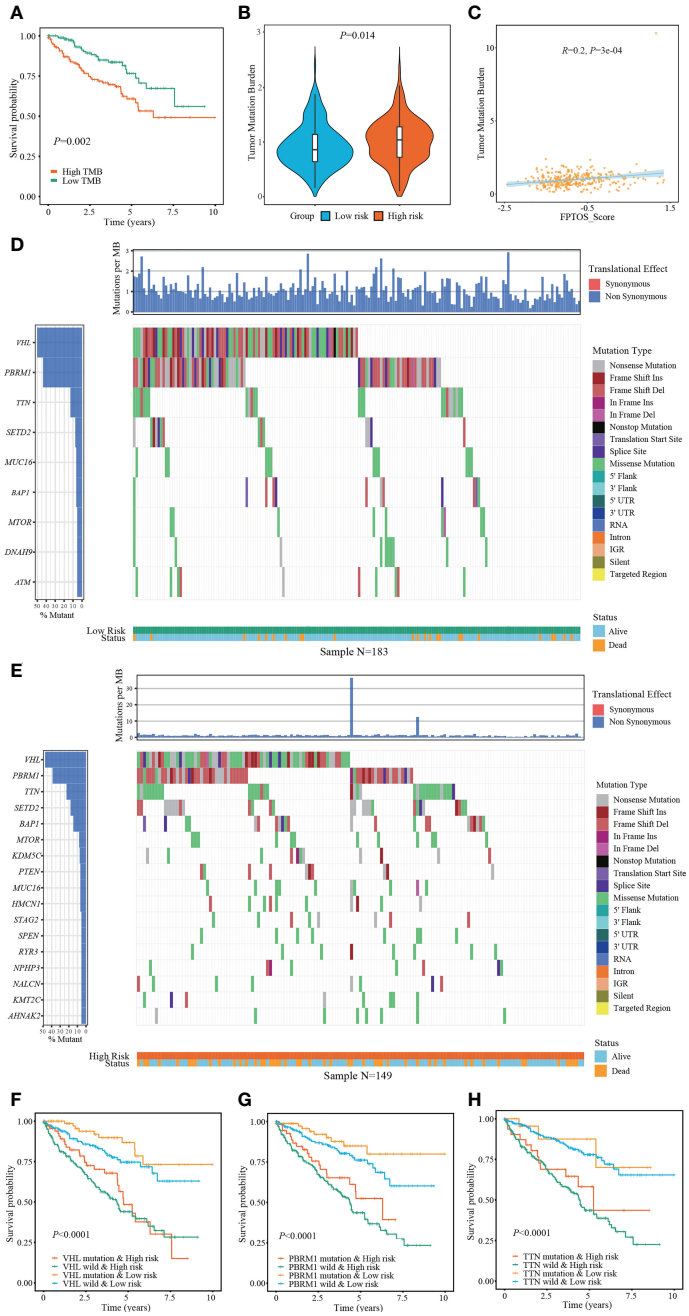

FIGURE 6
Exploring association between FPTOS_score and mutation profiles. **(A)** Kaplan-Meier survival analysis to explore the influence of TMB levels on the prognosis of ccRCC patients. **(B)** Differences of TMB levels between the two FPTOS-based risk stratifications. **(C)** Person's correlation analysis between FPTOS_score and TMB level. **(D, E)** Waterfall plot to exhibit the mutation landscape in the low- or high-risk group, respectively. The high-frequency mutated genes and events were illustrated. **(F–H)** Kaplan-Meier survival analysis among four groups stratified by the FPTOS-based risk stratifications and mutation profiles of driver genes *VHL*, *PBRM1*, or *TTN*, respectively.

3.8 Relationship between FPTOS_score and drug susceptibility

To explore available drugs for high-risk patients, we further investigated the relevance between FPTOS_score and IC50 values of corresponding drugs in the ccRCC cell lines *via* the pharmacogenomics database GDSC. In the light of inclusion criteria ($|R| > 0.15$, $P < 0.05$), 18 drugs (including cisplatin, BI-D1870 and docetaxel) performed sensitive responses towards high FPTOS_score, while 21 drugs (including AS601245, AKT Inhibitor VIII and AZD8055) performed resistant responses towards high FPTOS_score (Figure 9A). What else, the drug-involved pathways were analyzed. As shown in the Figure 9B, the sensitive drugs were enriched in the pathways associated with genome integrity,

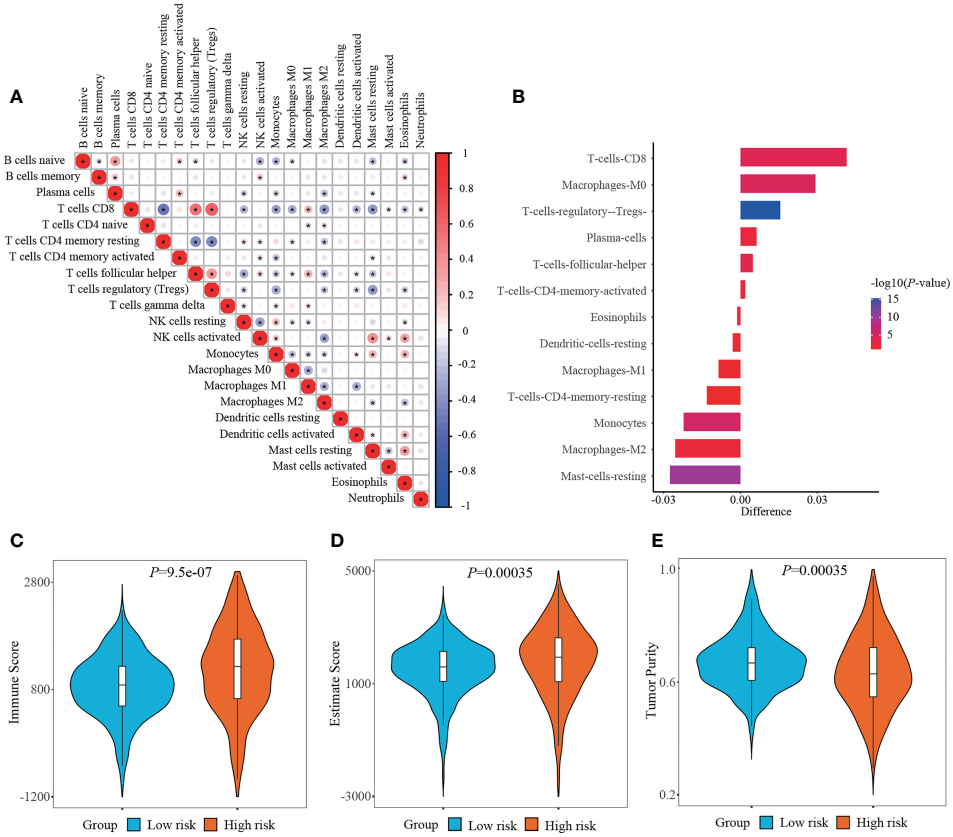

FIGURE 7
Determining immune cell infiltration and immune microenvironment between two risk stratifications. **(A)** Correlation matrix of all 22 immune cell populations. **(B)** Exploring the differentially infiltration of immune cell populations between low- and high-risk groups. **(C–E)** Comparison of immune score, estimate score or tumor purity using ESTIMATE algorithm between two risk stratifications.

metabolism, p53 pathway, protein stability and degradation, while the resistant drugs were involved in the pathways such as WNT signaling, RTK signaling, hormone-related, EGFR signaling, apoptosis regulation and Other. The above findings indicated that the FPTOS_score might influence the drug responsiveness of ccRCC cell lines, which might provide insights into the cancer treatment.

3.9 Exploring the expression pattern of the identified FPTOSs

The mRNA expression of prognostic FPTOSs in both renal tissue and cell samples was determined by RT-PCR method. As the results indicated, the expressions of *CDCA3*, *MYCN* and *TFAP2A* in ccRCC tumor tissue were significantly upregulated compared with those in adjacent normal kidney tissue, while the expressions of *ACADSB* and *CHAC1* were significantly downregulated (Figures 10A–E). Additionally, the mRNA expression of *ACADSB*, *CHAC1*, and *TFAP2A* were also significantly upregulated in ccRCC cell line 786-O, while the *CHAC1* was downregulated but *ACADSB* and *TFAP2A* were upregulated in another ccRCC cell line OS-RC-2 (Figures 10F–J).

4 Discussion

Resistance to cell death, genome instability and mutation are the basic hallmarks of cancer (26). Interestingly, RCC cells were more sensitive to erastin-induced ferroptosis than others tumor cell types, which might be attributed to the dependence of GSH content and GPX4 activity to regulate redox homeostasis (18). Mechanistically, peroxisomes promoted the biosynthesis of polyunsaturated ether phospholipids (PUFA-ePLs), substrates of lipid peroxidation, and triggered the occurrence of ferroptosis. A decrease of PUFA-ePLs will promote the conversion of ferroptosis-sensitive state to ferroptosis-resistant state of RCC cells (27). Chemerin, a hypoxia-inducible factor (HIF)-dependent adipokine, suppressed fatty acid oxidation and thus mediated ferroptosis resistance in ccRCC (28). Moreover, one analysis revealed that ccRCC patients occurred a 2-82% mutation frequency among 36 ferroptosis-related genes (29). The multi-kinase inhibitors sorafenib is recommended to be the first-line strategy for treating advanced ccRCC patients (30, 31). Interestingly, it can block the system Xc^- function, induce GSH consumption and lipid ROS accumulation, and thus trigger ferroptosis in RCC cells (32–34). Therefore, comprehensive exploration of the FPTOSs expression profiles could deepen the understanding of occurrence and progression of ccRCC.

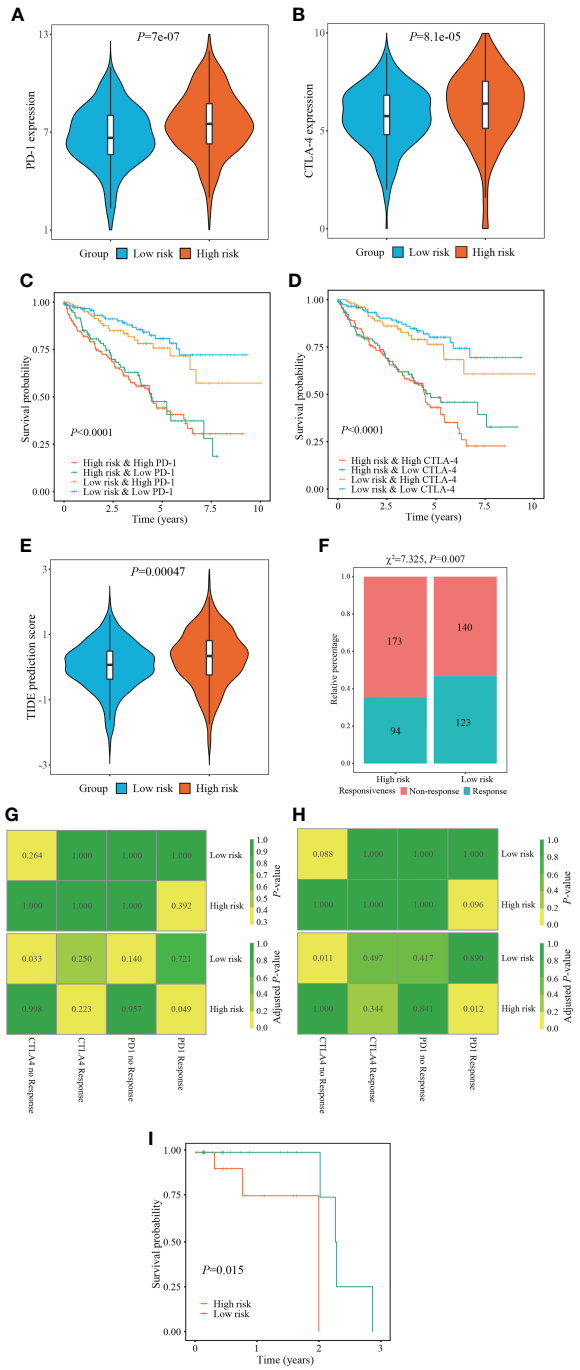

FIGURE 8
Evaluation of immunotherapy responsiveness based on FPTOS risk stratification. **(A, B)** Expression patterns of ICI targeted gene PD-1 or CTLA-4 in two FPTOS-based risk stratifications. **(C, D)** Kaplan-Meier survival analysis for OS among four groups stratified by the FPTOS-based risk stratifications and PD-1 or CTLA-4 expression level, respectively. **(E)** Difference of TIDE prediction score between the low- and high-risk groups. **(F)** Comparison of immunotherapy responsiveness between low- and high-risk groups. **(G, H)** SubMap analysis to predict the immunotherapy responsiveness in the low- and high-risk groups from the TCGA cohort or GEO cohort, respectively, according to the anti-PD-1 or anti-CTLA-4 responsiveness from the open-access metastatic melanoma cohort. **(I)** Kaplan-Meier survival analysis of progression-free survival (PFS) between the low- and high risk groups in the Riaz's cohort who have received anti-PD-1 immunotherapy.

In the current study, using univariate Cox regression, LASSO regression, and multivariate Cox regression analyses, 5 FPTOSs with crucial prognostic significances were identified, including *ACADSB*, *CDCA3*, *CHAC1*, *MYCN*, and *TFAP2A*. Among them, *ACADSB* and *MYCN* were discovered as the protective factors, while *CDCA3*, *CHAC1* and *TFAP2A* were discovered as the detrimental factors. ACADSB is a member of acyl-CoA dehydrogenase family, and is predominantly involved in the processes of fatty acid metabolism, branch-chained amino acid metabolism and ferroptosis (35, 36). It was reported that *ACADSB* expression was positively associated with the expression of ferroptosis driving genes. Suppression of ACADSB was observed in ccRCC samples, which was accompanied with advanced grade and stage, and might function as an independent prognostic factor of ccRCC patients (37). CDCA3 engaged in cell cycle regulation through mediating ubiquitin degradation of mitosis-inhibitory kinase WEE1 (38). It was considered to be a prognostic factor of RCC, and the upregulation of *CDCA3* was associated with advanced TNM stage, tumor grade and immune cell infiltration (39). In addition, lncRNA SNHG12 increased *CDCA3* expression and thus mediated tumor progression and sunitinib resistance in RCC patients (40). CHAC1 was implicated in the processes of endoplasmic reticulum (ER) stress and ferroptosis (41). It could serve as a biomarker to independently forecast the prognostic outcomes of ccRCC patients, and was positively associated with the expression signatures of various immune cells (memory B cell, NK cell and Th1 cell) and ICI genes (*ADORA2A*, *CD200*, *CD44*) (42). Aberrant *MYCN* amplification was previously considered as a driving event of high-risk neuroblastoma (43). However, inhibition of MYCN contributed to the drug resistance of cisplatin through repressing apoptosis in epithelial ovarian cancer (44). The specific roles of MYCN in ccRCC progression still requires further verification. Transcriptional factor TFAP2A controlled the expression of various tumor-related genes including *VEGF*, *BCL-2*, *c-Kit* and *c-Myc*, and was reported to be widely upregulated in tumor samples (45). Additionally, suppression of TFAP2A inhibited cell proliferation, migration and invasion *via* initiating oxidative stress and ferroptosis in gallbladder carcinoma (46).

These 5 FPTOS genes were then included into a prognostic model, which was utilized to develop a risk scoring system, named FPTOS_score. All patients were allocated into low- and high-risk groups on the basis of the median value of FPTOS_score. The results indicated a poor prognosis existed in the high-risk group, and the prognostic model presented preferable predictive sensitivity and accuracy. What else, the FPTOS-based risk stratification was able to distinguish patients with undesirable outcomes, and the results were robust even after considering the influence of various clinical parameters.

miRNAs served as a class of crucial molecules that regulate gene expression in a post-transcriptional modification manner. It was reported that miRNAs were responsible for regulating ROS generation and thus promoting ferroptosis occurrence in ccRCC (47). Hence, we carried out a co-expression analysis to explore the crosstalk between differentially expressed miRNAs and prognostic FPTOSs, and a total of 30 miRNA-FPTOS regulatory pairs were

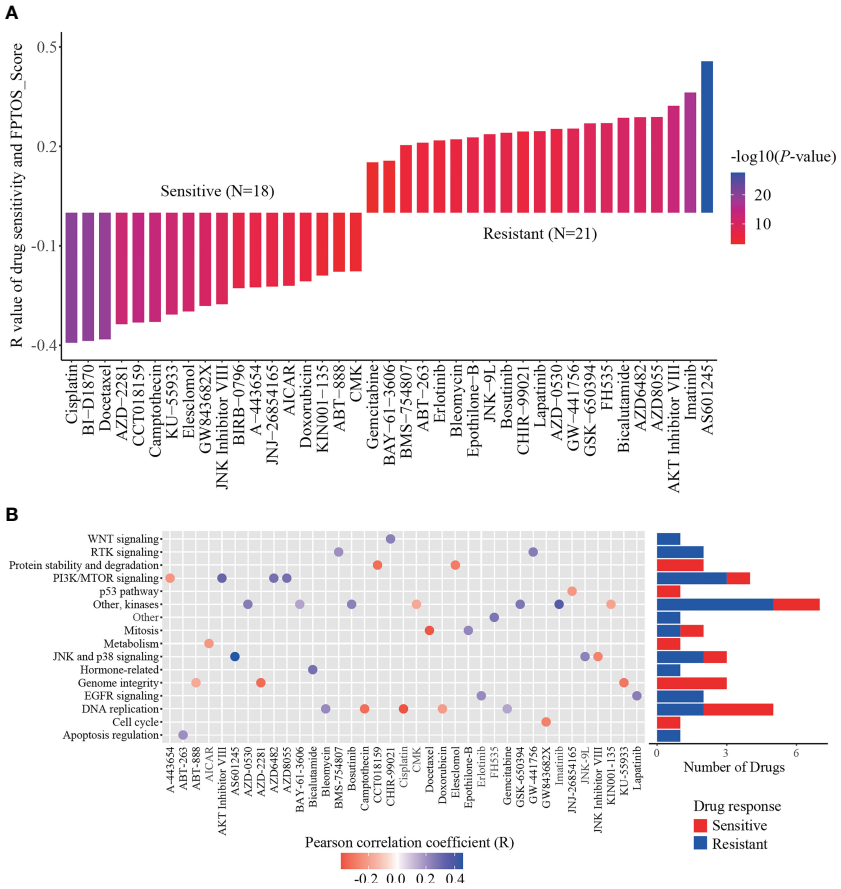

FIGURE 9
Identification of sensitive drugs for ccRCC patients based on FPTOS_score. **(A)** Person correlation analysis between FPTOS_score and drug susceptibility in the GDSC database. **(B)** Screening for involved pathways of identified drugs.

obtained, which might bring novel insights into the gene regulation patterns in ccRCC.

Emerging evidences demonstrated that accumulation of somatic mutation events is responsible for the tumorigenesis and progression (48). TMB is newly considered as a substitute for neoantigen load to act as a prognostic biomarker for cancer (49). Therefore, identification of mutated genes especially driver genes of ccRCC may provide promising opportunities for personalized therapy and prognosis prediction. The findings indicated that patients from high-risk group performed elevated TMB level, which was accompanied with a poor prognosis. Abundance mutation events were existed in patients with high-risk, and the well-defined driver genes *VHL*, *PRBM1* and *TTN* occupied the most frequent mutation sites in both the low- and high-risk groups. Interestingly, patients from the high-risk groups experienced a worse prognosis than those from the low-risk groups when the mutation of these diver genes was taken into account. A recently accepted notion of RCC progression is that *VHL* mutation function as an initial event to drive tumorigenesis, while *PBRM1*, *BAP1* and *SETD2* subsequent trigger defects in DNA repair system and abnormal tumor growth (50). *TTN* mutation has been reported to be correlated with myopathy and cancer, and one study showed that lncRNA TTN-AS1, which is transcribed in the opposite direction of TTN, was upregulated in ccRCC samples and positive associated with poor clinicopathological performances (51).

The infiltration of immune cell was predicted using CIBERSORT algorithm. Herein, the tumor samples from high-risk group were infiltrated with $CD8^+$ T cells, whereas those from low-risk group were infiltrated with resting mast cells. Unlike other solid tumors, there is a generally accepted viewpoint that increased $CD8^+$ T cells infiltration in RCC samples was positively associated with weak outcome (52). This phenomenon might owe to a relative lack of tertiary lymphoid structures, which suppressed the mature process of dendritic cell, and thus prevented $CD8^+$ T cells from recognizing tumor antigen (52, 53). Conversely, ccRCC tumor samples with abundant mast cell population performed better OS and PFS than those with scare mast cell population (54). Meanwhile, the immune score and estimate score were increased but the tumor purity was decreased in the high-risk group. The diversities of immune microenvironment might confer distinct drug susceptibilities to chemotherapy and immunotherapy. When compared with the low-risk group, the expression of ICI targeted genes (*PD-1, CTLA-4*) were significantly increased in the high-risk group. Patients with advanced or metastatic RCC have exhibited a desirable response rate to FDA-approved ICI drugs, such as anti-PD-1 antibody (nivolumab, pembrolizumab, atezolizumab) and/or

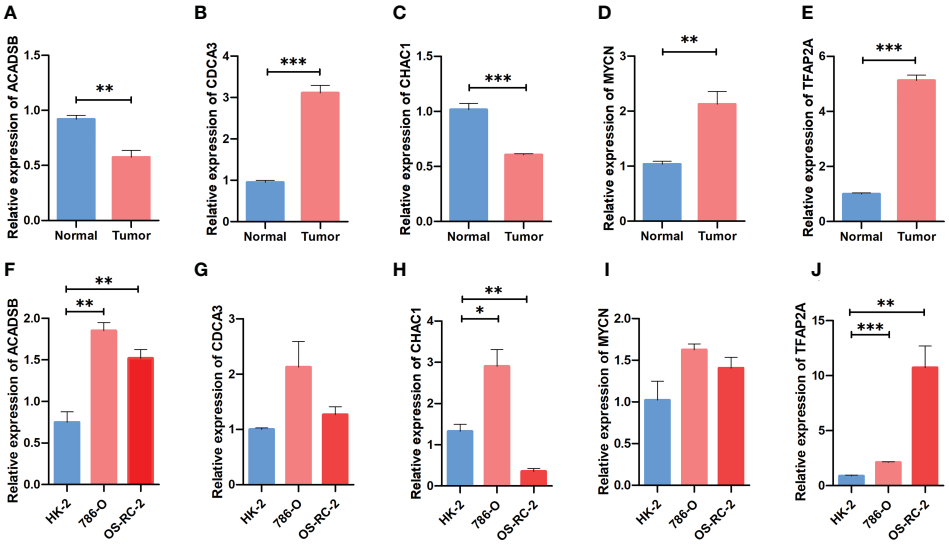

FIGURE 10
Comparing the expression pattern of the identified FPTOSs between ccRCC and normal renal sample using RT-PCR method. **(A–E)** The mRNA expression level of *ACADSB*, *CDCA3*, *CHAC1*, *MYCN*, *TFAP2A* in human ccRCC tumor samples and adjacent normal samples. **(F–J)** The mRNA expression level of *ACADSB*, *CDCA3*, *CHAC1*, *MYCN*, *TFAP2A* in human ccRCC cell lines (786-O, OS-RC-2) and normal renal proximal tubular cell line (HK2). Results were presented as mean ± standard error of mean (SEM), and $P < 0.05$ was considered to have statistically significant. $^{*}P < 0.05$, $^{**}P < 0.01$, $^{***}P < 0.001$.

anti-CTLA-4 antibody (ipilimumab) (55–58). Despite these advantages, most patients could not gain a durable response to immunotherapy. Encouragingly, the current study demonstrated that patients with high-risk performed a better response probability to anti-PD-1 immunotherapy than those with low-risk. Therefore, applying the FPTOS-based risk stratification might bring great benefits to metastatic RCC patients through distinguishing patients who respond positively to immunotherapy. Finally, correlation analysis indicated that cisplatin, BI-D1870 and docetaxel might serve as sensitive drugs to treat patients with high FPTOS_score.

Generally, the present study had mapped a ferroptosis and oxidative stress-associated landscape of ccRCC, and developed a prognostic model with a preferable predictive accuracy and stability. However, limitations should not be ignored. First, the transcriptome data were extracted from a retrospective cohort, and thus the prognostic model should be revaluated by a prospective cohort. Second, although robust results from bioinformatic analysis, the molecular functions and pathological mechanisms of the identified FPTOSs in ccRCC were still required experimental verification. Third, despite ICI-based immunotherapy and easily accessible drugs have shown the therapeutic potential for high-risk group, how to choose the optimum treatment protocol deserve further exploration.

5 Conclusion

Overall, we identified the FPTOSs with potential prognostic significance in ccRCC patients. A reliable score system to distinguish high-risk patients was established and performed a preferable predictive accuracy and stability. Subsequently, the miRNA-FPTOS regulatory network, driver gene mutation status, immune cell population, immunotherapy responsiveness, and drug susceptibility were examined. The results supply novel insights into the expression profiles of FPTOSs in ccRCC, and provide opportunities to identify therapeutical targets or prognostic biomarkers for ccRCC.

Data availability statement

The clinical information of ccRCC patients is included in the supplementary material. The other original contributions presented in the study are publicly available. The data can be found here: TCGA database (https://portal.gdc.cancer.gov/) and ArrayExpress database (https://www.ebi.ac.uk/arrayexpress/). Further inquiries can be directed to the corresponding author.

Author contributions

YW designed the study, performed the data analysis and interpretation. DL performed the data analysis and manuscript writing. BH performed the data collection. SZ revised the manuscript. All authors contributed to the article and approved the submitted version.

Funding

This work was supported by the National Natural Science Foundation of China (grant number 81874165).

Conflict of interest

The authors declare that the research was conducted in the absence of any commercial or financial relationships that could be construed as a potential conflict of interest.

Publisher's note

All claims expressed in this article are solely those of the authors and do not necessarily represent those of their affiliated organizations, or those of the publisher, the editors and the reviewers. Any product that may be evaluated in this article, or claim that may be made by its manufacturer, is not guaranteed or endorsed by the publisher.

Supplementary material

The Supplementary Material for this article can be found online at: https://www.frontiersin.org/articles/10.3389/fonc.2023.1131473/full#supplementary-material

References

1. Sung H, Ferlay J, Siegel RL, Laversanne M, Soerjomataram I, Jemal A, et al. Global cancer statistics 2020: GLOBOCAN estimates of incidence and mortality worldwide for 36 cancers in 185 countries. *CA Cancer J Clin* (2021) 71(3):209–49. doi: 10.3322/caac.21660

2. Siegel RL, Miller KD, Wagle NS, Jemal A. Cancer statistics, 2023. *CA Cancer J Clin* (2023) 73(1):17–48. doi: 10.3322/caac.21763

3. Linehan WM. Genetic basis of kidney cancer: Role of genomics for the development of disease-based therapeutics. *Genome Res* (2012) 22(11):2089–100. doi: 10.1101/gr.131110.111

4. Jonasch E, Gao J, Rathmell WK. Renal cell carcinoma. *BMJ* (2014) 349:g4797. doi: 10.1136/bmj.g4797

5. Siegel RL, Miller KD, Jemal A. Cancer statistics, 2017. *CA Cancer J Clin* (2017) 67 (1):7–30. doi: 10.3322/caac.21387

6. Heng DY, Mackenzie MJ, Vaishampayan UN, Bjarnason GA, Knox JJ, Tan MH, et al. Primary anti-vascular endothelial growth factor (VEGF)-refractory metastatic renal cell carcinoma: Clinical characteristics, risk factors, and subsequent therapy. *Ann Oncol* (2012) 23(6):1549–55. doi: 10.1093/annonc/mdr533

7. van der Mijn JC, Mier JW, Broxterman HJ, Verheul HM. Predictive biomarkers in renal cell cancer: Insights in drug resistance mechanisms. *Drug Resist Update* (2014) 17 (4-6):77–88. doi: 10.1016/j.drup.2014.10.003

8. Ren J-X, Li C, Yan X-L, Qu Y, Yang Y, Guo Z-N, et al. Crosstalk between oxidative stress and Ferroptosis/Oxytosis in ischemic stroke: Possible targets and molecular mechanisms. *Oxid Med Cell Longev* (2021) 2021:6643382. doi: 10.1155/2021/6643382

9. Lin D, Zhang M, Luo C, Wei P, Cui K, Chen Z. Targeting ferroptosis attenuates inflammation, fibrosis, and mast cell activation in chronic prostatitis. *J Immunol Res* (2022) 2022:6833867. doi: 10.1155/2022/6833867

10. Bartolacci C, Andreani C, El-Gammal Y, Scaglioni PP. Lipid metabolism regulates oxidative stress and ferroptosis in RAS-driven cancers: A perspective on cancer progression and therapy. *Front Mol Biosci* (2021) 8:706650. doi: 10.3389/fmolb.2021.706650

11. Dixon SJ, Lemberg KM, Lamprecht MR, Skouta R, Zaitsev EM, Gleason CE, et al. Ferroptosis: an iron-dependent form of nonapoptotic cell death. *Cell* (2012) 149 (5):1060–72. doi: 10.1016/j.cell.2012.03.042

12. Jiang X, Stockwell BR, Conrad M. Ferroptosis: mechanisms, biology and role in disease. *Nat Rev Mol Cell Biol* (2021) 22(4):266–82. doi: 10.1038/s41580-020-00324-8

13. Forman HJ, Zhang H. Targeting oxidative stress in disease: promise and limitations of antioxidant therapy. *Nat Rev Drug Discov* (2021) 20(9):689–709. doi: 10.1038/s41573-021-00233-1

14. Farhood B, Najafi M, Salehi E, Hashemi Goradel N, Nashtaei MS, Khanlarkhani N, et al. Disruption of the redox balance with either oxidative or anti-oxidative overloading as a promising target for cancer therapy. *J Cell Biochem* (2019) 120 (1):71–6. doi: 10.1002/jcb.27594

15. Yang G, Ni JS, Li Y, Zha M, Tu Y, Li K. Acceptor engineering for optimized ROS generation facilitates reprogramming macrophages to M1 phenotype in photodynamic immunotherapy. *Angew Chem Int Ed Engl* (2021) 60(10):5386–93. doi: 10.1002/anie.202013228

16. Ames BN, Shigenaga MK, Hagen TM. Oxidants, antioxidants, and the degenerative diseases of aging. *Proc Natl Acad Sci USA* (1993) 90(17):7915–22. doi: 10.1073/pnas.90.17.7915

17. Kremer DM, Nelson BS, Lin L, Yarosz EL, Halbrook CJ, Kerk SA, et al. GOT1 inhibition promotes pancreatic cancer cell death by ferroptosis. *Nat Commun* (2021) 12 (1):4860. doi: 10.1038/s41467-021-24859-2

18. Yang WS, SriRamaratnam R, Welsch ME, Shimada K, Skouta R, Viswanathan VS, et al. Regulation of ferroptotic cancer cell death by GPX4. *Cell* (2014) 156(1-2):317–31. doi: 10.1016/j.cell.2013.12.010

19. Newman AM, Liu CL, Green MR, Gentles AJ, Feng W, Xu Y, et al. Robust enumeration of cell subsets from tissue expression profiles. *Nat Methods* (2015) 12 (5):453–7. doi: 10.1038/nmeth.3337

20. Yoshihara K, Shahmoradgoli M, Martinez E, Vegesna R, Kim H, Torres-Garcia W, et al. Inferring tumour purity and stromal and immune cell admixture from expression data. *Nat Commun* (2013) 4:42612. doi: 10.1038/ncomms3612

21. Jiang P, Gu S, Pan D, Fu J, Sahu A, Hu X, et al. Signatures of T cell dysfunction and exclusion predict cancer immunotherapy response. *Nat Med* (2018) 24(10):1550–8. doi: 10.1038/s41591-018-0136-1

22. Ro W, Che PL, Reube A, Spence CN, Prieto PA, Mille JP, et al. Integrated molecular analysis of tumor biopsies on sequential CTLA-4 and PD-1 blockade reveals markers of response and resistance. *Sci Transl Med* (2017) 9(379):eaah3560. doi: 10.1126/scitranslmed.aah3560

23. Banerjee J, Khanna S, Bhattacharya A. MicroRNA regulation of oxidative stress. *Oxid Med Cell Longev* (2017) 2017:2872156. doi: 10.1155/2017/2872156

24. Diaz-Montero CM, Rini BI, Finke JH. The immunology of renal cell carcinoma. *Nat Rev Nephrol* (2020) 16(12):721–35. doi: 10.1038/s41581-020-0316-3

25. Kubli SP, Berger T, Araujo DV, Siu LL, Mak TW. Beyond immune checkpoint blockade: emerging immunological strategies. *Nat Rev Drug Discov* (2021) 20(12):899–919. doi: 10.1038/s41573-021-00155-y

26. Hanahan D. Hallmarks of cancer: New dimensions. *Cancer Discov* (2022) 12 (1):31–46. doi: 10.1158/2159-8290.Cd-21-1059

27. Zou Y, W. S. H, Ricq EL, Graham ET, Phadnis VV, Maretich P, et al. Plasticity of ether lipids promotes ferroptosis susceptibility and evasion. *Nature* (2020) 585 (7826):603–8. doi: 10.1038/s41586-020-2732-8

28. Tan SK, Mahmud I, Fontanesi F, Puchowicz M, Neumann CKA, Griswold AJ, et al. Obesity-dependent adipokine chemerin suppresses fatty acid oxidation to confer ferroptosis resistance. *Cancer Discov* (2021) 11(8):2072–93. doi: 10.1158/2159-8290.CD-20-1453

29. Wu G, Wang Q, Xu Y, Li Q, Cheng L. A new survival model based on ferroptosis-related genes for prognostic prediction in clear cell renal cell carcinoma. *Aging* (2020) 12(14):14933–48. doi: 10.18632/aging.103553

30. Inamoto T, Azuma H, Adachi M, Okayama Y, Sunaya T, Oya M. Outcomes of sorafenib treatment of advanced renal cell carcinoma according to IMDC risk criteria: Analysis of Japanese real-world data from postmarketing all-patient surveillance of sorafenib. *Future Oncol* (2022) 18(11):1371–80. doi: 10.2217/fon-2021-1001

31. Escudier B, Eisen T, Stadler WM, Szczylik C, Oudard S, Siebels M, et al. Sorafenib in advanced clear-cell renal-cell carcinoma. *N Engl J Med* (2007) 356(2):125–34. doi: 10.1056/NEJMoa060655

32. Dixon SJ, Patel DN, Welsch M, Skouta R, Lee ED, Hayano M, et al. Pharmacological inhibition of cystine-glutamate exchange induces endoplasmic reticulum stress and ferroptosis. *Elife* (2014) 3:e02523. doi: 10.7554/eLife.02523

33. Zhang W, Luo M, Xiong B, Liu X. Upregulation of metallothionein 1 G (MT1G) negatively regulates ferroptosis in clear cell renal cell carcinoma by reducing glutathione consumption. *J Oncol* (2022) 2022:4000617. doi: 10.1155/2022/4000617

34. Zhu T, Xiao Z, Yuan H, Tian H, Chen T, Chen Q, et al. ACO1 and IREB2 downregulation confer poor prognosis and correlate with autophagy-related ferroptosis and immune infiltration in KIRC. *Front Oncol* (2022) 12:929838. doi: 10.3389/fonc.2022.929838

35. Jiang P, Iqbal A, Wang M, Li X, Fang X, Yu H, et al. Transcriptomic analysis of Short/Branched-chain acyl-coenzyme a dehydrogenase knocked out bMECs revealed its regulatory effect on lipid metabolism. *Front Vet Sci* (2021) 8:744287. doi: 10.3389/fvets.2021.744287

36. Lu D, Yang Z, Xia Q, Gao S, Sun S, Luo X, et al. ACADSB regulates ferroptosis and affects the migration, invasion, and proliferation of colorectal cancer cells. *Cell Biol Int* (2020) 44(11):2334–43. doi: 10.1002/cbin.11443

37. Liu X, Zhang W, Wang H, Zhu L, Xu K. Decreased expression of ACADSB predicts poor prognosis in clear cell renal cell carcinoma. *Front Oncol* (2021) 11:762629. doi: 10.3389/fonc.2021.762629

38. Zhang W, Lu Y, Li X, Zhang J, Zheng L, Zhang W, et al. CDCA3 promotes cell proliferation by activating the NF-kappaB/cyclin D1 signaling pathway in colorectal cancer. *Biochem Biophys Res Commun* (2018) 500(2):196–203. doi: 10.1016/j.bbrc.2018.04.034

39. Bai Y, Liao S, Yin Z, You B, Lu D, Chen Y, et al. CDCA3 predicts poor prognosis and affects CD8(+) T cell infiltration in renal cell carcinoma. *J Oncol* (2022) 2022:6343760. doi: 10.1155/2022/6343760

40. Liu Y, Cheng G, Huang Z, Bao L, Liu J, Wang C, et al. Long noncoding RNA SNHG12 promotes tumour progression and sunitinib resistance by upregulating CDCA3 in renal cell carcinoma. *Cell Death Dis* (2020) 11(7):515. doi: 10.1038/s41419-020-2713-8

41. He S, Zhang M, Ye Y, Zhuang J, Ma X, Song Y, et al. ChaC glutathione specific gamma-glutamylcyclotransferase 1 inhibits cell viability and increases the sensitivity of prostate cancer cells to docetaxel by inducing endoplasmic reticulum stress and ferroptosis. *Exp Ther Med* (2021) 22(3):997. doi: 10.3892/etm.2021.10429

42. Li D, Liu S, Xu J, Chen L, Xu C, Chen F, et al. Ferroptosis-related gene CHAC1 is a valid indicator for the poor prognosis of kidney renal clear cell carcinoma. *J Cell Mol Med* (2021) 25(7):3610–21. doi: 10.1111/jcmm.16458

43. Brodeur GM, Seeger RC, Schwab M, Varmus HE, Bishop JM. Amplification of n-myc in untreated human neuroblastomas correlates with advanced disease stage. *Science* (1984) 224(4653):1121–4. doi: 10.1126/science.6719137

44. Yu R, Zhang H, Wang R, Xiao L. Low expression of MYCN promotes cisplatin resistance by suppressing cisplatin-induced apoptosis in epithelial ovarian cancer. *Oncol Lett* (2022) 24(6):423. doi: 10.3892/ol.2022.13543

45. Pellikainen JM, Kosma VM. Activator protein-2 in carcinogenesis with a special reference to breast cancer–a mini review. *Int J Cancer* (2007) 120(10):2061–7. doi: 10.1002/ijc.22648

46. Huang HX, Yang G, Yang Y, Yan J, Pan Q. TFAP2A is a novel regulator that modulates ferroptosis in gallbladder carcinoma cells *via* the Nrf2 signalling axis. *Eur Rev Med Pharmacol Sci* (2020) 24(9):4745–55. doi: 10.26355/eurrev_202005_21163

47. Zhu C, Song Z, Chen Z, Lin T, Lin H, Xu Z, et al. MicroRNA-4735-3p facilitates ferroptosis in clear cell renal cell carcinoma by targeting SLC40A1. *Anal Cell Pathol (Amst)* (2022) 2022:4213401. doi: 10.1155/2022/4213401

48. Cancer Genome Atlas Research N. Comprehensive molecular characterization of clear cell renal cell carcinoma. *Nature* (2013) 499(7456):43–9. doi: 10.1038/nature12222

49. Devarakonda S, Rotolo F, Tsao MS, Lanc I, Brambilla E, Masood A, et al. Tumor mutation burden as a biomarker in resected non-Small-Cell lung cancer. *J Clin Oncol* (2018) 36(30):2995–3006. doi: 10.1200/JCO.2018.78.1963

50. Dizman N, Philip EJ, Pal SK. Genomic profiling in renal cell carcinoma. *Nat Rev Nephrol* (2020) 16(8):435–51. doi: 10.1038/s41581-020-0301-x

51. Lin K, Chen H, Su C, Zhu H, Lai C, Shi Y. Long non-coding RNA TTN-AS1 serves as a competing endogenous RNA of miR-195 to facilitate clear cell renal cell carcinoma progression. *Cancer Manag Res* (2020) 12:3091–7. doi: 10.2147/CMAR.S249456

52. Fridman WH, Zitvogel L, SautÃ¨s-Fridman C, Kroemer G. The immune contexture in cancer prognosis and treatment. *Nat Rev Clin Oncol* (2017) 14 (12):717–34. doi: 10.1038/nrclinonc.2017.101

53. Giraldo NA, Becht E, Vano Y, Petitprez F, Lacroix L, Validire P, et al. Tumor-infiltrating and peripheral blood T-cell immunophenotypes predict early relapse in localized clear cell renal cell carcinoma. *Clin Cancer Res* (2017) 23(15):4416–28. doi: 10.1158/1078-0432.Ccr-16-2848

54. Yao J, Xi W, Chen X, Xiong Y, Zhu Y, Wang H, et al. Mast cell density in metastatic renal cell carcinoma: Association with prognosis and tumour-infiltrating lymphocytes. *Scand J Immunol* (2021) 93(4):e13006. doi: 10.1111/sji.13006

55. Motzer RJ, Penkov K, Haanen J, Rini B, Albiges L, Campbell MT, et al. Avelumab plus axitinib versus sunitinib for advanced renal-cell carcinoma. *N Engl J Med* (2019) 380(12):1103–15. doi: 10.1056/NEJMoa1816047

56. Motzer RJ, Tannir NM, McDermott DF, Aren Frontera O, Melichar B, Choueiri TK, et al. Nivolumab plus ipilimumab versus sunitinib in advanced renal-cell carcinoma. *N Engl J Med* (2018) 378(14):1277–90. doi: 10.1056/NEJMoa1712126

57. McDermott DF, Lee JL, Ziobro M, Suarez C, Langiewicz P, Matveev VB, et al. Open-label, single-arm, phase II study of pembrolizumab monotherapy as first-line therapy in patients with advanced non-clear cell renal cell carcinoma. *J Clin Oncol* (2021) 39(9):1029–39. doi: 10.1200/JCO.20.02365

58. McDermott DF, Sosman JA, Sznol M, Massard C, Gordon MS, Hamid O, et al. Atezolizumab, an anti-programmed death-ligand 1 antibody, in metastatic renal cell carcinoma: Long-term safety, clinical activity, and immune correlates from a phase ia study. *J Clin Oncol* (2016) 34(8):833–42. doi: 10.1200/JCO.2015.63.7421

frontiers | Frontiers in Oncology

TYPE Original Research
PUBLISHED 27 April 2023
DOI 10.3389/fonc.2023.1131191

OPEN ACCESS

EDITED BY
Linhui Wang,
Second Military Medical University, China

REVIEWED BY
Jianfeng Chen,
University of Texas MD Anderson Cancer Center, United States
Richard Kumaran Kandasamy,
Norwegian University of Science and Technology, Norway

*CORRESPONDENCE
Chengxiao Liu
liuchengxiao@163.com

†These authors have contributed equally to this work and share first authorship

RECEIVED 24 December 2022
ACCEPTED 19 April 2023
PUBLISHED 27 April 2023

CITATION
Pan H, Lu W, Zhang M and Liu C (2023) Construction of an interferon regulatory factors-related risk model for predicting prognosis, immune microenvironment and immunotherapy in clear cell renal cell carcinoma.
Front. Oncol. 13:1131191.
doi: 10.3389/fonc.2023.1131191

Construction of an interferon regulatory factors-related risk model for predicting prognosis, immune microenvironment and immunotherapy in clear cell renal cell carcinoma

Hao Pan[1†], Wei Lu[2†], Mengyuan Zhang[1] and Chengxiao Liu[1*]

[1]Department of Anesthesiology, Shandong Provincial Hospital Affiliated to Shandong First Medical University, Jinan, China, [2]Department of Oral and Maxillofacial Surgery, Shandong Provincial Hospital Affiliated to Shandong First Medical University, Jinan, China

Background: Interferon regulatory factors (IRFs) played complex and essential roles in progression, prognosis, and immune microenvironment in clear cell renal cell carcinoma (ccRCC). The purpose of this study was to construct a novel IRFs-related risk model to predict prognosis, tumor microenvironment (TME) and immunotherapy response in ccRCC.

Methods: Multi-omics analysis of IRFs in ccRCC was performed based on bulk RNA sequencing and single cell RNA sequencing data. According to the expression profiles of IRFs, the ccRCC samples were clustered by non-negative matrix factorization (NMF) algorithm. Then, least absolute shrinkage and selection operator (LASSO) and Cox regression analyses were applied to construct a risk model to predict prognosis, immune cells infiltration, immunotherapy response and targeted drug sensitivity in ccRCC. Furthermore, a nomogram comprising the risk model and clinical characteristics was established.

Results: Two molecular subtypes with different prognosis, clinical characteristics and infiltration levels of immune cells were identified in ccRCC. The IRFs-related risk model was developed as an independent prognostic indicator in the TCGA-KIRC cohort and validated in the E-MTAB-1980 cohort. The overall survival of patients in the low-risk group was better than that in the high-risk group. The risk model was superior to clinical characteristics and the ClearCode34 model in predicting the prognosis. In addition, a nomogram was developed to improve the clinical utility of the risk model. Moreover, the high-risk group had higher infiltration levels of $CD8^+$ T cell, macrophages, T follicular helper cells and T helper (Th1) cells and activity score of type I IFN response but lower infiltration levels of mast cells and activity score of type II IFN response. Cancer immunity cycle showed that the immune activity score of most steps was remarkably higher in the high-risk group. TIDE scores indicated that patients in the low-risk group were more likely responsive to immunotherapy. Patients in different risk

groups showed diverse drug sensitivity to axitinib, sorafenib, gefitinib, erlotinib, dasatinib and rapamycin.

Conclusions: In brief, a robust and effective risk model was developed to predict prognosis, TME characteristics and responses to immunotherapy and targeted drugs in ccRCC, which might provide new insights into personalized and precise therapeutic strategies.

KEYWORDS

interferon regulatory factors, clear cell renal cell carcinoma, tumor microenvironment, immunotherapy, drug sensitivity

Introduction

Clear cell renal cell carcinoma (ccRCC) is the most common histological subtype of renal cell carcinoma and accounts for approximately 80%-90% of cases (1). Radical nephrectomy remains the effective option for localized ccRCC, however, nearly 30% of patients develop distant metastatic or recurrence after surgery (2, 3). TKIs-targeted and mTOR-targeted therapies have been widely adopted, but the clinical benefits are limited (4). In recent years, immune checkpoint inhibitors (ICIs) therapy targeting PD-1/PD-L1 and/or CTLA-4 has made significant breakthroughs in ccRCC (5, 6). However, the therapeutic response rate of ICIs in ccRCC remains poor (7). Despite the combination treatment of ICIs and targeted therapeutic drugs may improve the response rate, these patients receiving the combination therapy often suffer from adverse events (5, 8, 9). Moreover, ccRCC exhibits extremely high heterogeneity, so the responses and prognoses after immunotherapy in patients with the same degree of progression vary extensively (10). Therefore, it is essential to explore the heterogeneity of the ccRCC patients and develop novel biomarkers or therapeutic targets to predict the prognosis and improve ICIs therapeutic efficacy, thereby optimizing immunotherapy for ccRCC.

Interferon regulatory factors (IRFs), which comprise nine gene family members (IRF1, IRF2, IRF3, IRF4, IRF5, IRF6, IRF7, IRF8 and IRF9), are a family of transcription factors that regulate the transcription process of interferons by acting at their gene sites (11). Cumulative evidences revealed IRFs played critical roles in the regulation of cell cycle, cell differentiation, cell apoptosis and cancer immune responses (11). Multiple studies suggested that IRFs played complex and essential roles in progression, prognosis, and immune microenvironment in ccRCC. Kong et al. reported that PD-L1 expression in ccRCC cells was induced by IFNγ stimulation through activation of JAK2/STAT1/IRF1 signaling (12). In addition, the high expression of IRF3 and IRF4 was found to be significantly associated with the advanced clinical stage and poor prognosis in ccRCC (13, 14). Moreover, Bai et al. found high expression of IRF5 was significantly associated with poor overall survival (OS) and recurrence free survival (RFS) in ccRCC (15). Furthermore, Ma et al. revealed that IRF6 overexpression could attenuate proliferation, migration and invasion of ccRCC cells by downregulating the KIF20A expression (16). IRF8 expression by tumor-associated macrophages (TAMs) was negatively associated with tumor stage and positively correlated with prognosis in ccRCC patients (17). As a component of IFN-stimulated gene factor 3 (ISGF3), IRF9 expression in ccRCC cells was negatively associated with tumor growth (18). The above results indicated that IRFs played a diverse regulatory role in the oncogenesis and progression of ccRCC. Cumulative evidences showed that carcinogenesis and progression of cancer was the consequence of the interaction of multiple genes and/or signal pathways (19). A single gene as biomarkers may be not sufficient to accurately predict prognosis and estimate immune status in ccRCC. Hence, we utilized all IRF family members to construct a novel risk model to provide new insights into predicting prognosis and promoting the individualized immunotherapy.

In our study, we classified ccRCC patients into different molecular subtypes based on IRFs and constructed a novel risk model. Moreover, we estimated the clinical performance of this risk model in terms of prognosis, immune microenvironment, response to immunotherapy and targeted drug sensitivity.

Materials and methods

Ethical statement

This study was approved by the Ethical Committee of Shandong Provincial Hospital Affiliated to Shandong First Medical University (SWYX: NO.2021-277). Written informed consent was obtained from all patients.

Data preparation

Transcriptomic RNA (HTseq-FPKM) including 539 ccRCC tissues and 72 adjacent nontumor tissues with clinical information were acquired from The Cancer Genome Atlas (TCGA) database. The gene annotation of the gene transfer

format (GTF, release 37, GRCh38.p13) file downloaded from GENECODE (http://gencodegenes.org) was used to annotate gene symbols. Somatic mutation data and copy number variation (CNV) data of TCGA-KIRC patients were downloaded from the USUC Xena (https://xena.ucsc.edu). In addition, three gene expression profiles of the GSE40435, GSE53757 and GSE66272 datasets with a total of 400 samples were downloaded from the Gene Expression Omnibus (GEO) database. After the batch effects were corrected using "sva" R package, the three datasets (GSE40435, GSE53757 and GSE66272) were merged into a single dataset. The single-cell RNA-sequencing (scRNA-seq) raw count files of the GSE156632 dataset was also obtained from the GEO database. The E-MTAB-1980 cohort comprising 101 ccRCC patients with clinical data was obtained from the EMBL-EBI database (https://www.ebi.ac.uk/).

scRNA-seq data analysis

The 10× scRNA-seq data was converted to Seurat object using "Seurat" R package. The clusters with cells less than 3, cells that were detected less than 50 genes and cells that expressed more than 5% of mitochondrial genes were removed. Principal component analysis (PCA) was performed using the top 1500 most variable genes. The "FindNeighbors" and "FindClusters" functions were used for cell clustering analysis based on the top 15 principal components (PCs). The "FindAllMarkers" function was applied to identify marker genes of different cell clusters based on the threshold of FDR< 0.01 and $|\log_2 FC| > 1$. Furthermore, cluster annotation was performed to recognize different cell type using "SingleR" package.

Differential expression analysis of the IRF family members and gene-gene interaction network

The mRNA expression levels of the IRF family members in non-paired samples and paired samples were analyzed using Wilcoxon rank-sum test and Wilcoxon signed-rank test respectively based on the TCGA-KIRC dataset. The mRNA expression levels of the IRF family members between ccRCC samples and normal samples were validated based on the GEO dataset using the Wilcoxon signed-rank test. In addition, UALCAN (http://ualcan.path.uab.edu) was used to analyze the protein expression levels of IRF family members between ccRCC samples and normal samples according to data from the Clinical Proteomic Tumor Analysis Consortium (CPTAC). P< 0.05 was considered statistically significant. The correlation analysis of the IRF family members was performed on basis of their mRNA expression data from the TCGA-KIRC dataset.

Prognostic values of the IRF family members

Kaplan-Meier (KM) survival curves were plotted to evaluate OS of the IRF family members in ccRCC based on the optimal cutoff value using "survival" R package. A receiver operating-characteristic (ROC) curve was plotted using the "pROC" R package, and the area under curve (AUC) was calculated to evaluate diagnostic capability of the IRF family members.

Identification of molecular subtypes based on IRF family members

Based on the expression profiles of IRF family members, non-negative matrix factorization (NMF) with "brunet" method for 10 iterations was performed to cluster the TCGA-KIRC samples. The number of clusters was set as 2 to 10 and the average contour width of the common member matrix was determined using the "NMF" R package. The minimum number of each subset was set as 10. Then, the optimal number of clusters was determined according to cophenetic, dispersion and silhouette indexes. KM survival curve was used to explore the difference of OS between the different molecular subtypes. Besides, the difference in mRNA expression of IRF family members between the different molecular subtypes was analyzed. Differentially expressed genes (DEGs) between different molecular subtypes were identified using the "limma" R package with the threshold of FDR< 0.05 and $|\log_2 FC| > 1$.

Gene set variation analysis (GSVA) and functional enrichment analysis

GSVA was applied to explore the difference in biological pathways between the different molecular subtypes through "GSVA" R package. The gene sets of "c2.cp.kegg.v2022.1.Hs.symbols.gmt" were obtained from the MSigDB database. Gene Ontology (GO) and Kyoto Encyclopedia of Genes and Genomes (KEGG) pathway enrichment analyses were performed with the "clusterprofiler", "org.Hs.eg.db", "enrichplot" and "circlize" R packages. The enrichment categories were considered as statistically significant if a false discovery rate (FDR)< 0.05.

Construction and validation of an IRFs-related prognostic model

Subsequently, the prognostic-related DEGs were identified by univariate Cox regression analysis based on the TCGA-KIRC cohort (p<0.01). To avoid the overfitting risk, least absolute shrinkage and selection operator (LASSO) Cox regression analysis was performed to narrow down the candidate genes using the "glmnet" R package. Finally, multivariate Cox regression analysis was conducted to determine the target genes for constructing an IRFs-related prognostic model. The risk score was calculated as follows: risk score = $\sum_{i=1}^{n} \mathrm{Expi} * \mathrm{coefi}$(where n, Expi and coefi represent the number of genes, the expression of each gene, and risk coefficient of each gene, respectively). According to the median value of the risk score, patients were divided into the high-risk and low-risk groups. Survival analysis was conducted to explore differences in the OS between the high-risk and low-risk groups.

Additionally, time-dependent ROC curve using "timeROC" R package was plotted, and the 1-, 3- and 5-year AUCs were calculated to evaluate the sensitivity and specificity of the prognostic model. PCA and t-distributed stochastic neighbor embedding (*t*-SNE) were performed to explore the distribution of the two risk groups. The E-MTAB-1980 cohort was used as an external independent cohort to validate the prognostic model.

Furthermore, we evaluated the relationships between the risk score and clinical characteristics. Univariate and multivariate Cox regression analyses were used to evaluate whether the risk score could serve as an independent prognostic biomarker. A nomogram combining the risk score and clinical characteristics (age, gender and stage) was constructed to predict the 1-, 3- and 5-year OS of ccRCC patients. To evaluate the predictive accuracy of the nomogram, the calibration curve and concordance index (C-index) curve were plotted. Decision curve analysis (DCA) was performed to evaluate the clinical utility and net benefit of the nomogram.

Evaluation of immune characteristics

To explore the immune status in ccRCC, the ESTIMATE algorithm was used to calculate the stromal score and immune score of each sample. The abundance of 22 immune cells was estimated using the CIBERSORT algorithm. The infiltration levels of 16 immune cells and activity scores of 13 immune-related pathways were calculated by the single sample gene set enrichment analysis (ssGSEA). The cancer immunity cycle including seven steps could reflect anticancer immune response in tumor microenvironment (TME) (20). Therefore, we compared the differences in the immune activity scores of the seven steps between the high-risk and low-risk groups based on the Tracking Tumor Immunophenotype (TIP; http://biocc.hrbmu.edu.cn/TIP/index.jsp) database. Furthermore, tumor mutation burden (TMB) of each patient in the TCGA-KIRC cohort was calculated. The difference in TMB between the high-risk and low-risk groups was compared, and the correlation between the risk score and TMB was also analyzed.

Assessment of immunotherapy response

To evaluate the immunotherapy response between the high-risk and low-risk groups, the tumor immune dysfunction and exclusion (TIDE; http://tide.dfci.atherard.edu/) was used to calculate the TIDE score of each patient according to myeloid-derived suppressor cell (MDSC), macrophage M2, T cell Dysfucntion and Exclusion (21). Moreover, the T-cell inflammatory signature (TIS) score was calculated based on the mean value of a log2-scaled normalized expression of 18 signature genes (22). The ROC curve was conducted to compare the predictive ability of risk model, TIDE and TIS using "timeROC" R package.

Drug sensitivity analysis

Based on the Genomics of Drug Sensitivity in Cancer (GDSC; https://www.cancerrxgene.org/) database, the half-maximal inhibitory concentration (IC50) of chemotherapeutic drugs was estimated using the "oncoPredict" R package. Thereafter, the difference in IC50 between the high-risk and low-risk groups was analyzed by Wilcoxon signed-rank test.

RNA extraction and quantitative real-time polymerase chain reaction (qRT-PCR)

20 pairs of ccRCC tissues and adjacent normal tissues were collected and stored at -80°C for qRT-PCR. Total RNA was extracted from 20 pairs of ccRCC tissues and adjacent normal tissues using TRIzol (TaKaRa, Japan) in accordance with the manufacturer's instructions. The T100 Thermal Cycler (Bio-Rad, USA) was used to reverse-transcribe RNA into cDNA. qPCR reactions were performed using Fast Start Universal SYBR Green Master (Roche, Switzerland) in the LightCycler 480 (Roche, Switzerland). The qPCR conditions were as follows: (1) 30 s at 95°C; (2) 5 s at 95°C, and 30 s at 60°C for 45 cycles; and (3) melt curve analysis. The sequences of primers are shown in Supplementary Table S1. The relative mRNA expression levels of IRF family members were calculated by the $2^{-\triangle\triangle CT}$ method.

Immunohistochemistry (IHC)

In addition, ccRCC tissues and adjacent normal tissues were fixed in formalin and embedded in paraffin for IHC analysis. Tissue sections (4 μm in thickness) were cut from the clinical samples (ccRCC tissues and normal tissues). The sections were placed in an oven at 72°C for two hours to prevent the tissues from falling out. Then, the sections were deparaffinized with xylene, rehydrated with ethanol and placed in sodium citrate buffer in a pressure cooker for antigen retrieval. Next, the sections were immersed into 3% hydrogen peroxide solution for 4 min at room temperature to inactivate endogenous peroxidase, and then they were rinsed in phosphate-buffered saline (PBS). The sections were incubated with primary antibodies against IRF1 (Abclonal, Wuhan, China), IRF2 (Abclonal), IRF3 (Abclonal), IRF4 (Abcam, Cambridge, UK), IRF5 (Abclonal), IRF6 (HUABIO, Hangzhou, China), IRF7 (Proteintech, Wuhan, China), IRF8 (Abcam) and IRF9 (Proteintech) at 4°C overnight. Then, the sections were incubated with secondary antibodies at room temperature for 40 min. Subsequently, the sections were stained with 3,3'-diaminobenzidine (DAB) and counterstained with hematoxylin. We examined three fields of view (200x) selected randomly from each section. The average optical density (AOD) value of each image was measured by Image J software, and the difference in AOD value between

ccRCC tissues and normal tissues was compared using Wilcoxon test.

Results

Multi-omics landscape of IRF family members in ccRCC

Based on the TCGA-KIRC dataset, the mRNA expression levels of IRF1/2/3/4/5/7/8/9 in 539 ccRCC samples were significantly higher than those in 72 normal samples, whereas the mRNA expression level of IRF6 in 539 ccRCC samples was significantly lower than that in 72 normal samples (Figure 1A). Moreover, the mRNA expression trends of the IRF family members, except for IRF5, in paired samples were consistent with those in non-paired samples (Supplementary Figure S1). The result in the GEO dataset showed that the expression levels of IRF1/2/3/4/5/7/8/9 in ccRCC samples were significantly upregulated compared with those in the normal samples, whereas the expression level of IRF6 in ccRCC samples was significantly downregulated compared with that in the normal samples (Figure 1B). On basis of the scRNA-seq data, we further validated the expression of the IRF family members in different types of cells in the TME. Eight cell clusters, namely endothelial cells, macrophage, monocyte, tissue stem cells, T cells, hepatocytes, epithelial cells and DC, were identified (Figure 1C) and the expression levels of the IRF family members in different types of cell clusters were shown in Figure 1D. Furthermore, we found that the protein levels of IRF2/3/4/7/8/9 in ccRCC samples were higher than those in the normal samples, while the protein level of IRF6 in ccRCC samples was lower than that in the normal samples (Supplementary Figure S2). The incidence of somatic mutation and CNVs of IRFs were also estimated. Among the 336 samples, only 5 samples (1.49%) had mutations in IRF family members (Figure 2A). We also found IRF1 and IRF9 had copy number amplification, while IRF2 had copy number deletion (Figure 2B). The location of CNV alterations of IRF family members on the chromosomes were shown in Figure 2C. A correlation network of IRF family members was constructed to show the whole landscapes of their interactions and prognostic values (Figure 2D). KM survival curves showed that the high expression of IRF1 ($p = 0.049$), IRF3 ($p< 0.001$), IRF4 ($p< 0.001$), IRF5 ($p< 0.001$), IRF7 ($p< 0.001$) and IRF9 ($p< 0.001$), and the low expression of IRF2 ($p = 0.049$) and IRF6 ($p< 0.001$) were significantly associated with poor OS (Supplementary Figure S3). We also found that IRF1, IRF3, IRF4, IRF5 and IRF7 were significantly higher in tumor stage III/IV or grade 3/4 compared with tumor stage I/II or grade 1/2, whereas the expression level of IRF6 was lower in tumor stage III/IV or grade 3/

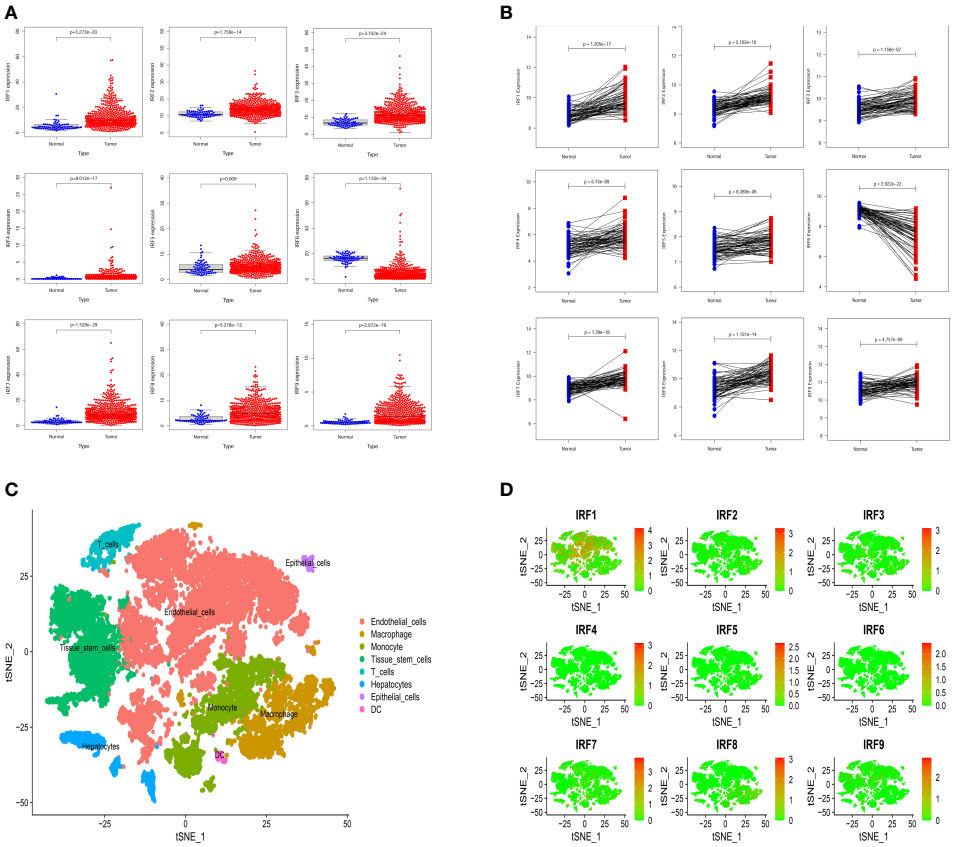

FIGURE 1
The expression levels of the IRF family members between ccRCC samples and normal samples. **(A)** The mRNA expression levels of the IRF family members in the TCGA-KIRC dataset. **(B)** The mRNA expression levels of the IRF family members in the GEO dataset. **(C)** The cell types were identified by single-cell RNA-sequencing analysis. **(D)** The expression levels of the IRF family members in different types of cell clusters.

4 (Supplementary Figure S4). These findings suggested that IRF family members might serve an important role in the oncogenesis and progression of ccRCC. Subsequently, multivariate Cox regression analysis identified that IRF9 (HR: 1.174; 95% CI: 1.051-1.311; $p = 0.004$) was an independent prognostic risk factor (Supplementary Figures S5A, B). ROC curve revealed that IRF9 (AUC = 0.826) had good diagnostic value for ccRCC (Supplementary Figure S5C). Nonetheless, time-dependent ROC curves indicated that *IRF9* (1-, 3-, 5-year AUC: 0.581, 0.581 and 0.656, respectively) had low predictive capability for the OS (Supplementary Figure S5D).

Validation of the IRF family members by qRT-PCR and IHC

We performed qRT-PCR to examine the mRNA expression levels of the IRF family members in clinical specimens. As shown in Figure 3A, the relative mRNA expression levels of IRF1/2/3/7/8/9 in ccRCC tissues were significantly higher than those in the normal tissues, whereas the relative mRNA expression levels of IRF4/5/6 in ccRCC tissues were significantly lower than those in the normal tissues. The mRNA expression trends of the IRF family members, except for IRF4/5, were consistent with the results of the above bioinformatics analysis. Meanwhile, IHC was conducted to validate the protein expression levels of the IRF family members between ccRCC tissues and normal tissues (Figures 3B, C). The result revealed that the protein levels of IRF1/2/3/7/8/9 in ccRCC tissues were higher than those in the normal tissues, while the protein level of IRF6 in ccRCC tissues was lower than that in the normal tissues.

Identification of IRFs-related molecular subtypes

According to the expression profile of IRF family members, unsupervised NMF algorithm was performed to identify novel IRF-related molecular subtypes in ccRCC. The optimal number of the clusters was identified as two (k =2). Consequently, the TCGA-KIRC cohort was divided into C1 (n = 62) and C2 (n = 468) subtypes (Figure 4A). PCA showed diverse clustering of the two molecular subtypes (Figure 4B). Survival analysis showed that the patients in C2 subtype had a worse OS than those in C1 subtype (Figure 4C). The distribution of clinical characteristics between the two molecular subtypes was illustrated in Supplementary Figure S6. As expected, all IRF family members showed significant differences between the two molecular subtypes (Figure 4D). In addition, GSVA enrichment analysis showed that C1 subtype was enriched in Wnt signaling pathway, thyroid cancer, colorectal cancer, regulation of autophagy and fatty acid metabolism, while C2 subtype was enriched in cytosolic DNA-sensing pathway, cytokine-cytokine receptor interaction and primary

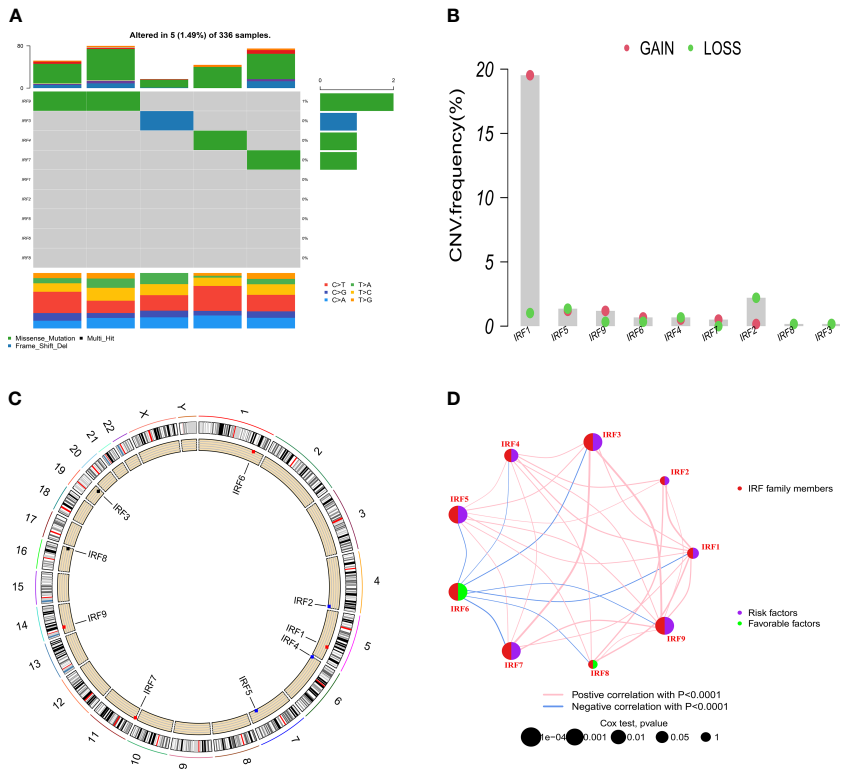

FIGURE 2
Somatic mutation and CNVs frequencies of the IRF family members in ccRCC. **(A)** Mutation frequency of the IRF family members in 336 patients with ccRCC. **(B)** CNVs of the IRF family members. **(C)** Locations of the CNV alterations of the IRF family members on 23 chromosomes. **(D)** Correlations and prognosis of the IRF family members in ccRCC patients.

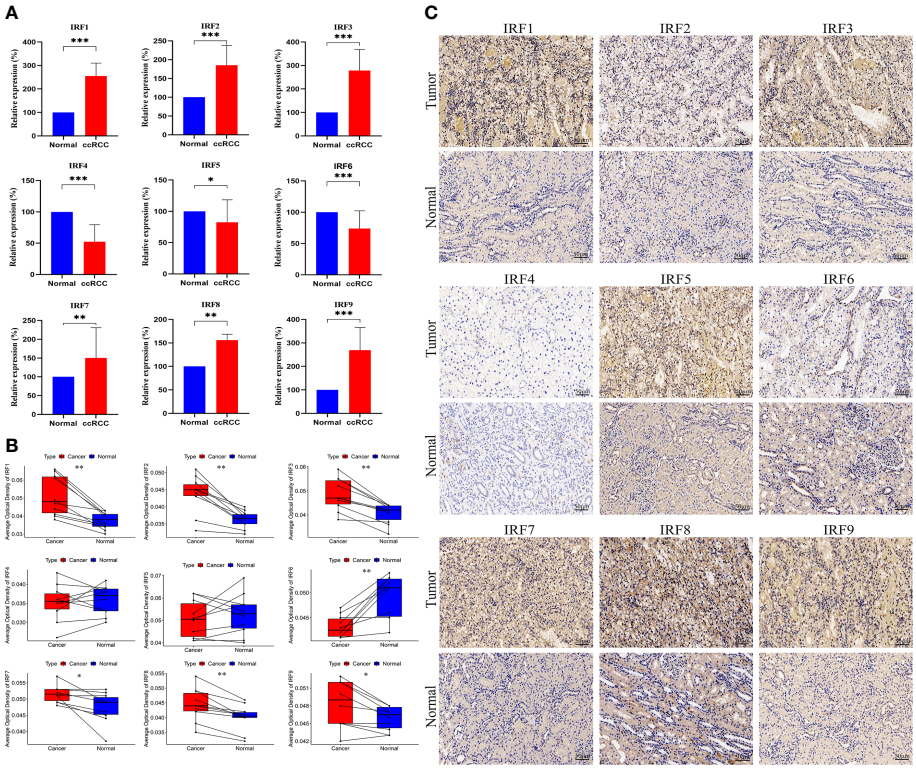

FIGURE 3
QRT-PCR and IHC analyses of the IRF family members. **(A)** The relative mRNA expression levels of the IRF family members between ccRCC and normal tissues were validated by qRT-PCR. **(B)** The AOD values of the IRF family members between ccRCC and normal tissues were compared. **(C)** Representative IHC staining of the IRF family members between ccRCC and normal tissues were shown. * $p<0.05$, ** $p<0.01$, *** $p<0.001$.

immunodeficiency (Figure 4E). Simultaneously, we estimated the differences in immune score, stromal score and immune infiltrating cells between the two molecular subtypes. The result revealed that immune score and stromal score in C2 subtype were significantly higher than those in C1 subtype. Additionally, naïve B cells, M2 macrophages, activated dendritic cells, resting mast cells and eosinophils were remarkably higher in C1 subtype, whereas plasma cells, CD8 T cells, T follicular helper cells (Tfh) and T regulatory cells (Tregs) were significantly higher in C2 subtype (Figure 4F). These results all indicated that there was a significant difference in immune microenvironment between the two molecular subtypes.

To further explore the heterogeneity between the two molecular subtypes, 1425 DEGs were identified with the threshold of FDR< 0.05 and $|\log_2 FC| > 1$. GO and KEGG pathway enrichment analyses for these DEGs were performed. GO analysis revealed that these DEGs were mainly concentrated on biological processes related to immune regulatory processes, such as positive regulation of lymphocyte activation, B cell mediated immunity, T cell receptor complex, and chemokine activity (Figure 4G). Moreover, KEGG pathway analysis showed that these DEGs were mainly enriched in cytokine-cytokine receptor interaction, Th17 cell differentiation, Th1 and Th2 cell differentiation, T cell receptor signaling pathway, TNF signaling pathway, NF-κB signaling pathway, and PD-L1 expression and PD-1 checkpoint pathway in cancer (Figure 4H). Hence, it is supposed that IRFs might be closely involved in regulating immune cells and immune responses in the TME of ccRCC.

Construction and validation of an IRFs-related prognostic model

By performing univariate Cox regression analysis, 421 prognostic-related DEGs were identified based on TCGA-KIRC cohort (Supplementary Table S2). To avoid overfitting risk and narrow down the range of candidate genes, LASSO Cox regression analysis was conducted to further filter out 19 candidate genes (Figure 5A). Finally, 9 genes (NPNT, BCL3, KISS1, PABPC1L, DBH-AS1, PYCR1, BACE2, MELTF, and TOX3) were retained to construct an IRFs-related prognostic model using the multivariate Cox regression analysis (Figure 5B). The risk score of each patient in both TCGA-KIRC and E-MATB-1980 cohorts was calculated using the following formula: risk score = expression of NPNT*(-0.12142) + expression of BCL3*(0.278869) + expression of KISS1*(0.3112) + expression of PABPC1L*(0.193679) + expression of DBH-AS1*(0.225393) + expression of PYCR1*(0.156245) + expression of BACE2*(0.208868) + expression of MELTF*(0.155669) + expression of TOX3*(-0.21914). Then, we examined the expression levels of the nine genes based on the TCGA-KIRC cohort and found that the expression levels of BCL3, PABPC1L and PYCR1 in ccRCC samples were higher than those in normal

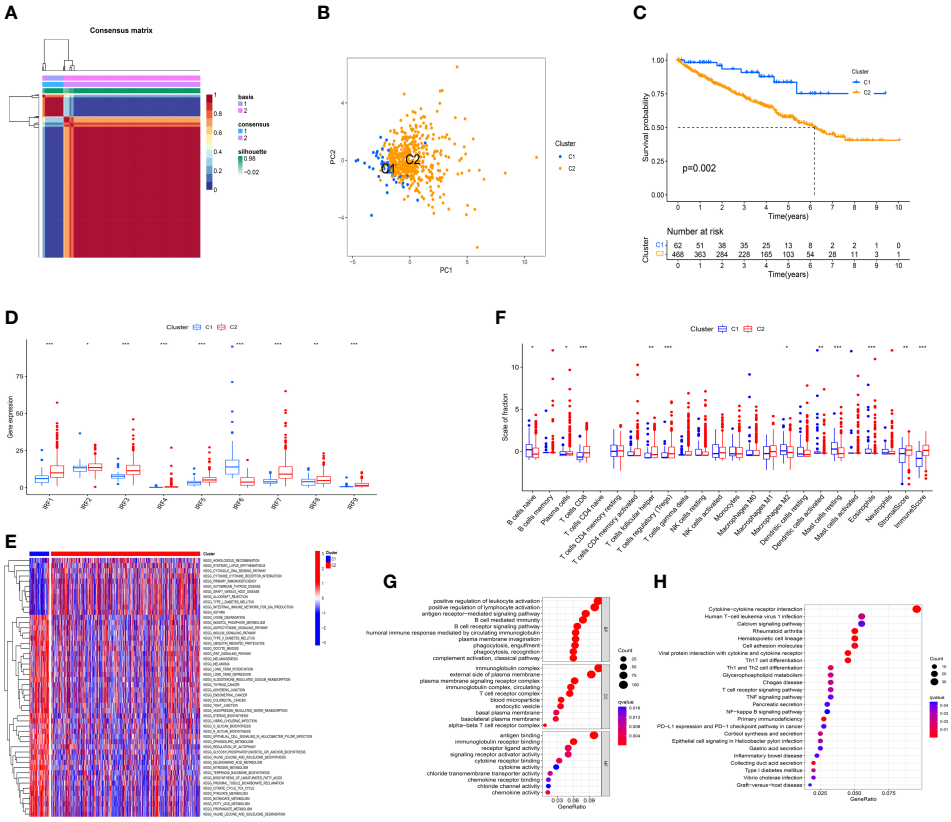

FIGURE 4
Identification of IRFs-related molecular subtypes. **(A)** Consensus map of NMF clustering (k = 2). **(B)** PCA plot of the expression profiling of IRFs. **(C)** KM analysis of OS between the two molecular subtypes. **(D)** The differences in the expression levels of IRF family members between the two molecular subtypes. **(E)** Heatmap of biological pathways between the two molecular subtypes. Activated and inhibited pathways are colored by red and blue, respectively. **(F)** The differences in immune score, stromal score and immune infiltrating cells between the two molecular subtypes. **(G)** GO enrichment analysis of DEGs between the two molecular subtypes. **(H)** KEGG pathway enrichment analysis of DEGs between the two molecular subtypes. * p<0.05, ** p<0.01, *** p<0.001.

samples, while the expression levels of NPNT, BACE2, MELTF and TOX3 in ccRCC samples were lower than those in normal samples (Figure 5C).

Patients were stratified into low-risk and high-risk groups according to the median value of risk score. PCA and t-SNE revealed that patients in the two risk groups were distributed in diverse directions in both TCGA-KIRC and E-MTAB-1980 cohorts (Supplementary Figures S7A–D). Additionally, there were remarkably differences in expression levels of IRF1/3/4/5/6/7/9 between the high-risk and low-risk groups (Supplementary Figure S7E). Meanwhile, we found that IRF family members were positively or negatively correlated with risk score and target genes in the risk model (Figure 5D). Survival analysis indicated that the patients in the low-risk group had a better OS than those in the high-risk group whether in the TCGA-KIRC (Figure 5E) or E-MTAB-1980 cohorts (Figure 5F). Furthermore, time-dependent ROC curves were plotted to explore the predictive capability of the prognostic model. The 1-, 3- and 5-year AUCs in TCGA-KIRC cohort were 0.807, 0.776 and 0.809, respectively (Figure 5G). Similarly, the 1-, 3- and 5-year AUCs in E-MTAB-1980 cohort were 0.773, 0.807 and 0.867, respectively (Figure 5H).

Correlation between risk score and clinical characteristics

To evaluate the independent prognostic value of the IRFs-related prognostic model, univariate and multivariate Cox regression analyses were performed in both TGCA-KIRC and E-MTAB-1980 cohorts. Univariate Cox regression analysis revealed that the risk score in both the TCGA-KIRC (Figure 6A; HR = 1.127, 95% CI:1.100-1.154, p< 0.001) and E-MTAB-1980 (Figure 6B; HR = 1.559, 95% CI:1.306-1.860, p< 0.001) cohorts was significantly associated with OS. After adjusting for confounding factors by multivariate Cox regression analysis, the risk score was confirmed to be an independent prognostic indicator in ccRCC patients (TCGA-KIRC: Figure 6C, HR = 1.098, 95% CI: 1.066-1.130, p< 0.001; E-MTAB-1980: Figure 6D, HR = 1.251, 95% CI: 1.024-1.528, p = 0.028). According to the TCGA-KIRC cohort, the relationships between clinical characteristics and risk score were explored, and the result revealed a significant difference in age, grade and TNM stage (Figure 6E). Furthermore, Figure 6F showed that there were more ccRCC patients with stage I-II in the low-risk group, but there were more ccRCC patients with stage III-IV in the high-risk group (p< 0.001). Besides, the C-index and ROC curve were conducted to

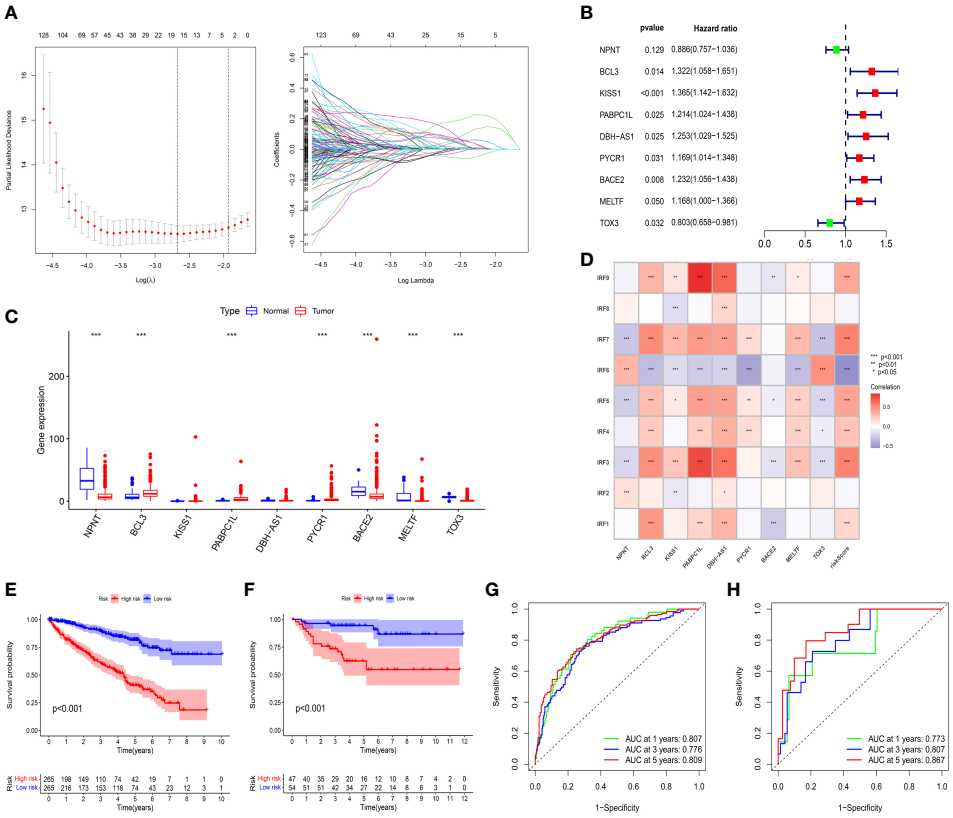

FIGURE 5
Construction and validation of an IRFs-related prognostic model. **(A)** The LASSO Cox regression analysis was performed to filter out the candidate genes. **(B)** 9 genes were retained to construct a prognostic model using the multivariate Cox regression analysis. **(C)** The mRNA expression levels of the nine genes between ccRCC samples and normal samples in the TCGA-KIRC dataset. **(D)** Correlations between IRF family members and risk score. **(E, F)** KM curves of OS between the low- and high-risk groups in TCGA-KIRC and E-MTAB-1980 datasets. **(G, H)** ROC curves of the IRFs-related prognostic model in predicting the 1-, 3- and 5-year OS in the TCGA-KIRC and E-MTAB-1980 datasets. * $p<0.05$, ** $p<0.01$, *** $p<0.001$.

evaluate the predictive performance of the risk model. We found that the C-index of the risk score was higher than those of other clinical characteristics (Figure 7D), suggesting the risk score could better predict the prognosis of ccRCC patients. Similarly, ROC curves also revealed that the AUC of the risk score was higher than those of other clinical characteristics, indicating that the risk score had higher sensitivity and specificity in predicting prognosis of ccRCC patients (Figures 7A–C). As reported, the robust predictive power of a ClearCode34 model has been validated in clinical cohorts (23, 24). We performed the 1-, 3-, and 5-year ROC curves of the ClearCode34 model (Figure 7E), and found that the 1-, 3-, and 5-year AUCs of IRFs-related risk model were higher than those of the ClearCode34 model, indicating that IRFs-related risk model was superior to the ClearCode34 model in predicting the prognosis of ccRCC.

Construction and evaluation of the prognostic nomogram

A nomogram scoring system comprising age, gender, stage and risk score was constructed to predict the 1-, 3- and 5-year OS of ccRCC patients based on the TCGA-KIRC cohort (Figure 7G). The excellent consistency of the calibration curve suggested that the nomogram had a high accuracy to predict the 1-, 3- and 5-year OS in ccRCC patients (Figure 7F). ROC curves revealed that the 1-, 3- and 5-year AUCs of the nomogram were 0.866, 0.822 and 0.793, indicating the nomogram showed satisfactory predictive ability, which was superior to other clinical characteristics (Supplementary Figures S8A–C). Furthermore, DCA revealed that the nomogram had better net benefit than other clinical characteristics (Figure 7H).

Evaluation of immune characteristics and immunotherapeutic response

To further explore the correlation between immune landscape and the risk score, the ESTIMATE algorithm was used to calculate the immune score, stromal score and ESTIMATE score. The high-risk group had a higher ESTIMATE score and immune score than the low-risk group (Figure 8A), indicating that ccRCC patients in the high-risk group might present more active immune status. Subsequently, the ssGSEA was used to explore the infiltration levels of 16 immune cells and activity scores of 13 immune-related pathways between the two risk groups. We found that the high-risk group had higher infiltration levels of $CD8^+$ T cell, $CD4^+$

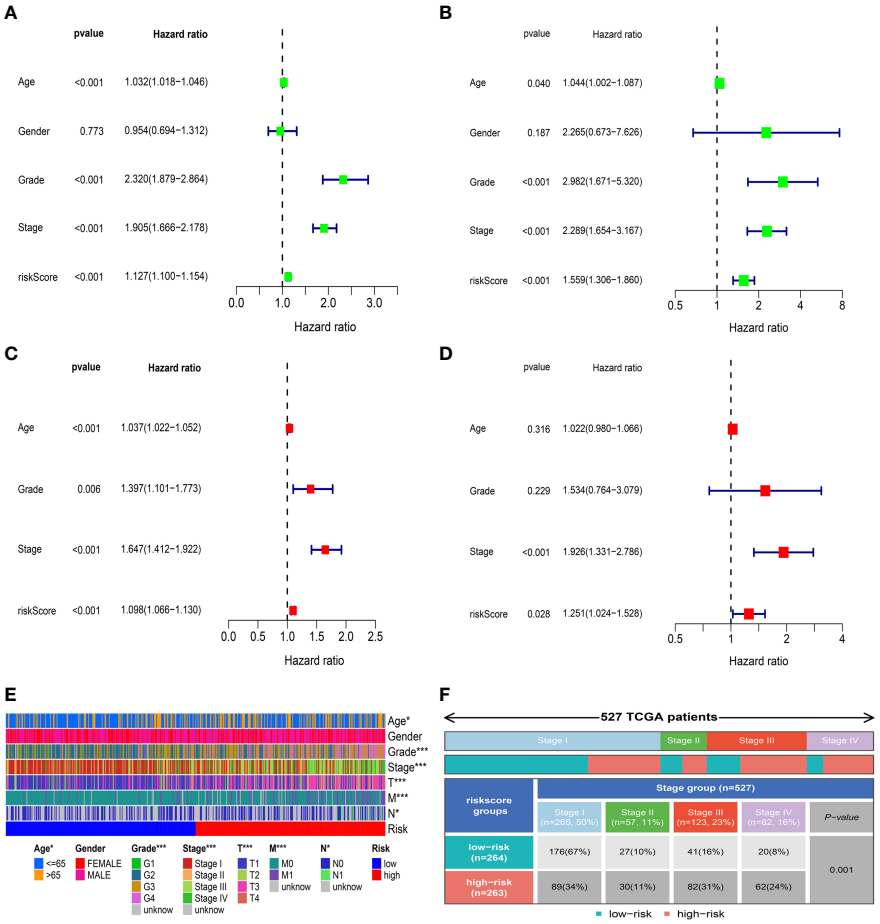

FIGURE 6
Correlation between risk score and clinical characteristics. **(A, C)** Univariate and multivariate Cox regression analyses showed that risk score was an independent prognostic indicator in the TCGA-KIRC dataset. **(B, D)** Univariate and multivariate Cox regression analyses showed that risk score was an independent prognostic indicator in the E-MTAB-1980 dataset. **(E)** Differences in clinical characteristics between the low- and high-risk groups in the TCGA-KIRC dataset. **(F)** Distribution of tumor stages between the low- and high-risk groups. * p<0.05, *** p<0.001.

T cell, macrophages, T helper (Th) cells, Tfh, Type 1 T helper (Th1) cells and Type 2 T helper (Th2) cells, whereas the low-risk group had higher infiltration levels of immature dendritic cells (iDCs) and mast cells (Figure 8B). Moreover, the activity scores of APC co-stimulation, CCR, check point, cytolytic activity, inflammation promoting, parainflammation, T cell co-inhibition, T cell co-stimulation and type I IFN response were higher in the high-risk group, whereas the activity score of type II IFN response was lower in the high-risk group (Figure 8B). Thorsson et al. (25) have identified six cancer immune subtypes (IS) including IS1 (wound healing), IS2 (IFN-γ dominant), IS3 (inflammatory), IS4 (lymphocyte depleted), IS5 (immunologically quiet), and IS6 (TGF-β dominant). As shown in Supplementary Figure 8D, there was significant difference in immune subtypes between the two risk groups and there were more patients with IS3 immune subtype in both the high-risk and low-risk groups ($p< 0.001$). To further explore the activity of immune cells in ccRCC, we calculated the immune activity score of each step based on TIP database. We discovered that the immune activity scores of most steps in the high-risk group were remarkably higher than those in the low-risk group (Figure 8D). Furthermore, we found that the high-risk group presented a more extensive TMB level than the low-risk group, and TMB level was positively associated with the risk score (Figure 8C). However, clinical researches have demonstrated that TMB could not predict the therapeutic response to ICIs in ccRCC (26, 27).

To evaluate the value of the risk model in immunotherapy, the relationships between risk score and TIDE, T-cell dysfunction, T-cell exclusion score and MSI score were explored. The result showed that TIDE score in the high-risk group was higher than that in the low-risk group, indicating patients in the low-risk group were more likely to benefit from ICIs therapy than those in the high-risk group (Figure 9A). Besides, we found that high-risk group showed a higher T-cell dysfunction and lower MSI score than low-risk group (Figures 9B–D). Meanwhile, ROC curve showed that the AUC of IRF-related risk model was remarkably higher than that of TIS and TIDE (Figure 9E), which suggested that the risk model displayed better predictive value for prognosis in ccRCC than TIS and TIDE.

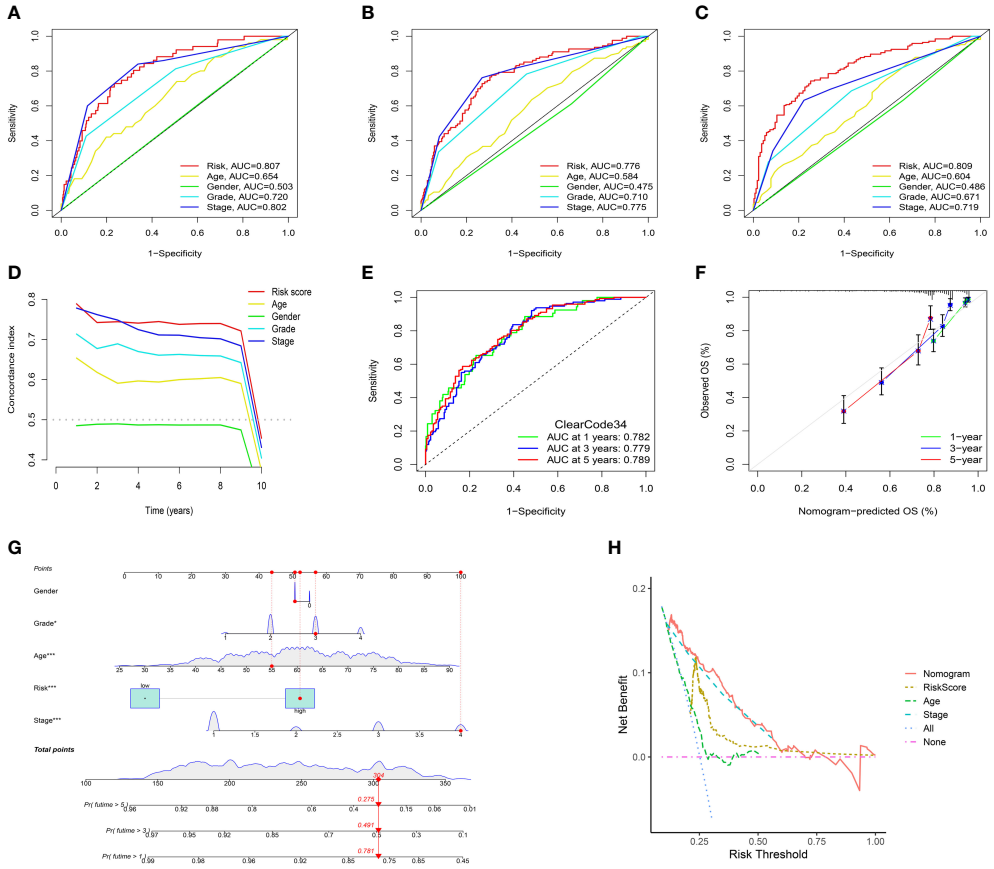

FIGURE 7
Assessment of the IRFs-related prognostic model and construction of a nomogram to predict the OS. **(A-C)** ROC curves of the nomogram in predicting the 1-,3- and 5-year OS in the TCGA-KIRC dataset. **(D)** C-indexes of the risk score and clinical characteristics. **(E)** ROC curves of the ClearCode34 model in predicting the 1-, 3- and 5-year OS. **(F)** The calibration curve of the nomogram in predicting the 1-, 3- and 5-year OS. **(G)** Construction of a nomogram based on age, gender, stage and risk score. **(H)** DCA curve of the nomogram. * p<0.05, *** p<0.001

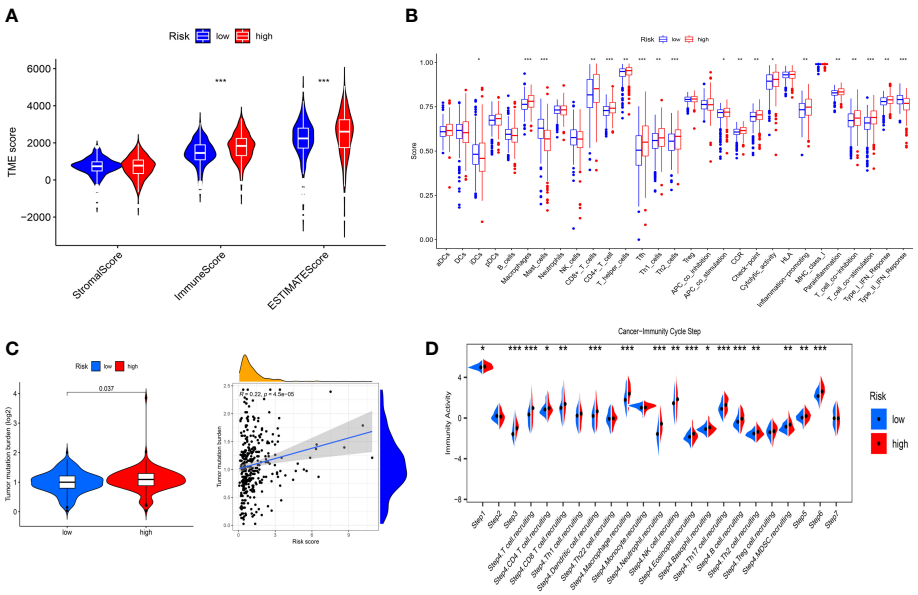

FIGURE 8
Immune landscape between the low- and high-risk groups. **(A)** Differences in the stromal score, immune score and ESTIMATE score. **(B)** Differences in the 16 immune cells and 13 immune-related pathways between the low- and high-risk groups. **(C)** Correlation between TMB and risk score. **(D)** Differences in the immune activity score of cancer-immunity cycle steps between the low- and high-risk groups. * p<0.05, ** p<0.01, *** p<0.001.

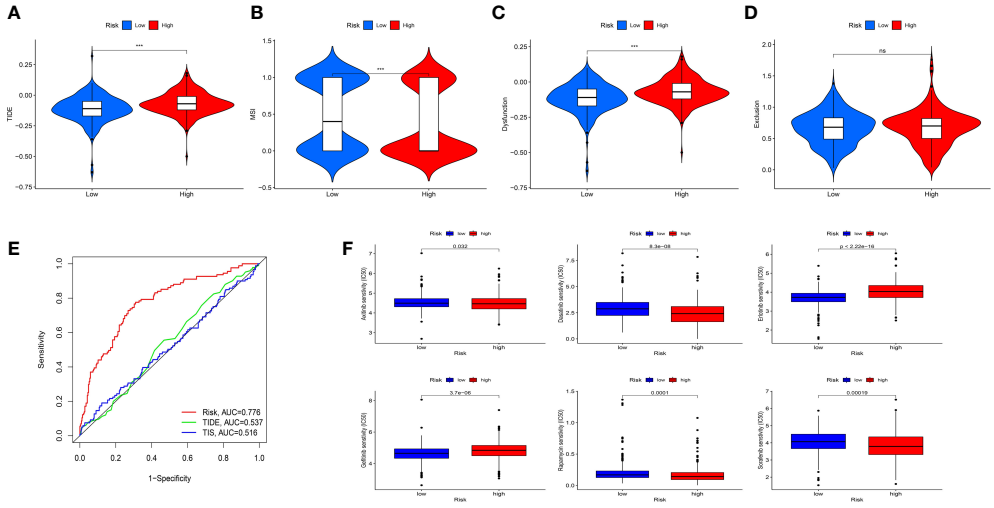

FIGURE 9
Evaluation the value of the IRFs-related prognostic model in immunotherapy and drug sensitivity. **(A-D)** Differences in TIDE, MSI, T cell dysfunction and T cell exclusion between the low- and high-risk groups. **(E)** ROC curve of IRFs-related prognostic model, TIDE and TIS in predicting the OS. **(F)** Correlation between risk score and drug sensitivity. *** $p<0.001$. ns, no significance.

Drug sensitivity analysis

To explore the correlation between the risk score and response to targeted drugs of ccRCC, we compared the differences in IC50 of these drugs between the high-risk and low-risk groups. We observed that the IC50 of axitinib, sorafenib, dasatinib, and rapamycin in the high-risk group were lower than those in the low-risk group, while the IC50 of erlotinib and gefitinib in the high-risk group were higher than those in the low-risk group (Figure 9F). Thus, we proposed that IRFs-related risk model could serve as a potential predictive factor for the sensitivity of targeted drugs.

Discussion

ccRCC is a heterogeneous tumor with high infiltration levels of immune cells, high aggressiveness and poor prognosis (28, 29). Intratumor heterogeneity in ccRCC is considered to be related to patterns of metastatic spread and prognosis, which makes it complex to predict prognosis and determine the appropriate therapeutic strategies (30). Moreover, the heterogeneity of tumor microenvironment (TME) might be responsible for the distinct therapeutic responses to ICIs in ccRCC patients (10). Cumulative evidences showed that IRFs participated in regulating immune cells and immune-related pathways in cancers (11), which suggested that IRFs might play an essential role in TME. Hence, identifying IRFs-related risk model is naturally significant to stratify ccRCC patient heterogeneity, predict prognosis and develop the individualized immunotherapeutic strategies.

Herein, multi-omic analysis of IRF family members in ccRCC indicated that IRFs might play an important role in oncogenesis and progression of ccRCC. Subsequently, the NMF algorithm was used to classify ccRCC patients into two distinct molecular subtypes based on the expression profile of IRF family members. We discovered that the patients in C2 subtype showed a worse OS than those in C1 subtype. In addition, there were differences in immune score, stromal score and abundance of various immune cells between the two molecular subtypes. Furthermore, GO and KEGG pathway enrichment analyses showed enrichment of immune-related pathways, such as positive regulation of lymphocyte activation, B cell mediated immunity, chemokine activity, cytokine-cytokine receptor interaction, Th17 cell differentiation, Th1 and Th2 cell differentiation, T cell receptor signaling pathway, TNF signaling pathway, NF-κB signaling pathway, and PD-L1 expression and PD-1 checkpoint pathway in cancer. It was evidenced that regulatory B cells could attenuate antitumor immune responses by suppressing the T-cell immune response (31). Cytokines and chemokines were found to play a crucial role in cancer-related inflammation and immune escape (32). Qu et al. revealed that the TNF-α/TNFR2 pathway was activated to enhance the immunosuppressive phenotype and function of Tregs in TME of gastric cancer (33). Overexpression of miR-210-3p could promote epithelial-mesenchymal transition, invasion, migration and bone metastasis in prostate cancer by activating NF-κB signaling pathway (34). IFNγ could promote tumor immune escape by regulating the PD-L1 expression *via* the JAK/STAT and PI3K-AKT signaling pathways (35). Taken together, it is reasonable to propose that IRFs were significantly involved in oncogenesis and progression of ccRCC through regulating immune responses and/or immune-related pathways.

We identified 9 target genes (NPNT, BCL3, KISS1, PABPC1L, DBH-AS1, PYCR1, BACE2, MELTF, and TOX3) to construct an effective and robust prognostic model in the TCGA-KIRC cohort, and validated the performance of the prognostic model in the E-MTAB-1980 cohort. Some target genes in the prognostic model have been explored in ccRCC. For instance, Braga et al. revealed that p50 together with Bcl-3 played an important role in the regulation of gene transcription in RCC (36). The invasiveness

and colonized ability in RCC cells were inhibited through the activation of KISS1/KISS1R signaling by honokiol (37). Bioinformatic analysis showed that PYCR1 may contribute to create an immunosuppressive microenvironment in the TME, and thus it could be as potential target in the immunotherapy for ccRCC (38). Jiang et al. found that TOX3 overexpression could inhibit the epithelial-mesenchymal transition (EMT) to reduce cell migration and invasion *via* transcriptionally repressing SNAI1 and SNAI2 in ccRCC cells (39). However, the other genes were revealed for the first time, which remains to be further explored in ccRCC. Survival analysis demonstrated that patients in the low-risk group had a remarkably better prognosis. Multivariate Cox regression analysis indicated that the risk model was an independent prognostic indicator. Moreover, IRFs-related risk model was superior to the ClearCode34 model in predicting the prognosis. To improve the predictive performance of the risk model, we then constructed a nomogram comprising risk score and clinical characteristics to accurately predict prognosis for ccRCC, which was superior to conventional clinical characteristics.

The ccRCC is reported to be one of the cancers with highly immune infiltration by pan-cancer analysis (40). In the TME, immune cells serve a critical role in cancer growth, invasion, migration and regulating anticancer immunity (41). Recent studies revealed that high infiltration of $CD8^+$ T cells was observed in ccRCC, which was closely correlated with the poor prognosis (42, 43). In addition, overexpression of immune escape markers and enhanced the infiltration levels of immunosuppressive cells were related to the high infiltration of $CD8^+$ T cells in ccRCC (44, 45). Similarly, it was evidenced that the infiltration of Tregs and Tfh in ccRCC indicated a poor prognosis (46, 47). Moreover, high infiltration of tumor-associated macrophages (TAMs) correlated with the poor prognosis and tumor metastasis of cancers (48, 49). Şenbabaoğlu et al. found that the infiltration of mast cells was significantly negatively associated with OS and progression-free survival (PFS) in ccRCC (46). Consistent with these studies, we discovered that high infiltration of $CD8^+$ T cells, macrophages and Tfh but low infiltration of mast cells in the high-risk group were associated with a worse prognosis. Interestingly, we also found higher activity scores of inflammation promoting and type I IFN response were in the high-risk group. Type I IFNs could be induced by IRF1/3/5/7/8 through Toll-like receptor (TLR) signaling and cGAS-STING pathways (50, 51). Meanwhile, evidences showed that type I IFNs offered proinflammatory mediators that contribute to tumor progression and increased negative regulatory cells and factors to promote immune escape (52). However, patients in the high-risk group presented lower activity of type II IFN response and showed higher expression of IRF1, which seemed to contradict the theory that activation of IFN-γ can induce IRF1 expression (51). In fact, IRF1 transcription can be driven not only by IFN-γ but also by proinflammatory NF-κB (51, 53). Previous studies showed that the excessive activation of NF-κB was closely associated with increased resistance to chemotherapy or cytokine therapy and a worse prognosis in ccRCC patients (54). Combined with KEGG enrichment analysis showing that NF-κB signaling pathway had a close relationship with IRFs-related molecular subtypes, it is supposed that NF-κB rather than IFN-γ played a major role in the regulation of IRF1 expression in ccRCC patients with high-risk. Additionally, IRF4 expression was excessively elevated in exhausted T cells that reduced IFN-γ production, which was in accordance with our results (55). To summarize, the reciprocal crosstalk between IRFs and IFNs might be responsible for the immune evasion and poor outcome in ccRCC patients. Furthermore, we also found that patients in high-risk group had higher immune scores and ESTIMATE scores. In accordance with the above findings, we believed that IRFs-related risk model could be an effective indicator for predicting prognosis and reflecting immune cells infiltration in the TME of ccRCC.

In recent years, ICIs have been widely used in immunotherapy for ccRCC. However, ccRCC patients exhibited diverse therapeutic responses to ICIs, which might be due to the heterogeneity of TME (10). Thus, it is extremely important to predict which patients can respond to ICIs. TIDE scores were associated with the potential of anticancer immune evasion, thereby predicting the therapeutic response to anti-PD1 and anti-CTLA4 (21). Moreover, high MSI showed a better response to immunotherapy (56). Our analysis showed that patients in low-risk group had lower TIDE score and T-cell dysfunction but a higher MSI than those in high-risk group, indicating that patients in low-risk group had a better response to ICIs. At the moment the combination of immunotherapy with targeted therapy have been deemed to be the first-line treatment for advanced ccRCC (57, 58). Thus, we next explored the response to targeted drugs in different risk groups. As expected, patients in different risk groups showed diverse drug sensitivity to axitinib, sorafenib, gefitinib, erlotinib, dasatinib and rapamycin. To summarize, the IRF-related risk model may be a valid tool to evaluate the response to both immunotherapy and targeted therapy, which can promote the development of personalized therapy for ccRCC patients.

In conclusion, we explored the different molecular subtypes of ccRCC based on IRF family members and evaluated the clinical prognosis, immune cell infiltration and signaling pathways of different molecular subtypes. Furthermore, we developed a robust and effective risk model to predict prognosis and responses to ICIs and targeted drugs and reflect the TME characteristics in ccRCC. These findings might provide new insights into personalized and precise therapeutic strategies. However, there were several limitations in our study. First, the public TCGA-KIRC and E-MTAB-1980 retrospective cohorts were used to construct and validate the risk model. Prospective research with a larger sample size is required to verify the clinical performance of the risk model. Besides, more functional experiments are needed to explore the potential biological mechanisms of IRFs in ccRCC.

Data availability statement

The original contributions presented in the study are included in the article/Supplementary Material. Further inquiries can be directed to the corresponding author.

Ethics statement

This study was approved by the Ethical Committee of Shandong Provincial Hospital Affiliated to Shandong First Medical University (SWYX: NO.2021-277). The patients/participants provided their written informed consent to participate in this study.

Author contributions

HP and WL have contributed equally to this work. HP and WL conceived and designed the study, performed the experiments, performed statistical analyses and wrote the manuscript. HP and MZ interpreted data and prepared the figures. CL edited and revised the manuscript. All authors contributed to the article and approved the submitted version.

Funding

This study was supported by the National Natural Science Foundation of China (NSFC81971010).

Conflict of interest

The authors declare that the research was conducted in the absence of any commercial or financial relationships that could be construed as a potential conflict of interest.

Publisher's note

Supplementary material

The Supplementary Material for this article can be found online at: https://www.frontiersin.org/articles/10.3389/fonc.2023.1131191/full#supplementary-material

SUPPLEMENTARY FIGURE 1
The expression levels of the IRF family members between paired ccRCC samples and normal samples in the TCGA-KIRC dataset.

SUPPLEMENTARY FIGURE 2
The protein expression levels of the IRF family members between ccRCC samples and normal samples based on CPTAC using UALCAN database.

SUPPLEMENTARY FIGURE 3
Prognostic value of the IRF family members in ccRCC in the TCGA-KIRC dataset.

SUPPLEMENTARY FIGURE 4
The correlation between the IRF family members and clinical stage/histological grade.

SUPPLEMENTARY FIGURE 5
Prognostic and diagnostic values of the IRF family members in ccRCC. **(A, B)** Univariate and multivariate Cox regression analyses showed that IRF9 was an independent prognostic indicator in the TCGA-KIRC dataset. **(C)** ROC curve of IRF9 in evaluating diagnostic value for ccRCC. **(D)** ROC curve of IRF9 in predicting the 1-, 3- and 5-year OS.

SUPPLEMENTARY FIGURE 6
The distribution of clinical characteristics between the two molecular subtypes.

SUPPLEMENTARY FIGURE 7
PCA and *t*-SNE showed the distribution of the two risk groups in the TCGA-KIRC **(A, C)** and E-MTAB-1980 **(B, D)** datasets. **(E)** Differences in the expression levels of IRF family members between the low- and high-risk groups. * $p<0.05$, ** $p<0.01$, *** $p<0.001$.

SUPPLEMENTARY FIGURE 8
(A–C) ROC curves of the nomogram in predicting the 1-, 3-, and 5-year OS. **(D)** Distribution of the immune subtypes between the low- and high-risk groups.

References

1. Ljungberg B, Bensalah K, Canfield S, Dabestani S, Hofmann F, Hora M, et al. EAU guidelines on renal cell carcinoma: 2014 update. *Eur Urol* (2015) 67:913–24. doi: 10.1016/j.eururo.2015.01.005

2. Motzer RJ, Hutson TE, Cella D, Reeves J, Hawkins R, Guo J, et al. Pazopanib versus sunitinib in metastatic renal-cell carcinoma. *New Engl J Med* (2013) 369:722–31. doi: 10.1056/NEJMoa1303989

3. Rini BI, Campbell SC, Escudier B. Renal cell carcinoma. *Lancet (London England)* (2009) 373:1119–32. doi: 10.1016/S0140-6736(09)60229-4

4. Gill DM, Agarwal N, Vaishampayan U. Evolving treatment paradigm in metastatic renal cell carcinoma. American society of clinical oncology educational book. American society of clinical oncology. *Annu Meeting* (2017) 37:319–29. doi: 10.1200/EDBK_174469

5. Motzer RJ, Penkov K, Haanen J, Rini B, Albiges L, Campbell MT, et al. Avelumab plus axitinib versus sunitinib for advanced renal-cell carcinoma. *New Engl J Med* (2019) 380:1103–15. doi: 10.1056/NEJMoa1816047

6. Kim MC, Jin Z, Kolb R, Borcherding N, Chatzkel JA, Falzarano SM, et al. Updates on immunotherapy and immune landscape in renal clear cell carcinoma. *Cancers 13* (2021):5856. doi: 10.3390/cancers13225856

7. Roviello G, Corona SP, Nesi G, Mini E. Results from a meta-analysis of immune checkpoint inhibitors in first-line renal cancer patients: does PD-L1 matter? *Ther Adv Med Oncol* (2019) 11:1758835919861905. doi: 10.1177/1758835919861905

8. Rini BI, Plimack ER, Stus V, Gafanov R, Hawkins R, Nosov D, et al. Pembrolizumab plus axitinib versus sunitinib for advanced renal-cell carcinoma. *New Engl J Med* (2019) 380:1116–27. doi: 10.1056/NEJMoa1816714

9. Choueiri TK, Powles T, Burotto M, Escudier B, Bourlon MT, Zurawski B, et al. Nivolumab plus cabozantinib versus sunitinib for advanced renal-cell carcinoma. *New Engl J Med* (2021) 384:829–41. doi: 10.1056/NEJMoa2026982

10. Gulati S, Martinez P, Joshi T, Birkbak NJ, Santos CR, Rowan AJ, et al. Systematic evaluation of the prognostic impact and intratumour heterogeneity of clear cell renal cell carcinoma biomarkers. *Eur Urol* (2014) 66:936–48. doi: 10.1016/j.eururo.2014.06.053

11. Chen YJ, Li J, Lu N, Shen XZ. Interferon regulatory factors: a key to tumour immunity. *Int Immunopharmacol* (2017) 49:1–5. doi: 10.1016/j.intimp.2017.05.010

12. Kong SK, Kim BS, Lim H, Kim HJ, Kim YS. Dissection of PD-L1 promoter reveals differential transcriptional regulation of PD-L1 in VHL mutant clear cell renal

cell carcinoma. *Lab investigation; J Tech Methods Pathol* (2022) 102:352–62. doi: 10.1038/s41374-021-00703-5

13. Wu J, Leng X, Pan Z, Xu L, Zhang H. Overexpression of IRF3 predicts poor prognosis in clear cell renal cell carcinoma. *Int J Gen Med* (2021) 14:5675–92. doi: 10.2147/IJGM.S328225

14. Dannenmann SR, Thielicke J, Stöckli M, Matter C, von Boehmer L, Cecconi V, et al. Tumor-associated macrophages subvert T-cell function and correlate with reduced survival in clear cell renal cell carcinoma. *Oncoimmunology* (2013) 2:e23562. doi: 10.4161/onci.23562

15. Bai Q, Liu L, Xia Y, Wang J, Xi W, Qu Y, et al. IRF5 is associated with adverse postoperative prognosis of patients with non-metastatic clear cell renal cell carcinoma. *Oncotarget* (2017) 8:44186–94. doi: 10.18632/oncotarget.17777

16. Ma X, Wang X, Dong Q, Pang H, Xu J, Shen J, et al. Inhibition of KIF20A by transcription factor IRF6 affects the progression of renal clear cell carcinoma. *Cancer Cell Int* (2021) 21:246. doi: 10.1186/s12935-021-01879-y

17. Muhitch JB, Hoffend NC, Azabdaftari G, Miller A, Bshara W, Morrison CD, et al. Tumor-associated macrophage expression of interferon regulatory factor-8 (IRF8) is a predictor of progression and patient survival in renal cell carcinoma. *J immunotherapy Cancer* (2019) 7:155. doi: 10.1186/s40425-019-0630-0

18. Liao L, Liu ZZ, Langbein L, Cai W, Cho EA, Na J, et al. Multiple tumor suppressors regulate a HIF-dependent negative feedback loop *via* ISGF3 in human clear cell renal cancer. *eLife* (2018) 7:e37925. doi: 10.7554/eLife.37925

19. Mak TK, Li X, Huang H, Wu K, Huang Z, He Y, et al. The cancer-associated fibroblast-related signature predicts prognosis and indicates immune microenvironment infiltration in gastric cancer. *Front Immunol* (2022) 13:951214. doi: 10.3389/fimmu.2022.951214

20. Chen DS, Mellman I. Oncology meets immunology: the cancer-immunity cycle. *Immunity* (2013) 39:1–10. doi: 10.1016/j.immuni.2013.07.012

21. Jiang P, Gu S, Pan D, Fu J, Sahu A, Hu X, et al. Signatures of T cell dysfunction and exclusion predict cancer immunotherapy response. *Nat Med* (2018) 24:1550–8. doi: 10.1038/s41591-018-0136-1

22. Ayers M, Lunceford J, Nebozhyn M, Murphy E, Loboda A, Kaufman DR, et al. IFN-γ-related mRNA profile predicts clinical response to PD-1 blockade. *J Clin Invest* (2017) 127:2930–40. doi: 10.1172/JCI91190

23. Brooks SA, Brannon AR, Parker JS, Fisher JC, Sen O, Kattan MW, et al. ClearCode34: a prognostic risk predictor for localized clear cell renal cell carcinoma. *Eur Urol* (2014) 66:77–84. doi: 10.1016/j.eururo.2014.02.035

24. Ghatalia P, Rathmell WK. Systematic review: ClearCode 34 - a validated prognostic signature in clear cell renal cell carcinoma (ccRCC). *Kidney Cancer (Clifton Va.)* (2018) 2:23–9. doi: 10.3233/KCA-170021

25. Thorsson V, Gibbs DL, Brown SD, Wolf D, Bortone DS, Ou Yang TH, et al. The immune landscape of cancer. *Immunity* (2018) 48:812–830.e14. doi: 10.1016/j.immuni.2018.03.023

26. Motzer RJ, Escudier B, McDermott DF, George S, Hammers HJ, Srinivas S, et al. Nivolumab versus everolimus in advanced renal-cell carcinoma. *New Engl J Med* (2015) 373:1803–13. doi: 10.1056/NEJMoa1510665

27. McDermott DF, Lee JL, Bjarnason GA, Larkin JMG, Gafanov RA, Kochenderfer MD, et al. Open-label, single-arm phase II study of pembrolizumab monotherapy as first-line therapy in patients with advanced clear cell renal cell carcinoma. *J Clin Oncol Off J Am Soc Clin Oncol* (2021) 39:1020–8. doi: 10.1200/JCO.20.02363

28. Tan P, Chen H, Huang Z, Huang M, Du Y, Li T, et al. MMP25-AS1/hsa-miR-10a-5p/SERPINE1 axis as a novel prognostic biomarker associated with immune cell infiltration in KIRC. *Mol Ther oncolytics* (2021) 22:307–25. doi: 10.1016/j.omto.2021.07.008

29. Zhong W, Li Y, Yuan Y, Zhong H, Huang C, Huang J, et al. Characterization of molecular heterogeneity associated with tumor microenvironment in clear cell renal cell carcinoma to aid immunotherapy. *Front Cell Dev Biol* (2021) 9:736540. doi: 10.3389/fcell.2021.736540

30. Au L, Hatipoglu E, Robert de Massy M, Litchfield K, Beattie G, Rowan A, et al. Determinants of anti-PD-1 response and resistance in clear cell renal cell carcinoma. *Cancer Cell* (2021) 39:1497–1518.e11. doi: 10.1016/j.ccell.2021.10.001

31. Sarvaria A, Madrigal JA, Saudemont A. B cell regulation in cancer and anti-tumor immunity. *Cell Mol Immunol* (2017) 14:662–74. doi: 10.1038/cmi.2017.35

32. Quezada SA, Peggs KS, Simpson TR, Allison JP. Shifting the equilibrium in cancer immunoediting: from tumor tolerance to eradication. *Immunol Rev* (2011) 241:104–18. doi: 10.1111/j.1600-065X.2011.01007.x

33. Qu Y, Wang X, Bai S, Niu L, Zhao G, Yao Y, et al. The effects of TNF-α/TNFR2 in regulatory T cells on the microenvironment and progression of gastric cancer. *Int J Cancer* (2022) 150:1373–91. doi: 10.1002/ijc.33873

34. Ren D, Yang Q, Dai Y, Guo W, Du H, Song L, et al. Oncogenic miR-210-3p promotes prostate cancer cell EMT and bone metastasis *via* NF-κB signaling pathway. *Mol Cancer* (2017) 16:117. doi: 10.1186/s12943-017-0688-6

35. Zhang X, Zeng Y, Qu Q, Zhu J, Liu Z, Ning W, et al. PD-L1 induced by IFN-γ from tumor-associated macrophages *via* the JAK/STAT3 and PI3K/AKT signaling pathways promoted progression of lung cancer. *Int J Clin Oncol* (2017) 22:1026–33. doi: 10.1007/s10147-017-1161-7

36. de Souza Braga M, da Silva Paiva KB, Foguer K, Barbosa Chaves KC, de Sá Lima L, Scavone C, et al. Involvement of the NF-κB/p50/Bcl-3 complex in response to antiangiogenic therapy in a mouse model of metastatic renal cell carcinoma. *Biomedicine pharmacotherapy = Biomedecine pharmacotherapie* (2014) 68:873–9. doi: 10.1016/j.biopha.2014.07.008

37. Cheng S, Castillo V, Eliaz I, Sliva D. Honokiol suppresses metastasis of renal cell carcinoma by targeting KISS1/KISS1R signaling. *Int J Oncol* (2015) 46:2293–8. doi: 10.3892/ijo.2015.2950

38. Wei X, Zhang X, Wang S, Wang Y, Ji C, Yao L, et al. PYCR1 regulates glutamine metabolism to construct an immunosuppressive microenvironment for the progression of clear cell renal cell carcinoma. *Am J Cancer Res* (2022) 12:3780–98.

39. Jiang B, Chen W, Qin H, Diao W, Li B, Cao W, et al. TOX3 inhibits cancer cell migration and invasion *via* transcriptional regulation of SNAI1 and SNAI2 in clear cell renal cell carcinoma. *Cancer Lett* (2019) 449:76–86. doi: 10.1016/j.canlet.2019.02.020

40. Vuong L, Kotecha RR, Voss MH, Hakimi AA. Tumor microenvironment dynamics in clear-cell renal cell carcinoma. *Cancer Discovery* (2019) 9:1349–57. doi: 10.1158/2159-8290.CD-19-0499

41. Pitt JM, Marabelle A, Eggermont A, Soria JC, Kroemer G, Zitvogel L. Targeting the tumor microenvironment: removing obstruction to anticancer immune responses and immunotherapy. *Ann Oncol Off J Eur Soc Med Oncol* (2016) 27:1482–92. doi: 10.1093/annonc/mdw168

42. Giraldo NA, Becht E, Pagès F, Skliris G, Verkarre V, Vano Y, et al. Orchestration and prognostic significance of immune checkpoints in the microenvironment of primary and metastatic renal cell cancer. *Clin Cancer Res an Off J Am Assoc Cancer Res* (2015) 21:3031–40. doi: 10.1158/1078-0432.CCR-14-2926

43. Díaz-Montero CM, Rini BI, Finke JH. The immunology of renal cell carcinoma. *Nat Rev Nephrol* (2020) 16:721–35. doi: 10.1038/s41581-020-0316-3

44. Clark DJ, Dhanasekaran SM, Petralia F, Pan J, Song X, Hu Y, et al. Integrated proteogenomic characterization of clear cell renal cell carcinoma. *Cell* (2019) 179:964–983.e31. doi: 10.1016/j.cell.2019.10.007

45. Zhang S, Zhang E, Long J, Hu Z, Peng J, Liu L, et al. Immune infiltration in renal cell carcinoma. *Cancer Sci* (2019) 110:1564–72. doi: 10.1111/cas.13996

46. Şenbabaoğlu Y, Gejman RS, Winer AG, Liu M, Van Allen EM, de Velasco G, et al. Tumor immune microenvironment characterization in clear cell renal cell carcinoma identifies prognostic and immunotherapeutically relevant messenger RNA signatures. *Genome Biol* (2016) 17:231. doi: 10.1186/s13059-016-1092-z

47. Pan Q, Wang L, Chai S, Zhang H, Li B. The immune infiltration in clear cell renal cell carcinoma and their clinical implications: a study based on TCGA and GEO databases. *J Cancer* (2020) 11:3207–15. doi: 10.7150/jca.37285

48. Komohara Y, Hasita H, Ohnishi K, Fujiwara Y, Suzu S, Eto M, et al. Macrophage infiltration and its prognostic relevance in clear cell renal cell carcinoma. *Cancer Sci* (2011) 102:1424–31. doi: 10.1111/j.1349-7006.2011.01945.x

49. Kadomoto S, Izumi K, Hiratsuka K, Nakano T, Naito R, Makino T, et al. Tumor-associated macrophages induce migration of renal cell carcinoma cells *via* activation of the CCL20-CCR6 axis. *Cancers* (2019) 12:89. doi: 10.3390/cancers12010089

50. Honda K, Takaoka A, Taniguchi T. Type I interferon [corrected] gene induction by the interferon regulatory factor family of transcription factors. *Immunity* (2006) 25:349–60. doi: 10.1016/j.immuni.2006.08.009

51. Negishi H, Taniguchi T, Yanai H. The interferon (IFN) class of cytokines and the IFN regulatory factor (IRF) transcription factor family. *Cold Spring Harbor Perspect Biol* (2018) 10:a028423. doi: 10.1101/cshperspect.a028423

52. Boukhaled GM, Harding S, Brooks DG. Opposing roles of type I interferons in cancer immunity. *Annu Rev Pathol* (2021) 16:167–98. doi: 10.1146/annurev-pathol-031920-093932

53. Feng H, Zhang YB, Gui JF, Lemon SM, Yamane D. Interferon regulatory factor 1 (IRF1) and anti-pathogen innate immune responses. *PLoS Pathog* (2021) 17:e1009220. doi: 10.1371/journal.ppat.1009220

54. Zhang J, Zhang Q. VHL and hypoxia signaling: beyond HIF in cancer. *Biomedicines* (2018) 6:35. doi: 10.3390/biomedicines6010035

55. Man K, Gabriel SS, Liao Y, Gloury R, Preston S, Henstridge DC, et al. Transcription factor IRF4 promotes CD8(+) T cell exhaustion and limits the development of memory-like T cells during chronic infection. *Immunity* (2017) 47:1129–1141.e5. doi: 10.1016/j.immuni.2017.11.021

56. Ganesh K, Stadler ZK, Cercek A, Mendelsohn RB, Shia J, Segal NH, et al. Immunotherapy in colorectal cancer: rationale, challenges and potential. nature reviews. *Gastroenterol Hepatol* (2019) 16:361–75. doi: 10.1038/s41575-019-0126-x

57. Atkins MB, Tannir NM. Current and emerging therapies for first-line treatment of metastatic clear cell renal cell carcinoma. *Cancer Treat Rev* (2018) 70:127–37. doi: 10.1016/j.ctrv.2018.07.009

58. Motzer RJ, Robbins PB, Powles T, Albiges L, Haanen JB, Larkin J, et al. Avelumab plus axitinib versus sunitinib in advanced renal cell carcinoma: biomarker analysis of the phase 3 JAVELIN renal 101 trial. *Nat Med* (2020) 26:1733–41. doi: 10.1038/s41591-020-1044-8

frontiers | Frontiers in Oncology

TYPE Original Research
PUBLISHED 01 May 2023
DOI 10.3389/fonc.2023.1133902

OPEN ACCESS

EDITED BY
Linhui Wang,
Second Military Medical University, China

REVIEWED BY
Jianming Lu,
Guangzhou First People's Hospital, China
Weimin Zhong,
Xiamen Fifth Hospital, China

*CORRESPONDENCE
Huiyang Yuan
2020120139@mail.sdu.edu.cn
Yidong Fan
fanyd@sdu.edu.cn
Dawei Xu
Dawei.Xu@ki.se

†These authors have contributed equally to this work

RECEIVED 29 December 2022
ACCEPTED 21 April 2023
PUBLISHED 01 May 2023

CITATION
Wang C, Qin X, Guo W, Wang J, Liu L, Fang Z, Yuan H, Fan Y and Xu D (2023) The chromosomal instability 25 gene signature is identified in clear cell renal cell carcinoma and serves as a predictor for survival and Sunitinib response.
Front. Oncol. 13:1133902.
doi: 10.3389/fonc.2023.1133902

The chromosomal instability 25 gene signature is identified in clear cell renal cell carcinoma and serves as a predictor for survival and Sunitinib response

Chang Wang[1,2†], Xin Qin[2†], Wei Guo[2], Jing Wang[3], Li Liu[4], Zhiqing Fang[2], Huiyang Yuan[2*], Yidong Fan[2*] and Dawei Xu[5*]

[1]Department of Emergency, The Second Hospital of Shandong University, Jinan, China, [2]Department of Emergency, Qilu Hospital of Shandong University, Jinan, China, [3]Department of Urologic Oncology, Division of Life Sciences and Medicine, University of Science and Technology of China, The First Affiliated Hospital of University of Science and Technology of China (USTC), Hefei, China, [4]School of Nursing, Beijing University of Chinese Medicine, Beijing, China, [5]Department of Medicine, Division of Hematology, Bioclinicum and Center for Molecular Medicine, Karolinska Institute and Karolinska University Hospital Solna, Stockholm, Sweden

Background: Chromosomal instability (CIN) is a cancer hallmark and it is difficult to directly measure its phenotype, while a CIN25 gene signature was established to do so in several cancer types. However, it is currently unclear whether there exists this signature in clear cell renal cell carcinoma (ccRCC), and if so, which biological and clinical implications it has.

Methods: Transcriptomic profiling was performed on 10 ccRCC tumors and matched renal non-tumorous tissues (NTs) for CIN25 signature analyses. TCGA and E-MBAT1980 ccRCC cohorts were analyzed for the presence of CIN25 signature, CIN25 score-based ccRCC classification, and association with molecular alterations and overall or progression-free survival (OS or PFS). IMmotion150 and 151 cohorts of ccRCC patients treated with Sunitinib were analyzed for the CIN25 impact on Sunitinib response and survival.

Results: The transcriptomic analysis of 10 patient samples showed robustly upregulated expression of the CIN25 signature genes in ccRCC tumors, which were further confirmed in TCGA and E-MBAT1980 ccRCC cohorts. Based on their expression heterogeneity, ccRCC tumors were categorized into CIN25-C1 (low) and C2 (high) subtypes. The CIN25-C2 subtype was associated with significantly shorter patient OS and PFS, and characterized by increased telomerase activity, proliferation, stemness and EMT. The CIN25 signature reflects not only a CIN phenotype, but also levels of the whole genomic instability including mutation burden, microsatellite instability and homologous recombination deficiency (HRD). Importantly, the CIN25 score was significantly associated with Sunitinib response and survival. In IMmotion151 cohort, patients in the CIN25-C1 group exhibited 2-fold higher remission rate than those in the CIN25-C2 group (P = 0.0004) and median PFS in these two groups was 11.2 and 5.6 months, respectively (P = 7.78E-08). Similar results were obtained from the IMmotion150 cohort analysis. Higher EZH2 expression and poor angiogenesis,

well characterized factors leading to Sunitinib resistance, were enriched in the CIN25-C2 tumors.

Conclusion: The CIN25 signature identified in ccRCC serves as a biomarker for CIN and other genome instability phenotypes and predicts patient outcomes and response to Sunitinib treatment. A PCR quantification is enough for the CIN25-based ccRCC classification, which holds great promises in clinical routine application.

KEYWORDS

ccRCC, chromosomal instability, CIN25, prognosis, Sunitinib, telomere

Introduction

Sporadic clear cell renal cell carcinoma (ccRCC) is the major subtype of renal cell carcinoma (RCC) (up to 80% of all RCCs) and originates from the epithelial cells in the nephron (1–3). Most patients are diagnosed early when tumors are localized, and thus successfully removed *via* nephrectomy, but the disease will eventually recur in about 30% of them post-surgery (2, 4). Clinical and pathological variables have been traditionally applied to stratify recurrence risk and survival, however, there exist certain limitations (4). To further improve the robustness of ccRCC prognostication, molecular biomarkers, such as multigene expression signature models, have recently been established to make molecular classifications or to combine with clinic-pathological factors for stratifications (5–11). Despite so, a substantial gap remains between all the models currently applied in the clinic and the prediction accuracy. Therefore, looking for more reliable prognostic factors is an unmet demand.

Metastasis readily occurs in approximately 1/3 of ccRCC patients at diagnosis, which requires adjuvant treatments (4, 12, 13). These same interventions are also requisite for patients with recurrent ccRCC or even patients with localized ccRCC (12, 14, 15). However, ccRCC tumors are intrinsically insensitive to conventional chemo- and radio-therapies (12, 14). Fortunately, over the last decades, targeted therapies, immunotherapies, and other multi-therapeutic modalities have been developed, which has revolutionized ccRCC treatment landscapes (14). For instance, immune checkpoint inhibitors (ICIs) are used to target immune checkpoint proteins PD-1/PDL-1 and/or CTLA4, thereby boosting anti-cancer immune response and showing a great efficacy in ccRCC (14, 16). Targeted therapeutic drugs, which mainly includes tyrosine kinase receptor inhibitors (TKRis), such as the small molecule Sunitinib, have been approved for the first-line treatment of metastatic ccRCC (13–15, 17). However, subsets of patients do not respond or develop resistance to ICI and/or TKRi treatments (6, 13–15, 17). Distinguishing responders from non-responders should be clinically important for personalized interventions of ccRCC.

It has long been documented that aneuploidies, or somatic copy number alterations (SCNAs), are associated with ccRCC outcomes, including recurrence, and metastasis, survival and drug resistance (4, 18–21). Therefore, aneuploidies and SCNAs have been used as genomic prognostic biomarkers in ccRCC (19–21). Mechanistically, aneuploidies or SCNAs are primarily driven by chromosomal instability (CIN), the cancer hallmark event resulting from persistent high-rates of chromosome mis-segregations during mitosis (22–25). The direct assessment of the CIN phenotype is difficult, and Carter et al. identified a 25 gene expression signature of CIN, so-called CIN25, for the CIN measurement (22). The genes included in the CIN25 are involved in spindle assembly checkpoint signaling, proliferation, and DNA replication and repair (Figure 1A) (22). By calculating their expression score, the authors showed a strong correlation between the CIN25 score and levels of CIN (22). The CIN25 was further observed to serve as a prognostic factor in breast, lung and several other cancers (22, 26). It is currently unclear whether this CIN25 signature is present in ccRCC, and if so, whether it has any clinical implications. Moreover, because CIN plays an important part in the cancer evolution, progression, and drug resistance (23), it is warranted to elucidate the relationship between CIN25 and targeted therapies of ccRCC. The present study is thus designed to address these issues. To this end, we performed the transcriptomic profiling in ccRCC tumors together with their matched renal tissues and analyzed TCGA and other cohorts of ccRCC.

Materials and methods

Primary ccRCC tumor specimens and their matched renal noncancerous tissues

Nineteen patients with ccRCC, diagnosed at Qilu Hospital of Shandong University, were randomly recruited and their clinical information was listed in Table S1. Tumors and their matched NT specimens were collected from these patients who underwent nephrectomy. All the samples were stored in nitrogen tanks until use. The study was approved by the Institutional review board of Qilu Hospital of Shandong University (#KYLL-2021(KS)-192) and the signed informed consent was obtained from all patients.

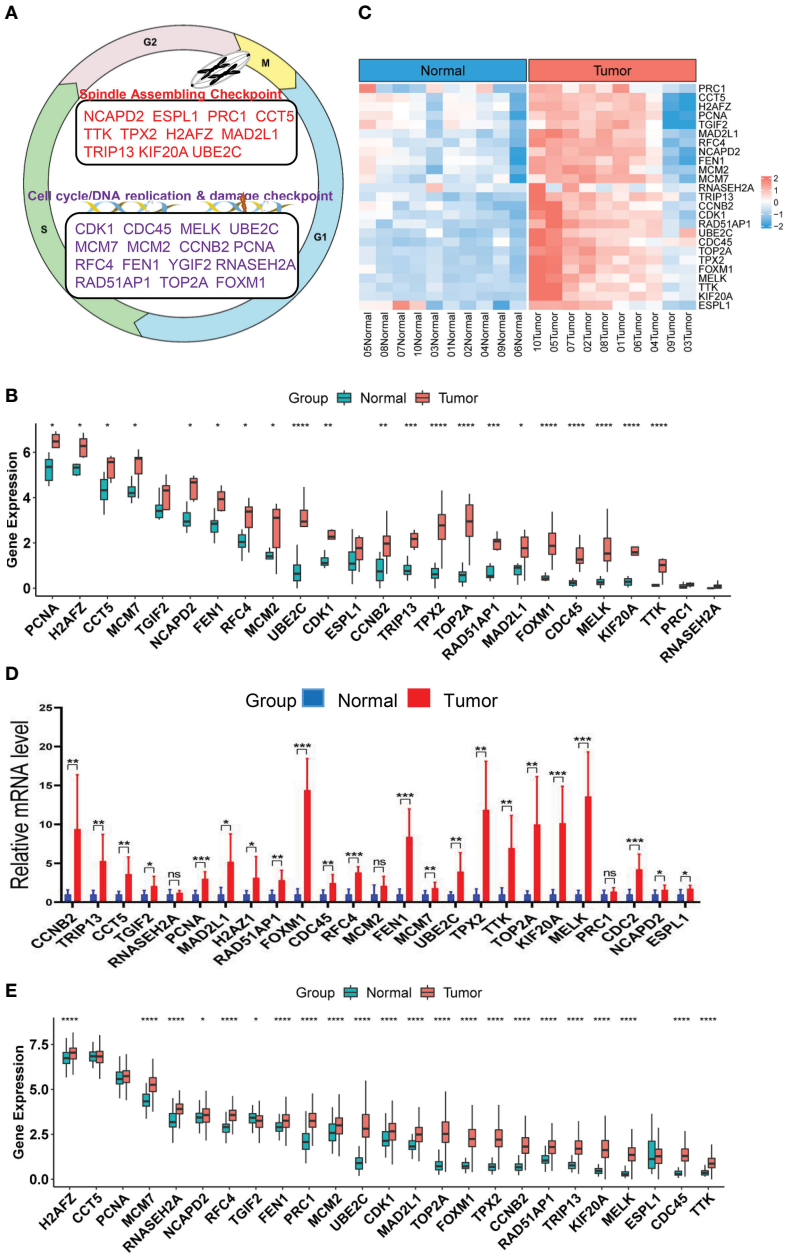

FIGURE 1
Upregulation of CIN25 genes in ccRCC tumors. **(A)** The CIN25 signature genes and their function. **(B)** Upregulated expression of 25 genes included in the CIN25 signature in primary ccRCC tumors. Tumors and matched non-tumorous tissues (NTs) from 10 patients were analyzed for transcriptomic profile and expression levels of CIN25 genes were expressed as Transcripts Per Million (TPM) counts. **(C)** The heatmap showing CIN25 ssGSEA scores between 10 ccRCC tumors and their matched NTs. **(D)** The qPCR validation of upregulated CIN25 gene expression in primary ccRCC tumors. Paired specimens from 9 ccRCC patients were analyzed for mRNA levels of CIN25 genes. mRNA levels of target genes were based on 2 (−ΔΔCT) values and normalized by β-actin expression. **(E)** Differences in expression of 25 CIN25 signature genes between 530 ccRCC tumors and 72 NTs in the TCGA cohort. TPM was used for expression level. *, **, *** and **** indicate *P* values <0.05, 0.01, 0.001 and 0.0001, respectively. ns, Not significant.

RNA extraction and RNA sequencing

RNA was extracted from primary tissues and cells using a RNAfast2000 kit (Fastagen) and quality control was performed using NanoDrop ND-1000 (Thermo Fisher Scientific). RNA sequencing was performed on 10 paired specimens. Sequencing libraries were generated using NEBNext^{R} Ultra^{TM} RNA Library Prep Kit (New England Biolabs) according to the manufacturer's recommendation. RNA sequencing was carried out using Illumina HiSeq 4000 sequencer at Metware Biotechnology (Wuhan, China). Paired-end reads were quality controlled by Q30 and Cutadapt software (v 1.9.3) was used to remove low-quality reads and 3' adaptor-trimming. Hisat2 (v 2.0.4) was further used to align clean reads from sequencing, and sequencing depth and gene length were

adjusted by Fragments Per Kilobase of transcript per Million (TPM) fragments mapped. The sequencing data were deposited in the GEO database (GSE217386).

Reverse transcription and qPCR analysis

The qPCR evaluation of CIN25 gene expression was performed on paired specimens from 9 patients with ccRCC. cDNA was synthesized using a PrimeScript™ RT reagent Kit (TAKARA). qPCR was carried out using SYBR Green of RT Master Mix (TAKARA) to assess mRNA levels of target genes based on 2 (−ΔΔCT) values. β-actin mRNA levels were used as the internal control for normalization of target gene expression. All the primers were synthesized at Wuhan Genecreate Biotech (Wuhan, China) and primer sequences are listed in Table S2.

Data collection and processing of ccRCC tumors

The TCGA cohort of ccRCCs included 530 tumor samples with survival information available and 72 renal NTs. Patient clinical data were summarized in Table S3 (27). Transcriptome, mutation, copy number variations (CNAs) and clinical-pathological data were downloaded from https://gdc.cancer.gov/. One hundred and one patients with ccRCC were in the E-MTAB-1980 cohort (28), and RNA array and clinical information were downloaded from http://www.ebi.ac.uk. Patient clinical characteristics were listed in Table S4. For RNA sequencing data, mRNA abundances were expressed as TPM. For array results (determined by 4×44K v2 microarray kit) from the E-MTAB-1980 cohort, probe-set values were used to quantify mRNA levels. ccRCC patients receiving Sunitinib treatments were contained in IMmotion150 (Table S5) (29, 30) and IMmotion151 (Table S6) trials (31, 32). Expression differences in CIN25-containing 25 genes were compared between ccRCC tumors and NTs in the TCGA cohort. For RNA expression, log2 (TPM+1) based on RNA sequencing data was from https://gdc.cancer.gov/ as stated above. Protein expression data was obtained from Clinical Proteomic Tumor Analysis Consortium (http://ualcan.path.uab.edu/index.html).

CIN25 signature

The CIN25 gene signature includes the following genes responsible for spindle assembling/checkpoint, DNA damage checkpoint and cell cycle regulation: NCAPD2, ESPL1, CDK1, MELK, PRC1, KIF20A, TOP2A, TTK, TPX2, UBE2C, MCM7, MCM2, RFC4, FEN1, CDC45, FOXM1, RAD51AP1, H2AFZ, MAD2L1, PCNA, RNASEH2A, TGIF2, CCT5, TRIP13 and CCNB2 (22) (Figure 1A). The CIN25 score for each sample were expressed as mean Z-scores based on the Z-normalized mRNA level of 25 CIN-related genes above. We also calculated the CIN25 score based on single sample gene set enrichment analysis (ssGSEA) to confirm the accuracy of the Z-score method and other purposes.

Copy number alterations and aneuploidy score analysis

Somatic CNAs were downloaded from https://xenabrowser.net/. CNA plots were made using R package 'oncoPrint' in 'ComplexHeatmap'. Aneuploidy scores were the sum total of altered (amplified or deleted) chromosome arms. TMB is defined as the number of non-silent mutations per million bases and the data were downloaded from https://xenabrowser.net/.

Analyses for proliferation, cancer stemness, Epithelial–mesenchymal transition, angiogenesis and telomerase score

Proliferation statuses were estimated using expression levels of Ki-67 mRNA and cell cycle scores, respectively. ccRCC cell cycle, stemness, EMT and angiogenesis signature scores were calculated based on ssGSEA or as the median z-score of genes included in each signature for each sample. These signatures are as follow: Angiogenesis: VEGFA, KDR, ESM1, PECAM1, ANGPTL4 and CD34 (33). Cell Cycle: CDK2, CDK4, CDK6, BUB1B, CCNE1, POLQ, AURKA, KI-67 and CCNB2 (34, 35). EMT: VIM, CDH2, FOXC2, SNAI1, SNAI2, TWIST1, FN1, ITGB6, MMP2, MMP3, MMP9, SOX10, GCS, CDH1, DSP and OCLN (36).

Telomere length and telomerase activity assessments

Telomere length data in the TCGA cohort of ccRCCs were from Bartheal et al. (37). Telomerase activity was evaluated using the telomerase score based on expression levels of the following 10 telomerase factors: TERT, TERC, DKC1, NHP2, NOP10, TCAB1, GAR1, NVL, RUVBL1 and RUVBL2 (38).

GSEA analysis

GSEA (http://www.gsea-msigdb.org/) analyses were performed to enrich KEGG pathways and hallmarks in two CIN25 subtypes of ccRCC tumors. P <0.05 and False discovery rate (FDR) <0.05 was considered statistically significant.

Nomograms for survival prediction

Cox regression analysis was conducted to assess the effect of the CIN25 cluster and clinical variables on survival. Then according to multivariate Cox regression analysis results, we constructed predictive nomograms including CIN25 and stage to predict 1-, 3-, and 5-year OS and/or PFS). Predicted survival of the nomogram against observed ones was plotted using the calibration curve. All nomograms and assessments of their predicative powers were made using R package regplot. Time-dependent Receiver Operator Characteristic (ROC) curves were used to determine sensitivity

and specificity of OS and PFS predictions. Time-dependent ROCs and AUCs were made using Rpackage timeROC.

Statistical analysis

All statistical analyses were carried out using R package version 4.0.5. Wilcox and K-W sum tests were used for analysis of differences between two groups and among multi groups, respectively. Spearman's Rank-Order Correlation coefficient was applied to determine correlation coefficients r between two variables. Survival analyses were made using log-rank test. The Survival and Survminer packages were employed to draw Kaplan–Meier survival curves for visualization of OS and PFS. Univariate and multivariate Cox regression analyses were used to determine the effect (HR and 95% CI) of various quantitative predictor variables on OS and PFS. $P < 0.05$ were considered as statistically significant.

Results

Robust upregulation of the CIN25 signature genes in primary ccRCC tumors

Although aneuploidies and SCNAs have been well documented in ccRCCs, it remains unclear whether there exists the CIN25 signature as identified in other tumor types. We thus probed this issue first. RNA sequencing was performed on primary ccRCC tumors and their matched NTs from 10 patients who underwent nephrectomy. Expression levels of 25 genes in the CIN25 signature were evaluated in both tumors and NTs. As shown in Figure 1B, tumors exhibited significantly upregulated expression of 21/25 genes. The analysis of CIN25 ssGSEA in these samples further unraveled enhanced CIN25 levels in tumors (Figure 1C). For validation, we did qPCR-based expression analyses of these 25 genes in paired tumors and NTs from 9 patients, and largely similar results were obtained (Figure 1D). To confirm this finding obtained from our small patient cohorts, we analyzed the TCGA ccRCC sequencing data for their CIN25 signature expression. The comparison between 530 tumors and 72 NTs revealed significantly higher mRNA levels of 22/25 genes in tumors than in NTs (Figure 1E). Protein information was available in 20 of 25 genes, and protein levels were similarly higher in tumors, which is consistent with the transcriptomic analysis data (Figure S1).

CIN25 expression-based classification of ccRCCs

The results above demonstrate highly upregulated expression of almost all CIN25 genes in ccRCC tumors, however, a significant heterogeneity was observed among them. To determine whether ccRCC tumors could be classified based on the CIN25 expression score, we performed consensus cluster analyses of the TCGA cohort. Nonnegative matrix factorization clustering of CIN25 mRNA data showed consistency K = 2, indicating that a two-cluster classification was optimal (Figure 2A). In a total of 530 tumors, CIN25-cluster 1 (CIN25-C1, low CIN level) and cluster 2 (CIN25-C2, high CIN level) were 350 (66%) and 180 (34%), respectively (Figure 2B). Because the CIN phenotype is characterized by the presence of aneuploidy, we further compared global CNAs, and calculated aneuploidy, amplified and deleted scores between two CIN25 clusters (Figures 2C, D). Indeed, the aneuploidy score was significantly higher in CIN25-C2 tumors (CIN25-C1 vs CIN25-C2, P = 1.78E-04) (Figures 2C, D). Interestingly, the amplified score was more robustly higher in the CIN25-C2 tumors than in CIN25-C1 ones (CIN25-C1 vs CIN25-C2, the amplified and deleted scores, P = 2.86E-18 and 4.95E-02, respectively) (Figure 2D). Moreover, we also calculated CIN25 ssGSEA score of each tumor based on the expression of 25 genes and observed a drastically higher CIN25 ssGSEA score in CIN25-C2 tumors (Figure 2E). To validate the CIN25 clustering classification of ccRCC tumors, we carried out the same analysis of the E-MTAB1980 ccRCC cohort, and tumors were readily categorized into two distinct CIN25 clusters, with higher CIN25 ssGSEA scores in CIN25-C2 tumors (Figures 2F, G).

Association between CIN25 subtypes and clinic-pathological variables

We next determined the potential association between CIN25 subtypes and clinic-pathological variables in ccRCC tumors. We first examined the distribution of two clusters between two genders and different age groups (≥60 and <60 years) in the TCGA cohort and did not observe significant differences, although male patients had a slightly higher frequency of CIN25-C2 than did females (38.6% vs 29.4%, P = 0.055) (Figure 3A). CIN25-C2 was more frequently observed in higher-stage (P = 5E-06) and higher-grade tumors (P = 0.007) (Figure 3B). Very similar results were obtained from the analysis of the E-MTAB1980 cohort (Figures 3C, D).

We further performed the same analysis of 10 ccRCC patients whose tumors were with transcriptomic profiling. Because 10 tumors were too few to make a CIN classification, we calculated ssGSEA score to express CIN25 levels in each tumor. The CIN25 ssGSEA score was significantly increased in higher-stage (III/IV vs I/II, P = 0.019) and grade (III/IV vs I/II, P = 0.032) tumors (Figure 3E), which was consistent with the result obtained from the TCGA patient analysis.

Telomere length, telomerase and genomic aberrations in CIN25 subtypes of ccRCC tumors

It is well established that telomere dysfunction drives CIN in oncogenesis (39). We thus sought to determine whether telomere length was altered in the TCGA ccRCC cohort. Telomeres were significantly shorter in tumors than in matched NTs (Figure 4A), but there was no statistically significant difference in telomere length between CIN25-C1 and C2 subtypes (Figure 4A). Because telomeric DNA is synthesized by telomerase, while telomerase

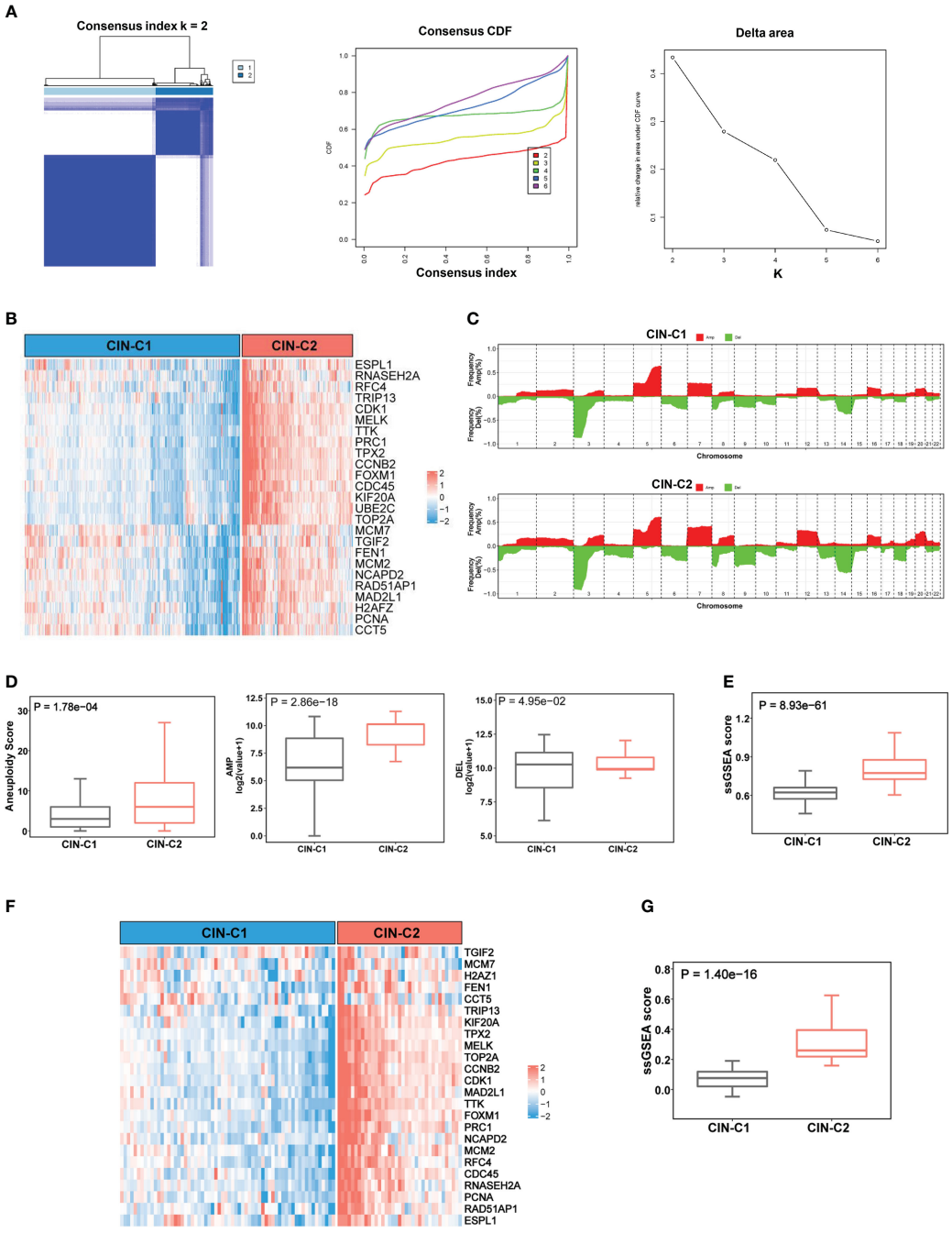

FIGURE 2
CIN25 signature-based classification of ccRCCs. **(A)** Consensus clustering of ccRCC tumors according to expression of CIN25 genes. A two-cluster classification of ccRCC tumors was optimal CIN25 signature-based clustering based on the K value from nonnegative matrix factorization. CDF: Cumulative distribution function. **(B)** TCGA ccRCC tumor clustering. Tumors were categorized into two clusters: CIN25-C1 (low) and CIN25-C2 (high). **(C)** Global copy number alterations (CNAs) in CIN25-C1 and CIN25-C2 tumors. The plots show frequencies of gain/amplification (Red) and deletion (Green) in 22 chromosomes. Top and bottom: CIN25-C1 and CIN25-C2, respectively. **(D)** Differences in the total aneuploidy score, and amplified and deleted scores between CIN25-C1 and CIN25-C2 tumors. **(E)** Differences in CIN25 ssGSEA score between CIN25-C1 and CIN25-C2 tumors. **(F)** CIN25 signature-based clustering of ccRCC tumors in the E-MTAB1980 cohort. **(G)** Differences in CIN25 ssGSEA score between CIN25-C1 and CIN25-C2 tumors in the E-MTAB1980 cohort.

activity is primarily governed by its catalytic component telomerase reverse transcriptase (TERT) (40), we further compared TERT expression and telomerase activity between CIN-C1 and C2 tumors. As shown in Figure 4B, TERT mRNA levels were significantly higher coupled with the increased frequency of TERT copy number gain in CIN25-C2 tumors (C2 vs C1 for TERT mRNA and copies: P = 1.84E-08, and 0.018, respectively). Telomerase activity, as determined using telomerase score (38), increased markedly in the CIN25-C2 tumors compared with that in CIN25-C1 tumors (P = 2.15E-05) (Figure 4C). Moreover, there was

10.3389/fonc.2023.1133902

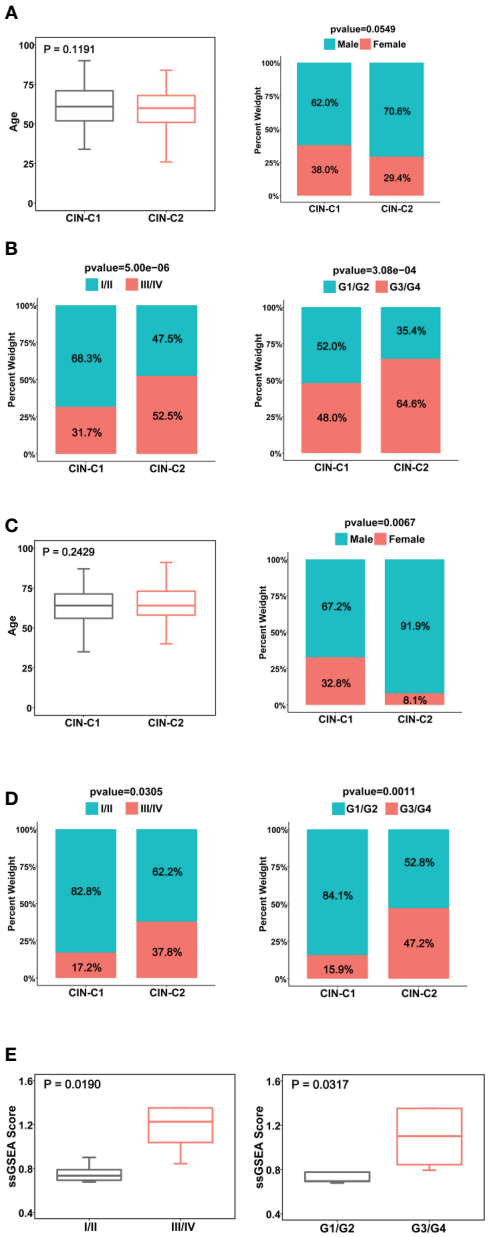

FIGURE 3
Association between CIN25 subtypes and clinic-pathological characteristics in ccRCCs. **(A, B)** The TCGA cohort. CIN25 subtypes were associated with stages and grades, but not age and gender. **(C, D)** The E-MTAB1980 cohort. CIN25 subtypes were associated with stages and grades but not age. More female patients were in the CIN25-C1 group. **(E)** The present cohort of 10 patients. Advanced stages and grades of ccRCC tumors exhibited significantly higher CIN25 ssGSEA scores. The CIN25 ssGSEA score was calculated as described in the Method.

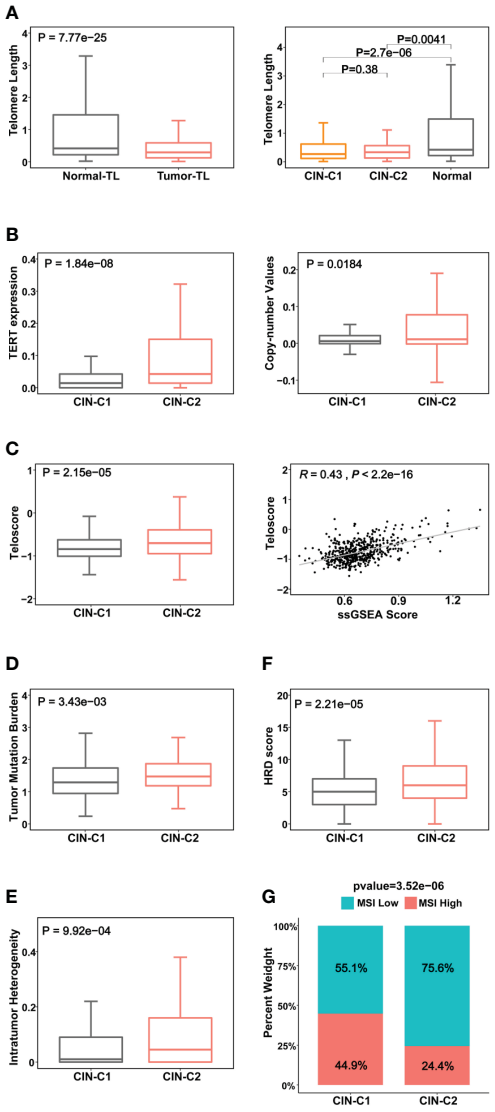

FIGURE 4
Association between CIN25 subtypes and telomere length, telomerase and other genomic alterations in ccRCCs. The TCGA cohort of ccRCCs were analyzed. Telomere length data were from reference 33. **(A)** Telomere shortening occurred in ccRCC tumors independently of CIN25 subtypes. Left panel: ccRCC tumors had significantly shorter telomeres than did renal nontumorous tissues (NTs). Right panel: Both CIN25-C1 and C2 tumors had similar telomere length, shorter than NTs. **(B)** Robustly higher TERT expression (left) and increased *TERT* copy numbers (right) in CIN25-C2 tumors. **(C)** Left panel: Significantly higher levels of telomerase activity, as assessed using the telomerase score in CIN25-C2 tumors. Right panel: The strong correlation between telomerase score and CIN25 ssGSEA score in ccRCC tumors. **(D–G)** CIN25-C2 tumors coupled with higher levels of other types of genomic instability. Higher tumor mutation burden (TMB) **(D)**, intratumoral heterogeneity (ITH) **(E)**, homologous recombination deficiency (HRD) **(F)** and microsatellite instability (MSI) **(G)** in CIN25-C2 tumors.

a significantly positive correlation between telomerase and CIN25 ssGSEA scores (R = 0.43, P <2.22E-16) (Figure 4C).

CIN is one subtype of genomic instability, whereas the later also includes several other forms of genomic aberrations such as nucleotide instability (NIN), microsatellite instability (MSI), homologous recombination deficiency (HRD), etc. (41). Thus, we further addressed the association of CIN25 clusters with the following important alterations: (i) Tumor mutation burden (TMB) (P = 0.034) (Figure 4D). Moreover, we compared the top 10 mutated genes between two subtypes. As expected, VHL, PBRM1, BAP1, MTOR and SETD2 are among the top mutated genes in both subtypes, however, significantly higher mutated frequencies of BAP1 and SETD2 were observed in the CIN25-C2 tumors (BAP1 and SETD2: P = 0.0003 and 0.018, respectively (Figure S3). In addition, KDM5C

mutation was more frequent in the CIN25-C1 tumors (P = 0.04). (ii) Intratumor genetic heterogeneity (P = 0.01) (Figure 4E). (iii) HRD (P = 0.0002) (Figure 4F). (iv) MSI (P = 0.00004) (Figure 4G). CIN25-C2 tumors exhibited significantly higher levels or frequencies of all the aberrations analyzed above.

CIN25 clusters for prediction of ccRCC patient survival

We then wanted to assess whether this CIN25 classification system could predict patient survival. The TCGA cohort of 530 ccRCC patients was first evaluated as the discovery set. Log-rank test analysis unravelled that those patients in the CIN25-C2 group had significantly shorter OS and PFS, as shown by Kaplan–Meier survival curves (P = 7.57E-06 and 4.83-07 for OS and PS, respectively) (Figure 5A). We further performed univariate COX regression analyses by including patient age, gender, stage, and grade together with the CIN25 clustering system. Advanced Stages, higher grades and CIN25-C2 were all associated with shorter OS and PFS (Figures 5B, C). Multivariate COX regression analyses showed that all three of them were independent prognostic factors for shorter OS and PFS (Figures 5B, C).

The E-MTAB-1980 ccRCC cohort as the validation set were further analyzed in the same manner. There was no PFS information available, and we only evaluated OS. Kaplan–Meier survival analysis showed that CIN25-C2 was associated with significantly shorter OS (P = 0.0003) (Figure 5D), and the CIN25 subtype and stages were independent OS predictors, as assessed using univariate (Figure 5E) and multivariate COX regression analyses (Figure 5F).

The data above consistently show that CIN25-C2 subtype and advanced stages are independent prognostic variables for OS and/or PFS in both TCGA and E-MTAB-1980 cohorts. We thus established a prognostic nomogram composed of CIN25 subtypes and stages. For the TCGA cohort, the nomograms exhibited a highly accurate estimation of OS and PFS possibilities at 1-, 3- and 5-years (Figures S2A, B). Similar results were obtained for OS prediction in the E-MTAB-1980 cohort (Figure S2C). To further evaluate the sensitivity and specificity of their prediction, we did time-dependent ROC analyses. In the TCGA cohort, Area under ROC curves (AUCs) for 1-, 3- and 5-year OS were 0.799, 0.767 and 0.740, respectively, while the AUCs for 1-, 3- and 5-year PFS were 0.825, 0.797 and 0.798, respectively (Figures S2D, E). For 1-, 3- and 5-year OS in the E-MTAB-1980 cohort, AUCs were 0.886, 0.871 and 0.838, respectively (Figure S2F). Separate analyses of these two variables showed that AUCs were largely between 0.6 and 0.7, between 0.7 and 0.8 for all CIN25- and stage-based predictions of 1-, 3- and 5-year survival (Figures S2G, H). AUCs obtained from stage-prediction were bigger in all the estimations.

The CIN25 cluster as a predictor for patient response to Sunitinib treatment

Sunitinib has long been applied for advanced ccRCC treatment as the first line drug (14), however, reliable biomarkers to predict its efficacy or patient response are few (6, 8). We thus determined whether the CIN25 cluster classification could help distinguish responders from non-responders in patients treated with Sunitinib. Toward this end, the IMmotion151 cohort of 416 ccRCC patients treated with Sunitinib was first analyzed as the discovery set (31, 32). Patient response to Sunitinib was categorized into complete remission (CR), partial remission (PR), stable disease (SD) and progressive disease (PD), respectively. A total of 416 patients were classified into CIN25-C1 (273 patients) and C2 (143 patients) groups. The CR and PR (CRPR) rate was 42% and 26% in CIN25-C1 and C2 groups, respectively (P = 0.0004) (Figure 6A). The disease progression during the Sunitinib treatment occurred in 14.9% and 30.9% for CIN25-C1 and C2 patients, respectively. The median PFS for C1 and C2 patients was 5.6 and 11.2 months, respectively (P = 7.78E-08; HR, 1.90 (95% CI: 1.45 – 2.47) (Figure 6B). We then analyzed the IMmotion150 cohort (29, 30) to validate the findings obtained from IMmotion151 cohort. In a total of 85 available patients, CIN25-C1 and C2 were 58 and 27, respectively. The total CRPR rate was 41.4% and 14.8% in CIN25-C1 and C2 groups, respectively (P = 0.002) (Figure 6C). Almost the half of CIN25-C2 patients (48.1%) underwent progression during the treatment, while only 13.8% of CIN25-C1 patients did so (Figure 6C). Higher CRPR rates in CIN25-C1 group led to longer PFS, and the median PFS for C1 and C2 patients was 4.4 and 9.8 months, respectively (P = 0.002; HR, 2.13 (95% CI: 1.18 – 3.84) (Figure 6D).

Signaling pathways enriched in CIN25-C2 tumors and phenotypic association

We next performed the GSEA analysis to probe differences in signaling pathways between two tumor groups. Figures 7A, B showed significantly enriched KEGG and hallmark pathways in CIN25-C2 tumors, and almost all of them are oncogenic and play key parts in ccRCC development and progression, such as G2/M checkpoint, E2F and MYC targets, IL6-JAK-STAT3, glycolysis, EMT and others (Figure 7C). Consistent with these enriched pathways, CIN25-C2 tumors had robustly strong proliferation activity compared to CIN25-C1 tumors, as assessed using proliferation marker Ki-67 and cell cycle score, and stemness score (Figure 7D); furthermore, an established EMT 16 gene signature (36) was further used to evaluate EMT between CIN25-C1 and C2 tumors and significantly increased EMT scores were observed in the CIN25-C2 group (Figure 7D) (P = 0.035).

Increased EZH2 expression and diminished angiogenesis in CIN25-C2 tumors

EZH2, a histone methyltransferase catalyzing H3K27 trimethylation (H3K27me3), has been shown to promote stemness, EMT and Sunitinib resistance in ccRCC and other tumors (42–44). Given the results above, we set out to determine whether EZH2 expression differed between CIN25-C1 and C2 tumors. The analysis of both TCGA and E-MTAB1980 ccRCC cohorts showed robustly higher EZH mRNA levels in CIN25-C2 than in C1 tumors (CIN25-C1 vs C2: P = 2.21E-38 and 3.12E-06,

10.3389/fonc.2023.1133902

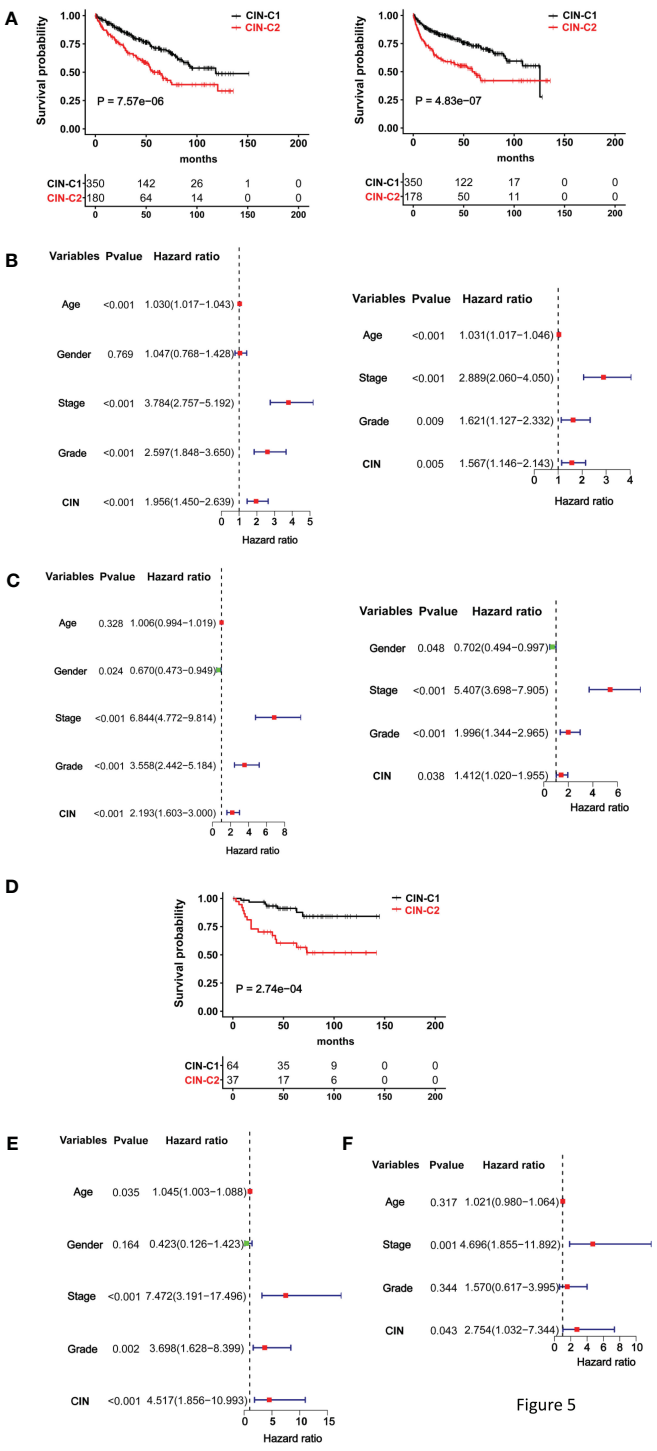

FIGURE 5
The CIN25 subtypes for survival prediction in ccRCCs. **(A–C)** The TCGA cohort analysis and **(D, E)** The E-MTAB1980 cohort analysis. **(A)** Significantly shorter overall and progression-free survival (OS and PFS) in the CIN25-C2 group. Left and right panel: OS and PFS, respectively. **(B)** Univariate and multivariate COX regression analyses of OS for the TCGA ccRCCs. **(C)** Univariate and multivariate COX regression analyses of PFS for the TCGA ccRCCs. **(D)** Significantly shorter OS in the CIN25-C2 group in the E-MTAB1980 cohort. **(E, F)** Univariate and multivariate COX regression analyses of OS for the E-MTAB1980 cohort.

respectively) (Figure 8A). In the Sunitinib-treated IMmotion150 and IMmotion151 cohorts, similar results were obtained (CIN25-C1 vs C2: P = 9.40E-08 and 1.71E-27 for IMmotion150 and 151, respectively) (Figure 8B). We further compared differences in EZH2 expression between responders and non-responders to Sunitinib. As expected, tumors from resistant patients expressed significantly higher levels of EZH2 than did those from responders (P = 0.021 and 0.004, respectively) (Figure 8C).

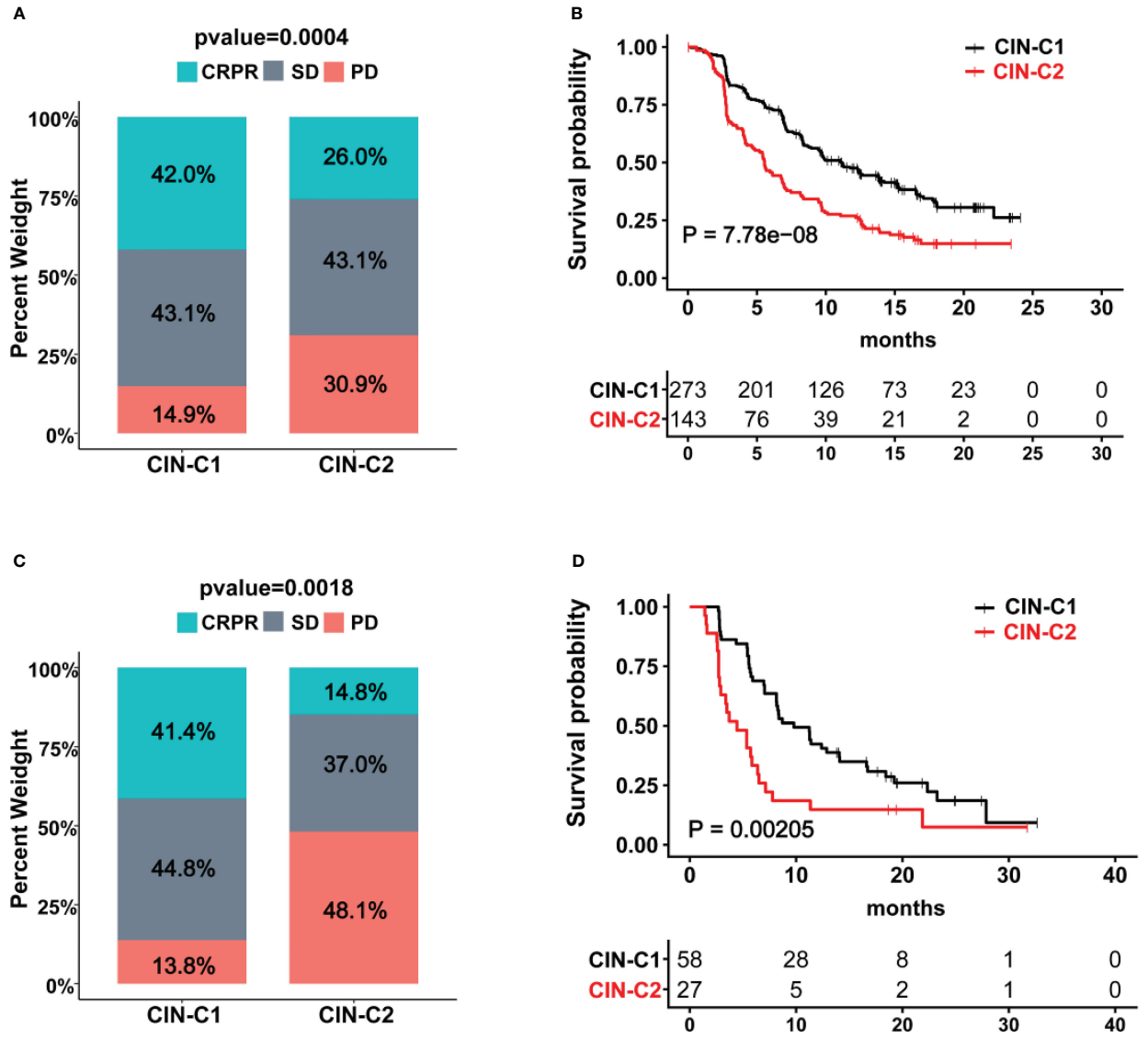

FIGURE 6
The CIN25 subtypes for prediction of Sunitinib response in ccRCCs. **(A, B)** IMmotion151 cohort of ccRCC patients treated with Sunitinib. Poor response to Sunitinib and shorter patient PFS in the CIN25-C2 group. **(C, D)** IMmotion150 cohort of ccRCC patients treated with Sunitinib. Poor response to Sunitinib and shorter patient PFS in the CIN25-C2 group.

In addition to higher EZH2 expression, poor angiogenesis is also a well characterized predictor for Sunitinib resistance (34, 35), and we thus analyzed the angiogenesis score in CIN25 subtypes of ccRCC tumors. As shown in Figure 8D, a significantly lower angiogenesis score was observed in the CIN-C2 tumors from the IMmotion151 (CIN25-C1 vs C2: P = 9.78E-17) and IMmotion150 (P = 0.0096) cohorts of ccRCC patients treated with Sunitinib. The TCGA and E-MTAB1980 ccRCC analyses showed similar results, which validated the observations above (Figure 8E).

Discussion

CIN is an important cancer hallmark (23–25). Because of the difficulty in directly assessing a CIN phenotype, a CIN25 signature has been developed, and the CIN25 expression-based score system roughly reflected levels of CIN in several cancer types (22). By analyzing primary ccRCC tumors and TCGA ccRCC cohort, we observed that expression of genes included in the CIN25 signature was robustly upregulated but significantly heterogenous. Based on CIN25 scores calculated from their mRNA levels, we categorized ccRCC patients into two clusters: CIN25-C1 (CIN25-low) and CIN25-C2 (CIN25-high), respectively. Our findings demonstrate that the CIN25 signature is present in ccRCC and this cluster system is useful in predicting patient outcomes and therapeutic response to TKR inhibitors.

CIN has been shown as a key driver of chromosomal alterations in human malignancies and primarily characterized by aneuploidy or SCNAs (23–25). Consistent with this, we observed that CIN25-C2 ccRCC tumors exhibited robustly increased aneuploidy. CIN-

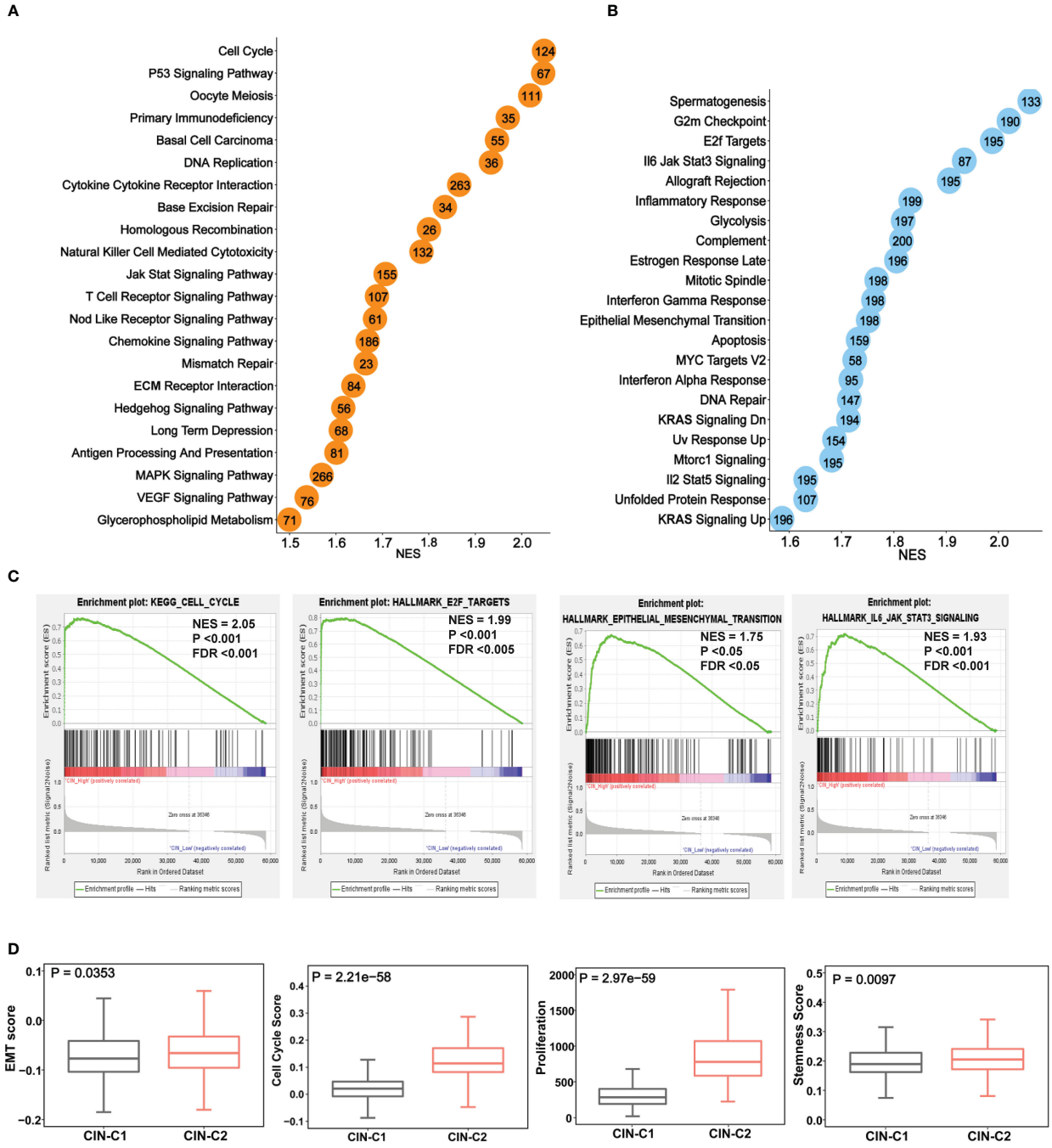

FIGURE 7
The enriched oncogenic pathways and aggressive phenotypes in the CIN25-C2 subtype of ccRCC tumors. The TCGA cohort analysis. **(A, B)** Enrichments of overrepresented KEGG **(A)** and hallmark **(B)** pathways in CIN25-C2 tumors. **(C)** Representative enriched pathways in CIN25-C2 tumors: Cell cycle, E2F targets, EMT and IL6-JAK-STAT3. **(D)** Higher EMT, proliferation and stemness scores in CIN-C2 tumors.

triggered aneuploidy creates intratumour genetic heterogeneity, thereby promoting phenotypic adaptation during cancer evolution and progression. On the other hand, aneuploidy or SCNAs further accelerate CIN rates. Thus, CIN and aneuploidy affect each other, establishing positive feedback.

CIN underpins much of the intratumoural heterogeneity observed in cancers and drives phenotypic adaptation during tumor evolution (23–25). It has been shown that the CIN phenotype is associated with resistance to chemo- and radiotherapies, however, it remains to be defined whether it has impacts on targeted therapeutic drugs. Sunitinib, a TKR inhibitor, has been applied as the first-line drug for advanced ccRCC treatment (12–14). Clinical studies showed that the intrinsic resistance to Sunitinib occurred in approximately 1/3 of patients,

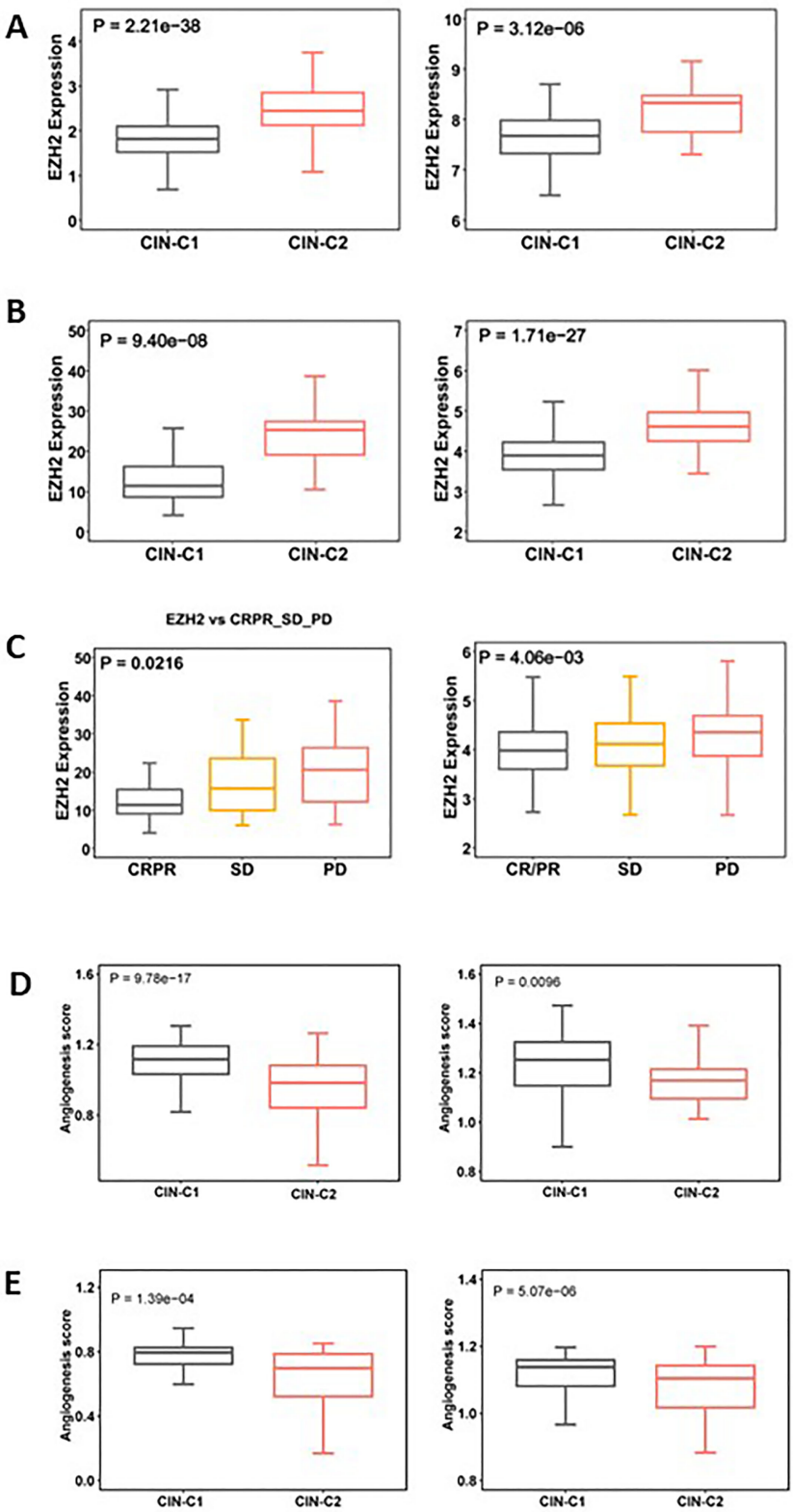

FIGURE 8
Differences in EZH2 expression and angiogenesis between CIN25-C1 and C2 subtypes of ccRCC tumors. **(A, B)** CIN25-C2 tumors expressed significantly higher levels of EZH2 mRNA. **(A)** TCGA (left) and E-MTAB1980 (right) ccRCC cohorts. **(B)** IMmotion150 (left) and 151 (right) cohorts. **(C)** Differences in EZH2 expression in tumors from CRPR, SD and PD patients (left and right: IMmotion150 and 151 cohorts, respectively). **(D)** Lower angiogenesis scores in CIN25-C2 tumors (left and right: TCGA and E-MTAB1980 ccRCC cohorts, respectively). **(E)** Lower angiogenesis scores in CIN25-C2 tumors (left and right: IMmotion150 and 151 cohorts, respectively).

while many of them initially responded to Sunitinib but the treatment failure developed eventually (6, 12, 15). Several molecules and signaling pathways have been implicated in Sunitinib irresponsiveness, however, the development of reliable biomarkers that distinguish Sunitinib responders from non-responders remains challenging. Our present findings suggest that the CIN25 signature serves as a useful stratifier to predict the therapeutic efficacy of Sunitinib and PFS in ccRCC patients. EZH2 upregulation and poor angiogenesis are likely the mechanism underlying lower efficacy observed in CIN25-C2 patients. Further studies are required to elucidate how CIN25 signature affects EZH2 expression and angiogenesis.

A link between telomere dysfunction and CIN has been well characterized in human malignancies and animal carcinogenesis models (39). Telomeric DNA repeats, when sufficient long, together with their binding-factors or sheltering proteins, form protective structures at the ends of linear chromosomes that prevent CIN (39, 45). Telomeric DNA is synthesized by telomerase, an RNA-dependent DNA polymerase activated in most human malignancies for telomere length maintenance (40). However, telomerase activation usually occurs at the late stage during a stepwise malignant transformation (45). Therefore, telomeres already become shortened in precursor lesions, which leads to telomere dysfunction as a driving event for CIN in early carcinogenesis (39, 45, 46). Shorter or dysfunctional telomere-bearing chromosomes are prone to fusion, thereby triggering the dicentric chromosome formation that missegregate or break in mitosis during anaphase (39). The resultant chromosomal breaks are fusogenic, through which a cycle of chromosome fusion and breakage is propagated. In the present study, we observed significantly shorter telomeres in ccRCC tumors than in their matched renal tissues. There were no differences in telomere length between CIN25-C1 and C2 tumors, but TERT expression and telomerase activity was noticeably higher in CIN25-C2 tumors. Likely, increased telomerase activity attenuates or compensates for telomere attrition in CIN25-C2 tumors.

CIN is one subtype in the genomic instability category that encompasses a variety of DNA alterations, including single nucleotide to whole chromosome changes (41). Interestingly, we observed that CIN25-C2 tumors also had increased genomic alterations reflecting all other aspects of genomic instability. In addition, HRD has been implicated in genomic instability including CIN, and consistently, HRD scores were significantly higher in CIN25-C2 tumors. Thus, the CIN25 clustering system help measure not only the CIN phenotype, but also the whole genomic instability level. From this point of a view, assessment of CIN25 signature may have broader implications both biologically and clinically. For instance, HRD occurs frequently in breast and ovarian cancer, and those patients are in general sensitive to PARP inhibitors. Conceivably, the CIN25 assessment may also be useful to stratify patients who respond to PARP inhibitor treatment. A PCR method is sufficient to quantify expression levels of 25 CIN genes, which is cost- and time-friendly, and easily applied for clinical routine.

In conclusion, the CIN25 clustering model can categorize ccRCC tumors into CIN25-C1 and C2 subtypes, and this classification hold great promises in predicting patient survival and response to Sunitinib. CIN25-C2 tumors are characterized by active proliferation, stemness and EMT phenotypes. EZH2 overexpression and poor angiogenesis may drive all these aggressive phenotypes, shorter survival and drug resistance. Importantly, the CIN25 clustering model not only represents a CIN phenotype, but also is strongly associated with other genomic instability-related alterations. Thus, the assessment of CIN25 reflects levels of CIN and whole genomic instability. Moreover, a PCR quantification is enough for the CIN25-based tumor classification, which is suitable for clinical routine application. Taken together, the present findings will contribute to improved personalized management of ccRCCs.

Data availability statement

The datasets presented in this study can be found in online repositories. The names of the repository/repositories and accession number(s) can be found in the article/Supplementary Material.

Ethics statement

The studies involving human participants were reviewed and approved by Institutional review board of Qilu Hospital of Shandong University. The patients/participants provided their written informed consent to participate in this study.

Author contributions

All authors participated in the conception and design of the study. CW, HY, JW, XQ, LL and WG performed bioinformatic analysis. XQ and ZF analyzed patient data and RNA sequencing. CW, XQ, HY, ZF, YF and DX participated in the data process, analysis and interpretation. CW, XQ, HY, YF and DX conceived and drafted the manuscript. HY, YF and DX revised the manuscript. All authors contributed to the article and approved the submitted version.

Funding

This work was supported by grants from Scientific Research Foundation of Qilu Hospital of Shandong University (Qingdao) (No. QDKY2019QN17), National Natural Science Foundation of China (No. 82103557, 82002674 and 81972475), Shandong Provincial Natural Science Foundation (No. ZR2020QH245), the Swedish Cancer Society No. 22 1989 Pj), Swedish Research Council (2018-02993), the Cancer Society in Stockholm (201393), and Karolinska Institutet (2022-01889).

Conflict of interest

The authors declare that the research was conducted in the absence of any commercial or financial relationships that could be construed as a potential conflict of interest.

Publisher's note

All claims expressed in this article are solely those of the authors and do not necessarily represent those of their affiliated organizations, or those of the publisher, the editors and the reviewers. Any product that may be evaluated in this article, or claim that may be made by its manufacturer, is not guaranteed or endorsed by the publisher.

Supplementary material

The Supplementary Material for this article can be found online at: https://www.frontiersin.org/articles/10.3389/fonc.2023.1133902/full#supplementary-material

References

1. Siegel RL, Miller KD, Jemal A. Cancer statistics, 2020. *CA Cancer J Clin* (2020) 70 (1):7–30. doi: 10.3322/caac.21590

2. Znaor A, Lortet-Tieulent J, Laversanne M, Jemal A, Bray F. International variations and trends in renal cell carcinoma incidence and mortality. *Eur Urol* (2015) 67(3):519–30. doi: 10.1016/j.eururo.2014.10.002

3. Fang Z, Zhang N, Yuan X, Xing X, Li X, Qin X, et al. GABPA-activated TGFBR2 transcription inhibits aggressiveness but is epigenetically erased by oncometabolites in renal cell carcinoma. *J Exp Clin Cancer Res* (2022) 41(1):173. doi: 10.1186/s13046-022-02382-6

4. Graham J, Dudani S, Heng DYC. Prognostication in kidney cancer: recent advances and future directions. *J Clin Oncol* (2018) JCO2018790147. doi: 10.1200/JCO.2018.79.0147

5. Ghatalia P, Rathmell WK. Systematic review: ClearCode 34 - a validated prognostic signature in clear cell renal cell carcinoma (ccRCC). *Kidney Cancer* (2018) 2(1):23–9. doi: 10.3233/KCA-170021

6. Yuan H, Qin X, Wang J, Yang Q, Fan Y, Xu D. The cuproptosis-associated 13 gene signature as a robust predictor for outcome and response to immune- and targeted-therapies in clear cell renal cell carcinoma. *Front Immunol* (2022) 13:971142. doi: 10.3389/fimmu.2022.971142

7. Rini B, Goddard A, Knezevic D, Maddala T, Zhou M, Aydin H, et al. A 16-gene assay to predict recurrence after surgery in localised renal cell carcinoma: development and validation studies. *Lancet Oncol* (2015) 16(6):676–85. doi: 10.1016/S1470-2045(15)70167-1

8. Chen S, Zhang E, Jiang L, Wang T, Guo T, Gao F, et al. Robust prediction of prognosis and immunotherapeutic response for clear cell renal cell carcinoma through deep learning algorithm. *Front Immunol* (2022) 13:798471. doi: 10.3389/fimmu.2022.798471

9. Tao J, Li X, Liang C, Liu Y, Zhou J. Expression of basement membrane genes and their prognostic significance in clear cell renal cell carcinoma patients. *Front Oncol* (2022) 12:1026331. doi: 10.3389/fonc.2022.1026331

10. Zeng R, Li Y, He DM, Sun MZ, Huang WQ, Wang YH, et al. Potassium channel-related genes are a novel prognostic signature for the tumor microenvironment of renal clear cell carcinoma. *Front Oncol* (2022) 12:1013324. doi: 10.3389/fonc.2022.1013324

11. Zheng D, Ning J, Xia Y, Ruan Y, Cheng F. Comprehensive analysis of a homeobox family gene signature in clear cell renal cell carcinoma with regard to prognosis and immune significance. *Front Oncol* (2022) 12:1008714. doi: 10.3389/fonc.2022.1008714

12. Angulo JC, Shapiro O. The changing therapeutic landscape of metastatic renal cancer. *Cancers (Basel)* (2019) 11(9). doi: 10.3390/cancers11091227

13. Motzer RJ, Escudier B, McDermott DF, George S, Hammers HJ, Srinivas S, et al. Nivolumab versus everolimus in advanced renal-cell carcinoma. *N Engl J Med* (2015) 373(19):1803–13. doi: 10.1056/NEJMoa1510665

14. Srivastava A, Doppalapudi SK, Patel HV, Srinivasan R, Singer EA. The roaring 2020s: a new decade of systemic therapy for renal cell carcinoma. *Curr Opin Oncol* (2022). doi: 10.1097/CCO.0000000000000831

15. Sharma R, Kadife E, Myers M, Kannourakis G, Prithviraj P, Ahmed N. Determinants of resistance to VEGF-TKI and immune checkpoint inhibitors in metastatic renal cell carcinoma. *J Exp Clin Cancer Res* (2021) 40(1):186. doi: 10.1186/s13046-021-01961-3

16. Braun DA, Hou Y, Bakouny Z, Ficial M, Sant' Angelo M, Forman J, et al. Interplay of somatic alterations and immune infiltration modulates response to PD-1 blockade in advanced clear cell renal cell carcinoma. *Nat Med* (2020) 26(6):909–18. doi: 10.1038/s41591-020-0839-y

17. Deng H, Liu W, He T, Hong Z, Yi F, Wei Y, et al. Comparative efficacy, safety, and costs of sorafenib vs. sunitinib as first-line therapy for metastatic renal cell carcinoma: a systematic review and meta-analysis. *Front Oncol* (2019) 9:479. doi: 10.3389/fonc.2019.00479

18. Turajlic S, Xu H, Litchfield K, Rowan A, Horswell S, Chambers T, et al. Deterministic evolutionary trajectories influence primary tumor growth: TRACERx renal. *Cell* (2018) 173(3):595–610 e11. doi: 10.1016/j.cell.2018.03.043

19. Brugarolas J. Molecular genetics of clear-cell renal cell carcinoma. *J Clin Oncol* (2014) 32(18):1968–76. doi: 10.1200/JCO.2012.45.2003

20. Correa AF, Ruth KJ, Al-Saleem T, Pei J, Dulaimi E, Kister D, et al. Overall tumor genomic instability: an important predictor of recurrence-free survival in patients with localized clear cell renal cell carcinoma. *Cancer Biol Ther* (2020) 21(5):424–31. doi: 10.1080/15384047.2020.1721251

21. Klatte T, Rao PN, de Martino M, LaRochelle J, Shuch B, Zomorodian N, et al. Cytogenetic profile predicts prognosis of patients with clear cell renal cell carcinoma. *J Clin Oncol* (2009) 27(5):746–53. doi: 10.1200/JCO.2007.15.8345

22. Carter SL, Eklund AC, Kohane IS, Harris LN, Szallasi Z. A signature of chromosomal instability inferred from gene expression profiles predicts clinical outcome in multiple human cancers. *Nat Genet* (2006) 38(9):1043–8. doi: 10.1038/ng1861

23. Lukow DA, Sheltzer JM. Chromosomal instability and aneuploidy as causes of cancer drug resistance. *Trends Cancer* (2022) 8(1):43–53. doi: 10.1016/j.trecan.2021.09.002

24. Al-Rawi DH, Bakhoum SF. Chromosomal instability as a source of genomic plasticity. *Curr Opin Genet Dev* (2022) 74:101913. doi: 10.1016/j.gde.2022.101913

25. Bakhoum SF, Cantley LC. The multifaceted role of chromosomal instability in cancer and its microenvironment. *Cell* (2018) 174(6):1347–60. doi: 10.1016/j.cell.2018.08.027

26. Weiler SME, Pinna F, Wolf T, Lutz T, Geldiyev A, Sticht C, et al. Induction of chromosome instability by activation of yes-associated protein and forkhead box M1 in liver cancer. *Gastroenterology* (2017) 152(8):2037–51 e22. doi: 10.1053/j.gastro.2017.02.018

27. Cancer Genome Atlas Research N. Comprehensive molecular characterization of clear cell renal cell carcinoma. *Nature* (2013) 499(7456):43–9. doi: 10.1038/nature12222

28. Sato Y, Yoshizato T, Shiraishi Y, Maekawa S, Okuno Y, Kamura T, et al. Integrated molecular analysis of clear-cell renal cell carcinoma. *Nat Genet* (2013) 45 (8):860–7. doi: 10.1038/ng.2699

29. McDermott DF, Huseni MA, Atkins MB, Motzer RJ, Rini BI, Escudier B, et al. Clinical activity and molecular correlates of response to atezolizumab alone or in combination with bevacizumab versus sunitinib in renal cell carcinoma. *Nat Med* (2018) 24(6):749–57. doi: 10.1038/s41591-018-0053-3

30. Powles T, Atkins MB, Escudier B, Motzer RJ, Rini BI, Fong L, et al. Efficacy and safety of atezolizumab plus bevacizumab following disease progression on atezolizumab or sunitinib monotherapy in patients with metastatic renal cell carcinoma in IMmotion150: a randomized phase 2 clinical trial. *Eur Urol* (2021) 79 (5):665–73. doi: 10.1016/j.eururo.2021.01.003

31. Motzer RJ, Powles T, Atkins MB, Escudier B, McDermott DF, Alekseev BY, et al. Final overall survival and molecular analysis in IMmotion151, a phase 3 trial comparing atezolizumab plus bevacizumab vs sunitinib in patients with previously untreated metastatic renal cell carcinoma. *JAMA Oncol* (2022) 8(2):275–80. doi: 10.1001/jamaoncol.2021.5981

32. Rini BI, Powles T, Atkins MB, Escudier B, McDermott DF, Suarez C, et al. Atezolizumab plus bevacizumab versus sunitinib in patients with previously untreated metastatic renal cell carcinoma (IMmotion151): a multicentre, open-label, phase 3, randomised controlled trial. *Lancet* (2019) 393(10189):2404–15. doi: 10.1016/S0140-6736(19)30723-8

33. Masiero M, Simoes FC, Han HD, Snell C, Peterkin T, Bridges E, et al. A core human primary tumor angiogenesis signature identifies the endothelial orphan receptor ELTD1 as a key regulator of angiogenesis. *Cancer Cell* (2013) 24(2):229–41. doi: 10.1016/j.ccr.2013.06.004

34. Hakimi AA, Voss MH, Kuo F, Sanchez A, Liu M, Nixon BG, et al. Transcriptomic profiling of the tumor microenvironment reveals distinct subgroups of clear cell renal cell cancer: data from a randomized phase III trial. *Cancer Discovery* (2019) 9(4):510–25. doi: 10.1158/2159-8290.CD-18-0957

35. Motzer RJ, Banchereau R, Hamidi H, Powles T, McDermott D, Atkins MB, et al. Molecular subsets in renal cancer determine outcome to checkpoint and angiogenesis blockade. *Cancer Cell* (2020) 38(6):803–17 e4. doi: 10.1016/j.ccell.2020.10.011

36. Gibbons DL, Creighton CJ. Pan-cancer survey of epithelial-mesenchymal transition markers across the cancer genome atlas. *Dev Dyn* (2018) 247(3):555–64. doi: 10.1002/dvdy.24485

37. Barthel FP, Wei W, Tang M, Martinez-Ledesma E, Hu X, Amin SB, et al. Systematic analysis of telomere length and somatic alterations in 31 cancer types. *Nat Genet* (2017) 49(3):349–57. doi: 10.1038/ng.3781

38. Wang J, Dai M, Xing X, Wang X, Qin X, Huang T, et al. Genomic, epigenomic, and transcriptomic signatures for telomerase complex components: a pan-cancer analysis. *Mol Oncol* (2022). doi: 10.1002/1878-0261.13324

39. Herate C, Sabatier L. Telomere instability initiates and then boosts carcinogenesis by the butterfly effect. *Curr Opin Genet Dev* (2020) 60:92–8. doi: 10.1016/j.gde.2020.01.005

40. Yuan X, Larsson C, Xu D. Mechanisms underlying the activation of TERT transcription and telomerase activity in human cancer: old actors and new players. *Oncogene* (2019) 38(34):6172–83. doi: 10.1038/s41388-019-0872-9

41. Pikor L, Thu K, Vucic E, Lam W. The detection and implication of genome instability in cancer. *Cancer Metastasis Rev* (2013) 32(3-4):341–52. doi: 10.1007/s10555-013-9429-5

42. Adelaiye-Ogala R, Budka J, Damayanti NP, Arrington J, Ferris M, Hsu CC, et al. EZH2 modifies sunitinib resistance in renal cell carcinoma by kinome reprogramming. *Cancer Res* (2017) 77(23):6651–66. doi: 10.1158/0008-5472.CAN-17-0899

43. Lyu C, Wang L, Stadlbauer B, Noessner E, Buchner A, Pohla H. Identification of EZH2 as cancer stem cell marker in clear cell renal cell carcinoma and the anti-tumor effect of epigallocatechin-3-Gallate (EGCG). *Cancers (Basel)* (2022) 14(17). doi: 10.3390/cancers14174200

44. Bakhoum SF, Ngo B, Laughney AM, Cavallo JA, Murphy CJ, Ly P, et al. Chromosomal instability drives metastasis through a cytosolic DNA response. *Nature* (2018) 553(7689):467–72. doi: 10.1038/nature25432

45. Yuan X, Dai M, Xu D. Telomere-related markers for cancer. *Curr Top Med Chem* (2020) 20(6):410–32. doi: 10.2174/1568026620666200106145340

46. Zhang A, Wang J, Zheng B, Fang X, Angstrom T, Liu C, et al. Telomere attrition predominantly occurs in precursor lesions during *in vivo* carcinogenic process of the uterine cervix. *Oncogene* (2004) 23(44):7441–7. doi: 10.1038/sj.onc.1207527

frontiers | Frontiers in Oncology

TYPE Original Research
PUBLISHED 22 June 2023
DOI 10.3389/fonc.2023.1095775

OPEN ACCESS

EDITED BY
Linhui Wang,
Second Military Medical University, China

REVIEWED BY
Xuedong Wei,
The First Affiliated Hospital of Soochow University, China
Aimin Jiang,
Fudan University, China

*CORRESPONDENCE
Chaozhao Liang
liang_chaozhao@ahmu.edu.cn
Jun Xiao
xiaojun0551@126.com
Song Xue
xs580155@163.com

†These authors share first authorship

RECEIVED 11 November 2022
ACCEPTED 20 April 2023
PUBLISHED 22 June 2023

CITATION
Tai S, Xu D-d, Yu Z, Guan Y, Yin S, Xiao J, Xue S and Liang C (2023) Genomic profiles of renal cell carcinoma in a small Chinese cohort.
Front. Oncol. 13:1095775.
doi: 10.3389/fonc.2023.1095775

Genomic profiles of renal cell carcinoma in a small Chinese cohort

Sheng Tai[1,2,3†], Dan-dan Xu[4,5†], Zhixian Yu[6†], Yu Guan[2,3], Shuiping Yin[1,2,3], Jun Xiao[7*], Song Xue[8*] and Chaozhao Liang[1,2,3*]

[1]Department of Urology, The First Affiliated Hospital of Anhui Medical University, Hefei, Anhui, China, [2]Institute of Urology, Anhui Medical University, Hefei, Anhui, China, [3]Anhui Province Key Laboratory of Genitourinary Diseases, Anhui Medical University, Hefei, Anhui, China, [4]Department of Oncology, Hospital of Anhui Medical University, Hefei, Anhui, China, [5]Department of Oncology, Anhui Public Health Clinical Center, Hefei, China, [6]Department of Urology, The First Affiliated Hospital of Wenzhou Medical University, Wenzhou, China, [7]Department of Urology, The First Affiliated Hospital of University of Science and Technology of China (USTC), Division of Life Sciences and Medicine, University of Science and Technology of China, Hefei, China, [8]Department of Urology, General Hospital of Eastern Theater Command, Nanjing, China

Objectives: Our aim was to describe the molecular characteristics of Renal Cell Carcinoma (RCC) and develop a small panel of RCC-associated genes from a large panel of cancer-related genes.

Materials and methods: Clinical data of 55 patients with RCC diagnosed in four hospitals from September 2021 to August 2022 were collected. Among the 55 patients, 38 were diagnosed with clear cell RCC (ccRCC), and the other 17 were diagnosed with non-clear cell RCC (nccRCC), including 10 cases of papillary renal cell carcinoma, 2 cases of hereditary leiomyomatosis and RCC syndrome (HLRCC), 1 eosinophilic papillary RCC, 1 tubular cystic carcinoma, 1 TFE3 gene fusion RCC, and 2 RCC with sarcomatoid differentiation. For each patient, 1123 cancer-related genes and 79 RCC-associated genes were analyzed.

Results: the most frequent mutations in a large panel of 1123 cancer-related genes in the overall population of RCC patients were VHL (51%), PBRM1 (35%), BAP1 (16%), KMT2D (15%), PTPRD (15%), and SETD2 (15%). For ccRCC patients, mutations in VHL, PBRM1, BAP1, and SERD2 can reach 74%, 50%, 24%, and 18%, respectively, while for nccRCC patients, the most frequent mutation was FH (29%), MLH3 (24%), ARID1A (18%), KMT2D (18%), and CREBBP (18%). The germline mutation rate in all 55 patients reached 12.7% (five with FH, one with ATM, and one with RAD50). The small panel containing only 79 RCC-associated genes demonstrated that mutations of VHL, PBRM1, BAP1, and SETD2 in ccRCC patients were 74%, 50%, 24%, and 18% respectively, while for the nccRCC cohort, the most frequent mutations were FH (29%), ARID1A (18%), ATM (12%), MSH6 (12%), BRAF (12%), and KRAS (12%). For ccRCC patients, the spectrum of mutations by large and small panels was almost the same, while for nccRCC patients, the mutation spectrum showed some differences. Even though the most frequent mutations (FH and ARID1A) in nccRCC were both demonstrated by large panels and small panels, other less frequent mutations such as MLH3, KMT2D, and CREBBP were not shown by the small panel.

Conclusion: Our study revealed that nccRCC is more heterogeneous than ccRCC. For nccRCC patients, the small panel shows a more clear profile of genetic characteristics by replacing MLH3, KMT2D, and CREBBP with ATM, MSH6, BRAF, and KRAS, which may help predict prognosis and make clinical decisions.

KEYWORDS

renal cell carcinoma (RCC), clear cell renal cell carcinoma (ccRCC), non-clear cell renal cell carcinoma (nccRCC), mutation, VHL, FH

1 Introduction

In 2020, 4.3 million patients were diagnosed with kidney cancer, accounting for 1.79 million deaths worldwide (1). There were 75800 newly diagnosed kidney cancer cases and 27800 patients who died of kidney cancer in China (2). Renal cell carcinoma (RCC) is the most common renal tumor in adults, including clear cell RCC (ccRCC), type 1 and type 2 papillary RCC (pRCC), chromophobe carcinoma, and other rare RCCs. ccRCC is the most common subtype, accounting for 75–85% of all cases. Early-stage renal cell carcinoma can be cured by surgical resection. However, recurrent, unresectable, and metastatic RCCs (mRCCs) have a high mortality rate, with a 5-year survival rate of only 12% (3). With the development of targeted therapy and immunotherapy, mRCC survival has been significantly prolonged; however, cancer progression and resistance to therapy need to be resolved, and comprehensive genomic profiles are important for RCC management.

Previous genetic characterization of RCC has significantly increased our knowledge of tumor biology and disease progression. The Cancer Genome Atlas (TCGA) accrued flash-frozen samples of tumor resections and adjacent normal kidneys (or an aliquot of blood if no normal kidney was available) for whole exome sequencing and analyzed the genomic information and related clinical and pathological patient data (4). This project revealed that ccRCC had a specific deletion on chromosome 3 in approximately 90% of patients and most ccRCCs harbored VHL gene mutations. Besides the 3p deletion, TCGA analysis confirmed a frequent occurrence in chromosome 5 (67%) and chromosome 14q (45%) deletions, and the top ten mutated genes in ccRCC were VHL, PBRM1, BAP1, SETD2, KDM5C, TP53, mTOR, SMARCA, PTEN, and ARID1A (5, 6). Numerous epigenomic-related genes are mutated in ccRCC, suggesting that epigenetic regulation plays an important role in the molecular pathways underlying ccRCC leading to the development of possible epigenetic therapies. pRCC is a heterogeneous RCC subtype in which the unifying feature is the presence of papillae in the tumor, which is most commonly separated into type 1 pRCC that has basophilic cytoplasm and type 2 pRCC that has abundant eosinophilic cytoplasm. Genomic profiles have also been described in TCGA studies. Type 1 pRCC is associated with frequent concurrent gains in chromosomes 7 and 17, and numerous potential oncogenes are encoded on chromosome 7, including MET, EGFR, and BRAF. Type 2 papillary RCC was the only loss of chromosome 22 that occurred consistently as a specific copy number alteration (frequency, 30.4%) (7, 8). Compared with type 1 pRCC, type 2 pRCC had low-frequency mutations, and the FH gene (encoding fumarate hydratase) germline and/or somatic mutations were discovered in type 2 pRCC. TCGA has characterized somatic genetic and genomic alterations in RCC; however, these databases are based on Western patients, and only 1.8% of Asian patients were included. Therefore, it is necessary to elucidate Chinese RCC genomic symbols and clinical characteristics of Chinese RCC.

We enrolled 55 patients with RCC from multiple hospitals and performed a panel of 1123 genes sequence, focusing on 79 RCC cancer-related gene target sequences. This study aimed to describe the genomic map of Chinese renal cell cancer and explore the differences between ccRCC and nccRCC, achieving precision medicine for RCC.

2 Methods

2.1 Patients

Patients were enrolled in three hospitals between November 1, 2021, and August 31, 2022. The pathologist confirmed the diagnosis of renal cell cancer, including ccRCC and pRCC. All participants provided signed informed consent. The specimens used were formalin fixed paraffin-embedded (FFPE) and fresh tumor specimens and were tested by DNA NGS. Clinical demographic parameters, cancer stage using the American Joint Committee on Cancer guidelines, and pathological data including tumor stage and lymph node status were collected.

2.2 Next-generation sequence

Tumor samples were collected, and next-generation sequencing tests of all samples were performed at ChosenMed Technology (Beijing) Co., Ltd., Beijing, China). Genomic DNA extraction and library preparation with TruSight™ Oncology 500 (TSO 500) Library Preparation Kit (Illumina, San Diego, CA, United States) were performed following the manufacturer's protocols. The library was sequenced on an Illumina NextSeq 550Dx platform with a paired-end run of 150 base pairs. Sequence alignment to the human genome

(hg19) (9) was completed using the BWA-MEM (version 0.7.11) alignment algorithm. SAMtools (version 1.3) (10) was used to perform the bam-sam conversions. We used the Genome Analysis Toolkit (GATK, version 3.6) (11) module IndelRealigner to perform local realignment of indels. Germline variants were filtered using an in-house built database, and all parameters were set according to the standard protocol (12). Copy number variants (CNVs), including amplification and deletion, were identified using CRAFT copy-number callers from the TSO500 pipeline. Manta (version 1.6.0) (13) was employed to detect large-scale structural variations (SVs) in the RNA library, and only fusions with at least three unique supporting reads, one of which is a split read crossing the fusion breakpoint, were considered candidate fusions. The process of SNVs and indel mutation calling, TMB measurement, and read filtering was performed as described in a previous study. Germline variants were filtered using an in-house built database, and all parameters were set according to the previous workflow. We finally obtained two R packets with 1,123 genes named ChosenOne® and 79 genes named ChsenFocus®.

2.3 Statistical analysis

The assessment of clinical characteristics between different cohorts, including age, sex, histological subtype, location, and TNM stage, was performed using SPSS 20.0. The R package "maftools package" (Mayakonda et al., 2018) was applied to perform the mutation analysis and provide a visualized process of variant analysis results. All statistical analyses were performed using R version 3.6.3. All the p-values presented are for a two-tailed test, and $p < 0.05$ represents statistical significance.

3 Results

3.1 Patients summary

A total of 55 patients diagnosed with renal cell cancer were enrolled from the First Affiliated Hospital of Anhui Medical University, the First Affiliated Hospital of Wenzhou Medical University, and the General Hospital of Eastern Theater Command between November 1, 2021, and August 31, 2022. Among the 55 patients, 78.2% were men and 21.8% were women, with a median age of 57 years. Approximately 69.1% of the patients had ccRCC and 30.9% had nccRCC, including eight with type 2 pRCC and two with type 1 pRCC. Of the tumors, 40.0% were localized to the left kidney, and 58.2% were located on the right side. Of the patients, 52.7% were diagnosed with TNM stage I, and 10% had distant metastases (Table 1; Table S1).

TABLE 1 Clinical characteristics of 55 RCCs.

Age, median (range)	57 (10~79)
Sex, n (%)	
Men	43 (78.2%)
Women	12 (21.8%)
Histological subtype, n (%)	
ccRCC	38 (69.1%)
nccRCC	17 (30.9%)
Tumor location, n (%)	
Right	22 (40.0%)
Left	32 (58.2%)
Unknown	1(1.8%)
TNM, n (%)	
I	29 (52.7%)
II	5 (9.1%)
III	10 (18.2%)
IV	11 (10.0%)

3.2 Somatic mutation of RCC in 1123 gene panel

All the samples were sequenced in an 1123 gene panel. VHL (51%), PBRM1 (35%), BAP1 (16%), KMT2D (15%), PTPRD (15%), and SETD2 (15%) were the most common mutations in all RCC patients (Figure 1). The mutation frequency in ccRCC was higher than that in nccRCC. Common gene mutations in ccRCC patients were VHL (74%), PBRM1(50%), BAP1(24%), SETD2 (18%), and ARID1B (16%) (Figure S1). The mutation copies were lower in nccRCC than in ccRCC, and the most frequent mutations in nccRCC were MLH3(24%), ARID1B (18%), CREBBP (18%), and KMT2D (18%) (Figure S2). Missense mutations accounted for the most prevalent mutation in ccRCC, while the most common genetic variation in nccRCC was Fram_Shift. Furthermore, Frame Shift Del and Frame Shift Ins have higher rates of mutation in nccRCC. Specifically, missense mutations in KRAS, NKX2-1, BRAF, CUL3, PRSS1, ABCC6, CYLD, ANKRD11, and BLM only have Frame Shift Ins, whereas BCL10 and MSH6 only have frameshift delay. KMT2D had the highest mutation rate in all three groups when the results of

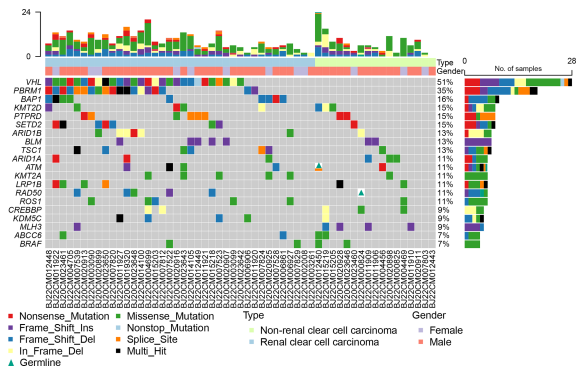

FIGURE 1
Genomic landscape of 55 RCC patients with 1123 gene.

the three groups were examined, and the mutation results of ccRCC were equivalent to those of all RCC patients.

3.3 Somatic mutation of RCC in 79 gene small panel

Based on an analysis of 79 genes associated with renal cancer, we found that VHL, PBRM1, BAP1, SETD2, and TSC1 mutation rates were higher in all RCCs at 51%, 35%, 16%, 15%, and 13%, respectively (Figure 2). VHL (74%), PBRM1 (50%), BAP1 (24%), SETD2 (18%), and TSC1 (16%) were the most frequently mutated genes in ccRCC (Figure S3). nccRCC mutations are highly specific, with high rates of mutations in FH, ARID1A, ATM, BRAF, and KRAS. nccRCC was more heterogeneous than ccRCC (Figure S4). The most common type of mutation in both groups of patients was missense mutation, and many genes had only missense mutations. Splice site, Frame Shift Del, Nonsense Mutation, and In Frame Del have all shown independent mutations in nccRCC patients. It seems that ccRCC has a clear driver gene mutation, and patients with ccRCC have a higher mutation rate than those with nccRCC. For ccRCC patients, the mutation profiles in the 1123 gene panel and 79 gene panels were nearly identified, whereas for nccRCC patients, the mutation profiles showed some differences. The most frequent mutations (FH and ARID1A) in nccRCC were both demonstrated by the 1123 gene panel and 79 gene panel; other less frequent mutations such as MLH3, KMT2D, and CREBBP were not detected in the 79 gene panel.

3.4 germline mutation of RCC

In 55 patients, we discovered six germline mutations in five (5/55, 9.1%) patients, including four FH genes, one ATM gene, and one RAD50 gene (Figure S4); it's important to note that all six of these germline mutations were discovered in nccRCC (5/17, 29.4%), and no germline mutations were discovered in ccRCC. Four of the five germline mutation patients were diagnosed with type 2 pRCC, three with FH germline mutations, and one with FH mutation concurrent with ATM germline mutation. Patients with a TFE3 fusion have a RAD50 germline mutation.

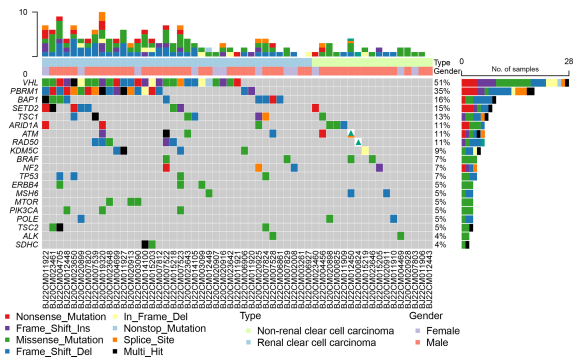

FIGURE 2
Genomic landscape of 55 RCC patients with 79 gene.

4 Discussion

Since kidney cancer is the most common cancer in urology, we report a comprehensive genomic analysis of 55 RCCs including 38 ccRCCs and 17 nccRCCs to reveal the genomic characteristics of a small Chinese RCC cohort. We discovered that the VHL gene is the most frequent mutation in ccRCC, which was similar to the conclusion that the VHL mutation is the most common mutation of ccRCC according to the TCGA project. Some Chinese researchers have reported that approximately 50% of ccRCC patients have VHL mutations (14), and our results show that VHL is approximately 51% in all RCCs and 78% in ccRCCs, which is similar to that in previous reports. VHL is a key component of the VHL E3 ubiquitin ligase complex that recognizes and binds hydroxylated target proteins in an oxygen-dependent manner. Loss of VHL stabilizes the protein levels of hypoxia-inducible factors HIF1α and HIF2α, which results in a loss of oxygen sensing, induces cellular proliferation, and promotes angiogenesis (15). Besides, VHL, PBRM1, BAP1, and SETD2 are regarded as driver mutations in ccRCC, which also act as biomarkers for ccRCC treatment and prognosis. The PBRM1 gene codes for BAF180, a subunit of the PBAF subtype of the SWI/SNF chromatin remodeling complex, and the PBAF complex suppress the hypoxic transcriptional signature. A study has reported that loss-of-function mutations in the PBRM1 gene were associated with the clinical benefit of using PD-1 inhibitor because PBAF loss shows that RCC is more sensitive to T-cell-mediated cytotoxicity than its PBAF-intact counterparts. Some clinical trials have shown that PBRM1 is a biomarker for immunotherapy (16, 17), but the results are still controversial. Some researchers have reported that PBRM1 loss defines a non-immunogenic tumor phenotype associated with checkpoint inhibitor resistance in renal carcinoma (17). Therefore, more evidence is required to reveal the relationship between PBRM1 mutation and immunotherapy response. In our study, mutations in VHL, PBRM1, BAP1, and SERD2 can reach 74%, 50%, 24%, and 18%, respectively, for ccRCC patients; while for nccRCC patients, the most frequent mutation was FH (29%), MLH3 (24%), ARID1A (18%), KMT2D (18%) and CREBBP (18%). As we know, the inactivation of the Von Hippel–Lindau (VHL) gene is by far the most common oncogenic driver event in ccRCC. Gene mutations in RCC patients were revealed by next-generation sequencing techniques, and the altered genes were then utilized to predict patients' prognosis and develop therapeutic drugs. The molecular fingerprints described by next-generation sequencing techniques categorize ccRCC into different subtypes that are clinically and therapeutically important. Specific mutations that seem to influence immune cell populations can be discovered in ccRCC tumors because of the interaction between these subtypes and the tumor microenvironment. Opportunities for illness prevention, early identification, prognosis, and therapy have been presented in these studies (18). PBRAM1, BAP1, and SETD2 are chromatin-remodeling genes that are present in the commonly lost region of chromosome arm 3p, which is critical for chromosome stability and remodeling. A lot of studies have revealed that the mutation of BAP1 is associated with poor prognosis (19, 20) even though how

PBRM1 gene mutations promote carcinogenesis and tumor progression is still unknown. PBRM1 is considered a tumor suppressor gene by *in vitro* experiments in ccRCC-derived cell lines, which show that PBRM1 gene silencing results in increased proliferation, migration, and colony formation (21).

Joseph RW et al. found that the loss of PBRM1 expression in 1330 ccRCC tumor samples was associated with an increased risk of metastasis without affecting the overall survival (22). The gene mutation of FH was the driving cause of hereditary leiomyomatosis and renal cell carcinoma (HLRCC). The median relapse-free survival for patients with FH gene mutation was only 9 months, so the 2022 WHO classification of renal cell carcinoma has changed the term from HLRCC to FH-deficient RCC which represents a new subtype in nccRCC. FH gene mutation of RCC was the golden standard for FH-deficient RCC, which requires more active treatment.

NccRCC is a rare subtype of RCC, accounting for 15–20% of RCCs, and it is a heterogeneous disease that comprises various types of renal cancer. We recruited 17 nccRCCs to perform the next-generation sequencing techniques, and the results showed that nccRCC has distinct genomic characteristics compared to ccRCC. There were no major mutated genes in nccRCC, and the highest mutated genes were MLH3(24%), ARID1B (18%), CREBBP (18%), and KMT2D (18%), which were lower than those in ccRCC. Numerous potential oncogenes of type 1 pRCC have been reported, including MET, EGFR, and BRAF, and somatic or germline activating mutations of MET has been found in a subset of type 1 pRCC; however, our study did not observe MET mutations due to the small sample size. Nevertheless, we found a higher frequency of FH mutations in type 2 pRCC, which is consistent with a previous report. Some research found that Cabozantinib plus nivolumab is effective in most non-clear cell variants of RCCS, especially those with prominent papillary features, but limited in chromophobe RCCS (23). Over the past two decades, a variety of options have been recognized as the dominant treatment for metastatic renal cell carcinoma (mRCC), including angiogenesis inhibitors, vascular endothelial growth factor receptor inhibitors, other tyrosine kinase inhibitors (TKIs), as well as MET inhibitors and mammalian targeted rapamycin (mTOR) inhibitors. More recently, immunotherapy or combination targeting agents have been shown to significantly improve outcomes in patients with mRCC compared to TKI alone (24).

For all solid tumor gene tests, an 1123 gene panel was designed; however, some genes were not frequently mutated in RCC. We searched for literature and clinical trials and then constructed a panel of 79 genes that were significantly associated with RCC tumorigenesis. Compared to the COSMIC and TCGA databases, the mutation of ccRCC by 79 gene panels is more consistent with the RCC driver mutation. For example, BLM and LRP1B are not significantly associated with the prognosis of ccRCC, but in the 1123 panel, we observed that the frequency exceeded 10%, so the 79 gene panel may be more suitable for profiling RCC gene mutation.

Kidney cancer is an inherited cancer. Several well-known hereditary RCC syndromes account for 5-9% of all RCC cases, including VHL disease, BHD syndrome, and HLRCC. Patients with a family history of RCC have an approximated two-fold increased risk of RCC. Early onset RCC diagnosed before the age of 46 years was reported to be associated with hereditary RCC. In a study of 190 Chinese patients under the age of 45 years who presented with renal tumors, 9.5% had a pathogenic/likely pathogenic (P/LP) germline mutation (25). Our study of 55 RCC patients revealed six germline mutations in five patients (5/55, 9.1%), which was consistent with previous reports. Interestingly, all germline mutations were found in nccRCC, indicating that nccRCC is associated with a high risk of hereditary diseases. We enrolled only seven cases of type 2 pRCC; surprisingly, four of them had FH pathogenic/likely pathogenic germline mutations and one had FH somatic loss. This could be higher than that reported in previous studies of the pRCC germline. FH-deficient RCC is a new WHO 2022 category with more aggressive habits and poor prognosis. A large study cohort including 77 FH-deficient RCC patients observed in the real world has been reported in China (26), with a median progression time of only 21 months, among which 70 patients were confirmed with FH germline mutation and the other 7 patients confirmed with somatic mutation. Therefore, it is necessary to test for germline mutations in nccRCC patients. Furthermore, we found two DDR genes (ATM and BRIP1) germline mutations. Although the DDR germline mutation is not an inherited gene of RCC, some publications have reported DDR germline mutations in kidney cancer in approximately 5% of cases (27, 28); however, the clinical and biological aspects of DDR germline kidney cancer are unknown. There are also differences in genetic mutations between Chinese and Western populations due to ethnic differences. Researchers have found that the five genes with the most mutations in the Chinese population are TP53, KRAS, ARID1A, PBRM1, and SMAD4, while the five most mutated genes in western populations were IDH1, ARID1A, BAP1, TP53, and KRAS. VHL (59.7%), PBRM1 (18.0%), SETD2 (12.2%), BAP1 (10.2%), and TP53 (9.4%) were the most common somatic cell alteration sites in our study. Compared with the TCGA database, the mutation frequency of VHL (59.7% vs. 50.0%, $p< 0.001$) and TP53 (9.4% vs. 3.5%, $p <0.001$) in our cohort were higher, while the mutation frequency of PBRM1 was lower (18.0% vs. 31.0%, $p < 0.001$) in the Chinese cohort (14). Therefore, we believe that racial disparities influence the emergence and progression of RCC. Thus, clinicians would greatly benefit from our work in the prognosis and clinical treatment counseling for RCC in the Chinese population.

Our results described the genomic characteristics of Chinese RCC, revealing that nccRCC has a higher frequency of germline mutations. However, our study had some limitations. First, the study's limited sample size of Chinese participants raises the possibility that not all RCC genomic alterations are present. This is because, in general, we only performed genetic testing on patients who have reached stage 3 or above. Moreover, genetic testing is still inaccessible for most patients as a result of the price, and some patients cannot afford the entire process. To further enhance our study, we will continue to gather sequencing information from kidney cancer patients in the follow-up study. Second, the gene panel of 1123 and 79 genes could not avoid selection bias. Finally, the mean follow-up time was not long enough; we did not explore the relationship between gene mutations and recurrence.

In conclusion, the present study described commonly mutated genes associated with RCC in a small Chinese cohort and revealed

that nccRCC was more heterogeneous than ccRCC, which may help to predict the prognosis and make clinical decisions.

Data availability statement

The original contributions presented in the study are included in the article/Supplementary Material, further inquiries can be directed to the corresponding authors. We declare that the data and materials in this study will be provided free of charge to scientists for noncommercial purposes.

Ethics statement

The studies involving human participants were reviewed and approved by Ethics Committee of the First Affiliated Hospital of Anhui Medical University. The patients/participants provided their written informed consent to participate in this study.

Author contributions

ST, D-DX, ZY, and CL contributed to the concept and design of the study. TS, ZY, YG, and SY participated in the writing, review, and/or modification of the manuscript. CL, SX, and JX provided administrative, technical, or material support. All authors contributed to the article and approved the submitted version.

Funding

This study was supported by the Clinical Research Special Fund of Wu Jieping Medical Foundation(320.6750.2021-04-05), and the National Natural Science Foundation of China (82102788).

Conflict of interest

The authors declare that the research was conducted in the absence of any commercial or financial relationships that could be construed as a potential conflict of interest.

Publisher's note

Supplementary material

The Supplementary Material for this article can be found online at: https://www.frontiersin.org/articles/10.3389/fonc.2023.1095775/full#supplementary-material

SUPPLEMENTARY FIGURE 1
Genomic landscape of ccRCC patients with 1123 gene.

SUPPLEMENTARY FIGURE 2
Genomic landscape of nccRCC patients with 1123 gene.

SUPPLEMENTARY FIGURE 3
Genomic landscape of ccRCC patients with 79 gene.

SUPPLEMENTARY FIGURE 4
Genomic landscape of nccRCC patients with 79 gene.

SUPPLEMENTARY TABLE 1
Clinical characteristics of all the patients.

References

1. Sung H, Ferlay J, Siegel RL, Laversanne M, Soerjomataram I, Jemal A, et al. Global cancer statistics 2020: GLOBOCAN estimates of incidence and mortality worldwide for 36 cancers in 185 countries. *CA: Cancer J Clin* (2021) 71(3):209–49. doi: 10.3322/caac.21660

2. Zheng R, Zhang S, Zeng H, Wang S, Sun K, Chen R, et al. Cancer incidence and mortality in China, 2016. *J Natl Cancer Center* (2022) 2(1):1–9. doi: 10.1016/j.jncc.2022.02.002

3. Hsieh JJ, Purdue MP, Signoretti S, Swanton C, Albiges L, Schmidinger M, et al. Renal cell carcinoma. *Nat Rev Dis Primers* (2017) 3:17009. doi: 10.1038/nrdp.2017.9

4. Linehan WM, Ricketts CJ. The cancer genome atlas of renal cell carcinoma: findings and clinical implications. *Nat Rev Urol* (2019) 16(9):539–52. doi: 10.1038/s41585-019-0211-5

5. Ricketts CJ, De Cubas AA, Fan H, Smith CC, Lang M, Reznik E, et al. et al: The cancer genome atlas comprehensive molecular characterization of renal cell carcinoma. *Cell Rep* (2018) 23(1):313–26.e315. doi: 10.1016/j.celrep.2018.03.075

6. Comprehensive molecular characterization of clear cell renal cell carcinoma. *Nature* (2013) 499(7456):43–9. doi: 10.1038/nature12222

7. Cancer Genome Atlas Research N, Linehan WM, Spellman PT, Ricketts CJ, Creighton CJ, Fei SS, et al. et al: Comprehensive molecular characterization of papillary renal-cell carcinoma. *N Engl J Med* (2016) 374(2):135–45. doi: 10.1056/NEJMoa1505917

8. Trpkov K, Hes O, Agaimy A, Bonert M, Martinek P, Magi-Galluzzi C, et al. et al: Fumarate hydratase-deficient renal cell carcinoma is strongly correlated with fumarate hydratase mutation and hereditary leiomyomatosis and renal cell carcinoma syndrome. *Am J Surg Pathol* (2016) 40(7):865–75. doi: 10.1097/PAS.0000000000000617

9. Li H, Durbin R. Fast and accurate short read alignment with burrows-wheeler transform. *Bioinf (Oxf Engl)* (2009) 25(14):1754–60. doi: 10.1093/bioinformatics/btp324

10. Li H, Handsaker B, Wysoker A, Fennell T, Ruan J, Homer N, et al. The sequence Alignment/Map format and SAMtools. *Bioinf (Oxf Engl)* (2009) 25(16):2078–9. doi: 10.1093/bioinformatics/btp352

11. McKenna A, Hanna M, Banks E, Sivachenko A, Cibulskis K, Kernytsky A, et al. et al: The genome analysis toolkit: a MapReduce framework for analyzing next-generation DNA sequencing data. *Genome Res* (2010) 20(9):1297–303. doi: 10.1101/gr.107524.110

12. He X, Chen S, Li R, Han X, He Z, Yuan D, et al. Comprehensive fundamental somatic variant calling and quality management strategies for human cancer genomes. *Briefings Bioinf* (2021) 22(3):bbaa083. doi: 10.1093/bib/bbaa083

13. Chen X, Schulz-Trieglaff O, Shaw R, Barnes B, Schlesinger F, Källberg M, et al. Manta: rapid detection of structural variants and indels for germline and cancer sequencing applications. *Bioinf (Oxf Engl)* (2016) 32(8):1220–2. doi: 10.1093/bioinformatics/btv710

14. Huang J, Cai W, Cai B, Kong W, Zhai W, Zhang J, et al. et al: Comprehensive genomic landscape in Chinese clear cell renal cell carcinoma patients. *Front Oncol* (2021) 11:697219. doi: 10.3389/fonc.2021.697219

15. Kaelin WGJr. Molecular basis of the VHL hereditary cancer syndrome. *Nat Rev Cancer* (2002) 2(9):673–82. doi: 10.1038/nrc885

16. Miao D, Margolis CA, Gao W, Voss MH, Li W, Martini DJ, et al. et al: Genomic correlates of response to immune checkpoint therapies in clear cell renal cell carcinoma. *Sci (New York NY)* (2018) 359(6377):801–6. doi: 10.1126/science.aan5951

17. Braun DA, Hou Y, Bakouny Z, Ficial M, Sant' Angelo M, Forman J, et al. et al: Interplay of somatic alterations and immune infiltration modulates response to PD-1 blockade in advanced clear cell renal cell carcinoma. *Nat Med* (2020) 26(6):909–18. doi: 10.1038/s41591-020-0839-y

18. Jonasch E, Walker CL, Rathmell WK. Clear cell renal cell carcinoma ontogeny and mechanisms of lethality. *Nat Rev Nephrol* (2021) 17(4):245–61. doi: 10.1038/s41581-020-00359-2

19. Voss MH, Reising A, Cheng Y, Patel P, Marker M, Kuo F, et al. et al: Genomically annotated risk model for advanced renal-cell carcinoma: a retrospective cohort study. *Lancet Oncol* (2018) 19(12):1688–98. doi: 10.1016/S1470-2045(18)30648-X

20. Hsieh JJ, Chen D, Wang PI, Marker M, Redzematovic A, Chen YB, et al. et al: Genomic biomarkers of a randomized trial comparing first-line everolimus and sunitinib in patients with metastatic renal cell carcinoma. *Eur Urol* (2017) 71 (3):405–14. doi: 10.1016/j.eururo.2016.10.007

21. Varela I, Tarpey P, Raine K, Huang D, Ong CK, Stephens P, et al. Exome sequencing identifies frequent mutation of the SWI/SNF complex gene PBRM1 in renal carcinoma [J]. *Nature* (2011) 469(7331):539–42. doi: 10.1038/nature09639

22. Joseph RW, Kapur P, Serie DJ, Parasramka M, Ho TH, Cheville JC, et al. Clear cell renal cell carcinoma subtypes identified by BAP1 and PBRM1 expression [J]. *J Urol* (2016) 195(1):180–7. doi: 10.1016/j.juro.2015.07.113

23. Lee CH, Voss MH, Carlo MI, Chen YB, Zucker M, Knezevic A, et al. Phase II trial of cabozantinib plus nivolumab in patients with non-Clear-Cell renal cell carcinoma and genomic correlates. *J Clin Oncol* (2022) 40(21):2333–41. doi: 10.1200/JCO.21.01944

24. Sepe P, Ottini A, Pircher CC, Franza A, Claps M, Guadalupi V, et al. Characteristics and treatment challenges of non-clear cell renal cell carcinoma. *[J]. Cancers (Basel)* (2021) 13(15):3807. doi: 10.3390/cancers13153807

25. Wu J, Wang H, Ricketts CJ, Yang Y, Merino MJ, Zhang H, et al. et al: Germline mutations of renal cancer predisposition genes and clinical relevance in Chinese patients with sporadic, early-onset disease. *Cancer* (2019) 125(7):1060–9. doi: 10.1002/cncr.31908

26. Xu Y, Kong W, Cao M, Wang J, Wang Z, Zheng L, et al. Genomic profiling and response to immune checkpoint inhibition plus tyrosine kinase inhibition in FH-deficient renal cell carcinoma. *Eur Urol* (2022) 83(2):163–72. doi: 10.1016/j.eururo.2022.05.029

27. Truong H, Sheikh R, Kotecha R, Kemel Y, Reisz PA, Lenis AT, et al. Germline variants identified in patients with early-onset renal cell carcinoma referred for germline genetic testing. *Eur Urol Oncol* (2021) 4(6):993–1000. doi: 10.1016/j.euo.2021.09.005

28. Abou Alaiwi S, Nassar AH, Adib E, Groha SM, Akl EW, McGregor BA, et al. Trans-ethnic variation in germline variants of patients with renal cell carcinoma. *Cell Rep* (2021) 34(13):108926. doi: 10.1016/j.celrep.2021.108926

Frontiers in Oncology

Advances knowledge of carcinogenesis and tumor progression for better treatment and management

The third most-cited oncology journal, which highlights research in carcinogenesis and tumor progression, bridging the gap between basic research and applications to imrpove diagnosis, therapeutics and management strategies.

Discover the latest Research Topics

See more →

Frontiers

Avenue du Tribunal-Fédéral 34
1005 Lausanne, Switzerland
frontiersin.org

Contact us

+41 (0)21 510 17 00
frontiersin.org/about/contact